Springer Proceedings in Physics 393

Hexu Sun · Wei Pei · Yan Dong ·
Hongmei Yu · Shi You *Editors*

Proceedings of the 10th Hydrogen Technology Convention, Volume 1

WHTC 2023, 22–26 May, Foshan, China

Springer

Springer Proceedings in Physics **393**

Indexed by Scopus

The series Springer Proceedings in Physics, founded in 1984, is devoted to timely reports of state-of-the-art developments in physics and related sciences. Typically based on material presented at conferences, workshops and similar scientific meetings, volumes published in this series will constitute a comprehensive up to date source of reference on a field or subfield of relevance in contemporary physics. Proposals must include the following:

- Name, place and date of the scientific meeting
- A link to the committees (local organization, international advisors etc.)
- Scientific description of the meeting
- List of invited/plenary speakers
- An estimate of the planned proceedings book parameters (number of pages/articles, requested number of bulk copies, submission deadline).

Please contact:

For Americas and Europe: Dr. Zachary Evenson; zachary.evenson@springer.com
For Asia, Australia and New Zealand: Dr. Loyola DSilva; loyola.dsilva@springer.com

Hexu Sun · Wei Pei · Yan Dong · Hongmei Yu · Shi You
Editors

Proceedings of the 10th Hydrogen Technology Convention, Volume 1

WHTC 2023
22–26 May, Foshan, China

Springer

Editors
Hexu Sun
Hebei University of Science and Technology
Shijiazhuang, China

Yan Dong
Department of New Energy Science
and Engineering
Hebei University of Technology
Tianjin, China

Shi You
Department of Wind and Energy Systems
Technical University of Denmark
Kongens Lyngby, Denmark

Wei Pei
Power Grid Sciences and Technology Lab
Institute of Electrical Engineering
Beijing, China

Hongmei Yu
Department of Fuel Cells
Dalian Institute of Chemical Physics, Chinese
Academy of Sciences
Dalian, China

ISSN 0930-8989 ISSN 1867-4941 (electronic)
Springer Proceedings in Physics
ISBN 978-981-99-8630-9 ISBN 978-981-99-8631-6 (eBook)
https://doi.org/10.1007/978-981-99-8631-6

This Springer imprint is published by the registered company Springer Nature Singapore Pte Ltd.
The registered company address is: 152 Beach Road, #21-01/04 Gateway East, Singapore 189721, Singapore

Paper in this product is recyclable.

Preface

The 10th World Hydrogen Technology Convention (WHTC2023), organized by the International Association for Hydrogen Energy, China Association for Science and Technology and China Machinery Industry Federation was held in Foshan, Guangdong Province, China, during 23–26 May 2023.

These proceedings highlight the latest advances in fundamental research, technologies and applications of hydrogen energy and fuel cells. In recent years, energy conversion between electricity and hydrogen energy has attracted increasing attention as a way to adjust the load of the grid. These conference records discuss and exchange cutting-edge findings and technological developments in fields such as new proton exchange membrane electrolysers, new electrode materials and catalysts, renewable energy, off-grid/grid-connected water electrolysis for hydrogen production, key materials and components of fuel cells, high-temperature solid oxide water electrolysis, energy storage technologies and research, CO_2 hydrogenation to methanol, nitrogen to ammonia and other applications with industrial potential.

The main topics of the proceedings include but are not limited to:

(1) Policies and strategies for hydrogen energy and fuel cells;
(2) Advanced proton exchange membranes, electrodes and catalyst materials for water electrolysis;
(3) Advanced hydrogen compression, storage, transportation and distribution technologies;
(4) Safety and related standards; and
(5) Manufacture and R&D of key materials and components of fuel cells and stack systems.

Shijiazhuang, China — Hexu Sun
Beijing, China — Wei Pei
Tianjin, China — Yan Dong
Dalian, China — Hongmei Yu
Kongens Lyngby, Denmark — Shi You

Contents

Analysis and Treatment of Gas Pulsation in the Pipeline of a Hydrogen Diaphragm Compressor

Jun Xiao(✉) and Maofei Geng

National Key Laboratory of High-End Compressor and System Technology, Hefei General Machinery Research Institute Co., Ltd., Hefei 230031, China
xjcompressor@163.com

Abstract. Based on the plane wave theory and the transfer matrix method, the modeling, calculation and analysis of gas pulsation in a complex pipeline system of a hydrogen diaphragm compressor were carried out. The calculations show that the gas pulsations of the intake and exhaust pipelines of the cylinder gradually attenuate along the pipeline upstream and downstream, and the gas pulsation of the exhaust pipeline of the second stage cylinder is larger. The gas pulsations of the exhaust pipelines of the first and second stage cylinders are significantly higher than the limit values of API 618. From the perspective of pulsation control, an attempt was made to add orifice plates at appropriate positions of the pipeline to reduce the pulsation amplitude. The trial calculations show that the added orifice plate can effectively reduce the maximum gas pulsation of the pipeline, and can provide a useful reference for the treatment of gas pulsation.

Keywords: Gas pulsation · Hydrogen diaphragm compressor · Pipeline system · Plane wave theory

1 Introduction

Hydrogen energy, as an important technology path for sustainable energy development and strategic transformation, is becoming a hot spot in the field of global energy and transportation. With the rapid development of the hydrogen energy industry, the demand for terminal hydrogen will increase significantly. Hydrogen compressor is an important power source for compressing and transporting hydrogen, which is widely used in hydrogen storage and transportation, hydrogen station and gas hydrogen canning. As the core equipment of the pressurization system in the hydrogen storage and transportation process, the reliability of the diaphragm hydrogen compressor has received increasing attention. The diaphragm hydrogen compressor is a positive displacement compressor. The intermittent suction and discharge will cause strong gas pulsation in the pipeline. Gas pulsation not only affects the working performance of the compressor, but also induces severe vibration of the pipeline, which has a significant impact on the safe operation of the hydrogenation station. Therefore, studying the gas pulsation characteristics

H. Sun et al. (Eds.): WHTC 2023, SPPHY 393, pp. 1–14, 2024.
https://doi.org/10.1007/978-981-99-8631-6_1

of the hydrogen compressor pipeline and finding the methods to suppress the gas pulsation have important theoretical significance and application value for improving the long-term safety and reliability of the hydrogen compressor and the hydrogen storage and transportation system.

At present, the existing studies on pipeline gas pulsation, mainly adopt the electro-acoustic analogy method [1, 2], transfer matrix method [3] based on the plane wave theory [4], full three-dimensional CFD method [5] and one-dimensional CFD method [6–8]. Pipeline gas pulsation is essentially a fluid dynamics problem, which can be solved theoretically by CFD. However, there are many branches and pipeline elements in the actual pipeline system, and the internal structures of mixers, separators, heat exchangers, valves and other elements as well as the suction and exhaust passages of cylinders are very complex, which brings huge modeling difficulties and time costs to the three-dimensional flow field analysis. The frequency domain method based on the plane wave theory is suitable for the acoustic analysis of complex pipelines, which can directly obtain the accurate analytical solution of gas pulsation. It has low computational complexity and can accurately simulate the pressure pulsation of the pipeline gas flow. In this paper, the gas pulsation of a two-stage diaphragm hydrogen compressor is analyzed based on the plane wave theory, and the gas pulsation is effectively suppressed by adding orifice plates at appropriate positions of the pipeline.

2 Calculation Method of Gas Pulsation

2.1 Plane Wave Theory

The pipeline gas flow is an oscillating system. According to the combination of different pipeline elements (such as constant cross-section pipe, snubber, tee branch) and different boundaries (such as close end, open end, anechoic end, etc.), the gas pulsation presents different characteristics. In the early 1960s, Kinsler and Frey [4] proposed the plane wave theory. Based on the continuity equation and motion equation, the theory describes the transfer of mass and momentum in the pipeline fluid, and can accurately simulate the pressure pulsation of gas flow.

Under normal circumstances, the pulsation value of the gas pressure in the pipeline is a small value relative to the average value of the pressure (generally within 8% in terms of amplitude), which conforms to the assumption of the plane wave theory. Therefore, the gas pulsation in the pipeline of the reciprocating compressor can be analyzed using the plane wave theory. The wave equation with linear damping can be expressed as

$$\frac{\partial^2 p_t}{\partial x^2} - \frac{R}{a^2}\frac{\partial p_t}{\partial t} - \frac{1}{a^2}\frac{\partial^2 p_t}{\partial t^2} = 0 \tag{1}$$

where p is the pressure, and the subscript t denotes the pulsation value. a is the sound of speed, $R = 4fu/D$ is the damping coefficient along the pipeline, f is the friction coefficient between gas and pipe wall, D is the pipe diameter, and u is the average flow velocity of pipe gas. The solution of (1) is

$$p_t = [A * e^{(\alpha + j\omega/a)x} + B * e^{-(\alpha + j\omega/a)x}]e^{j\omega t} \tag{2}$$

where $\alpha = R/(2a)$.

The equation of motion with damping can be expressed as

$$\frac{\partial \xi_t}{\partial t} + R\xi_t + S\frac{\partial p_t}{\partial x} = 0 \tag{3}$$

where $\xi_t = \rho S u_t$ is the pulsation massflow, and S is the cross-sectional area of pipe. The solution of (3) is

$$\xi_t = -[A * e^{(\alpha + j\omega/a)x} - B * e^{-(\alpha + j\omega/a)x}]e^{j\omega t} S/a \tag{4}$$

A complex pipeline system is composed of basic elements such as constant cross-section pipes, vessels, confluence points, reducers, etc. During the calculation, the pipeline system is first divided into many elements, each element representing different pipeline elements. First the transfer matrix of each element is obtained, and then the relationship of the pulsating pressure and the pulsating velocity between the nodes of each element can be established according to the transfer matrix. Assuming that the pulsating pressure and pulsating velocity at the beginning and terminal end of the compressor pipeline system are $p_{t,1}$、$u_{t,1}$、$p_{t,n}$、$u_{t,n}$ respectively, then the following transfer relationship exists

$$\begin{bmatrix} p_{t,n} \\ u_{t,n} \end{bmatrix} = \boldsymbol{M}_{n,n-1}\boldsymbol{M}_{n-1,n-2}\cdots\boldsymbol{M}_{21}\begin{bmatrix} p_{t,1} \\ u_{t,1} \end{bmatrix} \tag{5}$$

where $\boldsymbol{M}_{n,n\text{-}1}$ is the transfer matrix between nodes. According to the boundary conditions at both ends of the pipeline system, the natural frequency of the gas column in the pipeline system can be obtained.

2.2 Limitation of Pipeline Pressure Pulsation

The fifth edition of API 618 defines the pressure pulsation p-p value of general pipes with average pressure below 350 bar as follows:

$$P_1 = \sqrt{\frac{a}{350}}\frac{400}{(P_L \times D_I \times f)^{0.5}} \tag{6}$$

where P_1 is the p-p value of pulsation pressure corresponding to fundamental frequency and harmonic frequency, expressed as a percentage of the average pipeline pressure P_L. D_I is the inner diameter of the pipe, f is the fundamental frequency and harmonic frequency, and a is the speed of sound. The pressure pulsation p-p value of the suction and exhaust pipes of the compressor cylinder is limited as follows:

$$P_1 = 0.03R \tag{7}$$

where P_1 is the same as the above, and R is the exhaust/suction pressure ratio of the cylinder.

3 Acoustic Analysis

The research object is a two-stage double cylinder water-cooled hydrogen diaphragm compressor. The secondary exhaust pressure is more than 20 MPa. The gas pulsation in the inlet and outlet pipeline may cause strong vibration of pipeline components. The compression process of the two-stage double cylinder water-cooled hydrogen diaphragm compressor is to compress the hydrogen stored in the hydrogen storage tank to a pressure of more than 20 MPa through two stages and send it into the high-pressure hydrogen bottle. The inlet pressure range is 1.6 ~ 2.0 MPa, the rotation speed is 420 rpm, the piston stroke is 180 mm, the exhaust pressure is 20 ~ 22 MPa, the exhaust temperature is $\leq$ 150 °C, and the capacity of the compressor is 1000 Nm^3/H. Figure 1 shows the CAD modeling of the compressor cylinder and intake and exhaust pipeline. In the drawing, the primary intake pipeline is marked with white, the primary exhaust to secondary intake pipeline is marked with blue, and the secondary exhaust pipeline is marked with purple and red.

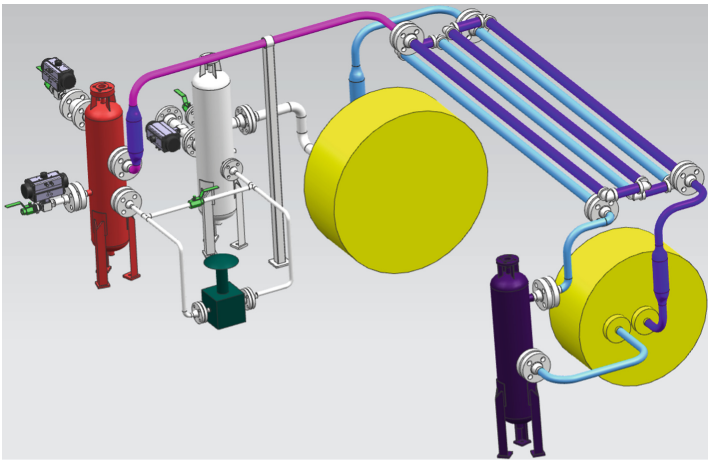

Fig. 1. Pipeline system model of a two-stage hydrogen diaphragm compressor

The compressed working medium is hydrogen. For the interstage pipeline, the first stage exhaust temperature is 6.2 MPa, and the second stage inlet pressure is 6 MPa.

Any changes to the drawings and process parameters can lead to changes in the calculation results. Considering that the primary intake snubber and the secondary exhaust snubber are connected to the upstream and downstream pipelines respectively, and the pulsation boundary conditions of upstream and downstream pipelines cannot be accurately given, and the volume of the snubber is much larger than the stroke volume, the primary intake snubber and its upstream pipeline, the secondary exhaust snubber and its downstream pipeline are not modeled in this study, and the open end boundary condition is given at the position of the pipeline connecting the snubber for pulsation calculation. The first stage cylinder is close to the intake snubber, and the pressure pulsation of this segment of pipeline is low. The calculation shows that the pressure pulsation of the intake

pipeline is far lower than the limit value in API 618, so the following discussion is only for the interstage pipeline and the second stage exhaust pipeline.

3.1 Pipeline from Primary Exhaust to Secondary Intake

The acoustic model of the pipeline from the 1st-stage exhaust to the 2nd-stage intake is shown in Fig. 2. The calculation results show that the pressure pulsation of the pipeline segment from the 1st-stage cylinder to the outlet of the 1st-stage cooler significantly exceeds the limit value of API 618. The pulsation amplitudes excited by the 6th and 14th harmonics are the largest. Within the ± 5% change range near the rated speed, the maximum pressure pulsation is excited by the 14th harmonic of 420 rpm. The maximum pressure pulsation location is the cylinder outlet node. The pressure pulsation of the pipeline after the outlet of the primary cooler is significantly reduced, and the pressure pulsation of the pipeline segments before and after the snubber downstream of the cooler is not weakened.

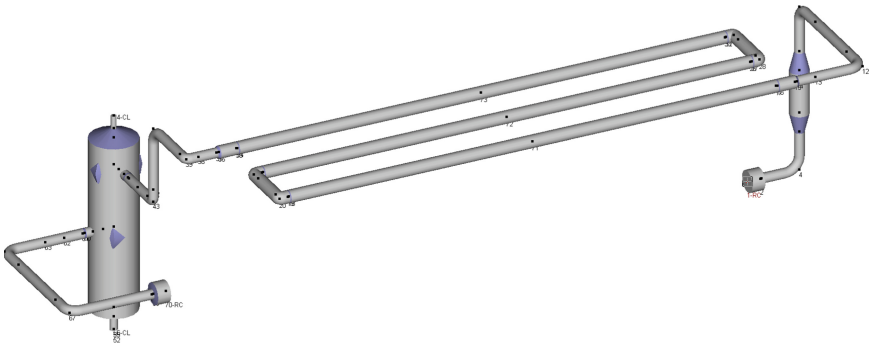

Fig. 2. Acoustic model of interstage pipeline

Figures 3, 4 and 5 respectively show the time-domain and frequency-domain data of pressure pulsation at the outlet node of the 1st-stage cylinder, the inlet node of the 1st-stage cooler and the outlet node of the 1st-stage cooler. The time-domain curve shows the pressure pulsation in several cycles under the rated speed, and the spectrum distribution shows the pulsation amplitude of each harmonic within the ± 5% speed change range and the curve representing the limit value of API 618. It can be seen from the figure that the sixth and fourteenth harmonic amplitudes of the pressure pulsation at the inlet node of the primary cooler have exceeded the limit value of API 618, and the sixth harmonic amplitudes at the outlet node of the cooler have been fully attenuated, but the fourteenth harmonic amplitudes are still significantly higher than the limit value.

3.2 Secondary exhaust pipeline

The acoustic model of the secondary exhaust pipeline is shown in Fig. 6. The calculation results show that the pressure pulsation of the secondary exhaust pipeline has greatly

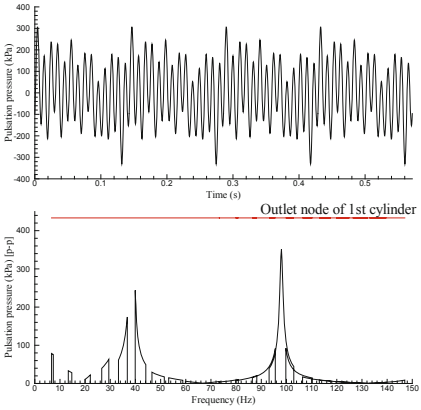

Fig. 3. Temporal and spectrum diagrams of pressure pulsation at the outlet node of 1st cylinder

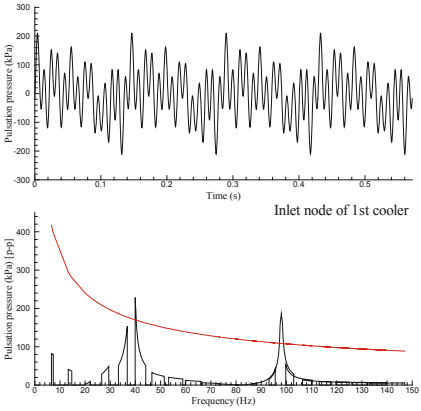

Fig. 4. Temporal and spectrum diagrams of pressure pulsation at the inlet node of 1st cooler

exceeded the limit value of API 618. The pulsation energy is basically contributed by the 4th and 14th harmonic components. Within the ± 5% change range near the rated speed, the maximum pressure pulsation is excited by the 4th harmonic of 421 rpm. The maximum pressure pulsation is located at the outlet node of the secondary cylinder. After the cylinder outlet, the pressure pulsation gradually decreases with the decrease of the distance from the exhaust snubber, and the pressure pulsation in the cooler pipeline segment decreases greatly.

Figures 7, 8 and 9 respectively show the time-domain and frequency-domain data of pressure pulsation at the outlet node of the secondary cylinder, the inlet node of the secondary cooler and the outlet node of the secondary cooler. It can be seen from the figure that the amplitudes of the 4th harmonic and the 14th harmonic of pressure pulsation at the inlet and outlet nodes of the cooler are much higher than the limit value of API 618, and the amplitudes of the 14th harmonic at each node are similar. However, the limit value of the cylinder outlet pipe calculated according to formula (7) is higher than

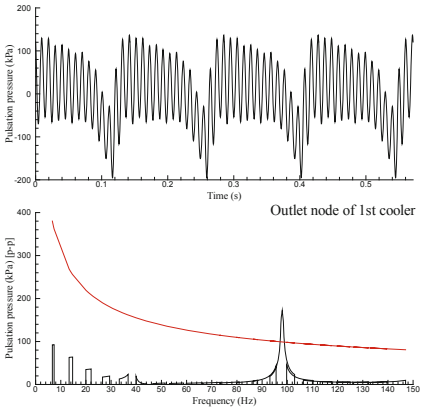

Fig. 5. Temporal and diagrams of pressure pulsation at the outlet node of 1st cooler

the limit value of the general pipe calculated according to formula (6), so the pulsation excited by the 14th harmonic here does not exceed the limit value.

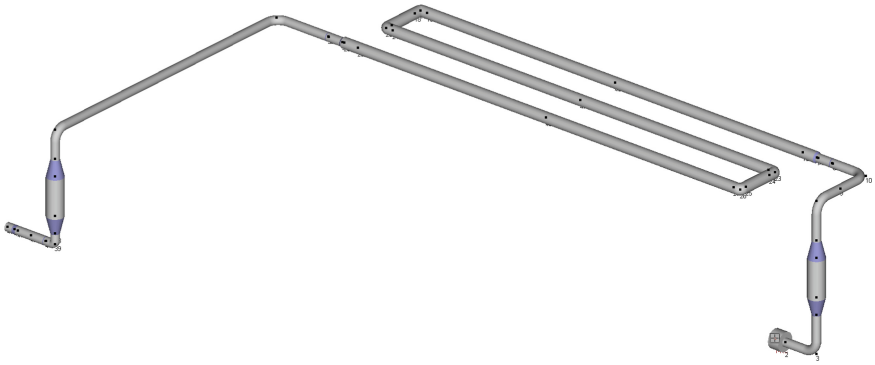

Fig. 6. Acoustic model of 2nd discharge pipeline

4 Study on pulsation suppression

In the relevant standards of petrochemical pipelines, it is clearly required that for the pulsation suppression of super-high pressure pipelines, the rectification scheme must be determined through acoustic analysis. On the basis of acoustic calculation of pipeline and from the perspective of pulsation control, this paper attempts to add orifice plates at the proper positions of pipeline to weaken the pulsation amplitude.

4.1 Pulsation suppression scheme of interstage pipeline

An orifice plate was added to the interstage pipeline from the primary exhaust to the secondary intake to control the gas pulsation. It was found that the orifice plate with

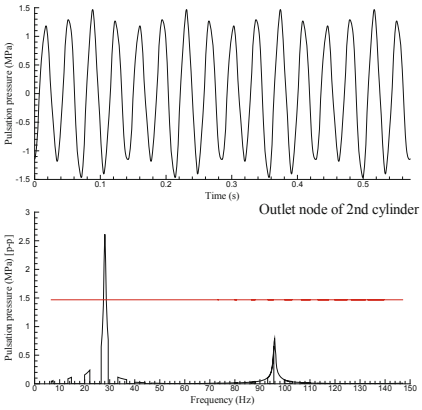

Fig. 7. Temporal and spectrum diagrams of pressure pulsation at the outlet node of 2nd cylinder

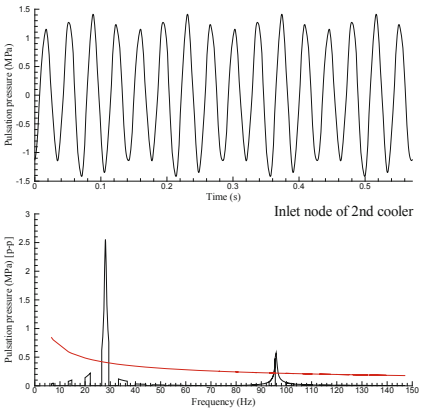

Fig. 8. Temporal and spectrum diagrams of pressure pulsation at the inlet node of 2nd cooler

a thickness of 35mm and a hole-diameter ratio of 0.25 was added after the primary cylinder outlet and before the reducer pipe in front of the cooler, which had a better effect on suppressing the high-order pressure pulsation. After the orifice plate is added at this position, the pulsation amplitudes excited by the 6th and 14th harmonics at the cooler and its front and rear pipeline segments are significantly reduced. The pipeline model near the location where the orifice plate is added is shown in Fig. 10, and the yellow component in the drawing is the added orifice plate. Figures 11, 12 and 13 are time-domain and frequency-domain diagrams of pressure pulsation at the outlet of the primary cylinder, the inlet and outlet nodes of the primary cooler after adding orifice plates. It can be seen from the figures that the low-frequency pulsation amplitude at the cylinder outlet node increases, but it does not exceed the limit value of API 618, and the highest amplitude pulsation component caused by the 14th harmonic has been seriously weakened.

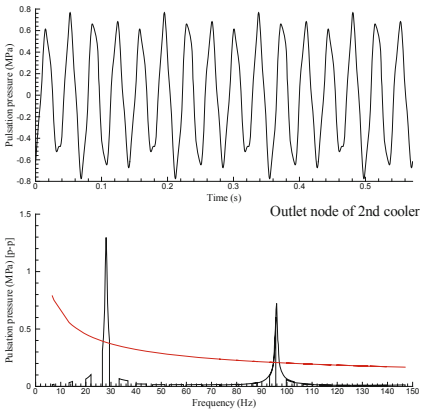

Fig. 9. Temporal and spectrum diagrams of pressure pulsation at the outlet node of 2nd cooler

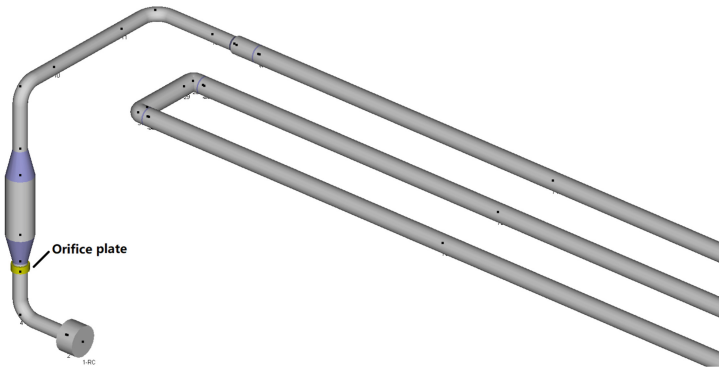

Fig. 10. Pipeline near the orifice plate (interstage pipeline)

4.2 Pulsation Suppression Scheme of 2nd-Stage Exhaust Pipeline

It is found that adding orifice plates with a thickness of 35mm and a hole-diameter ratio of 0.2 in front of the elbow after the outlet of the secondary cylinder and before the cooler has a better effect on suppressing gas pulsation. After the orifice plate is added at this position, the pulsation amplitudes excited by the 4th and 14th harmonics in the whole pipeline is greatly reduced. The pipeline model near the location of the added orifice plate is shown in Fig. 14. Figures 15, 16 and 17 are time-domain and frequency-domain diagrams of pressure pulsation at the outlet of the secondary cylinder, the inlet and outlet nodes of the secondary cooler. It can be seen from the figure that after the orifice plate is added, the low-frequency pressure pulsation of the 1st to 3rd harmonics at the cylinder outlet is slightly enlarged, but it is still far below the limit value of API 618. The large-scale pressure pulsation component of the 4th harmonic is greatly suppressed, and the high-frequency pressure pulsation including the 14th harmonic basically disappears.

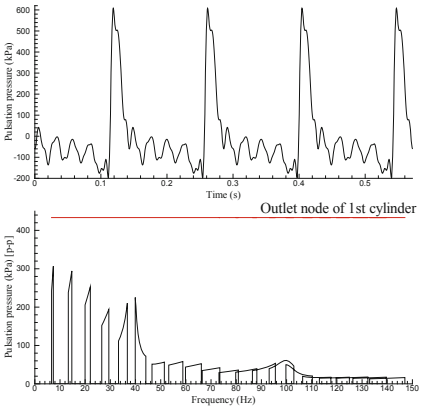

Fig. 11. Temporal and spectrum diagrams of pressure pulsation at the outlet of 1st cylinder after adding orifice plate

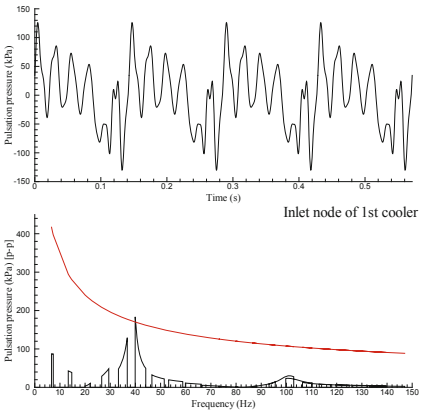

Fig. 12. Temporal and spectrum diagrams of pressure pulsation at the inlet of 1st cooler after adding orifice plate

5 Conclusions

Aiming at the analysis of gas pulsation in complex pipeline system of hydrogen compressor, on the basis of mastering the compressor parameters and pipeline data, the gas pulsation modeling and calculation analysis of two-stage pipeline of compressor are carried out based on the plane wave theory and transfer matrix method. The results show that the pressure pulsations of the primary intake and secondary exhaust pipelines gradually attenuate along the pipeline upstream and downstream. The pressure pulsation of the primary intake pipeline is relatively small, and the pulsation value is lower than the limit value of API 618. The pressure pulsation of the exhaust pipeline of the secondary cylinder is larger, and the pressure pulsations of exhaust pipelines of the primary and secondary cylinders are significantly higher than the limit values of API 618. On the basis of pulsation analysis, the attempt to add orifice plates to suppress gas pulsation is

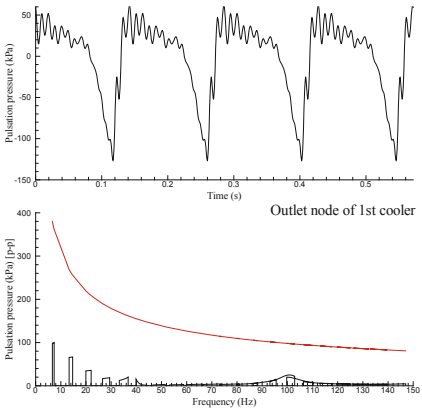

Fig. 13. Temporal and spectrum diagrams of pressure pulsation at the outlet of 1st cooler after adding orifice plate

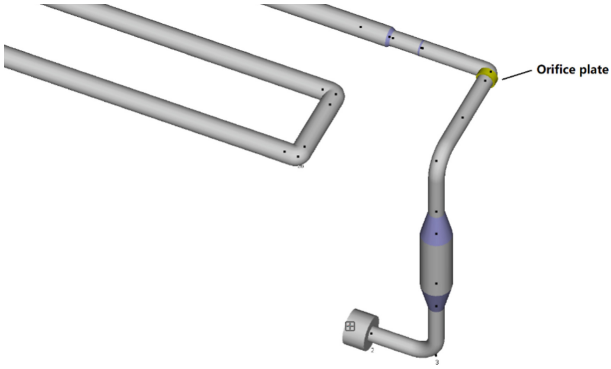

Fig. 14. Pipeline near the orifice plate (2nd discharge pipeline)

further carried out. The results show that the added orifice plates effectively reduce the maximum pressure pulsation of the pipeline, which can provide a useful reference for the follow-up pulsation treatment.

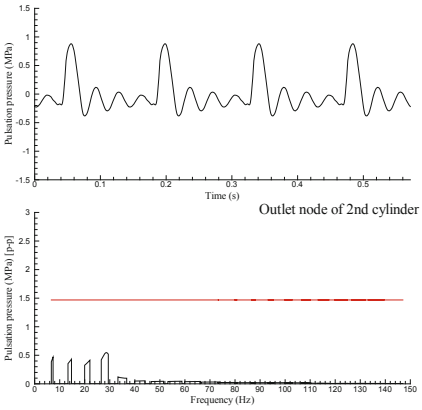

Fig. 15. Temporal and spectrum diagrams of pressure pulsation at the outlet of 2nd cylinder after adding orifice plate

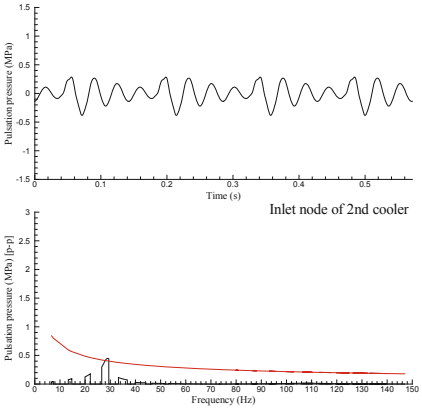

Fig. 16. Temporal and spectrum diagrams of pressure pulsation at the inlet of 2nd cooler after adding orifice plate

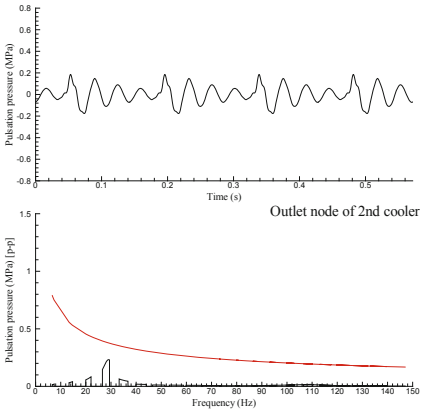

Fig. 17. Temporal and spectrum diagrams of pressure pulsation at the outlet of 2nd cooler after adding orifice plate

Acknowledgments. This work was supported by the Natural Science Foundation of Anhui Province (No. 2208085ME141), and the Natural Science Foundation of Hefei (No. 2021039), the Major science and technology project of China National Machinery Industry Corporation (SINOMAST-ZDZX-2018-01-04), and the Natural Science Foundation of Anhui Province (2208085QE159).

References

1. Xu, C., Hao, D., Yan, Y.: Calculation of the natural frequencies of the gas column of the piping system based on the electro-acoustic theory. Pipeline Tech. Equip. **2**, 10–12 (2007)
2. Chen, H., Hao, D., Sui, Z.: Electro-acoustic analogy of pressure piping air pulsation on reciprocating compressors. Compress. Technol. **6**, 7–9+32 (2008)
3. Dang, X., Chen, S.: Air Pulsation and Pipeline Vibration Of Piston Compressor. Xi'an Jiaotong University Press (1984)
4. Kinsler, L., Frey, A.R.: Fundamentals of Acoustics, 2nd edn. Wiley (1962)
5. Han, W., Han, S., Bai, C.: Numerical and experimental research on gas pulsation in reciprocating compressor piping system. J. Xi'an Jiaotong Univ. **47**(5), 61–66+71 (2013)
6. Chen, S., Huang, Y.: A research on the solution and application of one dimension unsteady gas flow system of equations. J. Xi'an Jiaotong Univ. **16**(1), 55–64 (1982)
7. Tweten, D., Nored, M., Brun, K.: The physics of pulsations. In: Gas Machinery Conference 2008. Albuquerque, NM (2008)
8. Zhao, D.: Research on Noise Control of the Automobile Intake System. Chongqing University (2018)

Airworthiness Design and Verification Analysis of Unconventional Thermodynamic Cycle Hydrogen Aero-Turbine Engines

Xinhao Tang[1(✉)], Suhua Shen[1], Yanjie Hu[2], and Chunxiao Wang[1]

[1] AECC Commercial Aircraft Engine Co., Ltd., Shanghai 200241, China
txh0926@sina.com

[2] COMAC Commercial Corporation of China Ltd., Shanghai 200135, China

Abstract. Hydrogen fuel is an extremely ideal aviation power with its characteristics of high power density and zero carbon emission. Hydrogen fuel is stored in a low-temperature liquid state in aircraft, and the liquid hydrogen needs to be warmed up to hydrogen gas by heat transfer before entering the combustion chamber to participate in combustion. Since liquid hydrogen has the traits of low temperature and high specific heat capacity, large amount of heat is required to complete the heat transfer process. And the engine thermal cycle process can be fully utilized for heat transfer of liquid hydrogen. This paper presents the design and verification of unconventional thermal cycle system based on an unconventional thermal cycle configuration for hydrogen aero-turbine engines under the existing airworthiness regulations. This paper can provide support for the airworthiness design and verification of hydrogen aero-turbine engines with unconventional thermal cycle configurations, and provide a reference for the introduction of the airworthiness validation special conditions policy applicable to hydrogen aero-turbine engines.

Keywords: Hydrogen · Unconventional thermodynamic cycle · Airworthiness

1 Introduction

The rapid growth of the air transport industry has made aviation emissions one of the main sources of pollution emissions in the transportation sector, and the impact of aircraft on climate and the environment has become more and more significant, among which carbon dioxide emissions have received the most attention from governments. The United Nations Framework Convention on Climate Change, adopted in June 1992, first proposed comprehensive control of carbon dioxide emissions [1]; the Kyoto Protocol, signed in 1997, began seeking to cut greenhouse gas emissions from aircraft and ships and proposed the idea of carbon trading [2]. The European Union adopted Directive 2008/101/EC in November 2008 to include the aviation industry in the Greenhouse Gas Emissions Trading System (ETS) [3]; ICAO added the "Environmental Technical Paper Annex 16, Volume 3" in March 2017, which specifies the calculation method and limitation standards for aircraft carbon emissions [4]; China's 2021 In the 14th Five-Year

H. Sun et al. (Eds.): WHTC 2023, SPPHY 393, pp. 15–24, 2024.
https://doi.org/10.1007/978-981-99-8631-6_2

Plan of China, the goal of "double carbon" is also clearly proposed, striving to achieve peak carbon emissions by 2030 and neutral carbon emissions by 2060 [5]; in the newly revised CCAR-34 "Turbine Engine Emissions and Exhaust Emissions" by Civil Aviation Administration of China (CAAC) in 2022 In 2022, "Aircraft Fuel Discharge and Exhaust Emissions Regulations" of the Civil Aviation Administration of China (CAAC) also clarified the calculation method and limitation requirements for aircraft carbon emissions [6].

Under the guidance of a series of civil aviation transportation low-carbon and energy-saving emission reduction requirements, in addition to the continuous optimization of traditional gas turbine engine design and aircraft operating procedures, new aviation power technologies such as hydrogen energy and electric motors have also seen vigorous development. Among them, hydrogen aero-turbine engine has the advantage of high power density because it directly uses part or all of liquid hydrogen as fuel, and can be adapted on the basis of the existing configuration of gas turbine engines, without making disruptive design changes to the current aircraft and aero-engine configuration, so hydrogen aero-turbine engine has a great potential to realize the civil aviation industry's "double carbon" goal in civil aviation.

Hydrogen fuel is stored in ultra-low temperature liquid form in aircraft and needs to be heated to gaseous state by unconventional thermodynamic cycle which is different from that of conventional gas turbine aero-engine before participating in combustion. In this paper, the design and verification of the unconventional thermodynamic cycle configuration of hydrogen aero-turbine engine is proposed based on the safety principle under the existing CCAR33 aero-engine airworthiness regulations.

2 Unconventional Thermodynamic Cycle Hydrogen Power Scheme

The ultra-low temperature (usually below − 260 °C) liquid hydrogen fuel in the aircraft storage tank cannot be directly mixed with petroleum hydrocarbon fuel through direct atomization but needs to be transformed into hydrogen gas through heat exchange and warming before entering the combustion chamber. Liquid hydrogen is one of the liquids with the highest specific heat capacity, which is about 5000 J/(kg K), and it consumes a lot of heat in the heat exchange process. In this context, the onboard electric heating supplemented by unconventional thermodynamic cycle engine modification design, so that the hydrogen as a fuel at the same time takes on the cooling function of the engine thermal cycle, can greatly reduce the extra energy consumption of liquid hydrogen heat exchange warming and improve the engine performance [7, 8], and thus improve the economy of the engine.

The purpose of using unconventional thermodynamic cycle hydrogen power scheme is to make full use of the engine thermal cycle to raise the temperature of liquid hydrogen and improve the performance of the engine. The current unconventional thermodynamic cycle schemes that can better heat the liquid hydrogen and significantly improve the engine performance are mainly two kinds of compress flow path pre-cooling (CPC) and turbine cooling gas pre-cooling (TPC).

The core structure of the compressor flow path pre-cooling scheme is the pre-cooler installed on the wall of the booster stage cassette. The lead pipe introduces part of the air

after the fan into the pre-cooler, which is cooled down by liquid hydrogen pre-cooling and then pressurized and discharged into the core. The principle of this scheme is to reduce the total inlet gas temperature in front of the core machine booster pole, increase the total temperature rise of the compressor and thus increase the pressurization ratio of the compressor, thus improve the efficiency of the compressor and reduce the fuel consumption rate. For the gas entering the compressor, the isentropic temperature ratio can be simplified as a relationship with the pressure ratio, see (1).

$$\frac{T_{2S}}{T_1} = \left(\frac{P_2}{P_1}\right)^{\frac{\kappa-1}{\kappa}} \tag{1}$$

T1 is the inlet temperature of the compressor (K), T2s is the end temperature of the isentropic compression process (K), T2 is the end temperature of the actual compression process (K), and k is the adiabatic index. Considering the specific heat and adiabatic index of the work mass as temperature-independent constants, the isentropic efficiency is therefore given in (2).

$$\eta_{ad} = \left(\left(\frac{P_2}{P_1}\right)^{\frac{\kappa-1}{\kappa}} - 1\right) / \left(\frac{T_2}{T_1} - 1\right) = \left(\pi_c^{\frac{\kappa-1}{\kappa}} - 1\right) / \left(\frac{T_2}{T_1} - 1\right) \tag{2}$$

where πc is the total pressure ratio of the compressor and k is taken as a constant value of 1.4.

The schematic diagram of the compressor flow path pre-cooling scheme is shown in Fig. 1.

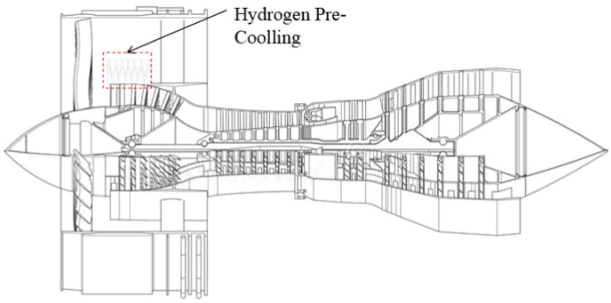

Fig. 1. Compressor flow path pre-cooling scheme

The core structure of the turbine cooling gas pre-cooling solution is an external pre-cooler installed between the high-pressure compressor and the turbine. The lead pipe introduces the turbine cooling gas from the high-pressure compressor into the external pre-cooler, where the cooling gas is further cooled by liquid hydrogen and then used for impact cooling and air film cooling of the turbine blades.

The turbine efficiency is used to measure the extent to which hysteresis isentropic work is converted to actual turbine output work, as shown in (3).

$$\eta_{T4} = N_T / N_{Ts} = N_T / W_4 \frac{k-1}{k} R T_4^* \left(1 - 1/\pi_T^{*\frac{k-1}{k}}\right) \tag{3}$$

where NT is the shaft work, NTs is the stagnant isentropic work, R is the gas constant; πT* is the expansion ratio; k is the specific heat ratio; W4 is the sum of the mainstream flow and the cold gas flow in front of the blades, and T4* is the total turbine inlet temperature.

Reducing the turbine cooling gas temperature through the heat exchanger can significantly improve the cooling effect of the turbine, allowing the turbine to withstand higher temperatures based on the existing design, increasing the turbine inlet temperature T4* and improving the turbine efficiency ηT4, while reducing the fuel consumption rate (Fig. 2).

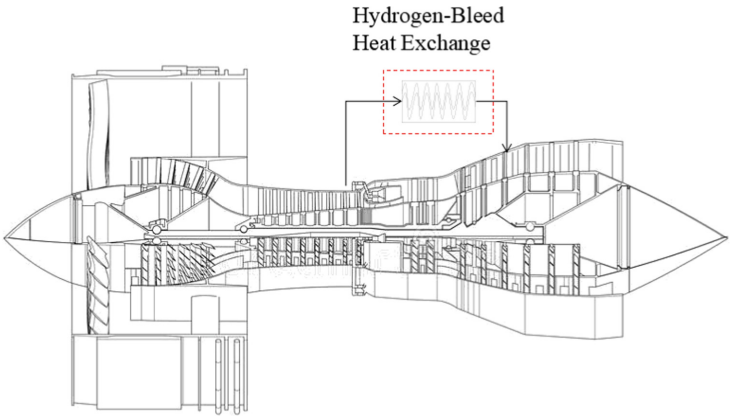

Fig. 2. Turbine flow path pre-cooling scheme

In the European cryogenic civil aircraft project CRYOPLANE, researchers have simulated the performance of a turbofan engine in two hydrogen-fueled unconventional thermodynamic cycle modes based on the performance parameters of a V2527-A5 engine [9]. The result indicates that engine using unconventional thermodynamic cycle has significant improvement on efficiency, as shown in Fig. 3.

The hydrogen turbine engine with unconventional thermodynamic cycle design has excellent performance, however, there are differences in configuration between the modified engine and the pre-modification engine, whether using the pressurized flow path pre-cooling or turbine cooling gas pre-cooling scheme, and the design changes need to be supplemented with the airworthiness design and verification of the unconventional thermodynamic cycle system.

3 Unconventional Thermodynamic Cycle Airworthiness Compliance Design and Verification

According to the two solutions of unconventional thermodynamic cycle hydrogen power, the main differences between the configuration and before modification are mainly in the compressor flow path pre-cooling device and turbine cooling gas pre-cooling device, and

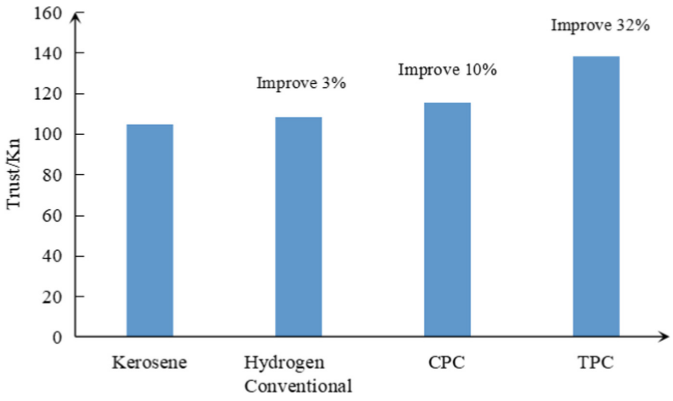

Fig. 3. Performance improvement with unconventional thermodynamic cycle

the airworthiness design should be carried out for the compressor flow path pre-cooling structure and turbine cooling gas pre-cooling structure under the principle of security analysis.

3.1 Design of Pre-cooling Device for Compressor Flow Path

The pre-cooling device of the compressor flow path does pre-cooling on the front end of the engine thermal cycle, and is also installed on the front end of the engine, which bring the influence of icing and foreign matter inhalation into consideration when doing the airworthiness compliance design.

According to the icing requirements of the airworthiness regulations for the intake system, the engine should not have icing conditions on engine components that affect engine operation or cause serious loss of power or thrust during its operation over its entire flight power range. A pressurized flow path pre-cooling device installed in front of the booster pole will make the risk of icing near the manifold ring significantly increased, especially in the high-altitude and low-temperature environment, traditional gas turbine engines often need to install hot gas anti-icing devices to prevent the manifold ring icing, the aero-engine icing phenomenon is shown in Fig. 4.

Therefore, it is necessary to carry out the airworthiness compliance design of the control system for the pre-cooling device of the compressor flow path accordingly, and open the pre-cooling device in front of the booster pole when the total temperature of the inlet air is high to reduce the total temperature in front of the fan booster pole to improve the boost ratio, and keep the pre-cooling device closed when the total temperature of the inlet air drops to a certain threshold. In addition, the total temperature sensor is set at the outlet of the pre-cooling device, and the low-temperature shutdown temperature control logic is also set to automatically shut down the pre-cooling device if the airflow is excessively cooled during the normal operation of the pre-cooling device and the total outlet temperature drops to a level that may cause icing.

In accordance with the requirements of the Airworthiness Regulations for inhalation of foreign objects, no unacceptable mechanical damage, loss of sustained power or thrust,

Fig. 4. Aero-engine icing

or engine stoppage shall be caused in the event that flying birds, ice, or large hail are inhaled, the aero-engine suction bird is shown in Fig. 5.

Fig. 5. Aero-engine bird strike

The pre-cooling device of the compressor flow path is installed on the wall of the booster box, and there is a certain probability that birds, ice, and large hailstones will hit the pre-cooling device when it is sucked into the engine, and there is a large amount of liquid hydrogen used for heat exchange in the pre-cooling device, which may cause liquid hydrogen leakage and fire if it is hit by foreign objects. Therefore, it is necessary to design the airworthiness of the pre-cooling device of the compressor flow path for structural strength and conduct strength assessments to ensure that its structure and

installation will not be damaged under the conditions of inhalation of foreign objects as required by airworthiness regulations.

3.2 Turbine Cooling Gas Pre-cooling Device Airworthiness Compliance Design

Turbine cooling gas pre-cooling device to do pre-cooling of the engine thermal cycle of the cooling gas, in doing airworthiness compliance design should mainly consider the impact of the cooling gas temperature range.

According to the airworthiness regulations for engine cooling, the engine must be designed and constructed to provide the necessary cooling under the intended operating conditions of the aircraft. Conventional configurations of aircraft turbine engines usually use a high-pressure compressor intermediate or final stage to induce gas to cool the turbine blades. The gas from the high-pressure compressor enters through the induced gas line from the hollow turbine blade roots and forms a gas film on the turbine blade surface to cool the turbine blades, which can isolate the flame and significantly reduce the temperature of the turbine blade body, the air film cooling structure is shown in Fig. 6.

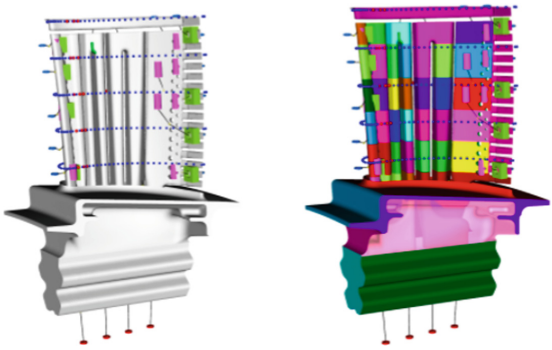

Fig. 6. Schematic diagram of hollow turbine blade air film cooling

The temperature of the air after multi-stage pressurization by the high-pressure compressor has a significant increase, and the total temperature of the high-pressure compressor outlet of large turbofan engines can usually reach more than 350 K. After using the turbo cooling air pre-cooling device to pre-cool the air leading from the high-pressure compressor, the temperature of the cooling air can be effectively reduced to enhance the cooling effect and further increase the temperature before the turbine. However, the turbine cooling air is not allowed to be overly pre-cooled. If the cold air is used directly for cooling the hot end components, it may produce too large a temperature gradient and lead to thermal stress problems in the turbine blades and other hot end components. Therefore, it is necessary to design the turbine cooling gas pre-cooling device to comply with the temperature range of the cooling gas. Determine the temperature range of the cooling gas that can be used for direct cooling according to the temperature field and thermal stress calculation results of the turbine blades and other hot end components.

Then, set the control logic of the turbine cooling gas pre-cooling device according to the determined temperature range of the cooling gas.

3.3 Unconventional Thermodynamic Cycle System Airworthiness Compliance Verification Ideas

The pre-cooling device in the unconventional thermodynamic cycle system designed according to the above principles, as an accessory of the engine, also needs to pass the corresponding environmental test according to the requirements of 33.91. The design and verification of the piping for transporting liquid hydrogen needs to meet the requirements of 33.17 Fire Resistance, 33.63 External Component Vibration, 33.64 Overpressure, etc. Therefore, the design and verification of the unconventional thermodynamic cycle system, represented by the pre-cooling of the compressor flow path and the pre-cooling of the turbine cooling gas, is shown in the Fig. 7.

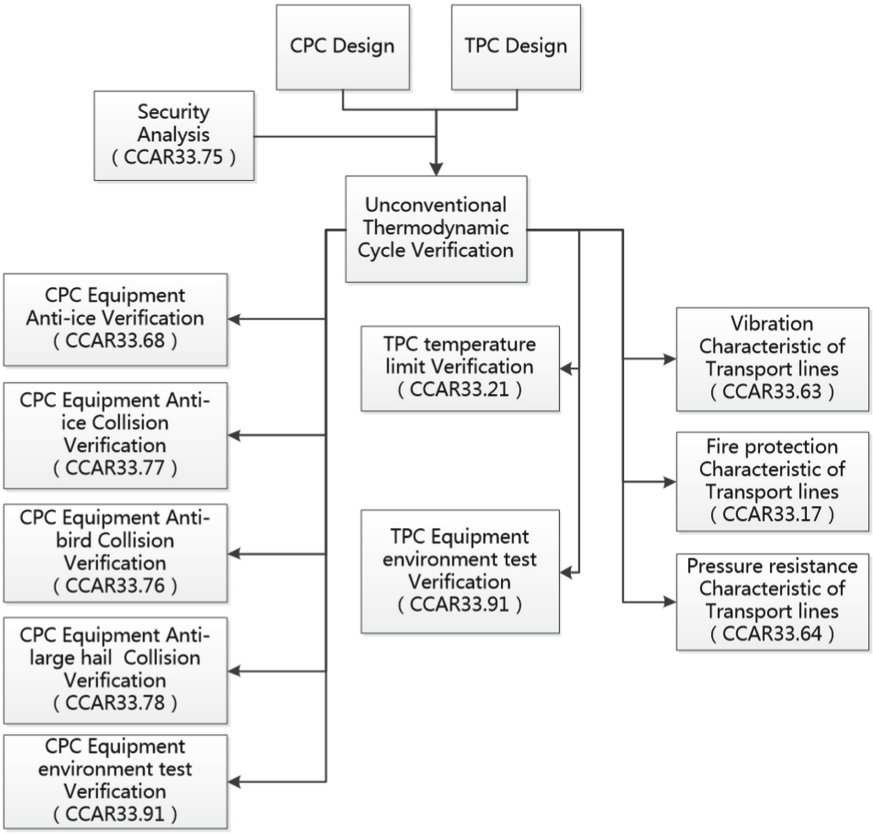

Fig. 7. Unconventional thermodynamic cycle system design and verification ideas

When carrying out airworthiness verification, under the current system of aero-engine airworthiness regulations, the verification of unconventional thermodynamic

cycle systems can fall under the existing CCAR33.68, CCAR33.77 and dozens of other provisions of the conformity work, and the specific conformity verification methods can be determined in consultation with the airworthiness authorities in conjunction with the industrial side's technology maturity assessment and verification strategy. For all evidence of conformity shown to the bureau, it is necessary to prove the validity of the evidence through test verification or validated methods.

3.4 Potential Special Conditions

During the airworthiness review process, the Bureau will establish special conditions for novel and unique design features that do not contain sufficient safety requirements in the regulations. According to CCAR-21 Civil Aviation Product and Component Qualification Validation [10], Section 21.16 of the regulations governs the special conditions as follows (Table 1).

Table 1. Civil aviation administration of China special conditions requirements

Elements			Safety level
Novel or unique design features	The intended use of the product is unconventional	Experience from the use of similar civil aviation products or civil aviation products with similar design features indicate that unsafe conditions may arise	Same as applicable regulation

The design of turbine engines using hydrogen as fuel, especially the unconventional thermodynamic cycle design in this paper, is highly novel, and the physical and chemical properties of hydrogen differ greatly from those of conventional fuel, which is highly flammable and explosive. In the previous paper, we have carried out airworthiness design and verification of unconventional thermodynamic cycle system, taking the verification of piping for liquid hydrogen transport as an example. If not, when the applicant adopts the design of unconventional thermodynamic cycle, the corresponding special conditions should be introduced by the airworthiness authority.

4 Conclusion and Outlook

This paper focuses on the unconventional thermodynamic cycle scheme adopted in conventional aero-turbine engines, and carries out the airworthiness design and verification of the unconventional thermodynamic cycle system, which can provide ideas for the airworthiness of conventional gas turbine engines converted to hydrogen-powered configurations. At the same time, due to storage, transport, ignition, and explosion characteristics, compressibility of hydrogen differ greatly from those of traditional fuel, and there is hydrogen corrosion effect on metal materials, further design and verification of

fire protection, component durability, and operating characteristics of the whole engine are needed in addition to the design and verification for compliance of unconventional thermodynamic cycle systems focused on in this paper, and based on the results of safety assessment, the airworthiness authorities and industry will identify the current novel or unique design features, and timely introduction of the corresponding special conditions.

References

1. UN. United Nations Framework Convention on Climate Change. UN, Rio de Janeiro (1992)
2. UN. Kyoto Protocol. UN, Tokyo (1997)
3. EU. DIRECTIVE 2008/101/EC. EU, Brussels (2008)
4. ICAO. Annex 16 to the Convention on International Aviation, Environmental Protection, vol. III, CO_2 Certification Requirement. ICAO, Montréal (2017)
5. Outline of the 14th Five-Year Plan and 2035 Visionary Goals for National Economic and Social Development of the People's Republic of China. Propaganda Department of the Central Committee of the Communist Party of China, Beijing (2021)
6. CAAC. Decision on Amending the Regulations on Fuel Discharge and Exhaust Emissions from Turbine Engine Aircraft (CCAR-34) (Draft for Comments) [EB/OL] (2022). http://www.caac.gov.cn/big5/www.caac.gov.cn/PHONE/HDJL/YJZJ/202202/P020220223522902445854.pdf. Accessed 21 Nov 2022
7. Boggia, J.S.: Unconventional cycles for aero gas turbine engines burning hydrogen. In: ISOABE Conference Proceedings (2001)
8. Boggia, S.: Four Unconventional Aero Gas Turbine Engines Burning Hydrogen—Cryoplane Project. Thesis, Cranfield University (2001)
9. Stefano, B., Anthony, J.: Some Unconventional Aero Gas Turbines Using Hydrogen Fuel. ASME Turbo Expo (2002)
10. Civil Aviation Administration of China. CCAR-21 Qualification Validation Regulations for Civil Aviation Products and Parts. Civil Aviation Administration of China, Beijing (2017)

Numerical Investigation of Combustion Characteristics of the Port Fuel Injection Hydrogen-Oxygen Internal Combustion Engine Under the Low-Temperature Intake Condition

Changwei Ji(✉), Jianpu Shen, and Shuofeng Wang

College of Energy and Power Engineering, Beijing Lab of New Energy Vehicles and Key Lab of Regional Air Pollution Control, Beijing University of Technology, Beijing 100124, People's Republic of China

Chwji@bjut.edu.cn

Abstract. The flammability limits of the hydrogen-oxygen mixture are extremely wide, and the ignition energy is low. Due to its excellent combustion properties, the hydrogen-oxygen mixture can be used as fuel in internal combustion engines (ICEs). However, the combustion of hydrogen-oxygen mixture is too intense, which results in limited research on its application in ICEs and is limited to low-temperature conditions in aerospace. This research aims to numerically discuss the coupling effects of equivalence ratio and ignition timing on the port fuel injection hydrogen-oxygen ICE under the low-temperature intake condition. The three-dimensional geometric model of a single-cylinder ICE was established using the CONVERGE software and validated against the mean in-cylinder pressure and reaction mechanism. The results indicate that adjusting equivalence ratio and ignition timing operating parameters is beneficial for controlling the temperature and pressure in the cylinder within a reasonable range during the total combustion process. In general, under the low-temperature intake condition, adopting a high equivalence ratio and optimal ignition timing strategy improve the combustion process and power performance of the port fuel injection hydrogen-oxygen ICE.

Keywords: Hydrogen-oxygen internal combustion engine · Port fuel injection · Combustion characteristics

1 Introduction

Liquid rocket engines are considered the preferred power device for launch vehicles and various spacecraft due to their advantages such as reliable operation and long working time [1]. Liquid hydrogen and liquid oxygen have significantly high specific impulse characteristics, and their combustion products are pollution-free, making them particularly suitable for the upper stage [2, 3]. The sub stage with an independent control system added based on the basic stage of the rocket is called the upper stage, which has the ability to fly independently and work in orbit for a long time. It is widely used

H. Sun et al. (Eds.): WHTC 2023, SPPHY 393, pp. 25–34, 2024.
https://doi.org/10.1007/978-981-99-8631-6_3

in tasks such as orbital gliding and deep space exploration [4–6]. With the continuous development of space technology, the duration of astronauts' deep space exploration missions has increased from 1 to nearly 2000 days [7]. It is difficult to control the evaporation of liquid hydrogen and liquid oxygen propellant and the evaporation gas cannot be used, which greatly restricts the development of the hydrogen-oxygen upper stage [8]. Liquid hydrogen and liquid oxygen propellant has a low boiling point and is easily vaporized into low-temperature gas hydrogen and gas oxygen when heated, resulting in an increase in pressure inside the storage tank. It is necessary to discharge gas hydrogen and gas oxygen to meet the safety pressure standards of the storage tank. In order to avoid fuel waste, gas hydrogen and gas oxygen are introduced into the ICE to burn and provide power.

As early as the 1960s, NASA (National Aeronautics and Space Administration) [9] proposed the concept of the hydrogen-oxygen ICE in the Apollo program. ULA (United Launch Alliance) [10] proposed an integrated vehicle liquid system in 2011, which introduces low-temperature hydrogen and oxygen into the ICE for combustion and work. ULA [11, 12] successively manufactured a single-cylinder ICE, a Wankel engine, and a 6-cylinder ICE using hydrogen-oxygen mixture as fuel, and conducted performance tests. Furuhama et al. [13] found that adopting a fuel strategy with a larger equivalence ratio of 3 to 6 can significantly suppress abnormal combustion in the hydrogen-oxygen ICE. Li et al. [14], based on the two-zone quasi-dimensional model, found that with the increase of the equivalence ratio, the indicated thermal efficiency (ITE) of the ICE increases to 40%. Fu et al. [15] conducted numerical simulation research on the combustion characteristics of the hydrogen ICE under oxygen-pure conditions.

The above research indicates that the application prospects of hydrogen-oxygen ICEs are extremely broad. However, previous research was mostly limited to the structural parameters and operational stability of hydrogen-oxygen ICEs, and there has been no in-depth study on the combustion characteristics of hydrogen-oxygen ICEs. In order to study the combustion characteristics of the hydrogen-oxygen ICE in detail, a three-dimensional geometric model was established and verified based on experimental data. The effects of different equivalence ratios and ignition timing on the combustion characteristics of the hydrogen-oxygen ICE were compared.

2 Model Establishment and Validation

2.1 Geometric Model and Boundary Conditions

This research is based on a commercial hydrogen internal combustion engine, whose geometric model is established by CONVERGE software. 2 mm mesh with adaptive mesh refinement (AMR) was used in this study to improve computational efficiency while ensuring accuracy. The geometric model and its mesh refinement are shown in Fig. 1. Table 1 lists the main technical parameters of the engine.

In order to improve the accuracy of the calculation, the boundary conditions of the engine model are set according to the experimental conditions. The ambient temperature of the model is set to 293 K. The engine speed is 1500 rpm, and the inlet pressure of the intake port and the outlet pressure of the exhaust port are both set to 100 kPa.

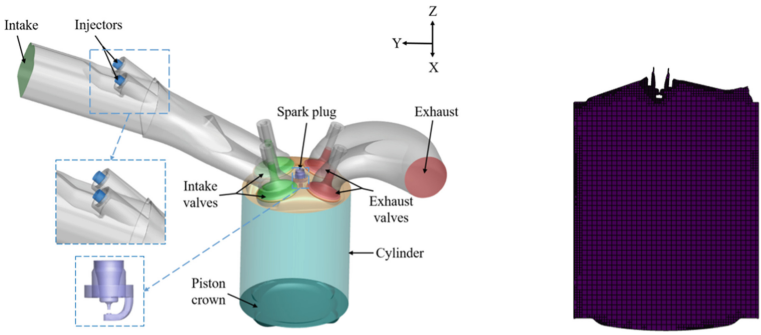

Fig. 1. The geometric model and mesh refinement.

Table 1. Main technical parameters of the engine.

Specification	Value
Engine type	4-stroke
Compression ratio	10.7
Bore/mm	74.5
Stroke/mm	85.9
Rod length/mm	140

2.2 Selection of Mathematical Models

Choosing a suitable turbulence model can accurately calculate the in-cylinder flow field of the engine. The turbulence situation in the cylinder of this model is predicted using the RNG k-ε model [16]. The SAGE model with detailed chemical reaction mechanisms developed by Li et al. is used in this study [17]. The wall heat transfer loss of the model is characterized and calculated by the wall-function model [18] to describe the influence of various parameters on wall heat transfer loss.

2.3 Experimental Setup and Model Validation

Experimental setup and uncertainty analysis. The entire test bench includes an engine system, a dynamometer system, a hydrogen supply system, and a data acquisition system. The schematic diagram of the test bench is indicated in Fig. 2. There is a PowerLink eddy current dynamometer in the dynamometer system used to control engine speed and load. The hydrogen supply system is composed of a hydrogen bottle group, pressure regulating valve, flame arrester and integrated hydrogen flowmeter (S4–33 A/MT, SevenStar, China). The Tociel 20 N060 thermal flow meter is used to measure the air mass flow rate. The data acquisition system consists of an electronic control unit (ecu), a horiba mexa-730λ lambda analyzer, and a kistler kibox combustion analyzer. The measurement uncertainty of the above experimental parameters is shown in Table 2.

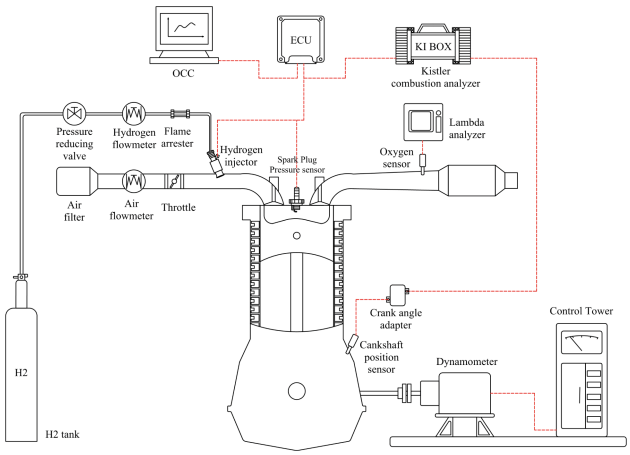

Fig. 2. The schematic diagram of the test bench of the engine.

Table 2. The information of main measurement devices.

Parameter	Manufacture	Type	Uncertainty
Engine speed	Power link	GW160	$\leq \pm 1$ rpm
Torque	Power link	GW160	$\leq \pm 0.28$ Nm
Air mass flow rate	Tociel	20 N060	$\leq \pm 0.1$ L/min
Hydrogen mass flow rate	Seven star	S4-33A/MT	± 0.1 L/min
Air-to-fuel ratio	Horiba	MEXA-730λ	$\leq \pm 0.1$
Cylinder pressure	Kistler	6177BCD17	$\leq \pm 0.3$ bar

Model validation. In order to demonstrate the accuracy of the engine model, the mean in-cylinder pressure of the model was simulated and compared with the experimental results. Due to limitations in experimental conditions, only hydrogen-air experiments were conducted on this engine. In this study, the engine speed was 1500 rpm and the equivalence ratio was 0.5. According to the results in Fig. 3, the curves of the simulation results and the experimental values are nearly overlapped. The mean cylinder pressure difference under different crankshaft angles is less than 0.2 bar. The above verification result indicates that the simulation results have achieved good consistency with the experimental values, and the predictive ability of the engine model has been verified.

In order to validate the accuracy of the hydrogen/oxygen reaction mechanism, the ChemkinPro software was used to calculate the laminar flame velocity. Based on the Grimech and Li schemes, the improved CANTERA was used by Kuznetsov et al. to calculate the laminar flame velocity of hydrogen-oxygen mixture under different initial pressures [19]. Figure 4 shows the calculation results of laminar flame velocity using ChemkinPro and compares them with Kuznetsov et al. The results indicate that this mechanism has

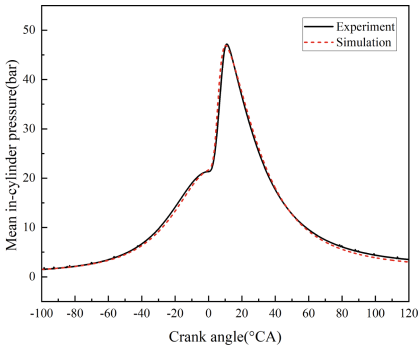

Fig. 3. Model validation for in-cylinder pressure.

excellent consistency with the laminar flame velocity results in the literature, and the error is within an acceptable range.

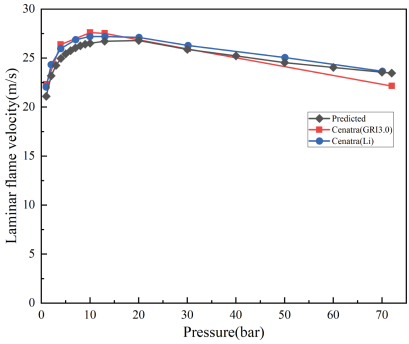

Fig. 4. The laminar flame velocity of hydrogen-oxygen mixture.

3 Result and Discussion

3.1 Combustion Analysis

In this study, the equivalence ratio was taken as 3.4, 3.6, 3.8, 4.0, 4.2, and 4.4, and the ignition timing was set to − 2°CA after top dead center (ATDC) and 0°CA ATDC, respectively. Figure 5 shows the variations of in-cylinder pressure with equivalence ratio at different ignition timing. As shown in Fig. 5, the variations of in-cylinder pressure with equivalence ratio at different ignition timing are consistent. During the compression stroke, the upward movement of the piston causes in-cylinder pressure to gradually increase, reaching a value of 2.2 MPa at TDC. After ignition, in-cylinder pressure rises to peak instantly. This is determined by the combustion characteristics of the hydrogen-oxygen mixture, which is well mixed in the cylinder and burns rapidly after ignition. After ignition, in-cylinder pressure decreases as the combustion of the mixture ends and the cylinder volume increases.

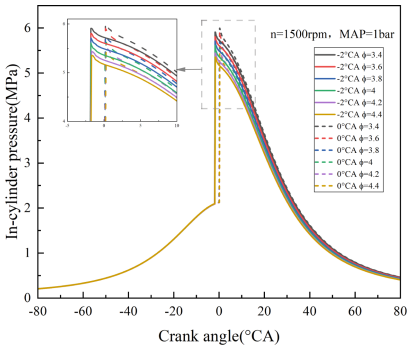

Fig. 5. Variations of in-cylinder pressure with equivalence ratio at different ignition timing.

It is necessary to investigate the peak in-cylinder pressure (Pmax) during the combustion process. Figure 6 shows the variations of Pmax with equivalence ratio at different ignition timing. From Fig. 6, it can be seen that when the equivalence ratio is 3.4 and the ignition timing is 0°CA ATDC, Pmax is 6.0 MPa. On the contrary, when the equivalence ratio is 4.4 and the ignition timing is − 2°CA ATDC, Pmax is 5.3 MPa. When the equivalence ratio is 4.0, Pmax at different ignition timing is similar. It can be observed that as the equivalence ratio continues to increase, Pmax decreases. This is because the increasing equivalence ratio leads to a continuous decrease in the mass of oxygen entering the cylinder, which determines a decrease in the mass of burned hydrogen and leads to a decrease in Pmax. Moreover, the combustion rate of the hydrogen-oxygen mixture is inhibited by excess hydrogen, which reduces Pmax. At the same time, The Pmax is decreased with the delay of ignition timing. This indicates that by increasing the equivalence ratio and adjusting the ignition timing, Pmax is reduced to ensure that it does not exceed the maximum pressure that a typical engine withstand.

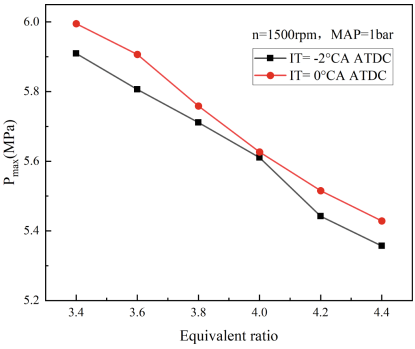

Fig. 6. Variations of Pmax with equivalence ratio at different ignition timing.

Due to the way of low-temperature intake, the analysis of the cylinder temperature is particularly crucial. Figure 7 shows the variations of cylinder temperature with equivalence ratio at different ignition timing. When the ignition timing is advanced to

− 2°CA ATDC, the equivalence ratio increases from 3.4 to 4.4, and the peak temperature decreases from 2700 to 2550 K. It can also be seen that the trend of in-cylinder temperature change is consistent with that of in-cylinder pressure change. The in-cylinder temperature instantly rises to its peak after ignition and gradually decreases after combustion.

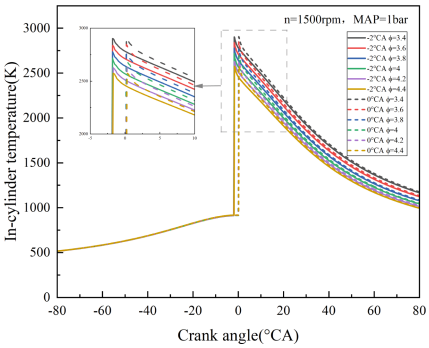

Fig. 7. Variations of in-cylinder temperature with equivalence ratio at different ignition timing.

Figure 8 shows the temperature distribution in the cylinder at the time of intake bottom dead center under different equivalence ratios. From the figure, it can be seen that 150 K gas with different equivalence ratios enters the cylinder, which is cooled by low-temperature gas. After the end of the intake, the temperature distribution in the cylinder tends to be consistent, except that the temperature near the spark plug is higher. This indicates that low-temperature hydrogen has an inhibitory effect on the formation of hot areas in the cylinder.

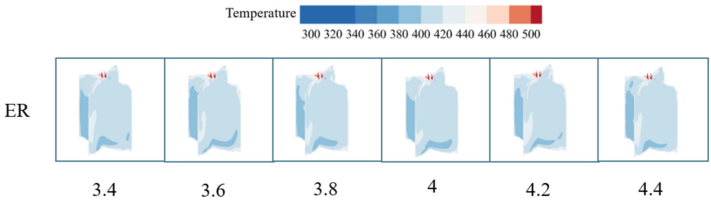

Fig. 8. The temperature distribution in the cylinder under different equivalence ratios.

3.2 Engine Performance

Indicated mean effective pressure (IMEP) is used to evaluate the operational performance of engines. Figure 9 shows the variations of IMEP with equivalence ratio at different ignition timing. From the figure, it can be seen that under the condition of engine speed of 1500 rpm and intake pressure of 1 bar, IMEP gradually decreases as the equivalence ratio gradually increases. When the ignition timing is postponed to 0°CA ATDC, the

equivalence ratio increases from 3.4 to 4.4, and the IMEP decreases from 0.40 to 0.31 MPa.

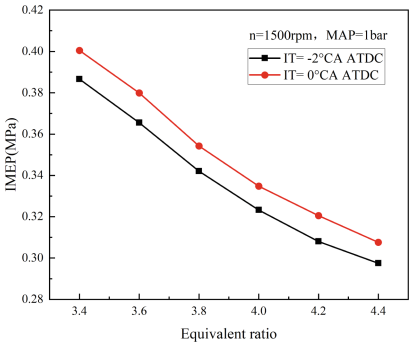

Fig. 9. Variations of IMEP with equivalence ratio at different ignition timing.

When the equivalence ratio is specific, delaying the ignition timing will increase the IMEP. When the equivalence ratio is 4, the IMEP at ignition timing of − 2°CA ATDC and 0°CA ATDC are 0.32 MPa and 0.34 MPa, respectively. This is because when the ignition timing is delayed to 0°CA ATDC, the hydrogen-oxygen mixture burns and releases heat instantly at TDC, completing the constant volume combustion process. On the contrary, when the ignition timing is − 2°CA ATDC, the combustion process is completed before reaching the compression TDC, resulting in the negative work during the compression stroke.

ITE is a parameter that measures the effectiveness of converting thermal energy into indicated work and is used to evaluate the economic performance of engines. Figure 10 shows the variations of ITE with equivalence ratio at different ignition timing. From the figure, it can be seen that the ITE at ignition timing of − 2°CA ATDC and 0°CA ATDC are around 21% and 22%, respectively. When the ignition timing is 0°CA ATDC, the maximum ITE is 22.5% at the equivalence ratio of 3.4, and the minimum ITE is 21.7% at the equivalence ratio of 4.0. It can be observed that at different ignition timing, ITE first decreases and then slightly increases with the increasing equivalence ratio. This is because as the equivalence ratio increases, the mass of oxygen entering the cylinder to participate in the reaction decreases, resulting in a decrease in the mass of hydrogen burned. However, the mass of hydrogen entering the cylinder increases, and the heat release of fuel per unit time decreases, resulting in a decrease in ITE. Furthermore, for a specific equivalence ratio, delaying ignition timing increases the ITE. As the ignition timing is further delayed to TDC, the ITE is improved due to the extremely fast combustion speed of the hydrogen-oxygen mixture which instantly burns at the TDC.

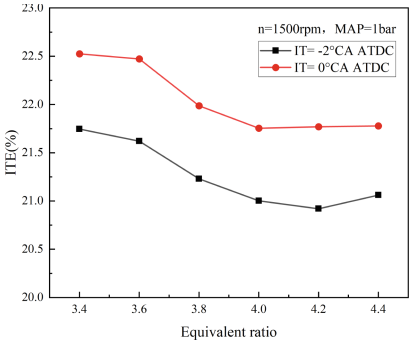

Fig. 10. Variations of ITE with equivalence ratio at different ignition timing.

4 Conclusion

In this study, the CONVERGE software is used to numerically study the combustion characteristics of the port fuel injection hydrogen-oxygen ICE at different ignition timing as a function of equivalence ratio. The main conclusions are as follows:

(1) The strategy of using a large equivalence ratio can effectively reduce the peak temperature and pressure in the cylinder, and as the equivalence ratio gradually increases, the peak temperature and pressure in the cylinder further decrease.
(2) Preliminary results indicate that low-temperature intake is beneficial for the uniform distribution of temperature inside the cylinder and reduces the formation of hot areas inside the cylinder.
(3) When the equivalence ratio is specified and the ignition timing is delayed, the IMEP is increased. On the contrary, when the ignition timing is specified, the IMEP decreases with the increase of the equivalence ratio.
(4) The variations of the ITE with equivalence ratio are irregular. When the equivalence ratio is specified, the ITE increases with the delay of ignition timing.

References

1. Naderi, M.: Modeling the effect of reusability on the performance of an existing LPRE. Acta Astronaut. **181**, 201–206 (2021)
2. Dai, J.: Numerical and experimental investigations of geometrical parameters on GH2/GO2 injector. Aerosp. Sci. Technol. **106**, 106187 (2020)
3. Satoh, D.: Estimating model parameters of liquid rocket engine simulator using data assimilation. Acta Astronaut. **177**, 373 (2020)
4. Wilson, J.: Deep space environments for human exploration. Adv. Space Res. **34**, 1281 (2004)
5. Nikischenko, I.: Improving the performance of LOX/kerosene upper stage rocket engines. Propul Power Res **6**, 157 (2017)
6. Pontani, M.: Simple method for performance evaluation of multistage rockets. Acta Astronaut. **94**, 434 (2014)
7. Zhou, C.: Analysis of dynamic characteristics and sensitivity of hydrogen-oxygen expansion cycle rocket engine system. Acta Astronaut. **189**, 624 (2021)

8. GuoBiao, C.: Combustion behaviors of GO2/GH2 swirl-coaxial injector using non-intrusive optical diagnostics. Acta Astronaut. **123**, 246 (2016)
9. Morgan, N.E.: Development of a hydrogen-oxygen internal combustion engine space power system. In: NASA Contractor Report. National Aeronautics and Space Administration, Washington (1965)
10. Holguin, M.: Enabling long duration spaceflight via an integrated vehicle fluid system. In: AIAA SPACE 2016 Conference and Exposition. California, USA (2016)
11. Zegler, F.: An integrated vehicle propulsion and power system for long duration cryogenic spaceflight. In: AIAA SPACE 2011 Conference and Exposition. California, USA (2011)
12. Zegler, F.: Development status of an integrated vehicle propulsion and power system for long-duration cryogenic spaceflight. In: AIAA SPACE 2012 Conference and Exposition. California, USA, 2012
13. Furuhama, S.: Combustion improvement in a hydrogen fueled engine. Int. J. Hydrogen Energy **2**(3), 329–340 (1977)
14. Li, H.: The performance of a hydrogen-oxygen S.I. engine. In: Powertrain and Fluid Systems Conference and Exhibition. California, USA (2002)
15. Fu, H.: Combustion characteristics and energy distribution of hydrogen engine under high oxygen concentration. Int. J. Hydrogen Energy **47**, 38031 (2022)
16. Li, Y.: Effects study of injection strategies on hydrogen-air formation and performance of hydrogen direct injection internal combustion engine. Int. J. Hydrogen Energy **44**, 26000 (2019)
17. Li, J.: An updated comprehensive kinetic model of hydrogen combustion. Int. J. Chem. Kinet. **36**(10), 566–575 (2004)
18. Han, M.: Effects of wall function model in lattice Boltzmann method-based large-eddy simulation on built environment flows. Build. Environ. **195**, 107764 (2021)
19. Kuznetsov, M.: Laminar burning velocities of hydrogen-oxygen-steam mixtures at elevated temperatures and pressures. Proc. Combust. Inst. **33**, 895 (2011)

Mechanical Behavior and Failure Analysis of Diaphragm in Diaphragm Compressor for Hydrogen Refueling Station

Xiao-Ming Liu[1(✉)], Zhilong Liu[1], Yang Yu[1], and Shunzeng Wang[2]

[1] State Key Laboratory of High-End Compressor and System Technology, Hefei General Machinery Research Institute, Hefei 230031, Anhui, People's Republic of China
liuxiaoming_4109@163.com

[2] School of Intelligent Manufacturing, Nanyang Institute of Technology, Nanyang 473006, Henan, People's Republic of China

Abstract. Diaphragm compressor is widely used to pressurize hydrogen and is one of the key equipment in hydrogen refueling station. And the Diaphragm is one of the wearing parts of diaphragm compressor. The failure of the diaphragm makes the maintenance cost of diaphragm compressor high. Because of the large deflection of the diaphragm in the diaphragm compressor, its mechanical behavior has strong nonlinear characteristics, especially after considering the constraints on the diaphragm by the cavity of the cylinder head, it is difficult to accurately calculate with the analytical method. Therefore, considering the constraint condition of the cylinder, the finite element model of the diaphragm working in the diaphragm compressor is established. By the calculations of the diaphragm deformation and stress, the fractures of the hydrogen side of the diaphragm in the fault cases are analyzed. The results of static structure analysis and dynamic analysis are compared with diaphragm fault cases respectively, which shows the necessity of dynamic analysis in the failure analysis of diaphragm. Besides, the mechanical behavior of the diaphragm's deformation indicates that the inertial effect of the diaphragm and collision between the diaphragm and the cavity cannot be ignored.

Keywords: Diaphragm compressor · Finite element analysis · Diaphragm failure

1 Introduction

Hydrogen refueling station is a hub connecting the production, transportation and application of hydrogen, where the pressurization of hydrogen is a necessary step to improve the energy density and practicality of hydrogen as an energy source. In this process, hydrogen needs to be pressurized to an extremely high pressure of 45 MPa or 90MPa, while its high purity must be guaranteed [1]. Diaphragm compressor is widely used as the hydrogen compressor in hydrogen refueling stations due to its high compression ratio and superior sealing performance [2]. However, as the core component of diaphragm compressor, the diaphragm is also one of the vulnerable parts [3]. Due to the fact that the cost of compression devices can account for about half of installed capital cost of

H. Sun et al. (Eds.): WHTC 2023, SPPHY 393, pp. 35–43, 2024.
https://doi.org/10.1007/978-981-99-8631-6_4

a hydrogen refueling station [4], and the failure of diaphragm will further increases the operating cost of the station, reasonable analysis of diaphragm failure is of great significance for reducing the cost of the hydrogen refueling station.

The diaphragm of the diaphragm compressor is generally composed of three plates, which are the process plate contacting with hydrogen, the hydraulic plate contacting with hydraulic oil, and the middle plate avoiding possible leaks while the diaphragm's failure happens. Usually, the failure of the diaphragm occurs on the process plate, i.e., the hydrogen side plate, or hydraulic plate [5], while the former is more frequent. Furthermore, the fracture of the process plate can be found at the edge, the center and the middle area [5].

Most literature used static structure analysis of the diaphragm when it clings to the cavity of the cylinder head or the perforated plate and concluded that the stress at the edge or center of the process plate or the middle area of the hydraulic plate exceeds the allowable stress, which gave the reasons for the cracks at these locations [5–8]. However, little literature discussed the cracks appearing in the middle area of the process plate. The static structure analysis and dynamic analysis based finite element method (FEM) simulation are applied to the diaphragm respectively, and the results are compared and discussed in this paper. It is found that the result of dynamic analysis is more consistent with the failure mode of the diaphragm, which explain the reason for the failure in the middle area of the process plate.

2 Fault Cases

In some diaphragm failure events of the diaphragm compressors for hydrogen refueling station, cracks are found in the middle area of the process plates. Figure 1(a, b) display two fault cases of the diaphragm with the cracks of the process plates appearing in the middle area near the exhaust holes. The cases belonged to the diaphragm compressors with the same design parameters which are listed in Table 1.

Table 1. Parameters of diaphragm compressors with diaphragm failure.

Parameters	Values
Radius of the diaphragm/mm	187.5
Thickness of the diaphragm/mm	0.5
Radius of the cavity/mm	165
Young modulus E/GPa	210
Poisson's ratio μ	0.3
Allowable stress σ/MPa	450
Discharge pressure $p(A)$/MPa	45
Maximal pressure difference between oil and gas/MPa	10
Rotational speed/rpm	382

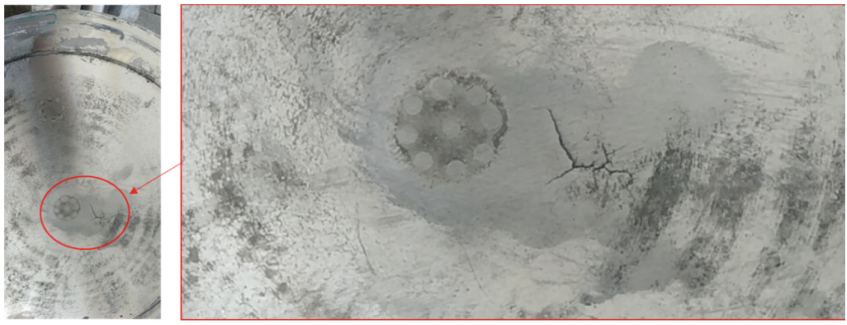

(a) Case 1

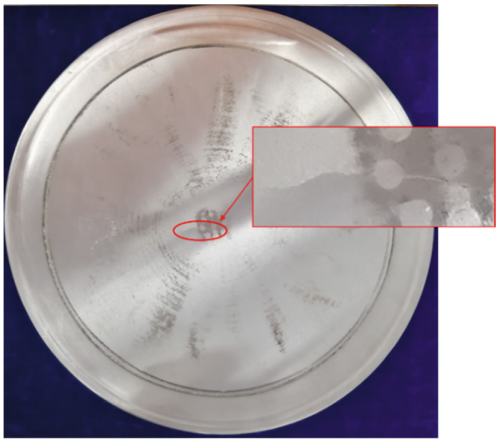

(b) Case 2

Fig. 1. Fault cases of the diaphragm

3 Failure Analysis of the Diaphragm

In the diaphragm compressor, the diaphragm is clamped by the cylinder head and cylinder block at the edge, and the middle part undergoes reciprocating deformation. Since the diaphragm is constrained by the cavity of the cylinder head and the perforated plate, which means it is not free to deform, the deformation cannot be calculated with theoretical method of thin-plate large deflection theory neither small deflection theory, particularly for the state when the diaphragm has not yet fully fitted the cavity. Thus, the FEM simulations are used to analyze the failure of the diaphragm. In which, the process plate is subjected to the uniform pressure of hydrogen with the maximum of 45 MPa and the minimum of 15 MPa, while the hydraulic plate to the uniform pressure of hydraulic oil with the maximum of 55 MPa and the minimum of 5 MPa. Furthermore, the hydrogen pressure and the oil pressure are assumed to change according to the sinusoidal manners represented by Eqs. (1) and (2) respectively.

$$p_g = 30 + 15\sin(\omega t) \tag{1}$$

$$p_o = 30 + 25\sin(\omega t) \tag{2}$$

In addition, the cavity surface of the cylinder head is generated by the traditional generatrix Eq. (3) which is a single exponential polynomial with the exponential term z taking 3.

$$w = \frac{4.2}{z-1}\left[2\left(\frac{r}{165}\right)^{z+1} - (z+1)^2 + (z-1)\right] \tag{3}$$

where r and w are the radius and the height of any point on the cavity. Considering the additional stress may be caused by the discharge holes and suction holes, the fine structure is added on the cylinder head model. To carry out the simulations, each plate of the diaphragm is divided into two layers with uniform thickness and 21,024 elements with 31,755 nodes in total. Particularly, the elements at the center area are refined to the size of 0.1 mm to capture the impact of discharge holes, and those in the edge where is clamped are refined to the size of 0.3 mm to capture the effect of clamping conditions on the deformation of the diaphragm. The modeling of the diaphragm and the mesh division are illustrated in Fig. 2(a) and (b) respectively. Besides, it is supposed that the deformation three plates always remain consistent and adhere tightly to each other, while the friction coefficient at the contact between the process plate and the cylinder head, as well as at the contact between the hydraulic plate and the cylinder block, is 0.15.

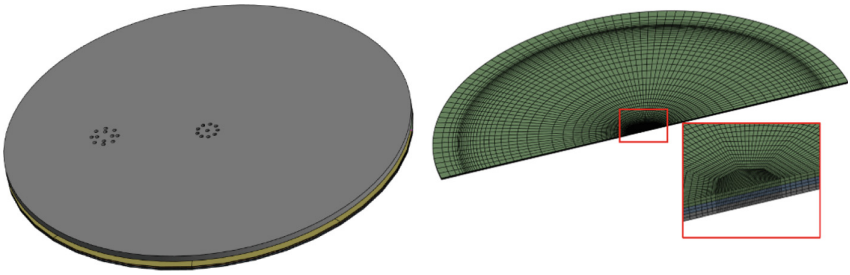

Fig. 2. Modeling of the diaphragm and its mesh division.

3.1 Static Structure Analysis

In the traditional analysis of the diaphragm of diaphragm compressor, inertia effect and collision of the diaphragm and the cavity is ignored, the loads and the structure's response are assumed to vary slowly with respect to time. And any state during the diaphragm's deformation process is believed to be at static equilibrium. Thus, the analysis becomes a statics problem. In this section, static structural analysis is used to obtain the deformation and the stress of the diaphragm as the pressure difference between the oil and hydrogen varies.

Figure 3 shows the von-Mises stress distribution cloud map of the diaphragm while the maximum stress happens. Figure 4(a)–(f) illustrate some representative moments of

the deflection distribution and the stress distribution of the process plate along the radius, from undeformed state to fitting the cylinder head. According to the static structure analysis, the maximal von-Mises stress of the diaphragm appears at the center of the process plate when the diaphragm clings to the cylinder head. In the beginning, the stress at the center of the process plate is smaller than that at the edge. As pressure difference rises, the stress at the center gradually increases and always occupies the maximum value of the entire plate. In addition, the deflection at the center of the process plate is the largest and those of other positions decrease as the radii increase. From the results, the value of the maximal von-Mises stress is 248 MPa which is lower than the allowable stress limit of the diaphragm material. Apparently, the results of the static structure analysis cannot explain the fault cases shown in Fig. 1.

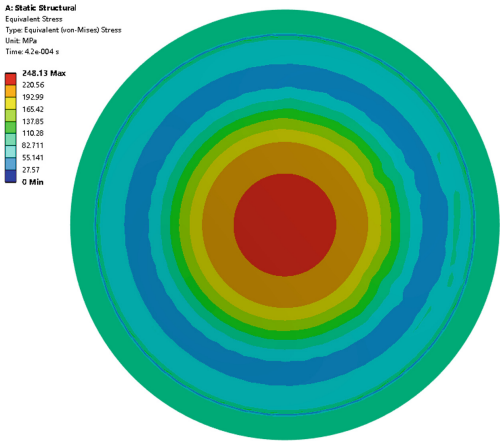

Fig. 3. The von-Mises stress distribution cloud map of the diaphragm while the maximum happens obtained by static structure analysis.

3.2 Dynamic Analysis

As the deformation of the diaphragm is actually a dynamic process, the inertial effect of the diaphragm and the collision between the diaphragm and the cavity of cylinder head should be considered to obtain more accurate results. Explicit dynamics is used in the dynamic analysis to obtain the transient response of the diaphragm during deforming.

Figure 5 shows the von-Mises stress distribution cloud map of the diaphragm while the maximum happens. Figure 6(a)–(f) illustrate some representative moments of the deflection distribution and the stress distribution of the process plate along the radius during the deformation from the undeformed state to fitting the cylinder head. According to the dynamic analysis, the maximal von-Mises stress of the diaphragm appears at the process plate, particularly, at the center and the ring with a radius of about 60 mm before the diaphragm clings to the cylinder head. From the beginning, the stress near the edge is higher than that at the center. Though the stress on the entire diaphragm increases as pressure difference rises, the maximum stress is distributed on the ring near the edge

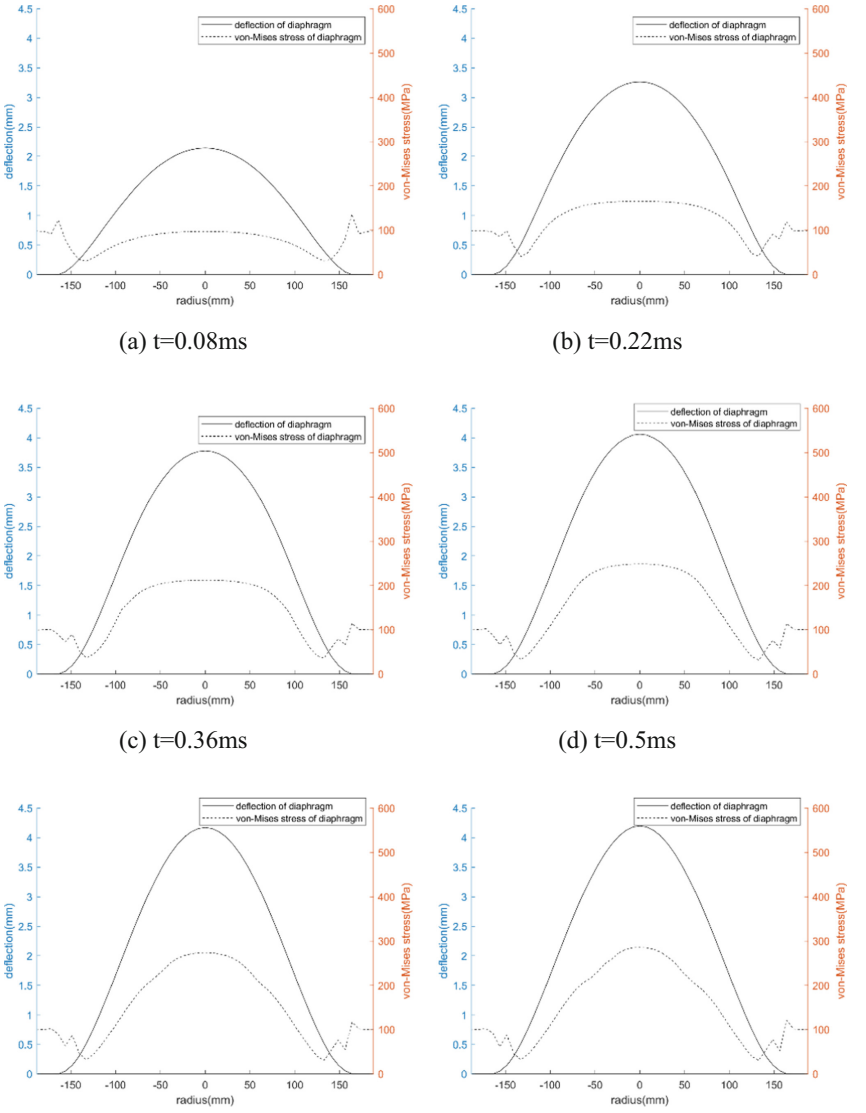

(a) t=0.08ms (b) t=0.22ms

(c) t=0.36ms (d) t=0.5ms

(e) t=0.64ms (f) t=0.78ms

Fig. 4. The deflection and von-Mises stress of the process plate along the radius at different moments calculated by static structure analysis.

of the process plate and the ring shrinks towards the center during the deformation process. On the other side, the stress at the center of the process plate oscillates in the deformation and reach the highest at t = 0.78 ms before the diaphragm clings to the cavity. Correspondingly, the deflection of the maximum stress ring is largest before t = 0.78 ms. After that, the largest deflection of the process plate occurs at the center during

the oscillation of the center area which clings to the cavity finally. From the results, the value of the maximal von-Mises stress is 564 MPa which is higher than the allowable stress limit of the diaphragm material and is able to cause the diaphragm cracking at these regions. This conclusion is consistent with the fault cases shown in Fig. 1.

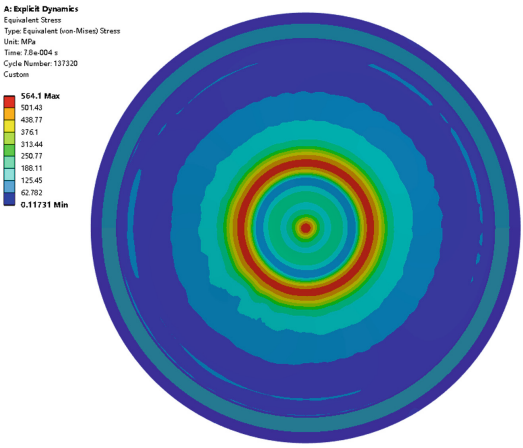

Fig. 5. The von-Mises stress distribution cloud map of the diaphragm while the maximum happens, which is obtained by dynamic analysis.

4 Conclusions

By calculating the deformation and stress of the diaphragm, the fractures of the process plate of the diaphragms of the diaphragm compressor in the fault cases are analyzed. The results of statics structure analysis and dynamics analysis are compared with diaphragm fault cases respectively, in which the latter can explain well the cause of the diaphragm rupture. During the deformation, the center area of the diaphragm oscillates and collides with the cavity of the cylinder head as the pressure difference changes, which leads to the maximum stress at the center and on the ring nearby. The process of deformation is very different from the results of static structure analysis, which shows the inertial and the collision of the diaphragm cannot be ignored, as well as the necessity of dynamic analysis in the failure analysis of diaphragm.

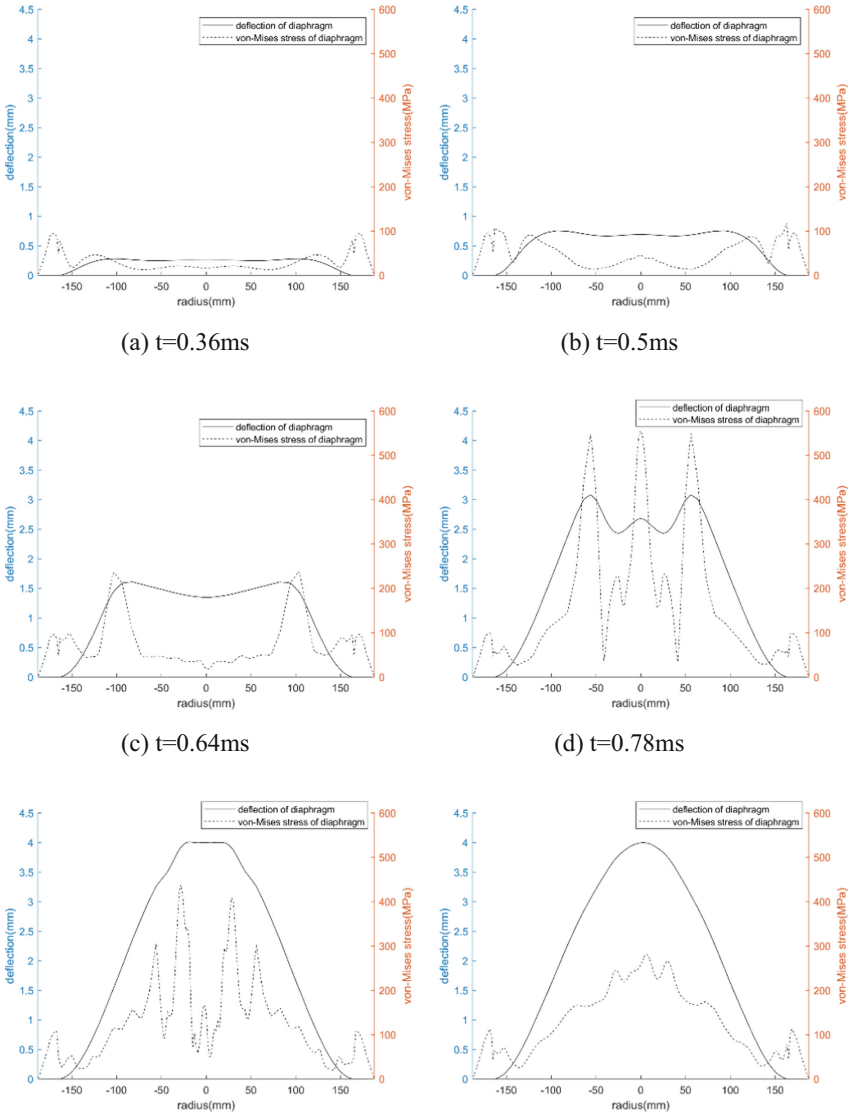

(a) t=0.36ms (b) t=0.5ms

(c) t=0.64ms (d) t=0.78ms

(e) t=0.92ms (f) t=1.06ms

Fig. 6. The deflection and von-Mises stress of the process plate along the radius at different moments calculated by dynamic analysis.

Acknowledgements. This research work had been supported by the National Natural Science Foundation of China (Grant No. 12102118) and by the Natural Science Foundation of Anhui Province, China (Grant No. 2108085QA42) and by the Science and Technology Major Project of Anhui Province, China (Grant No. 2021d05050007) and by the Natural Science Foundation of Hefei, Anhui, China (Grant No. 2021039).

References

1. Ananthachar, V., Duffy, J.J.: Efficiencies of hydrogen storage systems onboard fuel cell vehicles. Sol. Energy **78**(5), 687–694 (2005)
2. Ahmed, S., Sutherland, E.: Hydrogen compression, storage, and dispensing cost reduction workshop final report. In: Proceedings from the Hydrogen Compression, Storage, and Dispensing Cost Reduction Workshop, Argonne National Laboratory, Argonne, Illinois (2013)
3. Sdanghi, G., Maranzana, G., Celzard, A., Fierro, V.: Review of the current technologies and performances of hydrogen compression for stationary and automotive applications. Renew. Sustain. Energy Rev. **102**, 150–170 (2019)
4. Elgowainy, A., Reddi, K., Sutherland, E., Joseck, F.: Tube-trailer consolidation strategy for reducing hydrogen refueling station costs. Int. J. Hydrogen Energy **39**(35), 20197–20206 (2014)
5. Jia, X., Chen, J., Hu, H., Peng, X.: Study on the diaphragm fracture in a diaphragm compressor for a hydrogen refueling station. Int. J. Hydrogen Energy **41**(15), 6412–6421 (2016)
6. Hu, Y., Xu, X., Wang, W.: A new cavity profile for a diaphragm compressor used in hydrogen fueling stations. Int. J. Hydrogen Energy **42**(38), 24458–24469 (2017)
7. Li, J., Jia, X., Wu, Z., Peng, X.: The cavity profile of a diaphragm compressor for a hydrogen refueling station. Int. J. Hydrogen Energy **39**(8), 3926–3935 (2014)
8. Jia, X., Zhao, Y., Chen, J., Peng, X.: Research on the flowrate and diaphragm movement in a diaphragm compressor for a hydrogen refueling station. Int. J. Hydrogen Energy **41**(33), 14842–14851 (2016)

Global Trends in PEM Electrolyzer Research Based on Published Articles

Ziwei Bai[1(✉)], Jiahua Li[1], Zhanfeng Deng[1], Hui Tan[1], Lu Li[1], Guizhi Xu[1], Wei Kang[1], and Min Liu[2]

[1] State Grid Smart Grid Research Institute, Beijing 102206, China
baiziwei0427@sina.com
[2] Research Institute of State Grid Zhejiang Electric Power Co., Ltd., Hangzhou, Zhejiang, China

Abstract. As one of the representative new energy, hydrogen has received widely attention in recent years. PEM electrolyzer plays a central role in hydrogen production process. In this paper, 411 publications related to PEM electrolyzer collected from Web of Science released between 2005 and 2022 were analyzed through bibliometric to explore research hot-spots and future trends by analyzing publication and citation, countries and authors, journals and keywords. According to statistics and analysis, (1) Iran and Dincer Ibrahim were the most productive countries and authors, respectively. (2) International Journal of Hydrogen Energy was the mainly journal of PEM electrolyzer related publications. (3) Component and Hybrid System are likely to remain prominent areas of research in the foreseeable future. (4) Current hot-spots, such as Two Phase Flow and Hybrid System, may receive even more attention in the foreseeable future.

Keywords: PEM electrolyzer · Bibliometric · Hydrogen energy · Trend expectation

1 Introduction

Hydrogen has become one of the most promising clean and sustainable energy [1] due to its non-carbon emissions, which could make great contributions to the construction of global carbon neutral energy system. Hydrogen can be produced from various resources including fossil fuels [2–4], biomass [5], biological sources [6], and water electrolysis [7]. In contrast, electrolysis is the most economical method for large-scale production of high-purity (> 99.99%) hydrogen, which could be further classified into alkaline water electrolysis (AWE), solid oxide electrolysis (SOE), and proton exchange membrane (PEM) water electrolysis.

SOE is easy to achieve high producing efficiency [8], but the technology is still trapped in the laboratory stage and lacks of industrial application. AWE has become a well matured technology for hydrogen production up to the megawatt range, and constitutes the most extended electrolytic technology at a commercial level worldwide [9]. But its disadvantages including low partial load range and limited current density [10] limit the promotion of this technology and the enthusiasm of relevant academic research.

H. Sun et al. (Eds.): WHTC 2023, SPPHY 393, pp. 44–60, 2024.
https://doi.org/10.1007/978-981-99-8631-6_5

PEM by contrast, as a novel electrolysis method, has the advantages of high flexibility, compact equipment and high current density [11]. With the trial of non-noble metal catalysts utilization [12], more and more important achievements were accomplished in recent years, and in summary, the disadvantages of PEM are gradually overcome and the number of published papers related to PEM electrolysis is rapidly increasing (as summarized in Sect. 3.1).

Over the past two decades, more than 400 articles are published on the R&D of PEM electrolyzer, and the development road map of PEM electrolyzer over the years has been gradually clear. Thus, the purpose of this paper is to analyze the modification of research hot-spots in the field of PEM electrolyzer based on the publications, in order to offer beneficial inspirations and new frontiers for relevant scholars.

2 Methods

2.1 Data Collection

Relevant articles are identified from the Web of Science Core Collection (WoSCC) database. To avoid issues due to daily updates of the database, we conducted our search and downloaded relevant items on January 3, 2023, Tuesday (Fig. 1). We used search formulae as TS = ("PEM Electrolyzer"). The search terms were selected from the Science Citation Index Expanded (SCI-EXPANDED). A total of 444 publications were retrieved. After excluding 33 publications including early access, proceeding paper, corrections, meeting abstract, 411 articles were included in the final data set. Full records and cited refernces were exported as plaint text files for further analyses.

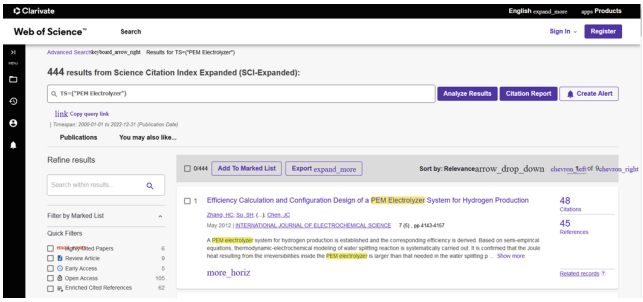

Fig. 1. Screenshot of web of science searching

The obtained data were imported into Citespace software (version 6.1.6) for deduplication. The number of publications, citations, countries, authors, journals, highly cited references, keywords, and other data were extracted by several independent researchers (JH Li, ZF Deng, H Tan, L Li) for data recheck. The H-index and average citations per items (ACI) utilized in the paper are calculated by ZW Bai based on information at WoS Online.

2.2 Data Analyses

Data collected from WoSCC needed to be further analyzed to accurately acquire the impact of each part. Citespace (version 6.1.6) and VOSviewer were introduced to bibliometric analysis and visual display. Microsoft Excel (version 16.58) was used to summarize relevant information in tables. Flow chart of publication filtering and analysis was shown in Fig. 2.

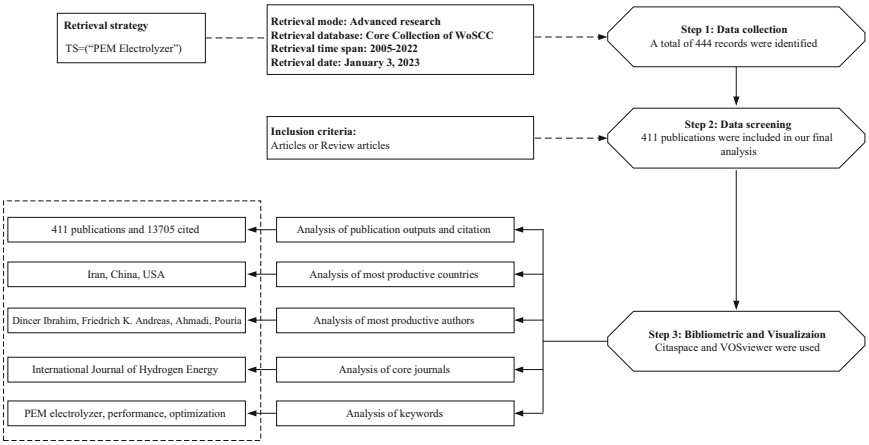

Fig. 2. Flow chart of publication filtering and analysis

3 Results

The above mentioned 411 samples published in 99 Journals were completed by 1382 authors from 60 countries/regions and affiliated to 506 organizations. These contents would be further described and analyzed through Publication and Citation, Regions and Countries, Authors, Journals, and Keywords, respectively. Details are shown as following.

3.1 Publication and Citation

As can be seen from Fig. 3, the total publications was relatively flat before 2017, and then the numbers displayed a sharply increasing trend since 2018. Almost 73.6% of total were published between 2018 and 2022. Citations almost rose straightly after 2018 too. It can be seen that the PEM Electrolytic is a research hot-spots indeed. Relevant research increases year by year.

The top 10 most-cited articles were listed in Table 1 in order to outcome the most influential paper in this field. The most-cited paper [13] is written by Barbir, F with 708 times cited, followed by papers [14–16] which has been cited for 307 times, 294 times, and 286 times, up to now, respectively.

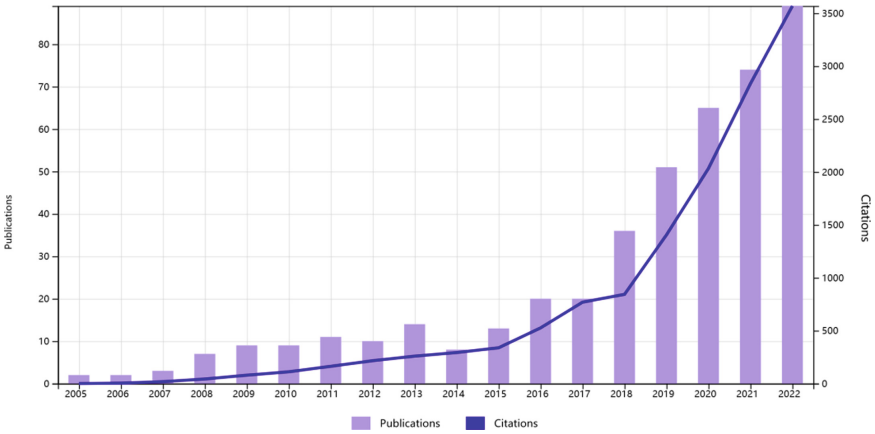

Fig. 3. Trends of publications and citations

The first mentioned one [13] is the first published paper related to PEM electrolyzer which discussed several possible applications for PEM electrolyzer including grid connected hydrogen generation, grid peak shaving, and power storage cooperated with fuel cell. Furthermore, several specific issues including size, operation, and efficiency are discussed in the paper. The second article [14] in the table should be paid specially attention. Because it published recently and been cited for 43.9 times annually. This paper is mainly study about the active and highly stable catalysts and several experiments and analysis were cleverly made. The fourth publication [16] in Table 1 is the most-cited article in 2022 which is mainly focus on the Energy and exergy analysis of a PEM electrolyzer system, and offered better understanding of the characteristics of PEM electrolyzer plant. This paper represents the boom of PEM electrolyzer system related research.

3.2 Publication and Citation

Figure 4 displays the distribution of total publications about PEM electrolyzer. Iran (88), China (61), USA (59), Germany (52), Canada (50), Turkey (50), Italy (32), France (27), South Korea (14), Japan (12) as the top 10 most productive countries up till 2022. These countries are mainly located in Asia, Europe and North America. Data in Fig. 4 is not directly equal to value in Fig. 3, because some articles are finished through global cooperation and will be duplicated statistics.

3.3 Authors

Tabel 2 summaries the top 10 authors in terms of the number of publications. Dincer, Ibrahim from University of Ontario was the most productive author with 22 publishments up to 2022. His outstanding investigation has significantly increased the number of related papers published from Canada, accounting for about 44%. In the same way, Iran, as the most productive country mentioned in Sect. 3.2, also owes its outstanding scientific

Table 1. High cited references in PEM electrolyzer

Rank	Title	Author	PY	Citation						
				2018	2019	2020	2021	2022	APY	Total
1	PEM electrolysis for production of hydrogen from renewable energy sources	Barbir, F.	2005	52	66	61	64	53	39.33	708
2	Oxide-Supported IrNiOx Core-shell particles as efficient, Cost-effective, and stable catalysts for electrochemical water splitting	Nong, H. N.; Oh, H. S.; Reier, T.	2015	38	51	56	47	32	38.38	307
3	Power management strategies for a stand-alone power system using renewable energy sources and hydrogen storage	Ipsakis, D.; Voutetakis, S.; Seferlis, P.	2009	21	19	22	22	12	21	294
4	Energy and exergy analysis of hydrogen production by a proton exchange membrane (PEM) electrolyzer plant	Ni, M.; Leung, M. K. H.; Leung, D. Y. C.	2008	22	36	41	45	63	19.07	286
5	Oxide-supported Ir nanodendrites with high activity and durability for the oxygen evolution reaction in acid PEM water electrolyzers	Oh, H. S.; Nong, H. N.; Reier, T.	2015	24	47	44	55	35	31.25	250

(*continued*)

Table 1. (*continued*)

Rank	Title	Author	PY	Citation						
				2018	2019	2020	2021	2022	APY	Total
6	Dynamic modelling of a proton exchange membrane (PEM) electrolyzer	Gorgun, H.	2006	10	13	13	18	22	11.06	188
7	Optimization of solar powered hydrogen production using photovoltaic electrolysis devices	Gibson, T. L.; Kelly, N. A.	2008	6	12	7	20	6	11.6	174
8	Energy and exergy analyses of hydrogen production via solar-boosted ocean thermal energy conversion and PEM electrolysis	Ahmadi, P.; Dincer, I.; Rosen, M. A.	2013	16	25	25	22	33	17.1	171
9	Ultrathin IrO_2 Nanoneedles for electrochemical water oxidation	Lim, J.; Park, D.; Jeon, S. S.	2018	5	28	38	45	41	31.6	158
10	Nanosized IrOx-Ir catalyst with relevant activity for anodes of proton exchange membrane electrolysis produced by a cost-effective procedure	Lettenmeier, P.; Wang, L.; Golla-Schindler, U.	2016	27	22	29	29	21	20.57	144

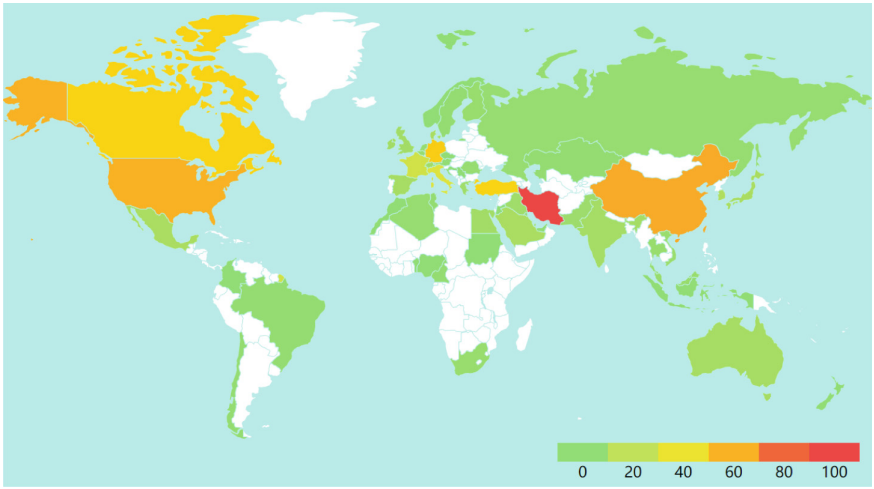

Fig. 4. Geo visualization of research distribution of PEM electrolyzer. *Note* Color relates to the paper released (*Note* Taiwan belongs to China; England, Northern Ireland, Scotland and Wales belongs to UK.)

research contributions to research teams led by Afshari, Ebrahim and Baniasadi, Ehsan. As can be seen, the rise of an outstanding scholar (team) has a significant impact on the research status of the country in relevant fields. While it is also important to find that as the second largest publication country, China, do not have any outstanding researcher being recorded in Table 2. It is considered as up to now, this topic has been greatly attracted by Chinese researchers but no one has become the academic leader.

3.4 Journals

There were 99 journals used to publish PEM electrolyzer related papers, in which the International Journal of Hydrogen Energy contributed the most articles with total publications of 147 (33.1%), and Energy Conversion and Management ranked second (36, 8.1%), followed by Journal of Power Sources (23, 5.2%) (Fig. 5).

3.5 Keywords

VOS viewer which could be used to classified the similar keywords was introduced, 411 publications contained 1891 keywords, and 180 left after merging of similar items. Heat map of Keywords (Fig. 6) highlights the top keywords including PEM Electrolyzer, Performance, Energy, Hydrogen Production, and Optimization. These keywords related to the deep research around PEM electrolyzer especially on catalyst and system performance.

Table 2. Most productive authors in PEM Electrolyzer.

Rank	Author	Country	Counts	Institutions	H-Index	ACI*
1	Dincer, Ibrahim	Canada	22	University of Ontario	104	34.43
2	Friedrich, K. Andreas	Germany	14	University of Stuttgart	48	35.09
3	Ahmadi, Pouria	USA	12	University of Illinois at Urbana-Champaign	47	54.68
4	Bazylak, Aimy	Canada	11	University of Toronto	34	20.17
5	Afshari, Ebrahim	Iran	11	University of Isfahan	25	27.98
6	Ozturk, Murat	Holland	11	Isparta University of Applied Sciences	20	19.40
7	Gago, A. Saul	Germany	10	Helmholtz Association	23	33.72
8	Baniasadi, Ehsan	Iran	10	University of Isfahan	21	23.52
9	Guilbert, Damien	France	9	Universite de Lorraine	13	12.11
10	Alirahmi, S. Mojtaba	Denmark	9	Aalborg University	10	33.07

**ACI* average cited index

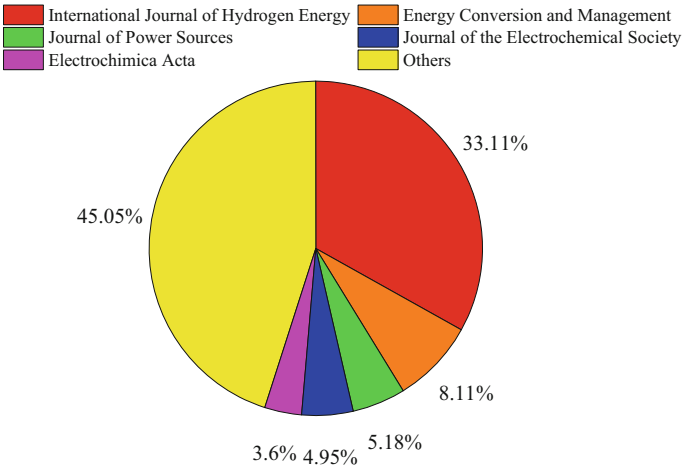

Fig. 5. Pie chart visualization of the top journals of PEM electrolyzer

4 Discussion

4.1 Countries and Authors

Figure 7 demonstrates the annual publications of top 10 most productive countries since 2014. Iran, China and USA are the top 3 countries who contributed the most publications as previous shown in Fig. 4. Iran has far more publications than any other country (20%), most of which are finished in recent 5 years [17–21]. Iran remains the most producer in recent five years, until been surpassed by China (23) in 2022.

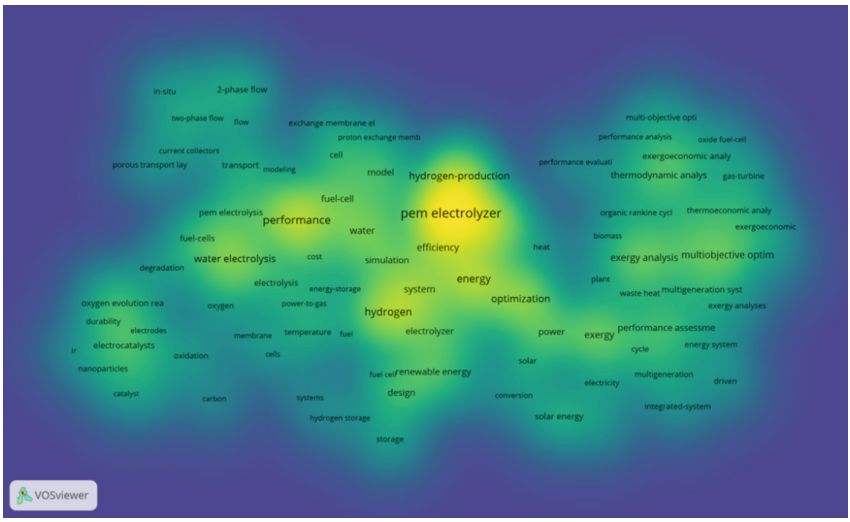

Fig. 6. Heat map of keywords in 2022

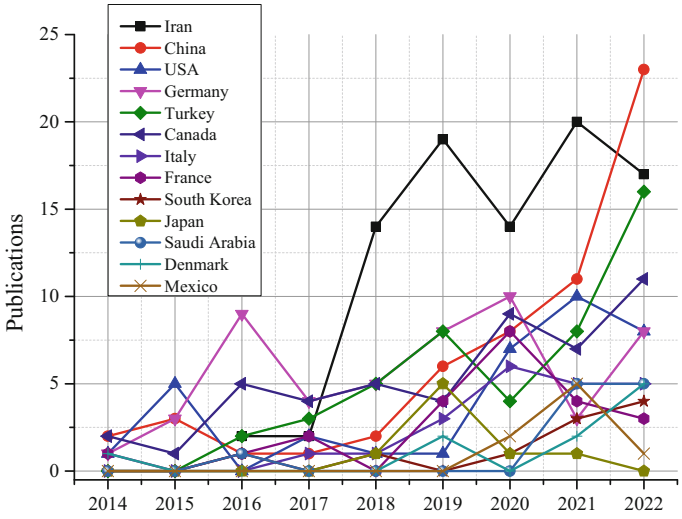

Fig. 7. Trends of publications of the top 10 countries/regions

Author cooperation analysis revealed inter-author connection networks. In the PEM Electrolyzer research area, Dincer Ibrahim (22), Friedrich K Andreas (14), Ahmadi, Pouria (12) are the top 3 authors with the most paper publications. And it can be seen from Fig. 8, which summarised the authors with more than 4 papers published, as some of these authors have quiet close stable team cooperation. Dincer, Ibrahim and Ahmadi, pouria used to co-work on the energy analysis and optimization of electrolyzer included system since 2013 [22–25]. Friedrich, Wang, Abouatallah, and bazylak are together

engaged in the characteristics investigation of gas diffusion layer and bipolar of PEM electrolyzer [26–31].

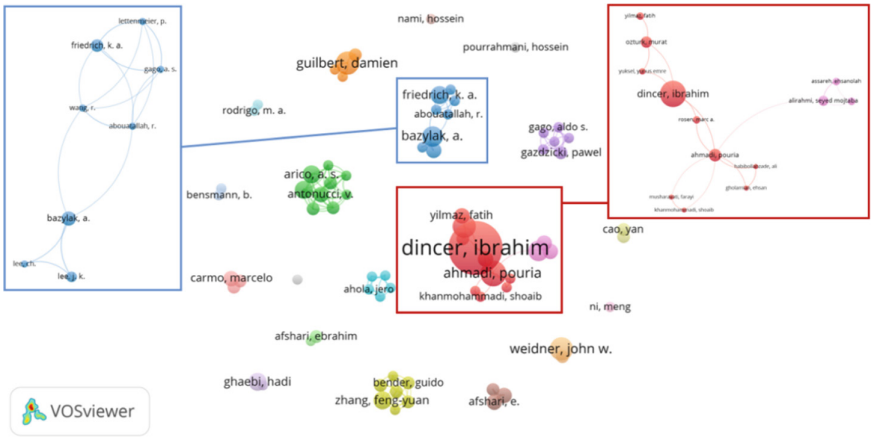

Fig. 8. Network visualization map of co-authorship. *Notes* the size of the nodes reflects the strength of their cooperation.

4.2 The Changing of Keywords

The keywords clarification through these papers are summarized as Fig. 9. It could be seen as three cluster are summarized with different colors, System type (Exergy Analysis, Multi-objective Optimization, et al.), component type (Two Phase Flow, Oxygen Evolution Reaction, et al.), and modeling type (Simulation, Design, et al.), which may related to system, component, and electrolyzer, respectively. Furthermore, the annual keywords in Fig. 10b clearly shows that the keywords on the right are newer, which emphasize that the research focus shifted from system into component gradually. This phenomenon is predictable, as technical research should gradually modification from application demonstration to theoretical verification.

Moreover, the verification of the keywords are summarized as Fig. 10. It is partial similar with the result presented in Fig. 9. Not only the component study related keywords, such as Modelling and Degradation [32–35] shows increment these years, but also the Hybrid System related keywords, such as Geothermal and Photovoltaic [21, 36–38], show a boom increment these years. As for the System Optimum Analysis and Oxygen Evolution Reaction, these keywords fail to present a continuous research trend and seem suspended.

4.3 Recent Research Trends

To analyze the subtle changes in research over recent years, the heat map of keywords till 2020 is drawn(as shown in Fig. 11) to compare with Fig. 6. The hot keywords related

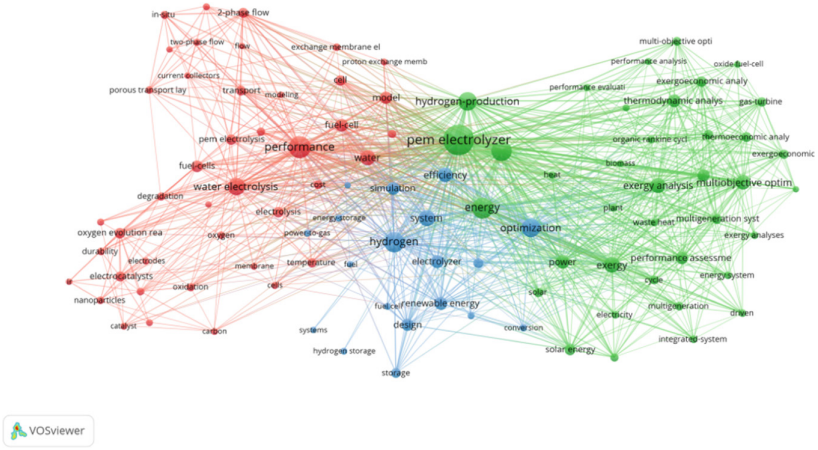

(A)Network visualization map of keywords

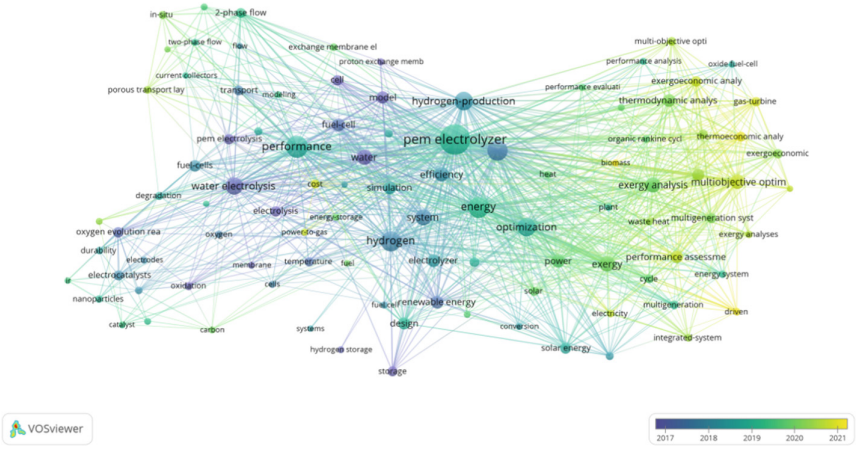

(B)Overlay visualization of keywords co-occurrence year

Fig. 9. Analysis of keywords for PEM electrolyzer (*Notes* the size of the nodes reflects the strength of their frequency)

to Performance and Optimization are slightly decreased during 2020–2022, which are replaced by publications about Modelling and Two Phase Flow. This trend modification is consistent with the research topic timeline as shown in Fig. 10.

Moreover, several outstanding authors are chosen for case analysis for the trend modification on researching area in PEM electrolyzer. The most prolific authors in the area are summarized in Table 3 as basic data, and their latest publications during 2020–2022 are utilized for special analysis.

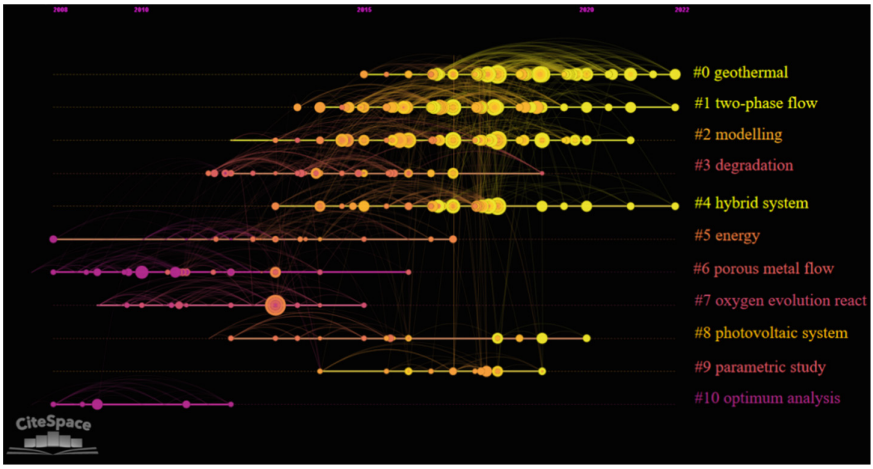

Fig. 10. Cluster timeline of co-cited reference (*Notes* the size of the nodes reflects the strength of their frequency)

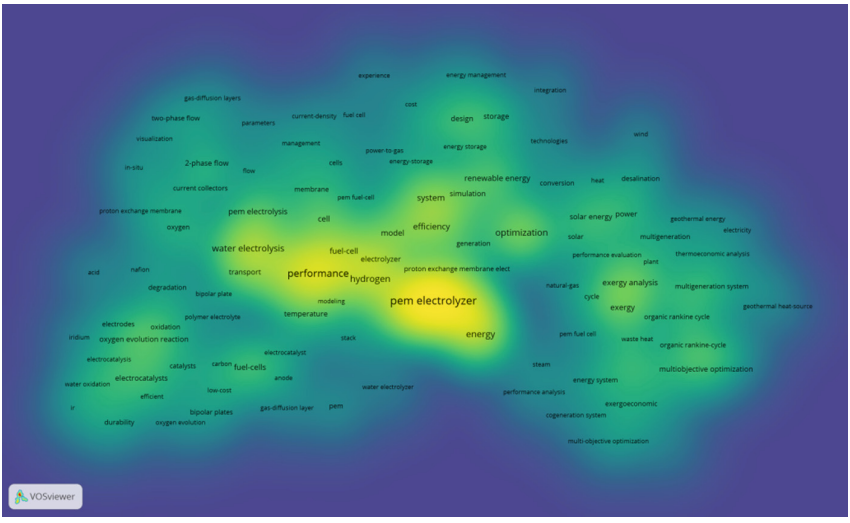

Fig. 11. Heat map of keywords in 2020

Based on the chosen publications, it should be mentioned that Aimy and Kieran are closely cooperated [32, 39, 40] around porous transport layers research. Meanwhile, Mojtaba and Ehsanolah were deeply co-worked [41–43] on electrolyzer related hybrid system investigation. Ibrahim is one of the greatest researchers who has made a significant contribution on PEM electrolyzer utilizing renewable energy [44, 45]. Marcelo was devoted to improve the electrolysis efficiency through novel components and operating conditions [46, 47]. These researchers have carried out their previous research directions in the past three years.

Table 3. Most productive authors in PEM electrolyzer during 2020–2022

Rank	Author	2020	2021	2022	Summary
1	Guilbert, Damien	5	3	0	8
2	Bazylak,Aimy	4	2	0	6
3	Alirahmi, Seyed Mojtaba	2	1	3	6
4	Fahy, Kieran F.	3	2	0	5
5	Assareh, Ehsanolah	0	1	4	5
6	Dincer, Ibrahim	1	3	1	5
7	Carmo, Marcelo	2	1	2	5
	Summary	17	13	10	40

Damien engaged in electrolyzer modeling and experimental verification for several year. His latest publication on 'Journal of Processes' in 2021 turn to study electrolyzer related testing applications [48]. This slightly variation maybe signify the further development of electrolysis related technology in application level.

Journal statistics help researchers choose the most suitable journal for their work. The publication Journal clusters show a clearly verification for the chosen publications, changing from 'Journal of International Journal of Hydrogen Energy' into other Journals instead, such as Energies and sustainable energy technology, which can easily be seen in Fig. 12.

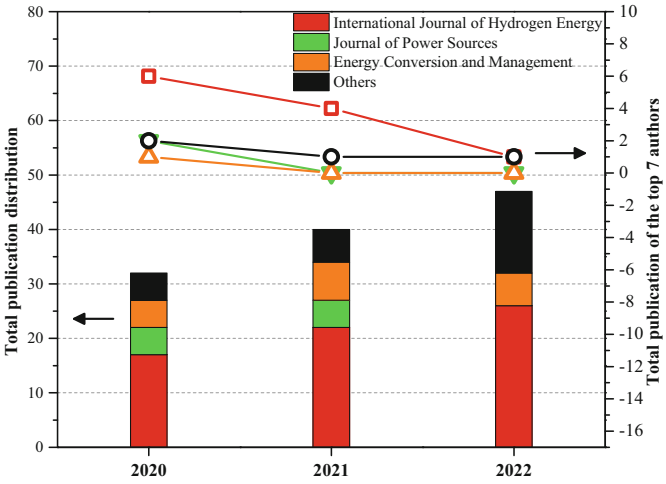

Fig. 12. Analysis of publication journals

However, even the weight of 'International Journal of Hydrogen Energy' among the articles significantly decreased, this Journal is still the mainly journal for publishing

work about PEM electrolyzer for most researchers. Data analysis indicates that some Journals, such as Sustainable Energy Technologies, Journal of Power Sources, Energies, are becoming more attractive to the related research. This phenomenon maybe related to the transfer of the research topics of the journals, so that gives authors more choices (Fig. 13).

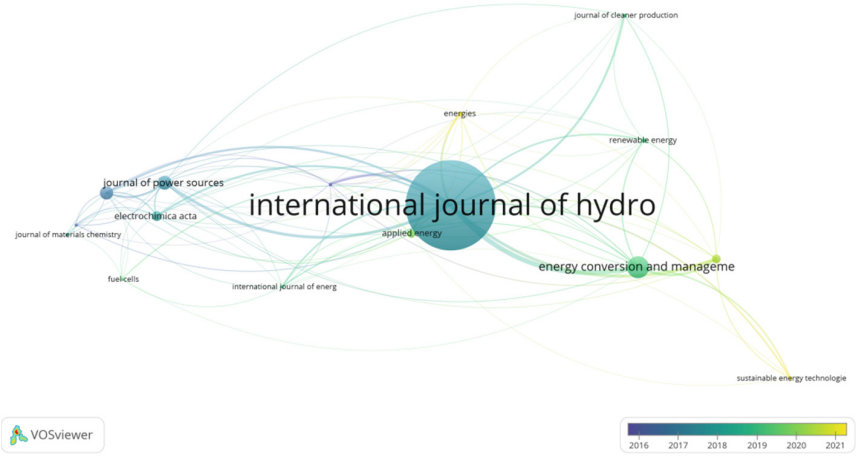

Fig. 13. Overlay visualization of journals co-occurrence year (*Notes* the size of the nodes is weighted by publications)

5 Conclusion

Based on the bibliometric analysis of the 411 PEM Electrolyzer publications released between 2005 and 2022, it is found that the research has increased explosively with the Iran being the leading producer, especially in recent 5 years. China lacks top scholars and core leader in the field. Most researchers have stable cooperative relationships, and continues their research direction in recent years. Component and hybrid system related study are investigation hot-spots recently. Furthermore, keywords including two phase flow and geothermal hybrid systemare more concerned than ever. More journals are joining the publications about hydrogen, but the status of the main journal (International Journal of Hydrogen Energy) is still unshakable.

Overall, electrolysis is a novel production method for clean energy. Bibliometrics is a useful tool to discover the current research hot-spots and future trends of a field. PEM electrolyzer related analysis in this paper clearly exhibits the research topic modification and research trend in recent years. This paper is hoping to offer beneficial inspirations and new frontiers for relevant scholars.

Acknowledgments. This material is based in part upon work supported by the State Grid Co., Ltd. Science and Technology Project: Research and Demonstration on Key Technologies of 100kW Hydrogen Utilization (Project No. 5400-201919487A-0-0-00).

References

1. Kazim, A., Veziroglu, T.N.: Utilization of solar hydrogen energy in the UAE to maintain its share in the world energy market for the 21st century. Renew. Energy **24**, 259–274 (2001)
2. Boyano, A., Blanco-Marigorta, A.M., Morosuk, T., Tsatsaronis, G.: Exergy environmental analysis of a steam methane reforming process for hydrogen production. Energy **36**, 2202–2214 (2011)
3. Rahimpour, M.R., Jafari, M., Iranshahi, D.: Progress in catalytic naphtha reforming process: a review. Appl. Energy **109**, 79–93 (2013)
4. Seyitoglu, S.S., Dincer, I., Kilicarslan, A.: Energy and exergy analyses of hydrogen production by coal gasification. Int. J. Hydrogen Energy **42**, 2592–2600 (2017)
5. Mujeebu, M.A.: Hydrogen and syngas production by superadiabatic combustion—a review. Appl. Energy **173**, 210–224 (2016)
6. Sivagurunathan, P., Kumar, G., Kim, S.H., Kobayashi, T., Xu, K.Q., Guo, W., et al.: Enhancement strategies for hydrogen production from wastewater: a review. Curr. Org. Chem. **20**, 2744–2752 (2016)
7. Dawood, F., Anda, M., Shafiullah, G.M.: Hydrogen production for energy: an overview. Int. J. Hydrogen Energy **45**(7), 3847–3869 (2020)
8. Dönitz, W., Erdle, E.: High-temperature electrolysis of water vapor-status of development and perspectives for application. Int. J. Hydrogen Energy **10**, 291e5 (1985)
9. Ursua, A., Gandia, L.M., Sanchis, P.: Hydrogen production from water electrolysis: current status and future trends. Proc. IEEE **100**(2), 410e26 (2012)
10. Schroder, V., Emonts, B., Janssen, H., Schulze, H.P.: Explosion limits of hydrogen/oxygen mixtures at initial pressures up to 200 bar. Chem. Eng. Technol. **27**(8), 847e51 (2004)
11. Stolten, M.D.: A comprehensive review on PEM water electrolysis. Int. J. Hydrogen Energy (2013)
12. Tajuddin, A., Elumalai, G., Xi, Z., et al.: Corrosion-resistant non- noble metal electrodes for PEM-type water electrolyzer. Int. J. Hydrogen Energy **78**, 46 (2021)
13. Barbir, F.: PEM electrolysis for production of hydrogen from renewable energy sources. Sol. Energy **78**(5), 661–669 (2005)
14. Nong, H.N., Oh, H.S., Reier, T., Willinger, E., Willinger, M.G., Petkov, V., Teschner, D., Strasser, P.: Oxide-supported IrNiOxCore-shell particles as efficient, cost-effective, and stable catalysts for electrochemical water splitting. Angewandte Chemie (2015)
15. Ipsakis, D., Voutetakis, S., Seferlis, P., et al.: Power management strategies for a stand-alone power system using renewable energy sources and hydrogen storage. Int. J. Hydrogen Energy **34**(16), 7081–7095 (2009)
16. Ni, M., Leung, M.K., Leung, D.Y.: Energy and exergy analysis of hydrogen production by a proton exchange membrane (PEM) electrolyzer plant. Energ. Conv. Manage.**49**(10), 2748–2756 (2008)
17. Akrami, E., Nemati, A., Nami, H., Ranjbar, F., et al.: Exergy and exergoeconomic assessment of hydrogen and cooling production from concentrated PVT equipped with PEM electrolyzer and LiBr-H_2O absorption chiller. Int. J. Hydrogen Energy **43**(2), 622–633
18. Toghyani, S, Afshari, E., Baniasadi, E., et al.: Energy and exergy analyses of a nanofluid based solar cooling and hydrogen production combined system. Renew. Energy (2019)
19. Seyedmatin, P., Karimian, S., Rostamzadeh, H., et al.: Electricity and hydrogen co-production via scramjet multi-expansion open cooling cycle coupled with a PEM electrolyzer. Energy **199**, 117364 (2020)

20. Musharavati, F., Ahmadi, P., Khanmohammadi, S.: Exergoeconomic assessment and multiobjective optimization of a geothermal-based trigeneration system for electricity, cooling, and clean hydrogen production. J. Therm. Anal. Calorim.Calorim. **145**(3), 1673–1689 (2021)
21. Mehrenjani, J.R., Gharehghani, A., Sangesaraki, A.G.: Machine learning optimization of a novel geothermal driven system with LNG heat sink for hydrogen production and liquefaction. Energy Convers. Manage. **254**, 115266 (2022)
22. Ahmadi, P., Dincer, I., Rosen, M.A.: Energy and exergy analyses of hydrogen production via solar-boosted ocean thermal energy conversion and PEM electrolysis. Int. J. Hydrogen Energy **38**(4), 1795–1805 (2013)
23. Ahmadi, P., Dincer, I., Rosen, M.A.: Performance assessment and optimization of a novel integrated multigeneration system for residential buildings. Energy Build. **67**, 568–578 (2013)
24. Ahmadi, P., Dincer, I., Rosen, M.A.: Multi-objective optimization of a novel solar-based multigeneration energy system. Solar Energy **108**, 576–591 (2014)
25. Ahmadi, P., Dincer, I., Rosen, M.A.: Performance assessment of a novel solar and ocean thermal energy conversion based multigeneration system for coastal areas. J. Sol. Energy Eng. **137**(1), 352–362 (2014)
26. Lettenmeier, P., Wang, R., Abouatallah, R., et al.: Durable membrane electrode assemblies for proton exchange membrane electrolyzer systems operating at high current densities. Electrochimica Acta, 502–511 (2016)
27. Lee, C.H., Zhao, B., Abouatallah, R., et al.: Compressible-gas invasion into liquid-saturated porous media: application to polymer-electrolyte-membrane electrolyzers. Phys. Rev. Appl. **11**(11), 54029 (2019)
28. Lee, C.H., Banerjee, R., Ge, N., et al.: The effect of cathode nitrogen purging on cell performance and in operando neutron imaging of a polymer electrolyte membrane electrolyzer. Electrochimica Acta (2018)
29. Lettenmeier, P., Ansar, A., Gago, A., et al.: Protective coatings for low-cost bipolar plates and current collectors of proton exchange membrane electrolyzers. In: International Conference on Electrolysis (2017)
30. Lee, C.H., Hinebaugh, J., Banerjee, R., et al.: Influence of limiting throat and flow regime on oxygen bubble saturation of polymer electrolyte membrane electrolyzer porous transport layers. Int. J. Hydrogen Energy **42**(5), 2724–2735 (2016)
31. Lettenmeier, P., Wang, R., Abouatallah, R., et al.: Coated stainless steel bipolar plates for proton exchange membrane electrolyzers. J. Electrochem. Soc.Electrochem. Soc. **163**(11), F3119 (2016)
32. Lee, C.H., Lee, J.K., Zhao, B., et al.: Temperature-dependent gas accumulation in polymer electrolyte membrane electrolyzer porous transport layers. J. Power Sour. **446**, 227312 (2020)
33. De Lorenzo, G., Agostino, R.G., Fragiacomo, P.: Dynamic electric simulation model of a proton exchange membrane electrolyzer system for hydrogen production. Energies **15**(17), 6437 (2022)
34. Hernández-Gómez, Á., Ramirez, V., Guilbert, D., et al.: Cell voltage static-dynamic modeling of a PEM electrolyzer based on adaptive parameters: development and experimental validation. Renew. Energy **163**, 1508–1522 (2021)
35. Kheirrouz, M., Melino, F., Ancona, M.A.: Fault detection and diagnosis methods for green hydrogen production: a review. Int. J. Hydrogen Energy (2022)
36. Sun, W., Feng, L., Abed, A.M., et al.: Thermoeconomic assessment of a renewable hybrid RO/PEM electrolyzer integrated with Kalina cycle and solar dryer unit using response surface methodology (RSM). Energy **260**, 124947 (2022)
37. Zhang, X., Zeng, R., Du, T., et al.: Conventional and energy level based exergoeconomic analysis of biomass and natural gas fired polygeneration system integrated with ground source heat pump and PEM electrolyzer. Energy Convers. Manage. **195**, 313–327 (2019)

38. Shapiro, D., Duffy, J., Kimble, M., et al.: Solar-powered regenerative PEM electrolyzer/fuel cell system. Sol. Energy **79**(5), 544–550 (2005)
39. Kim, P.J., Lee, C.H., Lee, J.K., et al.: In-plane transport in water electrolyzer porous transport layers with through pores. J. Electrochem. Soc.Electrochem. Soc. **167**(12), 124522 (2020)
40. Kim, P.J., Lee, J.K., Lee, C.H., et al.: Tailoring catalyst layer interface with titanium mesh porous transport layers. Electrochim. Acta. Acta **373**, 137879 (2021)
41. Alirahmi, S.M., Assareh, E., Chitsaz, A., et al.: Electrolyzer-fuel cell combination for grid peak load management in a geothermal power plant: power to hydrogen and hydrogen to power conversion. Int. J. Hydrogen Energy **46**(50), 25650–25665 (2021)
42. Alirahmi, S.M., Assareh, E., Pourghassab, N.N., et al.: Green hydrogen & electricity production via geothermal-driven multi-generation system: Thermodynamic modeling and optimization. Fuel **308**, 122049 (2022)
43. Alirahmi, S.M., Assareh, E., Arabkoohsar, A., et al.: Development and multi-criteria optimization of a solar thermal power plant integrated with PEM electrolyzer and thermoelectric generator. Int. J. Hydrogen Energy **47**(57), 23919–23934 (2022)
44. Temiz, M., Dincer, I.: A unique ocean and solar based multigenerational system with hydrogen production and thermal energy storage for Arctic communities. Energy **239**, 122126 (2022)
45. Yuksel, Y.E., Ozturk, M., Dincer, I.: Development of a novel combined energy plant for multigeneration with hydrogen and ammonia production. Int. J. Hydrogen Energy **46**(57), 28980–28994 (2021)
46. Zaccarine, S., Shviro, M., Nelson Weker, J., et al.: Multi-scale multi-technique characterization approach for analysis of PEM electrolyzer catalyst layer degradation. J. Electrochem. Soc. (2022)
47. Keller, R., Rauls, E., Hehemann, M., et al.: An adaptive model-based feedforward temperature control of a 100 kW PEM electrolyzer. Control. Eng. Pract.Pract. **120**, 104992 (2022)
48. Yodwong, B., Guilbert, D., Hinaje, M., et al.: Proton exchange membrane electrolyzer emulator for power electronics testing applications. Processes **9**(3), 498 (2021)

The Preparation of Iridium-Based Catalyst with Different Melting Point-Metal Nitrate and Its OER Performance in Acid Media

Jiayao Deng[1,2], Xiao Hu[1,2], Guizhi Xu[1,2], Zhanfeng Deng[1], Lan Yang[1], Ding Chen[3], Ming Zhou[3], and Boyuan Tian[1(✉)]

[1] Beijing Institute of Smart Energy, Changping, Beijing 102209, China
tianboyuan@bise.hrl.an.cn
[2] State Key Laboratory of Advanced Transmission Technology, State Grid Smart Grid Research Institute Co.,Ltd., Changping, Beijing 102209, China
[3] State Grid Jiaxing Power Supply Company, Jiaxing, Zhejiang, China

Abstract. Oxygen evolution reaction (OER) is the main factor limiting the large-scale development of proton-exchange membrane (PEM) hydrogen production. It is urgent to develop catalysts with excellent OER catalytic performance and stability. Herein, several Iridium-based catalysts were prepared by simple mixing and calcination, the OER properties of catalysts with different melting points of nitrates as calcinating additives were investigated. The $RbNO_3$ treated catalyst displayed a low overpotential(η) of 297.6 mV versus RHE, which is lower than the catalyst calcinated without nitrate (323.8 mV vs. RHE). Moreover, the $RbNO_3$ treated catalyst displayed good acid stability over 20 h Chronopotentiometric test. The high OER catalytic activity and stability of RbNO3 treated catalyst may be attribute to the smaller nanoparticle morphology, pure IrO_2 structure and high electrochemical surface area (ECSA), which increase the number of active sites and the intrinsic catalytic activity. This work indicated that the catalyst with excellent OER performance can be obtained by selecting nitrate with moderate melting point as the calcinating additive. Nitrates (like $RbNO_3$) treated catalyst with excellent catalytic activity and stability has good application prospect in hydrogen production of PEM water splitting.

Keywords: Oxygen evolution reaction · Nitrates · PEM water splitting

1 Introduction

Hydrogen energy [1–3] is a kind of renewable energy, which has the advantages of high energy density, environmental protection and pollution-free, so it has obtained the support of a number of national policies. At present, hydrogen production by proton-exchange membrane (PEM) electrocatalytic water splitting is regarded as a promising

The original version of the chapter has been revised: The author name from Gnauizhi Xu to Guizhi Xu has been updated. A correction to the chapter can be found at https://doi.org/10.1007/978-981-99-8631-6_48

H. Sun et al. (Eds.): WHTC 2023, SPPHY 393, pp. 61–68, 2024.
https://doi.org/10.1007/978-981-99-8631-6_6

technical route. However its practical application is influenced by the slow kinetics [4, 5] of the oxygen evolution reaction (OER). Hence, it's urgent to develop catalysts with excellent OER performance.

Among OER catalysts, Iridium components are widely studied because of the good catalytic activity as well as acid stability. There are various IrO_2 preparation method such as Adams Fusion method [6, 7], sol-gel method [8, 9], liquid reduction method [10], template method [11] and so on. Adams Fusion method is a traditional method having the advantages of simple preparation process and low cost, but the catalyst's overpotential prepared by this method is relatively high compared with other method [7]. Traditional Adams Fusion method mixes metal chloride precursor with $NaNO_3$ and then calcinate at proper temperature, $NaNO_3$ acts as an oxidation in the formation of new oxides. The presence of chlorine in the precursors can adversely affect PEM, and many studies have shown that chlorine-contained precursor should be avoided in future work to get rid of Cl^- contaminations [12]. Catalyst with nano size often shows better catalytic performance. With the increase of calcinating temperature, the grain grows [13, 14]. Research [15] shows that the addition of salt has effect on crystal growth. In consequence, inspired by above researches, several nitrates with different melting points (low melting point nitrate: Fe and La nitrate; middle melting point nitrate: Na and Rb nitrate; high melting point nitrate: Mg and Ba nitrate) were introduced to control grain size. After simple mixing and calcination with Ir black, Iridium based catalysts were prepared.

In this work, we have developed an innovative additive oxidation process that on the one hand effectively inhibits particle size growth during calcinating and on the other hand extends the raw material from harmful chloride precursor to iridium black. The properties of different catalysts were studied by electrochemical measurement, and the reasons for the differences were explored by a series of characterization methods.

2 Experimental

2.1 Catalysts Preparation

The catalysts were prepared by mixed drying and calcination. Firstly, the nitrate and iridium black (Premetek, P40V40) were weighed at a mass ratio of 20:1, after which 20ml deionized water was added for ultrasonic mixing for 30 min. Then the solvent was evaporated and dried, the resulting mixture was placed in a crucible and transferred to a furnace with a temperature control system. The calcinating treatment was performed at 600 °C for 6 h with a heating time of 3 h. The obtained product was centrifuged, washed with deionized water three times, and then dried at 80 °C in a drying oven for 12 h. For comparison, the sample prepared by direct calcination without adding nitrates was used as the contrast.

2.2 Physical Characterization

X-ray diffraction (XRD) data were collected on a Rigaku D/MAX 2500 X-ray diffractometer equipped with a Cu Kα source. The morphology and compositions of the samples were examined by scanning electron microscopy (SEM, SU8020) and transmission

electron microscopy (TEM) on a Tecnai G2 F30 configured with scanning transmission electron microscopy (STEM).

2.3 Electrochemical Analysis

The electrochemical performance (activity and stability) was performed in a typical three-electrode system by using CHI 660E instrument. The catalyst ink was prepared by adding 10 mg catalyst, and 100 μL Nafion (Alfa Aesar, D520 dispersion) into 1 mL ethanol and then ultrasonicating for 30 min. A certain amount of ink was loaded on the surface of the pre-polished glassy carbon electrode (GCE, φ3.0 mm) or carbon paper for drying, and the load of the catalyst is 0.5 mg cm^{-2}. A catalyst-modified GCE or carbon paper was used as the working electrode, and a Pt wire and a saturated calomel electrode (SCE) electrode were used as the counter and reference electrodes, respectively. A 0.5 M H_2SO_4 solution was chosen as the electrolyte, and oxygen was bubbled into the electrolyte for at least 30 min to reach saturation before testing. The saturated calomel electrode was calibrated by the reversible hydrogen electrode (RHE), giving their conversion equation: E(RHE) = E(SCE) + 0.059PH + 0.24 V. The current densities are normalized by the geometric area.

3 Results and Discussion

3.1 Structural Characterizations

Figure 1 shows the X-ray diffraction (XRD) patterns of the nitrate treated catalysts and the contrast. As can be seen from the figures, different phases were formed after calcinating with nitrates with different melting point ranges. As the temperature rises, the crystalline water is removed first at a relatively low temperature and then the decompose of nitrate occurs, the melting point of anhydrous nitrates is shown in the Table 1. As for the $NaNO_3$ and $RbNO_3$ treated catalyst and the contrast, the diffraction peaks correspond well to IrO_2 phase (PDF No. 43-1019, tetragonal, P42/mnm, and a = b = 4.4983 Å, c = 3.1544 Å). Additionally, with the addition of nitrates, XRD diffraction peak widened. As for low melting point $Fe(NO_3)_3{\cdot}9H_2O$ and $La(NO_3)_3{\cdot}6H_2O$, IrO_2 was observed, but the main phase is Fe_2O_3 for $Fe(NO_3)_3{\cdot}9H_2O$ treated catalyst and $La(OH)_3$ for $La(NO_3)_3{\cdot}6H_2O$ treated catalyst. For high melting point nitrates, $Ba(NO_3)_2$ treated catalyst contains IrO_2 and $BaIrO_{2.73}$ phase, and $Mg(NO_3)_2{\cdot}6H_2O$ treated catalyst has IrO_2 and Ir phase. The XRD results proved that different structure may be formed by introducing different melting point nitrate. By introducing nitrates with appropriate melting points, pure IrO_2 can be synthesized.

Table 1. Melting points

	$Fe(NO_3)_3$	$La(NO_3)_3$	$NaNO_3$	$RbNO_3$	$Mg(NO_3)_2$	$Ba(NO_3)_2$
Melting point (°C)	47.2	40	306.8	310	648	592

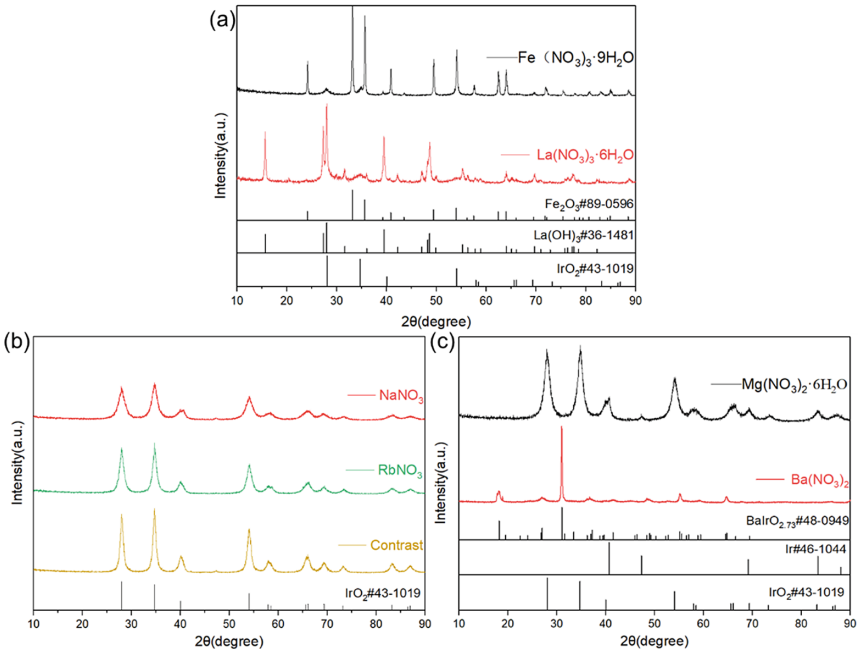

Fig. 1. X-ray diffraction (XRD) patterns of the catalysts.

The SEM images of the synthesized catalysts are shown in Fig. 2. As can be seen from the figures, the contrast showed a nanoparticle morphology. After adding sodium nitrate and rubidium nitrate with moderate melting points, the size of the particles is reduced. In order to further explore the morphology of catalyst, TEM and HRTEM images are shown in Fig. 3. Same as the morphology that observed by SEM, $NaNO_3$, $RbNO_3$ treated catalyst and the contrast has the morphology of nanoparticle, the average particle size of $RbNO_3$ and $NaNO_3$ treated catalyst is about 8 and 11 nm, which is smaller than the contrast (about 16 nm). The HRTEM images of the two catalysts revealed a lattice fringe spacing of 0.318 nm, which correspond to the (1 1 0) plane of IrO_2, which further verified the formation of pure IrO_2.

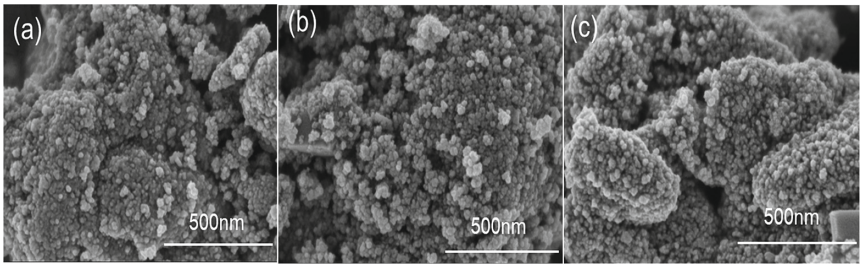

Fig. 2. SEM images of the catalysts. (a) $NaNO_3$, (b) RbO_3, (c) Contrast.

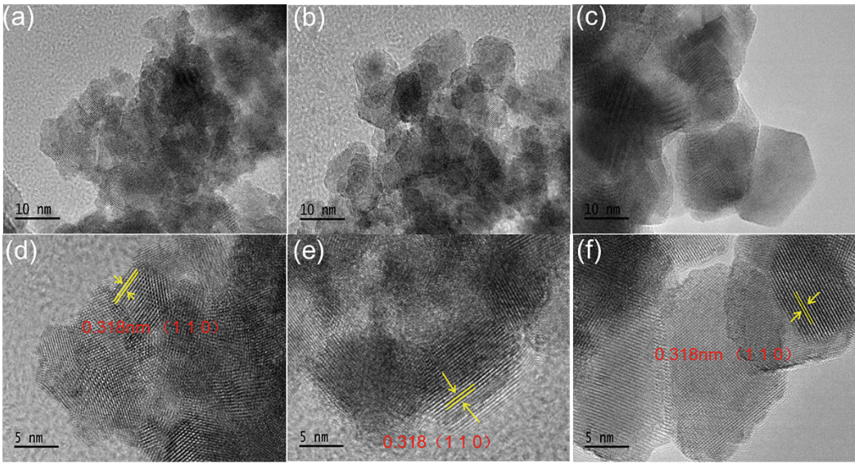

Fig. 3. TEM and HRTEM images of the catalysts. (a, d) $NaNO_3$, (b, e) $RbNO_3$, (c, f) Contrast.

3.2 Electrochemical Characterizations

To investigate the OER performance, the catalysts treated with several nitrates and the contrast were applied as anodic materials in a three-electrode system in 0.5 M H_2SO_4. The mass loading of all samples is 0.5 mg cm^{-2}. The OER activities of all catalysts were evaluated by LSV with 85% iR-compensation. As shown in Fig. 4(a), catalyst treated with $RbNO_3$ displayed a low overpotential(η) of 297.6 mV at 10 $mAcm^{-2}$, which is lower than that of contrast (323.8 mV). Figure 4(b) gives the OER activity at 1.55 V (vs. RHE), the current density of $RbNO_3$ treated catalyst is the highest, about 3 times higher than that of the contrast one. And Nitrates of Fe and La have almost no catalytic performance, which may because the calcinated material is basically oxide or hydroxide.

Tafel slope is a vital parameter for evaluating catalytic activity, as can be seen in Fig. 4(c) (the data is obtained from the LSV plots), these catalysts can be roughly divided into two classes according to the tafel value. Different tafel slope indicates that the catalyst has different rate-determining step (RDS) [16]. The contrast and $RbNO_3$ treated catalyst have a tafel slope approach 40 mV/dec, the $NaNO_3$ treated catalyst has a tafel slope about 60 mV/dec. The $RbNO_3$ treated catalyst's slope is much lower, which indicates a fast reaction kinetics. Moreover, cyclic voltammetry (CV) curves were constructed at different scan rate to obtain double-layer capacitance (C_{dl}), further evaluate electrochemical surface area (ECSA). $RbNO_3$ treated catalyst has a larger C_{dl} (73.32 mF cm^{-2}) than the contrast (23.52 mF cm^{-2}), implying the $RbNO_3$ treated catalyst has more active sites [17]. Due to that ECSA is a parameter to reflect intrinsic activity of the catalyst, it can conclude that $RbNO_3$ treated catalyst has a larger intrinsic catalytic area. Catalysts prepared with nitrates at different melting points showed different OER catalytic performance, $RbNO_3$ and $NaNO_3$ with moderate melting points are more superior, probably because they really act as calcinating aids at the calcinating temperature of 600 °C.

In addition to electrocatalytic activity, stability is another crucial parameter to evaluate the performance of the catalyst. The stability of $RbNO_3$ treated catalyst and the

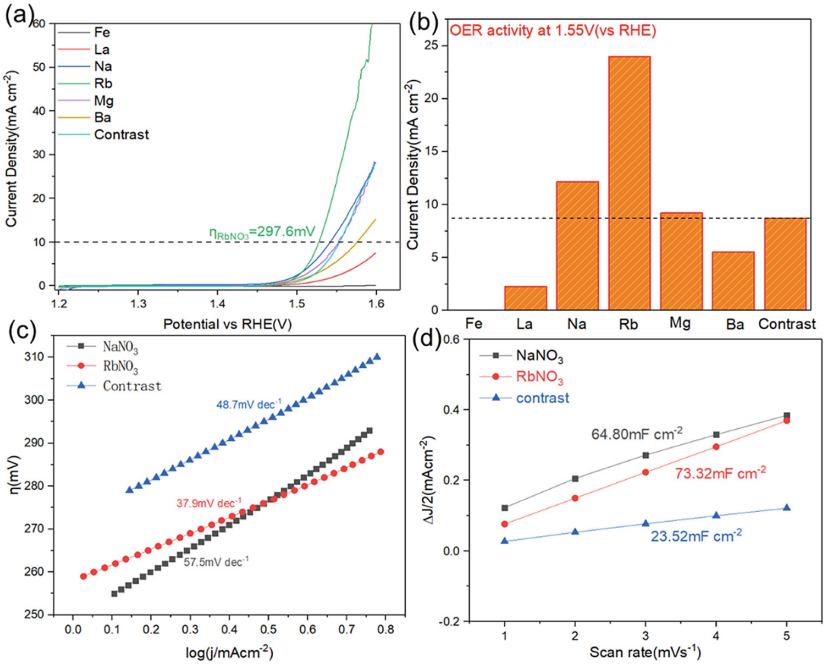

Fig. 4. Electrocatalytic properties of the catalysts (a) a LSV curves in 0.5 M H_2SO_4 solution with 85% iR-compensations. (b) OER activity at 1.55 V versus RHE. (c) Tafel plots obtained from lsv curves. (d) C_{dl} calculated from the obtained CV curves.

contrast were recorded by a chronopotentiometry technique. As can be seen in Fig. 5, the $RbNO_3$ treated catalyst is extremely stable during the 20 h test at 10 $mAcm^{-2}$, having a smaller voltage rise rate than the contrast. Chronopotentiometry test results indicated that the $RbNO_3$ treated catalyst has a good stability in acid media.

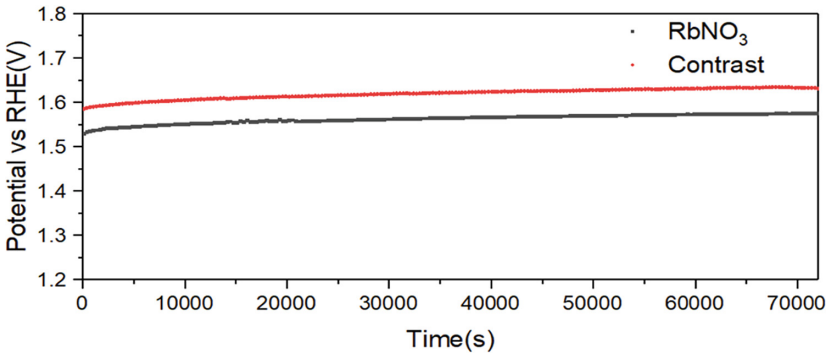

Fig. 5. Chronopotentiometric stability for $RbNO_3$ treated catalyst and the contrast (without iR compensations).

4 Conclusion

To summarize, we synthesized Iridium-based catalyst by introducing several nitrates with different melting point. The simple mixing and calcinating process makes the preparation of iridium-based catalysts easier for industrial operation. By introducing different melting point nitrates, different crystal structure characteristics were produced, which affected the performance of OER. The results revealed that the as-prepared catalysts exhibited different OER catalytic activity. The addition of moderate melting point nitrates facilitated the formation of pure IrO_2, achieving a low overpotential, especially for $RbNO_3$ ($\eta = 297.6$ mV vs. RHE). Meanwhile, $RbNO_3$ treated catalyst showed a long-term stability of 20 h. Sufficiently good catalytic activity and stability of $RbNO_3$ treated catalyst may attribute from the smaller nanoparticle morphology and high ESCA. This work put forward an innovative chlorine-free method to prepare high OER performance iridium-based catalyst, which can be well used in the acid media like PEM water splitting and other energy device applications.

Acknowledgements. This material is based in part upon work supported by the State Grid Corporation of China Science and Technology Funding Project: Research and experimental verification of current density increasing technology for PEM electrolyzer (5419-202158490A-0-5-ZN).

References

1. Midilli, A., Ay, M., Dincer, I., Rosen, M.A.: On hydrogen and hydrogen energy strategies. Renew. Sustain. Energy Rev. **9**(3), 255–271 (2005)
2. Sherif, S.A., Barbir, F., Veziroglu, T.N.: Wind energy and the hydrogen economy—review of the technology. Sol. Energy **78**(5), 647–660 (2005)
3. Dincer, I.: Technical, environmental and exergetic aspects of hydrogen energy systems (2002)
4. Zhou, Z.-H., Sun, W., Zaman, W.Q., Cao, L.-M., Yang, J.: Highly active and stable synergistic Ir–IrO_2 electro-catalyst for oxygen evolution reaction. Chem. Eng. Commun.Commun. **205**(7), 966–974 (2018)
5. Chen, S., et al.: Mn-doped RuO_2 nanocrystals as highly active electrocatalysts for enhanced oxygen evolution in acidic media. ACS Catal.Catal. **10**(2), 1152–1160 (2019)
6. Liu, Y., Wang, C., Lei, Y., Liu, F., Tian, B., Wang, J.: Investigation of high-performance IrO_2 electrocatalysts prepared by Adams method. Int. J. Hydrogen Energy **43**(42), 19460–19467 (2018)
7. Song, S., Zhang, H., Ma, X., Shao, Z., Baker, R.T., Yi, B.: Electrochemical investigation of electrocatalysts for the oxygen evolution reaction in PEM water electrolyzers. Int. J. Hydrogen Energy **33**(19), 4955–4961 (2008)
8. Ardizzone, S., et al.: Physico-chemical characterization of IrO_2–SnO_2 sol-gel nanopowders for electrochemical applications. J. Appl. Electrochem.Electrochem. **39**(11), 2093–2105 (2009)
9. Villullas, F.I.M.-C.H.M., Nascente, P.A.P., Bulhoes, L.O.S.: Sol-Gel Prepared Pt-Modified Oxide Layers: Synthesis,Characterization, and Electrocatalytic Activity (2006)
10. Lee, S.W., Baik, C., Kim, D.-H., Pak, C.: Control of Ir oxidation states to overcome the trade-off between activity and stability for the oxygen evolution reaction. J Power Sour **493** (2021)

11. Li, G., et al.: A hard-template method for the preparation of IrO(2), and its performance in a solid-polymer-electrolyte water electrolyzer. Chemsuschem **5**(5), 858–861 (2012)
12. Wang, L., et al.: Improving the activity and stability of Ir catalysts for PEM electrolyzer anodes by SnO_2: Sb aerogel supports: does V addition play an active role in electrocatalysis? J. Mater. Chem. A **5**(7), 3172–3178 (2017)
13. Huang, F., et al.: Insight into factors influencing thermal oxidation of iridium oxide electrode: thermostatic post-treatment temperature. J. Electrochem. Soc. **169**(3) (2022)
14. Daiane Ferreira da Silva, C., et al.: Oxygen evolution reaction activity and stability benchmarks for supported and unsupported IrO_x electrocatalysts. ACS Catalysis **11**(7), 4107–4116 (2021)
15. Wang, Y., Mumford, K.A., Shen, S., Li, Y.: Effects of low-melting temperature salt (Na_2SO_4) addition on the phase transformation, crystal growth, and chroma of titanium dioxide pigments. Powder Technol. **284**, 204–209 (2015)
16. Liu, Y., et al.: Iridium-containing water-oxidation catalysts in acidic electrolyte. Chin. J. Catal.Catal. **42**(7), 1054–1077 (2021)
17. Huang, H., et al.: Equilibrated $PtIr/IrO_{(x)}$ atomic heterojunctions on ultrafine 1D nanowires enable superior dual-electrocatalysis for overall water splitting. Small **18**(20), e2201333 (2022)

Development and Validation of a 100 kW-Class Fuel Cell System Controller for Passenger Cars

Ze Liu, Sichuan Xu(✉), and Baitao Zhang

School of Automotive Studies, Tongji University, Shanghai 201804, China
xusctj@163.com

Abstract. Fuel cell (FC) vehicle is an important technology route to achieve carbon neutrality in transportation. This paper examines the integration, system control, and performance test of a high-power self-humidifying fuel cell system for passenger cars. Firstly, a high specific power FC system integration scheme is designed, and a highly integrated 100 kW self-humidifying fuel cell system is realized based on the installation requirements of passenger cars. Then, the system controller application layer is developed using Matlab/Simulink and the controller rapid development prototype for complete closed-loop control of each subsystem, such as hydrogen supply, air supply, cooling, and electrical management. Finally, the performance dynamics experiment of the 100 kW FC system is conducted based on the developed system controller. The results show that the developed system controller provides high-quality control effects of operating parameters such as air flow and pressure, hydrogen supply pressure, and cooling water temperature for the stack to meet different operating requirements. The highest efficiency of the system reaches 62%, and the coefficient of variation (C_V) of the cell voltages is controlled to be less than 1%. This study contribute to accelerate the deployment and application of high-power FC systems in passenger cars.

Keywords: Fuel cell system · System controller · Software development · Performance test

1 Introduction

Proton exchange membrane fuel cell is an energy conversion device with high power density, high efficiency, zero pollution, and good low-temperature starting characteristics, which is an important research orientation for the revolution of future automotive power systems [1]. Fuel cell vehicles equipped with fuel cell systems have the advantages of short hydrogen refueling time, long range and good environmental adaptability to become an important technological route to achieve carbon neutrality in new energy vehicles worldwide [2]. The performance and durability of automotive fuel cell systems during service are two extremely important objectives [3].

Currently, the development route of fuel cell systems for passenger cars is moving toward high integration, high power density, and long durability [4]. Toyota motor released its state-of-the-art fuel cell passenger cars in 2014 and 2020 [5–7], The 2nd-generation MIRAI has a volumetric power of up to 5.4 kW/L [6], and system components

H. Sun et al. (Eds.): WHTC 2023, SPPHY 393, pp. 69–75, 2024.
https://doi.org/10.1007/978-981-99-8631-6_7

such as DC/DC converters, auxiliary components, and controller hardware are highly integrated with the electric stack. China's fuel cell vehicle technology is booming but still falls short of the world's most advanced level. FC systems are subject to variable environmental conditions and operating conditions, which is a huge challenge for performance and durability [8]. Innovative designs from the perspective of key materials and structures to achieve performance and endurance improvements from monolithic cells to systems have made significant contributions, but it takes a long lead-time as well as a great expense [9]. The development of superior controllers based on existing materials to improve the net power output, power generation efficiency, and durability of the system has been strongly demanded [10]. The system controller regulates the operating parameters such as airflow, pressure, and temperature at the macroscopic level to improve the electrochemical reaction efficiency and mitigate material degradation such as carbon corrosion, platinum agglomeration, and membrane dry cracking at the microscopic level [11–13]. The automotive fuel cell system controller consists of air supply subsystem, hydrogen supply subsystem, cooling subsystem, electrical management subsystem and monitoring subsystem. Coordinated control of each subsystem to achieve high performance and long life operation of the fuel cell system.

In this study, a 100 kW-class high specific power self-humidification fuel cell system is integrated for the R&D requirements of FC passenger cars. On the developed system bench, the system controller software is developed using Matlab/Simulink and Motohawk rapid development prototype. The developed FC system controller ensures optimal conditions in the FC stack by manipulating system components considering hardware limitations to achieve maximum system performance such as system efficiency and power.

2 FC System Integration

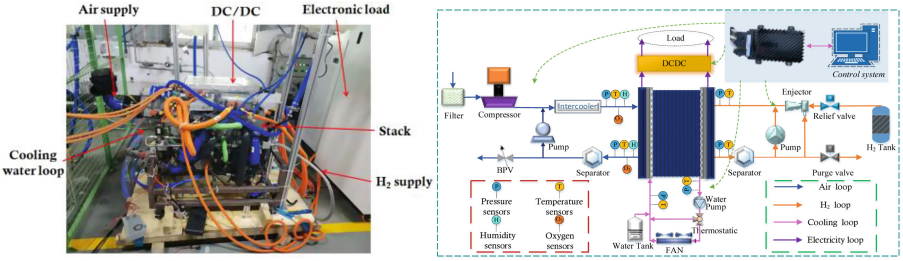

Fig. 1. 100 kW-class high specific power self-humidifying fuel cell system schematic and bench diagram.

The integrated solution of FC system starts from the demand of the whole vehicle, targeting high specific power density, and puts forward the requirements for fuel cell system, power stack, and components level by level. The schematic and the integrated system are shown in Fig. 1. The innovation of the system integration is the removal of the traditional external humidifier and instead the self-humidification function through

material and structural innovation, hydrogen recirculation and hydrogen-air counter-flow configuration, which is significant for the high integration of the whole system.

3 FC System Controller Development

Figure 2 shows the software architecture of the FC controller application layer and the Simulink flow diagram. SECM-112 controller has 33 analog input interfaces for all temperature, pressure, flow and other sensors in the fuel cell system. The system contains 7 CAN signals for air compressor, circulation pump, thermostat, DCDC, PTC, CVM, and water pump. The information interaction between FCU and each component is realized through CAN bus. Some valves and fans involved in the system are driven by low-side output (Boolean or PWM) and H-bridge.

In this developed system controller, setpoint of the FC-system net power, the ambient temperature, and atmospheric pressure are inputs. The calculated system net power is the output as well as the other values in the FC system, the polarization state of the stack, such as current, voltage, the state variables of system, such as flow rate, pressure, temperature, humidity, and oxygen concentration, the actuation values of components, such as compressor speed, pump speed, valve position, and fan speed. According to the vehicle operating conditions, the system state machine consists of nine states: power on, self-test, standby, automatic operation, purge, discharge, shutdown, and emergency stop. Different control calculations are performed within each state, and then the components are driven to achieve the appropriate function. The controllers in Fig. 2 consist of the electric power controller, the monitoring controller, and the actuator controllers for the system components in air, H2, and cooling subsystems. Such a hierarchical and simple controller architecture enables independent investigation of optimal stack operating conditions and hardware specifications.

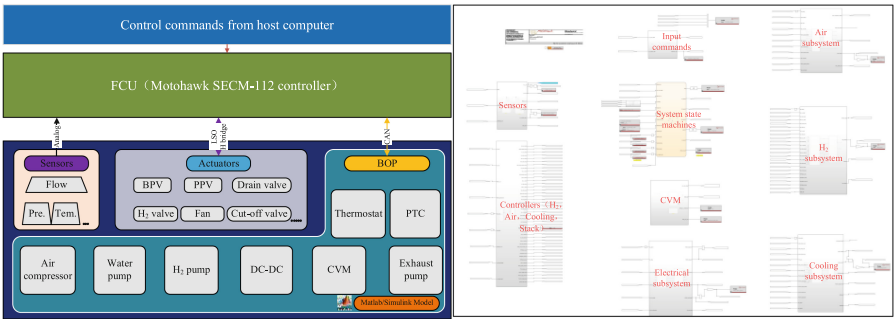

Fig. 2. Software development architecture and closed-loop control procedures for the entire FC system.

In general, the control of the air subsystem is the key to determine the high efficiency, high performance and long life of the FC system [14]. The control goal is to quickly provide precise air flow and pressure to the stack during cyclic load changes to avoid oxygen starvation and excessive air compressor power consumption. In this study, a

decoupled flow and pressure control algorithm is implemented for the air subsystem. The stack current and is given to the pre-determined functions, which are built based on experimental data to achieve the maximum system net power considering the stack power, compressor power loss, and pump power loss. Then, the setpoints of air pressure and flow are is determined. The setpoints of the flow and pressure are converted to the compressor speed and back pressure valve opening by a double PI controller including the supplemental functions of integral anti-windup and feedforward compensation methods for the stable operation.

Figure 3 shows the results of the close-loop setpoint tracking performance of the air flow rate and pressure by a series of step load profile. The current operation curves are shown in Fig. 5(a), and the results show that the DC/DC responds to the set current command almost indistinguishably, indicating that the reactant supply adequately meets the current loading demand. It is also confirmed that the air flow rate could trace the setpoint within an acceptable deviation less than ± 2.5 g/s as shown in Fig. 5 (b), the OER fluctuation range within 0.2 as shown in Fig. 5(c), and pressure fluctuation within ± 1.5kPa. It indicates that the error effect is within the acceptable range and meets the practical application requirements considering the influence of sensors and controllers in acquisition, measurement, and noise.

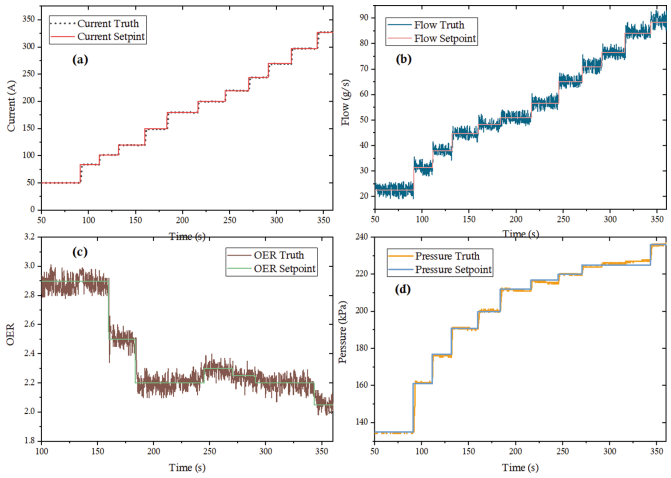

Fig. 3. Performance evaluation of closed-loop setpoint tracking with decoupled air flow and pressure.

4 FC System Performance Discussion

4.1 System Power and Efficiency

The developed system control algorithm is written into the fuel cell system controller, and performance experiments of the 100kW system are conducted. Figure 4 shows that the average output voltage of the individual cell is 0.62 V when the current density is

loaded to 1781 mA/cm^2, and the output power of the stack reaches a peak of 120.2 kW, at which the peak net power of the system reaches 97.8 kW and the power consumption of the auxiliary components accounts for 18.6%.With the rise of the net power of the system, the efficiency shows a decreasing trend. The maximum efficiency of the system reaches 62%, which is the advanced level of current FC systems for passenger cars.

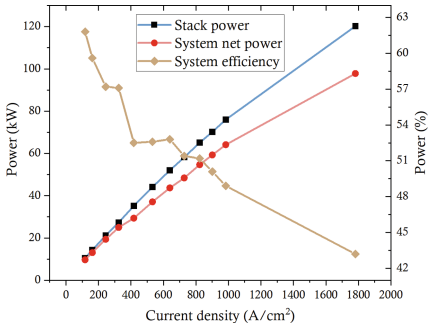

Fig. 4. 100 kW-class FC system output performance analysis with the implementation of the developed system controller.

4.2 Stack Consistency

Figure 5 shows the cell voltage coefficient of variation (C_v) during the load variation. The trend of C_v is observed during the period when the stack is loaded from start-up to 70 kW. In the start-up phase (around 0 s), the instability of the cell voltage is due to the lagging response of the hydrogen and air supply, which results in a C_v of 4.5%. Afterwards, the voltage stabilizes quickly and C_v drops rapidly. The C_v is kept within 1% during the entire load variation, which is a really bright result and provides the basis for the high reliability and durability of the system operation. After 2100 s, the system enters into the shutdown procedure, the reactants are cut off and start discharging, thus C_v increases.

5 Conclusions

In this paper, we developed a system controller for high efficiency and long durability on an integrated 100 kW passenger car fuel cell system. The complete control program is developed in conjunction with Matlab/Simulink and the Motohamk rapid control prototype. The closed-loop control performance of the controller is discussed, represented by the air subsystem. With the implementation of the developed FC system controller, the dynamic performance of the entire system is investigated. The results show that the FC system demonstrates excellent potential in terms of net power, system efficiency, and consistency. The implementation of this study is important for advancing the commercialization of fuel cell passenger vehicles.

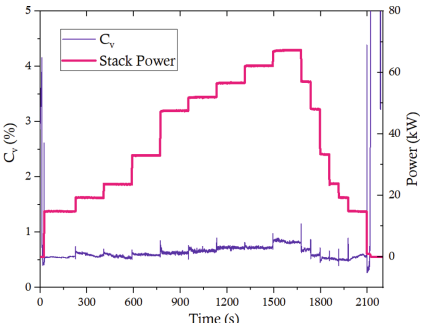

Fig. 5. Consistency analysis of 100 kW-class FC system under dynamic conditions output performance analysis with the implementation of the developed system controller.

References

1. Wu, D., Peng, C., Yin, C., Tang, H.: Review of system integration and control of proton exchange membrane fuel cells. Electrochem. Energy Rev. **3**(3), 466–505 (2020)
2. Chuan, F.A.N.G., Dian, Y.U.A.N., Yangbin, S.H.A.O., et al.: Technical breakthrough of new generation fuel cell system for winter Olympics application environment. Automot. Eng.. Eng. **44**(04), 535–544 (2022)
3. Pengcheng, L.I.U., Sichuan, X.U.: Experimental study on dynamic response performance for PEMFC stack. Chem. Industry Eng. Progress **40**(06), 3172–3180 (2021)
4. Wang, J.: System integration, durability and reliability of fuel cells: challenges and solutions. Appl. Energy **189**, 460–479 (2017)
5. Hasegawa, T., Imanishi, H., Nada, M., Ikogi, Y.: Development of the Fuel Cell System in the Mirai FCV. SAE Technical Paper Series (2016)
6. Itoga, M., Hamada, S., Mizuno, S., Nishiumi, H., Murata, K., Tonuma, T.: Development of Fuel Cell Stack for New FCV. SAE Technical Paper Series (2016)
7. Yoshizumi, T., Kubo, H., Okumura, M.: Development of High-Performance FC Stack for the New MIRAI. SAE Technical Paper Series (2021)
8. Zhang, B., Wang, X., Gong, D., Xu, S.: Experimental analysis of the performance of the air supply system in a 120 kW polymer electrolyte membrane fuel cell system. Int. J. Hydrogen Energy **47**(50), 21417–21434 (2022)
9. Baolian, Y.I., Ming, H.O.U.: Solutions for the durability of fuel cells in vehicle applications. J. Autom. Safety Energy **2**(02), 91–100 (2011)
10. Wang, Y., Wang, K., Zhong, S., et al.: Research progress on durability enhancement-oriented electric control technology of automotive fuel cell system. Autom. Eng. **44**(04), 545–559 (2022)
11. Daud, W.R.W., Rosli, R.E., Majlan, E.H., Hamid, S.A.A., Mohamed, R., Husaini, T.: PEM fuel cell system control: a review. Renew. Energy **113**, 620–638 (2017)
12. Yang, B., Li, J., Li, Y., Guo, Z., Zeng, K., Shu, H., et al.: A critical survey of proton exchange membrane fuel cell system control: summaries, advances, and perspectives. Int. J. Hydrogen Energy **47**(17), 9986–10020 (2022)
13. Li, Q., Liu, Z., Sun, Y., Yang, S., Deng, C.: A review on temperature control of proton exchange membrane fuel cells. Processes **9**(2) (2021)
14. Liu, Z., Zhang, B., Xu, S.: Research on air mass flow-pressure combined control and dynamic performance of fuel cell system for vehicles application. Appl. Energy **309** (2022)

Dual-Layer Characteristic Temperature Model for AWES Dynamic Thermal Detection Based on IR

Zixuan Shangguan[1,2] and Cunman Zhang[1,2(✉)]

[1] School of Automotive Studies, Tongji University, Shanghai 201804, China
zhangcunman@tongji.edu.cn
[2] Clean Energy Automotive Engineering Center, Tongji University, Shanghai 201804, China

Abstract. With the increasing application of the AWES, the dynamic thermal detection of the electrolyzer inspires great interest. The dimension of dynamic thermal detection of the AWES is currently limited to only the inlet and outlet temperatures. This study proposes a dual-layer characteristics temperature model for AWES temperature monitoring. The DLCT model deals with the difficulty of extracting characteristic temperature with its first layer of multi gaussian distribution regression. The second layer model can clarify the disturbing signal using linear regression and provide a quantized temperature distribution pattern of the surface temperature. This DLCT model does not require additional modifications to the AWES, nor any temperature sensor inside or on its surface. With the DLCT model implemented during dynamic operation, the AWES can be more comprehensive monitored, and more insights can be gathered regarding the DLCT for better thermal uniformity.

Keywords: Alkaline electrolyzer · Dynamic thermal detection · Characteristic temperature · Multi gaussian regression · Machine learning

1 Introduction

Hydrogen energy system can replace the fossil fuel system as a solution for many global environmental issues, and water-electrolysis-based hydrogen production has gain its maturity in term of both technology [1] and economic [2]. The alkaline water electrolysis system (AWES) is one of the most widely used, technically mature and cost-effective high-power water electrolysis hydrogen production technology [1]. The AWES is considered to be able to provide medium term large-scale Renewable Energy-based green hydrogen for the hydrogen energy system [3]. However, the fluctuating power output of the renewable power system requires AWES to operate under similar unsteady conditions, which brings up the necessity of thermal detection over AWES for more detailed dynamic response. As status quo, in the operation and maintenance of AWES, the only thermal parameters recorded are normally inlet and outlet temperature for the electrolyzer.

H. Sun et al. (Eds.): WHTC 2023, SPPHY 393, pp. 76–82, 2024.
https://doi.org/10.1007/978-981-99-8631-6_8

For the dynamic thermal detection of AWES, only recording the inlet and outlet temperature means only acquiring the temperature of the inlet fluid and the gas-liquid mixture at two positions on the end-face of the electrolyzer. The temperature of the bulk structure is not recorded, neither on the surface nor from the inside. Such a lack of understanding of dynamic thermal detection leads to the inability for the uniformity of its temperature distribution and may even cause the ignorance of its inside hot spots. In addition, the limit of indicative temperature also leads to over-simplification of the evaluation criteria of the electrolyzer and brings difficulties in collecting sufficient temperature distribution data over the dynamic operating conditions. In conclusion, only recording the inlet and outlet temperature of the electrolyzer makes it difficult to understand the thermal characteristics of the AWES, and, also, to provide more improvement guidance as well as more analysis dimensions for the AWES, such as multi-physics approaches [4, 5].

Hence, this study puts forward the dual-layer characteristic temperature (DLCT) model, which is composed of two layers of the characteristic temperature (CT) regression analysis over the side surface of the electrolyzer.

2 Modeling Method

As demonstrated in Fig. 1(a), the IR recorder is stationed to the side of the electrolyzer, the captured IR image is drawn in Fig. 1 (b). As can be seen, due to characteristics of the lye-gas mixture in the electrolyzer [5], the temperature is higher in the upper region of the electrolyzer. The temperature of the metal plate (70.4 °C) is quite higher than the gasket region (57.52 °C) in its adjacency. This unevenness is the first problem to be dealt with, in collecting the CT of the electrolyzer surface. And there are the current collectors with higher temperatures near the bottom, the CT analysis must be able to distinguish these disturbing signals.

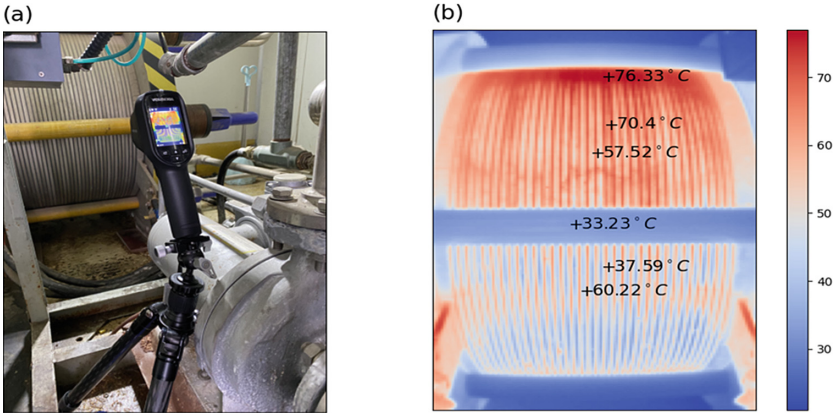

Fig. 1. (a) The apparatus of the infrared image collection, and (b) the recorded IR image with temperature noted at different locations.

The second problem comes with the obstacles and auxiliary parts on the electrolyzer. As in Fig. 1 (b), the clamping bolts of the electrolyzer are positioned at the top, middle and the bottom blocking the direction detection of the surface temperature. With larger rated power, the AWES grows in size, and the number of clamping bolts also grows, leading to more blocked surface area. And finally, the model should filter out the obstacles and provide the overall surface temperature distribution with quantized parameters.

This study aims to tackle these two problems with two layers of CT analysis model. The first layer CT model can extract the CT of the metal structure within the segment of the IR image, implemented with MGD regression. The second layer model can clarify the disturbing signal using linear regression, resume the surface temperature over the side of the electrolyzer and provide an overall quantized temperature distribution pattern of the surface temperature of the electrolyzer. This DLCT model does not require additional modifications to the AWES, nor does it attach any temperature sensor inside or on the surface of the electrolyzer.

3 First-Layer Characteristic Temperature Model

The IR image is first segmented as in Fig. 2 (a). The image is segmented into 12 vertical segments as demonstration, and the IR image can also be horizontally segmented or divided into a mesh grid.

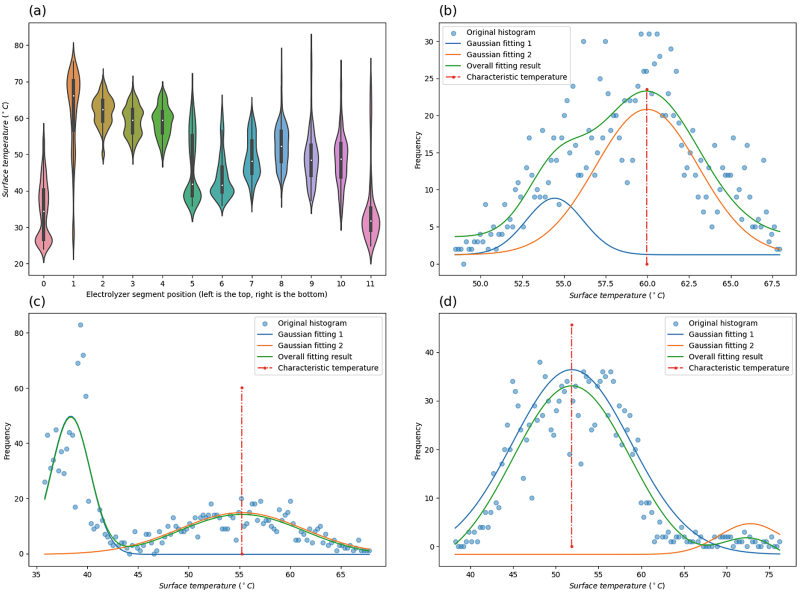

Fig. 2. (a) The violin graphs of each segment in an IR image, (b) the temperature distribution and MGD analysis results of segment No. 4, (c) the temperature distribution and MGD analysis results of segment No. 5, and (d) the temperature distribution and MGD analysis results of segment No. 8.

3.1 Multi-Gaussian Distribution Analysis

Here, MGD regression is performed to extract the CT within each segment. The gaussian distribution is also called the normal distribution [6]. In this study, for convenience, the gaussian distribution is converted to the frequency of occurrence, rather than probability. As a result, the temperature gaussian distribution formula can be changed into:

$$h(t) = h \times e^{-\frac{(t-t_0)^2}{2w^2}} + h_0 \tag{1}$$

In which, t represents temperature, $h(t)$ represents the frequency of occurrence of a certain temperature within in the adjacency of t. h represents the height of the frequency peak and is used to determine the significance of this distribution. t_0 is the expectation of the distribution, and the potential CT in the segment. w represents the width of the gaussian distribution and the h_0 represents the bottom noise of the segment.

However, as in Fig. 2 (b), (c), (d) the complexity of the distribution within on segment does not fit a single gaussian distribution. Hence, this study combines several gaussian distributions into the MGD model [7]. Within each segment, the distribution of the temperature signals can be described by:

$$h_i(t) = h_1 \times e^{-\frac{(t-t_{0,1})^2}{2w_1^2}} + h_2 \times e^{-\frac{(t-t_{0,2})^2}{2w_2^2}} + h_3 \times e^{-\frac{(t-t_{0,3})^2}{2w_3^2}} + h_0 \tag{2}$$

$(h_1, t_{0,1}, w_1)$, $(h_2, t_{0,2}, w_2)$ and $(h_3, t_{0,3}, w_3)$ three sets of parameters represent the relevant parameters of three Gaussian distributions, among which $t_{0,1}$, $t_{0,2}$, $t_{0,3}$ are the three potential CT of the region. In this paper, SciPy based on python is used to carry out the regression of the above equation [8].

3.2 First Layer CT Model Results

The result CTs within each segment come from the actual surface of the electrolyzer. For in Fig. 2 (b) and compared with Fig. 1 (b), the higher CT represents the temperature of the metal plate, whereas the lower CT represents the gasket. Likewise, the clamping bolts, and the current collectors, can also be screened out of the CTs. Finally, the CT with higher height of frequency of occurrence is chosen as the CT of the temperature of this segment. Likewise, in Fig. 2 (c), the lower, however, more concentrated represents the clamping bolts at the middle in Fig. 1 (b), and the peak with higher temperature is the surface of the electrolyzer, which is recognized as the CT of the segment. And in the Fig. 2 (d), there are also two peaks in the figure. The peak with higher CT represents the hot current collectors near the bottom of the IR image, and the lower peak represents the surface temperature of the electrolyzer and should be acknowledged as the CT of the segment.

4 Second-Layer Characteristic Temperature Model

4.1 Regression Method

The potential CTs of each segment of the IR image are plotted in the Fig. 3(a), and CTs have been selected. In the top and bottom segment, there is no CT of the surface because a large proportion of the image is taken up by the clamping bolts and background. Rest

of the segments have CT on the surface, except segment No. 6 where the clamping bolt is dominant. And the linear relationship between CTs on the electrolyzer surface and segment positions is explicit.

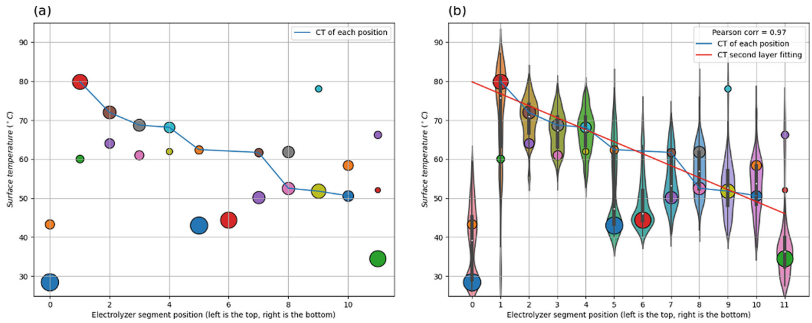

Fig. 3. **(a)** The potential CTs of each segment, and (b) the result of the second layer CT model.

Hence linear regression should be applied to analyze the distribution pattern. The temperature distribution of each segment on the electrolyzer surface can be expressed as:

$$T_i = a \times x_i + b, i \in [1, n] \tag{3}$$

In which, T_i represents the CT of a certain segment, $x_i \in N$ represents the position of the segment, and $a, b \in R$ are the parameters for the temperature distribution pattern. a Stands for the slope of the linear equation and b for the intercept. This study also employs the built-in method from SciPy to conduct the second layer CT model.

4.2 Second Layer CT Model Results

The Pearson correlation is 0.97, which means the segment position has a very strong linear relationship with the CT [9]. As shown in the Fig. 3(b), the slope of the linear relationship between CT and segment position is − 3.06, which means every time we check one segment just beneath another, the CT will likely be 3.06 °C lower. The intercept of the equation is 79.80 °C, which means based on the estimation of the second-layer model, the CT on the top of the electrolyzer surface will be near 80 °C. And the CT s of any other segments hindered by obstacles can be derived from this linear relationship.

More importantly, the second-layer CT model provides us with the quantized temperature distribution pattern on the electrolyzer surface, which can be introduced to examine the thermal uniformity of the electrolyzer design and operation. The slope in linear regression can describe the significance of the temperature variation of the electrolyzer, and the intercept can predict the maximum temperature on the electrolyzer surface.

5 Conclusion

In summary, this study introduces the DLCT model to deal with two major problems of AWES dynamic thermal detection, the extraction of characteristic temperatures and hinderance of auxiliaries. The first layer employs MGD regression to evaluate the segment temperature and produces multiple potential CTs. The CT is then selected for each segment, and fed into the second layer, where linear regression is implemented to provide quantized distribution pattern.

And the results of the DLCT not only provide global AWES CT, but also quantized temperature distribution pattern, which will bring in richer dimensions for detecting and optimizing the dynamic operation of the electrolyzer. As a result, the AWES can be more comprehensive monitored during dynamic operation, and more guidance can be gathered with the DLCT for better thermal uniformity.

References

1. Bodner, M., Hofer, A., Hacker, V.: H2 generation from alkaline electrolyzer. Wiley Interdisc. Rev. Energy Environ. **4**, 365–381 (2015)
2. Bowen Yang, R.Z., Zhang, C.: The techo-economic evaluation of hydrogen production cost towards anion exchange membrane electrolyzer. In: 23rd World Hydrogen Energy Conference Proceedings; Track **15**, 1376–1378 (2022)
3. Chang Zhang, J.W., Ren, Z., Yu, Z., Wang, P.: Wind-powered 250 kW electrolyzer for dynamic hydrogen production: a pilot study. Int. J. Hydrogen Energy **46**, 34550–34564 (2021)
4. Le Bideau, D., Mandin, P., Benbouzid, M., Kim, M., Sellier, M.: Review of necessary thermophysical properties and their sensivities with temperature and electrolyte mass fractions for alkaline water electrolysis multiphysics modelling. Int. J. Hydrogen Energy **44**, 4553–4569 (2019)
5. Hammoudi, M., Henao, C., Agbossou, K., Dubé, Y., Doumbia, M.L.: New multi-physics approach for modelling and design of alkaline electrolyzers. Int. J. Hydrogen Energy **37**, 13895–13913 (2012)
6. Do, C.B.: The multivariate Gaussian distribution. Section Notes, Lecture on Machine Learning, CS, 229 (2008)
7. Ahrendt, P.: The Multivariate Gaussian Probability Distribution. Technical University of Denmark, Tech Report, 203 (2005)
8. Virtanen, P., Gommers, R., Oliphant, T.E., Haberland, M., Reddy, T., Cournapeau, D., et al.: SciPy 1.0: fundamental algorithms for scientific computing in python. Nat. Methods **17**, 261–272 (2020)
9. Benesty, J., Chen, J., Huang, Y., Cohen, I.: Pearson Correlation Coefficient. Noise Reduction in Speech Processing, pp. 1–4. Springer (2009)

Process Simulation of Green Ammonia Production Via Sorption-Enhanced Gasification of Biomass

Godknows Dziva and Liang Zeng(✉)

Key Laboratory for Green Chemical Technology of the Ministry of Education, School of Chemical Engineering and Technology, Tianjin University, Tianjin 300072, China
zengl@tju.edu.cn

Abstract. Ammonia is a crucial hydrogen carrier. This paper explores small-scale green ammonia production from two-stage sorption-enhanced gasification of biomass. ASPEN Plus was used to calculate the mass and energy balance of two novel process designs; configuration (a) employs fractional flue gas recycling to supply nitrogen for producing carbon-neutral ammonia without air separation, and configuration (b) uses air separation to produce carbon-negative ammonia by efficiently capturing CO_2. The mass balance shows that the ammonia yield of configuration (a) is about 5% higher than that of configuration (b). The energy analysis shows that additional biomass fed to the combustor is the primary energy penalty in configuration (a), while the primary energy penalty in configuration (b) is from the electricity consumption by the ASU and CO_2 compressor. The energy penalty for configuration (a) is considerably higher than that for configuration (b); hence, configuration (b) has lower energy consumption.(36.4 GJ/t NH_3 vs. 40.2 GJ/t NH_3). Overall, configuration (b) is superior to configuration (a) from a techno-environmental standpoint.

Keywords: Green ammonia · Bioenergy · Carbon capture · Process simulation

1 Introduction

About 27% of the hydrogen produced annually is used for producing ammonia via the Haber-Bosch process [1]. Ammonia is a vital hydrogen carrier due to its high hydrogen content(18 wt%) and relatively low energy demand for liquefaction. The maturity and flexibility of ammonia supply chains are set to make ammonia a key player in low-carbon economies [2]. Currently, blue or grey hydrogen from coal and natural gas and nitrogen air separation is used for ammonia synthesis. Hydrogen production accounts for most of the energy consumed in ammonia plants. Existing ammonia production routes have the following shortcomings: (i) high carbon footprint, accounting for up to 1.6% of annual global CO_2 emissions [3], (ii) rigorous and energy-intensive syngas cleanup to meet the standards required for the synthesis loop.

Green ammonia from biomass gasification has recently received interest as a pathway for lowering the carbon footprint. Carbon-negative ammonia can be produced from

H. Sun et al. (Eds.): WHTC 2023, SPPHY 393, pp. 83–89, 2024.
https://doi.org/10.1007/978-981-99-8631-6_9

biomass when carbon capture is employed. This study evaluates simplified and efficient biomass conversion to ammonia using two-stage sorption-enhanced gasification (SEG). Two processes for small-scale, decentralized ammonia production are analyzed using ASPEN Plus simulation. One process produces carbon-neutral ammonia, while the other produces negative-carbon ammonia by capturing CO_2.

2 Process Design and Simulation

2.1 Process Design

The proposed process is based on two-stage SEG of biomass. As shown in Fig. 1, the first stage involves steam gasification of biomass in a fluidized bed gasifier at 650–750 °C. Then the product gas from the gasifier undergoes sorption-enhanced reforming at 550–650 °C in an autothermal moving bed reformer with gas-solid countercurrent contacting. Continuous in situ separation of CO_2 by CaO (carbonation) in the gasifier and reformer promotes the WGS, resulting in a hydrogen-rich product gas with > 90%mol hydrogen(dry basis) [4–6]. CaO also catalyzes tar reforming. The $CaCO_3$ from the gasifier and reformer is decomposed back to CaO in a fluidized bed combustor using heat from char and supplementary fuel combustion.

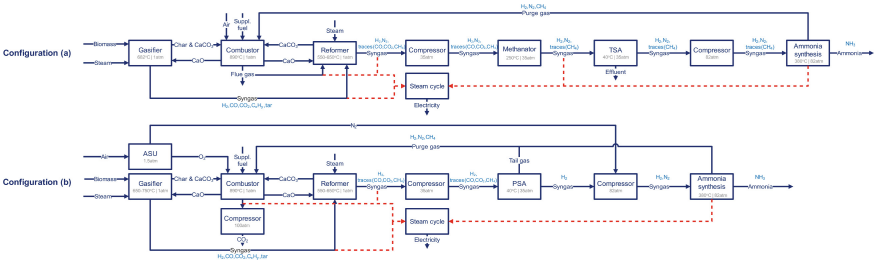

Fig. 1. Process flow diagrams of ammonia production using two-stage SEG of biomass; configuration (a) carbon-neutral ammonia synthesis; configuration (b) carbon-negative ammonia synthesis.

Figure 1 shows two routes for ammonia production. In configuration (a), part of the flue gas (mainly N_2 and CO_2) is introduced into the moving bed reformer, where CaO recaptures CO_2, and the N_2 required for ammonia synthesis is released into the syngas. The size of the flue gas recycle is adjusted such that H_2/N_2 is close to 3. Employing a flue gas recycle to supply nitrogen takes advantage of in-situ carbon capture by CaO to separate N_2 and CO_2, effectively eliminating the need for an air separation unit (ASU). After compression, methanation and temperature-swing adsorption (TSA) convert and remove oxygen compounds that can poison ammonia synthesis catalysts. Configuration (b) uses an ASU to supply nitrogen. Oxygen is used for combustion to capture CO_2. After compression, pressure-swing adsorption (PSA) removes almost all traces to produce pure hydrogen. The PSA tail gas supplement fuel for the combustor. The low inert content of syngas lessens the purge size for configuration (b) compared to configuration (a).

Ammonia synthesis uses a low-pressure loop (82 atm) based on the ICI leading concept for small-scale, modular ammonia production [7]. The purge gas from the synthesis loop supplements fuel for the combustor in both configurations. Waste heat recovered throughout the plant generates electricity in a three-stage steam turbine [8]. Steam for gasification and reforming is drawn after the medium-pressure turbine.

2.2 ASPEN Plus Simulation

This study considered a decentralized small-scale plant processing at least 128 tonnes per day (t/d) of dried wheat stalks (Table 1). This translates to 24 MWth of fuel fed to the gasifier. The mass and energy balance of the two designs was calculated using ASPEN Plus under steady-state conditions. Physical properties and thermodynamic relationships were calculated using steam tables and the Peng–Robinson equation of state with the Boston-Mathias modifications (PR-BM).

The operating parameters of each unit operation are shown in Fig. 1. The simulation used four-stage compressors with inter-stage cooling. The isentropic and mechanical efficiency of the compressors, pumps and turbines were assumed to be 80% and 95%, respectively. A 10 °C minimum temperature approach was assumed for all heat exchangers. The hydrogen recovery rate during PSA was assumed to be 85% [9]. Water removal by TSA is assumed to be 99.99% [10].

Table 1. Composition of wheat stalks biomass (dry basis) [11]

Proximate analysis (wt%)				Ultimate analysis (wt%)					Heating value (MJ/kg)	
Moisture	Ash	Volatiles	Fixed carbon	C	H	O	N	S	LHV	HHV
6.21	7.61	73.3	19.09	45.63	5.44	40.37	0.73	0.22	16.36	17.55

3 Results and Discussion

3.1 Mass Balance

The mass balance of the two configurations is summarized in Table 2. The flow rates and product distribution for the gasifier are identical for both processes. 53.1 t/d (40,545 Nm^3/h) of syngas are produced from the gasifier. The product gas composition is comparable to pilot-scale results for SEG [12]. The steam fed to the reformer is also equal due to identical raw syngas compositions. Hence, almost equivalent hydrogen yields are obtained from both cases. The calcium oxide flow rate of configuration (a) is double that of configuration (b) due to the additional CO_2 introduced by recycling 28% of the flue gas to the reformer. This higher sorbent load for configuration (a) results in a supplementary fuel demand for the combustor that is nearly six times higher than in configuration (b). Configuration (a) emits 3.1 tonnes of CO_2 per tonne of NH_3, while configuration (b) captures $> 99\%$ of the total carbon fed into the process.

After syngas cleanup, the syngas contains almost no oxygen compounds. Around 380 t/d and 353 t/d of syngas are fed to the synthesis loop of configuration (a) and (b), respectively. The hydrogen conversion in the synthesis loop is slightly higher for configuration (b) because of a lower inert content (6.4% vs. 1%). The overall ammonia yield from configuration (a) is 5% higher than from configuration (b) due to the higher syngas feed in the former.

Table 2. Mass balance of key unit operations

Unit operation	Parameter	Configuration (a)	Configuration (b)
Gasifier	Biomass feed [t/d]	128	128
	Steam flow rate [t/d]	35	35
	CaO flow rate [t/d]	132	132
	Product gas composition [mol%, dry basis]	75.4% H_2, 14.1% CO, 3.4% CO_2, 6.5% CH_4, 0.4% N_2	75.4% H_2, 14.1% CO, 3.4% CO_2, 6.5% CH_4, 0.4% N_2
Reformer	Steam flow rate [t/d]	69.2	69.2
	CaO flow rate [t/d]	242.3	121.1
	Product gas composition [mol%, dry basis]	75.1% H_2, 23.8% N_2, 0.3% CO, 0.3% CO_2, 0.1% CH_4	98.4% H_2, 0.3% CO, 0.3% CO_2, 0.06% CH_4
Combustor	Supplementary biomass fuel [t/d]	29.3	5.4
	Flue gas recycle [%]	27.7	0
	Product gas composition [dry basis]	52.4% N_2, 45.4% CO_2, 1.3% O_2	95.8% CO_2, 3.3% N_2, 0.8% O_2
	Specific CO_{2e} emissions [t CO_2/t NH_3]	3.1	0
	Carbon capture rate [%]	0	99.99
Ammonia synthesis	H_2 conversion each pass [%]	18.4	18.8
	Purge rate [%]	2	0.1
	Ammonia yield [t/d]	65.6	62.5

3.2 Energy Balance

Table 3 shows the overall energy balance for the two process designs. As seen in the material balance (Table 2), the supplementary fuel demand for configuration (a) is higher;

thus, the total biomass input of configuration (a) is about 16% higher than for configuration (b). Meanwhile, the electricity demand for configuration (b) is 40% higher than for configuration (b). The relatively higher power demand is mainly due to electricity used in the ASU and CO_2 compressor. The overall energy input of configuration (a) is higher than configuration (b).

The energy output in ammonia is higher for configuration (a) due to a higher overall yield (see Table 2). As shown in Fig. 1, configuration (a) has an extra stream available for waste heat recovery. Hence, configuration (a) generates more electricity than configuration (b). It should be noted both processes have a power deficit; 300 kW_e for configuration (a) and 2341 kW_e for configuration (b).

The biomass-to-ammonia efficiency of configuration (a) is relatively lower due to its high biomass requirement. Likewise, the biomass-to-ammonia + power efficiency of configuration (b) is relatively lower due to its high power demand. Therefore, the primary energy penalty in configuration (a) is from the combustor, while the primary energy penalty in configuration (b) is from the air separation and CO_2 compression.

The efficiency of ammonia production is typically measured by the net energy consumption per tonne of ammonia. As shown in Table 3, configuration (a) consumes 40.2 GJ to produce one tonne of ammonia. Configuration (b) consumes 36.4 GJ per tonne of ammonia. This indicates that the energy penalty of configuration (a) is higher than configuration (b). Therefore, better energy efficiency clearly makes configuration (b) the superior option.

It is worth mentioning that the energy consumption of the two configurations is significantly lower than processes based on coal gasification (42 GJ/t NH_3), electrolysis (43 GJ/t NH_3), biogas reforming (42 GJ/t NH_3) and biomass oxy-gasification (58 GJ/t NH_3) [13]. However, the proposed processes remain inferior to modern methane reforming plants (28 GJ/t NH_3).

4 Conclusions

This study used ASPEN Plus to analyze the mass and energy balance of two novel designs for small-scale green ammonia production using two-stage SEG of biomass. Configuration (a) uses flue gas recycling to produce carbon-neutral ammonia without air separation. Configuration (b) uses air separation to produce carbon-negative by capturing CO_2.

Results showed that the syngas and ammonia yield of configuration (a) is higher than configuration (b). Configuration (a) emits 3.1 tonnes of CO_2 per tonne of NH_3, while configuration (b) captures > 99% of the total carbon fed into the process. The primary energy penalty in configuration (a) is from additional fuel for sorbent regeneration, while the primary energy penalty in configuration (b) is from the ASU and CO_2 compressor. The energy penalty for configuration (b) is lower than for configuration (a); thus, configuration (b) retains a higher energy efficiency. Therefore, in addition to a lower carbon footprint, better energy efficiency makes configuration (b) the superior process.

Table 3. Overall energy balance of the process

	Configuration (a)	Configuration (b)
Energy input		
Biomass input [kWth, LHV basis]	30,182	25,251
Gasifier fuel	24,226	24,226
Combustor supplementary fuel	5956	1025
Electricity input [kW_e]	2837	4019
Air compressor	298	–
Water pumps	41	29
ASU	–	681
CO_2 compressor	–	964
Syngas compressors	2026	1675
Miscellaneous (20% of total power input)	473	670
Total energy input [kW]	33,019	29,270
Energy output		
Ammonia [kWth, LHV basis]	14,122	13,464
Electricity generated [kW_e]	2532	1678
Total energy output [kW]	16,655	15,142
Efficiency		
Biomass-to-ammonia efficiency [%]	46.8	53.3
Biomass-to-ammonia + power efficiency [%]	45.8	44.1
Energy consumption [GJ/t NH_3]	40.2	36.4

References

1. IEA: The Future of Hydrogen-Seizing Today's Opportunities (2019)
2. Thomas, G., Parks, G.: Potential Roles of Ammonia in a Hydrogen Economy (2006)
3. Rouwenhorst, K.H.R., Krzywda, P.M., Benes, N.E., et al.: Ammonia Production Technologies. Techno-Economic Challenges of Green Ammonia as an Energy Vector, pp. 41–83 (2021)
4. Chen, S., Wang, D., Xue, Z., et al.: Calcium looping gasification for high-concentration hydrogen production with CO_2 capture in a novel compact fluidized bed: Simulation and operation requirements. Int. J. Hydrogen Energy **36**(8), 4887–4899 (2011)
5. Zhao, H., Song, G., Shen, L., et al.: Novel technique route of coal gasification with CO_2 capture using CaO sorbents via three-stage interconnected fluidized beds. Energy Fuels **26**(5), 2934–2941 (2012)
6. Li, B., Fabrice Magoua Mbeugang, C., Liu, D., et al.: Simulation of sorption enhanced staged gasification of biomass for hydrogen production in the presence of calcium oxide. Int. J. Hydrogen Energy **45**(51), 26855–26864 (2020)
7. Arora, P., Sharma, I., Hoadley, A., et al.: Remote, small-scale, 'greener' routes of ammonia production. J. Clean. Prod. **199**, 177–192 (2018)

8. Spath, P., Aden, A., Eggeman, T., et al.: Biomass to Hydrogen Production Detailed Design and Economics Utilizing the Battelle Columbus Laboratory Indirectly-Heated Gasifier (2005)
9. Luberti, M., Ahn, H.: Review of Polybed pressure swing adsorption for hydrogen purification. Int. J. Hydrogen Energy **47**(20), 10911–10933 (2022)
10. Kemper, J., Sutherland, L., Watt, J., et al.: Evaluation and analysis of the performance of dehydration units for CO_2 capture. Energy Procedia **63**, 7568–7584 (2014)
11. Lu, Y., Guo, L., Ji, C., et al.: Hydrogen production by biomass gasification in supercritical water: a parametric study. Int. J. Hydrogen Energy **31**(7), 822–831 (2006)
12. Fuchs, J., Schmid, J.C., Müller, S., et al.: Dual fluidized bed gasification of biomass with selective carbon dioxide removal and limestone as bed material: a review. Renew. Sustain. Energy Rev. **107**, 212–231 (2019)
13. Tunå, P., Hulteberg, C., Ahlgren, S.: Techno-economic assessment of nonfossil ammonia production. Environ. Prog. Sustain. Energy **33**(4), 1290–1297 (2014)

Optimization of Energy Management Control Strategy for Hydrogen-Electric Hybrid Train

Shijie Sun[1](✉), Yang Gao[1], Jian Wang[1,2], Lei Shi[1], Limei Chen[1], Weiran Xiang[1], and Wenrong Li[1]

[1] CRRC Changchun Railway Vehicles Co., Ltd., Changke Road 2001, Changchun 130062, China
ssj_crrc@163.com

[2] Central South University, Lu Shan Nan Road 932, Changsha, Hunan, China

Abstract. In order to enhance the stability of the energy regulation of the hydrogen-electric hybrid train and reduce the impact on the train bus of the hybrid system during the energy regulation process, an improved rule-based instantaneous power control strategy is proposed, in which the bus voltage is introduced into the control link to enhance the system stability. The simulation results prove that the optimized control strategy improves the stability of the high-voltage DC link of the hybrid system, avoids the high-voltage surging to the super-capacitor system and the traction system, and extends the service life of the super-capacitor at the same time.

Keywords: Hydrogen energy · Hybrid · Energy management strategy · Optimization

1 Introduction

Among many sources of energy, hydrogen is relatively abundant, with high efficiency in conversion to electricity and only water as the conversion product, which is green and clean. At present, the capacity of hydrogen fuel cell is about 120 kW, the technology is relatively mature, and it can achieve the technical breakthrough of 200 kW capacity in a short time, so the application potential of hydrogen fuel cell in rail transit vehicles is infinite. Compared with diesel or electrical locomotive, the obvious advantages of hydrogen-electric hybrid train are as follows, such as no need to set up contact networks, saving line construction, operation and maintenance costs; green and pollution-free; short project construction cycle and low fixed investment.

Since the electrical output characteristics of hydrogen fuel cells are relatively "soft" and the demand power response is slow, the design of rail vehicles requires the use of super-capacitors or lithium-ion batteries to provide transient response energy for trains and to recover the braking energy generated under train braking conditions [1, 2]. Since trains are equipped with multiple energy sources to power the trains, unified energy management and energy distribution for different energy sources are required to ensure safe and stable operation of the vehicles. For multi-energy coupled power supply

H. Sun et al. (Eds.): WHTC 2023, SPPHY 393, pp. 90–99, 2024.
https://doi.org/10.1007/978-981-99-8631-6_10

technology, scholars at home and abroad have conducted a lot of research work. In the paper [3], the frequency of hydrogen consumption and power fluctuation of the hydrogen fuel cell is used as a reference in the control strategy, and a power-following control strategy is used to optimize the control of the fluctuation rate. In the paper [4], the control strategy of the state machine is optimized and a voltage equalization algorithm is used so that the train can guarantee the discharge equalization of the non-functional power supply under different operating conditions. Other scholars have proposed different optimal management control strategies in order to improve the economic effect of the power system, and the papers [5, 6] proposed an optimal control strategy with the minimum hydrogen consumption as the control objective, which can improve the efficiency of the power supply system and thus reduce the cost of hydrogen refueling. In the paper [7], an optimal control strategy based on dynamic planning was proposed, which is able to achieve coordinated control of the hybrid power system. Although scholars at home and abroad have proposed numerous optimal control strategies, the control strategies are relatively complex and not conducive to engineering practice, while a large number of optimal control strategies are based on optimization under fixed working conditions, without taking into account the complexity of the actual operating conditions of rail vehicles, and therefore do not have the feasibility of practical engineering applications.

In this paper, the rule-based instantaneous power control strategy is widely used as the benchmark of the whole vehicle energy management control strategy, and according to the problems encountered in the process of engineering practice, the control strategy is optimized, and an improved rule-based instantaneous power control strategy is proposed, which reduces the high-voltage impact on the super-capacitor system and traction system during the power regulation of the train, and helps to enhance the system stability and reduce the failure rate of the high-voltage system.

2 Train Configuration and Operation Mode

2.1 Train Configuration

In a typical series hybrid system, there shall be two or more power sources, including one energy storage system (ESS), and the traction equipment (TE) which serves as the primary power sink. The system may contain a secondary energy consuming device, such as a braking resistor (BR), in case the power system cannot fully recover or partially recover the energy regenerated by the traction system during regenerative braking. These subsystems shall be electrically connected to enable the exchange of energy between them. In addition to these main circuit subsystems, a series hybrid system may have one or more auxiliary power supplies (APS). The auxiliary loads have a large impact on energy consumption and should be considered if the APS is connected to the main circuit.

Figure 1 shows an example block diagram of the series hybrid system, which has four main subsystems, i.e. one main primary power source (PPS) with a hydrogen fuel cell as the main energy source, one energy storage system (ESS) with a super-capacitor as the auxiliary power source, a traction unit (TE), and an auxiliary equipment (Aux).

Key

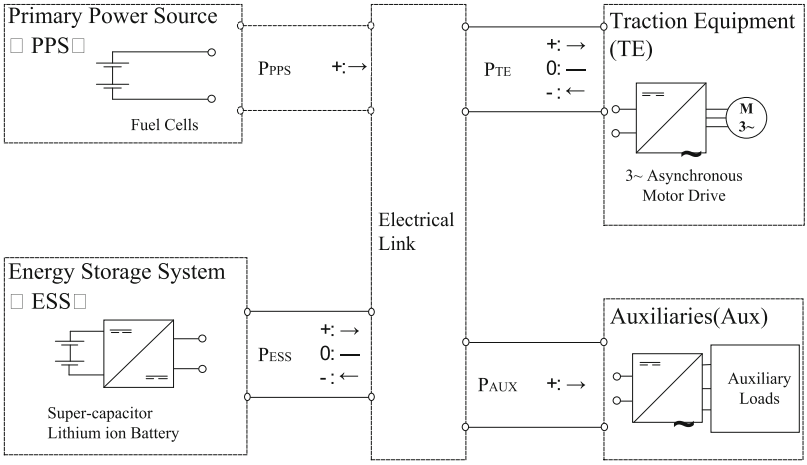

Fig. 1. Block diagram of a series hybrid system

P_{PPS} Power of primary power source (PPS)
P_{TE} Power of traction equipment (TE)
P_{ESS} Power of energy storage system (ESS)
P_{BR} Power of brake resistor (BR)
P_{AUX} Power of auxiliaries (AUX).

2.2 Major Operation Mode

In Fig. 1, when the train is in operation, there can be power flows in the power supply system for four main subsystems, namely

(a) between the PPS and the electrical link, denoted as P_{PPS} in Fig. 1.
(b) between the ESS and the electrical link, denoted as P_{ESS} in Fig. 1.
(c) between the electric link and the traction equipment, denoted as P_{TE} in Fig. 1.
(d) between the electrical link and the Aux, denoted as P_{AUX} in Fig. 1.

Among these:

(b) and (c) are bidirectional and their values P_{ESS} and P_{TE} can both be positive and negative;
(a) is unidirectional and its value P_{PPS} can only be positive;
(d) is also unidirectional, but unlike (a), its value P_{AUX} is always positive and non-zero when the system is running.

In Fig. 1, the possible symbols of these variables (+, 0 and −) and the corresponding directions are also marked. Note that the directions are defined so that the power flow from the power subsystem to the electrical link and from the electrical link to the power subsystem becomes positive, e.g. when the hybrid vehicle is accelerated with electrical energy from the PPS or ESS.

Using these symbols, the major modes of operation of the system can be classified according to the symbols of these variables, as shown in Table 1.

Among the modes shown in Table 1, Mode II (pure power source) is a power supply mode in which the PPS provides all the power required by the traction equipment. Similarly, Mode VI (idling) is a mode in which the PPS provides all the power required by the auxiliary equipment when the power required by the traction equipment is zero. In addition, Mode VII (sliding) is a mode in which the PPS and ESS provide all the power required by the auxiliary equipment when the power required by the traction equipment is zero. The train charges the ESS in Modes I (supplementary charging during motoring), IV (Power source charging ESS) and V (supplementary charging during braking).

Table 1. Major operating modes of the series hybrid system

Mode	P_{PPS}	P_{ESS}	P_{TE}	P_{AUX}	Description
I	+	−	+	+	Supplementary charging during motoring
II	+	0	+	+	Pure power source
III	+	+	+	+	Boosting
IV	+	−	0	+	Power source charging ESS
V	+	−	−	+	Supplementary charging during braking
VI	+	0	0	+	Idling
VII	+	+	0	+	Sliding

3 Energy Management Control Strategy Determination and Optimization

3.1 Proposal of Energy Management Control Strategy

In a typical series hybrid system, the control strategy generally uses a thermostat-based control strategy and a power-following-based control strategy. In the thermostat-based control strategy, the SOC limits of the super-capacitor need to be set according to the train operating conditions. In the case of super-capacitor discharging condition and the SOC value is lower than the pre-set lower limit, the output power of hydrogen fuel cell is adjusted to provide energy for the train and charge the super-capacitor; in the case of super-capacitor charging condition and the SOC value is higher than the pre-set upper limit, the output power of hydrogen fuel cell is adjusted to standby power and the super-capacitor and hydrogen fuel cell jointly provide energy for the train. Under this control strategy, the hydrogen fuel cell can be operated in the optimal working area for a long time and the consumption of hydrogen fuel can be reduced. However, the super-capacitor is frequently charged and discharged, which shortens the service life of the super-capacitor. In the power following-based control strategy, the operating state of the hydrogen fuel cell is adjusted according to the SOC of the super-capacitor and the power demand of the train. When the super-capacitor is full and there is no power demand of train, the hydrogen fuel cell runs in standby mode and provides the minimum

power output for the train; when the super-capacitor is hungry and there is power demand of train, the hydrogen fuel cell outputs power according to the demand and the power value is adjusted with the demand of train. Under such control strategy, the cycles of super-capacitor charging and discharging are reduced, which helps to extend the service life of super-capacitor, but the output power of hydrogen fuel cell fluctuates more and damages the fuel cell more.

The rule-based instantaneous power control strategy combines the advantages and disadvantages of the above two control strategies to realize the control of the super-capacitor SOC and the proper regulation of the hydrogen fuel cell output power to ensure the efficiency of the hydrogen fuel cell. This control strategy can make use of the fast response characteristic of super-capacitor energy output and alleviate the dynamic response requirement of hydrogen fuel cell power output. However, this control strategy is a switching control strategy based on a given threshold value. Under the extreme operating conditions of the train, such as when the super-capacitor is close to the discharge cutoff zone or the charging cutoff zone, the switching control strategy will cause a step change in the traction or electric braking load of the train, which will cause a shock to the high-voltage power supply system of the train. To address this problem, this paper proposes an optimized control strategy and introduces a bus voltage control strategy to realize the regulation of bus voltage, so as to avoid the high bus voltage caused by load fluctuation or other extreme operating conditions, which will impact on the hydrogen fuel cell and traction system and prolong the service life of the super-capacitor system.

3.2 Optimization of Energy Management Control Strategies

The main factors affecting the energy distribution of super-capacitor and hydrogen fuel cell in the hybrid system are the power demand of the train, such as the traction power, regenerative braking power and auxiliary power supply of the train, and the SOC of the super-capacitor (characterized by the voltage of the super-capacitor in this project), and the bus voltage control link is introduced in the energy management control strategy to enhance the stability of the system. This summary is presented in two aspects of super-capacitor's operating area division and rule-based optimization of transient power control strategy.

(1) Super-capacitor working area division

According to the output characteristics of the hybrid super-capacitor, the output voltage stability is relatively poor when the SOC of the super-capacitor is too higher or too lower, and the service life of the cell is seriously affected. In order to improve the smoothness of the power system during the train operation, avoid the over-charging or over-discharging condition of super-capacitor, and prolong the service life of super-capacitor, the working interval of super-capacitor is divided. According to the train operating conditions, the super-capacitor charging and discharging intervals are divided into five parts, namely, discharge reserve area, traction discharge area, SOC maintenance area, brake recovery area and charging reserve area, and the corresponding super-capacitor voltage judgment thresholds are set according to these five intervals for the energy management control strategy, details of which are shown in Fig. 2 and Table 2.

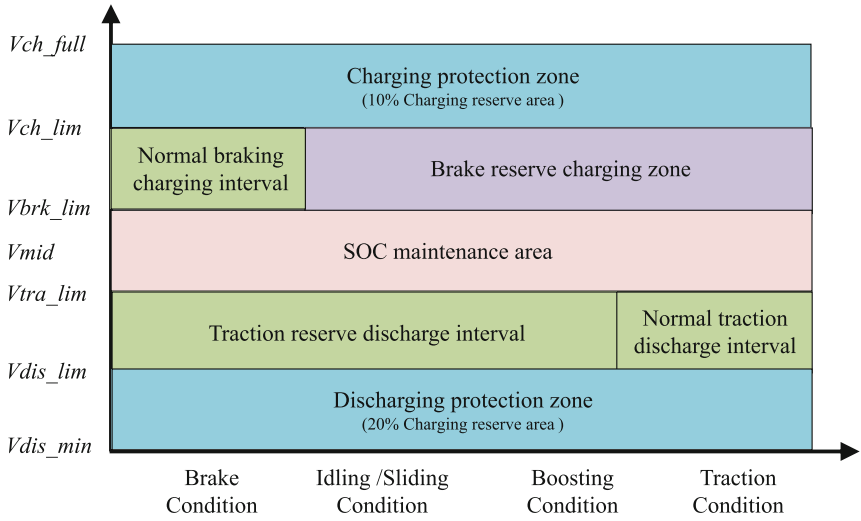

Fig. 2. The division of super-capacitor SOC working area

Table 2. The parameter description of voltage

Symbols	Description
V_{dis_lim}	Discharging limit voltage
V_{tra_lim}	Allowable traction voltage
V_{mid}	Operating median voltage
V_{brk_lim}	Upper limit voltage of hydrogen fuel cell charging
V_{chg_lim}	Charging limit voltage

In order to fully protect the super-capacitor and provide backup energy for emergency train traction, 20% SOC of the super-capacitor is reserved for this function. If the super-capacitor voltage is lower than V_{tra_lim} in non-traction conditions, the hydrogen fuel cell must be activated to charge the super-capacitor to ensure the traction demand of the train. In the electric braking condition, the super-capacitor needs to absorb the braking energy and ensure that the super-capacitor will not be overcharged, so it is necessary to set the upper limit of hydrogen fuel cell charging voltage V_{brk_lim} and the upper limit of charging voltage V_{chg_lim}.

(2) Control strategy optimization

According to the vehicle operating conditions, such as stopping, idling, starting acceleration, traction and braking conditions, and combined with the real-time voltage of the super-capacitor, the rules of the output power P_{fc} of the hydrogen fuel cell were formulated according to the demand power of the train, as detailed in Table 3, where P_{tc} is the power consumed by the train, V_c is the voltage of the super-capacitor, P_{aux} is the power

consumed by the train auxiliary equipment, P_{fc_max} is the maximum power output by the hydrogen fuel cell, and P_{fc_min} is the minimum power output by the hydrogen fuel cell.

The hydrogen fuel cell outputs power according to the above rule-based control strategy. If there is a sudden jump in the train power demand, the hydrogen fuel cell cannot change the output power, it will cause a sudden rise in the train high-voltage bus, which will endanger the super-capacitor system and the train traction system. Therefore, a bus voltage controller is introduced in the train energy management control strategy to stabilize the train bus voltage within the target voltage DC1450–DC1950 V to ensure the safe operation of the vehicle. The equivalent control structure diagram of the optimized rule-based instantaneous power control strategy is shown in Fig. 3, where V_{fc} is the hydrogen fuel cell output voltage, I^*_{fc} is the hydrogen fuel cell output reference current, and I_{fc} is the hydrogen fuel cell output current output by the controller. From the figure, it can be seen that two compensation loops are introduced in the control link, which are PI control compensation based on the lower limit voltage DC1475 V as the target and PI control compensation based on the upper limit voltage DC1925 V as the target, and after this compensation, the bus voltage can be effectively controlled in the range of DC1450–DC1950 V.

4 Simulation Verification

Matlab/Simulink simulations were performed to verify the proposed improved rule-based instantaneous power control strategy, and the key parameters involved in the simulations are shown in Table 4. To verify the effect of load fluctuation on the bus voltage, the pre-optimized and post-optimized control strategies were compared by abruptly removing traction at 70 s to simulate the effect of power fluctuation on the bus voltage. From Fig. 4, it can be seen that the peak bus voltage fluctuation after optimization is 1947 V, which does not exceed the upper bus voltage limit, but the bus voltage before optimization is nearly 2000 V, which far exceeds the upper bus voltage limit.

5 Summary and Prospect

The improved rule-based transient power control strategy proposed in this paper has significant effects on improving the train bus voltage stability and avoiding the shocks to the components. It can help to improve the stability of train operation, reduce the impact on the component life and reliability because of the voltage jumping, and reduce the operation and maintenance cost.

In view of the rule-based control strategy in the rail vehicles, there are still problems such as low conversion efficiency of hydrogen fuel cell, frequent charging and discharging of power battery, etc. It is necessary to optimize the control strategy in the future to enhance energy utilization and extend the service life of components.

Table 3. Hydrogen fuel cell output power rules

	P_{tc}			
V_c	$P_{tc} < 0$ Braking condition	$0 \leq Ptc < Paux$ Idling/sliding condition	$Paux \leq Ptc < Pfc\_max$ Boosting condition	$Ptc \geq Pfc\_max$ Traction condition
$V_c < V_{dis\_lim}$	P_{fc_min}	P_{fc_max}	Pfc_max	
$V_{dis\_lim} \leq V_c < V_{tra\_lim}$	P_{fc_min}	P_{fc_max}	P_{fc_max}	P_{fc_max}
$V_{tra\_lim} \leq V_c < V_{mid}$	P_{fc_min}	P_{fc_max}	P_{fc_max}	P_{fc_max}
$V_{mid} \leq V_c < V_{brk\_lim}$	P_{fc_min}	P_{aux}	P_{tc}	P_{fc_max}
$V_{brk\_lim} \leq V_c < V_{chg\_lim}$	P_{fc_min}	P_{fc_min}	P_{aux}	P_{fc_max}
$V_{chg\_lim} \leq V_c$	Shutdown	Shutdown	P_{fc_min}	P_{fc_max}

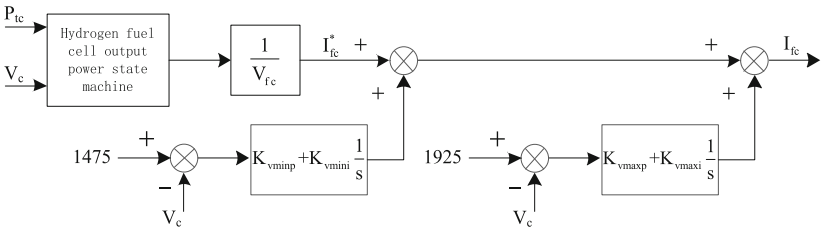

Fig. 3. Equivalent structure diagram of control strategy

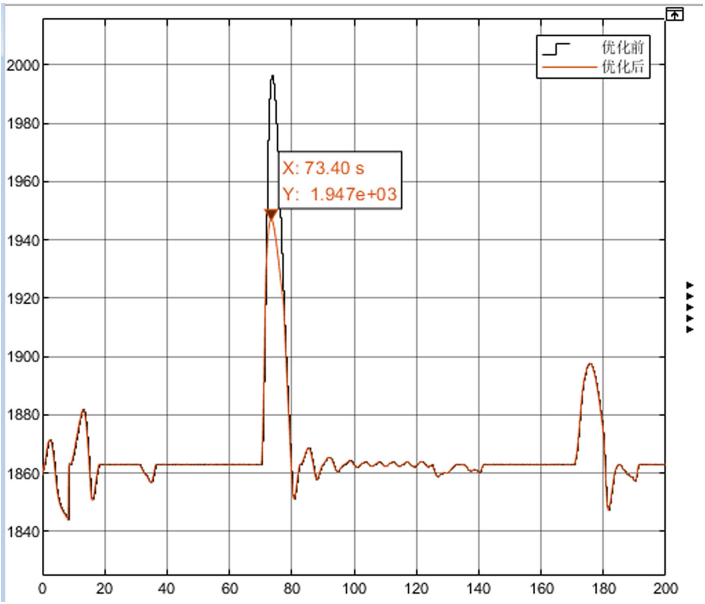

Fig. 4. The DC bus voltage fluctuation comparison

Table 4. Key parameters

Symbols	Value	Symbols	Value
V_{dis_lim}	1602 V	V_{chg_lim}	1917 V
V_{tra_lim}	1717 V	V_{brk_lim}	1894 V
V_{mid}	1765 V	P_{aux}	202 kW
P_{fc_max}	800 kW	P_{fc_min}	80 kW

References

1. García, P., Fernández, L.M., Torreglosa, J.P., et al.: Operation mode control of a hybrid power system based on fuel cell/battery/ultracapacitor for an electric tramway. Comput. Electr. Eng.. Electr. Eng. **39**(7), 1993–2004 (2013)
2. Wei, G.U.O., Hongshan, Z.H.A.O.: Grouping control strategy of battery energy storage array system based on an improved distributed consensus algorithm. Trans. China Electrotech. Soc. **34**(23), 4991–5000 (2019)
3. Nan, L.I.U., Boxuan, Y.U., Ai, G.U.O., et al.: Analysis of power tracking management strategy for fuel cell hybrid system. J. Southwest Jiaotong Univ. **55**(6), 1147–1154 (2020)
4. Yan, Y., Huang, W., Liu, J., et al.: The control strategy of fuel cell hybrid tram based on state machine control. In: IEEE. 2019 IEEE Sustainable Power and Energy Conference (iSPEC), pp. 699–703. IEEE, Beijing, China (2019)
5. Wang, T., Li, Q, Han, Y., et al.: Fuel cell hybrid power generation system equivalent hydrogen consumption instantaneous optimization energy management method. Proc. CSEE **38**(14), 4173–4182 (2018)
6. Qi, L.I., Bo, S.U., Yuchen, P.U., et al.: A state machine control based on equivalent consumption minimization for fuel cell/supercapacitor hybrid tramway. IEEE Trans. Transp. Electrif. **5**(2), 552–564 (2019)
7. Lei, X.U., Qing, T.I.A.N., Yankun, L.I.: Coordinated control of fuel cell hybrid power system for trams based on DP optimization optimization. Electr. Drive Locomotives **6**, 73–80 (2021)

Safety Technologies and Challenges of Hydrogen-Powered Rail Transport

Jian Wang[1,2(✉)], Yang Gao[2], Shijie Sun[2], and Lei Shi[2]

[1] Central South University, Lu Shan Nan Road 932, Changsha, Hunan, China
wangjian20.ck@crrcgc.cc
[2] CRRC Changchun Railway Vehicles Co., Ltd., Changke Road 2001, Changchun, Jilin, China

Abstract. As one of the many energy alternatives, the interest in hydrogen-powered rail transport is gradually increasing worldwide, and some railway vehicles powered by hydrogen are currently in operation or undergoing experimental projects. However, due to the unsafe and unstable nature of hydrogen energy, hydrogen has potential leakage and explosion hazards in all rail transport applications. This paper summarizes the main application technologies of hydrogen safety in light of the research progress and unsafe factors in the process in the field of hydrogen-powered rail transport in various countries, at the same time clarifies the development challenges and difficulties of hydrogen-powered rail transport in the future, and makes suggestions for the development of hydrogen-powered rail transport safety in China.

Keywords: Hydrogen-powered rail transport risk · Hydrogen safety technology · Hydrogen-powered rail transport challenges

1 Introduction

After the signing of the Paris Agreement in 2016, countries all over the world have started looking for a new type of energy that can replace traditional fossil fuels. Hydrogen energy is gradually favored by countries for its advantages of zero carbon emission, non-toxicity and high energy density. With the maturity of the technology, hydrogen energy is developing rapidly and gradually applied to passenger cars, subways and trams, becoming an important part of the urban transportation network. In the rail transport industry, hydrogen-powered vehicles are involved with the operation of hydrogen refueling, hydrogen storage and hydrogen reaction, which may lead to accidents such as hydrogen leakage and explosion. That raises more requirements on the engineering process and the safety measures. Therefore, how to apply hydrogen energy safely, stably and efficiently in the rail transport industry has become a key and difficult point for all countries today.

2 The Exploration of Hydrogen-Powered Rail Transport

More than 10 countries are implementing or planning to implement hydrogen-powered rail vehicles to date [1] and the first delivery peak of hydrogen-powered rail vehicles is expected to be in 2025.

H. Sun et al. (Eds.): WHTC 2023, SPPHY 393, pp. 100–107, 2024.
https://doi.org/10.1007/978-981-99-8631-6_11

The U.S. signed a related agreement in 2020 and expects to deliver the country's first commercial hydrogen-powered passenger train (Flirt H2) in 2023 and officially put it into service in 2024. The Korea Railway Research Institute announced on April 20, 2021 that it is researching on a 150 km/h liquid hydrogen-powered train with a maximum range expected to be 1.6 times that of the 700 bar gaseous hydrogen-powered trains. And the time required to refill with liquid hydrogen is expected to be 20% less than gaseous hydrogen, and the research is expected to continue until 2025. Germany was the first country in the world to put hydrogen-powered trains into commercial use, and has worked with Alstom on hydrogen fuel cell trains several times in recent years, with the first fleet of 14 iLINTs going into regular operation in Germany by the end of 2022. The first hydrogen-powered test train of Japan, the Hybari, was jointly developed by JR East, Hitachi Ltd. Toyota Motor Corp and unveiled in 2022. The train is scheduled to enter service in 2030 (Figs. 1 and 2).

Fig. 1. Flirt H_2 hydrogen fuel cell train

Fig. 2. Japanese "Hybari" train

By the end of 2022, the first hydrogen-powered locomotive jointly developed by Southwest Jiaotong University and CRRC Datong has exceeded 20,000 kilometers of safe operation, saving about 110 tons of fuel consumption and reducing carbon emissions by about 350 tons. In Guangdong, Foshan Gaoming tram, the first hydrogen -powered railway system in China has been operated commercially since 2019, and the train can travel 100 km when fully filled with hydrogen. The first hydrogen-powered regional express vehicle in the world was released by the end of 2022, which can achieve a long range of 600 km (Figs. 3 and 4).

Fig. 3. The first hydrogen-powered locomotive

Fig. 4. The world's first hydrogen-powered regional express vehicle

3 Safety Risks of Hydrogen in Rail Transport

3.1 Failure of On-board Hydrogen Energy Devices

For on-board hydrogen storage, hydrogen needs to be compressed, liquefied or materially combined to achieve higher energy density [2]. Compared to conventional diesel, hydrogen shows significantly lower volumetric and mass energy density at the storage system level, which severely limits the operation distance as well as the refueling process of the vehicle. During the refueling process, the rapid filling of hydrogen can lead to a rapid temperature increase in the hydrogen storage tank, and since the lateral stretching of the hydrogen storage tank can be significantly affected by temperature changes, the tank may fail under excessive pressure, thus triggering hydrogen leakage. Hydrogen storage tanks are also susceptible to accidents caused by human handling, material problems, etc. When hydrogen storage tanks are mixed with other gases, there is a risk of explosion due to dangerous chemical reactions under certain conditions. At the same time, hydrogen storage tanks have to face the problem of compatibility between hydrogen and its materials [3]. The phenomenon of "hydrogen embrittlement" threatens the material safety of certain equipment working in hydrogen environment for a long time, and the deterioration of metallic materials can be a serious threat to the safety of hydrogen systems.

3.2 Lack of Safety Regulations for Hydrogen Vehicles

There are no applicable regulations and standards for on-board hydrogen storage of rail transport. Although most hazardous accidents can be controlled by combining existing regulations in other hydrogen applications with existing rail-specific standards, the hydrogen technology standardization system of China suffers from a low number of industry standards, weak dominance of hydrogen industry consortia in industry standard development, and low coverage of some technology categories [3]. An acceptable level of residual risk must be reached to solve the residual risk. China has not yet formed a comprehensive risk evaluation system for hydrogen energy systems and mastered the identification method of major hazards related to hydrogen energy infrastructure in the field of hydrogen-powered rail transport, and at the same time has not established effective measures to deal with hydrogen-powered vehicle accidents and emergency safety response mechanisms [4].

In terms of the quality of hydrogen vehicle-related components, China's hydrogen safety quality evaluation system still needs to be improved, and there is still a lack of authoritative and commonly recognized third-party hydrogen safety testing and research center. At the same time, the capacity of safety testing, measurement and certification of relevant departments needs to be improved.

3.3 Inadequate Hydrogen Fire Prevention and Control Technology in Tunnels

Generally speaking, most of the hydrogen storage systems of railway vehicles are installed on the roof or in the engine room, and once the hydrogen fuel cell leaks in the open space, the released hydrogen gas will quickly dissipate upward by virtue of its small density and strong diffusivity, and cannot accumulate. However, in such a narrow and restricted space as tunnel, hydrogen gas is very easy to accumulate above the train, and due to the dangerous nature of hydrogen gas such as low ignition energy, flammable and explosive, the accumulation of hydrogen gas is more likely to cause combustion to form a jet fire or explosion. At the same time, the wind speed and direction inside the tunnel as well as the location of hydrogen leakage inside the tunnel also affect the diffusion process of hydrogen leakage [5].

In the event of a hydrogen ignition in a tunnel, the formation of a jet fire can quickly pyrolyze the surface materials or parts of the train, spreading smoke and flames through the cars and tunnel, resulting in reduced visibility, difficult evacuation, and even fatal poisoning of personnel. In addition to the ventilation conditions, the flammability and thermal response time of the interior materials and the mass of combustible materials, which are the main factors affecting the heat release rate of a train, the geometry of the tunnel entrance can also have an impact [6].

4 Hydrogen-Powered Rail Transport Safety Technology

4.1 On-board Hydrogen Safety Technology

Many researches have conducted to reduce the safety risks associated with the operation of hydrogen-powered vehicles in different aspects. Hydrail has made significant progress in passenger rail by deploying a highly visible demonstration system to monitor

the real-time status of fuel cells. China Railway Siyuan Survey and Design Group Co., Ltd. Has released a hydrogen-powered tram hydrogen power system temperature monitoring device [7], which will cool down and extinguish fire when abnormal temperature or open flame source is monitored and alarm occurs simultaneously, thus solving the problem of hydrogen-powered tram power system temperature rise and spark generation, which threatens the safety of hydrogen power system. For the problem of hydrogen leakage when the hydrogen-powered trams are parked in the depot, the hydrogen leakage monitoring and elimination system of hydrogen-powered tram depot [8] can automatically turn on the exhaust fan to discharge the hydrogen out of the depot, thus saving time for emergency treatment and greatly reducing the possibility of danger. Qingdao CRRC Sifang Rolling Stock Co., Ltd. Has invented a rail vehicle hydrogen energy equipment installation device [9], which enables the ready assembly and disassembly of facilities and equipment through modular design, and at the same time can be adjusted in size according to hydrogen energy equipment or similar products to meet the needs of different specifications of products, and uses cylindrical pressure cylinders to reduce the storage capacity under consideration of additional installation space such as pipes and shells.

4.2 Related Hydrogen Safety Standards

In recent years, the government of China has paid more attention to renewable energy, which aims to ensure safe production and application, and encourages all parties to pay attention to the production, storage and transportation processes and firefighting needs of hydrogen-powered vehicles. In terms of hydrogen refueling process and safety management of hydrogen-powered vehicles, temporary hydrogen refueling equipment configuration, temporary hydrogen refueling process, safety measures for hydrogen refueling operation and emergency treatment plan for hydrogen trains have been focused and effectively discussed [10], which provides partial reference for the hydrogen energy industry. Regional quantitative risk evaluation software is also gradually developed and recognized by many domestic safety evaluation agencies, gradually realizing that safety of hydrogen-powered vehicles can be measured, prevented and followed. Zhang Feng et al. [11] put forward requirements for hydrogen-related area management, hydrogen storage module safety design of trams and hydrogen storage module maintenance requirements in the safety design and maintenance management of hydrogen—powered trams, and elaborated the application practice of hydrogen-related component overhaul and maintenance of hydrogen energy trams, which provides action guidelines for subsequent operation and management. At present, relevant safety technical specification documents of hydrogen refueling stations have been released, in which further requirements are unified for technical requirements of hydrogen storage pressure vessel, safety assurance during transportation and hydrogen risk identification.

4.3 Tunnel Hydrogen Explosion Prevention and Control

The researchers analyzed the consequences and causes of railway tunnel fire safety accidents around the world by establishing relevant mathematical and physical models [12–18], studied the development of railway tunnel fire laws in more depth, and proposed

numerous measures to help reduce railway tunnel fire safety accidents and reduce the scale of train fires in tunnels, in order to further improve the level of safety operation inside railway tunnels and ensure the smooth operation of hydrogen-powered vehicles after entering the tunnels. These include the application of flame retardant technology, the use of partially non-combustible materials on the surface of the train, strict control of the size of the natural wind speed in the tunnel, the lowest possible number of open train doors and windows when meeting the requirements for personnel escape, and ensuring that the spacing between firefighting facilities in the tunnel meets the standards. In recent years, with the development of the Internet of Things, domestic and international institutions are currently developing an integrated information platform for fire safety and disaster mitigation and relief in tunnels [6], which mainly covers fire prediction and alarm system, tunnel fire intelligent consultation system, fire management system and safety emergency response system, etc. Under the normal working environment, each system automatically adjusts its working status through dynamic monitoring and real-time monitoring, etc. The system is designed to meet the requirements of tunnel fire safety and disaster mitigation and relief in a modern, informative and intelligent way [19, 20].

5 China's Hydrogen-Powered Rail Transport Challenges

5.1 On-board Hydrogen Device Research Needs to be More In-depth

Several challenges remain in using hydrogen fuel cells to power railway vehicles, and the safety of the hydrogen storage tank determines the level of risk for hydrogen-powered vehicles and becomes the basis for achieving smooth operation of hydrogen trains. Although it is technically possible to reduce the storage space required for hydrogen by compressing the hydrogen to high pressure, however, the mechanisms of hydrogen spontaneous combustion, flame acceleration and ignition-detonation transition are still unclear, there is a lack of test data on materials under the operating environment of hydrogen-powered vehicles over a long period of time, and the validity and applicability of risk assessment models still need to be further tested, all of which are technical challenges limiting the rapid development of hydrogen-powered rail transport.

5.2 Hydrogen Safety Regulations Need to be Improved

The technical standards and safety regulations related to hydrogen energy are not yet perfected and unified. According to statistics, the number of hydrogen energy-related standards in China is more than the sum of European, American and Japanese hydrogen energy standards, but they fail to effectively support industrial development, and there is still a cross-regional information gap.

5.3 Hydrogen Rail Accident Rescue Technology Still Needs to be Improved

Although numerous analytical studies have been conducted previously to evaluate the operational risk of vehicles in special transportation scenarios such as tunnels, ports and

high altitude areas, there is still a lack of data and experience in the field of hydrogen-powered rail transport to quantify the risk, and it is difficult to summarize the specific laws for the possible fire hazards. For different types of vehicles entering the tunnel, the level of tunnel operation management in China needs to be improved, and the emergency rescue countermeasures corresponding to the safety level of fire prevention in the tunnel still need to be unified.

6 Conclusion

Hydrogen energy is regarded as the second most important secondary energy source after electricity in the future by many countries, and it will occupy a large proportion in the transportation field. In the future, China still needs to strengthen the research on the safety technology of hydrogen energy infrastructure equipment operation, improve the accuracy of relevant risk assessment methods, accurately identify the major sources of danger in the abnormal operation of hydrogen-powered rail vehicles, form a mature risk response system for special transportation scenarios, and establish a rapid response mechanism. At the same time, we should further improve the hydrogen safety quality system in China, set up a professional research center for hydrogen equipment, strictly control all the industry chains involved with the domestic production and import and export of hydrogen equipment, accelerate the development of relevant standards, and form a standard on which the hydrogen-powered rail industry chain can jointly rely.

References

1. Q Liang 2020 Global countries explore the path of hydrogen fuel cell trains World Rail Transp 6 56 58
2. Böhm, M., Del Rey, A.F., Pagenkopf, J. et al.: Review and comparison of worldwide hydrogen activities in the rail sector with special focus on on-board storage and refueling technologies. Int. J. Hydrogen Energy
3. C Xianghong W Zhiqiang 2020 Considerations on hydrogen energy utilization safety technology research and standard system construction China Eng Sci 22 5 144 151
4. Shi, W.B., Chunming, C., Li, D.W. et al.: Comparison and suggestions on the standardization system of hydrogen energy technology between ISO/IEC, the United States, Japan and China. Chem. Prog. **41**(12):6275–6284 (2022)
5. Dongping, Z., Feng, W., Yanli, Y., et al.: A review of railway tunnel fire accidents and their scale. Tunn. Constr. **35**(3):227–231 (2015)
6. JX Lai H Zhou F Cheng 2017 Statistical analysis of fire accidents in highway tunnels and countermeasures for disaster prevention and mitigation Tunn. Constr. 37 4 409 415
7. Jing, W., Zexi, F., Yingfeng, Y. et al.: A device and method for monitoring the temperature rise of hydrogen power system of hydrogen energy tram (2021)
8. Wanyan, J., Feng, Z.X., Yao, Y.F., et al.: A hydrogen leakage monitoring and elimination system for hydrogen energy trams (2021)
9. Chen, J.H., Zeng, S.J., Cai, A.N.Z.U. et al.: A hydrogen energy equipment installation device for rail vehicles (2020)
10. S Shanglin L Xiaoman T Chengming 2022 Hydrogen refueling process and safety management of hydrogen energy locomotives Int. Combust. Engines Accessories 6 29 31

11. Z Feng 2022 Safety design and maintenance management of hydrogen storage system for hydrogen energy trams Electri. Mech. Eng. Technol. 51 10 267 270
12. Z Haoran Z Xin T Ying 2022 Analysis of the diffusion process of liquid hydrogen leakage from on-board hydrogen supply systems in tunnels China Automot. 8 34 39
13. Rajkumar, J., Aryai, V., Salehi, F., et al: Computational fluid dynamics modelling of a hydrogen fire safety in a scaled tunnel environment. Saf. Extreme Environ. 1–15 (2022)
14. X Gu J Zhang Y Pan 2020 Hazard analysis on tunnel hydrogen jet fire based on CFD simulation of temperature field and concentration field Saf. Sci. 122 104532
15. Y Xie N Lv Y Huang 2022 Comparative analysis on temperature characteristics of hydrogen-powered and traditional fossil-fueled vehicle fires in the tunnel under longitudinal ventilations Int. J. Hydrogen Energy 47 57 24107 24118
16. Y Xie N Lv X Wang 2021 Thermal and fire characteristics of hydrogen jet flames in the tunnel at longitudinal ventilation strategies Fuel 306 121659
17. Zhang, J., Ji, W., Yuan, Z., et al.: Pyrolysis, combustion, and fire spread characteristics of the railway train carriages: a review of development. Energy Built Environ. (2022)
18. F Salehi N Reddy S Jalalifar 2021 Ceiling temperature assessment of a reduced scale tunnel in the event of two hydrogen jet fires Saf. Extreme Environ. 3 2 133 142
19. JY Zheng ZL Liu ZL Hua 2020 Current status and challenges of hydrogen safety research J. Saf. Environ. 20 1 106 115
20. Wei, F., Ren, S., Gao, L., et al.: Transformation and characteristics of the U.S. hydrogen energy strategy under the carbon neutrality goal. J. Chin. Acad. Sci. **36**(9):1049–1057 (2021)

Research of Standard System on Fuel Cell Systems for Vehicles

Wang Mingrui[1](✉), Fang Yunlong[1], Xu Liyao[2], Zhao Minyu[1], and Chen Jie[1]

[1] DeepWay Technology, Beijing 100102, China
wangmingrui@deepway.ai
[2] Dongfeng Motor Corporation Technology Center, Wuhan 430058, China

Abstract. China attaches great importance to the development of hydrogen energy and fuel cell industry, and a series of industrial policies and relevant national departments have repeatedly mentioned the direction of industrial development. This paper comprehensively sorts out and analyzes the relevant domestic and foreign standards focusing on fuel cell system for vehicle use, suggest that the standard system construction of them should center on key components and performance indicators, and establishes a four-level system from performance indicators to components. On several key performance indicators that restrict the large-scale industrialization of fuel cell vehicles, the entire industry should strengthen research.

Keywords: Hydrogen energy · Fuel cell · Standards

1 Introduction

Hydrogen energy and hydrogen fuel cell are an important way to realize clean energy utilization and optimize the energy consumption structure in China. Hydrogen energy has characteristics and advantages such as diverse sources, large-scale stable storage, transportation and utilization, rapid replenishment, etc. It can be widely used in many fields, such as transportation, industrial production, domestic life and aerospace, etc. The development of hydrogen energy technology is an important way to realize the clean energy utilization.

As an important application scenario of it in transportation, hydrogen fuel cell vehicles are an important direction for transforming and upgrading the electric power system of vehicles worldwide. Hydrogen fuel cell vehicles have the advantages of "zero emission" during the use phase, efficient energy utilization, long driving range and short refueling time, etc. If renewable energy is used to produce hydrogen, fuel cell vehicles can even achieve zero emissions throughout their life cycle.

Supported by Beijing Municipal Science & Technology Commission,Administrative Commission of Zhongguancun Science Park No. Z221100000222030.

H. Sun et al. (Eds.): WHTC 2023, SPPHY 393, pp. 108–115, 2024.
https://doi.org/10.1007/978-981-99-8631-6_12

In 2020, the Chinese Society of Automotive Engineers published Technology Roadmap for Energy Saving and New Energy Vehicles 2.0, which covers the hydrogen energy system supply chain and the key system technology chain of the vehicle for hydrogen fuel cell vehicles [1].

Based on the classification of this roadmap, this paper focuses on the standard system of fuel cell systems for vehicles. Section 2 of this paper presents the guiding measures of national and local policies on the standard system of fuel cell system. Section 3 presents the paper's hierarchical classification of current standards for automotive fuel cell systems. Section 4 presents statistical information and a brief analysis of the current national, local, group and international standards on automotive fuel cell systems. Section 5 gives the conclusion and outlook for the future.

2 National and Local Policy Guidance on Fuel Cell System Standards

2.1 Purpose and Importance of Investigating Fuel Cell System Standards

In the past, the lack of an industry standard system was considered to be one of the obstacles to the rapid development of the hydrogen energy and fuel cell industry. China attaches great importance to the development of them, and a series of industrial policies as well as many mentions by relevant state departments have clearly defined the direction of industrial development. In 2019, hydrogen energy was included in the State Council's "Government Work Report" for the first time. In the same year, Ministry of Industry and Information Technology summarized work essentials of new energy vehicle standardization of 2019 which clearly included five key research areas, such as fuel cell electric vehicles [2].

With the introduction of a large deal of industrial standards in recent years, the domestic industrial standardization system is being rapidly established, but there are still a large number of sub-discipline areas with standard vacancies. At this stage, the requirements of national standards are becoming stricter and stricter, mainly applied to basic safety and major project support, while local and industry are encouraged to actively participate in the subdivision standard clauses.

Standardization is the feedback of science and technology and the accumulation of experience, and the process of "development-implementation-revision" of a standard is the process of "innovation-application-re-innovation" of science and technology. If a country wants to promote technological progress and the rapid and standardized development of a certain industry, it will certainly actively promote the development of relevant standards to guide society to rationally allocate the resources invested in this industry. If enterprises hope to win, they must use technical standards as a means to enhance the ability of enterprises to compete in the industrial market.

2.2 National Policy Guidelines for Fuel Cell System Standards

The National Development and Reform Commission pointed out in the mid-term and long-term plan for the development of the hydrogen energy industry (2021–2035): "A

perfect standard system for the hydrogen energy industry should be established. Leading enterprises are encouraged to actively participate in the development of various standards, and conditional social groups are supported to develop and publish relevant standards" [3]. In 2020, the Ministry of Finance, together with other four ministries, issued a notice on demonstration and application of fuel cell vehicles. In this notice, they proposed that, given the current situation of industrial development, incentives will be given to eligible city clusters to carry out the industrialization of fuel cell vehicle key core technologies and demonstration applications, forming a new model of fuel cell vehicle development with reasonable layout, focus and synergy. The notice emphasized that in the demonstration content to promote the establishment and perfection of hydrogen fuel cell vehicle-related technical indicator system and testing and evaluation standards, and continuously improve the technical level of the industrial chain and product safety and reliability [4].

3 Local Government Planning for Fuel Cell System Standards

Guangdong Province's planning for fuel cell system standards

Guangdong Province has been a key region in China's hydrogen energy industry, and in September 2021, the Ministry of Finance, with other four ministries, officially approved Guangdong fuel cell vehicle demonstration city cluster as the first demonstration city cluster [5].

In August 2022, Guangdong Provincial Development and Reform Commission issued an action plan accelerating construction of fuel cell vehicle demonstration city cluster for next four years. In this plan, it specified that they would support quality metrology supervision and testing institutions and relevant testing enterprises to establish professional standard research platforms for fuel cell vehicles. They would support leading enterprises, universities and research institutes to jointly develop technical standards for inspection and testing of key components of fuel cell vehicles and improve professional testing capabilities [6].

As early as September 2020, Guangdong Provincial Development and Reform Commission and other four institutions released Guangdong Provincial Hydrogen Fuel Cell Vehicle Standard System and Planning Roadmap (2020–2024). This is the first clearly proposed and comprehensive provincial-level hydrogen fuel cell vehicle standard and technology system plan in China. The roadmap comprehensively summarizes the existing standards related to hydrogen fuel cells at home and abroad, compiles the framework of the hydrogen fuel cell industry standard system, and puts forward the recommendations for the creation and revision of key standards and the standardization roadmap for the hydrogen fuel cell industry [7].

This standard system framework sorts and classifies national, industry, local, and group standards at all levels, and collects 127 national standards, 11 industry standards, 2 local standards, 3 group standards, and 94 standards to be developed for hydrogen fuel cell vehicles. As for the current standard system, the standards for storage and transportation, fuel cell system and vehicle application are relatively perfect, while the

standards for foundation and management, preparation and refilling are relatively lacking. However, there are not many standards for automotive fuel cell systems and their subdivisions.

Beijing's Planning for Fuel Cell System Standards

In August 2021, the Ministry of Finance and other four ministries jointly approved the Beijing-Tianjin-Hebei hydrogen fuel cell vehicle demonstration city cluster under the leadership of Beijing [8]. In November 2022, Beijing Municipal Bureau of Economy and Information Technology and the Bureau of Market Regulation released Beijing Fuel Cell Vehicle Standard System, in which the existing standards were sorted out according to the whole industrial chain and various links of fuel cell vehicles, a total of 151 items.

The standard system considers the requirements of fuel cell vehicle demonstration application and the needs of industrial development, and builds the standard system with the whole vehicle and key components as the core. Considering that the fuel cell system is the power center of fuel cell vehicles, the standard system chooses to subdivide under the first-level catalog of key components to further accelerate the research and application of new technologies.

Compared with the hydrogen fuel cell system standard system developed in Guangdong Province, this standard system clearly states that the standards related to the three main auxiliary systems of the fuel cell system, namely the hydrogen supply system, the air supply system and the thermal management system, should also be included in the construction of the standard system [9]. However, this standard system does not continue to subdivide the automotive fuel cell system downward according to the system-auxiliary system hierarchy.

3.1 A Four-Level Classification of Fuel Cell System Standards in This Paper

The above information shows that both national and local policies clearly point out that the construction of a standard system of automotive fuel cell system is a necessary element for the establishment of fuel cell vehicle industrialization. The standard system of automotive fuel cell system should land on key components and performance indicators. On this basis, the classification of the standard level of fuel cell system should be clarified. Only then can the outline of the standard system be verified, the gaps be filled, and the required standards be prepared or revised in a targeted manner.

In the development process, the industry usually classifies fuel cells according to the three-level structure of system, auxiliary system and components, and carries out the corresponding design development work. Therefore, the three major auxiliary systems of fuel cell systems should not be neglected in the development of standards. After research, there are indeed relevant standards for all three layers.

Meanwhile, the national industrial policy has set clear performance indicator requirements for both the fuel cell system and its major components. Although performance indicators can be further subdivided as a separate classification dimension, such as environmental adaptability, safety, and durability. However, these performance indicators are too abstract, and in practice they are realized through different levels of the fuel cell system, and it is not conducive to establishing a connection with key components if the performance indicators are singled out as the main level. Therefore, in this paper,

standards for automotive fuel cell systems are divided into four levels: performance indicators, systems, subsystems, and components.

In terms of standard types, standards for fuel cell systems can generally be divided into two categories: technical conditions and test methods. In the past, when some standards were prepared, some products with simpler principles and structures or more mature industrial development were prepared by combining technical conditions and test methods. However, the fuel cell system industry is still in the cultivation stage, and the technical routes of various products have not yet been completed. Therefore, this paper still divides the types of standards for automotive fuel cell systems into these two categories.

4 Domestic and Foreign Related Standards Statistics and Brief Analysis

4.1 Relevant National Standards Statistics and brief Analysis

The search yielded a total of fourteen existing national standards related to automotive fuel cell systems, as shown in Fig. 1 and eight of them are in the type of technical conditions, and six are in the type of test methods. There are nine standards at the system level, no standards at the subsystem or component level, and five standards related to performance indicators. There are also some standards under preparation, see Fig. 2.

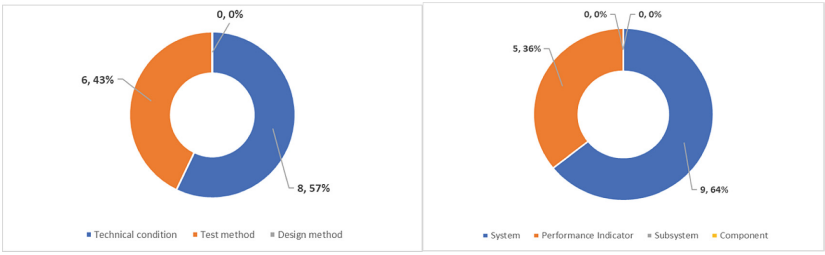

Fig. 1. Current national standards of fuel cell systems for vehicles

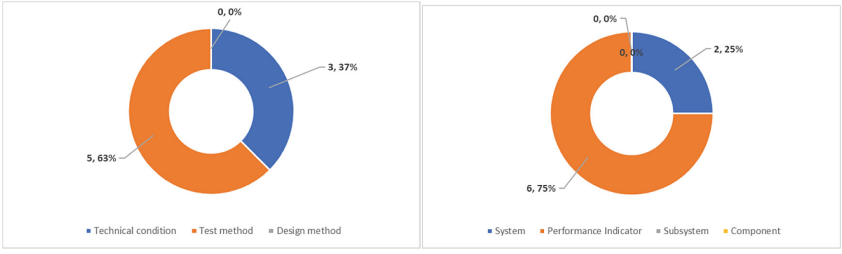

Fig. 2. National standards in preparation of fuel cell systems for vehicles

From the above information, the national standard mainly focuses on system-level standards and does not include key components. In terms of performance indicators,

the national standard is mainly concerned with environmental adaptability, safety, and durability.

4.2 Relevant Local Standards Statistics and Brief Analysis

Among the existing local standards, there are four standards related to automotive fuel cell systems, as shown in Fig. 3. Three of them are in the technical condition type and one is in the test method type. There is one system-level standard, one component-level standard, and two standards related to performance indicators. Local standards are also mainly concerned with safety and durability two performance indicators, and local standards have a strong access nature, so more attention to the technical conditions of the standards.

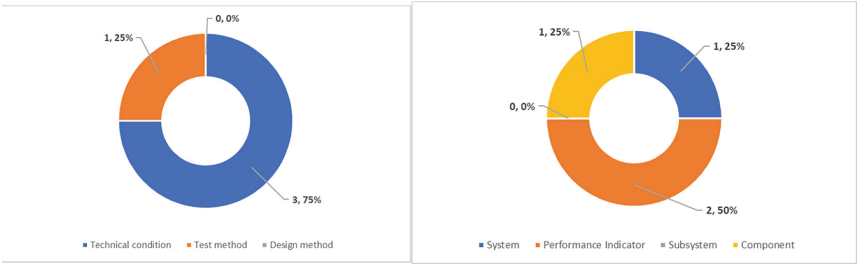

Fig. 3. Current local standards of fuel cell systems for vehicles

4.3 Relevant Group Standards Statistics and Brief Analysis

There are twenty-three group standards related to automotive fuel cell systems, as shown in the figure below. Among them, there are fifteen standards of technical conditions and eight standards of test methods. There are nine standards of system level, one standard of subsystem level, six standards of component level and seven standards of performance indicators (Fig. 4).

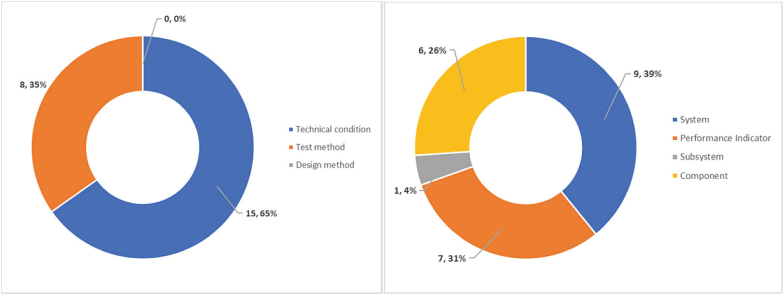

Fig. 4. Current group standards of fuel cell systems for vehicles

4.4 Relevant International Standards Statistics and Brief Analysis

The search yielded ten international standards related to automotive fuel cell systems, as shown in Fig. 5. Five of them are technical conditions, four are test methods and one is a design development method. There are eight standards at the system level and two standards at the performance indicator level.

The American Society of Automotive Engineers (SAE) has developed a relatively comprehensive set of international standards for fuel cell vehicles, mainly based on test methods. However, some of the standards were published relatively early and their contents may have lagged the development level of the industry. In addition, since SAE standards are not developed by international standards organizations, China rarely adopts SAE standards when developing relevant standards. Therefore, SAE standards have some significance for the development of national standards, but they need to be carefully selected in the process of specific transformation [10].

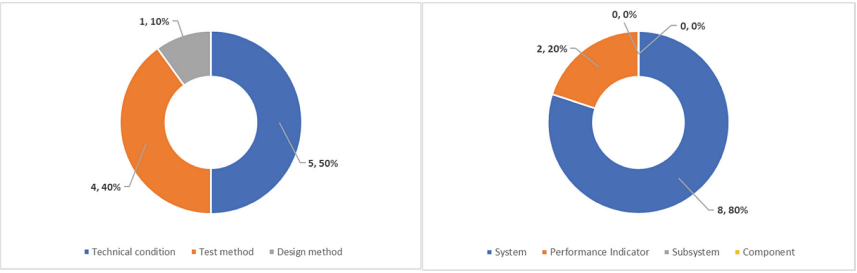

Fig. 5. Current international standards of fuel cell systems for vehicles

The International Electrotechnical Commission (IEC) has also published a few standards for automotive fuel cell systems, and the publication time is more recent, and the types of standards are mostly technical conditions, so these standards have more reference value for the preparation of national standards.

5 Conclusion and Outlook

The standard system of automotive fuel cell system should focus on key components and performance indicators. Whether it is an international standard, or a national standard, local standard or group standard, all have the role of guiding industrial development, so the concentration point should be on technical conditions and test methods from the type of standard. In the process of construction, it should be clearly established from the performance indicators, systems, auxiliary systems to parts of the four-tier system. In terms of level, national and international standards are more concerned with the system level, while group standards are more focused on the component level.

Although there are fewer standards dealing with the subsystem level, there are also relevant groups that have been established. Although the fuel cell subsystem cannot be a separate product at present, with the gradual development and growth of the fuel cell

industry, it is foreseeable that strong component suppliers in the industry will form strong alliance to provide separate fuel cell subsystem products and solutions to fuel cell system suppliers and even OEMs. Standards related to fuel cell subsystems will also gradually increase in the future. From the point of view of performance indicators, whether it is the national standard or the industry standard or the local standard, the most important performance indicators are mainly environmental adaptability, safety and durability, which are also the neck indicators that limit the large-scale industrialization of fuel cell vehicles. The whole industry should strengthen research and breakthrough in these performance indicators.

References

1. China society of automotive engineers: technology roadmap for energy saving and new energy vehicles 2.0. 2nd ed. China Machine Press, Beijing (2020)
2. Ministry of Industry and Information Technology of the People's Republic of China, https://www.miit.gov.cn/jgsj/zbes/gzdt/art/2020/art_d267bc68b1c745aabf843a86a507f259.html, Last accessed 15 May 2019
3. National Development and Reform Commission, http://zfxxgk.nea.gov.cn/2022-03/23/c_1310525630.htm, Last accessed 23 Mar 2022
4. National Energy Administration, http://www.nea.gov.cn/2020-09/21/c_139384465.htm, Last accessed 21 Sep 2020
5. People's Government of Guangdong Province, https://www.gd.gov.cn/gdywdt/bmdt/content/post_3502815.html, last accessed 03 Sep 2021
6. Guangdong Provincial Development and Reform Commission, http://drc.gd.gov.cn/ywtz/content/post_3993253.html, Last accessed 11 Aug 2022
7. Guangdong Administration for Market Regulation, http://amr.gd.gov.cn/zwgk/tzgg/content/post_3086069.html, Last accessed 15 Sep 2020
8. Beijing Municipal Finance Bureau, http://czj.beijing.gov.cn/zwxx/czyw/202108/t20210824_2475571.html, Last accessed 24 Aug 2021
9. Beijing Municipal Bureau of Economy and Information Technology, http://jxj.beijing.gov.cn/jxdt/tzgg/202211/t20221130_2869211.html, Last accessed 30 Nov 2022
10. Wang, X., Zhang, Y. et al.: Brief introduction of foreign standards of fuel cell vehicles. Chin. Standard. (6), 128–133 (2021)

Porous Heterogeneous Sulfide Nickel/Nickel Iron Alloy Catalysts for Oxygen Evolution Reaction of Alkaline Water Electrolysis at High Current Density

Songhu Bi, Zhen Geng(✉), Liming Jin, Mingzhe Xue(✉), and Cunman Zhang

Clean Energy Automotive Engineering Center, School of Automotive Studies, Tongji University, Shanghai 201804, People's Republic of China
{zgeng,mzxue}@tongji.edu.cn

Abstract. Alkaline water electrolysis is the important pathway for the green hydrogen production, where oxygen evolution reaction (OER) is the rate-limiting step due to the sluggish reaction kinetics. Transition metal heterogeneous catalyst is the kind of important OER catalyst for alkaline water electrolysis due to its good performance, low price and environmental friendliness. In this work, the porous sulfide nickel@nickel iron alloy catalyst (i.e. NM/NS@Ni_3Fe) is prepared by the designed high-temperature vulcanization and multi-step electrodeposition method. The NM/NS@Ni_3Fe catalyst exhibits an outstanding OER performance in an alkaline environment, with a low potential of 1.53 V at high current density of 1000 mA cm^{-2} and a low Tafel slope of 89 mV dec^{-1}. The excellent OER performance is attributed to the unique electronic structure of Ni_3S_2/Ni_3Fe heterogeneous interface and the catalyst layer with porous structure. The results indicate that Ni_3S_2 provides good electronic conductivity and the low electronegativity S atoms increase the formation of oxygen vacancies, which effectively improves the OER performance. In addition, the hydrophilic and porous structure of the electrode facilitates bubbles release and electrolyte flow at high current density. It provides the guidance for the design of porous heterogeneous OER catalysts with good-performance.

Keywords: Alkaline water electrolysis · Oxygen evolution reaction · Porous heterogeneous catalyst · High current density

1 Introduction

Green hydrogen, a "zero carbon emission" clean fuel, has been identified as having a crucial role in future energy innovation [1]. The eco-friendly energy gas can be obtained by many paths, such as water electrolysis to produce hydrogen, photo-splitting of water to produce hydrogen, biomass to produce hydrogen, and nuclear power to produce hydrogen [2]. Among them, the coupling of renewable energy power generation (such as wind energy, and solar energy) and water electrolysis hydrogen production technology is considered to be the main technical path to obtaining green hydrogen in the future [3, 4].

H. Sun et al. (Eds.): WHTC 2023, SPPHY 393, pp. 116–121, 2024.
https://doi.org/10.1007/978-981-99-8631-6_13

However, water electrolysis is limited by the slow oxygen evolution reaction (OER) [5]. Therefore, the high-performance OER catalysts that can speed up the electrochemical reaction and promote the decomposition of H_2O molecules are crucial for the electrolysis of water, especially for high current density conditions (>500 mA cm^{-2}) [6, 7].

In order to accelerate the decomposition of water molecules and obtain superior electrochemical performance at high current densities, the fabrication of heterojunction catalysts has become a research hotspot [8]. For NiS_x/Ni_3Fe, low reaction activation energies and unique coordination structures, are considered potential catalysts for water electrolysis [9, 10]. In this work, porous Ni_3S_2/Ni_3Fe heterojunction catalyst electrodes are successfully prepared to rely on vulcanization and multi-step electrodeposition techniques. The prepared NM/NS@Ni_3Fe catalyst exhibited an impressive OER performance in alkaline environment, showing a low high current potential of 1.53 V@1000 ma cm^{-2} and a low Tafel slope of 89 mV dec^{-1}. This heterogeneous catalyst shows good practical applications, especially for OER reactions at high currents.

2 Materials and Methods

2.1 Chemicals

All chemicals used in this work are analytical grade. $NiCl_2{\cdot}6H_2O$, NH_4Cl, $FeCl_2{\cdot}4H_2O$, H_3BO_3, sulfur powder and HCl are purchased from Sinopharm Reagent Co. Commercial RuO_2 is purchased from Aladdin Reagent Co., and NM (wire diameter of 100 μm, 80 mesh) is purchased from China Kangwei Wire Mesh Co.

2.2 Preparation of NM/NS

The nickel mesh (1 × 2 cm^2) is submerged in 3 M HCl for 20 min to remove the surface oxides, then ultrasonic cleaning in deionized water three times to remove HCl residue. Next, the cleaned nickel mesh is taken as the cathode and the high-purity nickel rod (99.5 wt%) as the anode. The electrodeposition solution is a mixture of 0.15 M $NiCl_2{\cdot}6H_2O$ and 2 M NH_4Cl. Electrodeposition is operated at room temperature for 10 min at a current density of 1000 mA cm^{-2} [11]. After drying at 60 °C for 4 h, it is placed in a crucible and vulcanized in a tube furnace containing 60 mg of S powder at 300 °C for 60 min. Then annealed in the air for 60 min to room temperature and it is denoted as NM/NS.

2.3 Preparation of NM/NS@Ni_3Fe

Continuously, 0.21 M $FeCl_2{\cdot}4H_2O$ and 0.6 M H_3BO_3 are added into the solution and the solution is heated to 80 °C. Next, NM/NS is maintained for 3 min at an electro-deposition current density of 10 mA cm^{-2}. The target electrode is denoted as NM/NS@Ni_3Fe.

2.4 Materials characterization

X-ray diffraction (XRD) data are acquired by X-ray scanning using a device (Bruker D8 Advanced) with a Rigaku 2550 light source (Cu Kα, λ = 1.5418 Å). The scanning range is 10–90° with a scanning rate of 0.2°/s. The surface morphologies are investigated by scanning electron microscopy (ZEISS GeminiSEM 300) at a scanning voltage of 3 kV.

2.5 Electrochemical Characterization

Electrochemical performances are estimated by a three-electrode system connected to an electrochemical workstation (Reference 3000) in 30 wt% KOH solution (pH = 14.6). A high-purity graphite rod is used as the counter electrode accompanied by a HgO/Hg reference electrode. Linear scanning voltammetric (LSV) curves are performed with the scan range of 1.0–1.9 V versus the reversible hydrogen potential (vs. RHE) and the scan rate is 5 mVs^{-1}. The potential (vs. RHE) is converted by the equation: $E_{(RHE)} = E_{(HgO/Hg)} + 0.0591 \times pH + 0.098$. All LSV curves are corrected by ir-compensation in the three-electrode system. Tafel slopes are obtained using a logarithmic transformation base on LSV curves. EISs are tested at a constant potential (0.49 V vs. HgO/Hg) scanning from 0.01 to 100,000 Hz.

3 Results and Discussion

Commercial NM is used as a substrate because of its lower price, resistance to alkaline corrosion, and two-dimensional planes conferring fast bubble release. The preparation process is shown in Fig. 1a. Initially, the high-current (1 A cm^{-2}) is used to electro-deposited porous nickel (PN), its porous property can confer a large loading area for catalysis. Then, the PN is vulcanized, the sulfur vapor reacts with the metallic Ni to produce Ni_3S_2 at high temperatures. Finally, the electrode NM/NS@Ni_3Fe is prepared by electro-depositing the nickel-iron alloy again in the nickel-iron solution. Figure 1b and c show NM/PN electrode that reflects a distinct porous property, which provides a large area for the active sites. Figure 1c shows the SEM image of NM/NS@Ni_3Fe, showing filamentous nickel sulfide on the surface relative to PN. The filamentous morphology can increase the roughness of the catalyst surface, which can improve the catalytic performance through its super-hydrophilicity.

As shown in Fig. 2, the composition of the prepared electrodes is determined by XRD testing. NM and PN exhibit strong characteristic response peaks at 44.50 (111) 51.85 (113) and 76.38 (220), respectively, indicating that Ni metal is the predominant component. After vulcanization, PN is vulcanized to generate Ni_3S_2, showing a strong response at the characteristic angles 21.75° (101), 31.10° (110), 37.78° (003), 49.93° (113), 55.16° (122), respectively. When the NiFe alloy is deposited on the surface, the characteristic peaks of Ni_3Fe do not emerge. The signal peak is blocked because of its low content and its close response to the Ni metal.

The alkaline OER performance of the prepared electrodes is examined in a 30 wt% KOH solution, illustrated in Fig. 3. NM/NS@Ni_3Fe exhibits a lower potential of 1.53 V at a high current density of 1000 mA cm^{-2}, which is much lower than the NM/NS (1.71 V) and commercial RuO_2 (1.60 V). At high current density (100–1000 mA cm^{-2}), NM/NS@Ni_3Fe possesses a small Tafel slope of 89 mV dec^{-1}, which is smaller than 201 for NM/NS and 110 for RuO_2, indicating that NM/NS@Ni_3Fe has a faster electrochemical reaction kinetics. The excellent OER performance is attributed to the Ni_3S_2 and Ni_3Fe heterostructures, whose unique electron transport properties confer a low reaction energy barrier to the active site. Moreover, NM/NS@Ni_3Fe exhibits a smaller electrochemical impedance value of 0.62 Ω, which is smaller than 3.8 Ω for NM/NS and 1.2 Ω for RuO_2, demonstrating the faster electron transfer ability of NM/NS@Ni_3Fe. The

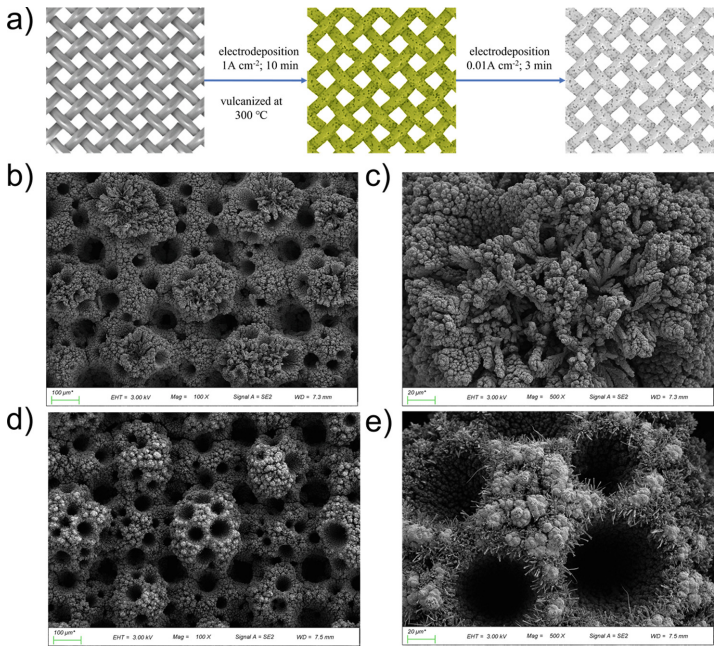

Fig. 1 **a** Schematic diagram of the preparation process of NM/NS@Ni_3Fe; **b** and **c** SEM images of NM/PN; **d** and **e** SEM images of NM/NS@Ni_3Fe.

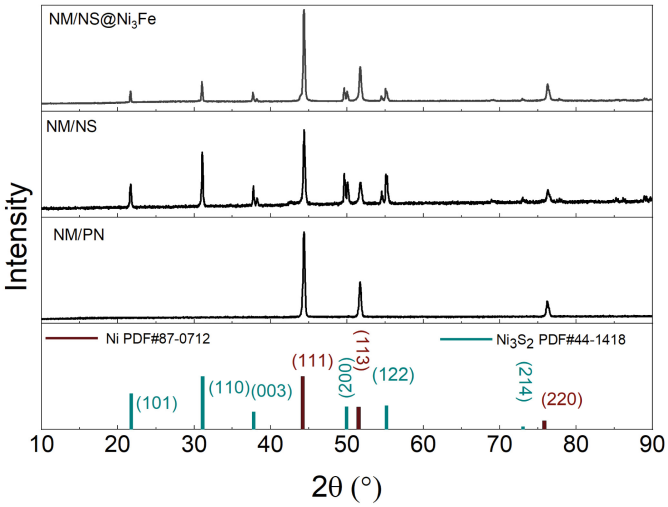

Fig. 2. XRD patterns of various electrodes (NM/PN; NM/NS; NM/NS@Ni_3Fe).

correlation between phase shift and frequency further confirms that NM/NS@Ni_3Fe possesses better electron transfer capability with phase peaks shifted to higher frequencies (Fig. 3d).

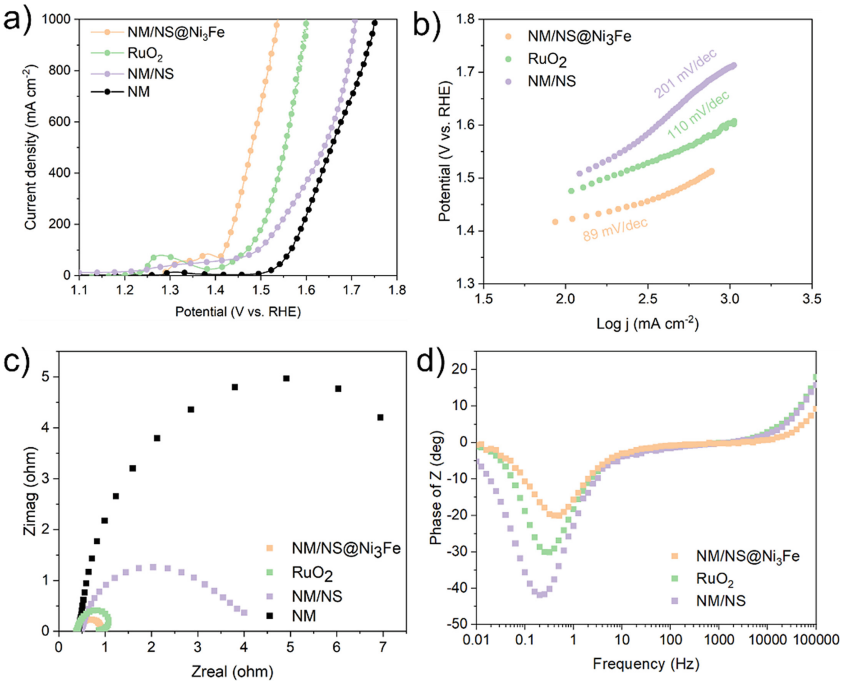

Fig. 3. Electrochemical properties of various electrodes (NM/NS@Ni_3Fe, NM/NS, RuO_2 and NM): **a** LSV curves, **b** Tafel slope, **c** EIS spectrum and **d** Relationship between frequency and phase shift.

4 Conclusion

Porous heterogeneous Ni_3S_2@Ni_3Fe electrodes are successfully prepared using a continuous hydrogen template method, high-temperature vulcanization and electrodeposition methods. NM/NS@Ni_3Fe exhibits a potential of only 1.53 V for a current density of 1000 mA cm^{-2} and a lower Tafel slope of 89 mV dec^{-1}, superior to commercial RuO_2. Its good performance is attributed to the unique electronic structure of the Ni_3S_2 and Ni_3Fe and the porous properties of the electrodes. Such porous heterogeneous NM/NS@Ni_3Fe electrode not only exhibits good catalytic properties but also has the potential to be applied due to its facile and inexpensive fabrication.

References

1. Lewis, N.S., Nocera, D.G.: Powering the planet: chemical challenges in solar energy utilization. Proc. Natl. Acad. Sci. **103**(43), 15729–15735 (2006)
2. Nikolaidis, P., Poullikkas, A.: A comparative overview of hydrogen production processes. Renew. Sustain. Energy Rev. **67**, 597–611 (2017)
3. Koroneos, C., Dompros, A., Roumbas, G.: Hydrogen production via biomass gasification—A life cycle assessment approach. Chem. Eng. Process. **47**(8), 1261–1268 (2008)
4. Grigoriev, S.A., Fateev, V.N., Bessarabov, D.G., Millet, P.: Current status, research trends, and challenges in water electrolysis science and technology. Int. J. Hydrogen Energy **45**(49), 26036–26058 (2020)
5. Ren, J., Antonietti, M., Fellinger, T.-P.: Efficient water splitting using a simple Ni/N/C paper electrocatalyst. Adv. Energy Mater. **5**(6), 1401660 (2015)
6. Yang, X., Guo, R., Cai, R., Shi, W., Liu, W., Guo, J., et al.: Engineering transition metal catalysts for large-current-density water splitting. Dalton Trans. **51**(12), 4590–4607 (2022)
7. Li, S., Li, E., An, X., Hao, X., Jiang, Z., Guan, G.: Transition metal-based catalysts for electrochemical water splitting at high current density: current status and perspectives. Nanoscale **13**(30), 12788–12817 (2021)
8. Xu, Q., Zhang, J., Zhang, H., Zhang, L., Chen, L., Hu, Y., et al.: Atomic heterointerface engineering overcomes the activity limitation of electrocatalysts and promises highly-efficient alkaline water splitting. Energy Environ. Sci. **14**(10), 5228–5259 (2021)
9. Xiong, Y., Xu, L., Jin, C., Sun, Q.: Interface-engineered atomically thin Ni_3S_2/MnO_2 heterogeneous nanoarrays for efficient overall water splitting in alkaline media. Appl. Catal. B **254**, 329–338 (2019)
10. Li, J., Jiang, L., He, S., Wei, L., Zhou, R., Zhang, J., et al.: Heterostructured $Ni(OH)_2/Ni_3S_2$ supported on Ni foam as highly efficient and durable bifunctional electrodes for overall water electrolysis. Energy Fuels **33**(11), 12052–12062 (2019)
11. Sengupta, S., Patra, A., Jena, S., Das, K., Das, S.: A Study on the effect of electrodeposition parameters on the morphology of porous nickel electrodeposits. Metall. and Mater. Trans. A. **49**(3), 920–937 (2018)

Study on Safety Risk of Railway Vehicle Hydrogen Refueling Station Based on T-S Fuzzy Fault Tree and Bayesian Network

Lei Shi[1(✉)], Yang Gao[1], Jian Wang[1,2], Shijie Sun[1], Limei Chen[1], and Weiran Xiang[1]

[1] CRRC Changchun Railway Vehicles Co., Ltd., Changke Road 2001, Changchun, Jilin, China
shilei8.ck@crrcgc.cc

[2] Central South University, Lu Shan Nan Road 932, Changsha, Hunan, China

Abstract. According to the requirements of operation safety in railway vehicle hydrogen refueling station, the risk factors affecting the operation safety were selected, the calculation formula of evaluation index was derived, and the Bayesian network model based on T-S fuzzy fault tree was constructed. The triangular membership function, the fuzzy subset of failure probability and the posterior probability formula were used to verify the availability of the safety risk assessment method.

Keywords: Railway vehicle hydrogen refueling station · T-S fuzzy fault tree · Bayesian network · Safety risk

1 Introduction

As a renewable, clean and efficient secondary energy source, hydrogen energy has many advantages such as wide source, high calorific value, pollution-free combustion and various forms of utilization. Hydrogen energy is widely used in the field of rail transportation [1]. The construction of hydrogen refueling stations is the basis for the large-scale application of hydrogen vehicles, and the safe operation of hydrogen refueling stations is a necessary guarantee for the movement of hydrogen rail vehicles. At present, more than 300 hydrogen refueling stations have been built nationwide, and the number of hydrogen refueling stations in China ranks the first in the world [2]. For the safe operation of hydrogen refueling stations for rail transportation, it is necessary to regularly evaluate the safety of hydrogen refueling stations and develop an effective emergency treatment plan.

Fault tree analysis method, as an effective tool for reliability and safety analysis of large complex systems, is widely used in safety risk evaluation [3]. However, the inadequacy of the probability, bimodal and with-or-with relationship assumptions in the traditional fault tree severely restricts the further application of the fault tree analysis method. In the literature [4], fuzzy set theory was introduced to describe the connection between events with T-S gates instead of with-or-gates, while the effects of multiple fault degrees on the system were considered to solve the problems of traditional fault

H. Sun et al. (Eds.): WHTC 2023, SPPHY 393, pp. 122–131, 2024.
https://doi.org/10.1007/978-981-99-8631-6_14

trees. Compared with the T-S fuzzy fault tree analysis method, Bayesian networks have advantages in dealing with logical relations of events, system polymorphism and computational simplicity. The literature [5] introduced fuzzy set theory into Bayesian network analysis to solve the problem of over-reliance on exact fault probability and successfully applied it to urban road traffic accident analysis. However, the study was only for two-state systems, and the conditional probability parameters of Bayesian networks are difficult to determine, making it difficult to perform real-time dynamic evaluation. In view of the superiority and complementarity of T-S fuzzy fault trees and Bayesian networks.

This paper proposes a safety risk evaluation method of rail transit hydrogen refueling station based on T-S fuzzy fault tree and Bayesian network. Through the transformation of T-S fuzzy fault tree to Bayesian network, the Bayesian network model and node conditional probability table are determined, and the fault states and fault probabilities of nodes are described by using fuzzy numbers and fuzzy subsets, and the safety risk evaluation method of rail transit hydrogen refueling station is calculated.

2 Basic Theory and Methods

2.1 Constructing Bayesian Networks Based on T-S Fuzzy Fault Trees

The T-S fuzzy fault tree model is shown in Fig. 1, where x_1, x_2, and x_3 are the bottom events, y_1 is the middle event, y_2 is the top event, and a and b are T-S fuzzy gates.

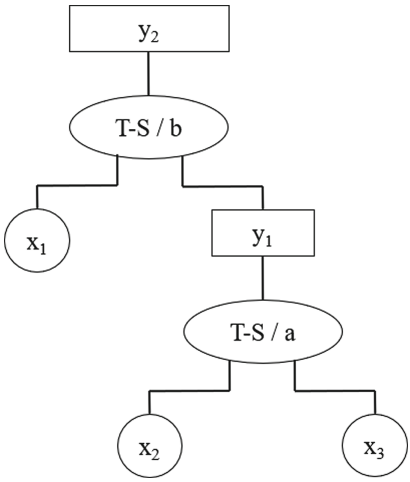

Fig. 1. T-S fuzzy fault tree

A Bayesian network is a loop-free network consisting of a conditional probability table and a directed acyclic graph. Vx and V_y in a Bayesian network denote node variables, and if there is an edge from V_x to V_y, V_x is said to be the parent node of V_y, while V_y is the child node of V_x. The structure of a simple Bayesian network is shown

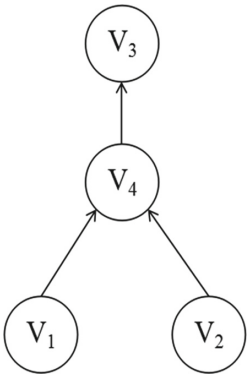

Fig. 2. A simple Bayesian network

in Fig. 2. The nodes without a parent are called root nodes (V_1, V_2), the nodes without children are called leaf nodes (V_3), and the rest are called intermediate nodes (V_4).

Firstly, the top event, middle event and bottom event in the T-S fuzzy fault tree correspond to the leaf node, middle node and root node of the Bayesian network, respectively, and then the corresponding nodes in the Bayesian network are connected with directed edges according to the T-S gate relationship, and the flow of the Bayesian network constructed based on the T-S fuzzy fault tree is shown in Fig. 3.

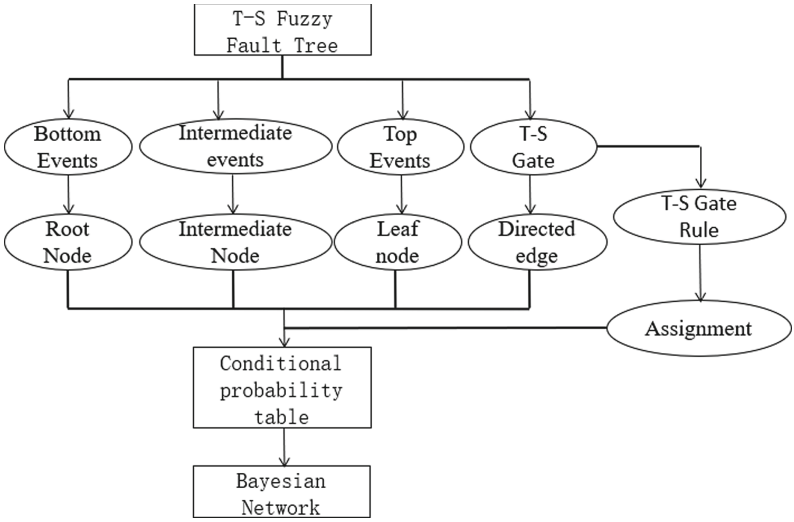

Fig. 3. A flow chart of Bayesian network based on T-S fuzzy fault tree construction

2.2 Node Description

In this paper, the fuzzy set represented by the triangular affiliation function is chosen to describe the failure probability of each node, and a fuzzy subset of the failure probability of $xj = xj^{a_j}$ is set.

$$F(x_j^{a_j}) = \{ f^m - \Delta f^1, f^m, f^m + \Delta f^r \} \tag{1}$$

In the above equation: $f^{\,m}$is the center of the fuzzy subset, Δf^1 and Δf^r are the left and right fuzzy regions, and the magnitude of the two values indicates the level of fuzziness. If $\Delta f^{\,1} = \Delta f^r = 0$, the fuzzy subset is the exact value, $F(x_j^{a_j})$ is shown in Fig. 4 according to the triangular affiliation function.

$$\mu F(x_j^{a_j})(f) = \begin{Bmatrix} \max\left\{0, 1 - \frac{f^m - f}{\Delta f^1}\right\}, 0 \le f \le f^m \\ \max\left\{0, 1 - \frac{f - f^m}{\Delta f^r}\right\}, f^m \langle f \le 1 \end{Bmatrix} \tag{2}$$

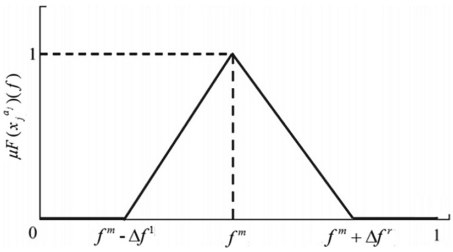

Fig. 4. Trigonometric affiliation function

2.3 T-S Fuzzy Fault Tree Inference Based on Bayesian Networks

If the fuzzy subset of fault probabilities of each node at each fault state is known to be $F(x_1^{a_1})$, $F(x_2^{a_2})$, …, $F(x_n^{a_n})$, the fuzzy subset of fault probabilities at $T = T_{\mathrm{m}}$ is obtained by the bucket elimination method.

$$\begin{aligned} F(T = T_m) &= \sum_{x_p; y_q} F(x_p; y_q; T = T_m) \\ &= \sum_{\pi(T)} F(T = T_m | \pi(T)) \times \sum_{\pi(y_1)} F(y_1 | \pi(y_1)) \\ &\quad \times \sum_{\pi(y_2)} F(y_2 | \pi(y_2)) \times \cdots \times \sum_{\pi(y_q)} F(y_q | \pi(y_q)) \\ &\quad \times F(x_1^{a_1}) \times F(x_2^{a_2}) \times \cdots \times F(x_n^{a_n}) \end{aligned} \tag{3}$$

In the above equation, $\pi(T)$ is the set of parent nodes for T and $\pi(y_{\mathrm{q}})$ is the set of parent nodes for y_{q}. In the practical case the current fault state of the root node is unique,

then the root node state importance is as follows.

$$Q_{T_q}^{D_e}(x_i') = \max\{(P(T = T_q|x_i = x_i') - P(T = T_q, x_i = 0)), 0\} \tag{4}$$

In the above equation, $P(T = T_q|x_i = x_i')$ is the $T = T_q$ probability of occurrence when $x_i = x_i'$ is the probability of occurrence of $T = T_q$ when the current fault state is 0.

Using the Bayesian conditional probability formula, the probability at $x_i = x_i^{ai}$ when $T = T_{\mathrm{q}}$ can be found as follows.

$$P(x_i = x_i^{a_i}|T = T_q) = E\left(\frac{P(x_i = x_i^{a_i}|T = T_q)}{P(T = T_q)}\right) \tag{5}$$

In the above equation, $P(x_i = x_i^{a_i}|T = T_q)$ is a fuzzy subset of the posterior probability of $x_i = x_i^{a_i}$ when $T = T_q$.

3 Safety Risk Assessment of Rail Transit Hydrogen Refueling Stations Based on T-S Fuzzy Fault Trees and Bayesian Networks

The workflow steps of a rail transit hydrogen refueling station are hydrogen supply, compression, storage, and refueling. The main safety risks come from gas leakage and fire during hydrogen transportation, storage and hydrogen refueling [6].

Combined with the relevant literature to analyze the process flow of hydrogen refueling station, the safety risk factors of hydrogen refueling station are mainly seven categories of station process, pressure system, control system, safety system, environmental factors, human factors and regulations.

From these seven categories as the top events of the assessment system, 26 possible basic events of safety accidents in hydrogen refueling stations were collated and the fault tree model constructed is shown in Fig. 5.

The T-S fuzzy fault tree in Fig. 5 is transformed into a Bayesian network graph, and the intermediate events corresponding to the intermediate nodes y1-y7 are shown in Table 1. Then the conditional probability table of the Bayesian network nodes is assigned by the T-S gate rule and the conditional probability of each node is determined according to the historical data survey weight method to complete the establishment of the Bayesian network.

In this paper, the likelihood level of occurrence of the nodes to be evaluated is determined according to the risk occurrence likelihood level criteria, as detailed in Table 2.

In this paper, a weighted average method is used for processing and analysis to obtain the fault probability f^{m} of each root node; the results of the survey are summarized, and fuzzification of f^{m} is performed to determine Δf^{l} and Δf^{r}. The fuzzy subset of fault probability of the root node is finally determined.

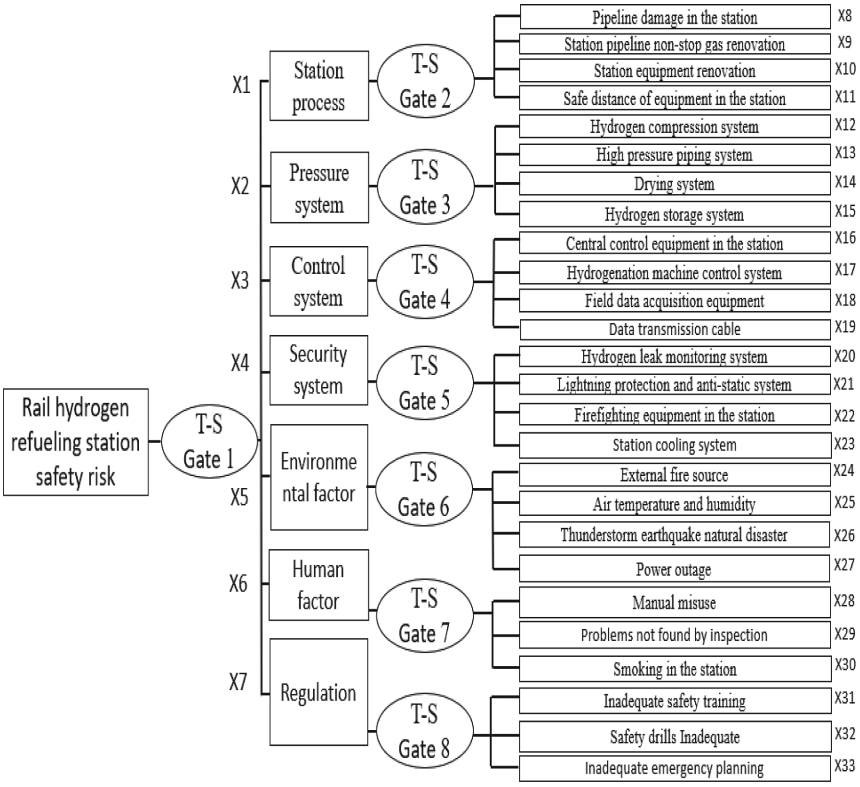

Fig. 5. Rail hydrogen refueling station safety risk fault tree

Based on the established Bayesian network, the fuzzy subset of failure probability of each node is obtained by reasoning using Eq. (3). According to the fault state of each root node, the posterior probability of each root node state is calculated using Eqs. (4) and (5), and the relative weakness of the system is determined under the condition that only the fault state of the root node is known, which facilitates the safety management of the rail transit hydrogen refueling station.

4 Application Analysis

In this paper, we assume that the fault states of root nodes X8 and X9 are no fault and severe fault, which are represented by fuzzy numbers 0 and 1, respectively, and the fault states of the remaining nodes are no fault, medium fault and severe fault, which are represented by 0, 0.5 and 1, respectively. Combined with the workflow of the rail transit hydrogen refueling station and the percentage of each safety risk factor in the operation of the station, the fuzzy subset $F(X_j = 1)$ of failure probability with failure state of each node is obtained, as shown in Table 3. Where the fuzzification parameter $\Delta f^{1} = \Delta f^{\mathrm{r}} = 0.15 f^{\mathrm{m}}$, and the middle element is the center of the fuzzy subset.

For the purpose of analysis, this paper assumes that the fuzzy subset of failure probabilities for root node failure states of 0.5 and 1 are the same. According to the root node failure probability subset, the conditional probability table of the intermediate node y1 of Bayesian network is listed as shown in Table 4, where rule 1 indicates that the probability of y1 being 0, 0.5 and 1 is 0 when X8 is 0 and X9 is 0, and other rules and so on.

$$
\begin{aligned}
F(y_1 = 0) &= \sum_{x_8;y_9} F(x_8, y_9; y_1 = 0) \\
&= \sum_{x_8;y_9} F(y_1 = 0|x_8, y_9) \times F(x_8) \times F(x_9) \\
&= (0.77565, 0.73276, 0.69835) \\
F(y_1 = 0.5) &= \sum_{x_8;y_9} F(x_8, y_9; y_1 = 0.5) \\
&= \sum_{x_8;y_9} F(y_1 = 0.5|x_8, y_9) \times F(x_8) \times F(x_9) \\
&= (0.10452, 0.12107, 0.13705) \\
F(y_1 = 1) &= \sum_{x_8;y_9} F(x_8, y_9; y_1 = 1) \\
&= \sum_{x_8;y_9} F(y_1 = 1|x_8, y_9) \times F(x_8) \times F(x_9) \\
&= (0.11852, 0.14255, 0.16002)
\end{aligned}
$$

Based on the constructed Bayesian network, the conditional probability table of the nodes is combined with the inference using Eq. (3) to obtain the fuzzy subset of failure probabilities when the failure states of the leaf nodes are 0, 0.5 and 1.

$$
\begin{aligned}
P(T = 0) &= (0.14855, 0.08732, 0.04123) \\
P(T = 0.5) &= (0.12687, 0.11872, 0.10982) \\
P(T = 1) &= (0.72562, 0.77851, 0.85625)
\end{aligned}
$$

In practical application, it is also necessary to consider the influencing factors that play a significant role in the safety risk of rail transit hydrogen refueling stations and pay attention to the order of each influencing factor. The posterior probability of each root node is calculated using Eqs. (4) and (5), as shown in Table 5.

The above calculation results show that the probability of moderate or serious failure is small, while the probability of no failure is large, which is consistent with the actual situation and verifies the accuracy and feasibility of the method in this paper. According to the principle of maximum affiliation, the safety risk level of this hydrogen refueling station can be determined and the countermeasures that should be taken can be analyzed. According to the existing safety risk management scheme, it is enough to strengthen the monitoring, but it is also necessary to pay attention to the changes of each influencing factor and take corresponding measures.

Table 1. Intermediate events corresponding to intermediate nodes

Node	Event	Node	Event
y1	Station process	y5	Environmental factor
y2	Pressure system	y6	Human factor
y3	Control System	y7	Regulation
y4	Security Systems	–	–

Table 2. Risk occurrence likelihood level criteria

Level	Possibility	Probability
I	Frequent	[0.1,1]
II	Probable	[0.01,0.1)
III	Occasional	[0.001,0.01)
IV	Rare	[0.0001,0.001)
V	Impossible	[0,0.0001)

Table 3. Subset of root node failure probabilities

Root node	F ($X_j = 1$)	Root node	F ($X_j = 1$)
X_8	(0.00042,0.00050,0.00058)	X_{21}	(0.00067,0.00080,0.00093)
X_9	(0.00681,0.00800,0.00919)	X_{22}	(0.00686,0.00800,0.00914)
X_{10}	(0.00050,0.00060,0.00070)	X_{23}	(0.00033,0.00040,0.00047)
X_{11}	(0.00339,0.00400,0.00461)	X_{24}	(0.00062,0.00070,0.00078)
X_{12}	(0.00680,0.00800,0.00920)	X_{25}	(0.00511,0.00600,0.00689)
X_{13}	(0.00008,0.00010,0.00012)	X_{26}	(0.00007,0.00008,0.00009)
X_{14}	(0.00420,0.00500,0.00480)	X_{27}	(0.00005,0.00006,0.00007)
X_{15}	(0.11020,0.13000,0.14980)	X_{28}	(0.08500,0.10000,0.11500)
X_{16}	(0.00007,0.00010,0.00013)	X_{29}	(0.00685,0.00800,0.00915)
X_{17}	(0.12744,0.15000,0.17256)	X30	(0.68000,0.80000,0.92000)
X_{18}	(0.02122,0.02500,0.02878)	X_{31}	(0.17000,0.20000,0.23000)
X_{19}	(0.68000,0.80000,0.92000)	X_{32}	(0.00542,0.00650,0.00758)
X_{20}	(0.00575,0.00700,0.00825)	X_{33}	(0.00008,0.00010,0.00012)

Table 4. Intermediate node y1 conditional probability table

Rule	X_8	X_9	$y1 = 0$	$y1 = 0.5$	$y1 = 1$
1	0	0	1	0	0
2	0	0.5	0.2	0.7	0.1
3	0.5	1	0	0.2	0.8
4	0.5	0	0.5	0.4	0.1
5	1	0.5	0.1	0.5	0.4
6	1	1	0	0	1

Table 5. Root node posterior probability

Root node	$P(X_i = 0)$	Root node	$P(X_i = 0)$
X_8	0.02752	X_{21}	0.05416
X_9	0.01625	X_{22}	0.03258
X_{10}	0.03251	X_{23}	0.03577
X_{11}	0.06106	X_{24}	0.07741
X_{12}	0.07565	X_{25}	0.06231
X_{13}	0.03758	X_{26}	0.04157
X_{14}	0.06583	X_{27}	0.02896
X_{15}	0.00785	X_{28}	0.03741
X_{16}	0.00228	X_{29}	0.01227
X_{17}	0.01571	X_{30}	0.05214
X_{18}	0.04332	X_{31}	0.07541
X_{19}	0.02771	X_{32}	0.01513
X_{20}	0.00225	X_{33}	0.05936

5 Conclusion

In this paper, the safety risks affecting the operation of rail transit hydrogen refueling stations are studied. Firstly, the safety risk factors affecting the operation of hydrogen refueling stations are selected and the formulae for the evaluation indexes are derived; then a Bayesian network model based on the T-S fuzzy fault tree analysis method is constructed and the conditional probability table of Bayesian network nodes is assigned with the basic events of potential hydrogen refueling station safety accidents; finally, the triangle affiliation function, the fuzzy subset of failure probabilities and the posterior probability formulae are used for the calculation. The usability of this safety risk evaluation method is verified.

References

1. Lin, W., Liu, W., Li, Y.: Study on the development strategy of China's hydrogen energy infrastructure industry. Strateg Study CAE J. **21**(3), 78–79 (2019)
2. Zhang, Z., Zhang, G., Liu, Y.: Current situation and prospect of hydrogen refueling station construction in China. Energy Conserv. J. **37**(6), 16–19 (2018)
3. Yao, C., Zhang, Y., Wang, X.: T-S fuzzy fault tree importance analysis method. Chin. Mech. Eng. J. **22**(11), 1261–1268 (2011)
4. Song, H., Zhang, H., Wang, X.: T-S fuzzy fault tree analysis method. Control Decis. J. **20**(8), 854–859 (2005)
5. Zhao, J., Deng, W., Wang, J.: Bayesian network-based analysis of urban road traffic accidents. J. Southeast Univ. (Nat. Sci. Ed.) **41**(6), 1300–1306 (2011)
6. Ruan, J., Luo, Y., Tang, J.: Discussion on the safe and reliable operation of hydrogen refueling mother stations and countermeasures. Saf. Health Environ. J. **21**(9), 28–31 (2021)

Design Method of the Hydrogen Liquefaction Process with Catalyst-Filled Heat Exchanger Model

Cui Lv[1], Gang Zhou[1(✉)], Jinzhen Wang[1], Ming He[1], Jihao Wu[1,2], and Linghui Gong[1]

[1] State Key Laboratory of Technologies in Space Cryogenic Propellants, Technical Institute of Physics and Chemistry, Chinese Academy of Sciences, Beijing, China
zhougang@mail.ipc.ac.cn

[2] University of Chinese Academy of Sciences, Beijing, China

Abstract. Hydrogen liquefaction is a crucial process in the liquid hydrogen industry, and the use of liquid hydrogen is becoming increasingly important for storing and transporting hydrogen over long distances. Hydrogen has two spin isomers, that is ortho and para hydrogen. One of the challenges in this process is the conversion of ortho to para hydrogen in the heat exchanger. As the conversion process releases heat and is a spontaneous behavior, it is important to ensure that the content of para hydrogen in the final product is at least 95%. Unfortunately, there are currently no known commercial models that contain catalyst-filled heat exchangers for converting ortho hydrogen to para hydrogen. In this paper, Aspen Hysys is used to construct a new design method for hydrogen liquefier with O-P hydrogen conversion heat exchanger. Using this model, one 5 ton per day hydrogen liquefier is designed, and the key parameters of the process are obtained, which will provide a new method for the design of hydrogen liquefaction process in the future.

Keywords: Hydrogen liquefaction · Catalyst-filled heat exchanger · Ortho hydrogen · Para hydrogen

1 Introduction

Hydrogen energy is an essential renewable energy carrier that provides a critical technical pathway to achieve low-carbon goals. Liquid hydrogen, with its high storage density and low storage pressure, is a crucial component of building hydrogen energy storage and transportation systems. As future hydrogen consumption gradually increases, the design of the liquefaction process is becoming a widely researched topic in liquid hydrogen production technology.

Hydrogen consists of two spin isomers, which are ortho-hydrogen and para-hydrogen, and their concentration ratio varies with temperature [1]. The common conversion of ortho- to para-hydrogen is an exothermic reaction that can occur with the help of catalyst, but this phenomenon can also occur in liquid hydrogen without the catalyst. In order to reduce the vaporization of liquid hydrogen products caused by conversion

H. Sun et al. (Eds.): WHTC 2023, SPPHY 393, pp. 132–140, 2024.
https://doi.org/10.1007/978-981-99-8631-6_15

heat, catalytic conversion is arranged in multiple temperature ranges of the liquid hydrogen production process. Catalytic conversion reaction can be categorized as adiabatic convention, isothermal convention and continuous convention. It is challenging to integrate the catalyst in the heat exchanger to realize the multistage continuous reaction. However, continuous reaction consumes the least amount of work, so it is more suitable for large-scale hydrogen liquefaction plant.

Despite being commercially available, current software lacks a heat exchanger model integrated with the ortho to para conversion reaction. Therefore, effectively and accurately designing a hydrogen liquefier with continuous conversion is the focus of researchers' attention. Son et al. [2] adopted an equivalent heat exchanger model using a conversion reactor unit to simulate the catalytic reaction, but the limitation of this work is that if a large amount of ortho- is converted to para-hydrogen, the results will be infeasible. Guocong et al. [3] replaced the module with a heater and heat exchanger, which is more suitable for adiabatic conversion. Meanwhile, Berstad et al. [4] used equilibrium hydrogen to optimize the design process. However, in the above design process, these methods have some limitations. Furthermore, if the hydrogen in the outlet of heat exchangers can't reach the equilibrium hydrogen,there is still a lack of a mature solution. In the present study, we provide a new design method for a hydrogen liquefier with ortho- and para-hydrogen conversion heat exchanger based on the Aspen Hysys V12.1. This will not only improve the calculation accuracy, but also provide a reference for other similar processes.

2 Hydrogen Liquefaction Process Model

2.1 Liquefaction Process Description

To assess the suitability of Aspen Hysys for simulating hydrogen liquefaction systems with continuous conversion, a 5 TPD (ton per day) liquefier system was chosen for the study. Different working media, such as hydrogen, helium, neon, and mixed working media, were evaluated for the pre-cooling component of the system.Considering the technical maturity, complexity and energy consumption, liquid nitrogen pre-cooling and helium cryogenic cooling scheme was ultimately selected, as shown in Fig. 1. Therefore, The system consists of a compressor, a liquid nitrogen pre-cooling section, a turbo-expander pre-cooling section, and a liquid hydrogen storage system. Hydrogen gas is gradually cooled in heat exchangers (HEX1-7) from 300K to 20K through throttling valves, with HEX3-7 containing a catalyst.HEX3 is designed as the thermosiphon heat exchanger where hydrogen undergoes isothermal conversion. HEX4-5 is used for near-continuous conversion.In this scheme, there are the following characteristics: (1) the cooling path and the liquefaction path are relatively independent. (2) the cooling medium is inert working medium, resulting in higher safety levels, and non-explosion compressors can be used to reduce initial equipment investment. (3) a thermosiphon heat exchanger is used for isothermal conversion in the liquid nitrogen temperature zone. Under the temperature of 80K, the continuous convection with catalytic filled heat exchangers were used. (4) two throttling valves are employed to further utilize the J-T effect of hydrogen.

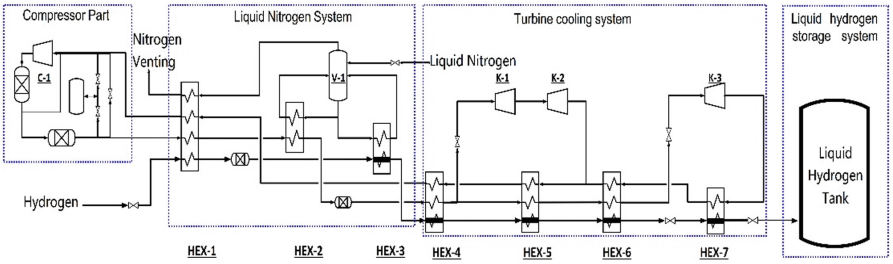

Fig. 1. Flow chart of hydrogen liquefaction

2.2 Simulation Method

Equivalent catalyst-filled heat exchanger model

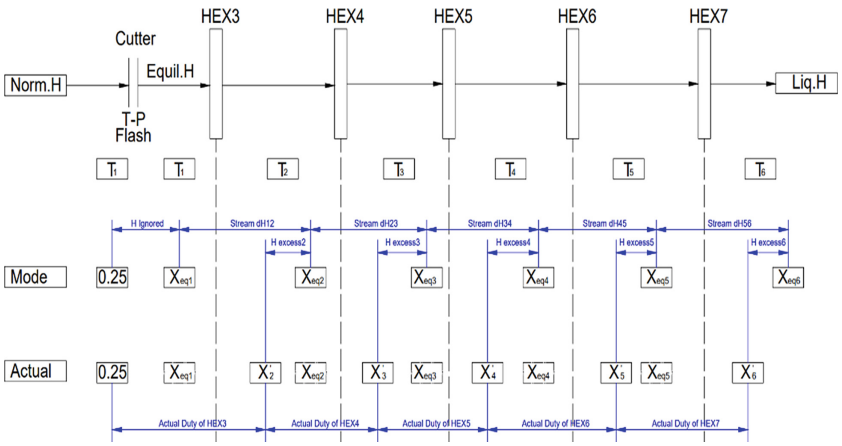

Fig. 2. Flow chart of hydrogen stream in HEX3-5

In the process shown in Fig. 1, HEX1-2 are typical plate-fin heat exchangers, and their calculations can be done using the LNG heat exchanger model in Aspen Hysys. As for the hydrogen properties, normal hydrogen (o-H2:75%, P-H2:25%) from NIST is used for HEX1-2. On the other hand, HEX3-7 are filled with a catalyst, so the hydrogen properties used in these heat exchangers employ the equilibrium hydrogen physical property method. This method can be obtained by modifying the heat capacity of the para hydrogen from NIST. By using these properties in Aspen Hysys, we can relative accurately simulate the performance of the heat exchangers in the hydrogen liquefaction process. Since Aspen Hysys doesn't have a built-in heat exchanger model for ortho-para H2 conversion, equivalent heat exchanger models need to be customized to simulate this process in catalyst-filled heat exchangers like HEX3-7. In cases where the para hydrogen content at the outlet doesn't reach the equilibrium state, the non-equilibrium conversion efficiency is used to calculate the actual exit para hydrogen fraction. This is done by

dividing the exit para hydrogen fraction by the equilibrium hydrogen fraction. The difference between the equilibrium and non-equilibrium conversion heat is then calculated and set as the heat loss in the heat exchanger. This can be implemented in Aspen Hysys using spreadsheets to perform the necessary calculations and provide a more accurate model of the heat exchanger's performance. The specific implementation process can be further explained as shown in Fig. 2, which shows a schematic diagram of the catalyst-filled heat exchanger and the attached hydrogen stream. The cutter is placed between HEX1 and HEX3 to convert the property package model of hydrogen. This is necessary because the hydrogen properties used in HEX1 and HEX3-7 differ due to the ortho-para H2 conversion process taking place in the catalyst-filled heat exchangers. The hydrogen outlet temperature of each heat exchanger is represented by T1-T6. At each temperature, the corresponding equilibrium hydrogen content is represented as $X_{eq1}-X_{eq6}$. After conversion through the catalyst-filled heat exchangers, the para hydrogen content is represented as $X'_1-X'_6$. By using these values, we can calculate the non-equilibrium conversion efficiency as the ratio of the para hydrogen content after conversion to the equilibrium hydrogen content at the corresponding temperature. The difference between the equilibrium and non-equilibrium conversion heat is then calculated and set as the heat loss in the heat exchanger, which can be implemented using spreadsheet tools. This allows for a more accurate simulation of the heat exchanger performance in Aspen Hysys.

In Fig. 2, the temperature decreases from left to right, so the corresponding para hydrogen content increases. The blue line represents the conversion heat that is released as the ortho-para H2 conversion takes place in the catalyst-filled heat exchangers. $H_{ignored}$ in HEX3 represents the heat duty difference between the enthalpy of normal hydrogen and the equilibrium hydrogen at T1, which needs to be taken away in HEX3. In each stage of heat exchanger, the equilibrium hydrogen enthalpy change is denoted as Stream dH(i), where the H represents the mass enthalpy in kJ/kg, as shown in Eq. 1.

$$\text{Stream dH(i)} = H_{Xeq(T_{i+1})} - H_{Xeq(T_i)} \text{ for i} = 1-6 \tag{1}$$

When the actual outlet para hydrogen content X′(i) does not reach the equilibrium content Xeq(i) at stage i, it creates an excess heat difference in the heat exchanger, $H_{excess(i)}$ represents the influence of this part which is shown in Eq. (3).

$$H_{ignored} = H_{Xeq(T_1)} - H_{(T_1,0.25)} \tag{2}$$

$$H_{excess(i)} = 2\left(X_{eq(i)} - X_i'\right) \times H_{reaction(i)} \quad \text{for } i = 2-6 \tag{3}$$

where the $H_{reaction(i)}$ is the reaction heat duty at temperature T_i. In addition to the excess heat term, the heat duty at each stage of the heat exchanger also includes the equilibrium hydrogen enthalpy change, Stream dH(i). Equations (4) and (5) represent the actual heat duty and the heat correction value of the heat exchanger that needs to be added to the actual heat duty to account for any deviations from the expected heat transfer performance of the heat exchanger, respectively.

$$Q_{\text{actual duty}} = \text{Stream dH} + H_{excess(i)} - H_{excess(i+1)} \tag{4}$$

$$\text{Heat loss} = H_{\text{excess(i)}} - H_{\text{excess(i+1)}} \tag{5}$$

For i = 1–6,when i = 1, $H_{\text{excess(1)}} = H_{\text{ignored}}$

Validation of the equivalent heat exchanger

In Aspen HYSYS, the stand-alone conversion process of O-H2 to P-H2 can be achieved through a conversion reactor. The conversion reactor is modeled by setting the reactants, feed rates of reactants, reaction conditions (such as pressure, temperature, and catalyst), and reaction kinetics models. To validate the accuracy of the conversion heat value achieved by the equivalent heat exchanger unit, comparisons with data are performed in this study. Following the model shown in Fig. 2, a calculation model for the conversion reactor can be established as shown in Fig. 3 which shows a calculation model for the conversion reactor, which consists of feed-in streams for normal hydrogen and catalyst, a reactor, and an outlet stream for non equilibrium hydrogen.

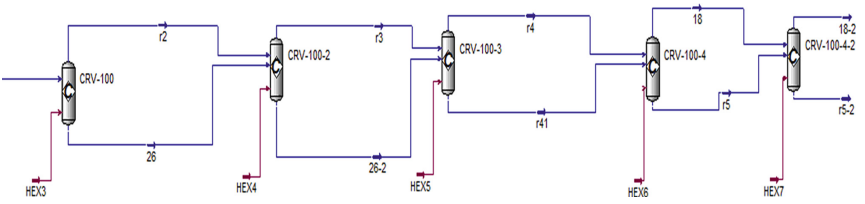

Fig. 3. Conversion reactor units to model the process of o-p hydrogen in HEX3-5

The conversion heat that is released during the conversion process is calculated based on the inlet and outlet conditions of the reactor. In order to ensure consistency between the conversion reactor and heat exchanger models, the parameters needed during the reaction process, such as temperature, pressure, flow rate, and other data, can be transferred to the corresponding variables in Fig. 3. Besides, the conversion rate in the conversion reactor can be calculated using the actual para-hydrogen content, which is obtained from the calculations in the equivalent heat exchanger model. The conversion rate is shown in Eq. (6):

$$\text{Conversion rate}\% = \frac{X'_{i+1} - X'_i}{1 - X'_i} \times 100\% \tag{6}$$

In this equation, X'_i represents the para hydrogen content at the inlet of stage i, and X'_{i+1} represents the para hydrogen content at the outlet of stage i + 1. The conversion rate calculation takes into account the fact that not all of the normal hydrogen is converted to para hydrogen in the conversion reactor due to equilibrium limitations.

As shown in Table 1, the results of heat duty of hydrogen stream calculated by the conversion reactors and customized heat exchanger models are compared with the HEX3-7. The results show that the customized models were able to produce accurate predictions for the heat duty of the hydrogen stream, with errors ranging from 0.84 to 5.55%. These errors are within an acceptable range and indicate that the customized models can be used to simulate the performance of the hydrogen liquefaction process.

Table 1. Heat duty compared with the conversion reactor and customized heat exchanger

	Heat duty of equivalent heat exchanger model	Heat duty of conversion reactor	Absolute error	Relative error	
	kW	kW	kW	%	
HEX-3	−19.04	−19.2	0.16	0.84	
HEX-4	−32.75	−33.02	0.28	0.84	
HEX-5	−41.53	−40.94	−0.59	1.45	
HEX-6	−6.02	−5.71	−0.32	5.55	
HEX-7	−10.15	−9.73	−0.42	4.33	

Process optimization

The performance of the hydrogen liquefaction cycle is influenced by the process organization and operating parameters. The behavior of these parameters is complex, and can be difficult to understand without the help of a process simulator. In this study, a commercial process simulator, Aspen Hysys V12.1, was selected to model and analyze the hydrogen liquefaction process. Aspen Hysys is a widely used process simulator that allows for the simulation and optimization of a range of chemical and physical processes. The use of a process simulator allows for the analysis of how different operating parameters and process organization can affect the performance of the hydrogen liquefaction process. By simulating the process under different conditions, we can optimize the design and operation of the process to achieve maximum efficiency and performance.

The study has been performed on the basis of the following main assumptions:

(1) The pressure drop of each streams in the heat exchanger is 5kPa;
(2) The inlet and outlet helium state of the compressor are respectively 4bar, 298Kand 20 bar, 300K;
(3) Liquid nitrogen gas holdup of the thermal siphon heat exchanger outlet is 0.2;
(4) The temperatures difference of the heat exchangers in the same end is determined by set;
(5) The nitrogen vent temperature is 298K;
(6) Non-equelium conversion efficiency of the hydrogen is 95%;
(7) The design mass flow rate of the hydrogen is 231kg/h.

Optimization objectives is in Eq. 7 and the optimization variables and variable bounds are showed in Table 2:

$$f(x)_{min} = (W1 + W_{LN} - W2 - W3 - W4)/Q_{LH} \tag{7}$$

W1 is the power consumption of the compressor, kW; W_{LN} is the power consumption of liquid nitrogen (0.6 kWh/Kg), kW; W2-W4 is the work of expander K-1, K-2, K-3,kW; Q_{LH} is the mass flow rate of liquid hydrogen, kg/h.

This paper uses the Eq. 7 without recover the turbine power as the objective function with the optimizer in Hysys and the equivalent heat exchanger model to optimize the process under the premise of the above variables and constraints.

Table 2. Optimization variables and variable bounds.

Variables	Stream	Lower bound	Upper bound
Turbine pressure(bar)		6	21
Heat exchanger temperature	T HX3 OUT	77	85
(K)	T HX4 OUT	50	80
	T HX5 OUT	30	70
	T HX6 OUT	20	30
	T HX6 OUT	20	30

3 Results

Specific power consumption is a crucial parameter in the design and operation of a hydrogen liquefier. It represents the direct operating cost of the process, and optimizing it is essential for maximizing the energy efficiency and reducing operating costs. The unit energy consumption of the optimized hydrogen liquefaction process was found to be12.61 kWh/kgLH2. From Fig. 4, the study found that the compressor and liquid nitrogen power consumption account for 68.34% and 31.66% of the total power consumption, respectively. This information is useful for identifying areas where energy efficiency can be improved. The total output power of the three expansion machines was found to be 104.4 kW, which accounts for about 3.58% of the total power consumption, so this part of power is not necessary to be recovered.

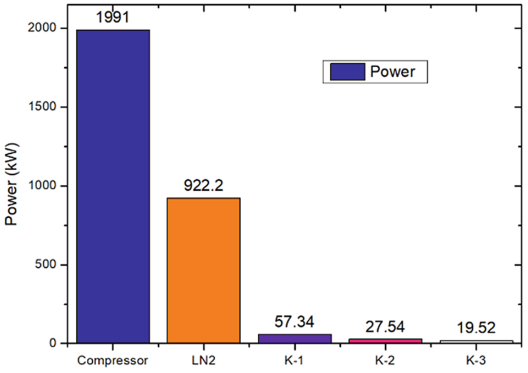

Fig. 4. The power of the critical components in the hydrogen liquefier

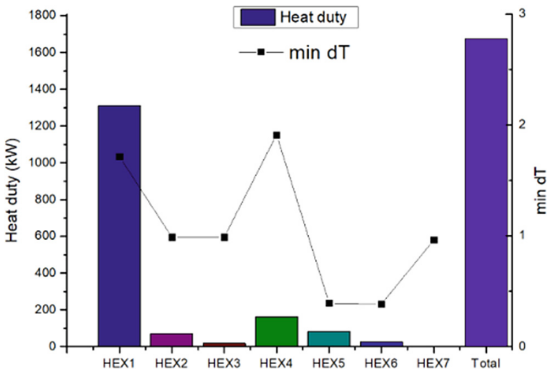

Fig. 5. The heat load and minimum temperature difference of the heat exchanger

To ensure that the heat exchangers operate efficiently and effectively, it is important to consider the temperature difference between the hot and cold fluids. By limiting the minimum temperature difference to 0.3-2K, the goal is to minimize the irreversible loss of energy. This requires careful consideration of the thermal characteristics of the system, including the design of the heat exchangers and the total investment. As shown in Fig. 5, HEX1 has the largest heat load among all the heat exchangers in the system and accounts for 78% of the total heat load. Therefore, its on-site installation limitations should be carefully considered in the actual design. HEX2 and HEX3, on the other hand, are designed as liquid nitrogen thermosiphon heat exchangers, which take advantage of the latent heat of evaporation of liquid nitrogen. This facilitates the provision of a cold source for isothermal conversion in HEX3. Below the liquid nitrogen temperature zone, the heat load of HEX4-7 decreases sequentially.

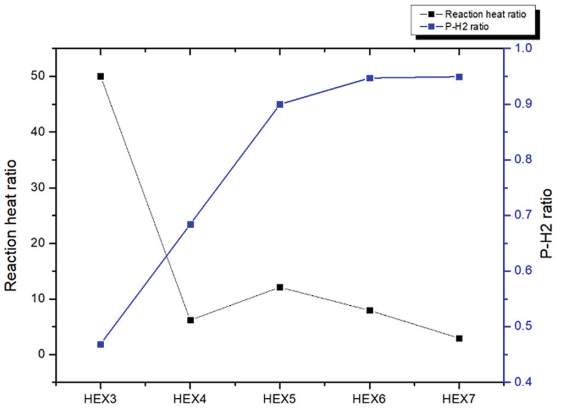

Fig. 6 Conversion heat ratio and para hydrogen content of hydrogen stream from HEX3-7

The conversion heat of HEX3 is the largest among all the heat exchangers in the system, accounting for about 50%, and the para hydrogen ratio is varied from 25 to

47%.The final exit para hydrogen content reaches 95%, meeting the requirements of the design requirement of the process, which shown in the Fig. 6.

4 Conclusion

In the process design of hydrogen liquefaction, the integral model of ortho and para hydrogen conversion heat exchanger is crucial to accurately calculate the process parameters. In this study, an equivalent heat exchanger model was constructed using Aspen Hysys to provide a new design method for hydrogen liquefaction, using the helium refrigeration hydrogen liquefaction model of 5tpd as an example. The method was validated through an analysis of the key process parameters. By using this simulation methodology, it is expected that future studies related to hydrogen liquefaction processes could be facilitated. This approach allows for a more efficient and accurate design of hydrogen liquefaction systems, which is crucial for the development of clean fuel technologies and the transition to a more sustainable energy future.

Acknowledgments. This work was supported by the National Science Foundation of China (Grant No.52106034), the Youth Innovation Promotion Association Innovative, Chinese Academy of Sciences (No.2020030).

References

1. Acobsen, R.T., Leachman, J.W., Penoncello, S.G., Lemmon, E.W.: Current status of thermodynamic properties of hydrogen. Int. J. Thermophys.Thermophys. **28**(3), 758–772 (2007)
2. Son, H., Taejong, Y., Hwang, J., Lim, Y.: Simulation methodology for hydrogen liquefaction process design considering hydrogen characteristics. Int. J. Hydrogen Energy **47**(61), 25662–25678 (2022)
3. Wang Guocong, X., Zelin, D.Z., Jianlu, Z., Yuxing, L.: Optimization of mixed refrigerant hydrogen liquefaction process. J. Northeast Dianlian Univ. **41**(06), 61–70 (2021)
4. Berstad, D., et al.: Dissecting the exergy balance of a hydrogen liquefier: analysis of a scaled-up claude hydrogen liquefier with mixed refrigerant pre-cooling. Int. J. Hydrogen Energy **46**, 8014–8029 (2021)

The Cracks Effect Analysis on In-Plane Diffusivity in Proton Exchange Membrane Fuel Cell Catalyst Layer by Lattice Boltzmann Method

Mingyang Yang, Song Yan, Aimin Du, and Sichuan Xu(✉)

School of Automotive Studies, Tongji University, 4800 Cao'an Road, Shanghai 201804, People's Republic of China
scxutj@163.com

Abstract. Crack is always considered as a kind of defect on a catalyst layer in a proton exchange membrane fuel cell (PEMFC), and its enhancement on mass transfer ability has always been ignored. In this work, the crack effect analysis on in-plane (IP) diffusivity on a catalyst layer is numerically evaluated by a D2Q9 lattice Boltzmann method (LBM). The effects on some key parameters like crack length, width, quantity and shape are carried out. The IP concentration distribution of crack CL shows deviation from the theoretical value, and this is because of the tortuosity caused by the CL cracks. The crack shape has almost no effect on the IP effective diffusivity, and the crack length shows a little bit more influence than the crack width and quantity. The crack ratio of the CL is the dominant effect on the IP mass diffusivity enhancement, and the lower the CL porosity is, the higher this enhancement achieve.

Keywords: Proton exchange membrane fuel cell · Catalyst layer · Crack

1 Introduction

Cracks formation on CLs during the operational process mostly bring unexpected defects, mostly regarded as degradations and failures. These defects occur at the crack formation reign, including crack propagation to membrane pinholes, increasing in-plane (IP) resistance (R_{IP}) of CLs, formation of flooding areas and catalyst degradation [1]. Some operation conditions are prone to crack initiation, such as freeze-thaw (F-T) cycles [2], dry-wet cycles [3], cyclic loadings [4], and ionomer degradation [5]. However, some work has claimed the mass transfer enhancement by the cracks on CL [6–8].

In this work, to understand the crack effect on the PEMFC catalyst layer IP diffusivity, a lattice Boltzmann method D2Q9 model was employed. The normalized concentration of air in the cracked CL was acquired, and the effective diffusivity of the complex crack zone was calculated by the flux field. This model was validated by the analytical result and shows relatively high accuracy. The effects on some key parameters like crack length, crack width, crack quantity and crack shape were carried out.

H. Sun et al. (Eds.): WHTC 2023, SPPHY 393, pp. 141–150, 2024.
https://doi.org/10.1007/978-981-99-8631-6_16

2 Random Crack Domain Regeneration

A processed base crack regeneration method was employed to obtain a computational field. The details of this method were described in our previous work [9]. The circle cracks were introduced in this simulation because some former work showed a significant enhancement in mass transfer using this CL structure [10]. The non-crack area (NCA), the intact porous catalyst layer, and the crack area (CA), the chapped crack, were defined in the computational domain. These two different regions have different properties on diffusion.

3 Physical and Mathematical Model

3.1 Physical Description

In a cracked CL, the effective diffusivity D^{eff} is determined by the NCA phase and CA phase properties. Although the exact value of the D^{eff} is hard to estimate, its value is in the range of D_{CA} and D_{NCA}.

$$D^{eff} \in [D_{CA}, D_{NCA}] \tag{1}$$

The NCA and CA phase in this research are porous CL structure and air, respectively. The mass diffusivity $D^{p}_{O_2}$ in the nanostructure is reported to be sensitive to the porous CL structure due to the effect of Knudsen diffusion [11], which is shown as

$$\frac{1}{D^{p}_{O_2}} = \frac{1}{D_{Kn}} + \frac{1}{D_{O_2}} \tag{2}$$

The D_{O_2} is oxygen diffusivity is equal to the D_{NCA}, and the D_{Kn} is Knudsen diffusivity. These values can be calculated as

$$D_{O_2} = 0.22 \times 10^{-4} \frac{(T/293.2\text{K})^{1.5}}{p/1\text{ atm}} \tag{3}$$

$$D_{Kn} = 4850 d_p \sqrt{\frac{T}{M}} \tag{4}$$

where p is the absolute pressure in atm, and is set to 2.5 atm (absolute pressure). T is temperature in K, and is set to 353 K. M is the molecular weight of oxygen in g/mol, and is set to 32 g/mol. d_p is the characteristic pore size in cm [11]. The mean d_p is used in the modeling and an empirical correlation of the mean d_p is given as

$$d_p = 140.50\varepsilon^2 + 68.35\varepsilon + 38.08 \tag{5}$$

To obtain the diffusivity D_{NCA} in the NCA media, a Bruggeman-like power law is employed as [11]

$$D_{NCA} = 1.07\varepsilon^{1.75} \times D^{p}_{O_2}$$

Combining Eq. (2)–(6), the diffusivity of NCA media at different porosities are acquired. In this research, the porosity is in 0.25~0.45.

3.2 Governing Equations

A 2D model is employed for the IP mass transfer analysis. Figure 1 illustrates the computational domain of a cracked CL, and the governing equations for mass diffusion can be expressed as following equations,

$$\frac{\partial C}{\partial t} = D_{NCA}\left(\frac{\partial^2 C}{\partial x^2} + \frac{\partial^2 C}{\partial y^2}\right) \tag{7a}$$

$$\frac{\partial C}{\partial t} = D_{CA}\left(\frac{\partial^2 C}{\partial x^2} + \frac{\partial^2 C}{\partial y^2}\right) \tag{7b}$$

The boundary conditions are described as

$$\begin{cases} C = C_1, \ y = L, 0 \le x \le L \\ C = C_2, \ y = 0, 0 \le x \le L \\ f_{1,5,8}\,|_{x=0} = f_{1,5,8}\,|_{x=L} \\ f_{3,6,7}\,|_{x=L} = f_{3,6,7}\,|_{x=0} \end{cases} \tag{8}$$

where C is the concentration. The top and bottom boundary are maintained at C_1 and C_2 using famous Zou-he boundary conditions [12]. To ensure stability of the numerical method, a small difference which is 0.01 is set between these two boundaries. The periodic boundary is set at the left and right boundaries as previous works [13].

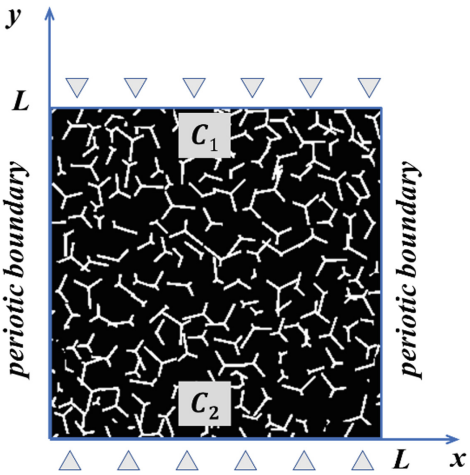

Fig. 1 Computational domain of cracked CL.

3.3 2D LBM Model Description

In this research, a two-dimensional (2D) LBM single relaxation time (SRT) model is employed to solve the mass transfer phenomenon in different phases. The density distribution function g_α evolution equation for a two-dimensional nine-speed (D2Q9) LBM

in both NCA and CA can be given as,

$$g_\alpha(\boldsymbol{r}+\boldsymbol{e}_\alpha\delta_t, t+\delta_t) - g_\alpha(\boldsymbol{r}, t) = -\frac{1}{\tau}\left[g_\alpha(\boldsymbol{r}, t) - g_\alpha^{eq}(\boldsymbol{r}, t)\right] \tag{9}$$

where $\boldsymbol{r}$ is the position vector, t is the real time, δ_t is the iteration time step, ${g_\alpha}^{eq}$ is the equilibrium distribution function of the evolution equation.

The gases phase in the NCA is assumed to be static, because the *Peclet Number* (*Pe*) in the porous structure is relatively low. Thus, the ${g_\alpha}^{eq}$ shows as [14].

$$g^{eq}(x, t) = \begin{cases} 0, & \mathrm{i} = 0 \\ \frac{1}{6}C, & \mathrm{i} = 1 \text{ - } 4 \\ \frac{1}{12}C, & \mathrm{i} = 5 \text{ - } 8 \end{cases} \tag{10}$$

The velocity vector $\boldsymbol{e}_i$ for D2Q9 scheme is

$$\boldsymbol{e}_i = \begin{cases} (0, 0) & i = 0 \\ \boldsymbol{e}\left(\cos\left[\frac{\pi}{2}(i-1)\right], \sin\left[\frac{\pi}{2}(i-1)\right]\right) & i = 1, 2, 3, 4 \\ \sqrt{2}\boldsymbol{e}\left(\cos\left[\frac{\pi}{2}(i-1)\right], \sin\left[\frac{\pi}{2}(i-1)\right]\right) & \sqrt{2}i = 5, 6, 7, 8 \end{cases} \tag{11}$$

and τ is the dimensionless relaxation time for NCA and CA, which is determined by the diffusivity coefficient [15],

$$\tau_{CA} = \frac{3}{2}\frac{D_{CA}}{(\rho c)_{CA}\cdot c^2\delta_t} + 0.5 \tag{12}$$

and

$$\tau_{NCA} = \frac{3}{2}\frac{D_{NCA}}{(\rho c)_{NCA}\cdot c^2\delta_t} + 0.5 \tag{13}$$

where c is a pseudo sound speed, D_{CA} and D_{NCA} are the diffusivity coefficient in crack area and non-cracked area, respectively. To ensure the continuities of the flux and density distribution functions at the interface of different phases, the ρc is set to 1 in this model [16]. Then the calculation of macroscopic quantities of the density and flux can be obtained by

$$T = \sum_i f_i, \tag{14}$$

$$J = \left(\sum_i c_i f_i\right)\frac{\tau - 0.5}{\tau}. \tag{15}$$

At the end of each computational loop, the effective diffusivity coefficient D^{eff} can be obtained by Fick's law [17, 18]:

$$D^{eff} = \frac{L_x \int J dA}{(C_2 - C_1)\int dA}. \tag{17}$$

where C_2 and C_1 are the boundary values of inlet and outlet boundaries, respectively. L_x is the distance between these two boundaries, and A is the computational width of the domain.

The normalized effective diffusivity coefficient D^n is defined as [19],

$$D^n = D^{eff}/D_{NCA}. \tag{18}$$

The D_{NCA} is equal to the D^{O_2}, which is the oxygen diffusivity in bulk. This normalized method makes the crack effect obviously on the diffusivity change of the CLs.

4 Results and Discussion

4.1 Model Validation

Two typical structures, the "parallel" and the "series" model which are introduced in the previous work are used to validate the LBM model [20]. In the model validation section, the CR is set to 0.5. The D_{CA}/D_{NCA} value is set to 1–1000. Meanwhile, the domain side length effect is also taken into consideration which is set from 300 to 5000 μm at the resolution of 10 μm. The model validation result is shown in Fig. 2. When the domain side length is small, the error value is big, and the error is sensitive to the ratio between two conductivity values. To balance the computational consumption and an error less than 1%, the domain side length is set to 3000 μm, and the conductivity ratio is limited at 1:100. In another word, the representative element volume (REV) in this case is 3000 μm × 3000 μm.

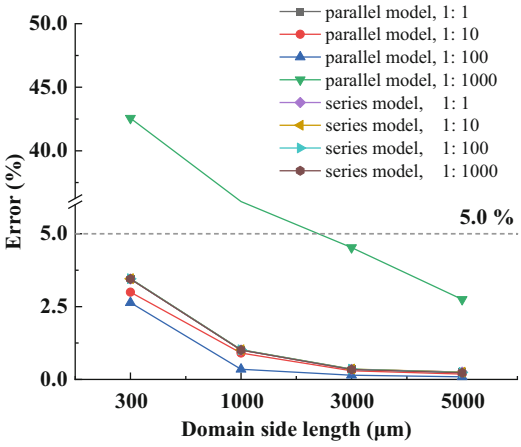

Fig. 2. Comparison between model prediction value and theoretical value.

4.2 IP Effective Transfer Properties Influenced by Cracks

Normalized Concentration with Diffusion Time. To evaluate the effect of diffusion time on normalized concentration in the crack area, a bunch of simulations are designed. The porosity of NCA is 0.3, and five different crack quantities are selected from 20 to 180. The triangle crack with 25 μm crack width are reconstructed, and every crack arm length is random from 0 to 200 μm. As shown in Fig. 3, the average temperature at each coordinate with 180 cracks is higher than that of 20 cracks. The D_{CA} is significant than the D_{NCA}, thus a higher *CR* is good for mass transport in the CLs. After 15e5 lattice steps, the computing converges, but none of the concentration reaches the theoretical linear line. This is because the existence of cracks changes the real tortuosity of the mass

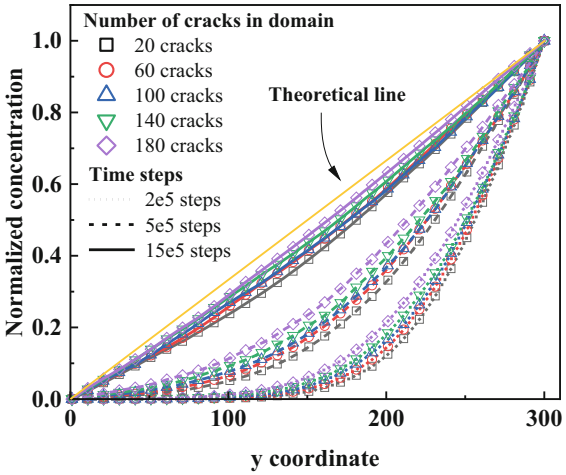

Fig. 3. The normalized concentration distribution with different time steps.

transfer. Furthermore, the more crack quantity, the farther the concentration deviates from the theoretical value.

Normalized Concentration with Crack Shape. To evaluate the effect of crack shape on the on normalized concentration in the crack area, three kinds of domains with different crack shape, which are linear cracks, circle cracks and triangle cracks were employed. The porosity of NCA is 0.3, and the *CR* were set to 0.15 ± 0.05. The triangle cracks case shows a little higher normalized concentration than that of linear crack and circle crack cases. However, when the calculation converges, all three cases shows similar normalized concentration distribution. In addition, the deviation of the computational value from the theoretical value is caused by the cracks affecting the tortuosity of the computational domain (Fig. 4).

Crack Ratio Effect on Diffusivity. To understand the effect of crack ratio on effective diffusivity, the relationship between crack ratio and normalized diffusivity was carried out. The NCA porosity is set to 0.2 and the D_{NCA}/D_{bulk} is 0.04111. Different crack width, length and quantity cases are carried out. Meanwhile, the parallel model and series model are also used as the upper and lower limit of the normalized diffusivity. With the CR increase from 0 to 0.15, the normalized diffusivity of crack width case, crack length case and crack quantity case increase from 0.0411 to 0.0682, 0.0780 and 0.0866, respectively. Thus, the crack length shows the highest influence on the IP mass transfer enhancement. The computational model result is between the parallel model and series model results (Fig. 5).

NCA Porosity Effect on Diffusivity. A lower porosity will cause a lower D_{NCA}, and the relationship between these two parameters is shown in Eqs. (2)–(6). When the porosities are 0.2, 0.3, 0.4 and 0.5, the D_{NCA}/D_{bulk} are 0.0411, 0.089, 0.1579 and 0.2452, respectively. And the simulation is carried out for these four cases. Result shows, with the crack ratio increase from 0 to 0.17, the IP diffusivity enhancements of 0.2, 0.3, 0.4

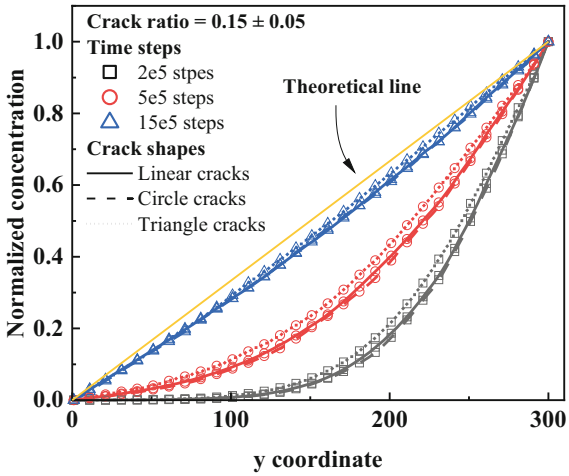

Fig. 4. The normalized concentration distribution of different crack shapes.

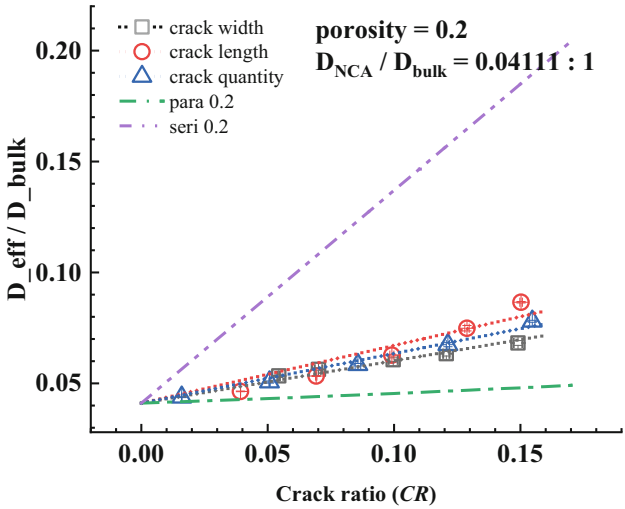

Fig. 5. Diffusivity change caused by crack ratio change.

and 0.5 porosity cases are about 96.93%, 63.86%, 43.40% and 30.08%, respectively. Considering the relative low porosity of CL structure, this enhancement shows great potential to enhance the IP mass transportation of oxygen phase and water vapor phase (Fig. 6).

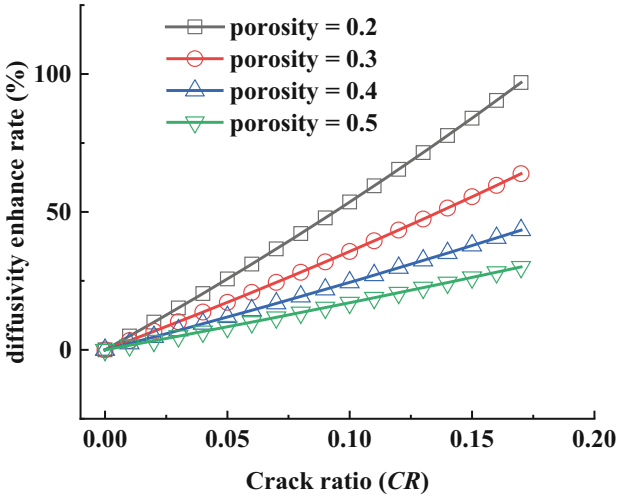

Fig. 6. Diffusivity change caused by NCA porosity change.

5 Conclusions

In order to understand the crack effect on the PEMFC catalyst layer IP diffusivity, a lattice Boltzmann method D2Q9 model was employed in this research. The normalized concentration of mass transport was acquired, and the effective diffusivity of the complex crack zone was calculated by the flux result. The following conclusions were mainly obtained:

1. The LBM model shows good accuracy when the diffusivity ratio is bigger than 1: 100. The error is below 5% when the domain size is 300 μm × 300 μm, and the error is below 0.5% when the domain size is 3000 μm × 3000 μm.
2. For a triangle crack, the crack length shows a little bit more influence than the crack width and quantity. However, comparing to the parameter including length, width, quantity and shape, the *CR* plays the dominant role in the diffusivity enhancing.
3. Considering the relative low porosity of CL structure, there is a great potential to enhance the IP mass transportation of oxygen phase and water vapor phase by design the cracked morphology.

References

1. Kundu, S., Fowler, M.W., Simon, L.C., Grot, S.: Morphological features (defects) in fuel cell membrane electrode assemblies. J. Power. Sources **157**(2), 650–656 (2006)
2. Lee, S.-Y., Kim, H.-J., Cho, E., Lee, K.-S., Lim, T.-H., Hwang, I.C., et al.: Performance degradation and microstructure changes in freeze–thaw cycling for PEMFC MEAs with various initial microstructures. Int. J. Hydrogen Energy **35**(23), 12888–12896 (2010)
3. Uchiyama, T,. Kumei, H., Yoshida, T.: Catalyst layer cracks by buckling deformation of membrane electrode assemblies under humidity cycles and mitigation methods. J. Power Sources **238**, 403–412 (2013)

4. Kai, Y., Kitayama, Y., Omiya, M., Uchiyama, T., Kato, M.: Crack formation in membrane electrode assembly under static and cyclic loadings. J. Fuel Cell Sci. Technol. **10**(2) (2013)
5. Singh, Y., Orfino, F.P., Dutta, M., Kjeang, E.: 3D failure analysis of pure mechanical and pure chemical degradation in fuel cell membranes. J. Electrochem. Soc. **164**(13), F1331–F1341 (2017)
6. Vengatesan, S., Panha, K., Fowler, M.W., Yuan, X.-Z., Wang, H.: Membrane electrode assembly degradation under idle conditions via unsymmetrical reactant relative humidity cycling. J. Power Sour. **207**, 101–110 (2012)
7. Yin, Y., Li, R., Bai, F., Zhu, W., Qin, Y., Chang, Y., et al.: Ionomer migration within PEMFC catalyst layers induced by humidity changes. Electrochem. Commun. 109 (2019)
8. Park, C.H., Lee, S.Y., Hwang, D.S., Shin, D.W., Cho, D.H., Lee, K.H., et al.: Nanocrack-regulated self-humidifying membranes. Nature **532**(7600), 480–483 (2016)
9. Yang, M., Yan, S., Du, A., Liu, J., Xu, S.: Effect of micro-cracks on the in-plane electronic conductivity of proton exchange membrane fuel cell catalyst layers based on lattice Boltzmann method. Int. J. Hydrogen Energy (2022)
10. Hou, Y., Deng, H., Pan, F., Chen, W., Du, Q., Jiao, K.: Pore-scale investigation of catalyst layer ingredient and structure effect in proton exchange membrane fuel cell. Appl. Energy **253**, 113561 (2019)
11. Zheng, W., Kim, S.H.: The effects of catalyst layer microstructure and water saturation on the effective diffusivity in PEMFC. J. Electrochem. Soc. **165**(7), F468–F478 (2018)
12. Zou, Q., He, X.: On pressure and velocity boundary conditions for the lattice Boltzmann BGK model. Phys. Fluids **9**(6), 1591–1598 (1997)
13. Chen, L., Kang, Q., Tao, W.: Pore-scale numerical study of multiphase reactive transport processes in cathode catalyst layers of proton exchange membrane fuel cells. Int. J. Hydrogen Energy **46**(24), 13283–13297 (2021)
14. Wang, M., He, J., Yu, J., Pan, N.: Lattice Boltzmann modeling of the effective thermal conductivity for fibrous materials. Int. J. Therm. Sci. **46**(9), 848–855 (2007)
15. Qu, Z.G., Fu, Y.D., Liu, Y., Zhou, L.: Approach for predicting effective thermal conductivity of aerogel materials through a modified lattice Boltzmann method. Appl. Therm. Eng. **132**, 730–739 (2018)
16. Wang, M., Wang, J., Pan, N., Chen, S.: Mesoscopic predictions of the effective thermal conductivity for microscale random porous media. Phys. Rev. E Stat. Nonlin. Soft Matter Phys. **75**(3 Pt 2), 036702 (2007)
17. Hu, B., Wang, J.G.: Fractal microstructure effects on effective gas diffusivity of a nanoporous medium based on pore-scale numerical simulations with lattice Boltzmann method. Phys. Rev. E. **104**(6–2), 065304 (2021)
18. Lange, K.J., Sui, P.-C., Djilalia, N. : Pore scale simulation of transport and electrochemical reactions in reconstructed PEMFC catalyst layers (2010)
19. García-Salaberri, P.A., Zenyuk, I.V., Shum, A.D., Hwang, G., Vera, M., Weber, A.Z., et al.: Analysis of representative elementary volume and through-plane regional characteristics of carbon-fiber papers: diffusivity, permeability and electrical/thermal conductivity. Int. J. Mass Transf. **127**, 687–703 (2018)
20. Tuncer, E., Gubański, S.M., Nettelblad, B.: Dielectric relaxation in dielectric mixtures: Application of the finite element method and its comparison with dielectric mixture formulas. J. Appl. Phys. **89**(12), 8092–8100 (2001)

Brief Review and Technical Insight of Liquefied Hydrogen Carriers Development

Wei Song, Zilong Zhu(✉), Zhong Wan, Chan Long, and Tao Liu

Hudong-Zhonghua Shipbuilding (Group) Co., Ltd, Shanghai 200129, China
zzlong_seu@sina.com

Abstract. Countries worldwide are shifting to a hydrogen economy in response to stringent environmental regulations, and hydrogen transport between countries is expected to increase in the medium to long term. Although hydrogen is traded between countries in different forms such as ammonia, liquid hydrogen, and methanol, from the perspective of volume density and production/demand area without a separate process, the transportation of hydrogen in liquid form is the potential way for large-scale transportation of hydrogen in the future. This article aims to highlight the opportunities and challenges technical for the ocean-going liquid hydrogen carriers. An overview of development state-of-the-art and key technical challenges of liquid hydrogen carrier ships are summarized, including regulation, the cargo containment structure and insulation, boil off ratio (BOR) evaluation, boil-off gas (BOG) handling system and propulsion system. Finally, detailed technical route of the key technology required by future liquid hydrogen carrier is extrapolated, and securing a possible design through various technological alternatives.

Keywords: Liquid hydrogen carrier · Insulation · Boil off ratio · BOG handling · Propulsion system · Technical insight

1 Background and Motivation

With the strengthening of international environmental regulations and the geopolitics of the Russia-Ukraine war, the energy market will undergo rapid changes in the future. The Paris Agreement adopted on December 12, 2015 is not only a substitute for emotion in Kyoto, but also a consensus of the international community on greenhouse gases (GHGs) [1]. Most advanced and developing countries have participated in the agreement, 186 countries put forward the goal and contribution plan of reducing greenhouse gas emissions. Investment in new renewable energy has being increased in recent years, but the fluctuations in new renewable energy production and difficulties in trading renewable energy resources across countries are considered the biggest hurdles obstacles to the utilization of renewable energy. To break through the limitations of this new renewable energy, hydrogen energy has attracted attention. Hydrogen uses fuel cells to generate carbon free electric energy and heat energy that can be easily converted into renewable energy [4]. Hydrogen energy produced by water electrolysis with renewable energy is

H. Sun et al. (Eds.): WHTC 2023, SPPHY 393, pp. 151–162, 2024.
https://doi.org/10.1007/978-981-99-8631-6_17

best solution to balance the problem of renewable energy fluctuation and imbalance in various countries. China is today the largest hydrogen consumer in the world, at about 24 MtH_2/year in 2020 [5].

Niermann et al. investigated hydrogen exports from Algeria to Hamburg [6] and analyzed the feasibility of different liquid organic hydrogen carriers (LOHC), pipeline transportation and bulk transportation of liquid hydrogen. In a similar study, chain energy efficiency and costs for ammonia and LH_2 sea transport from northern Norway to Rotterdam and global (Tokyo) were estimated by Ishimoto et al. [7]. The energy efficiency and life-cycle costs of energy transported by submarine high-voltage cables are compared with pipeline hydrogen transport, compressed hydrogen ship and liquid hydrogen with different distances in [8]. Hydrogen can be transported by ship in the form of LOHC, ammonia or liquefied hydrogen and ammonia carriers have been commercialized and widely used in industrial. For LOHC carriers, ordinary chemical carriers can be used, so it is not necessary to further develop new technologies [9]. The above three recently published overlap papers, they all agree that liquid hydrogen (LH_2) is the most promising option for long-distance seaborne hydrogen transport. Coincidentally, the liquefied hydrogen transport ship aims to the demonstration of liquefied hydrogen transport between Australia and Japan. At the end of 2019, Kawasaki Heavy Industry of Japan built a world's first liquid hydrogen carrier with two 1250 m^3 double-shell vacuum liquid hydrogen storage tank, which horizontal cylindrical pressure vessel freely enable thermal shrinkage for transporting LH_2 [10].

Several economic analyzes on the hydrogen supply chain including maritime transportation of liquefied hydrogen have been performed, but few studies has been done on the technical characteristics of liquefied hydrogen carriers. Although Japan has completed the construction of liquid hydrogen ships, this is only an experimental attempt. Therefore, this is a comprehensive and difficult task, because the volumes are vast and data sets, and the necessary methodology statement may not be fully available. A comprehensive comparison of theories and assumptions, methodological choices and levels of technical abstraction is beyond scope of this paper. Therefore, we review and discuss the most obvious differences in the existing liquid hydrogen carrier or conceptual design assumptions, and extrapolate the preliminary technical appearance of the future liquid hydrogen ship. While identifying detailed technologies necessary for the development of liquefied hydrogen carriers in the future and securing various technical alternatives, the technical feasibility of liquefied hydrogen carriers is analyzed.

2 Classification of Liquid Hydrogen Carrier Tanks

The capacity of the liquefied hydrogen carrier depends on the economics of the liquefied hydrogen supply chain which have a significant impact on the analysis. Therefore, referring to the LNG ship type, the possible capacity of each tank type of the liquefied hydrogen carrier is analyzed. As shown in Fig. 1, membrane and type B tanks are applied to large LNG carriers, and Type C tanks are mainly applied to small LNG carriers or bunkering ships.

The Type C tank has the advantage of higher design pressure and ability to store BOG in the tank due to its relatively pressure build-up (accumulation) system locking

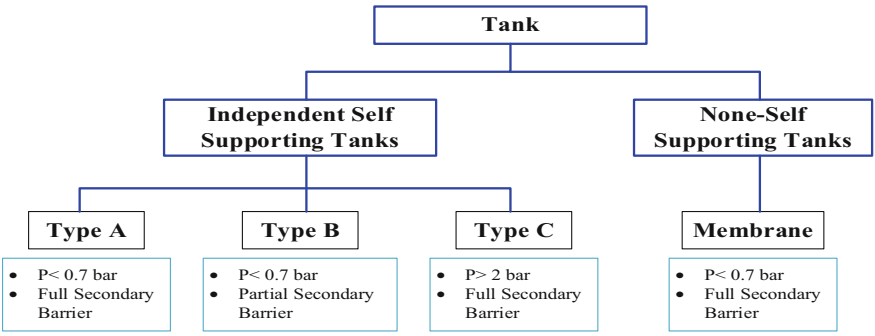

Fig. 1. Classification of cargo tanks for ships

BOG into the cargo tank, but has the disadvantage of being difficult to enlarge due to its shape and having low space efficiency. Hyundai Heavy Industries Group completed the conceptual design of a 20 K class liquid hydrogen carrier and received Approval in Principle (AIP) certification from the Korean Register of Shipping. Based on this, it is expected that it will be possible to manufacture up to 5000 ~ 6000 m^3 per type C tank, and it is judged that the capacity of the liquefied hydrogen carrier can be up to about 20 K depending on the number of tanks.

Membrane type tanks have high space efficiency and can be manufactured with a capacity of 160 K or higher based on LNG carriers. However, since this is a judgment from the viewpoint of manufacturability of the tank, it is also necessary to consider the possibility of applying an appropriate insulation system according to the capacity.

3 State of the Art and Extrapolations of Hydrogen Tanks Boil off Ratio

3.1 Type-C Tank

Liquid hydrogen storage and handling technology was first developed and applied by NASA aerospace projects [11]. The world's largest spherical LH_2 storage tank with approximately 3200 m^3 LH_2 capacity was built in the 1960s. The absolute value of the boil off gas is reported about 530 gal/day, which corresponds to boil off ratio of approximately 0.0625% per day [12]. Different types of LH_2 tanks have been designed and brought to market by Linde, the BOR of which is decided by size, shape, insulation, environment and usage pattern. For example, a cylindrical tank with a capacity of 300 m^3 has a boil off ratio of 0.3% per day, while a spherical tank with a capacity of 1100–2300 m^3 has a boil off ratio of less than 0.1% per day [13].

In the 1980s KHI built spherical LH_2 tanks with a volume of 600 m^3 and 540 m^3 LH_2 capacity which achieves a boil off ratio of 0.18% per day [14]. After 30 years of operation, no degradation in insulation performance has been detected by KHI [15]. By 2020, 1250 cubic meters of horizontal cylindrical seaborne tank have been put in operation [16], the spherical onshore terminal tank achieves thermal insulation performance with $\leq$ 0.1% per day boil off ratio [17]. Recently, a basic principle design of 11,200 m^3 volume

spherical LH_2 tank with $\leq 0.1\%$ per day boil off ratio performance have been completed by KHI and certified by the classification society [18].

Most hydrogen storage vessels are double-layered with a vacuum in the middle. The space between these can also contain other materials, such as aluminum-coated polyester sheets, alternating layers of aluminum foil as well as fiberglass. The vacuum aims to reduce losses by conduction and convection, while the alternated layer aims to reduce losses by radiation [19]. Heat loss can also be reduced by reducing the ratio of the exposed surface to the volume of the tank, which is the reason why spherical tanks are often used to store the liquid hydrogen. That can be seen as a trade-off with cost. Although the surface-volume ratio of cylindrical tanks is higher than that in spherical tanks, they are easier to manufacture due to the low costs, thus making them more common. The boil-off ratio depends on the size of the tank and the intended pattern of use. For example, a 300 m^3 small tank has boil off ratio of 0.3% per day, while tanks of 1100–2300 m^3 can already achieve boil off ratio of less than 0.1% per day [20].

Based on the brief review above, it is reasonable to assume that low boil off ratio can also be achieved when LH_2 cargo tanks are sized close to the capacity of today's Liquefied Natural Gas (LNG) carriers. Since boil off ratio of 0.06–0.25% per day is already achieved for tanks between 100 and 4000 m^3, a natural question is that whether it will facilitate or impede achievable performance of low boil off ratio if further scaling-up tanks volume. Under the assumption of well insulated tank with a uniform temperature distribution inside, the heat flow into tank LH_2 will proportional to the difference between the ambient temperature and the LH_2 temperature (K), overall heat transfer coefficien t(W m^{-2} K^{-1}) and the tank surface area (m^2), as shown in Eq. (1).

$$Q_{\text{in}} = (T_{\infty,ambient} - T_{\infty,\text{LH}_2}) U_{\text{overall}} A_{\text{surface}} \tag{1}$$

The boil off ratio is defined as the ratio of the amount of evaporated gas produced per unit time to the full tank inventory, but [% per day] is a more commonly used unit for cryogenic storage tanks. Qin is heat (kW), V_{tank} is volume (m^3), ρLH_2 is the density of liquid hydrogen (kg/m^3), Levap,LH_2 is the latent heat of vaporization (kJ/kg), A_{surface} is the surface area (m^2), and U_{overall} is overall heat transfer coefficient (W m^{-2} K^{-1}). The boil off ratio (% per day) can be expressed as:

$$BOR(\%/day) = \frac{Q\text{in}}{L_{\text{evap,LH}_2} \cdot \rho_{\text{LH}_2} \cdot V_{\text{tan k}}} \cdot 24 \cdot 3600 \cdot 100\% \tag{2}$$

where the units in the equation are international standard.

From (1) and (2), it can be found that the boil off ratio is proportional to the ratio of surface area to volume, which is usually called specific surface area. For spherical and cylindrical tanks, Fig. 2 gives how the specific surface area changes with size. It can be observed that it will decline sharply with the increase of trading volume, while on the other hand, it will rise sharply for sufficiently low trading volume.

To further illustrate the effect of size on the boil off ratio at the achievable design point, Fig. 3 shows the change of daily the boil off ratio with the total heat transfer coefficient and spherical tank volume. The ambient temperature is set at 288 K. For simplicity, it is assumed that the storage tank contains 1.2 bar (a) of pure saturated liquid to hydrogen, and the air-fuel rate is 10%. The liquid density and temperature can be

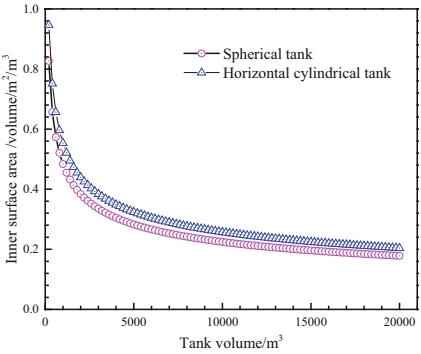

Fig. 2. Relation between internal surface area and volume for cylindrical and spherical tanks

retrieved respectively from the thermophysical properties in REFPROP [21], and the specific heat of evaporation (h_{evap}. LH_2) is 443.17 kJ/kg. For any fixed value of U, the daily the boil off ratio decreases significantly with the increase of tank size. The daily boil off ratio decreases by about 54% when the volume increases by 10 times (e.g. for 1000 m^3 relative to 100 m^3). Apart from these correlations based on equation, the rough data of three spherical tanks existed of different sizes and vintage [22], and the tank performance of other two indicators [13, 18] are also plotted in the same chart. Reference [6–8] is also included. The estimated value of the total heat transfer coefficient U of each tank can be read from the curve intersected with the data point, and it indicates that [12, 13, 17] is about 0.004 W m^{-2} K^{-1}. In theory, if the storage tank [13, 14] or [17] can be further scaled with U unchanged, the boil off ratio would be reduced to about 0.07% per day with a volume of 10,000 m^3. The corresponding figure of [22] would eventually reach about 0.17% per day.

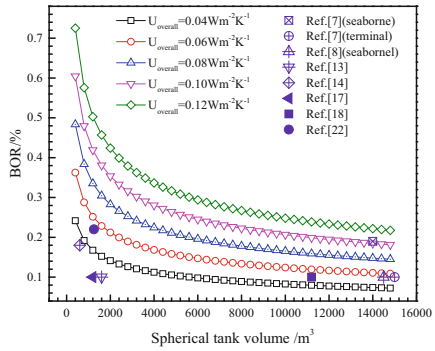

Fig. 3. Evaluation for the relation between spherical LH_2 tank volume, overall heat transfer coefficient and daily BOR.

As these illustrative examples show, due to the reduction of surface-to-volume ratio, the increase of size and diameter is usually beneficial to the low-voltage insulation system

[23]. It is still to be identified what is the best technical and economic boil off ratio of large LH_2 transport carriers in the future [24], and its size is equivalent to the current LNG tanker. This is an overall research and development task. It is necessary to weigh tank design and thermal insulation layout with a series of trade-offs, some of which may relax some restrictions, such as balancing boil off ratio and energy demand of propulsion and auxiliary systems. Multidisciplinary capabilities at different levels are required, including construction and materials technology, thermodynamics and fluid dynamics, mass and heat transfer, thermal process, naval architecture, and power and propulsion systems. In the research project, "LH_2 Pioneer—Super Insulated Marine Containment System for Global LH_2 Ship Transportation" led by SINTEF, LH_2 containment and thermal insulation, cargo loading and marine hydrogen re-liquefaction process are the key research topics [25].

3.2 Membrane Type Cargo Tank

Therefore, in order to determine the thermal insulation performance of membrane tank insulation, it is assumed well insulated membrane cargo tank with a uniform temperature distribution both inside and outside of insulation layer. Excluding insulation mounting members, piping, support members and cargo handling systems, only the thermal insulation and heat transfer around cargo tank which volume is assumed to be cubic are considered. The heat flowing into the cargo tank will be proportional to the difference between the outer surface temperature of the insulation layer and the LH_2 temperature (K), the outer surface area and the thermal conductivity, as represented in the Eq. (3).

$$Q_{\text{in}} = \lambda \cdot \frac{(T_{\infty,\text{out}} - T_{\infty,\text{LH}_2})}{D_{\text{thickness}}} \cdot A_{\text{surface}} \tag{3}$$

$$BOR(\%/day) = \frac{Q\text{in}}{L_{\text{evap,LH}_2} \cdot \rho_{\text{LH}_2} \cdot V_{\text{tan k}}} \cdot 24 \cdot 3600 \cdot 100\% \tag{4}$$

This paper only considers heat conduction for the outer surface temperature of the insulation layer of 0 °C and the inner temperature of − 253 °C, the volume of the cargo tank varies from 1000 to 60,000 m^3, and the thickness of the insulation layer is between 0.5 and 2.5 m. Due to the different areas of the hot and cold ends, the average value of the insulation outer area is considered as the outer area of the cargo volume for the conduction heat input calculations and following calculation formula is shown in (4). $D_{\text{thickness}}$ and λ represent the thickness (m) of the insulation layer and thermal conductivity (W m^{-1} K^{-1}).

Through the summary of the above literature, it is reasonable to assume that the boil off ratio of the liquid hydrogen cargo tank which is supposed to cube cargo tank is set at 0.2% per day. Figure 4 shows the requirements for the thermal conductivity of the thermal insulation layer in liquid hydrogen ships with different capacities and thicknesses of the thermal insulation layer. As mentioned above, since this is a calculation for a fully enclosed cargo tank that does not include other heat input components, it is necessary to apply an insulation with a lower thermal conductivity than that shown in this result when other heat leaking components are considered. It is obvious from the figure that with the increase of the volume of the cargo hold, the thermal conductivity gradually increases

but its increase rate gradually decreases, which means that when the volume of the cargo tank reaches a certain value, the benefits obtained by improving the thermal insulation performance of the insulation material are significantly reduced and the benefits are more pronounced with the thickness of the insulation. However, increasing the thickness of the insulation layer will affect the usable space of the cargo tank and bring about the problem of lower loading economy. Therefore, this is a pair of contradictions and need to find the best balance point.

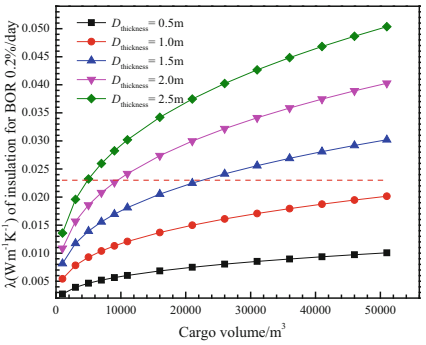

Fig. 4. Thermal conductivity of thermal insulation materials required for liquefied hydrogen tanks with different volumes

Table 1 shows the conductivities of insulation materials applicable to tanks of cryogenic cargo which are commonly used in current industry. Among the proposed materials, VIP is the only material with $\lambda < 0.01$ W m^{-1} K^{-1} and MLI exists as a better heat-insulating property than VIP. But considering the vacuum structure transformation of the membrane insulation system, it is judged to be technically difficult to apply.

Table 1. Thermal conductivity of insulation material

Insulation material	Thermal conductivity (W m^{-1} K^{-1})	Source
Mineral wool	0.035–0.045	[26]
Polyurethane	0.017–0.024	[26]
Expanded polystyrene	0.035–0.04	[26]
VIP	0.002–0.008	[26]
Glass bubble	0.047–0.2	[27]

When VIP is applied to the inter barrier space (IBS) of the liquefied hydrogen membrane tank, the temperature is lower than that of the IBS of the existing LNG cargo tank, so there is a difference in operating concept. The IBS of the existing LNG cargo tank was operated in the form of nitrogen purging, but the IBS of the hydrogen cargo hold cannot perform nitrogen purging because there is an area where the temperature

is lower than the freezing point of nitrogen (− 210 °C). A method of applying helium instead of nitrogen is also possible.

It is possible to apply a vacuum to the IBS space, but it is necessary to develop and verify the technology for applying/maintaining a vacuum in a large space. In the case of an LNG membrane tank, a vacuum of − 800 mbar is applied through a global test to confirm the airtightness of the primary barrier, so it is expected that a certain level of vacuum application is structurally possible. However, in a liquefied hydrogen carrier, it is necessary to verify whether the vacuum can be maintained during the life cycle of the ship and whether freezing of nitrogen or the like occurs at the corresponding level of vacuum. When vacuum is applied to the IBS, the effects of air condensation and oxygen enrichment due to air inflow in case of vacuum loss should be considered. In addition, the correlation between the reduction in vacuum and the amount of BOG generated due to VIP aging should be considered. Figure 5 is an example of an insulation system arrangement for a membrane tank.

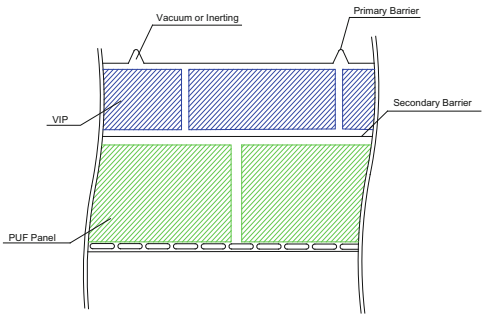

Fig. 5. Example of an insulation system for LH_2 membrane tank in the future.

4 BOG Handling System and Propulsion System

The development of BOG handling and propulsion systems needs to be considered together with the tank insulation system. In other words, it is anticipated that it will be necessary to develop an insulation system that will control BOG generation to levels required for propulsion/power generation. Furthermore, re-liquefaction of BOG and combustion via Gas Combustion Unit (GCU) is also possible. However, in the case of re-liquefaction, a large amount of energy is consumed compared with the re-liquefaction of LNG, so its application is limited and it is unrealistic to apply it in the short to medium term [28]. Example of BOG handling system and propulsion system in illustrated in Fig. 6.

LNG-based rules prohibit the release of BOG into the atmosphere except in emergency situations because air pollution is closely related to the greenhouse effect and methane emissions [29]. In the case of hydrogen, there is no risk of air pollution, so it is considered necessary to establish a certain area around the exhaust point as a safety

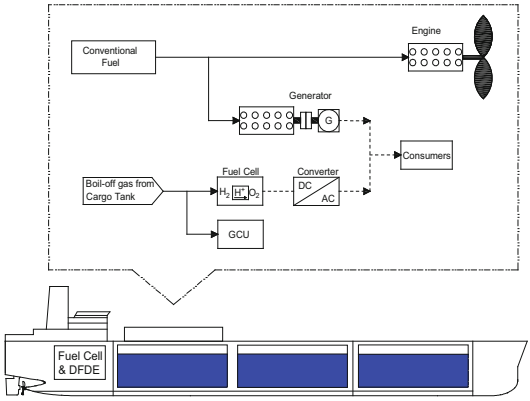

Fig. 6. Example of BOG handling system and propulsion system.

zone to eliminate the risk of fire/explosion, and to examine whether natural discharge after dilution can be performed without a separate BOG treatment facility.

Hydrogen can be usually used in the field of fuel cells (see Table 2). Due to the absence of moving parts, fuel cells have some advantages like very low noise, low vibration and low pollutant emissions. However, the tolerance to impurities are their challenges, especially the proton exchange membrane fuel cells (PEMFCs) and shock resistance. PEMFCs and solid oxide fuel cells (SOFCs) are both effective at about 60%. Besides, SOFCs has an additional advantage [30]. They can operate under high temperature (700–1000 °C), which implies that they can be used to generate steam and power needed in steam turbine. The overall system efficiency can be increased to about 80% [31]. As for the both technologies, the additional ancillary components (e.g. plant balancing) reduce the overall efficiency of a few percent. These losses become higher as long as the fuel cells become larger. The specific power (kg/kW) of SOFCs is lower than that of PEMFCs. They have high operating temperatures, long start-up times and poor tolerance to load variations. Internal combustion engines (ICEs) become more efficient owning to the larger sizes, which have a higher average power density, lower costs as well as more tolerance to load changes, and lasts longer. Some disadvantages of them can be noticed such as noise, vibration and low efficiency.

5 Conclusions

Trade of hydrogen between countries will be carried out in the form of ammonia, liquid hydrogen, LOHC, etc., taking into account the renewable energy resources of the exporting country and the hydrogen usage type and technological maturity of the importing country, and will not be traded in only one form. Therefore, in this article, the key technology or potential demand technology are listed.

(1) Development of efficient insulation system.

- For type C tank, vacuum and MLI/glass bubble insulation technology need to develop application technology.

Table. 2. Comparison between direct hydrogen use in fuel cells and ICEs

Performance	ICE	PEMFC	SOFC	GAS TURBINE
Conversion efficiency (%)	50	52	60	35
System efficiency (%)	50	56	80	58
Cost (USD/kW)	< 500	> 1500	> 4500	–
Specific power(kg/kW)	2–11	4	50	1.25–2
Partial load efficiency	High	High	High	Low
Tolerance to load variations	High	Medium	Low	High
Maturity	High	Medium	Low	High
Lifetime	High	Low	Low	–
Noise/vibration	High	Low	Low	High
NO_x and hydrocarbon emissions	Medium	Low	Low	Medium

- For Membrane tank, IBS vacuum maintenance and VIP aging technology research are required.

(2) Development of an efficient hydrogen BOG treatment system and propulsion system are needed.

- Large-capacity fuel cell (PEM or SOFC) needs to be developed.
- Hydrogen BOG dilution emission method needs further verification and inspection.

(3) Considering the low density of liquefied hydrogen, stability, propeller immersion, draft changes (cargo loading/unloading), etc., it is necessary to optimize the linear design of the hull.

At the beginning of the introduction of liquid hydrogen carriers, about 20,000–40,000 m^3 capacity liquid hydrogen carriers equipped with type C tanks with relatively low technical hurdles are suitable, and in the long term it is considered necessary to develop membrane-type liquid hydrogen carriers. In order to succeed in the commercialization of liquefied hydrogen carriers, the reliability and safety of the technology have to be ensured, and there are still technical challenges to be overcome. It is expected that domestic shipyards will successfully enter into the technology of liquefied hydrogen carriers by utilizing their know-how in developing LNG carriers, which is their strength, and that liquefied hydrogen will play an important role in the hydrogen supply chain.

References

1. Farid et al.: After Paris: fiscal, macroeconomic, and financial implications of climate change (2016)
2. Choi, B.I.: Liquid hydrogen-based hydrogen society infrastructure establishment plan. Superconduct. Cryogen. **22**(1), 9–12 (2020)

3. KHI. https://global.kawasaki.com/en/corp/newsroom,accessed (2021)
4. Appleby, A.J.: Fuel cells and hydrogen fuel. Int. J. Hydrogen Energy **19**(2), 175–180 (1994)
5. Song, P., Sui, Y., Shan, T., et al.: Assessment of hydrogen supply solutions for hydrogen fueling station: a Shanghai case study. Int. J. Hydrogen Energy **45**(58), 32884–32898 (2020)
6. Niermann, M., Timmerberg, S., Drünert, S., et al.: Liquid organic hydrogen carriers and alternatives for international transport of renewable hydrogen. Renew. Sustain. Energy Rev. **135**
7. Ishimoto, Y., Voldsund, M., Neksa, P., et al.: Large-scale production and transport of hydrogen from Norway to Europe and Japan: value chain analysis and comparison of liquid hydrogen and ammonia as energy carriers. Int. J. Hydrogen Energy **58**, 45 (2020)
8. d'Amore-Domenech, R., Leo, T.J., Pollet, B.G.: Bulk power transmission at sea: life cycle cost comparison of electricity and hydrogen as energy vectors. Appl. Energy **288**, 116625 (2021)
9. Wijayanta, A.T., Oda, T., Purnomo, C.W., et al.: Liquid hydrogen, methyl cyclohexane, and ammonia as potential hydrogen storage: comparison review. Int. J. Hydrogen Energy **44**(29), 15026–15044 (2019)
10. Takaoka, Y., Kagaya, H., Saeed, A., et al.: Introduction to a Liquefied Hydrogen Carrier for a Pilot Hydrogen Energy Supply Chain (HESC) Project in Japan. Gastech, Tokyo (2017)
11. Hedayat, A., Hastings, L.J., Bryant, C., et al.: Large scale demonstration of liquid hydrogen storage with zero boil off. In: AIP Conference Proceedings (2002)
12. Boucher, R.: An Overview of the NASA Composite. Liquid Hydrogen Cryotank Technologies and Demonstration (2015)
13. Decker, L.: Liquid hydrogen distribution technology. In: Presented at the Hyper Closing Seminar. Brussels, https://www.sintef.no/globalassets/project/hyper/presentations-day2/day2_1105_decker_liquid-hydrogen-distribution-technology_linde.pdf;2019
14. Kawasaki Heavy Industries. KHI Activity for Hydrogen Supply Chain (2016). http://www.jccp.or.jp/country/docs/Hydrogen%20Chain%20by%20Yoshimura.pdf
15. Kawasaki Heavy Industries. Japan's Largest Liquid Hydrogen Storage Tank (2017). https://global.kawasaki.com/en/stories/articles/vol39/
16. Kawasaki Heavy Industries. Kawasaki Technical Review. Special issue on hydrogen energy supply chain (2021). https://global.kawasaki.com/en/corp/rd/magazine/182/index.html
17. Kamiya, S.: World's first ocean going liquid hydrogen carrier. In: Dissemination Conference of the PRESLHY Project (2021). https://hysafe.info/wp-content/uploads/sites/3/2021/05/2_1_LH2-carrier-KHI-kamiya-for-publishing-1-1.pdf
18. Kawasaki Heavy Industries. Kawasaki Completes Basic Design for World's Largest Class (11,200-cubic-meter) Spherical Liquefied Hydrogen Storage Tank (2020). https://global.kawasaki.com/en/corp/newsroom/news/detail/?f=20201224_8018
19. Andersson, J., Grönkvist, S.: Large-scale storage of hydrogen. Int. J. Hydrogen Energy **44**(23), 11901–11919 (2019)
20. Berstad, D., Gardarsdottir, S., Roussanaly, S., et al.: Liquid hydrogen as prospective energy carrier: a brief review and discussion of underlying assumptions applied in value chain analysis. Renew. Sustain. Energy Rev. **154** (2022)
21. Leachman, J.W., Jacobsen, R.T., Penoncello, S.G., et al.: Fundamental equations of state for parahydrogen, normal hydrogen, and orthohydrogen. J. Phys. Chem. Ref. Data **38**(3), 721–748 (2009)
22. Krenn, A.G., Youngquist, R.C., Starr, S.O.: Annular air leaks in a liquid hydrogen storage tank. IOP Conf. Ser. Mater. Sci. Eng. **278** (2017). https://doi.org/10.1088/1757-899X/278/1/012065
23. Ghafri, S., Swanger, A., Jusko, V., et al.: Modelling of liquid hydrogen boil-off. Energies **15** (2022)

24. Heinrich, F., Roland, H., Gunter, H.: Safety valve for the outer vessel of a double wall vacuum-insulated storage tank for low boiling liquified gases: EP0303860A3 (1990)
25. LH_2 Pioneer—Ultra-insulated seaborne containment system for global LH_2 ship transport. Research Council of Norway (2021). https://prosjektbanken.forskningsradet.no/en/project/FORISS/320233
26. Pfundstein, M., Gellert, R., Spitzner, M., et al.: Insulating Materials: Principles, Materials, Applications (2012)
27. 3M™ Glass Bubbles K Series S Series. https://multimedia.3m.com/mws/media/619093O/3m-glass-bubbles-types-k-and-s-uk-data-sheet.pdf. Accessed 17 Feb 2022
28. Lee, H., Shao, Y., Lee, S., et al.: Analysis and assessment of partial re-liquefaction system for liquefied hydrogen tankers using liquefied natural gas (LNG) and H_2 hybrid propulsion. Int. J. Hydrogen Energy **44**(29), 15056–15071 (2019)
29. Kustov, M.V., Kalugin, V.D., Hristich, O.V., et al.: Recovery method for emergency situations with hazardous substances emission into the atmosphere. Int. J. Safety Secur. Eng. Interdisc. J. Res. Appl. **4**, 11 (2021)
30. Depcik, C., Cassady, T., Collicott, B., et al.: Comparison of lithium ion Batteries, hydrogen fueled combustion engines, and a hydrogen fuel cell in powering a small Unmanned Aerial Vehicle. Energy Convers. Manage. **207**, 112514 (2020)
31. Müller, K., Thiele, S., Wasserscheid, P.: Evaluations of concepts for the integration of fuel cells in liquid organic hydrogen carrier systems. Energy Fuels (2019)

Influence of Blade Geometry on Performance of Hydrogen Vortex Blower in Fuel Cell System

Hongshuai Li, Lei Tan(✉), and Huanxin Zhao

State Key Laboratory of Hydroscience and Engineering, Department of Energy and Power Engineering, Tsinghua University, Beijing 100084, China
tanlei@mail.tsinghua.edu.cn

Abstract. Hydrogen fuel cell has great potential in replacement of traditional fossil energy systems to decrease carbon dioxide emission. Vortex blower is a key device in the hydrogen recirculation system, which need to be studied deeply to improve the performance of the whole fuel cell. In this paper, the steady internal flow of a hydrogen vortex bower was numerical simulated, and the effect of blade number and blade flapping angle on the performance was studied. The simulation results were compared with experimental data, and the deviation of simulation in choking condition was observed. With the validated simulation method, the influence of blade number and flapping angle was studied. Higher blade number causes more friction, and less blade number leads to flow separation. The negative flapping angle also has the effect on depressing low-pressure region. This research illuminates the simulation method can be further applied to the aerodynamic study and structure optimization of vortex blower.

Keywords: Hydrogen vortex blower · Experiment · Blade number · Angle

1 Introduction

Hydrogen fuel cell is considered as a promising option in replacement of traditional fossil energy systems with high efficiency, low emission, and short refueling time. In the automotive industry, polymer electrolyte membrane fuel cell (PEMFC) is used widely. To ensure the operation stability and the duration of membrane, adequate hydrogen is critical for the anode, and same to the cathode with air. The hydrogen ratio defines the ratio of hydrogen inlet mole flow and mole flow consumed by fuel cell stack and it is usually greater than 1. Therefore, hydrogen recirculation system is required to reuse the excess hydrogen from anode exhaust gas, which improves the total efficiency of PEMFC and minimizes environmental pollution [1]. There are many researchers [2, 3] focusing the control strategy and control system simulation of hydrogen recirculation system.

Vortex blower is the key device in hydrogen recirculation system, which inputs work to anode exhaust hydrogen, and it is one of the most energy-consuming devices in PEMFC. Hence, a high efficiency vortex blower is desired for a superior performance PEMFC. Many researchers analyze vortex blower through experimental analysis, theoretical analysis, and simulation analysis. Song [4] discussed about the experimental characteristics of forward and backward bending impeller, which showed little difference in

H. Sun et al. (Eds.): WHTC 2023, SPPHY 393, pp. 163–173, 2024.
https://doi.org/10.1007/978-981-99-8631-6_18

large flow condition. Badami [5] proposed a theoretical model with the consideration of clearance to study leakage. Han [6] analyzed the effect of different blade thickness and blade number, and also predicted fatigue life of blade through simulation. Cai and Zhang [7, 8] studied the influence of blade bending direction and bending angle on flow characteristic of vortex blower with simulation method. In addition, many researchers focus on aero-acoustic and noise simulation [9–11]. This study simulated the flow characteristic of a compact hydrogen vortex blower with experimental data.

2 Numerical Simulation

2.1 Geometry Modelling

As shown in Figs. 1 and 2, the vortex blower consists of two main parts, stational flow path with inlet and outlet, and impeller with rotational flow path. The rotational speed of impeller is 10,000–23,000 rpm. The diameter of inlet and outlet is 5 mm. The impeller inner diameter is 27 mm and outer diameter is 76 mm. The impeller has 36 blades. The thickness of blade is 0.8 mm. The fluid domain was calculated by interference operation. To ensure the full development of the flow, extension is added to both inlet and outlet, with length as same as the impeller outer diameter of 76 mm.

Fig. 1. Stator of vortex blower.

2.2 Mesh Generation

Poly-Hexcore meshes were generated separately on stational flow domain and impeller domain by Fluent Meshing 2020 R1, Fig. 3 shows the Poly-Hexcore meshes of impeller domain and stational flow domain. Mesh independency was checked by refining the impeller domain and checking the pressure difference between inlet and outlet. The inlet flow of mesh independency checking state was set as 12.60 m^3/h with rotational speed 17,000 rpm. Four groups of impeller domain mesh were generated with 921,221, 1,228,781, 3,872,419, and 5,853,783. The static pressure differences between inlet and outlet were simulated, and compared with the result from experiment (see Table 1). By consideration of both accuracy and computational resource, mesh group 1 was finally chosen for following numerical simulation.

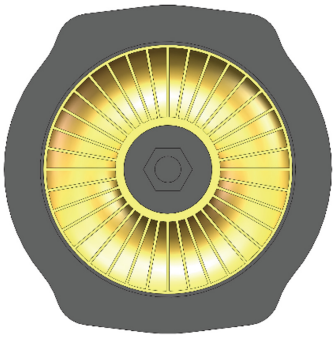

Fig. 2. Impeller of vortex blower.

Table 1. Mesh independency checking results.

Mesh group	Mesh number	Static pressure difference	Error (%)
1	921,221	3189.4	7.24
2	1,228,781	3146.9	5.81
3	3,872,419	3146.8	5.81
4	5,853,783	3205.9	7.80
Experimental data	–	2974.0	–

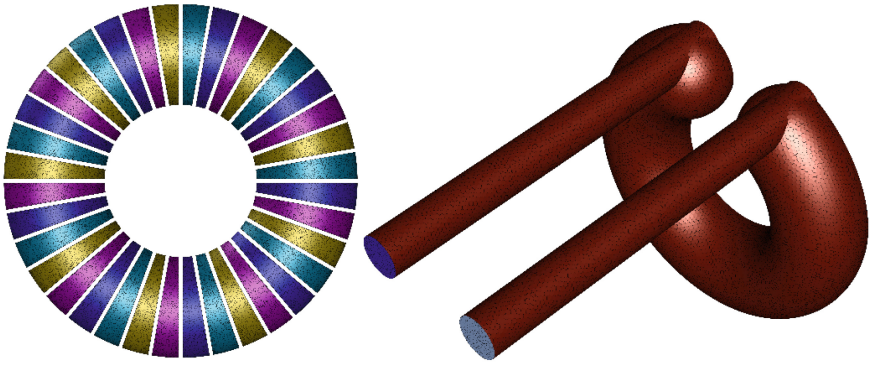

Fig. 3. Poly-hexcore meshes of impeller domain and stational flow domain.

2.3 Solver Setup

In this study, all numerical simulations were conducted by Fluent 2020 R1. To achieve temporal accuracy and numerical stability in transient simulation, Courant number *Co* is required less than 1. The Courant number is defined as:

$$Co = \frac{\delta t|\mathbf{U}|}{\delta x} \tag{1}$$

where δt is the where is the time step, $|\mathbf{U}|$ is the magnitude of the velocity and δx is the cell size. Because the rotational speed of the vortex blower is at the scale of ten thousand, according to *Co*, the time step should be chosen little than 10^{-5} s, which will cause enormous computational effort. Therefore, in this study, simulations were completed with MRF method. The interface between the stator and the impeller is not conformal. In Fluent, there are several methods dealing with non-conformal interface, periodic boundary condition, periodic repeats, coupled wall, matching, and mapped. Because the couple wall interface has no flow exchange between two sides of interface, it is not suitable for the simulation in this study, and neither is mapped method, which is always combined with coupled wall.

The viscous model was selected as realizable k-ε two equation model, which is suitable for high Reynolds number flow. With k-ε model, near-wall treatment method should be selected. Scalable wall functions, non-equilibrium wall functions, and enhanced wall treatment are all suitable for this kind of simulation. By comparison with experimental data, enhanced wall treatment was finally chosen. Coupled scheme was used for pressure velocity coupling, with all velocity-relative terms in second order upwind scheme. For better convergence, pseudo transient option was chosen. As to boundary conditions, mass flow inlet and pressure outlet were selected.

3 Results and Discussion

3.1 Internal Flow Simulation

The flow characteristic of the vortex blower was obtained by four groups experiments on a standard blower test rig. In every group of experiments, the valve opening was set as a constant, and by increasing impeller revolution speed from 10,000 to 23,000 rpm, the mass flow and pressure difference were recorded.

The internal flow simulation was conducted based on the experiments. The rotational speed and inlet mass flow were set as same as experimental data, and the pressure difference was computed numerically. The error was acceptable in engineering with less than 20%. Hence the validation of internal flow simulation was checked. In Fig. 4, four groups of simulation results and experimental data were plotted. From group 1 to group 4, the valve opening was increased. Black squares represent experimental data and red circles are simulation results. From left to right on x axis, the rotational speed is increased from 10,000 to 23,000 rpm.

From Fig. 4(a)–(d), the deviation between simulation results and experimental data is growing. The reason for this deviation is that the mass flow was increasing from group 1 to group 4, and the vortex blower was operated with over inlet flow outside the design region, which caused choking condition. This is also a characteristic phenomenon of vortex blower, that it is more sensitive to choking condition than surging condition.

In Fig. 5, the pressure contours of interface between stator and rotator was plotted. The fluid is pressured sequentially by blades with the high-speed rotation of impeller, and the blade structure has influence of the flow pattern on the interface. The flow pathlines were shown in Fig. 6 and a series complex eddy structures near inlet were observed with low velocity. The low-energy flow was gathered around the inner circle of impeller, which will cause flow separation. Because of the centrifugal force, the flow separation

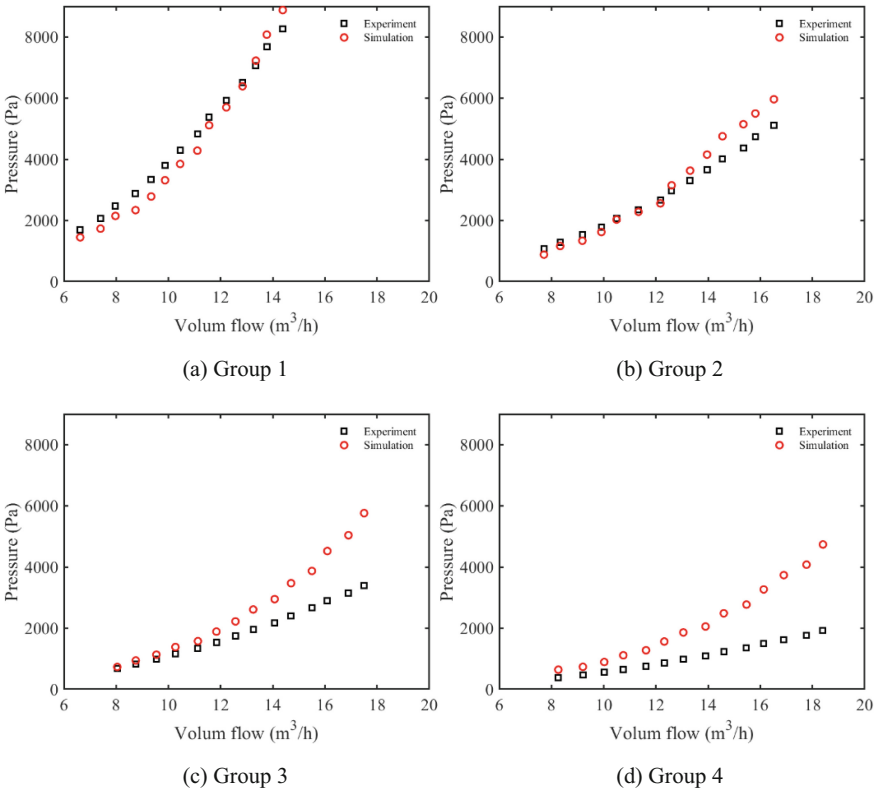

Fig. 4. Experimental data and simulation results of the vortex blower. Black squares represent experimental data. Red circles represent simulation results. The rotational speed is increased from 10,000 to 23,000 rpm from left to right on x axis.

near outer circle region was depressed. In the Fig. 7, the pressure contour of impeller also showed pressure gradient both from inlet to outlet and inner circle to outer circle.

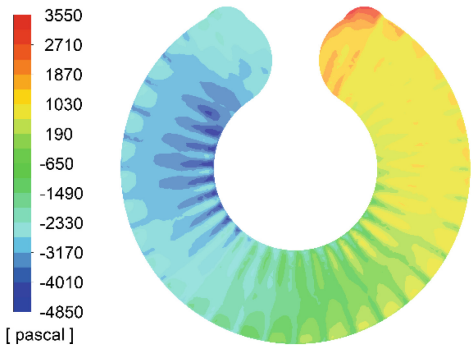

Fig. 5. Pressure contours of interface between stator and rotator.

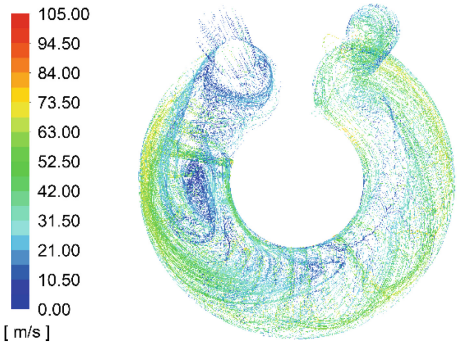

Fig. 6. Pathlines colored by velocity magnitude.

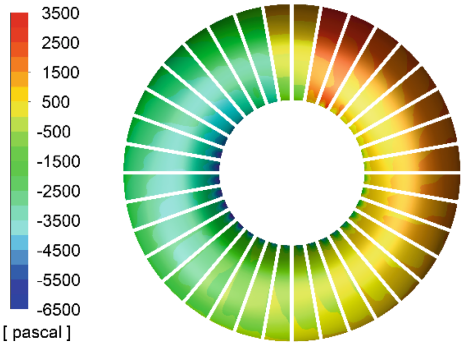

Fig. 7. Pressure contour of impeller.

3.2 Influence of Blade Parameters

In following simulation, the operation point with rotational speed of 17,000 rpm and inlet mass flow of 12.60 m^3/h was selected to study the influence of blade parameters to the performance of the vortex blower.

Firstly, the effect of blade number was studied. With the blade number changing evenly from 34 to 42 by 2, six new impeller models were generated. Under the selected operation point, the pressure difference between inlet and outlet was simulated as shown in Fig. 8. With the decrease of blade number, the pressure rise of the vortex blower is increasing. With the same revolution speed, the more blade number means the more friction between fluid flow and blades, which explain the tendency. Besides, the more blade number makes choking condition more easily to happen. So, higher blade number does not benefit the internal flow of vortex blower.

The pressure contours of the interface between stator and rotator are shown in Fig. 9. Blade number is 34 on the left. Blade number is 42 on the right. The main flow patterns with blade structure are observed on both sides. However, the pressure contour of 34-blade-number impeller is much more uneven compared with 42-blade-number impeller, though the pressure rise is higher.

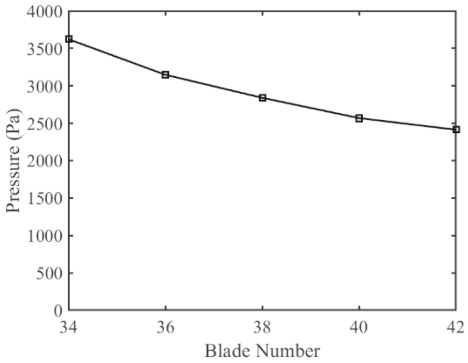

Fig. 8. The pressure rises of vortex blower with different blade number at rotational speed of 17,000 rpm and mass flow of 12.60 m^3/h.

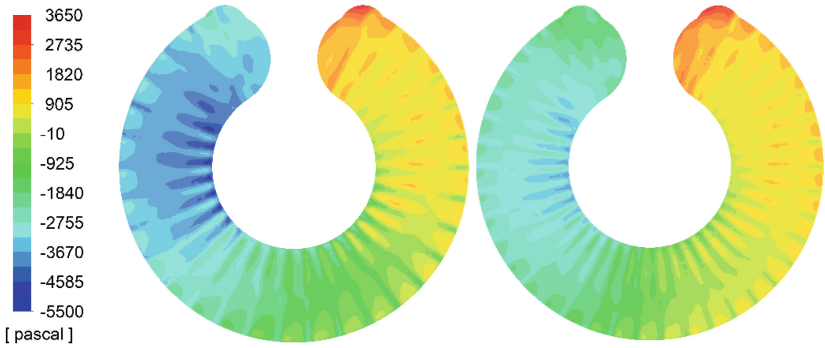

Fig. 9. Pressure contours of interface between stator and rotator. Blade number is 34 on the left. Blade number is 42 on the right.

Figure 10 shows that, in the 34-blade-number impeller, there is a large low-pressure region at the suction surface near inlet, which means sever flow separation. With flow separation, larger secondary flow and other eddy structures will lead to higher energy loss. To ensure the performance of vortex blower with less blade number, further experiments should be done, and there will be an optimal number of blades for specific vortex blower structure.

Secondly, the influence of blade flapping angle was simulated. Blade flapping angle is defined as the space angle between rotation axis and blade plate. In addition, the blade flapping angle is positive when the flapping direction is the same as the rotational direction. In the baseline impeller, all blade plates are parallel to rotation axis, and the blade flapping angle is 0°. New impeller models with blade flapping angle of 5° and − 5° were shown in Fig. 11 left and right. The rotational direction of impeller is counterclockwise face to the paper.

These two impeller models were simulated and compared with baseline impeller as shown in Table 2. The positive flapping angle got higher pressure rise than baseline, and the negative flapping angle got lower pressure rise than baseline. By observing the

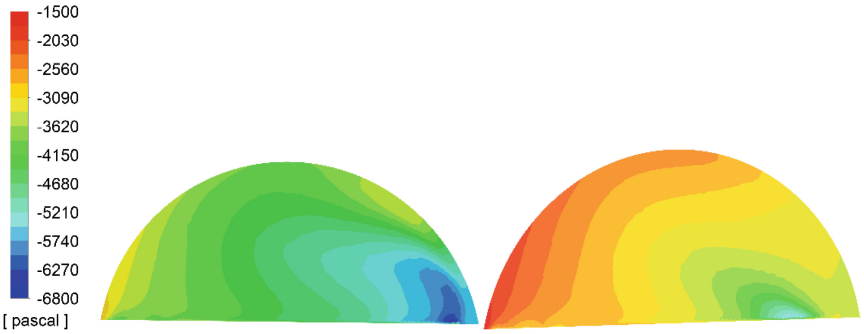

Fig. 10. Pressure contours of suction surface near the inlet. Blade number is 34 on the left. Blade number is 42 on the right.

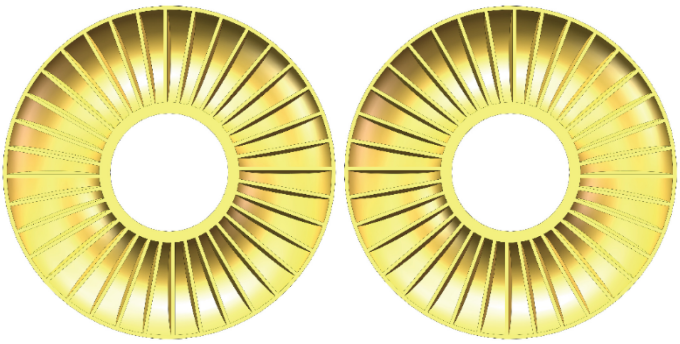

Fig. 11. Impeller models with blade flapping angle. Left: 5°. Right: − 5°.

pressure distribution on interface in Fig. 12, the positive blade flapping angle impeller has similar flow structure as low blade number, and the negative blade flapping angle influences flow like high blade number. The reason for negative flapping angle impeller has more smooth pressure contour is that the structure of the suction surface depressed the flow separation relatively. For further optimization of vortex blower, the optimal blade number combined with proper blade flapping angle is worth to discuss.

Table 2. Simulation results of impellers with different blade flapping angle.

Blade flapping angle	Static pressure difference (Pa)
5°	3900.2
0°	2609.4
−5°	2484.5

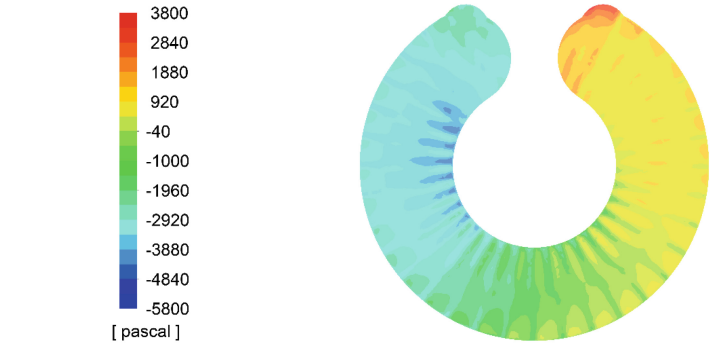

(a) Blade Flapping angle 0° (Baseline)

(b) Blade Flapping angle 5°

(c) Blade Flapping angle −5°

Fig. 12. Pressure contours of interface between stator and rotator.

4 Conclusions

In this paper, a simulation method of the steady internal flow in a vortex blower for hydrogen recirculation system was detailly illustrated. Multiple reference frame method was used to dealing with the relative motion between rotor and stator. The energy characteristic of the vortex blower was recorded through experiments. With the validated simulation method, the influence of blade number and blade flapping angle was discussed. The following conclusions can be drawn:

- The simulation of operation states within design condition region agreed well with experimental data. When the mass flow over the design region, choking condition will happen.
- Higher blade number causes more friction loss between fluid flow and blade because of the higher blade frequency. Lower blade number will get higher pressure rise.

- Positive blade flapping angle improves the pressure rise of the vortex blower. Negative blade flapping angle has the influence of depressing the flow separation at the impeller and make pressure field more even.

Acknowledgments. This work has been supported by the National Key Research and Development Program of China [2020YFB1901401], the Huaneng Group science and technology research project [KTHT-U22YYJC07], the Guoqiang Institute of Tsinghua University [2021GQG1003], the State Key Laboratory of Hydroscience and Engineering [2021-KY-04, sklhse-2022-Iow06], the Creative Seed Fund of Shanxi Research Institute for Clean Energy of Tsinghua University.

References

1. Tinz, S., Dirkes, S., Walters, M., Andert, J.: Fuel Cells, 2nd edn. WILEY-VCH, Weinheim (2022)
2. Chen, F., Zhang, J., et al.: Modeling and selection scheme of PEMFC hydrogen supply system. J. Jilin Univ. 1–11 (2022)
3. Zhou, S., Zhang, C., Chen, F.: Modeling and simulation of high-pressure automobile PEMFC Power system. J. Syst. Simul. **23**(7), 1469–1476 (2011)
4. Song, L., Nie, B.: Research on the comparing of the performance characteristics of regenerative blower with forward skewed and backward skewed impeller. Fluid Mach. **37**(1), 6–9 (2009)
5. Badami, M., Mura, M.: Leakage effects on the performance characteristics of a regenerative blower for the hydrogen recirculation of a PEM fuel cell. Energy Convers. Manage. **55**, 20–25 (2012)
6. Han, H., Zuo, S.: Effect of blade parameters on performance of regenerative blower. Fluid Mach. **40**(7), 15–19 (2012)
7. Cai, Z., Zhang, W.: Influence of impeller parameters on the performance of vortex blower. Fluid Mach. **32**(12), 19–22 (2004)
8. Cai, Z., Zhang, W.: The numerical simulation for the performance of H_2 vortex blower. Petro Chem. Equip. **34**(2), 25–28 (2005)
9. Zuo, S., Hu, Q., Han, H., Kang, Q.: Influence of blade thickness on regenerative blower's blade noise. J. Vib. Shock **33**(8), 130–133 (2014)
10. Heo, M., Seo, T., Shim, H., Kim, K.: Optimization of a regenerative blower to enhance aerodynamic and aeroacoustic performance. J. Mech. Sci. Technol. **30**(3), 1197–1208 (2016)
11. Lim, T., Lee, S., Jeon, W., Jang, C.: Characteristics of unsteady flow field and aeroacoustic noise in a regenerative blower. J. Mech. Sci. Technol. **29**(5), 2005–2012 (2015)

Relationship Between Stress Distribution and Current Density Distribution on Commercial Proton Exchange Membrane Fuel Cells

Weichen Ji and Rui Lin(✉)

School of Automotive Studies, Tongji University, 4800 Cao'an Road, Shanghai, China
ruilin@tongji.edu.cn

Abstract. The current density of proton exchange membrane fuel cells (PEMFCs) is directly linked to their electrochemical reaction. Its distribution over the active area can give the local performance of the cells, which is significant for exploration of internal process and optimization of performance. In this paper, segmented cell technology is applied to investigate the current density distribution for a commercial PEMFC with different clamping strategies. The stress distribution and current density distribution as well as the overall performance of the cell are tested under the same operating conditions. The results show that a more uniform stress distribution can lead to a more uniform reaction current density distribution and the good uniformity of the stress distribution and current density distribution has a positive impact on the improvement of the cell overall performance. Thus, it is significant to improve the clamping strategy in order to improve the uniformity of the stress distribution and reaction current density distribution, which ultimately improves the cell overall performance.

Keywords: Commercial proton exchange membrane fuel cells · Clamping strategies · Stress distribution · Contact form · Current density distribution

1 Introduction

The PEMFC is regarded as one of the most promising power sources for vehicles and various portable electronic applications due to its high energy conversion rate, high reliability and low pollution emission in operation [1]. Currently, commercial fuel cells usually need hundreds of cells and large active area for each single cell to realize high power applications [2]. Scaling up the active area from no more than 50 cm^2 in laboratory level to over 150 cm^2 for commercial use encounters challenges in reaction gas flow distribution, water-heat management, and reaction uniformity [3]. In order to optimize the design of commercial PEMFC, it is necessary to carefully consider the coupling relationship of various uneven parameters such as temperature, reaction gas concentration, stress distribution and current density distribution [4].

Conventional fuel cell diagnostic methods such as polarization curve can give an overall performance but lack of spatial information at different positions for the large

H. Sun et al. (Eds.): WHTC 2023, SPPHY 393, pp. 174–179, 2024.
https://doi.org/10.1007/978-981-99-8631-6_19

reaction active area. As current density is directly linked to electrochemical reaction of fuel cells, its distribution over the active area can give the local performance of the cells [5]. Thus, relevant diagnostic methods need to be developed to obtain the current density distribution in the reaction process of commercial PEMFCs with large active area. So far, various researches have been conducted to investigate the current density distribution inside PEMFCs with large active area. In order to study the influence of relative humidity (RH) on the performance and durability of reversal-tolerant-anodes (RTAs) during hydrogen starvation, Wang et al. [6] employed an advanced segmented technique to examine the coupling reactions by simultaneously measuring current density, RH and temperature in a PEMFC with large active area. It is found that the inlet of RTAs undergoes degradation earlier than the outlet and the membrane electrode assembly (MEA) with a RTA has an optimal humidity during cell reversal. Lin et al. [7] studied the changes of the overall performance and current density distribution of commercial PEMFCs under dynamic gas operating parameters especially transient process through fast segmented cell technology. The results showed that the cathode stoichiometric ratio has a more significant effect on the cell performance than the back pressure. The work leads to suggestions on the control strategy during dynamic load demands and lays a foundation for further study into the durability under variable gas operation parameters of the fuel cell operation.

Moreover, some researches have been conducted to study the relationship between stress distribution and current density distribution as well as the cell overall performance. Vijayakumar et al. [8] measured the current distribution profile along the cathode flow field channel using a segmented current measurement plate to understand the influence of uneven clamping pressure distribution on the MEA. Although scholars have done some research on the relationship between the stress distribution and the current density distribution affected by the clamping force, few studies on the stress distribution and its relationship with the current density distribution caused by the cell structure and clamping strategy have been conducted so far inside commercial PEMFCs with large active area.

In this work, two different clamping strategies are applied to a commercial PEMFC with the active area of 360 cm^2. The current density distribution is tested by segmented cell technology (from Yuanzhu technology, www.szfcet.com) and the stress distribution is obtained. The results of both strategies are compared not only to analyze the influence of different structures on stress distribution but also to examine the relationship between stress distribution and current density distribution as well as the cell overall performance.

2 Experimental Part

The research is carried out on a commercial single PEMFC with the active area of 360 cm^2 with two different clamping strategies (strategy 1 and strategy 2) under the standard operating conditions. The conditions contain: coolant temperature of 75°C, anode/cathode back pressure of 100/95 kPa, anode/cathode stoichiometry of 1.5/2.2, anode/cathode RH of 80%/80%. The segmented cell technology is from Yuanzhu technology (www.szfcet.com), which is applied to test the current density distribution of the fuel cell and the stress distribution is obtained by pressure measurement film.

3 Results and Discussion

3.1 Influence of Different Structures on Stress Distribution

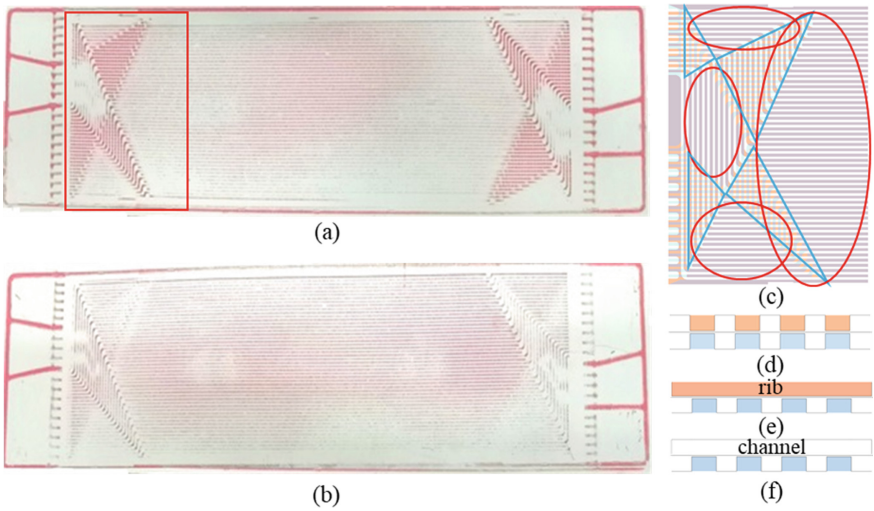

Fig. 1. The stress distribution (**a**) and the flow field structure (**c**) of the contact interface of the cell with strategy 1; the stress distribution (**b**) of the cell with strategy 2; cross section of the parallel areas (**d**) and the vertical areas (**e**, **f**) of the flow field structure.

Figure 1 analyzes the influence of different structures on stress distribution. It can be found that the stress distribution of the cell with strategy 1 (Fig. 1(a)) is less uniform than the stress distribution of the cell with strategy 2 (Fig. 1(b)). As shown in Fig. 1(c), the contact interface of the cell with strategy 1 can be divided into two parts. One is the area where the ribs on the contact interface are vertical to each other (the triangle areas of Fig. 1(c)), and the other is the area where the ribs on the contact interface are parallel to each other (the oval areas of Fig. 1 (c)). Comparing the stress distribution and the flow field structure on the contact interface, we can find that the contact where ribs are vertical to each other is better than that where ribs are parallel to each other. In vertical areas, the ribs and channels on both sides of the interface are interlaced. The contact forms of the interface can be divided into three types: rib to rib, rib to channel, channel to channel (Fig. 1(e, f)). From Fig. 1(a) we can find that both the rib-to-rib form and the rib-to-channel form can achieve good contact stress, while the channel-to-channel form gains poor contact. As most of the vertical areas are rib-to-rib and rib-to-channel forms, these areas generally result in good contact. On the other hand, the parallel areas only have rib-to-rib and channel-to-channel forms. And as the proportion of the channel-to-channel form which has poor contact is considerably large (near 50%), the parallel areas generally result in poor contact. As shown in Fig. 1(b), the interface of the cell with strategy 2 only has rib-to-channel and rib-to-rib forms (Fig. 1(e)). Thus, the stress distribution on the entire contact interface is more uniform and generally better.

3.2 Relationship Between Stress Distribution and Current Density Distribution

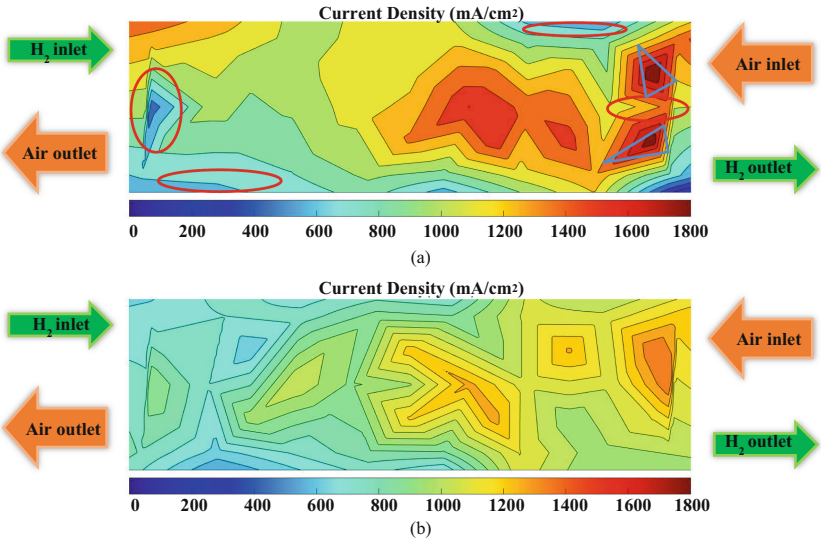

Fig. 2. The current density distribution of the cell with strategy 1 (**a**) and the cell with strategy 2 (**b**) at 1000 mA/cm^2.

Figure 2 shows the current density distribution of the cell with two clamping strategies at 1000 mA/cm^2 respectively, which investigates the relationship between stress distribution and current density distribution. As shown in Fig. 2(a), it is found that the local current density in some areas (the oval areas of Fig. 2(a)) is lower than the normal value. It can be found from the stress distribution and flow field structure in Fig. 1(c) that these low current density areas are consistent with the poor contact areas (parallel areas). Therefore, the local poor contact may affect the reaction in these areas and lead to low local current density. On the other hand, by comparing the triangle areas of the stress distribution (Fig. 1 (c)) and the current density distribution (Fig. 2(a)), the results show that local good contact contributes to the reaction in these areas, which leads to the increase of local current density. Moreover, the current density distribution of the cell with strategy 2 (Fig. 2(b)) is much more uniform than that of the cell with strategy 1 (Fig. 2(a)). By combining the phenomenon with the stress distribution of the cells with two clamping strategies respectively (Fig. 1(a) and (b)), we can find that a more uniform stress distribution can lead to a more uniform reaction current density distribution.

3.3 Relationship Between Current Density Distribution and the Cell Overall Performance

As shown in Fig. 3, the red line is the polarization curve of strategy 2, and the black line is the polarization curve of strategy 1. It can be found that the overall performance of the cell with strategy 2 is better than that of the cell with strategy 1, especially at medium and

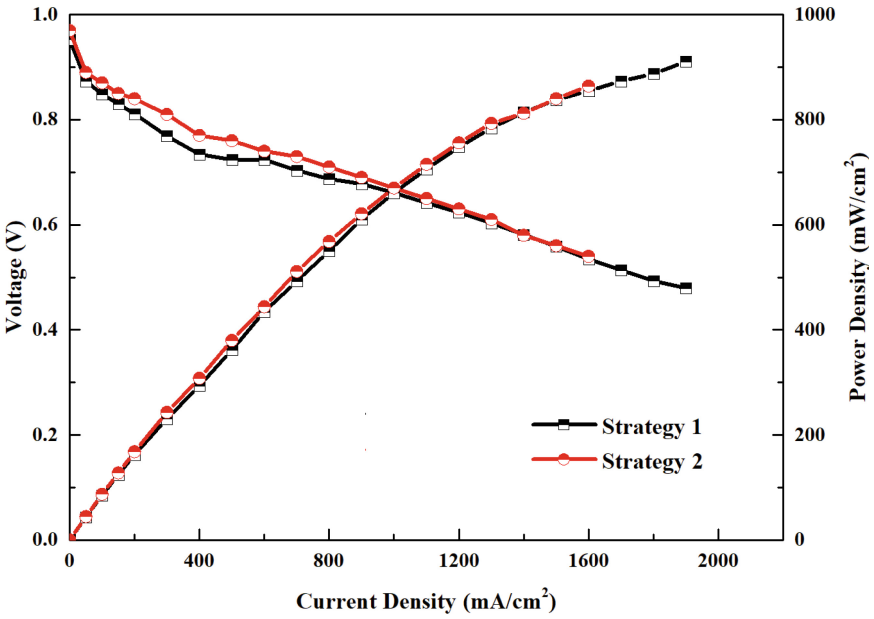

Fig. 3. Polarization curves of the cell with both clamping strategies.

low current density region. Since the stress distribution and current density distribution of the cell with strategy 2 is more uniform than that of strategy 1 (Figs. 1 and 2), it can be deduced that the well uniformity of the stress distribution and current density distribution has a positive impact on the improvement of the cell overall performance.

4 Conclusions

In this study, two different clamping strategies are applied to a commercial PEMFC with the active area of 360 cm^2. The stress distribution and current density distribution as well as the overall performance of the cell in both cases are tested under the same operating conditions. The results show that the vertical areas where rib-to-rib and rib-to-channel forms occupy the majority have good contact while the parallel areas where the proportion of the channel-to-channel form which has poor contact is considerably large have poor contact, which leads to the uneven stress distribution of the cell with strategy 1. The cell with strategy 2 of which the contact interface only has rib-to-channel and rib-to-rib forms has more uniform and generally better stress distribution on the entire contact interface. By comparing the relationship between the stress distribution and the current density distribution of both strategies, it is found that a more uniform stress distribution can lead to a more uniform reaction current density distribution. From the results of the overall performance of the cells in both strategies, it can be considered that the good uniformity of the stress distribution and current density distribution has a positive impact on the improvement of the cell overall performance. Thus, it is significant to improve the clamping strategy and the contact form of the flow field in order to improve

the uniformity of the stress distribution and reaction current density distribution, and ultimately improve the cell overall performance.

Acknowledgement. The authors gratefully acknowledge the financial support by Key projects of intergovernmental international scientific and technological innovation cooperation (No. 2022YFE0102900) and the International Cooperation Program of Science and Technology Commission of Shanghai Municipality (No. 22160712100).

References

1. Lin, R., Yu, X.T., Chen, L., et al.: Structure majorization on the surface of microporous layer in polymer electrolyte membrane fuel cells to optimize performance and durability. Energy Conv Manage **243**, 114319 (2021)
2. Shimpalee, S., Hirano, S., Debolt, M., et al.: Macro-scale analysis of large scale PEM fuel cell flow-fields for automotive applications. J. Electrochem. Soc. **164**(11), E3073 (2017)
3. Peng, L., Shao, H., Qiu, D., et al.: Investigation of the non-uniform distribution of current density in commercial-size proton exchange membrane fuel cells. J. Power. Sour. **453**, 227836 (2020)
4. Wu, H.-W., Shih, G.-J., Chen, Y.-B.: Effect of operational parameters on transport and performance of a PEM fuel cell with the best protrusive gas diffusion layer arrangement. Appl. Energy **220**, 47–58 (2018)
5. Belhadj, M., Aquino, A., Heng, J., et al.: Current density distributions in polymer electrolyte fuel cells: a tool for characterisation of gas distribution in the cell and its state of health. Chem. Eng. Sci. **185**, 18–25 (2018)
6. Wang, Y., Xie, X., Zhou, C., et al.: Study of relative humidity on durability of the reversal tolerant proton exchange membrane fuel cell anode using a segmented cell. J. Power. Sour. **449**, 227542 (2020)
7. Ma, Y.Y., Lin, R., Hou, Z.J., et al.: Research on the variation of current density distribution in a commercial-size proton exchange membrane fuel cell under dynamic gas operation parameters. Int. J. Heat Mass Transf. **196**, 123287 (2022)
8. Vijayakumar, R., Ramkumar, T., Maheswari, S., et al.: Current and clamping pressure distribution studies on the scale up issues in direct methanol fuel cells. Electrochim. Acta **90**, 274–282 (2013)

Hydrogen Leakage Detection in Confined Spaces with Drift Suppression Based on Subspace Alignment

Haifeng Se, Jinhai Jiang, Chuanyu Sun, and Kai Song(✉)

School of Electrical Engineering and Automation, Harbin Institute of Technology, Harbin 150001, China
kaisong@hit.edu.cn

Abstract. Gas sensor has been widely used in flammable gas detection. In order to solve the problem that gas sensors are susceptible to drift in hydrogen leakage detection in confined spaces, a drift compensation framework based on subspace alignment is proposed. First, global domains and subdomains are aligned simultaneously in the new subspace, thus reducing the distribution difference between the source domain and the target domain. Then, the proposed method utilizes extreme learning machine (ELM) to iteratively refine the prediction results of the target domain, and continuously optimizes the subspace and classifier. In this way, the proposed method realizes drift compensation at the feature level. Compared with the existing methods, the proposed method achieves the highest accuracy of 79.83% in the long-term drift scenario. Therefore, the experimental results show that the proposed method is competent for hydrogen leakage detection with drift, and can provide a reference for the design of drift compensation method based on gas sensors.

Keywords: Gas sensor · Hydrogen leakage detection · Drift compensation · ELM

1 Introduction

Compared with oil and natural gas, hydrogen energy has a higher conversion rate and lower carbon emissions, which is regarded as one of the feasible solutions to solve the problem of fossil fuel environmental pollution and energy crisis [1]. However, hydrogen is a flammable gas and hydrogen leakage in confined spaces may occur in the process of hydrogen transportation and hydrogen storage. In this case, it has potential risks of combustion and explosion. Therefore, it is necessary to design hydrogen leakage methods.

With the development of material science and artificial intelligence, gas sensors have been widely used in the field of explosive detection [2]. Most gas detection methods utilize gas sensors + machine learning to identify flammable gases. They generally assume that the training and test sets are independent and equally distributed. The prediction model is built on the training set and applied to the test set. However, due to aging,

H. Sun et al. (Eds.): WHTC 2023, SPPHY 393, pp. 180–186, 2024.
https://doi.org/10.1007/978-981-99-8631-6_20

temperature and humidity interference, even the same concentration of the target gas, the response of the gas sensor is still different, i.e., sensor drift. In this context, the methods which assume that the training set and the test are identically distributed are not competent for gas detection in the drift scene in practical application.

For gas detection with sensor drift, Zhang et al. [3] proposed a machine learning method based on subspace projection to suppress gas sensor drift. Artursson et al. [4] introduced a drift counteraction method based on principal component analysis and partial least squares, and thus suppress sensor drift by removing drift direction component. Vergara et al. [5] designed a machine learning approach, namely the integration of classifiers, to solve the problem of gas identification over long periods of time. However, the accuracy of existing methods is still low. Therefore, a gas sensor compensation method based on subspace alignment is proposed. This method is suitable for gas identification in drift scene with high accuracy by aligning global domains and subdomains in the new subspace.

2 Methodology

The source domain with D-dimension are denoted as $X_S = [x_s^1, x_s^2, \cdots, x_s^{N_S}] \in \Re^{D \times N_S}$, and the target domain with D-dimension are denoted as $X_T = [x_T^1, x_T^2, \cdots, x_T^{N_T}] \in \Re^{D \times N_T}$. $P \in \Re^{D \times d}$ represents a base matrix. $\|\cdot\|_2$ is the l_2-norm. $tr(\cdot)$ denotes the trace operator.

2.1 Subspace Alignment Method (SAM)

To suppress sensor drift, the proposed SAM utilizes P to achieve domain alignment, and thus reduce distribution divergence between source domain and target domain. First, we focus on the alignment of the global distribution based on marginal distribution distance in the subspace.

$$\min_P \|\mu_S - \mu_T\|_2^2 = \min_P \left\| \frac{1}{N_S} \sum_{i=1}^{N_S} y_S^i - \frac{1}{N_T} \sum_{j=1}^{N_T} y_T^j \right\|_2^2 \tag{1}$$

where μ denotes the centre of the domain in the subspace. $y_S^i = P^T x_S^i$ $(i = 1, 2, ..., N_S)$ and $y_T^j = P^T x_T^j$ $(j = 1, 2, ..., N_T)$ are the projected samples in the subspace. Then we rewrite (3) as:

$$\begin{aligned} &\min_P \left\| \frac{1}{N_S} \sum_{i=1}^{N_S} y_S^i - \frac{1}{N_T} \sum_{j=1}^{N_T} y_T^j \right\|_2^2 \\ &= \min_P tr(P^T (u_S - u_T)(u_S - u_T)^T P) \end{aligned} \tag{2}$$

where u is the centre of the domain in the original space. For example, $u_S = \frac{1}{N_S} \sum_{i=1}^{N_S} x_s^i$ and $u_T = \frac{1}{N_T} \sum_{j=1}^{N_T} x_T^j$.

We then consider aligning subdomains with the same category between domains, which is formulated as follows

$$\begin{aligned}&\min_{P}\sum_{c=1}^{C}\left\|\frac{1}{N_S^c}\sum_{y_S^i\in class\,c}y_S^i-\frac{1}{\hat{N}_T^c}\sum_{\hat{y}_S^i\in class\,c}\hat{y}_T^j\right\|_2^2\\&=\min_{P}tr\left(\sum_{c=1}^{C}P^T(u_S^c-\hat{u}_T^c)(u_S^c-\hat{u}_T^c)^TP\right)\end{aligned}\tag{3}$$

where $\hat{y}_T^j$ represents the j-th sample whose classifier prediction result belong to class c from the target domain. $\hat{N}_T^c$ is the number of samples whose classifier prediction result belong to class c. $\hat{u}_T^c$ is the centre of c-class samples from the target domain.

To prevent data distortion from source and target domains, it is necessary to maximize the following term

$$\begin{aligned}&\max_{P}((1-\alpha_1)\times tr(P^TX_SX_S^TP)+\alpha_1\times tr(P^TX_TX_T^TP))\\&=\max_{P}(tr((1-\alpha_1)\times P^TX_SX_S^TP+\alpha_1\times P^TX_TX_T^TP))\end{aligned}\tag{4}$$

where $\alpha_1\in[0,1][0,1]$.

Finally, the proposed SAM simultaneously optimizes (2), (3) and (4), which is formulated as:

$$\min_{P}\frac{\alpha_2\times tr(P^T(u_S-u_T)(u_S-u_T)^TP)+\alpha_3\times tr(\sum_{c=1}^{C}P^T(u_S^c-\hat{u}_T^c)(u_S^c-\hat{u}_T^c)^TP)}{tr((1-\alpha_1)\times P^TX_SX_S^TP+\alpha_1\times P^TX_TX_T^TP)}\tag{5}$$

To achieve a unique solution, (5) is rewritten as

$$\begin{cases}\min_{P}(\alpha_2\times tr(P^T(u_S-u_T)(u_S-u_T)^TP)+\alpha_3\times tr(\sum_{c=1}^{C}P^T(u_S^c-\hat{u}_T^c)(u_S^c-\hat{u}_T^c)^TP)\\s.t.(1-\alpha_1)\times P^TX_SX_S^TP+\alpha_1\times P^TX_TX_T^TP=I\end{cases}\tag{6}$$

where $I\in\Re^{d\times d}$ is the identity matrix.

After that, the Lagrange function L is introduced:

$$\begin{aligned}L=&\alpha_2\times tr(P^T(u_S-u_T)(u_S-u_T)^TP)+\alpha_3\times tr(\sum_{c=1}^{C}P^T(u_S^c-\hat{u}_T^c)(u_S^c-\hat{u}_T^c)^TP)\\&-tr((I-((1-\alpha_1)\times P^TX_SX_S^TP+\alpha_1\times P^TX_TX_T^TP))\Phi)\end{aligned}\tag{7}$$

where $\Phi=\mathrm{diag}(\phi_1,\phi_2,\ldots,\phi_d)\in\Re^{d\times d}$ denote the Lagrange multipliers.

According to $\frac{\partial L}{\partial P} = 0$, we can get

$$((1-\alpha_1) \times X_S X_S^T + \alpha_1 \times X_T X_T^T))^{-1}(\alpha_2(u_S - u_T)(u_S - u_T)^T + \alpha_3 \sum_{c=1}^{C}(u_S^c - \hat{u}_T^c)(u_S^c - \hat{u}_T^c)^T)P = P\Phi \tag{8}$$

P can be solved by eigenvalue decomposition based on A. i.e.,

$$AP = P\Phi \tag{9}$$

where

$$A = ((1-\alpha_2) \times X_S X_S^T + \alpha_2 \times X_T X_T^T)^{-1}\Big((1-\alpha_1) \times (u_S - u_T)(u_S - u_T)^T + \alpha_1 \times \sum_{c=1}^{C}(u_S^c - \hat{u}_T^c)(u_S^c - \hat{u}_T^c)^T\Big).$$

Therefor, P^* is formulated as

$$P^* = [P_1, P_2, ..., P_d] \tag{10}$$

where P_k $(k = 1, 2, ..., d)$ denotes the eigenvector with respect to the k-th minimum eigenvalue.

2.2 The Proposed Framework

The proposed framework first calculates P according to (10), and the source domain and target domain are projected into the subspace, thus reducing the distribution differences between domains. Then, the data of the subspace is input into ELM [6] for training, and thus obtain the prediction result of the target domain. Finally, the target domain is iteratively optimized to predict the results and P (see Fig. 1).

3 Experiments

3.1 Dataset

The benchmark sensor drift dataset was collected over 36-month from UCSD [5], including acetone, acetaldehyde, ethanol, ethylene, ammonia, and toluene. There are 13,910 samples in the data set and each sample consists of 128-dimensional feature vector. The benchmark sensor drift dataset is divided into ten batches, as shown in Table 1.

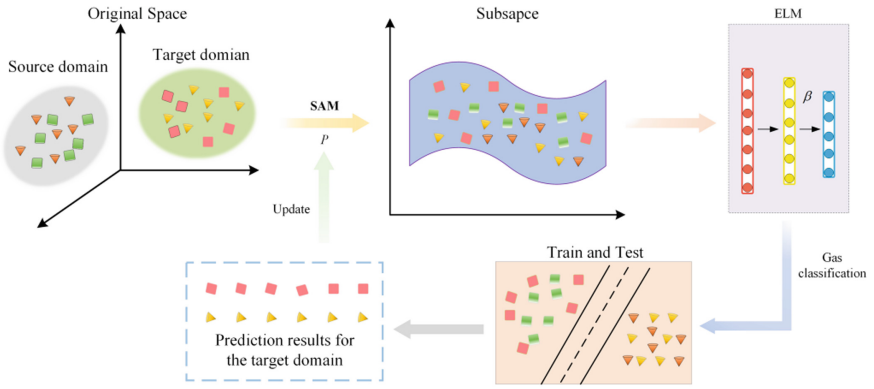

Fig. 1. Average accuracy with different Iterations.

Table 1. The sensor drift dataset.

Batch ID	Month	Acetone	Acetaldehyde	Ethanol	Ethylene	Ammonia	Toluene	Total
Batch 1	1, 2	91	99	82	31	71	75	445
Batch 2	3–10	165	333	101	108	531	6	1244
Batch 3	11–13	366	491	214	241	274	0	1586
Batch 4	14, 15	65	42	13	31	10	0	161
Batch 5	16	29	41	21	43	62	0	197
Batch 6	17–20	515	573	111	28	604	465	2300
Batch 7	21	648	663	361	745	631	567	3613
Batch 8	22, 23	32	31	41	34	142	18	294
Batch 9	24, 30	60	56	101	76	76	100	470
Batch 10	36	600	600	600	600	600	600	3600

3.2 Experimental Results

The experimental environment is an Intel(R) core (TM) i7-10750H CPU@2.60 GHz, 16 GB memory, Windows 11 and Python 3.6. We set batch 1 as the training set (source

domain) and batch t ($t = 2, 3, \ldots, 10$) as the test set (target domain). The proposed method is compared with several drift compensation methods, including SVM, ELM and DRCA [3].

The experimental results are shown in Table 2. Compared with SVM, ELM and DRCA, the proposed method achieves the highest classification accuracy by reducing the distribution difference. Therefore, these results show that the proposed drift compensation strategy is competent for gas detection in long-term drift scenarios.

Table 2. Experiment results.

Method	Batch2	Batch3	Batch4	Batch5	Batch6	Batch7	Batch8	Batch9	Batch10	Aver.
SVM	72.33	64.44	52.54	18.86	30.17	29.20	21.46	40.22	34.06	40.37
ELM	69.63	65.25	65.75	65.13	68.54	52.75	48.65	50.92	34.49	57.89
DRCA	90.46	91.45	85.21	94.88	87.14	63.46	61.53	71.04	53.55	77.65
Our	91.01	89.38	88.65	90.75	88.14	68.81	70.15	72.33	59.27	79.83

During training we hope to use as few iterations as possible to achieve the highest accuracy. Figure 2 shows the average accuracy of the proposed method with iterations. The results show that the proposed method is effective and the highest average accuracy is achieved in fewer iterations.

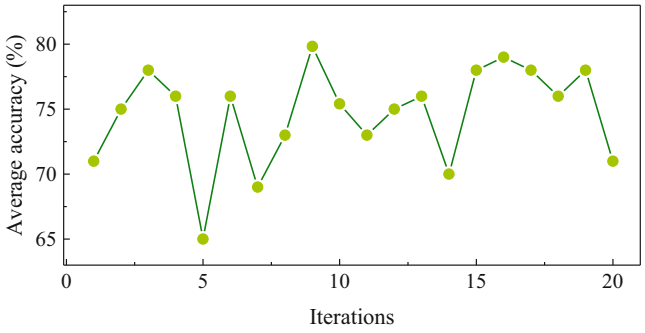

Fig. 2. Average accuracy with different Iterations.

4 Conclusion

Hydrogen leakage detection in confined spaces is the guarantee of successful hydrogen transport and hydrogen storage technology. In this paper, focusing on the practical application scenario, a drift compensation method for gas sensor is proposed. In this method, subspace alignment is realized by aligning subdomains and global domains, and thus reducing the distribution difference due to sensor drift. Experimental results show that the proposed method achieves the highest classification accuracy in the long-term drift with an average accuracy of 79.83%.

Acknowledgments. This work was supported by the Central Science and Technology Commission of China under grant JZKJW20200036.

References

1. Hao, D., Wang, X., Zhang, Y., et al.: Experimental study on hydrogen leakage and emission of fuel cell vehicles in confined spaces. Autom. Innov. **3**(19), 111–122 (2020)
2. Brudzewski, K., Osowski, S., Pawlowski, W.: Metal oxide sensor arrays for detection of explosives at sub-parts-per million concentration levels by the differential electronic nose. Sens. Actuators B Chem. **161**(1), 528–533 (2012)
3. Zhang, L., Liu, Y., He, Z., et al.: Anti-drift in E-nose: a subspace projection approach with drift reduction. Sens. Actuators B Chem. **253**, 407–417 (2017)
4. Artursson, T., Eklov, T., Lundstrom, I., et al.: Drift correction for gas sensors using multivariate methods. J. Chemom.Chemom. **14**(5–6), 711–723 (2015)
5. Vergara, A., Vembu, S., Ayhan, T., et al.: Chemical gas sensor drift compensation using classifier ensembles. Sens. Actuators B Chem. **166**, 320–329 (2012)
6. Ding, X., Liu, J., Yang, F., et al.: Random compact Gaussian kernel: application to ELM classification and regression. Knowl.-Based Syst..-Based Syst. **217**, 106848 (2021)

Design of 10 L/s Liquid Hydrogen Pump with Integrated Inducer and Centrifugal Impeller

ZiWei Li[1,2], Cui Lv[1(✉)], Jihao Wu[1,2], Linghui Gong[1], Jinzhen Wang[1], Jin Shang[1], and Ming He[1]

[1] Key Laboratory of Cryogenic Science and Technology, State Key Laboratory of Technologies in Space Cryogenic Propellants, Technical Institute of Physics and Chemistry, Chinese Academy of Sciences, Beijing, China
clv@mail.ipc.ac.cn

[2] Key Laboratory of Cryogenic Science and Technology, University of Chinese Academy of Sciences, Beijing, China

Abstract. With the global focus on energy and environmental issues, hydrogen energy development has become more and more important. The liquid hydrogen pump is an important equipment for hydrogen transportation, whose performance is significantly decided by the impeller. In this paper, we designed an integrated impeller with an inducer and an centrifugal impeller and optimized the axial length and outlet angle of the centrifugal impeller. Grid independence and cross validation prove that the simulation model and results are reliable. It is worth noting that a high roughness is given to the impeller surfaces in our simulation to obtain results closer to the real situation. By analyzing the pressure and relative liquid flow angle distribution in the fluid domain, the structural design of the impeller is optimized, and then the performance curve is obtained. The simulation results will provide a guidance for the manufacture of our liquid hydrogen pump, and also provide a reference for the design and manufacture of other liquid hydrogen pumps.

Keywords: Liquid hydrogen pump · Integrated impeller · High speed

The development of hydrogen energy has attracted global focus, which is greatly concerned with energy and environmental issues. Recently, many countries around the world have deployed hydrogen energy-related technologies. Due to the advantages of low energy consumption and high efficiency, the liquid hydrogen pump is widely valued for liquid hydrogen transferring. The impeller is the most important part of the pump. Considering the cavitation issue, we used an integrated impeller with an inducer and centrifugal impeller to improve the performance.

At present, there is less literature to be investigated. In 2015, Li et al. [1] designed a semi-open integrated impeller for aviation fuel pumps. The performance requirements are 8000 rpm, 77,000 L/h, and the inlet and outlet pressure difference is 0.956 MPa. According to calculations, the pump does not produce cavitation in the operating range, and the efficiency is 65%. And then, they optimized the profile line to improve the performance [2]. Liu et al. [3] optimized the blade wrapping angle. In 2018, Li et al.

H. Sun et al. (Eds.): WHTC 2023, SPPHY 393, pp. 187–192, 2024.
https://doi.org/10.1007/978-981-99-8631-6_21

[4] designed a fuel centrifugal pump with an integrated inducer and impeller influenced by an inlet flow ejector. The pump performance requirements are 1500 L/h, 10678 rpm, 23.07 m. And the simulation efficiency is 69%. The experiment efficiency is 65%. Tian et al. [5] designed an integrated impeller for an aero fuel pump and optimized the centrifugal impeller blade wrapping angle. The pump performance requirements are 3.9 kg/s, 9000 rpm, $\triangle P \geq 80$ kPa. And the simulation efficiency is 81.5%.

In this paper, we designed an integrated impeller with an inducer and centrifugal impeller and optimized axial length and outlet angle. By analyzing the flow field pressure and relative liquid flow angle distribution, the structural design of the impeller is determined, and the performance curve is obtained.

1 Preliminary Design of Integrated Impeller

1.1 Performance Parameters

Table 1. Performance parameters

Parameters	Q	Head	Rotating speed	Inlet pressure	Outlet pressure
Value	10 L/s	145 m	18000 rpm	1.3 bar	20.5 K

According to Table 1, the liquid hydrogen integrated impeller is designed as shown in Fig. 1. The impeller has 3 main blades and 3 auxiliary blades.

a. Overall impeller structure b. Impeller blade

Fig. 1. Closed integral impeller

1.2 Calculation and Boundary Conditions

Adopt the SST k − ω turbulence model and secondary windward space discrete format. The convergence residual is set to 10^{-5}. Set the inlet as pressure boundary condition as 1.3 bar and outlet as volume flow rate boundary as 10 L/s. Set wall roughness as 1.2 μm.

1.3 Results of Preliminary Impeller Design

The results of the preliminary design are shown in Table 2. The efficiency is 89.65%. The flow field pressure and velocity distribution are shown in Fig. 2.

Table 2. The results of preliminary impeller design

Parameters	rpm	Efficiency (%)	Head (m)	Power (W)	Outlet pressure (bar)
Value	18000	89.65%	167.92	1299.65	2.46

a. Total pressure b. Absolute velocity

Fig. 2. Total pressure and absolute velocity of the preliminary design

2 Optimization of the Integrated Impeller Structure

2.1 Optimization of the Axial Length

After changing the axial length of the centrifugal impeller from 15 to 40 mm with the interval of 5 mm, we get the calculation results as shown in Fig. 3. When the axial length of the centrifugal impeller is 25 mm, the efficiency is optimal.

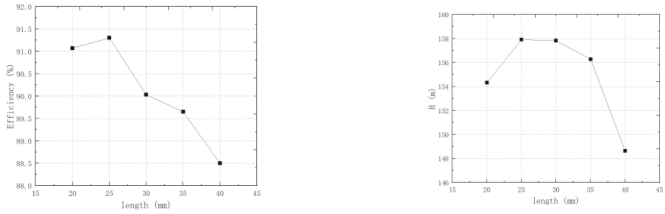

a. Efficiency b. Head

Fig. 3. Efficiency and head change with the axial length of the centrifugal impeller

Fig. 4. Relative flow angle of each plane when axial length of the centrifugal impeller is 25 mm.

The relative flow angle contribution is shown in Fig. 4. 20, 35, 45, and 55 mm correspond to the inducer plane, the inlet, the middle, and the outlet plane of the centrifugal impeller. On each plane, with the increase of radius, the circumferential direction velocity increases, and the relative flow angle decreases. At the 20 mm plane, the relative

flow angle is about 35° at the roof of the blade and about 18° at the top of the blade. The relative flow angle is consistent with the β angle of the blade design. At the 35 mm plane, the relative flow angle is about 34° at the roof of the blade and about 26° at the top of the blade. The design β angle is 43° and 23°. The low relative flow angle area at the inner diameter is affected by the leading edge of the auxiliary blade. At the 45 mm plane, the relative flow angle is about 39.5° at the roof of the blade and the design β angle is 41.5°. The relative flow angle is about 42.4° at the top of the blade and the design β angle is 24.5°. The β angle of the blade limits the development of fluid flow and the counter-current zone appears. At the 55 mm plane, the relative flow angle is about 45° at the roof of the blade and the design β angle is 32°. At top of the blade, the flow angle is 25°, which is close to the design of β angle 27°. In general, the impeller structure needs to be improved.

2.2 Optimization of the Outlet Angle

The outlet angle affects the pump performance including hydraulic efficiency, and characteristic curve. Six groups of outlet angles are shown in Table 3. And the calculation results are shown as follows.

Table 3. Impeller performance at different outlet angles

	①	②	③	④	⑤	⑥
0%	28	30	32	34	36	38
100	23	25	27	30	32	34
H (m)	147.8	154.4	169.64	178.74	183.89	188.71
Efficiency (%)	87.74	88.07	91.3	91.11	91.6	92.63

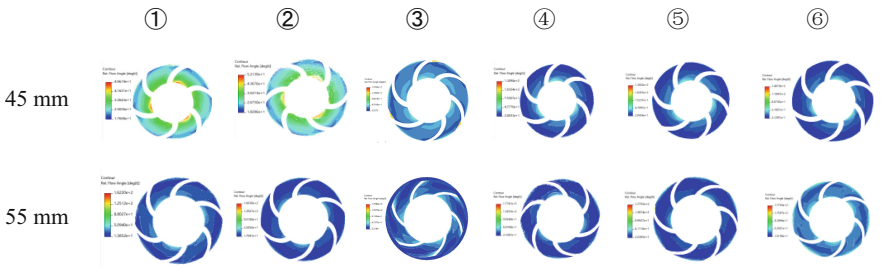

Fig. 5. Relative flow angle distribution at different outlet angles

As shown in Table 3, when selecting a larger outlet angle such as ⑥, the efficiency is highest under the design working conditions. Due to 2.1, the area where the blade angle is not reasonable is between the length of 45 and 55 mm. And the distribution of liquid flow angle at the shaft length section of 45 mm and 55 mm under the condition of six groups of blade shapes was analyzed.

As showed in Fig. 5, in group ①, at 45 mm plane, the liquid flow angles at the root and top of the leaf at 45 mm were about 35° and 24°, and the design β angles of the leaves were 38° and 23°, respectively. The design angle is appropriate. At 55 mm plane, the liquid flow angle at the root and top of the leaf is about 48° and 32°, and the design β angles of the blade are 28° and 23°. It can be seen that the outlet angle setting is too small. In group ②, at 45 mm plane, the design angle is appropriate. At 55 mm plane, the liquid flow angle at the root and top of the leaf is about 40° and 23°, and the design β angles of the blade are 30° and 25°. It can be seen that the outlet angle setting is small but has improved compared to ①. ③, ④, ⑤ is also gradually improving compared to the previous one. In group ⑥, the liquid flow angles at the root and top of the leaf were about 43° and 29° at 45 mm plane, and the design β angles of the leaves were 43° and 28.5°. At 55 mm plane, the liquid flow angle at the root and top of the leaf is about 38° and 33°, and the design β angles of the blade are 38° and 34°. The design outlet angle is appropriate. So we adopt the group ⑥.

3 Results

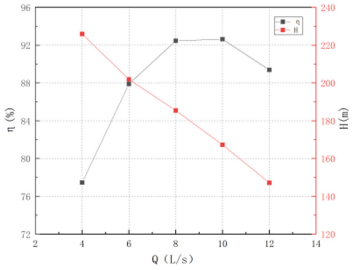

Fig. 6. Impeller performance curve

The Impeller performance curve is shown in Fig. 6. Under the design flow rate condition of 10 L/s, the impeller efficiency reaches the optimal value of 92.63%, and the head is 167.24 m (Fig. 7).

a. Total pressure b. Absolute velocity

Fig. 7. Total pressure and absolute velocity of the final design

Finally, the complete structure of the impeller and volute under the design condition was calculated, and the efficiency was 85.69%. The efficiency loss in volutes was 6.9%.

4 Conclusion

The liquid hydrogen pump impeller is designed with an integrated inducer and centrifugal impeller in this paper. After the axial length of the centrifugal impeller and are outlet angle are optimized, simulation is performed on the impeller with the design conditions. Even with the high surface toughness, the impeller efficiency and overall efficiency with the volute shell reach 92.63% and 85.69%, respectively. With the reliable results shown in this paper, our liquid hydrogen pump will build up and test soon, and the test performance will be published. This paper will benefit for the development of the low energy consumption and high efficiency liquid hydrogen pump.

Acknowledgments. This work was supported by the National Science Foundation of China (Grant No. 52106034), the Youth Innovation Promotion Association Innovative, Chinese Academy of Sciences, and the Talent Cultivation Project of Technical Institute of Physics and Chemistry, Chinese Academy of Sciences (Grant No. 2021-LC).

References

1. Jia, L., Huacong, L., et al.: Cavitation study of inducer and impeller combination aero centrifugal pump. J. Propulsion Technol. **36**(7), 1005–1012 (2015)
2. Jia, L., Huacong, L., et al.: Profile optimization of multi-diversion combination inducer and impeller. J. Beijing Univ. Aeronaut. Astronaut. **42**(5), 953–960 (2016)
3. Liu, Y., Wang, S., et al.: Numerical study on blade wrap angle on performance of combination impeller centrifugal pump. Sci. Technol. Eng. **15**(8), 244–252 (2015)
4. Li, J., Chen, X.: The flow simulation of a fuel centrifugal pump with integrated inducer and impeller influenced by inlet flow ejector. In: 9th International Conference on Mechanical and Aerospace Engineering (2018)
5. Tian, Q., Zhang, X., et al.: Numerical analysis on inducer and impeller combination with different blade wrap angle in aero fuel centrifugal pump. In: IET International Conference on Aircraft Utility Systems (AUS 2020)

Experimental Research on High-Pressure Hydrogen Leakage and Diffusion of Hydrogen Refueling Station

Bin Jiang(✉), Tongshen Zhen, and Fangfang Fang

State Power Investment Corporation R&D Institute, Changping Beijing 102209, China
bj_year@yeah.net

Abstract. As the infrastructure to provide hydrogen for hydrogen fuel cell vehicles, hydrogen refueling station is a very important part of hydrogen energy utilization. However, due to the characteristics of hydrogen, such as flammability and explosion, low density, wide range of explosive limit concentration, hydrogen refueling station accidents often occur. The existing research on hydrogen refueling stations often uses the method of numerical simulation, and mainly considers the leakage of hydrogen storage tank. There are few relevant experimental studies and little consideration is given to the case of hydrogen pipeline leakage. In order to explore the phenomenon and rule of high-pressure hydrogen leakage and diffusion in the pipeline of hydrogen refueling stations, a full-size high-pressure hydrogen leakage test facility is built based on a real hydrogen refueling station. The vehicle-mounted high-pressure hydrogen storage tank is used as the high-pressure hydrogen gas source to provide constant hydrogen pressure to the test section through the combination of different valves in the pipeline and the instrument control system. By changing different leakage sizes and pressures, the concentration distribution and influence factors after hydrogen leakage are analyzed, which provides an important basis for the optimal layout and operation and maintenance of the safety facilities of the existing hydrogen refueling station.

Keywords: Hydrogen leakage · Hydrogen refueling station · Test facility

1 Introduction

Hydrogen refueling station as the infrastructure to provide hydrogen for hydrogen fuel cell vehicles, hydrogen refueling station is a very important part of hydrogen energy utilization. However, due to the characteristics of hydrogen, such as flammability and explosion, low density, wide range of explosive limit concentration, hydrogen refueling station accidents often occur. The existing research on hydrogen refueling stations often uses the method of numerical simulation, and mainly considers the leakage of hydrogen storage tank. There are few relevant experimental studies and little consideration is given to the case of hydrogen pipeline leakage. In order to explore the phenomenon and rule of high-pressure hydrogen leakage and diffusion in the pipeline of hydrogen refueling stations, a full-size high-pressure hydrogen leakage test facility is built based on

H. Sun et al. (Eds.): WHTC 2023, SPPHY 393, pp. 193–199, 2024.
https://doi.org/10.1007/978-981-99-8631-6_22

a real hydrogen refueling station. The vehicle-mounted high-pressure hydrogen storage tank is used as the high-pressure hydrogen gas source to provide constant hydrogen pressure to the test section through the combination of different valves in the pipeline and the instrument control system. By changing different leakage sizes and pressures, the concentration distribution and influence factors after hydrogen leakage are analyzed, which provides an important basis for the optimal layout and operation and maintenance of the safety facilities of the existing hydrogen refueling station.

2 Experimental System

2.1 Experimental System Design

Based on the design of pipelines and valves for typical hydrogen energy facilities and equipment, a high-pressure hydrogen storage tank (with a pressure more than 35 MPa) is used as the high-pressure hydrogen gas source. through the combination of different valves in the pipeline and the instrument control system, a constant hydrogen pressure is provided to the pipeline in the test section, and a high-pressure hydrogen gas leakage diffusion test facility is built.

Using hydrogen concentration sensors, sound sensors, fiber optic sensors, and infrared sensors to monitor the diffusion behavior of hydrogen after high-pressure leakage, analyze the flow field structure and concentration spatiotemporal distribution of hydrogen under different leakage pressures and leakage ports, analyze the diffusion behavior, acceleration, and changes in hydrogen leakage vibration measured by sound sensors, and comprehensively analyze the impact of different fracture sizes on hydrogen diffusion behavior, Provide data support for the hydrogen leakage diffusion dynamics model and the prediction method of combustion and explosion risk areas.

2.2 Test Facility

The high pressure hydrogen leakage test facility is shown in Fig. 1.

The system mainly consists of a gas supply system, a pressurization system, a test section, and a relief system. Vibration sensors are arranged on the test section, sound sensors are arranged near the leakage port, and several hydrogen concentration sensors are arranged above the leakage port to monitor the leakage behavior of hydrogen. The actual test facility is shown in Fig. 2.

The experimental system is equipped with two leakage nozzles with diameters of 0.05 and 1 mm. The nozzle can be horizontal and vertical. The hydrogen booster can pressurize the hydrogen gas to a maximum of 35 MPa. The input parameters of this experimental system mainly refer to the relevant parameters of the actual demonstration hydrogen refueling station, as is shown in Table 1.

The material of the test section pipeline is Q345 or 316 L seamless steel pipe, and the maximum size of simulated leakage in the test section is the inner diameter of the pipeline. According to the actual operation of a hydrogen refueling station, the pipeline size is 3/4 inch, with an outer diameter of 19.05 mm, which corresponds to an inner diameter of 10.97 mm (0.432 in) at a working pressure of 35 MPa.

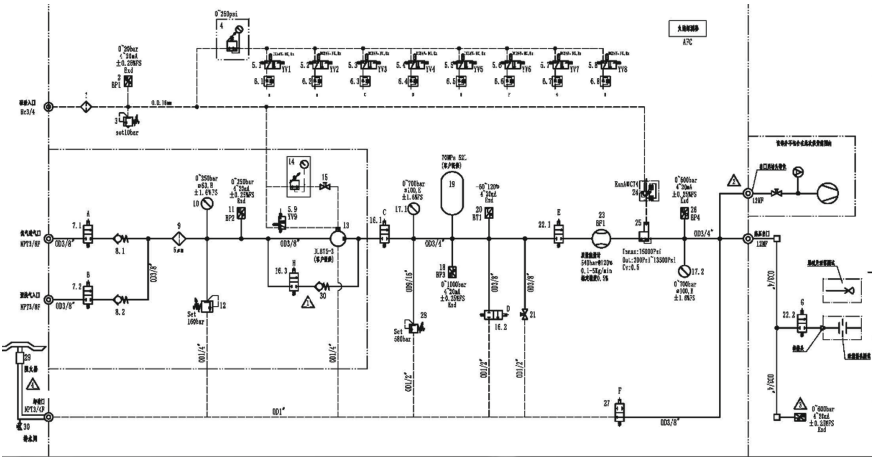

Fig. 1. Schematic diagram of the test facility

Fig. 2. High pressure hydrogen leakage and diffusion test facility

Table 1. Overall parameters of the test facility

Test parameters	Unit	Value
Operation pressure	MPa	0–35
Operation temperature	°C	− 30 to 50
Leakage nozzle size	Mm (diameter)	0.5/1
Test section length	m	2.0
Outer diameter of test section	mm	19.05
Inner diameter of test section	mm	10.97
Mass flow rate	g/s	26 (maximum)

3 Test Results

3.1 Horizontal Hydrogen Ejection Condition

Horizontal hydrogen ejection condition is shown in Fig. 3. Three sensors were arrange at a distance of 1m downstream of the nozzle, the lower sensor is located directly in front of the nozzle, and the distance between the upper two sensors is 50 cm. The pressure at the nozzle is 52 bars. Within 2 s after the start of hydrogen injection, the hydrogen sensor measures the hydrogen concentration value. The hydrogen sensor facing the nozzle measures the maximum value, and the middle hydrogen sensor delays for 1 s to measure the hydrogen concentration data. The top hydrogen sensor hardly measures the hydrogen gas data. When the hydrogen injection ends, the wake concentration is measured to be about 1%.

3.2 Vertical Hydrogen Ejection Condition

Vertical hydrogen ejection condition is shown in Fig. 4. Three sensors are arranged. The middle sensor is located directly above the nozzle, and the distance between the sensors on both sides is 70 cm from the middle sensor. The pressure at the nozzle is 42 bars. Within 2.5 s after the hydrogen gas is sprayed, the hydrogen sensor measures the hydrogen concentration value, while the middle hydrogen sensor measures the maximum value. The two symmetrically arranged side sensors measure a smaller value, and the maximum hydrogen concentration values of the two are almost the same.

4 Conclusions

1. Hydrogen will diffuse quickly ($\leq$ 2 s) even under lower pressure (45 bars), sensors need to be arranged above the pipelines.
2. Acceleration sensors can be used since they are not affected by wind or other factors.
3. Hydrogen will not spontaneously ignite under 50 bars.

Further research need to be done such as obstacles, different nozzle shapes and higher pressures (700 bars).

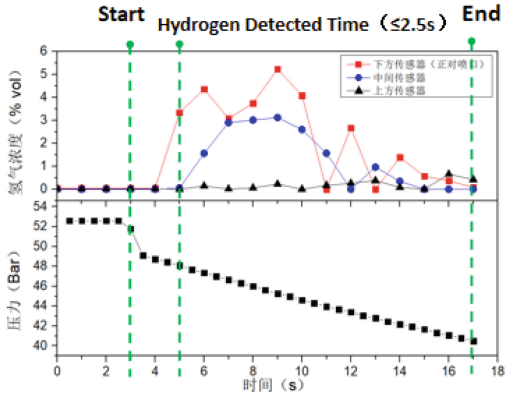

Fig. 3. High pressure hydrogen leakage—horizontal injection

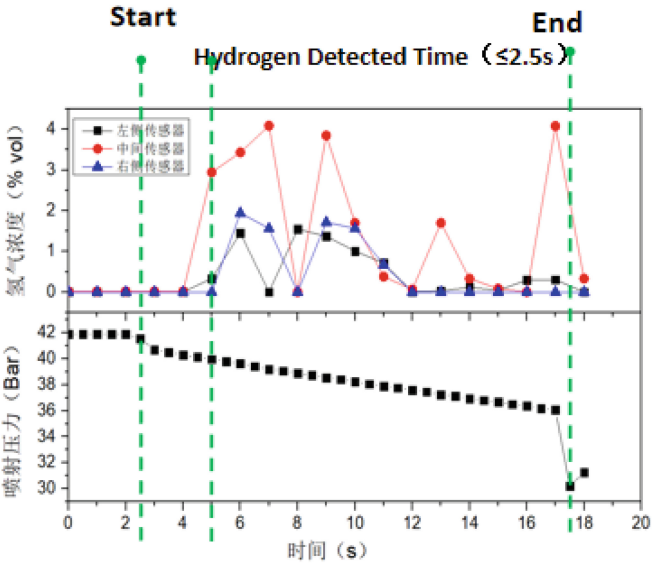

Fig. 4. High pressure hydrogen leakage—vertical ejection

References

1. Wang, Z.: Research challenges in high-pressure hydrogen spontaneous ignition. J. Nanjing Tech. Univ. (Nat. Sci. Edn.) **41**(5), 656–663 (2019)
2. Astbury, G., Hawksworth, S.: Spontaneous ignition of hydrogen leaks: a review of postulated mechanisms. Int. J. Hydrogen Energy **32**(13), 2178–2184 (2007)

3. Ekoto, I.W., Merilo, E.G., Houf, W.G., Evans, G.H., Groethe, M.A.: Experimental investigation of hydrogen release and ignition from fuel cell powered forklifts in enclosed spaces. In: 4th International Conference on Hydrogen Safety, San Francisco, CA, 12–14 Sept 2011
4. Hall, D.J., Walker, S.: Scaling rules for reduced-scale field releases of hydrogen fluoride. J. Hazard. Mater. **54**, 89–111 (1997)
5. Houf, W.G., Evans, G.H., James, S.C., Merilo, E., Groethe, M.: Simulation of hydrogen releases from fuel-cell vehicles in tunnels. In: Proceedings of World Hydrogen Energy Conference, Essen, Germany, 16–21 May 2010
6. Houf, W.G., Evans, G.H., Ekoto, I.W., Merilo, E., Groethe, M.: Hydrogen fuel-cell forklift vehicle releases in enclosed spaces. Int. J. Hydrogen Energy

Coupled Heat Transfer Characteristics of SiC High Temperature Heat Exchanger in Solid Oxide Fuel Cell

Jia-Liang Song[1(✉)], Hua Chen[2], Yong-Dong Chen[1], Gai-Ge Yu[1], Hong-Wei Zou[1], and Bing-Chuan Han[1]

[1] Hefei General Machinery Research Institute Co., Ltd. (HGMRI), Hefei 230031, China
sjl516516@126.com, chenyongdong@hgmri.com
[2] University of Science and Technology of China, Hefei 230027, China

Abstract. High temperature heat exchanger is a crucial equipment in the BOP of SOFC. Replacing the commonly used metal materials with high-temperature resistant SiC ceramic materials for the manufacturing of SOFC high-temperature heat exchanger is a revolutionary technology with great application potential. This paper focused on SiC-based cathodic air preheater which is a novel SOFC high temperature heat exchanger, and firstly investigated the coupled radiation-conduction-convection heat transfer characteristics between flue gas and air at extremely high temperature conditions. The DO model in ANSYS Fluent was utilized to analyze the radiation heat transfer characteristics of high-temperature flue gas and the effect of gas absorption coefficient, and the simulation results were compared with the S2S model and non-radiation model. The results showed that radiation heat transfer cannot be ignored at high flue gas inlet temperature. With flue gas inlet temperature in the range of 800–1100 °C and low air/flue gas flow rate ratio, the gas radiation heat transfer and the effect of flue gas absorption coefficient can be ignored.

Keywords: SOFC · Cathode air preheater · SiC · Heat radiation · Coupled heat transfer characteristics

1 Introduction

In China, Solid oxide fuel cell (SOFC) is favorable in heat power cogeneration and is of great significance in supporting the "dual carbon" target [1]. At present, the fledgling SOFC industry in China mainly focused on the research of stack, however the focus on the BOP (Balance of Plant), which is another major component of SOFC, is not enough. BOP is the crucial technology in SOFC including functions of inlet/outlet gas heat exchange, fuel/air flow distribution, waste heat utilization and so on. It is the key to ensure the efficient and stable operation of the stack.

The operating temperature of SOFC is in the range of 700–1000 °C. It is required that the cathode inlet air temperature of the stack should not be less than 700 °C after stable operation. The BOP recovers the unreacted anode fuel and cathode air of the stack, and

H. Sun et al. (Eds.): WHTC 2023, SPPHY 393, pp. 200–213, 2024.
https://doi.org/10.1007/978-981-99-8631-6_23

sends them to the catalytic combustion chamber for full combustion. The combustion exhaust preheats the cathode air in the high temperature heat exchanger to an appropriate temperature range and then enters the stack to participate in the reaction.

For the high temperature heat exchanger, on the one hand, the increasing stack reaction temperature has the risk of exceeding the temperature tolerance limit of metal heat exchanger represented by superalloy materials. On the other hand, the long-term use of typical commercial metal alloy heat exchanger suffers from the risk of chromium volatilization, which is a known cathodic degradation mechanism, reducing the performance and lifetime of SOFC [2]. Furthermore, the strength of metal alloy heat exchanger decreases rapidly above temperature of 550 °C [3], thus the long-term operation under adverse conditions such as high temperature and oxidation will affect the dynamic service performance of alloy heat exchangers. SiC ceramics and their composite materials are considered as the most promising ceramic materials for high temperature heat exchangers due to their high intensity at high temperature, low density, low thermal expansion coefficient, high thermal conductivity, anti-oxidation, low creep at high temperature and excellent thermal shock resistance [4, 5], thus the application prospects of SiC in SOFC power generation system are promising.

For the high temperature nonmetal heat exchanger, relevant research in China has not been carried out yet, while the international research is just getting started. José Luis Córdova et al. [6, 7] designed and developed a novel cathode air preheater made of alumina ceramics for SOFC. The heat exchanger comprised a group of overlapping quasi-spiral flow channels with rectangular cross section, which was tested to achieve high heat transfer efficiency of 92% and low pressure drop. M. Dev Anand [8] and Umayorupagam P. et al. [9] compared the performance of compact heat exchangers with rectangular channels using SiC and AlN materials. Moreover, researchers have also investigated the application of SiC based high temperature heat exchangers in other fields [10–12]. The research on heat transfer and flow process is relatively simple, and the effect of heat radiation is also ignored in order to simplify heat transfer calculation. However, the temperature of flue gas in SOFC cathode air preheater can be as high as 1100 °C, and the flue gas side contain polar molecules such as CO_2 and H_2O, thus the flus gas has a certain radiation capacity. Furthermore, SiC ceramic heat transfer element has a dark color and rough surface, thus exhibits high blackness at high surface temperature, which can be approximately considered as blackbody. Therefore, the effect of thermal radiation may not be negligible.

To sum up, replacing the commonly used metal materials with high-temperature resistant SiC ceramic materials for the manufacturing of SOFC high-temperature heat exchanger is a revolutionary technology with great application potential. However, the research on coupled radiation-conduction-convection heat transfer characteristics of SiC high temperature heat exchanger in SOFC needs to be carried out urgently. This paper focused on SiC-based cathodic air preheater which is a novel SOFC high temperature heat exchanger. Based on ANSYS Fluent, the coupled heat transfer characteristics between flue gas and air at extremely high temperature conditions were firstly investigated and the effect of radiation heat transfer were analyzed.

2 Structure and Operating Parameters of SOFC Air Preheater

SOFC cathode air preheater comprises a series of high-temperature flue gas channels and air channels. In order to study the coupled radiation-conduction-convection heat transfer characteristics between flus gas and air, the heat exchanger is simplified as a tubular heat exchanger composed of a hot channel and a cold channel. Figure 1 shows the structure and operating conditions of tubular heat exchanger simulated in this paper. Table 1 shows the simulation parameters of the structure and operating conditions of a natural gas SOFC air preheater. The hydraulic diameter of the internal air channel is 5–10 mm, the internal diameter of the external flue gas channel is 10–20 mm, and the length along the channel is within 500 mm. The heat exchanger material is SiC. The flue gas inlet temperature is in the range of 800–1100 °C, with pressure of 1 bar and flow rate of 1–5 m/s. The flue gas components are H_2O (20–30%), CO_2 (10–20%), O_2 (0–10%) and N_2. The inlet air temperature is 25 °C, with pressure of 1 bar and flow rate of 1–5 m/s. The outlet air temperature is required no less than 700 °C.

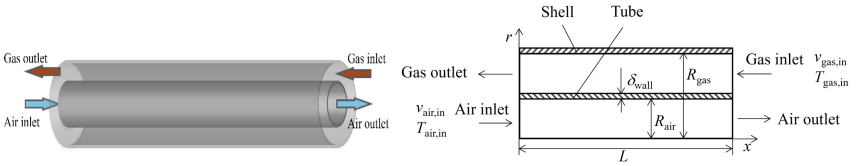

(a) Structure of heat exchanger (b) Two-dimensional axisymmetric operation conditions

Fig. 1. Structure and operating conditions of simulated heat exchanger

3 Numerical Model

3.1 Radiative Transfer Equation

Considering the effect of heat radiation, the radiation heat flux must be introduced into the energy equation. In order to calculate the radiation heat flux, the Radiative Transfer Equation (RTE) must be introduced, and the temperature field should be solved by coupling the energy equation and RTE.

The RTE for radiation participating medium at position $\vec{r}$, in the direction $\vec{s}$ is as follows:

$$\frac{\mathrm{d}I(\vec{r},\vec{s})}{\mathrm{d}s} + (\alpha+\sigma_s)I(\vec{r},\vec{s}) = \alpha n^2 \frac{\sigma T^4}{\pi} + \frac{\sigma_s}{4\pi}\int_0^{4\pi} I(\vec{r},\vec{s}')\Phi(\vec{s},\vec{s}')d\Omega' \tag{1}$$

where, $\vec{s}$ is the position vector. $\vec{r}$ is the direction vector. $\vec{s}'$ is the scattering direction vector. s is the path length. α is the absorption coefficient. n is the refractive index. σ_s is the scattering coefficient. σ is the Stefan-Boltzmann constant. I is the radiation intensity. T is the local temperature. Φ is the phase function. Ω' is the solid angle.

Table 1. Simulation parameters of the structure and operating conditions.

Parameter		Value
Inlet gas temperature		800–1100 °C
Inlet gas velocity		1–5 m/s
Inlet gas pressure		1–2 bar
Gas components	N_2	40–70%
	H_2O	20–30%
	CO_2	10–20%
	O_2	0–10%
Inlet air temperature		25 °C
Inlet air velocity		1–5 m/s
Inlet air pressure		1–2 bar
Inner diameter of air channel		5–10 mm
Inner diameter of gas channel		10–20 mm
Thickness of channel		1–3 mm
Channel length		400–500 mm

3.2 Optical Thickness

Optical thickness (τ_λ) represents the heat radiation attenuation ability of radiation participating gas at a specific wavelength along given path length. High optical thickness value corresponds to high attenuation effect of the radiation participating gas on the incident radiation energy. τ_λ is the line integral of the attenuation coefficient along any path in a scattering and absorbing medium which can be expressed as follows:

$$\tau_\lambda = \int_0^L \kappa_\lambda(l)\mathrm{d}l \tag{2}$$

where, κ_λ is the spectral attenuation coefficient which depends on the gas components, pressure, temperature and the wavelength of incident radiation energy. κ_λ is the sum of the spectral absorption coefficient (α_λ) and spectral scattering coefficient ($\sigma_{s,\lambda}$) at a specific wavelength:

$$\kappa_\lambda = \alpha_\lambda + \sigma_{s,\lambda} \tag{3}$$

For uniform medium, spectral attenuation coefficient is constant along the path length L, thus optical thickness has a simple physical interpretation as the length of a path in units of mean free path which can be expressed as follows:

$$\tau_\lambda = \kappa_\lambda L \tag{4}$$

In this simulation, the diameter of flue gas channel is in the range of 5–10 mm, and the flue gas contains two polar molecules, CO_2 and H_2O. The absorption coefficient of CO_2 is about 0.5 m^{-1}, and the concentration of CO_2 is in the range of 10–20%. The absorption coefficient of H_2O is about 0.4 m^{-1}, and the concentration of H_2O is in the range of 20–30%. Thus, the optical thickness of flue gas is less than 0.005, which belongs to optical thin gas. In engineering estimation, the absorption effect of CO_2 and H_2O on incident radiation energy cannot be ignored, but their scattering effect can be ignored. Therefore, to preliminarily analyze the effect of flue gas radiation on heat exchanger performance, the pure absorption and non-scattering condition of gray gas is simulated in this study.

3.3 Radiation Heat Transfer Model

In this paper, DO model was selected to simulate the radiation heat transfer between high-temperature flue gas and air. In addition, S2S model calculation results can be used as comparison to analyze the effect of gas radiation.

(1) **DO model**

DO model is applicable to radiation problems in entire range of optical thicknesses. It allows the solution of enclosure radiative transfer without participating media and participating radiation. The DO model solves the RTE of a finite number of discrete solid angles, and the solution precision is controlled by the precision of the discrete solid angles. DO model considers the RTE in the position $\vec{s}$ as a field equation as follows:

$$\nabla(I(\vec{r},\vec{s})\vec{s}) + (\alpha+\sigma_s)I(\vec{r},\vec{s}) = \alpha n^2\frac{\sigma T^4}{\pi} + \frac{\sigma_s}{4\pi}\int_0^{4\pi} I(\vec{r},\vec{s}')\Phi(\vec{s},\vec{s}')d\Omega' \tag{5}$$

(2) **S2S model**

The S2S model is suitable for the solution of enclosure radiative transfer without participating media, however it assumes that all surfaces are diffuse and gray radiation. Thus, S2S model cannot be used to model participating radiation problems. The emissivity (ε) equals the absorptivity (α) and the transmissivity could be neglected. When radiant energy (E) is incident on the surface, part (ρE) is reflected, part (αE) is absorbed, and part (τE) is transmitted. Considering the conservation of energy, that $\alpha + \rho = 1$. Since $\alpha = \varepsilon$, thus $\rho = 1 - \varepsilon$.

The radiation heat flux leaving a given surface consists of directly emitted heat flux and reflected heat flux. The reflected heat flux depends on the incident heat flux from the surroundings, which can be expressed by the radiant heat flux leaving all other surfaces. The radiation heat flux leaving from surface k can be expressed as follows:

$$q_{\text{out},k} = \varepsilon_k\sigma T^4 + \rho_k q_{\text{in},k} \tag{6}$$

where, $q_{\text{out},k}$ is the radiation heat flux leaving the surface. ε_k is the emissivity. ρ_k is the reflectivity. $q_{\text{in},k}$ is the radiation heat flux incident on the surface from the surroundings.

The radiant heat flux incident from one surface to another can be calculated by the surface to-surface view factor (F_{jk}). Therefore, incident radiant heat flux can be expressed as radiant heat flux leaving all other surfaces as:

$$q_{\text{in},k} = \sum_{j=1}^{N} F_{kj} q_{\text{out},j} \tag{7}$$

Then, the total radiant heat flux leaving surface k can be rewritten as:

$$q_{\text{out},k} = \varepsilon_k \sigma T^4 + \rho_k \sum_{j=1}^{N} F_{kj} q_{\text{out},j} \tag{8}$$

Equation (8) can be written as follows:

$$J_k = E_k + \rho_k \sum_{j=1}^{N} F_{kj} J_j \tag{9}$$

where, J_k represents the heat flux given off from surface k, and E_k represents the emissive heat flux of surface k.

3.4 Grid Independence Study

A two-dimensional axisymmetric model of coupled radiation-conduction-convection heat transfer between flue gas and water was built according Fig. 1a. The flue gas domain, air domain and channel domain were divided into grids as shown in Fig. 2. The RTE and energy equations are solved based on ANSYS Fluent. A grid independence study was conducted to assess the appropriate number of grid elements. Different grid elements of 2×10^3, 5×10^3, and 1×10^4 were evaluated. Figure 3 showed the comparison of air temperature variation along the channel length calculated with different grid elements. It is found that grid elements of 5×10^3 is adequate for the simulation.

Fig. 2. Meshing of simulated heat exchanger

4 Results and Discussion

4.1 Radiation Model Comparison

In this section, DO model and S2S model in ANSYS Fluent were utilized to analyze the coupled radiation-conduction-convection heat transfer characteristics between high-temperature flue gas and air, and the simulation results were compared with the non-radiation model to analyze the effect of radiation. The detailed simulation parameters were listed in Table 2.

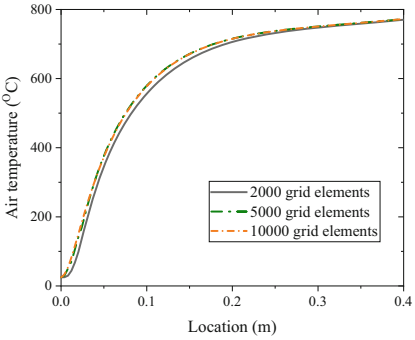

Fig. 3. Air temperature variation at different grid elements

Table 2. Simulation parameters of different cases.

Parameter		Case 1	Case 2	Case 3
Inlet gas temperature		800 °C		
Inlet gas velocity		3 m/s		
Inlet gas pressure		1 bar		
Gas components	N_2	40%		
	H_2O	30%		
	CO_2	20%		
	O_2	10%		
Inlet air temperature		25 °C		
Inlet air velocity		3 m/s		
Inlet air pressure		1 bar		
Inner diameter of air channel		5 mm	10 mm	10 mm
Inner diameter of gas channel		15 mm	20 mm	15 mm
Thickness of channel		1 mm		
Channel length		400 mm		

Figure 4 showed the temperature distributions of coupled heat transfer calculated by the DO radiation model, S2S radiation model and non-radiation model at case 1. It was found that the air outlet temperature was low without considering the radiation while the air outlet temperature is high considering the radiation. This means that the effect of radiation heat transfer cannot be ignored at high flue gas inlet temperature. Comparing the results of different radiation models, it can be seen that the calculation results of DO radiation model and S2S radiation model are very close. Thus, it was preliminarily considered that the effect of gas radiation on coupled heat transfer is tiny, and the effect of gas radiation can be ignored in the coupled heat transfer process, which indicates that the gray gas hypothesis is reasonable.

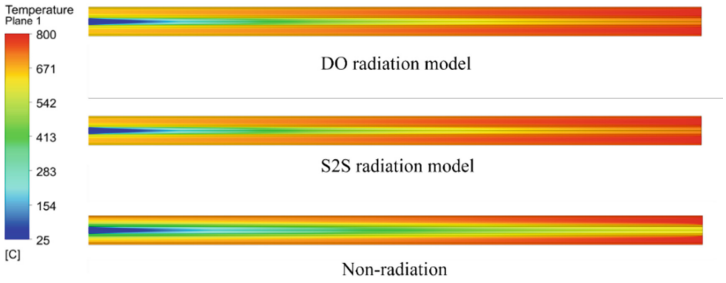

Fig. 4. Comparison of temperature distribution of different radiation models at case 1

Figures 5 and 6 showed the temperature variations of flue gas and air calculated by the DO radiation model, S2S radiation model and non-radiation model at case 1. It was found that the air temperature along the channel increases slightly when considering the radiation. When the flue gas inlet temperature is 800 °C, the air outlet temperature can only be heated to 600 °C. The air temperature along the channel increases greatly when considering the radiation, and the air outlet temperature can be heated to 700 °C. With high flue gas inlet temperature, the contribution of radiation heat transfer to air heating can be as high as 100 °C, thus the influence of radiation heat transfer is very important. Comparing the results of different radiation models, it can be seen that the calculation results of DO radiation model and S2S radiation model are very close, so the influence of gas radiation on heat transfer can be ignored at case 1.

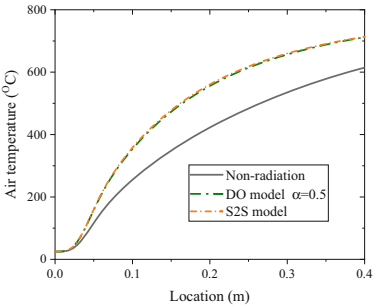

Fig. 5. Air temperature variation at case 1

Figures 7 and 8 showed the temperature variations of flue gas and air calculated by the DO radiation model, S2S radiation model and non-radiation model at case 2. The diameter of air channel in case 2 is larger than that in case 1, thus the ratio of air flow rate to flue gas flow rate in case 2 is larger than that in case 1 under the same inlet velocity, which leads to lower air outlet temperature in case 2. Regardless of radiation heat transfer, the air outlet temperature can only be heated to 320 °C. Considering the radiation heat transfer, the air outlet temperature calculated by S2S radiation model is 420 °C, and air outlet temperature calculated by DO radiation model is 400 °C. On one hand, the contribution of radiation heat transfer to air heating at case 2 is up to 100 °C,

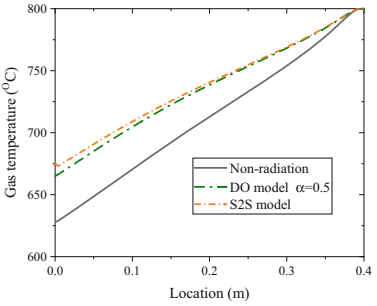

Fig. 6. Flue gas temperature variation at case 1.

which further proves the importance of radiation heat transfer to coupled heat transfer. On the other hand, comparing the results of different radiation models, it is found that there is a deviation between the DO radiation model and the S2S radiation model results, that is, the gas radiation will affect the proportion of radiation heat transfer at case 2, which indicates that the gas radiation has a certain effect on the coupled heat transfer when the air/gas flow ratio is large. In addition, the air outlet temperature calculated by the S2S radiation model is higher than that calculated by the DO radiation model, which indicates the existence of radiation participating gases slightly reduce the coupled heat transfer characteristics.

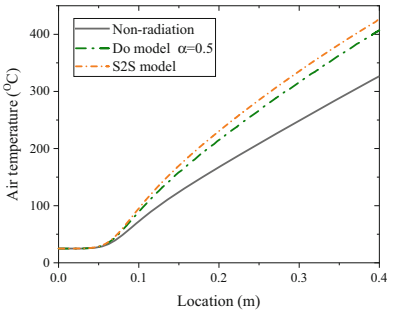

Fig. 7. Air temperature variation at case 2

Figures 9 and 10 showed the temperature variations of flue gas and air calculated by the DO radiation model, S2S radiation model and non-radiation model at case 3. The diameter of flue gas channel in case 3 is smaller than that in case 2, thus the ratio of air flow rate to flue gas flow rate in case 3 is larger than that in case 1 and case 2 under the same inlet velocity, which leads to lower air outlet temperature in case 3. The air outlet temperature can only be heated to 250 °C without considering radiation heat transfer. Considering the radiation heat radiation heat transfer, air outlet temperature calculated by the S2S radiation model is 290 °C and the DO radiation is 270 °C. On one hand, the contribution of radiation heat transfer to air heating is 20–40 °C in case 3, which means the effect of radiation heat transfer on coupled heat transfer is reduced in case 3. On the

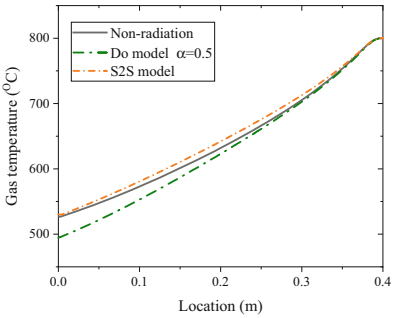

Fig. 8. Flue gas temperature variation at case 2.

other hand, comparing the results of different radiation models, it can be seen that the air outlet temperature calculated by S2S radiation model is higher than that calculated by DO radiation model, which further proves that gas radiation has certain effect on the coupled heat transfer when the air/gas flow ratio is large.

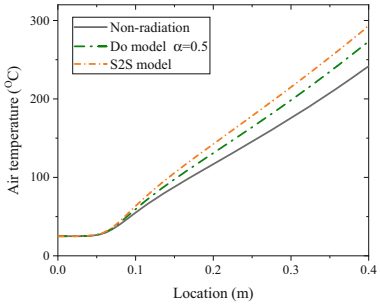

Fig. 9. Air temperature variation at case 3.

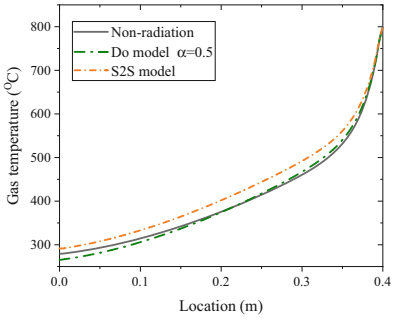

Fig. 10. Flue gas temperature variation at case 3.

4.2 Effect of Absorption Coefficient

According to above analysis, the gas radiation has a certain impact on the coupled heat transfer characteristics only at large air/gas flow ratio. Since the SOFC cathode air preheater in this study is designed to heat the air to above 700 °C using high-temperature flue gas, the air/ gas flow ratio is generally small, thus the effect of gas radiation is unapparent. In addition, the optical thickness of flue gas is very tiny (less than 0.005), thus the gas radiation effect is very tiny. Based on the above analysis, the flue gas radiation has little effect on the coupled heat transfer characteristics.

To further verify the effect of flue gas radiation on the coupled heat transfer characteristics, the gray gas assumption is adopted in this section considering the flue gas absorption coefficient to be independent of wavelength, thus the average absorption coefficient is used in calculation. The DO radiation model is used to analyze the effect of the absorption coefficient on the coupled heat transfer characteristics of flue gas and air with the flue gas absorption coefficient in the range of 0–1 m^{-1}. Figures 11, 12 and 13 showed the air and flue gas temperature variations along the channel with different absorption coefficients at case 1–3. It is found that the absorption coefficient of flue gas in the DO radiation model has little effect on the air and flue gas temperature variation with inlet flue gas temperature of 800 °C at each case. Thus, when inlet flue gas temperature is not very high, the effect of gas radiation can be ignored.

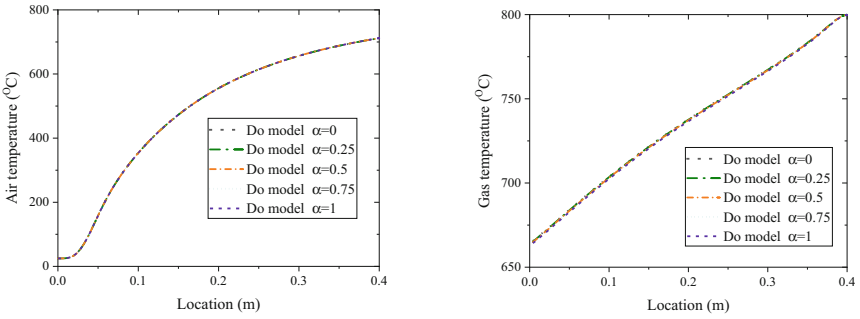

Fig. 11. Air and flue gas temperature variation along the channel at case 1 with different absorption coefficients.

Figures 14 and 15 showed the effect of absorption coefficient on air and flue gas temperature variation at case 2 with inlet flue gas temperature of 1100 °C and 1500 °C, respectively. It is found that the absorption coefficient of flue gas has little effect on the air temperature variation with high inlet flue gas temperature, while has small effect on the flue gas temperature variation. Moreover, the higher the inlet flue gas temperature, the greater the effect on the flue gas temperature variation. Since the flue gas temperature in the SOFC cathode air preheater is in the range of 800–1100 °C, the effect of flue gas absorption coefficient and gas radiation can be ignored.

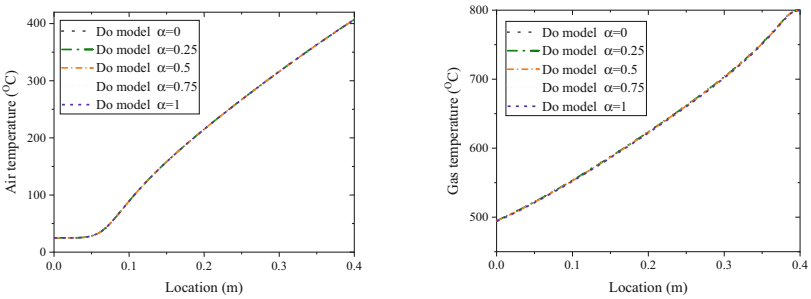

Fig. 12. Air and flue gas temperature variation along the channel at case 2 with different absorption coefficients.

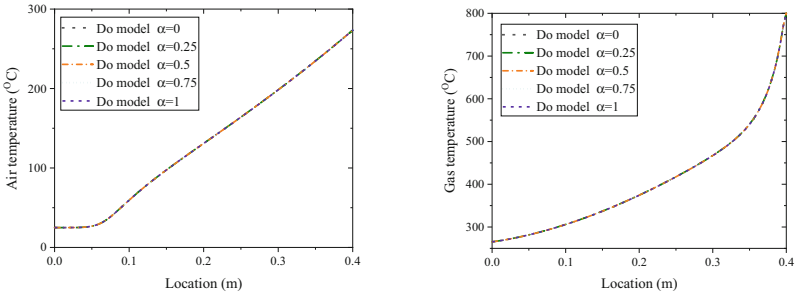

Fig. 13. Air and flue gas temperature variation along the channel at case 3 with different absorption coefficients

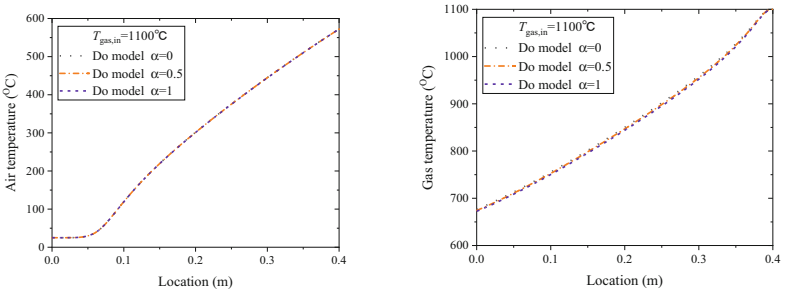

Fig. 14. Effect of absorption coefficient on flue gas temperature variation at inlet flue gas temperature of 1100 °C.

5 Conclusions

(1) The air outlet temperature calculated by the non-radiation model is apparently lower than that of DO radiation model and S2S radiation model, thus the effect of radiation heat transfer is very important and cannot be ignored at high flue gas inlet temperature.

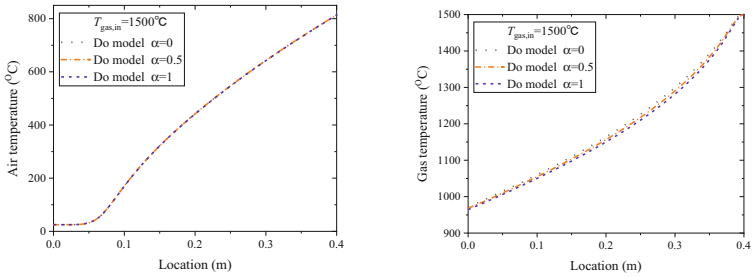

Fig. 15. Effect of absorption coefficient on flue gas temperature variation at inlet flue gas temperature of 1500 °C.

(2) Comparing different radiation models, the calculation results of DO radiation model and S2S radiation model are very close at small air/gas flow rate ratio, while the calculation results of S2S radiation model is slightly higher than DO radiation model at large air/gas flow rate ratio. Thus, the participating radiation effect of flue gas slightly deteriorates the coupled heat transfer characteristics.
(3) The absorption coefficient of flue gas has little effect on the air temperature variation, while has tiny effect on flue gas temperature variation at high flue gas inlet temperature of 1100–1500 °C. The higher the flue gas inlet temperature, the greater the effect on the flue gas temperature variation.

Acknowledgements. This research is sponsored by the Doctor's Science and Technology Fund of HGMRI (2020011749) and Youth's science and technology Fund of SINOMACH (QNJJ-ZD-2022-06).

References

1. Hu, L., Yang, Z.B., Xiong, X.Y., et al.: Development strategy for solid oxide fuel cell industry in China. Strateg. Study Chin. Acad. Eng. **24**(3), 118–126 (2022)
2. Giles, S., Lin, G., Mohanram, A., et al.: Saint-Gobain's all ceramic SOFC stack: architecture and performance. ECS Trans. **57**(1), 105–114 (2013)
3. Caccia, M., Tabandeh-Khorshid, M., Itskos, G., et al.: Ceramic–metal composites for heat exchangers in concentrated solar power plants. Nature **562**(7727), 346–347 (2018)
4. Sommers, A., Wang, Q., Han, X., et al.: Ceramics and ceramic matrix composites for heat exchangers in advanced thermal systems—a review. Appl. Therm. Eng. **30**(11–12), 1277–1291 (2010)
5. Li, Q., et al.: Compact heat exchangers: a review and future applications for a new generation of high temperature solar receivers. Renew. Sustain. Energy Rev. (2011)
6. Cordova, J.L.: Novel compact ceramic heat exchanger for solid oxide fuel cell cathode air preheater application. In *16th Annual Solid Oxide Fuel Cell Workshop* (2015)
7. Córdova, J.L., Heshmat, H.: Development of a ceramic heat exchanger for application as solid oxide fuel cell cathode air preheater. In *ASME Power & Energy Conference* (2016)

8. Anand, M.D., Devadhas, G.G., Prabhu, N., et al.: ceramic monolith heat exchanger—a theoretical study and performance analysis (2018)
9. Arunachalam, U.P., Edwin, M.: Theoretical investigation of a ceramic monolith heat exchanger using silicon carbide and aluminium nitride as heat exchanger material. Int. J. Heat Technol. **35**(3), 645–650 (2017)
10. Schulte-Fischedick, J., DreißIgacker, V., Tamme, R.: An innovative ceramic high temperature plate-fin heat exchanger for EFCC processes. Appl. Therm. Eng. **27**(8–9), 1285–1294 (2007)
11. Nagarajan, V., Chen, Y., Wang, Q., et al.: Hydraulic and thermal performances of a novel configuration of high temperature ceramic plate-fin heat exchanger. Appl. Energy **113**(Jan.), 589–602 (2014)
12. Takeuchi, Y., Park, C., Noborio, K., et al.: Heat transfer in SiC compact heat exchanger. Fusion Eng. Des. **85**(7–9), 1266–1270 (2010)

Deep Neural Network for Prediction of Adsorbent Selectivity on Hydrogen Purification

Chenglong Li[1,2], Chengsi Xie[1], Yi Zong[4], Richard Chahine[3], Tianqi Yang[2(✉)], Feng Ye[5(✉)], and Jinsheng Xiao[2,3]

[1] Automobile Technology and Service College, Wuhan City Polytechnic, Wuhan 430064, Hubei, China
lichenglong@whut.edu.cn

[2] School of Automotive Engineering, Hubei Research Center for New Energy & Intelligent Connected Vehicle, Wuhan University of Technology, Wuhan 430070, Hubei, China
tqyang@whut.edu.cn

[3] Hydrogen Research Institute, Université du Québec à Trois-Rivières, Trois-Rivières, QC G8Z 4M3, Canada

[4] Division for Power and Energy Systems, Department of Wind and Energy Systems, Technical University of Denmark, 4000 Roskilde, Denmark

[5] School of Artificial Intelligence, Jianghan University, Wuhan 430056, Hubei, China
Feng.Ye@jhun.edu.cn

Abstract. With emergence of new materials, more and more materials are available for adsorption and separation processes. The adsorption selectivity of adsorbent to adsorbate is one of the important indicators in choosing materials. Because the adsorption experiment of the mixture is time-consuming and difficult, the selectivity of the adsorbent is generally calculated by the ideal adsorbed solution theory (IAST). Taking the CO_2/H_2 gas mixture as an example, this paper proposes a new adsorption selectivity calculation method based on a deep neural network (DNN) with 5 hidden layers, which takes the molar fraction of CO_2, adsorption pressure and Langmuir adsorption isotherm parameters as the inputs of DNN. Combining the DNN and the NIST/ARPA-E database to quickly and accurately calculate the adsorption selectivity, the hydrogen purification and carbon dioxide storage materials can be quickly screened.

Keywords: Hydrogen purification · Ideal adsorbed solution theory · Langmuir isotherm · Selectivity · Deep neural network

1 Introduction

Integrated gasification combined cycle (IGCC) is an advanced power system that combines coal gasification technology and an efficient combined cycle. IGCC will produce a lot of CO_2 and H_2. It has a good development prospect to capture CO_2 efficiently and obtain high-purity H_2 by pressure swing adsorption (PSA) technology [1]. The commonly used commercial adsorbents are activated carbon (AC) and zeolite. However,

H. Sun et al. (Eds.): WHTC 2023, SPPHY 393, pp. 214–221, 2024.
https://doi.org/10.1007/978-981-99-8631-6_24

with the emergence of new materials, metal-organic frameworks (MOFs) are increasingly proven to be effective as adsorbents to separate CO_2 and H_2. Therefore, quickly and accurately selecting the appropriate adsorbent as the separation of CO_2 and H_2 becomes particularly important.

At present, the selectivity of the adsorbent is one of the important indicators to evaluate the performance of the adsorbent. Adsorption selectivity is the thermodynamic characteristic of the equilibrium-based separations system, which determines the separation efficiency [2]. The method commonly used to solve selectivity is the ideal adsorbed solution theory (IAST). The main practical advantage of IAST is that the adsorption selectivity of adsorbent can be estimated simply from the adsorption isotherm of a single gas, so no special equipment is required for the separation measurement of mixed gas [3]. However, the solution of IAST requires integral calculation from different adsorption isotherm models to solve the spreading pressure. Different adsorption isotherm models will obtain different analytical models, and the solution of selectivity is also relatively complex [4].

Deep neural network (DNN) has good advantages in processing non-linear characteristics and has been increasingly used in the simulation, prediction and optimization of gas adsorption and separation. In this paper, a DNN model is used to predict the separation selectivity. The inputs of DNN are CO_2 molar fraction, adsorption pressure and Langmuir adsorption isotherm parameters, and the output of DNN is separation selectivity. The training data of DNN comes from the selectivity by IAST calculations.

2 Mathematical Model

2.1 Langmuir Model for Calculating Adsorption Amount

Langmuir adsorption model is the most widely used isotherm model. The basic Langmuir adsorption model has simple from:

$$n = \frac{n_s b p}{1 + bp} \tag{1}$$

where n represents the equilibrium adsorption amount, p represents the equilibrium adsorption pressure, and n_s and b are saturation capacity and affinity, which are obtained by fitting the experimental values.

The extended Langmuir is used for the adsorption of multi-component gas:

$$n_i = \frac{n_{si} b_i p_i}{1 + \sum_i b_i p_i} \tag{2}$$

where i is the gas component.

2.2 Ideal Adsorbed Solution Theory (IAST) for Calculating Adsorption Amount

The ideal adsorbed solution theory (IAST) assumes that the adsorbed mixture is an ideal solution at constant spreading pressure and temperature. From the IAST, the spreading

pressure π is given by [5],

$$\boldsymbol{\pi_i^0\left(p_i^0\right) = \frac{RT}{A}\int_0^{p_i^0} nd\ln p} \tag{3}$$

where a is the adsorbent specific surface area, $\boldsymbol{R}$ is the molar gas constant. $\boldsymbol{p_i^0}$ is the gas pressure of component i that corresponds to the spreading pressure π.

The spreading pressure for a Langmuir isotherm via Eq. (3) is

$$\frac{A}{RT}\pi_i^0\left(p_i^0\right) = n_s \log\left(1 + bp_i^0\right) \tag{4}$$

At a constant temperature T, the spreading pressure of a single component is the same.

For binary adsorption of component 1 and 2, combining Eqs. (3) and (4),we can get,

$$n_{s1}\log\left(1 + b_1p_1^0\right) = n_{s2}\log\left(1 + b_2p_2^0\right) \tag{5}$$

The IAST requires

$$y_1p_t = x_1p_1^0,\ (1 - y_1)p_t = (1 - x_1)p_2^0 \tag{6}$$

where y_i and x_i are the molar fractions of component i in gas phase and adsorbed phase, respectively, and p_t is the total gas pressure.

2.3 Selectivity Calculated by IAST and Extended Langmuir Equation

Adsorption selectivity in a binary mixture of components 1 and 2 is defined as

$$S_{12} = \left(\frac{x_1}{y_1}\right)/\left(\frac{x_2}{y_2}\right) = \left(\frac{x_1}{x_2}\right)\left(\frac{y_2}{y_1}\right) = \left(\frac{n_1}{n_2}\right)\left(\frac{y_2}{y_1}\right) \tag{7}$$

The adsorption selectivity can be solved by combining Eqs. (5) and (6). If the extended Langmuir equation is used to solve the adsorption selectivity, combining Eqs. (2), (7) becomes

$$S_{12} = \left(\frac{n_{s1}b_1p_1}{1 + \sum_i b_ip_i}/\frac{n_{s2}b_2p_2}{1 + \sum_i b_ip_i}\right)\left(\frac{y_2}{y_1}\right) = \frac{n_{s1}b_1}{n_{s2}b_2} \tag{8}$$

where p_i is calculated from the total pressure p_t by multiplying the mole fraction y_i. In this paper, component 1 represents CO_2, and component 2 represents H_2. So here S_{12} represents the selectivity of an adsorbent for CO_2 compared to H_2. Higher S_{12} is good for hydrogen purification.

2.4 Deep Neural Network (DNN) for Selectivity

Artificial neural network (ANN) has strong nonlinear processing ability, which includes an input layer, hidden layers and an output layer. A deep neural network (DNN) is a neural network with multiple hidden layers. The more the number of hidden layers, the better the nonlinear fitting characteristics of the ANN, and the better it is to deal with complex problems. In this paper, the number of hidden layers is set to 5, and the number of neurons in each hidden layer is 10. The structure of the DNN in this paper is shown in Fig. 1. The inputs of DNN are CO_2 molar fraction, adsorption pressure and Langmuir adsorption isotherm parameters. And the output of DNN is separation selectivity. The chosen method of training data generation is via Latin hypercube sampling (LHS). The significant advantage of LHS is that a small number of samples can represent the entire sample space. The upper and lower boundaries of the LHS are shown in Table 1. The total number of sample points is set to 6000, and the adsorption selectivity values of the selected sample points are calculated by IAST. Due to the large difference between the input parameter values, the calculated selectivity difference is also large. The adsorption selectivity values are set between 3 and 1500. Finally, 3602 sample points are selected to train DNN.

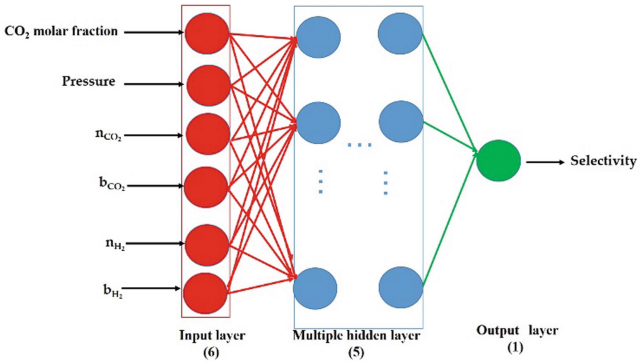

Fig. 1. DNN structure for predicting separation selectivity.

Table 1. Lower (lb) and upper (ub) boundaries of Latin hypercube sampling (LHS).

Condition	CO_2 molar fraction	Pressure (bar)	n_{CO_2} (mol/kg)	b_{CO_2} (bar^{-1})	n_{H_2} (mol/kg)	b_{H_2} (bar^{-1})
lb	0.1	0.1	5	0.1	0.5	0
ub	0.9	30	20	1.5	6	0.6

3 Results and Discussion

The NIST/ARPA-E database of Novel and Emerging Adsorbent Materials is a free, web-based catalog of adsorbent materials and measured adsorption properties of numerous materials, thus making it a treasure trove for data-driven analysis [6, 7]. As shown in Fig. 2, the Isotherm Visualization Tool of the NIST/ARPA-E database can quickly obtain the adsorption isotherm and Langmuir fitting parameters by searching the adsorbent material and gas species. The adsorption of CO_2 and H_2 on activated carbon and CuBTC is randomly selected in the NIST/ARPA-E database. Therefore, by combining NIST/ARPA-E Database and DNN model, the selectivity of different adsorbents to CO_2 and H_2 can be quickly calculated so as to achieve the purpose of fast screening materials.

The algorithm of DNN is completed by Matlab software. The correlation coefficients of the training set, validation set, test set and whole data set of the DNN are 0.99998, 0.9998, 0.99688 and 0.99948, respectively, indicating that the DNN model can well predict the selectivity. In order to further verify the accuracy of the DNN model, the selectivity of activated carbon and CuBTC under different pressures and CO_2 molar fractions is calculated by extended Langmuir, IAST and DNN. As shown in Fig. 3, by comparison, the selectivity values calculated by the IAST agree well with the values calculated by the DNN model, which further verifies the robustness of the DNN model. In Fig. 3 (a), for an 80:20 H_2/CO_2 mixture, CuBTC selectivity under different adsorption pressures is greater than activated carbon. In Fig. 3 (b), at 10 atm, the selectivity of CuBTC is also greater than that of activated carbon at different mole fractions of carbon dioxide. Therefore, for ideal H_2 purification and CO_2 capture materials, CuBTC is more suitable than activated carbon. Compared with activated carbon, CuBTC has a larger surface area and higher pore volume. There are also related articles about the application of CuBTC in PSA hydrogen purification. For the 81:19 H_2/CO_2 mixture, the purity 99.99+ of hydrogen can be obtained by a 4-step PSA cycle with CuBTC as an adsorbent [8].

Besides, after nonlinear treatment by DNN, the process optimization design of adsorption and separation can be carried out. For example, Ref. [9] predicts and optimizes CO_2 adsorption capacity, selectivity and adsorption heat through DNN and multi-objective optimization algorithm. It is worth noting that the selectivity at a fixed temperature calculated by extended Langmuir is a constant value, and the selectivity value does not change with adsorption pressure and mole fraction. Obviously, the calculation error of extended Langmuir is large. Ref. [10] points out that the IAST gives the most accurate predictions than the extended Langmuir and LRC for three binary systems. Therefore, more and more researchers use IAST to develop corresponding application programming interfaces (APIs) for calculating selectivity, such as pyIAST, pyGAPS and GraphIAST [11].

Compared with IAST, another advantage is that the DNN does not need to solve the integral solutions of different isotherm models. Actually, the DNN proposed in this paper can calculate the selectivity of any two-component gas, such as CO_2/CH_4, CH_4/H_2, etc. When the input parameters of DNN exceed the lower and upper boundaries of training data, the predicted results may deviate from the IAST theoretical calculations. The robustness of the DNN can be enhanced by increasing the dimension of input parameters and adjusting the structure of the DNN, which is not the focus of this paper. The DNN

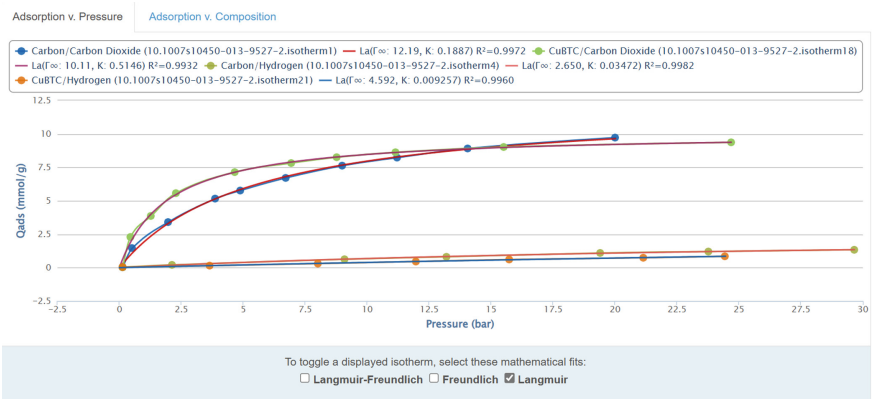

Fig. 2. Adsorption isotherms of CO_2 and H_2 on CuBTC and AC at 298K on NIST/ARPA-E (equilibrium data from Ref. [12]).

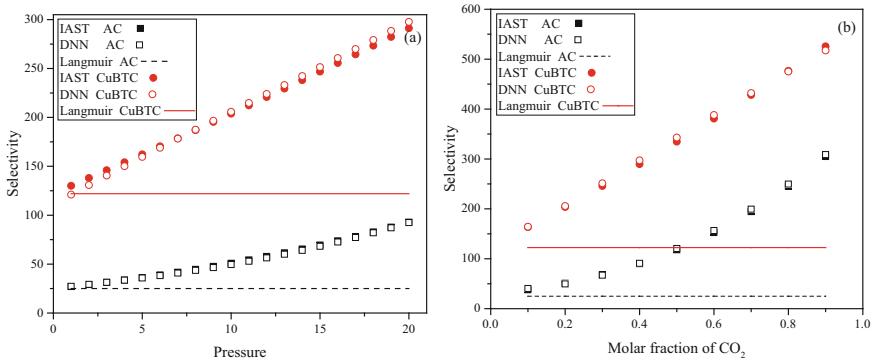

Fig. 3. Extended Langmuir, IAST and DNN calculated selectivities of activated carbon and CuBTC for a 20:80 CO_2/H_2 mixture at different pressure (a) and a 10 atm CO_2/H_2 mixture at a different molar fraction of CO_2 (b).

model is a new attempt at calculating selectivity and can improve the efficiency of adsorbent screening. In addition, the DNN model can also be extended to the calculation of adsorption selectivity of multi-component gases to optimize the design of layered beds with multi-adsorbent.

4 Conclusion

The deep neural network model constructed in this paper can quickly predict the adsorption selectivity of CO_2/H_2. The results show that the correlation coefficient of the DNN model for the whole data set can reach 0.99948. In addition, by combining with NIST/ARPA-E Database, this paper takes activated carbon and CuBTC as examples to compare the adsorption selectivity of the two adsorbents under different pressures and

CO_2 molar fraction at the same temperature. The results show that the adsorption selectivity of CuBTC is greater than that of activated carbon, so CuBTC is more suitable for H_2 purification and CO_2 storage than activated carbon.

Acknowledgments. This research is funded by the and the Shuguang Project of Knowledge Innovation Program from the Wuhan Science and Technology Bureau (2022010801020432, 2023010201020479) and the National Natural Science Foundation of China (52176191). The authors' team is partially supported by the Innovative Research Team Development Program of the Ministry of Education of China (IRT_17R83). Thanks to the International Network Programme supported by the Danish Agency for Higher Education and Science for the PRESS project "Proactive Energy Management Systems for Power-to-Heat and Powerto- Gas Solutions" (No. 8073-00026B).

References

1. Herm, Z.R., Swisher, J.A., Smit, B., Krishna, R., Long, J.R.: Metal-organic frameworks as adsorbents for hydrogen purification and precombustion carbon dioxide capture. J. Am. Chem. Soc. **133**, 5664–5667 (2011)
2. Xiang, H., Fan, X., Siperstein, F.R.: Understanding ethane/ethylene adsorption selectivity in ethane-selective microporous materials. Sep. Purif. Technol. **241** (2020)
3. Oschatz, M., Antonietti, M.: A search for selectivity to enable CO_2 capture with porous adsorbents. Energy Environ. Sci. **11**, 57–70 (2018)
4. Simon, C.M., Smit, B., Haranczyk, M.: PyIAST: ideal adsorbed solution theory (IAST) Python package. Comput. Phys. Commun. **200**, 364–380 (2016)
5. Zhou, X., Huang, W., Miao, J., Xia, Q., Zhang, Z., Wang, H., et al.: Enhanced separation performance of a novel composite material GrO@MIL-101 for CO_2/CH_4 binary mixture. Chem. Eng. J. **266**, 339–344 (2015)
6. Siderius, D., Shen, V.: NIST/ARPA-E database of novel and emerging adsorbent materials. National Institute of Standards and Technology, Gaithersburg (2014)
7. Iacomi, P., Llewellyn, P.L.: Data mining for binary separation materials in published adsorption isotherms. Chem. Mater. **32**, 982–991 (2020)
8. Silva, B., Solomon, I., Ribeiro, A.M., Lee, U.H., Hwang, Y.K., Chang, J.-S., et al.: H_2 purification by pressure swing adsorption using CuBTC. Sep. Purif. Technol. **118**, 744–756 (2013)
9. Yulia, F., Zulys, A., Saha, B.B., Mabuchi, T., Gonçalves, W., Nasruddin: Bio-metal-organic framework-based cobalt glutamate for CO_2/N_2 separation: experimental and multi-objective optimization with a neural network. Process Saf. Environ. Prot. **162**, 998–1014 (2022)
10. Park, J.-H., Kim, J.-N., Cho, S.-H.: Performance analysis of four-bed H_2 PSA process using layered beds. AlChE J. **46**, 790–802 (2000)
11. Dautzenberg, E., van Hurne, S., Smulders, M.M.J., de Smet, L.C.P.M.: GraphIAST: a graphical user interface software for ideal adsorption solution theory (IAST) calculations. Comput. Phys. Commun. **280** (2022)
12. Rother, J., Fieback, T.: Multicomponent adsorption measurements on activated carbon, zeolite molecular sieve and metal–organic framework. Adsorption **19**, 1065–1074 (2013)

Scheduling of Renewable Energy Hydrogen Production System Based on Two—Stage Distribution Robust Optimization

Luohui Xia[1], Bin Wu[2], Linwei Zhou[3(✉)], Tao Liang[2], and Zicong Liu[2]

[1] Science and Technology Innovation Research Academy (Hebei), CAICT Institute Co., Ltd., Baoding 071000, Hebei, China
[2] School of Artificial Intelligence, Hebei University of Technology, Tianjin 300130, China
[3] Baoding National High-tech Industrial Development Zone Administrative Committee, Baoding 071000, Hebei, China
191825524@qq.com

Abstract. Hydrogen energy has various advantages such as cleanliness, storage and high energy carrier, which is considered to be one of the key paths to achieve the goal of "double carbon". Utilization of hydrogen production in renewable energy is an important technical means to achieve new energy amazing and energy cleaning utilization. In response to the uncertainty characteristics of local scenery resources and local electricity load and hydrogen load demand, considering the investment cost of hydrogen storage system and the influence of flexible load of electric load on the optimal operation of the system, a two-stage distributed robust optimization model for hydrogen production system (H2-RES) from renewable energy is established, the capacity of the first stage hydrogen production system is determined by the system economy, and the second stage is designed to optimize the real-time scheduling of the system, aiming at the total operating cost, which is solved by C&CG algorithm, finally, an example is given to verify the validity of the proposed model.

Keywords: Renewable energy · Hydrogen production · Two stage robust · Optimal configuration · Operation optimization

1 Introduction

With the "carbon peak-carbon neutral" goal proposed, power, transportation, and production links to speed up the transition to a deep low-carbon clean, hydrogen energy as an important clean energy, several developed countries have promoted the development of hydrogen energy industry as a national strategy. China also plans to include hydrogen energy in the energy category [1]. And from the central to the local issued a number of renewable energy to promote the development of hydrogen and hydrogen vehicles [2, 3]. Now, during the Beijing Winter Olympic Games, hydrogen energy has been fully demonstrated in this Beijing Winter Olympic Games, including more than 1,000 hydrogen-powered vehicles, equipped with more than 30 hydrogen refueling stations,

H. Sun et al. (Eds.): WHTC 2023, SPPHY 393, pp. 222–243, 2024.
https://doi.org/10.1007/978-981-99-8631-6_25

in order to ensure the demand for hydrogen energy for the Winter Olympic Games, construction of large-scale hydrogen production projects in Zhangjiakou and other places. From the perspective of hydrogen demand, hydrogen-powered vehicles are more suitable for the "three north" winter low-temperature environment than electric vehicles because of their fast hydrogenation speed, long range and environmental friendliness, in recent years, it has gained wide attention and developed rapidly [4]. Hydrogen stations will also proliferate in the future, as they are a prerequisite for the rapid development of hydrogen-powered cars. The integration of renewable energy hydrogen production and power generation into the grid will not only enable new energy consumption and promote green energy development, but also be in line with the current situation of the Zhangjiakou region's energy supply for the Beijing Winter Olympic Games. Therefore, hydrogen production system based on renewable energy and supported by DC microgrid will be the best way to achieve low-carbon environmental protection, and zero-carbon power plus hydrogen energy is the only way to optimize the energy structure in the future [5], this has also become the current hot spot of scholars.

Literature [6] optimizes the operation of the comprehensive energy system of the hydrogen production unit containing wind power, which can meet the needs of electricity, hydrogen and heat at the same time. Reference [7] established a two-tier model for configuration optimization of grid connected offshore wind power hydrogen energy system, and studied the configuration and economy of the system by means of net present value. Literature [8] designed a hybrid new energy system including wind power, photovoltaic and hydrogen energy storage, and used the objective fitness function to model, and achieved good capacity optimization results Literature [9] designed the hydrogen energy storage system with heat balance system, established the wind hydrogen hybrid system, and proposed the optimal allocation method of hydrogen energy storage capacity of wind hydrogen hybrid system considering the uncertainty of heat balance. The above research optimizes the static capacity configuration of the integrated energy system containing hydrogen energy, and there is no subsequent dynamic optimization of the static configuration.

Literature [10] cooperates with three main body of the scene, based on the Nash negotiation theory, the operation model is established. Finally, through example verification, the operational operation of the proposed cooperative operation can be greatly improved. And the overall benefits of the cooperation alliance. Literature [11] is optimized by hydrogen energy-natural gas multi-energy storage systems, and the economics and environmental protection of electric hydrogen and electricity gas are verified. Literature [12] constructed the optimal scheduling model of wind hydrogen system with the optimization objective of hydrogen production efficiency, solved the optimal hydrogen production power by using artificial bee colony algorithm, and verified the effectiveness of the proposed method through simulation analysis. Literature [13] established the optimal scheduling model of integrated energy system with hydrogen production system with the goal of minimizing operation cost and environmental cost, and solved the optimal daily operation scheduling scheme of the system by using NSGA-II algorithm., Literature [14] proposed a low-carbon operation method of integrated energy system considering electrothermal flexible load and fine modeling of hydrogen energy.

The static capacity configuration of hydrogen production equipment is not considered in the above literature.

Literature [15] established an island microgrid model including hydrogen production system and cogeneration, used robust optimization method to deal with the uncertainty related to photovoltaic output, electric load and heat load demand, and verified the effectiveness of the robust optimization used to deal with relevant risks, but static configuration optimization was not considered in the system. Literature [16] is electrically and hydrogen into the energy carrier, and a double-layer mixed integer planning model is proposed. The upper layer model is intended to improve system economy, optimize the device configuration to meet regional energy demand; The lower layer model aims to minimize the average cost of hydrogen production in order to promote the development of hydrogen. Among them, in the upper equipment capacity configuration, the economy of the system is the goal to determine whether the equipment is put into construction, rather than determining the equipment to be put into construction first and then optimizing the optimal capacity. Literature [17] uses a two-stage distributed robust optimization model to deal with the uncertainty of load. In the first stage, it optimizes the equipment safety capacity and time in the integrated energy system. In the second stage, it mainly optimizes and determines the "worst" operation scenario that the integrated energy system may encounter in the future and optimizes the system operation scheduling. Literature [18] For the renewable energy area integrated energy system to improve economic and scheduling flexibility, a double robust game model is proposed, and multi-target whale optimization algorithm is used to address constraint complex mixing integers nonlinear planning issues, verify the feasibility of the model and the effectiveness of the algorithm of the model by case analysis. The system in the above two documents did not consider hydrogen energy. Based on this, aiming at the uncertain load and renewable energy output, a two-stage distributed robust optimization model based onH2-RES system is established. Firstly, the capacity of hydrogen production system is statically optimized, and then the dynamic operation of the system is scheduling optimized.

During the operating scheduling of theH2-RES system, the flexible load of the electric load can be changed by changing its own size and time period, and further optimizing the smooth load curve to improve the operational flexibility and economic benefits ofH2-RES.Literature [19] For the problem of low-carbon economy optimization operation in the integrated energy system of hydrogen energy to energy conversion medium, the impact of flexible load on adjustment system optimization operation, and established flexible load model. Literature [20] established IES two-stage distribution robust optimization scheduling model considering flexible loads, verifying that flexible loads can improve the economic benefits of the IES system operation.

Based on the existing literature, this paper takes the hydrogen production system from renewable energy sources as the research object. Firstly, the capacity of the hydrogen production system is optimized for the uncertainty of renewable energy sources and the local electric load and hydrogen load. After the static configuration optimization, the daily operation scheduling of the hydrogen production system from renewable energy sources is optimized. For the uncertainty of renewable energy, considering the investment cost of hydrogen production system and the impact of the flexible load of electric load participating in the electric load regulation on the optimal operation of the system. A

two-stage distributed robust optimization model of hydrogen production system from renewable energy driven by the worst scenario is constructed and applied to practical engineering projects, which has good feasibility.

The structure of the remainder of this paper is as follows. Section 2 introduce the structure and model of renewable energy hydrogen production system, Sects. 3 and 4 respectively introduce the objective function and model of static configuration and dynamic scheduling of the system, Sects. 5 and 6 respectively introduce the two-stage robust programming model and its solution method of the system, and Sect. 7 introduces the case analysis of the method proposed in this paper.

2 H2-RES Structure and Model

Figure 1 shows the complete structure diagram of renewable energy hydrogen production system. It mainly includes fan, photovoltaic, storage battery, power grid, alkaline water electrolyzer, hydrogen compressor, hydrogen storage tank, etc. Part of the fans and photovoltaic power generation is used for residential power load, and the other part is used for hydrogen load of hydrogen fuel vehicles. The hydrogen produced by the electrolytic cell is compressed by the hydrogen compressor and then sent to the hydrogen storage tank. The compressed hydrogen gas is transported to the hydrogenation station through the hydrogen long pipe trailer to supply the hydrogen demand of hydrogen fuel vehicles. The battery in the system plays a buffer role. When the available energy is insufficient, it is discharged through the battery first. If the electric load and hydrogen load are still not met, it is necessary to purchase electricity from the power grid. When there is still electricity left after the electricity load and hydrogen load can be met by generating electricity from renewable energy, the battery can be charged or sold to the power grid according to the actual situation. In order to deal with the uncertainty of wind and solar output, the worst scenario driven distributed robust method is used to optimize the system. In terms of power load demand, flexible load is considered in this paper.

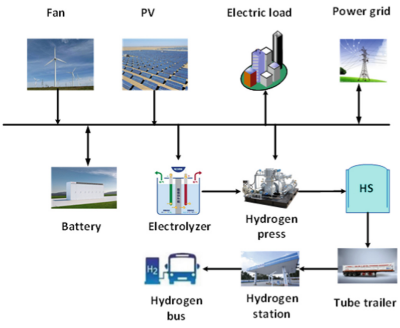

Fig. 1. H2-RES structure

3 The H2-RES Capacity Configuration Phase

The capacity configuration stage of H2-RES is mainly to configure the optimal capacity of electrolytic cell, hydrogen compressor and hydrogen storage tank in the hydrogen production system. The goal is to minimize the daily average investment cost on the premise that the system can operate normally under all the worst probability scenarios:

$$min\, F_1 = \frac{\rho_{ED} M_{ED} + \rho_{HC} M_{HC} + \rho_{HS} M_{HS}}{N} \tag{1}$$

In the formula, ρ_{ED} represents the unit capacity investment cost of the electrolyzer, ρ_{HC} represents the unit capacity investment cost of the hydrogen compressor, ρ_{HS} represents the unit capacity investment cost of the hydrogen storage tank; M_{ED}, M_{HC}, M_{HS} represents the capacity of the electrolyzer cell, hydrogen compressor and hydrogen storage tank respectively, and N represents the total number of days in a year, taking 365 days.

The upper and lower limits of the capacity of the electrolyzer, hydrogen compressor and hydrogen storage tank are as follows:

$$0 \le M_{ED} \le M_{ED,max} \tag{2}$$

$$0 \le M_{HC} \le M_{HC.max} \tag{3}$$

$$0 \le M_{HS} \le M_{HS,max} \tag{4}$$

$M_{ED,max}$, $M_{HC,max}$, $M_{HS,max}$ represents the maximum capacity of the electrolyzer, hydrogen compressor, and hydrogen storage tank, respectively.

4 The H2-RES Optimal Scheduling Phase

After determining the optimal capacity configuration of the hydrogen production system in the first stage, the next stage is to optimize the operation and scheduling of the hydrogen production system from renewable energy based on the optimal capacity of the hydrogen production system determined in the first stage. In view of the characteristics of difficult prediction and strong randomness of fan and photovoltaic output, the "worst" operation scenario that may be encountered by the microgrid is considered and the economy of its operation is estimated, and the flexible load in the electric load is considered to improve the economy of the system.

4.1 Flexible Electrical Load Model

The electrical load in the hydrogen production system of renewable energy includes flexible electrical load and rigid electrical load. The flexible electrical load is mainly used to regulate the overall load curve of the system and improve the overall energy consumption level of the system on the premise of meeting the basic rigid electrical load of the system. In order to tap the scheduling potential of flexible electric load and improve the economy of the system, two flexible load mathematical models are established, namely transferable and reducible flexible load.

4.1.1 Transferable Electric Load Model

The load can be transferred according to the real-time electricity price, the user carries on the transfer to some non-essential time period load, for example washing machine, water heater and so on. And the working hours of the transferable load and the size of the transfer time have no time continuity constraints, and have higher flexibility, the total power of the pre-and post-dispatch transferable loads must satisfy uniform invariance on the transferable interval $[t_{start}, t_{end}]$.

$$\sum_{t=1}^{T} F_t^{tr} \Delta t = \sum_{t=t_{start}}^{t_{end}} P_t^{tr} \Delta t \tag{5}$$

$$b_t^{tr} P_{min}^{tr} \leq P_t^{tr} \leq b_t^{tr} P_{max}^{tr} \tag{6}$$

In the formula: F_t^{tr} and P_t^{tr} denote the power of the transferable electric load at t time before and after the transfer respectively, P_{min}^{tr} and P_{max}^{tr} denote the transferable minimum electric load and the transferable maximum electric load respectively, b_t^{tr} is the 0-1 variable, which represents the transition state of the transferable electrical load t period and $b_t^{tr} = 1$ means that the electric transfer load occurs during the time period.

When electric load transfer, the user is transfer compensation adjustment

$$C_{tr} = r_{tr} \sum_{t=1}^{T} b_t^{tr} P_t^{tr} \tag{7}$$

In the formula: r_{tr} represents the unit compensation price of the transferable electric load.

4.1.2 Reduction of Electric Load Model

Reducible electric load refers to a certain reduction of load power within the allowable range without changing the purpose of users' power consumption, which alleviates the tension of energy consumption. The reducible load in each period after dispatching can be expressed as:

$$P_t^{cu} = \left(1 - b_t^{cu} \varepsilon_t\right) F_t^{cu} \tag{8}$$

In the formula: F_t^{cu} and P_t^{cu} for t time can reduce the electrical load before and after the reduction of electrical load power, b_t^{cu} for 0-1 variables, that can reduce the electrical load cut state, the load can be reduced by t when b_t^{cu} is equal to 1, ε_t represents the reduction of the load at t time, $0 \leqslant \varepsilon_t \leqslant 1$, when $\varepsilon_t = 1$ represents the complete reduction of the load.

$$C_{cu} = r_{cu} \sum_{t=1}^{T} b_t^{cu} \left(P_t^{cu} - F_t^{cu}\right) \tag{9}$$

In the formula: r_{cu} represents the unit power compensation cost that can reduce the electrical load.

4.2 Objective Function

The optimization objective of the second stage is to minimize the total cost under the operation of the hydrogen production system with renewable energy, and finally determine the start-up and shutdown plan of each unit, the power generation capacity, the charge and discharge plan of the energy storage system, and the power purchase and sales plan for trading with the power grid. The total cost includes the power purchase and sale expenses with the power grid, the flexible power load dispatching compensation cost of the microgrid, and the operation and maintenance expenses of the battery and hydrogen production system.

$$min\, F_2 = C_{grid} + C_{dr} + C_{op} \tag{10}$$

In the formula: C_{grid}, C_{dr}, C_{op} represents the transaction costs between the power grid, flexible load compensation costs, the operation and maintenance costs of equipment.

(1) transaction cost between system and power grid

Transaction costs between the system and the grid include the purchase of electricity to the grid and the sale of electricity to the grid

$$C_{grid} = \sum_{t=1}^{T} l_t^{buy} P_t^{buy} - l_t^{sell} P_t^{sell} \tag{11}$$

In the formula: l_t^{buy} represents the purchase price of t time Grid, l_t^{sell} represents the sale price of t time grid, P_t^{buy}, P_t^{buy} represents the purchase and sale power of t time system.

(2) flexible electric load dispatch compensation cost

The flexible power load dispatching compensation cost mainly includes the power load compensation cost which can be reduced and the power load compensation cost which can be transferred:

$$C_{dr} = C_{tr} + C_{cu} \tag{12}$$

In the formula: C_{tr}, C_{cu} respectively represents the transferable electric power compensation cost and can reduce the electric power compensation cost, its specific mathematical model is shown in the formula (7) and formula (9).

(3) system equipment operation and maintenance costs

System equipment operation and maintenance costs mainly include the main components of the system operation and maintenance costs. The main components of the hydrogen production system are based on the unit power consumption, and the storage battery is based on the charge/discharge capacity. The model is as follows:

$$C_{OP} = C_{OP}^{EH} + C_{OP}^{BAT} \tag{13}$$

$$C_{OP}^{EH} = \sum_{t=1}^{T} r_{OP}^{EH}(P_t^{ED} + P_t^{HC}) \tag{14}$$

$$C_{OP}^{BAT} = \sum_{t=1}^{T} r_{OP}^{BAT}(P_t^{BATC} + P_t^{BATD}) \tag{15}$$

In the formula: C_{OP}^{EH}, C_{OP}^{BAT} represents the operation and maintenance cost of hydrogen production equipment and storage battery respectively; r_{OP}^{EH}, r_{OP}^{BAT} represents the unit operation and maintenance cost of hydrogen production system and storage battery respectively; P_t^{ED}, P_t^{HC} represents the consumption power of electrolyzer and hydrogen press at time t, P_t^{BATC}, P_t^{BATD} represents the charge and discharge power of battery at time t.

4.3 Constraints

The constraints of the optimal scheduling model ofH2-RES mainly include power balance constraints, power storage equipment constraints and hydrogen production system constraints.

(1) Power balance constraint

$$P_t^{WD} + P_t^{PV} + P_t^{BATD} + P_t^{BUY} = P_t^{EL} + P_t^{tr} + P_t^{cu} + P_t^{BATC} + P_t^{ED} + P_t^{HC} + P_t^{SELL} \tag{16}$$

In the formula: P_t^{WD}, P_t^{PV} represents the fan output power and photovoltaic output power at time t respectively; P_t^{BATC}, P_t^{BATD} represents the battery charge/discharge power at time t respectively; P_t^{BUY}, P_t^{SELL} indicates the purchasing power and selling power between the hydrogen production system and the power grid at time t, P_t^{EL}, P_t^{tr}, P_t^{cu} represents the rigid electric load at time t, the transferable electric load and the reduced electric load respectively, and P_t^{ED}, P_t^{HC} represents the consumed electric power of the electrolyzer and the hydrogen compressor at time t.

(2) Constraint of storage equipment

$$\begin{cases} E_1 = \eta_0 E_{BAT} + \eta_{ch} P_t^{BATC} - \frac{P_t^{BATD}}{\eta_{dis}} \\ E_k = E_{k-1} + \eta_{ch} P_k^{BATC} - \frac{P_k^{BATD}}{\eta_{dis}}, 2 \le k \le 24 \\ \eta_{\min} E_{BAT} \le E_t \le \eta_{\max} E_{BAT}, 1 \le t \le 24 \\ 0 \le P_t^{BATC} \le I_t^{ch} P_{\max}^{BATC} \\ 0 \le P_t^{BATD} \le I_t^{dis} P_{\max}^{BATD} \\ 0 \le I_t^{ch} + I_t^{dis} \le 1 \\ \sum_{t=1}^{T} \eta_{ch} P_t^{BATC} \Delta t - \sum_{t=1}^{T} \frac{P_t^{BATD}}{\eta_{dis}} \Delta t = 0 \\ E_T = \eta_0 E_{BAT} \end{cases} \tag{17}$$

In the formula, E_1, E_t denote the capacity of the battery in the first time period and t the t time period battery capacity, E_{BAT} denote the total capacity of the battery, E_T denote the capacity of the battery in the last time period of a dispatch period, η_0, η_{min}, η_{max} represents the ratio coefficient of initial capacity, the minimum energy storage coefficient and the maximum energy storage coefficient, η_{ch}, η_{dis} represents the efficiency of charge/discharge energy, I_t^{ch}, I_t^{dis} represent the Battery t time charge and discharge energy mark bit 0-1 variable.

(3) Constraints of hydrogen production system

The hydrogen production system consists of an electrolytic cell, a Hydrogen compressor, and a hydrogen storage tank.

① Electrolytic cell model

At present, the most commonly used electrolyzer in industrial production is alkaline water electrolyzer, which has fast reaction speed and mature technology. The hydrogen production efficiency of the electrolyzer and the power of the electrolyzer can be regarded as a linear relationship under stable operation [21]. The unit hydrogen production rate is assumed to be η_{H_2}, kg/(kW h),The hydrogen yield $m_t^{H_2}$ at t time is the product of the hydrogen yield η_{H_2} and the power P_t^{ED} input to the cell [22]:

$$m_t^{H_2} = \eta_{H_2} P_t^{ED} \tag{18}$$

The electrolyzer shall meet the minimum safe power and maximum power constraints during operation:

$$P_{min}^{ED} \le P_t^{ED} \le P_{max}^{ED} \tag{19}$$

In the formula: P_{min}^{ED}, P_{max}^{ED} respectively represents the minimum safe power and the maximum operating power when the electrolyzer is running.

At the same time, the electrolytic cell should also meet the power climbing constraints:

$$\left| P_{t+1}^{ED} - P_t^{ED} \right| \le P_{rp}^{ED} \tag{20}$$

In the formula: P_{rp}^{ED} indicates the maximum climbing power of the electrolyzer.

② Hydrogen compressor model

To facilitate storage and transportation, hydrogen is compressed into high pressure hydrogen using Hydrogen compressor, and the power consumption of the hydrogen compressor [23] needs to be satisfied:

$$P_t^{HC} = \frac{R_{H_2} m_t^{H_2} T_{in} \kappa}{3600 \eta_{HC} (\kappa - 1)} \left[(P_{out}/P_{in})^{\frac{\kappa-1}{\kappa}} - 1 \right] \tag{21}$$

$$0 \le P_t^{HC} \le P_{max}^{HC} \tag{22}$$

In the formula: R_{H_2} is the specific heat capacity of hydrogen Changshu, T_{in} is the compressor input hydrogen temperature, η_{HC} is the compressor efficiency, κ is the isentropic index of hydrogen, P_{out}/P_{in} is the compression ratio.

③ Hydrogen storage tank model

The hydrogen storage tank is used to store the compressed hydrogen, and its mathematical model and constraints are:

$$\begin{cases} m_1^{HS} = \rho_0 M_{HS} + m_1^{H_2} - L_1^{H_2} \\ m_k^{HS} = m_{k-1}^{HS} + m_k^{H_2} - L_k^{H_2}, 2 \le k \le 24 \\ \rho_{\min} M_{HS} \le m_t^{HS} \le \rho_{\max} M_{HS}, 1 \le t \le 24 \\ m_T^{HS} = \rho_0 M_{HS} \end{cases} \tag{23}$$

In the formula, m_1^{HS} represents the hydrogen storage capacity of the hydrogen storage tank in the first period of the dispatching period, m_k^{HS} represents the hydrogen storage capacity of the hydrogen storage tank in the k period of the dispatching period, m_T^{HS} represents the hydrogen storage capacity of the hydrogen storage tank in the last period of the dispatching period, ρ_0, ρ_{min}, ρ_{max} represents the initial hydrogen storage ratio coefficient, the minimum hydrogen storage ratio coefficient and the maximum hydrogen storage ratio coefficient respectively, and M_{HS} represents the total capacity of the hydrogen storage tank.

5 Two-Stage Robust Programming Model for H2-RES

The first stage of the two-stage distributed robust optimization model based on renewable energy hydrogen production system proposed in this paper is to optimize the capacity of the hydrogen production system according to the local renewable energy characteristics, electric load and hydrogen load, including the capacity configuration of electrolytic cell, hydrogen compressor and hydrogen storage tank. The optimization goal is the construction cost. The second stage is to optimize the real-time scheduling scheme with the lowest system operation cost under the "worst" operation scenario that the system may encounter in the future. Then feed back the optimization results of the second stage to the first stage to further formulate the best planning scheme. The two-stage planning model is shown in Fig. 2.

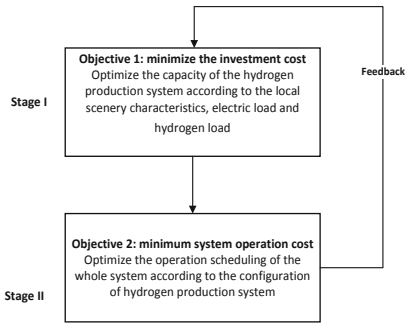

Fig. 2. Two-stage programming model

The two-stage robust optimization model is as follows:

$$F_3 = \min_x \left\{ F_1 + \max_u \min_y \{F_2\} \right\} \tag{24}$$

In the formula: x is the decision variable of the first stage, that is, the capacity configuration of the hydrogen production system; u is the scene of the worst scenery; y is the decision variable of the second stage, that is, after the configuration of the hydrogen production system and the worst-case scenario of the most economic scheduling scheme.

In this paper, we use the k-means Clustering Method to reduce M wind power and photovoltaic power scenes into typical discrete scenes with uncertain and random characteristics u1, u2, . . . , uk, the occurrence probabilities of various scenarios are obtained to simulate the output uncertainty of renewable energy. The initial probability of each discrete scenario is expressed in p_k^0.

The purpose of scene reduction analysis is to replace a large number of complex scene features with a small number of representative scenes, and construct an uncertain set to describe the distribution of scenery output. The comprehensive norm constraint set composed of [22] 1-norm and ∞-norm restricts the probability distribution of renewable energy output scenario, as shown in Eq. (25).

$$\Omega = \left\{ p_k \left| \begin{array}{c} p_k \geq 0, k = 1, 2, \ldots, K \\ \sum_{k=1}^{10} p_k = 1 \\ \sum_{k=1}^{10} |p_k - p_k^0| \leq \lambda_1 \\ \max_{k=1,2,\ldots,K} |p_k - p_k^0| \leq \lambda_\infty \end{array} \right. \right\} \tag{25}$$

In the formula: Ω is the probability distribution feasible region of renewable energy output scene, where P_k is the probability of the typical scene u_k, which λ_1, λ_∞ is the probability allowable deviation value of 1-norm and ∞-norm respectively, which can be obtained from Eq. (26).

$$\begin{cases} \lambda_1 = \frac{k}{2M} \ln \frac{2k}{1-\alpha_1} \\ \lambda_\infty = \frac{1}{2M} \ln \frac{2k}{1-\alpha_\infty} \end{cases} \tag{26}$$

In the formula: α_1, α_∞ is the confidence level of 1-norm and ∞-norm uncertainty probability respectively.

The two-stage distribution robust optimization model is a min max min structure. In order to facilitate analysis, the worst scenario of renewable energy output is represented by the worst probability distribution of renewable energy output. The two-stage distribution robust model of the proposed system can be transformed into the following form:

$$F_3 = \min_x \left\{ F_1 + \max \left\{ \sum_{k=1}^{10} p_k \min_y \{F_2\} \right\} \right\} \tag{27}$$

6 Two-Stage Robust Model Solving Method

To solve the two-stage distributed robust optimization problem, a column constraint generation algorithm (C & CG) is used to solve the decomposition problem. Compared with Benders decomposition algorithm, C & CG algorithm has fewer iterations and higher accuracy. C & CG algorithm is used to decompose the two-stage distributed robust problem into main problem and sub-problem.

The main problem is to solve the optimal capacity allocation of the hydrogen production system based on the probability distribution of the initial worst-case scenario, and to obtain the maximum real-time operating cost with the lowest operating cost as the objective in the worst-case scenario, and provide a lower bound for the model:

$$\begin{cases} min A^T x + U \\ U \geq \sum_{k=1}^{10} p_k min\left\{B^T y_k\right\} \end{cases} \tag{28}$$

In the formula, A^T is the coefficient matrix of the primary decision variable, x is the primary decision variable, U is the auxiliary variable of the main problem objective function and B^T is the coefficient matrix of the secondary decision variable.

Based on the optimal capacity configuration of the hydrogen production system solved by the main problem, the sub problem calculates the operation with the lowest operation cost as the goal in each scenario in parallel, and provides the upper bound value to the model. The worst scene probability is updated in the probability distribution feasible region Ω of the data-driven wind and solar output scenario, and the scheduling optimization of the system is carried out. The sub problem can be expressed as:

$$\max_{\{p_k\}\in\Omega} \sum_{k=1}^{K} P_k^q \left[\min_{y_k \in (x,p_k)} \left(B^q\right)^T y_k^q \right] \tag{29}$$

The iterative solution process of the main problem and sub problem by using C & CG algorithm is as follows:

Step 1: Initialization, set the maximum number of iterations n_{max}; convergence accuracy $\zeta = 10^{-3}$, the number of initialization iterations $n = 1$, set the scenery output benchmark scenario u_0 as the worst scenario u_q, initialization $U = +\infty$, The upper bound of the objective function is $U = +\infty$ and the lower bound is $L = -\infty$, the historical data are clustered to obtain K discrete scenes with typical time and the initial probability distribution p_k^0.

Step 2: substitute the worst scenario u_q into the main problem for solution, obtain the optimal capacity solution x^q of the hydrogen production system, and take the optimal solution obtained from the main problem as a new lower bound L^q.

Step 3: substitute x^q into the subproblem and consider the uncertainty of wind power output, and calculate the output plan of each unit when the operation cost is the lowest in each scenario in the subproblem in parallel.

Step 4: find the wind power output expectation and corresponding decision variables y^q that maximize the operation cost in the probability distribution feasible region Ω of the data-driven wind power output scene, take the sum of the sub problem optimization

result $\sum_{k=1}^{K} P_k^q\left[(B^q)^T y_k^q\right]$ and the main problem result $(A^q)^T x^q$ as the upper bound, and update the bad scene u_{q+1} and probability distribution P_k^{q+1}.

Step 5: determine $U^q - L^q \leq \varepsilon$ whether satisfied, if satisfied, the iteration convergence and get the optimal solution; If not satisfied, then update the worst scenario and its probability, $n = n + 1$, and return to step 2 (Fig. 3).

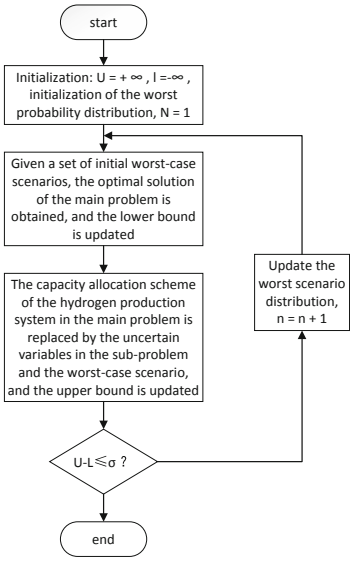

Fig. 3. Solution flow of two-stage robust optimization model

The framework of two-stage distributed robust optimization model based onH2-RES is shown in Fig. 4.

7 Case Analysis

7.1 Basic Data and Model Parameters

In order to verify the feasibility of the model and method in this paper, an example is constructed based on the actual data of Chongli renewable energy large-scale hydrogen production project in Zhangjiakou, Hebei Province. Taking the renewable energy hydrogen production system shown in Fig. 1 as the research object, CPLEX commercial solver is used for modeling and solving in matlab 2020a.

In Zhangjiakou renewable energy hydrogen production project, there are three fans and one photovoltaic array. The rated power of each fan is 2 MW and the rated power of photovoltaic array is 3 MW. Set the optimal scheduling cycle as 24 h, and take 1 h as the unit period. The renewable energy output data of the past one year is taken and reduced to 10 typical discrete renewable energy output scenarios with uncertain and random characteristics by K-means clustering method, and the corresponding probability of

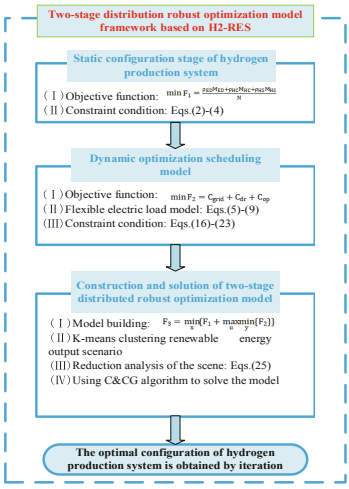

Fig. 4. The whole frame

each scenario is obtained to drive the two-stage distributed robust optimization model of H2-RES. The data of renewable energy output before and after clustering is shown in Figs. 5 and 6. Figure 5 (a) and (b) respectively show the historical data of fan output and photovoltaic output in the past year Fig. 6 shows the 10 types of renewable energy output scenarios obtained by clustering.

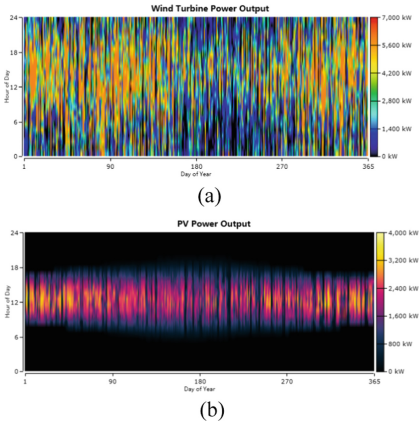

Fig. 5. Historical data of available in process energy output

During the 2022 Winter Olympic Games, more than 400 hydrogen buses were applied to Zhangjiakou competition area, and their daily hydrogen load was supplied by the renewable energy hydrogen production project in Zhangjiakou area. This paper selects the hydrogen load and electric load of typical days and the renewable energy output data of the next day predicted according to the historical renewable energy output data, and

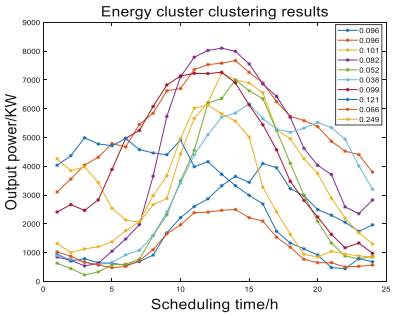

Fig. 6. Clustering results of renewable energy output

makes a case analysis on the dynamic scheduling optimization after the static configuration ofH2-RES hydrogen production system in the first stage. Figure 7 shows typical daily load demand and predicted renewable energy output data.

The purchase and sale price in the calculation case adopts the pricing method of time of use price. The prices of electricity purchased and sold in different time periods are shown in Fig. 8.

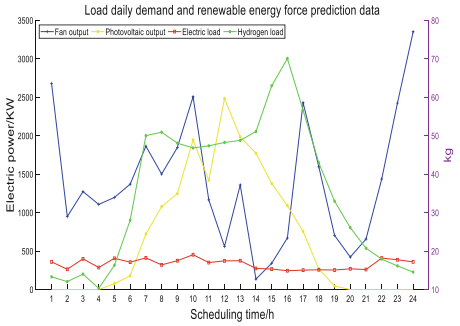

Fig. 7. Load daily demand and renewable energy force prediction data

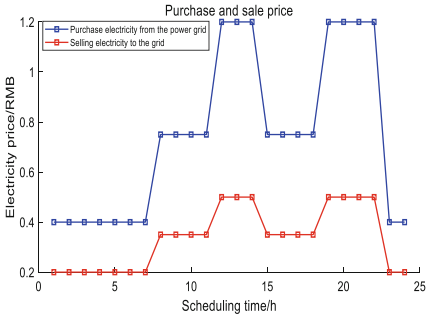

Fig. 8. Purchase electricity-based electricity price

The parameter values of main equipment of the H2-RES system are shown in Table 1.

Table 1. Important parameter values of H2-RES.

Parameter	Value	Parameter	Value
ρ_{ED}	6027	η_{ch}	0.95
ρ_{HC}	1071	η_{dis}	0.96
ρ_{HS}	3549	η_0	0.3
$M_{ED,\max}$	5000	η_{min}	0.1
$M_{HC,\max}$	1000	η_{max}	0.9
$M_{HS,\max}$	1000	R_{H_2}	14.304
r_{tr}	0.05	T_{in}	40
r_{cu}	0.5	η_{HC}	0.7
r_{OP}^{EH}	0.04	κ	1.4
r_{OP}^{BAT}	0.01	ρ_0	0.25
η_{H_2}	0.0192	ρ_{min}	0.2
E_{BAT}	600	ρ_{max}	0.9

7.2 Analysis of Optimizing Static Configuration Stage

In this paper, the historical scenery output data are clustered by K-means method, and 10 groups of initial scenes and their probabilities are obtained. The comprehensive norm constraint set is used to constrain the probability distribution of wind and solar output scenarios, in which the 1-norm constraint confidence is set to 0.5 and ∞-norm constraint confidence is set to 0.99. Build a two-stage robust optimization model forH2-RES system. The static configuration of hydrogen production system obtained by iteration according to C & CG algorithm is shown in Table 2.

The capacity configuration of the optimized hydrogen production system is close to that in the actual project. The capacity of the actual hydrogen production system in Zhangjiakou renewable energy hydrogen production project is shown in Table 3. According to the configuration obtained from the simulation of the example, it is suggested to increase the capacity of the hydrogen storage tank in the project to 220–250kg.

Table 2. Optimized capacity configuration of hydrogen production system

Equipment	Electrolyzer	Hydrogen press	Hydrogen storage tank
Capacity/kW (kg)	2715.3	93.5	213.4

Table 3. Actual capacity of hydrogen production system on site

Equipment	Electrolyzer	Hydrogen press	Hydrogen storage tank
Capacity/kW (kg)	3000	132	210

7.3 Flexible Electric Load Optimization Analysis

The response of electric load demand after considering flexible load is shown in Fig. 9. The blue bar represents the electric load predicted at the dispatching time, the orange bar represents the flexible electric load that can be transferred at the dispatching time, the yellow bar represents the flexible electric load that can be reduced at the dispatching time, and the red curve represents the electric load after considering the flexible load, which can also be expressed as the electric load after demand response.

It can be seen from the figure that the transferable electric load in period 1, period 3, period 5, period 7, period 9–10 and period 22–24 is transferred to period 14–21, and the reducible load in period 2, period 4, period 6, period 8–9 and period 11–21 is reduced on the basis of meeting the acceptable reduction times of users. It effectively smoothes the power load curve of the system, and then improves the wind power consumption and economic benefits of the dispatching plan.

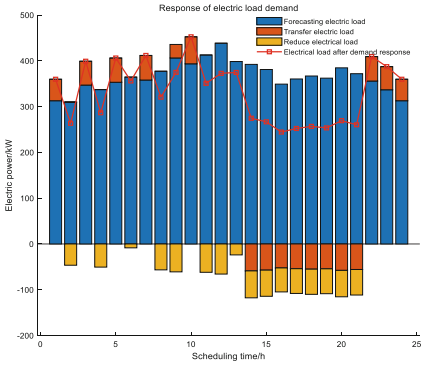

Fig. 9. Response of electric load demand

7.4 Optimized Dynamic Dispatching Operation Analysis

Based on the capacity configuration of hydrogen production system, the dynamic dispatching operation ofH2-RES system is optimized. The optimal operation strategy of each unit of the system is shown in Fig. 10. The blue bar represents the renewable energy output plan, the orange bar represents the power purchase plan of the system to the power grid, the green bar represents the power sales plan of the system to the power grid, and the yellow bar represents the charging and discharging plan of the battery. Above the horizontal axis represents the charging plan, below the horizontal axis represents the

discharge plan, the purple bar represents the power consumption plan of the hydrogen production system, and the red curve represents the power load after demand response.

It can be seen from the figure that in these 24 periods, most of the power output of renewable resources is used for the power consumption of hydrogen production system. In periods 1–7 and 14, the output of renewable energy can not meet the power load and power consumption of hydrogen production system. It is necessary to purchase power from the power grid to meet the power demand. In periods 10, 12–13, 15 and 17, 22–24, the output of renewable energy can fully meet the electrical load and the electrical power required by the hydrogen production system, and the excess electricity is used to sell electricity to the power grid and charge the battery. In this strategy, more electricity is purchased to charge the battery in the first and seventh periods when the output of the available energy is insufficient and the electricity price is low, and the battery is discharged in the eighth to ninth periods, the eleventh periods, the fourteenth periods and the eighteenth to twenty-first periods when the output of the available energy cannot meet the required electric power, so as to achieve the effect of peak shaving and valley filling. The charging and capacity status of the battery are shown in Fig. 11. The total capacity of the battery set in this paper is 1000 kW, the minimum capacity is limited to 100 kW and the maximum capacity is limited to 900 kW. The maximum charging and discharging power is 400KW. It can be seen that the charging power of the battery reaches the maximum charging state in period 1, 11 and 17, and the discharging power reaches the maximum discharging state in period 6 and 21. The capacity of the storage battery is 300 kW at the beginning of the dispatching period, reaches the allowable maximum capacity state in 11, 13 and 18 periods, and returns to the initial state at the last moment of the dispatching period.

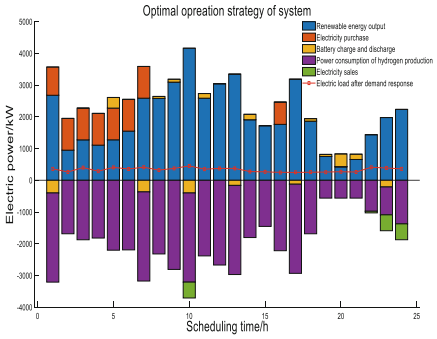

Fig. 10. Electric power optimal operation strategy

7.5 Hydrogen Load Supply Situation

The hydrogen load supply is shown in Fig. 12. The green curve represents the real-time change of hydrogen in the hydrogen storage tank during the 24-h dispatching period, the red curve represents the change of hydrogen load during the 24-h dispatching period, and the blue curve represents the real-time change of hydrogen production of

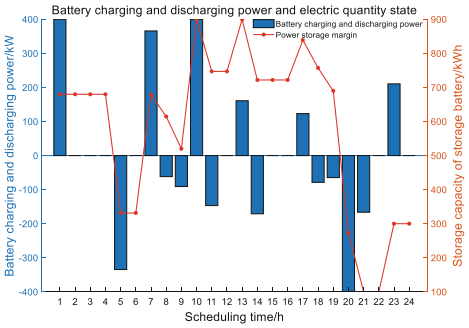

Fig. 11. Battery charging and discharging power and electric quantity status

the hydrogen production system during the 24-h dispatching period. During the period 1–7, the hydrogen production of the hydrogen production system has excess hydrogen load. The excess hydrogen is stored in the hydrogen storage tank. It can be seen that the hydrogen in the hydrogen storage tank has been increasing. During the period 8, the hydrogen load has excess hydrogen production. At this time, the hydrogen in the hydrogen storage tank makes up for the hydrogen load. There is little difference between the hydrogen load and the hydrogen production during the period 9–13. In the period 14–21, except for the period 18, the hydrogen load is more than the hydrogen output, and the hydrogen load is far more than the hydrogen output in the period 15 and 19. In this period, the hydrogen load in the hydrogen storage tank is used to supplement the hydrogen load, the hydrogen load in the period 22–23 is nearly equal to the hydrogen output, and the hydrogen output in the period 24 is more than the hydrogen load, It can be seen that the hydrogen storage tank plays a role in maintaining the stability of hydrogen load during the whole dispatching period.

The capacity status of the hydrogen storage tank is shown in Fig. 13. It can be seen that the initial capacity proportion of the hydrogen storage tank is 0.25. When the hydrogen production of the hydrogen production system exceeds the hydrogen load, the hydrogen capacity status in the hydrogen storage tank will increase, otherwise it will decrease. In the last period of the dispatching period, the capacity status of the hydrogen storage tank will return to the initial capacity proportion, ensuring the normal and stable operation of the hydrogen storage tank in the next dispatching cycle.

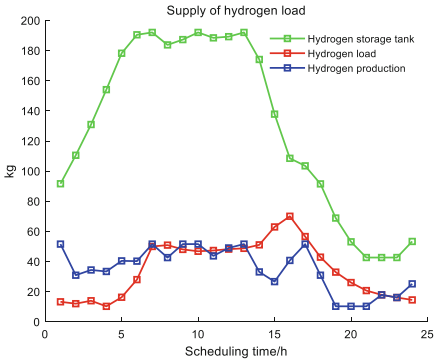

Fig. 12. Hydrogen load supply situation

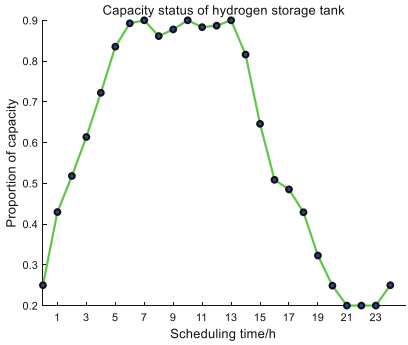

Fig.13. Capacity status of hydrogen storage tank

8 Conclusion

This paper takes the hydrogen production system from renewable energy sources (H2-res) as the research object, fully considers the uncertainty of wind and solar output and the flexible load of electric load, and establishes a two-stage distributed robust optimization model. In the first stage, the system economy is taken as the optimization objective to determine the capacity of the hydrogen production system. The second stage takes the system operation cost as the goal, aims to optimize the real-time scheduling of the system, and uses the CCG algorithm to solve it. Finally, an example is given to verify the effectiveness of the proposed model, and the following conclusions are drawn:

(1) Different from the previous two-stage distributed robust optimization of pre scheduling and re scheduling of microgrid system, this paper is the static configuration of H2-RES system considering the uncertainty of wind and solar output and the two-stage distributed robust optimization model of system dynamic scheduling based on static configuration.
(2) The flexible load of electric load is considered in the operation optimization of H2-RES system, which can reduce the cost of dispatching scheme and improve the economic benefit of the system.

(3) By considering the wind solar output scenario under the worst scenario, the capacity of the hydrogen production system obtained through the iteration of the algorithm is very close to the actual project, which can provide practical application value.

Acknowledgement. This research was supported by the Science and Technology Plan Project of Hebei Province of China (Grant No. 19210108D, 19214501D, 20314501D, F2021202022).

References

1. Wang, Y., Guo, C., Chen, X., Jia, L., Guo, X., Chen, R., Zhang, M., Chen, Z., Wang, H.: Carbon peak and carbon neutrality in China: goals, implementation path and prospects. China Geol. **4**(04), 720–746 (2021)
2. Chen, S., Kumar, A., Wong, W.C., Chiu, M.S., Wang, X.N.: Hydrogen value chain and fuel cells within hybrid renewable energy systems: advanced operation and control strategies. Appl. Energy **269**, 321–337 (2019). https://doi.org/10.1016/j.apenergy.2018.10.003
3. He, X., Wang, F., Wallington, T.J., Shen, W., Melaina, M.W., Kim, H.C., et al.: Well-to-wheels emissions, costs, and feedstock potentials for light-duty hydrogen fuel cell vehicles in China in 2017 and 2030. Renew. Sustain. Energy Rev. **137**, 110477 (2021). https://doi.org/10.1016/j.rser.2020.110477
4. Xu, X., Xu, B., Dong, J., Liu, X.: Near-term analysis of a roll-out strategy to introduce fuel cell vehicles and hydrogen stations in Shenzhen China. Appl. Energy **196** (2016)
5. Shao, Q.: Analysis of future development trend of hydrogen energy production with water electrolysis technology. Int. Core J. Eng. **8**(1) (2022)
6. Tooryan, F., Hassanzadeh Fard, H., Dargahi, V., Jin, S.: A cost-effective approach for optimal energy management of a hybrid CCHP microgrid with different hydrogen production considering load growth analysis. Int. J. Hydrogen Energy **47**(10) (2022)
7. Hou, P., Enevoldsen, P., Eichman, J., et al.: Optimizing investments in coupled offshore wind—electrolytic hydrogen storage systems in Denmark. J. Power Sour. **359**, 186–197 (2017)
8. Bakhtiari, H., Naghizadeh, R.A.: Multi-criteria optimal sizing of hybrid renewable energy systems including wind, photovoltaic, battery, and hydrogen storage with ε-constraint method. IET Renew. Power Gener. **12**(8) (2018)
9. Si, Y., Chen, L., Ma, L., Gao, M., Ma, H., Mei, S.: Modeling the heat-hydrogen balance characteristic of hydrogen energy storage and cooperative dispatch of wind-hydrogen hybrid system. Front. Energy Res. (2021)
10. Wang, X., Li, B., Wang, Y., Lu, H., Zhao, H., Xue, W.: A bargaining game-based profit allocation method for the wind-hydrogen-storage combined system. Appl. Energy **310** (2022)
11. Liu, J., Zhou, C., Gao, H., et al.: A day-ahead economic dispatch optimization model of integrated electricity-natural gas system considering hydrogen-gas energy storage system in microgrid. Power Syst. Technol. **42**(1), 170–178 (2018)
12. Hong, Z., Wei, Z., Han, X.: Optimization scheduling control strategy of wind-hydrogen system considering hydrogen production efficiency. J. Energy Storage 103609 (2022)
13. Fang, R.: Multi-objective optimized operation of integrated energy system with hydrogen storage. Int. J. Hydrogen Energy **44**(56) (2019)
14. Deng, J., Jiang, F., Wang, W., et al.: Low-carbon optimized operation of integrated energy system considering electric heating flexible load and hydrogen energy refined modeling. Power Syst. Technol. 1–12 (2022). https://doi.org/10.13335/j.1000-3673.pst.2021.1373

15. Nojavan, S., Akbari Dibavar, A., Farahmand Zahed, A., Zare, K.: Risk-constrained scheduling of a CHP-based microgrid including hydrogen energy storage using robust optimization approach. Int. J. Hydrogen Energy **45**(prepublish) (2020)
16. Pan, G., Gu, W., Qiu, H., et al.: Bi-level mixed-integer planning for electricity-hydrogen integrated energy system considering levelized cost of hydrogen. Appl. Energy **270**, 115176 (2020)
17. Zhang, X., Liu, X., Zhong, J.: Integrated energy system planning considering a reward and punishment ladder-type carbon trading and electric-thermal transfer load uncertainty. Proc. CSEE **40**(19), 6132–6142 (2020). https://doi.org/10.13334/j.0258-8013.pcsee.191302
18. Li, X., Wang, W., Wang, H.: A novel bi-level robust game model to optimize a regionally integrated energy system with large-scale centralized renewable-energy sources in Western China. Energy **228** (2021)
19. Al Hajri, I., Ahmadian, A., Elkamel, A.: Stochastic day-ahead unit commitment scheduling of integrated electricity and gas networks with hydrogen energy storage (HES), plug-in electric vehicles (PEVs) and renewable energies. Sustain. Cities Soc. **67**(prepublish) (2021)
20. Hou, J., Yu, W., Xu, Z., Ding, S.: Distributionally robust optimal dispatching of integrated energy system with flexible electrical/thermal load. Electr. Meas. Instrum. 1–10 (2022). http://kns.cnki.net/kcms/detail/23.1202.TH.20211019.1225.004.html
21. Korpas, M., Holen, A.T.: Operation planning of hydrogen storage connected to wind power operating in a power market. IEEE Trans. Energy Convers. **21**(3) (2006)
22. El-Taweel, N.A, Khani, H., Farag, H.E.Z.: Hydrogen storage optimal scheduling for fuel supply and capacity-based demand response program under dynamic hydrogen pricing. IEEE Trans. Smart Grid **10**(4) (2019)
23. Gokcek, M., Kale, C.: Techno-economical evaluation of a hydrogen refuelling station powered by wind-PV hybrid power system: a case study for İzmir-Çeşme. Int. J. Hydrogen Energy **43**(23), 10615–10625 (2018)

Capacity Optimization of Hybrid Energy Storage System in Microgrid

Yanwei Jing[1], Zhihao Zhao[2], Wen Jiang[3], and Tao Liang[2(✉)]

[1] Hebei Construction & Investment New Energy Group Co., Ltd., Shijiazhuang 050006, China
[2] School of Artificial Intelligence, Hebei University of Technology, Tianjin 300130, China
liangtao@hebut.edu.cn
[3] Jointo Energy Investment Co., Ltd. Hebei, Shijiazhuang 050051, China

Abstract. A hydrogen fuel station is an infrastructure for commercializing hydrogen energy using fuel cells, especially in the automotive field. Hydrogen, produced through microgrid systems of renewable energy sources such as solar and wind, is a green fuel that can greatly reduce the use of fossil fuels in the transportation sector. In this study, taking the Winter Olympics as the background, hydrogen production was carried out through the wind-solar hybrid microgrid system installed in Chongli, Zhangjiakou, so as to meet the fuel supply of hydrogen buses during the Winter Olympics. This analysis is the capacity optimization configuration design of the microgrid including the hydrogen production system, and the simulation analysis is carried out by using the Homer simulation software. In this study, NASA's ground-based meteorology and solar databases were used. Therefore, the annual average wind speed of the site is 5.72 m/s, and the annual average solar radiation is 5.08 kWh/m^2/d. According to the optimization results obtained for the proposed configuration, different system configuration schemes are found, and a variety of schemes are compared to select the most economical capacity configuration scheme. It was finally shown that a microgrid including a hydrogen production system powered by renewable energy is economically feasible.

Keywords: Microgrid · Energy storage system · Hydrogen energy storage · Storage battery · HOMER Pro software

1 Research Status

1.1 Research Status of Microgrid Capacity Optimization Configuration

In recent years, with the construction of complementary microgrid optimization projects, my country has overcome many technical difficulties in energy. In the energy development stage, the "Eleventh Five-Year Plan for Energy Development" in 2007 proposed a renewable energy industrialization project [1], by reducing construction costs and adopting renewable energy as a key development technology on a large scale. Make full use of the abundant renewable energy sources such as wind energy, solar energy, biomass energy, etc., to drive the development of energy industrial production, and realize the scope construction. This is also the first time that the "distributed energy supply system"

H. Sun et al. (Eds.): WHTC 2023, SPPHY 393, pp. 244–268, 2024.
https://doi.org/10.1007/978-981-99-8631-6_26

has been identified as the key to develop cutting-edge technologies. In terms of electric energy, the energy system adopts the dispatching method to realize the interactive operation between renewable energy such as wind and light and the energy storage system. In terms of electric energy demand, the complementary electric energy system realizes the co-generation of cooling, heating and electricity, and configures and operates in an optimal way according to the load demand, so as to realize the coordinated operation between energy sources [2]. In 2016, the country proposed the "Internet+" smart energy model, and the development time was determined in the interval of 2016–2030 [3]. Therefore, in the future, the complementary model will occupy an extremely important position in energy utilization.

In the aspect of capacity optimization design of microgrid, many scholars have made in-depth research on it. Qi Yan and other scholars have used intelligent algorithms such as the improved gray wolf algorithm and particle swarm algorithm to study the scheduling problem and economic optimization of the microgrid system from the perspective of intelligence, so as to obtain the optimal solution of the microgrid [4, 5]. Due to the late start of microgrid technology and related technologies have not yet matured, the investment in technology will generate huge costs, so economy is the key inspection criterion [6, 7]. Shao Zhifang and other scholars comprehensively considered the power supply side and the load side, studied the configuration optimization of the coordinated operation of the supply and demand sides of the off-grid microgrid, and obtained the configuration result with the minimum cost of the distributed microgrid system [8]. Zhang Zhiwen et al. took the remote areas of Guizhou as the background, and studied the capacity optimization configuration scheme of wind, solar, water, and storage power stations [9]. Tan Ying and other scholars have achieved the goal of reducing pollutant emissions by introducing renewable energy on the basis of diesel generators [10].

1.2 Research Status of Hydrogen Energy Technology

Hydrogen energy is a green and efficient secondary energy, so in the future, hydrogen energy will inevitably become an important part of my country's energy structure. At the same time, the relevant links of hydrogen production, hydrogen storage and hydrogen consumption have great economic value. As an intermediate medium, hydrogen energy can realize the conversion between electric energy and other energy sources. It is an ideal energy medium and can realize large-scale application of energy storage medium in the future [11].

A large number of foreign scholars and researchers use hydrogen as a renewable resource to generate energy savings. Hydrogen is a novel energy storage method. By combining with wind power and photovoltaic power generation systems, the impact of distributed power generation systems on the power grid can be improved [12, 13]. In remote mountainous areas, traditional resources cannot guarantee power quality, and the investment cost is high. As an energy carrier and conversion medium, hydrogen has the advantages of hydrogen-hydrogen refueling station-hydrogen bus construction.

The United States is the first country to use hydrogen and fuel cells as energy sources. Around the 1960s and 1970s, the United States had put forward the concept of "hydrogen economy". The United States has solved a series of technical problems in the hydrogen industry through a large amount of human and financial investment. In 1990, the United

States formulated the "Five-Year Plan for Hydrogen Energy Research and Development", and in 1996, the "Hydrogen Energy Prospects Act" was promulgated, with the purpose of creating the universality of hydrogen energy. In 2012, US President Barack Obama submitted a financial plan totaling 3.8 trillion US dollars, of which 6.3 billion yuan was used for the development and construction of hydrogen energy, automotive alternative fuels and other projects. As of 2019, the United States has adopted hydrogen fuel vehicles as commercial vehicles, and at the same time has invested heavily in related hydrogen energy innovations. A series of events have proved that the hydrogen energy industry occupies an extremely important position in the energy development of the United States.

The EU is also one of the early regions involved in the field of hydrogen energy, and the EU has taken hydrogen energy as an important guarantee for energy security and transformation. In 1956, the University of Cambridge invented the total temperature alkaline fuel cell, which opened the prelude to the development of fuel cells. The EU has promulgated a series of policies to ensure the development and construction of the hydrogen energy industry, and plans to reach 33% of power generation by renewable energy in 2020, 45% by 2030, and 50% by 2040., the proportion of power generation will reach 97% in 2050 [14]. In 2011, Germany built the world's first wind-hydrogen power station with a power generation scale of 6 MW. In 2013, the German Audi company built a 6-megawatt E-Gas power conversion hydrogen project, marking that Audi became the world's first automobile company to use renewable energy. In 2019, Germany invested a total of 250 million euros in research on hydrogen energy vehicle projects, and plans to build 400 hydrogen energy filling stations by 2030.

China is also a big country in the use of hydrogen energy. In the "Energy Technology Revolution Innovation Action Plan (2016–2030)" [25], hydrogen energy has been classified as a key project of the energy technology revolution, and the construction and development of the hydrogen energy industry has also been included in my country. Energy strategy: My country has always focused on replacing some fossil fuels such as coal and oil by abandoning wind, water and other renewable energy sources, which can reduce costs and improve stability, which is more conducive to the construction of the hydrogen energy industry system and the construction of a national hydrogen energy industry network.

The continuous development of hydrogen energy technology has not only carried out in-depth research in key laboratories of universities, but also built a large number of hydrogen energy industry demonstration projects. In terms of hydrogen energy demonstration projects, it is mainly for applications in distributed power generation and new energy vehicles. Up to now, the number of hydrogen energy stations in operation in China has reached 14, which are located in Shanghai, Beijing, Guangdong and other places, and the first hydrogen refueling station in China that uses wind-solar hybrid electrolysis of water to produce hydrogen has been in Dalian has been completed, and the scale level has reached 70 MPa, which can provide energy for hydrogen vehicles in the three northeastern provinces [15].

2 Microgrid Structure and Modeling Research

2.1 Microgrid Structure

Complementary microgrid is based on the characteristics of various distributed power sources to perform joint power generation, thereby effectively avoiding the disadvantage of poor reliability of a single power source. Through the differences in the output characteristics of distributed power sources such as wind power generation, photovoltaic power generation and lithium-ion batteries, they are combined into a complementary micro-grid system to ensure that the output power of the micro-grid remains balanced at various time periods and under different conditions, and improve the micro-grid. System stability: The complementary microgrid takes its own structural characteristics as a reference, and obtains the effects of the lowest total cost, the best power supply reliability and stability. Figure 1 is the microgrid architecture diagram of the research object of this paper. Among them, wind turbines and solar cells are the main power sources of the system, which are set to maintain the maximum output power all the time, and the lithium-ion battery system is the backup power supply of the system. When the output of wind turbines and solar cells is insufficient, the stable operation of the microgrid system is guaranteed.

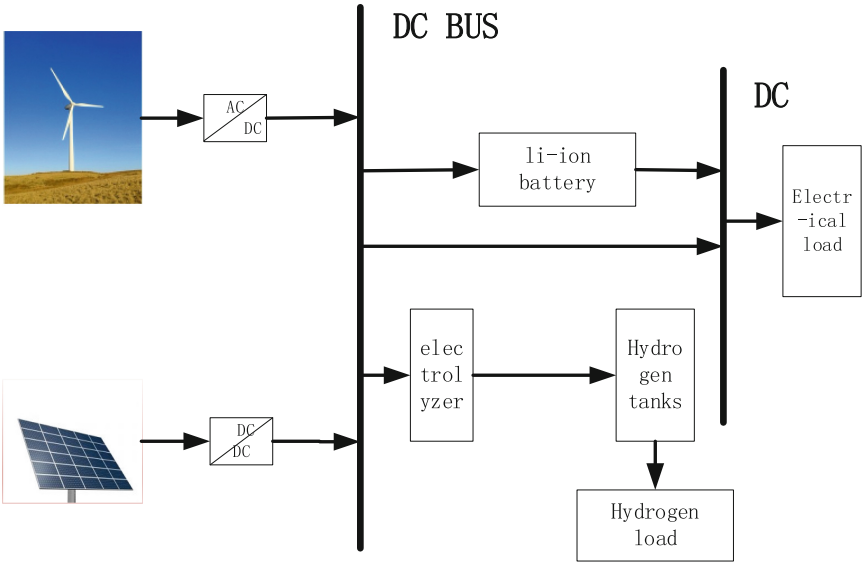

Fig. 1. Overall structure of the wind-solar-hydrogen integrated microgrid system

2.2 Distributed Power Model

2.2.1 Fan Model

Wind power generation is a process of energy conversion. First, wind energy is converted into mechanical energy of a motor by a fan and then converted into electrical energy. At present, three-phase permanent magnet synchronous generators are mostly used in small wind power generation systems, and grid-connected generators such as double-feedback asynchronous generators, cage asynchronous generators, and permanent magnet synchronous generators are also widely used [16].

The size of the wind speed directly determines the power generation of the wind turbine, because the wind resource has relatively large fluctuation and randomness. At present, domestic and foreign scholars have carried out a lot of research on the distribution of wind speed, among which the most representative is the two-parameter Weibull distribution model [17]. This model has a good fit to the wind speed, and the probability density formula is as follows:

$$f(v) = \frac{k}{c}(\frac{v}{c})^{k-1} \cdot \exp\left[-(\frac{v}{c})^{k}\right] \tag{1}$$

where: v represents the wind speed here; k represents the Weibull shape factor, $k > 0$; c represents the Weibull scale parameter, $c > 1$; v_c represents the cut-out wind speed; v_e represents the rated wind speed.

The Weibull shape factor, the scale parameter is calculated as follows:

$$f(v) = \frac{k}{c}(\frac{v}{c})^{k-1} \cdot \exp\left[-(\frac{v}{c})^{k}\right] \tag{2}$$

$$c = \overline{v}/[\Gamma(1 + 1/k)] \tag{3}$$

where σ represents the standard deviation; $\overline{v}$ represents the average wind speed; Γ represents the Gamma function.

The functional relationship between the output power of the wind turbine and the wind speed can be obtained as the output power function [4]:

$$P_{WT}(v) = \begin{cases} 0, & 0 \le v < v_{ci} \\ P_r \frac{v - v_{ci}}{v_r - v_{ci}}, & v_{ci} \le v < v_r \\ P_r, & v_r \le v < v_{\infty} \end{cases} \tag{4}$$

In the formula: P_{WT} represents the real-time power generated by the fan; v represents the real-time wind speed; v_{ci} represents the cut-in wind speed; v_{∞} represents the cut-out wind speed; v_r represents the rated wind speed.

Fans are mainly divided into two categories: fixed pitch fans and variable pitch fans. The pitch of the fixed pitch fan cannot be changed, so when the actual wind speed is greater than the rated wind speed, the power output of the fan will decrease instead; since the variable pitch fan can change its own pitch, when the wind speed is greater than the rated wind speed, its output power remains rated Power does not change. In this paper, the variable pitch fan is selected as the research object (Table 1; Fig. 2).

Table 1. Air fan parameters

Number	Fan parameters	Value
1	Rated capacity	2 MW
2	Rotor diameter	82 m
3	Control mechanism	Pitch control
4	Rotor type	Reverse wind rotor
5	Hub height	85 m

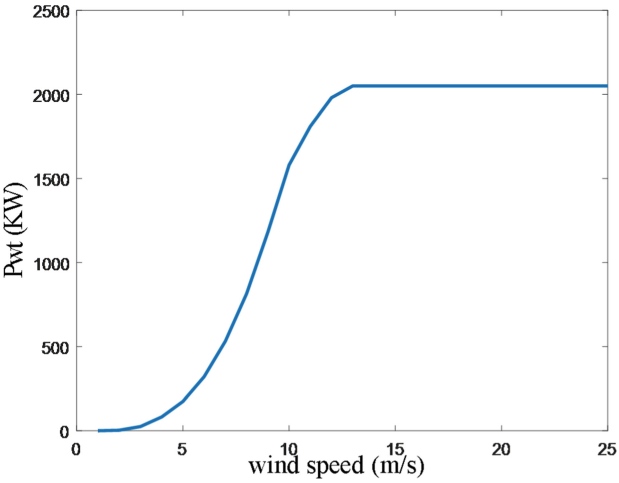

Fig. 2. Power output curve of the wind power generator

2.2.2 Photovoltaic Model

As a kind of renewable energy, solar energy comes from the energy generated by the continuous nuclear fusion reaction inside the sun [18]. It can be regarded as a kind of energy with huge reserves and no pollution. With the continuous consumption of fossil resources, photovoltaic power generation has received more and more attention due to its cleanliness and pollution-free. Photovoltaic power generation has the characteristics of safety, no resource consumption, random installation, and simple construction. The principle of solar photovoltaic power generation is to use the photovoltaic effect (Photovoltaic effect) [19] generated when semiconductor materials receive light, thereby converting light energy into direct current electricity.

There are many factors that affect the output power of photovoltaic cells, such as light intensity, temperature of photovoltaic cells, panel shadows, etc. [30]. The output power of photovoltaic cells is as follows:

$$P_{pv}(t) = P_{STC}\frac{L_C(t)}{L_{STC}}[1 + \mu(T_C - T_{STC})] \tag{5}$$

In the formula: P_{pv} represents the actual power generated by the solar photovoltaic panel; P_{STC} represents the rated power of the solar photovoltaic panel; L_C represents the current ambient light intensity; L_{STC} represents the light intensity in the ideal environment, 1 kW/m^2; μ represents the power temperature coefficient, − 0.0047 °C; T_C represents the solar photovoltaic panel during operation Surface temperature; T_{STC} indicates the surface temperature of the solar photovoltaic panel in an ideal environment.

Among them, the comprehensive calculation of real-time temperature and light intensity is adopted through the HOMER Pro simulation software, as follows:

$$T_C = T_a + (T_{C,noct} - T_{a,noct})(\frac{G_T}{G_{T,noct}})(1 - \frac{\eta_c}{\tau a}) \tag{6}$$

In the formula, T_a represents the actual temperature; $T_{C,noct}$ represents the photovoltaic panel temperature under the rated state; $T_{a,noct}$ represents the actual temperature defined by NOCT; G_T represents the light intensity; $G_{T,noct}$ represents the light intensity defined by NOCT; η_c represents the efficiency of the solar photovoltaic panel; τ, a indicates the care for the penetration and absorption rate of solar photovoltaic panels.

2.2.3 Lithium-Ion Battery

The service life and discharge degree of a lithium-ion battery have a great relationship with the number of times the battery is charged and discharged. The degree of discharge of the battery is the ratio of the amount of electricity released by the battery to the rated capacity, expressed by. Usually the condition is less than or equal to 80% to prolong the life of the battery. The state of charge represents the ratio between the battery capacity and the rated capacity of the battery in a steady state at a temperature of 25 °C, and is generally expressed. The state of charge of the lithium battery is constantly changing dynamically, and its state of charge will calculate the amount of electricity consumed or absorbed in the previous period and update it at each time point.

The state-of-charge formula for charging and discharging a lithium-ion battery is shown in. The relationship between the state of charge and the depth of discharge is shown below.

$$SOC(t+1) = SOC(t) - \frac{P_{BAT}(t) \cdot \Delta t}{Q_R \cdot \eta_{dis}} \quad P_{BAT}(t) \geq 0 \tag{7}$$

$$SOC(t+1) = SOC(t) - \frac{P_{BAT}(t) \cdot \Delta t}{Q_R \cdot \eta_{ch}} \quad P_{BAT}(t) \leq 0 \tag{8}$$

$$DOD = 1 - SOC \tag{9}$$

In the formula, $SOC(t+1)$, $SOC(t)$ represents the state of charge of the lithium ion battery at $t+1, t$; $P_{BAT}(t)$ represents the charge and discharge power of the lithium ion battery per unit time, the value during charging is less than 0, and the value during discharging is greater than 0; η_{dis} represents the discharge efficiency of the lithium ion battery; η_{ch} represents The charging efficiency of a lithium-ion battery; Q_R is the rated capacity of the battery.

2.2.4 Electrolyzer Model

The working process of the electrolytic cell is a redox reaction, which conforms to the law of conservation of matter. In the process of electrolysis of water, 96485.31 C of electricity will be consumed for every 1 mol of electron change. Therefore, the amount of gas produced by the electrolysis process is positively related to the current. The alkaline solution is only to improve the conductivity of the solution, and does not participate in the actual electrolysis process, so it will not produce consumption.

According to the formula, it can be concluded that 1 unit of hydrogen is generated by electrolysis and 2 units of electrons are transferred. The specific relationship between the rated power of the electrolyzer and the hydrogen content is expressed as follows:

$$P_{N-ele} = \frac{Q_N \cdot 2 \cdot N_A}{V_M \cdot C_O \cdot 3600} V_N \frac{1}{\eta_{ele}} \tag{10}$$

$$Q = \frac{P_{\tan k}}{P_{N-ele}} Q_N \tag{11}$$

In the formula: P_{N-ele} is the rated power of the electrolysis process of the electrolytic cell; Q_N is the rated hydrogen production rate; $P_{\tan k}$ is the equivalent power of volume hydrogen; N_A is the constant 6.021023; V_M is the molar volume, 24.5 L/mol; η is the electrolytic cell efficiency of 75%.

2.2.5 Hydrogen Storage Tank Model

The hydrogen storage tank is a device that stores the hydrogen produced by the electrolyzer and provides fuel for the fuel cell. The hydrogen storage tank is generally composed of a container, a valve, a hydrogen storage material, and a gas guiding structure. The hydrogen storage method of the hydrogen storage tank has the advantages of large capacity and high safety factor. By electrolyzing water to produce hydrogen from excess electrical energy, it not only reduces the charging and discharging pressure of batteries in the microgrid, but also can store hydrogen to meet the use of hydrogen. The specific energy conversion relationship:

$$P_{el-\tan k}(t) = P_{gen-el}(t) \times \eta_{el} \tag{12}$$

In the formula, $P_{el-\tan k}(t)$ represents the energy of hydrogen charged in the time hydrogen storage tank, $P_{gen-el}(t)$ represents the excessive power generation in the microgrid and the energy flowing to the electrolyzer, η_{el} is the efficiency of the alkaline electrolyzer.

2.2.6 Converter Model

As a device that converts electrical energy, converters are generally divided into DC/AC inverters, DC/DC choppers, AC/DC rectifiers, AC/DC/AC voltage conversion and frequency conversion, etc. [20]. The use of current transformers can meet the input and output requirements of distributed power and energy storage equipment.

In the microgrid system, wind turbines and solar photovoltaics can generate alternating current and direct current, and the converter can convert the electric energy to

alternating current and direct current. In the entire microgrid system, converters are required between the supply and demand of equipment to ensure the power exchange between AC and DC system components. The capacity expression of the converter is shown below.

$$P_{inverter} = \frac{E_{load,\max}}{\eta_{inverter}} \tag{13}$$

In the formula: $E_{load,\max}$ represents the maximum load in the microgrid; $\eta_{inverter}$ represents the power conversion efficiency of the converter, and the calculation formula is as follows.

$$\eta_{inverter} = \frac{P_{out}}{P_{in}} \tag{14}$$

When the converter is working, the input electrical power will be consumed as the energy inside the device, and no power will be generated. An electrical power proportional to the input is then output. When the rated power is reached, the output will be limited due to temperature and its own limitations. When the input is too large, the output power remains unchanged, and the efficiency is reduced by the formula. The converter selected in this paper has a conversion efficiency of 90%.

3 Optimization Objectives and Constraints

3.1 Optimization Goals

In this microgrid system, the optimization objective is selected as the total net present cost of the system (Net Present Cost, NPC).

Total System Cost

The total net cash cost of the system refers to the difference between the total cost and the benefit obtained in the whole life cycle of the microgrid. The cost of microgrid mainly includes initial equipment investment, operation cost, replacement consumption, fuel consumption cost, environmental pollution control cost and power grid purchase cost. The total benefit of the microgrid is the grid-connected benefit of the residual value of equipment and excess electricity. The microgrid system in this paper is an off-grid type and does not require an external power grid. Moreover, the distributed power sources in the microgrid system are all renewable and clean energy sources, and there is no environmental pollution problem. Therefore, the pollution emission penalty can be ignored in the net cash cost of this system. Compared with the power purchase cost of the power grid, only four parts are considered: the investment cost of the equipment in the system, the operation and maintenance cost, the replacement cost and the equipment residual [21].

The total net cash cost of the microgrid system is:

$$C_{NPC} = C_{CNPC} + C_{RNPC} + C_{SNPC} + C_{OMNPC} \tag{15}$$

In the formula, C_{CNPC} represents the investment cost of related devices in the microgrid; C_{RNPC} represents the replacement cost of the device in the microgrid; C_{SNPC} represents the residual value of the device in the microgrid; C_{OMNPC} represents the operation and maintenance cost of the device in the microgrid.

3.2 Constraints

3.2.1 Equipment Operation Constraints

(1) Power generation constraints of the fan system

$$0 \le P_{WT} \le P_{WT.\max} \tag{16}$$

In the formula, represents the maximum generating power of the fan system.

(2) Power generation constraints of photovoltaic solar panels

$$0 \le P_{PV} \le P_{PV.\max} \tag{17}$$

In the formula, represents the maximum power generation of photovoltaic solar panels.

(3) Li-ion battery output power and SOC constraints

$$SOC_{\min} \le SOC(t) \le SOC_{\max} \tag{18}$$

$$-P_{bat.d\max} \le P_{bat} \le P_{bat.c\max} \tag{19}$$

$$SOC(t+\Delta t) = SOC(t) - \frac{\eta_{bat} P_{bat}(t)\Delta t}{E_{bat}} \tag{20}$$

In the formula: $SOC_{\min}$, $SOC_{\max}$ respectively represent the minimum and maximum state of charge of the lithium-ion battery; $P_{bat.c\max}$, $P_{bat.d\max}$ respectively, represent the maximum charge and discharge power of the lithium-ion battery; η_{bat} represent the conversion efficiency of the lithium-ion battery; E_{bat} represent the lithium-ion battery capacity; Δt represent the time step.

3.2.2 Capacity Constraints of Microgrid-Related Equipment

$$S_{WT.\min} \le S_{WT} \le S_{WT.\max} \tag{21}$$

$$S_{PV.\min} \le S_{PV} \le S_{PV.\max} \tag{22}$$

$$S_{BAT.\min} \le S_{BAT} \le S_{BAT.\max} \tag{23}$$

$$S_{HESS.\min} \le S_{HESS} \le S_{HESS.\max} \tag{24}$$

$$S_{CON.\min} \le S_{CON} \le S_{CON.\max} \tag{25}$$

In the formula: $S_{WT.\max}$, $S_{WT.\min}$ respectively represent the maximum and minimum capacity of the fan system; $S_{PV.\max}$, $S_{PV.\min}$ respectively represent the maximum and minimum capacity of the photovoltaic solar panel; $S_{BAT.\max}$, $S_{BAT.\min}$ respectively represent the maximum and minimum capacity of the lithium-ion battery; $S_{HESS.\max}$, $S_{HESS.\min}$ respectively represent the hydrogen energy storage system capacity The maximum and minimum values; $S_{CON.\max}$, $S_{CON.\max}$ represent the maximum and minimum values of the converter capacity.

3.3 Comparison of Hydrogen Production Capacity and Gasoline Production Capacity

In this paper, the use of hydrogen generated by wind and solar resources can effectively reduce the demand for gasoline, thereby greatly reducing the production of carbon dioxide, carbon monoxide and other particulate matter. According to the lower heating value of hydrogen and gasoline fuel [22], the microgrid system is calculated. The consumption of gasoline (kg) that can be replaced by the hydrogen produced, the specific calculation relationship is as follows:

$$M_{GFuel} = \frac{M_{H_2} \times LHV_{H_2}}{LHV_{GFuel}} \tag{26}$$

where: represents the annual hydrogen production of the microgrid system; represents the minimum heating value of hydrogen (119.9 MJ/kg) [23], and represents the minimum heating value of gasoline (43.4 MJ/kg) [24].

Therefore, the annual emissions of carbon dioxide and carbon monoxide that can be reduced by hydrogen production in the microgrid system are expressed as follows:

$$A_{CO_2} = M_{GFuel} \times SE_{CO_2} \tag{27}$$

$$A_{CO} = M_{GFuel} \times SE_{CO} \tag{28}$$

In the formula:, respectively represent the specific emission factors of carbon dioxide and carbon monoxide in the combustion process of gasoline, in which the emission coefficient of carbon dioxide is 2.3 kg per kilogram of gasoline, and the emission coefficient of carbon monoxide is 0.00766 kg per kilogram of gasoline [25].

4 Simulation Results and Analysis

4.1 Introduction of HOMER Simulation Software

The HOMER simulation software is developed by the US Department of Energy Renewable Energy Laboratory (NREL) based on C/C++. It has been widely used in microgrid systems and distributed power sources in renewable energy. HOMER contains a large number of ready-made models, mainly including wind turbine models, solar photovoltaic models, grid models and load models, and operators can build new models according to their own needs. The biggest advantage of this simulation software is that it can convert the microgrid system model built by the operator into a set of related schemes, and use the scheme sensitivity to analyze, and can conduct simulation on the investment situation, energy and capital flow conditions in the simulation on the premise of actual operation. Simulation: After building the microgrid system model, the operator can use the HOMER software to obtain the capacity configuration with the lowest net cash cost, and perform data analysis on the required results [22, 26]. HOMER simulation software has the following features.

(1) System simulation

The characteristic of HOMER software is that it can simulate the system model. By simulating a system, the operator can obtain the model of the combination of various equipments. By setting different parameters, HOMER software can generate a large number of simulated systems. The operator can set the time step of the simulation according to the needs, which is generally between 1 min and 1 h. During the simulation process, the software takes into account the investment cost of the equipment. Operation and maintenance costs. Replacement costs and environmental treatment costs, etc.; finally obtain the corresponding system configuration results, the cost ratio of each equipment, the proportion of power generation, the operation of the equipment, etc.

(2) Process optimization

The HOMER software considers all possible combinations during operation and ranks the system results according to the selected optimization variables. Due to the "no-derivative" algorithm, the design process of determining the minimum cost of the microgrid system can be greatly simplified, and the simulation optimization results of the system will be arranged in an increasing manner according to the total net cash cost.

(3) Sensitivity analysis

Under normal circumstances, the built system is relatively complex, and the operator cannot master all aspects of the system. Therefore, a large number of simulations and comparisons are required to better understand the importance of some variables and parameters. HOMER software has a sensitivity analysis function, which can provide the operator with the functions of all variables, such as light intensity, wind speed, etc., and can also understand the changes of various variables and parameters in the microgrid system under the optimal state conditions. At present, HOMER software has become the software of choice when many foreign scholars study the economics of distributed energy and microgrid.

4.2 HOMER Software Principle and Evaluation Index

4.2.1 Software Principle

HOMER simulation software has now been widely used in the planning and construction of smaller-scale microgrid systems. In the construction of the model, the first step is to select the constituent equipment and models in the microgrid system, such as fan systems, photovoltaic solar panels, electrolyzers, hydrogen storage tanks, energy storage batteries, etc.; in the second step of the model system Input of relevant parameters, such as the local geographical location of the research object, natural resources such as wind and light, the relevant cost of the equipment in the system, and the service life, etc.; Finally, through simulation, various combination schemes and each equipment in the system can be obtained. Sensitivity analysis can also be used to obtain the influence of different parameter conditions on the capacity configuration results of the microgrid system. For the situation that cannot be run, the HOMER simulation software will give specific adjustment parameters [26]. The flow chart of the calculation principle of the simulation software is shown in Fig. 3.

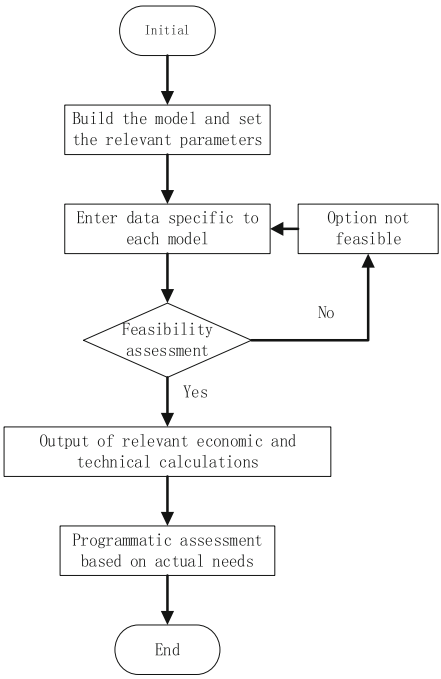

Fig. 3. Flowchart of software calculation principle

4.3 Microgrid System Modeling Based on HOMER Software

4.3.1 Optimal Capacity of Microgrid System

Taking Chongli, Zhangjiakou as the research object, the capacity allocation optimization of the microgrid system is carried out through the timing load and local wind and solar resources. The installed capacity of the hydrogen storage tank and the installed capacity of the converter.

$$S = [S_{WT}, S_{PV}, S_{BAT}, S_{ELE}, S_{HT}, S_{CON}] \tag{4.1}$$

where: S_{WT} represents the installed capacity of the fan system; S_{PV} represents the installed capacity of the solar photovoltaic system; S_{BAT} represents the installed capacity of the lithium-ion battery energy storage system; S_{ELE} represents the installed capacity of the electrolyzer; S_{HT} represents the installed capacity of the hydrogen storage tank; S_{CON} represents the installed capacity of the converter.

4.3.2 Microgrid System Structure

In this paper, Zhangjiakou Chongli (latitude: 40.5; longitude: 114.5; altitude: 1200 m; the test wind speed altitude is 10 m) is used as the research object. The specific local data are shown in Table 2. Build a simulation structure through the HOMER simulation software, and set relevant parameters: the power of the electrical load is 2400 kWh/d,

of which the peak power is 183.32 kWh/h, and the demand of the hydrogen load is 730 kg/d, of which the peak demand is 72.11 kg/h; The initial capacity of the hydrogen storage tank is 80%, the initial capacity of the lithium-ion battery is 80%, the minimum capacity is 30%, and the working efficiency of the electrolyzer is 75%. The life of the simulated system is 35 years, the maximum allowable power shortage rate is 0.5%, the actual annual interest rate is 8%, and the expected expansion rate is 2%. The load following strategy (LC) and the cyclic charging strategy (CC) are adopted. Controls the run strategy.

Table 2. Local scenery and natural resources of the study subjects

Month	Solar light intensity (kWh/m^2/day)	Wind speed (m/s)
1	2.73	6.55
2	3.66	6.40
3	4.80	6.88
4	5.96	7.35
5	6.34	6.54
6	6.31	5.37
7	5.69	4.63
8	5.16	4.41
9	4.68	5.07
10	3.79	6.09
11	2.84	6.62
12	2.37	6.82

According to Table 2, it can be concluded that the local wind energy and sunlight resources of the research object are sufficient, and a micro-grid system with wind turbine system and solar photovoltaic power generation based on renewable energy can be built. In this microgrid system, the installed capacity of the distributed power generation is restricted by its own volume and floor area, and the optimal variables of the microgrid system are in the range of (units), kW, kg, and kW. Other equipment variables in the microgrid system are not constrained, and the given equipment optimization variables are optimally configured and combined within the specified variation range. Figure 4 shows a typical local daily load curve. The cost parameters of related equipment in the microgrid system are shown in Table 3.

According to the data in Table 2, the HOMER simulation software is used to obtain the discrete data of local wind energy, light resources and load throughout the year. The discrete annual hourly wind speed data and light intensity data are shown in Figs. 5 and 6. The obtained discrete data is used as the input data of the system simulation, and the system simulation is carried out.

In the HOMER simulation software, by referring to the inputted microgrid system parameters, load data and the local wind speed, light intensity and other data of the

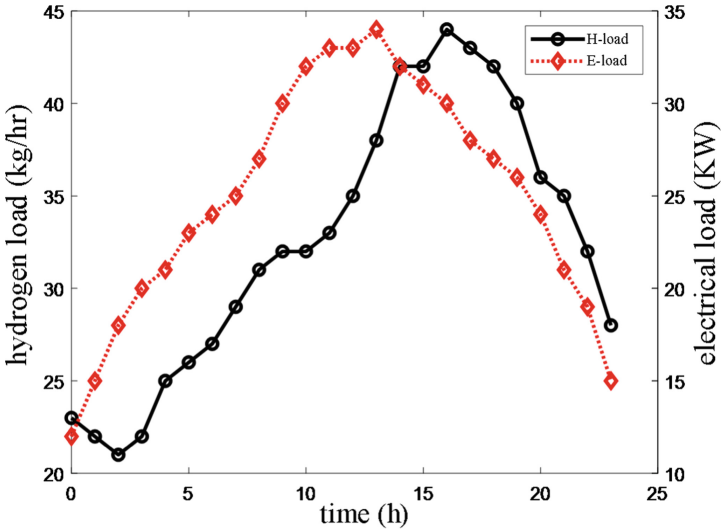

Fig. 4. Typical daily load curve

Table 3. Cost parameters of the equipment related to the microgrid

Equipment	Installation cost	Replacement cost	Operation & maintenance cost (year)	Life
Wind turbine generator (Yuan)	9500000	7000000	600000	20
Photovoltaic cell (Yuan/kW)	4300	3500	25	15
Lithium-ion battery (Yuan)	45000	30000	700	6
Electrolytic tank (Yuan/kW)	5000	4000	400	10
Hydrogen storage tank (Yuan/kg)	6000	5000	300	25
Converter (Yuan/kW)	3000	2500	200	13

research object, the power generation of the distributed power generation in the microgrid system for 8760 h in a year can be obtained. The hourly power generation is compared with the load. The simulation step size of each hour not only proves the accuracy of the simulation optimization results, but also reduces the calculation time of the optimization process. The discrete hourly load data for the whole year are shown in Figs. 7 and 8.

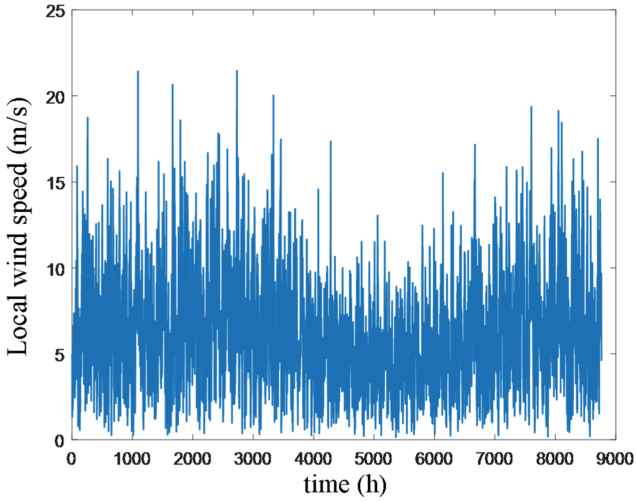

Fig. 5. Hourly wind speed data for the year after discrete

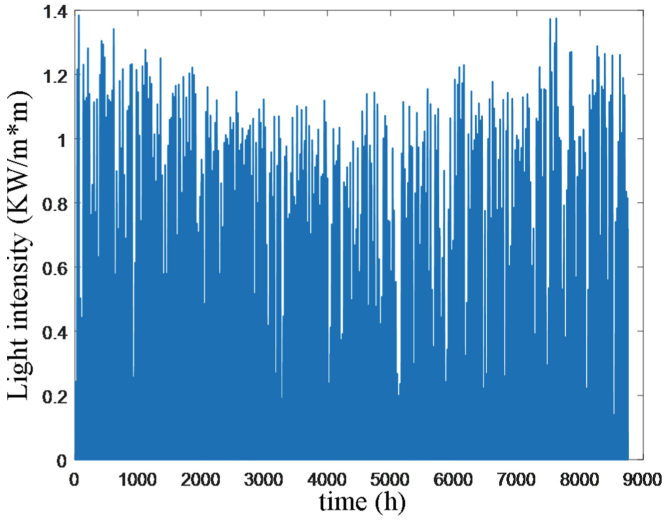

Fig. 6. Data on hourly light intensity for the year after discrete

4.4 System Simulation Results and Analysis

4.4.1 Optimization Results and Analysis

Compared with other professional optimization software, HOMER simulation software simulates with the conditions set in advance, arranges the simulation results and the size of the net cash cost, and outputs the equipment configuration scheme required by the load, and the configuration scheme of the final equipment optimization results. As shown in Table 4.

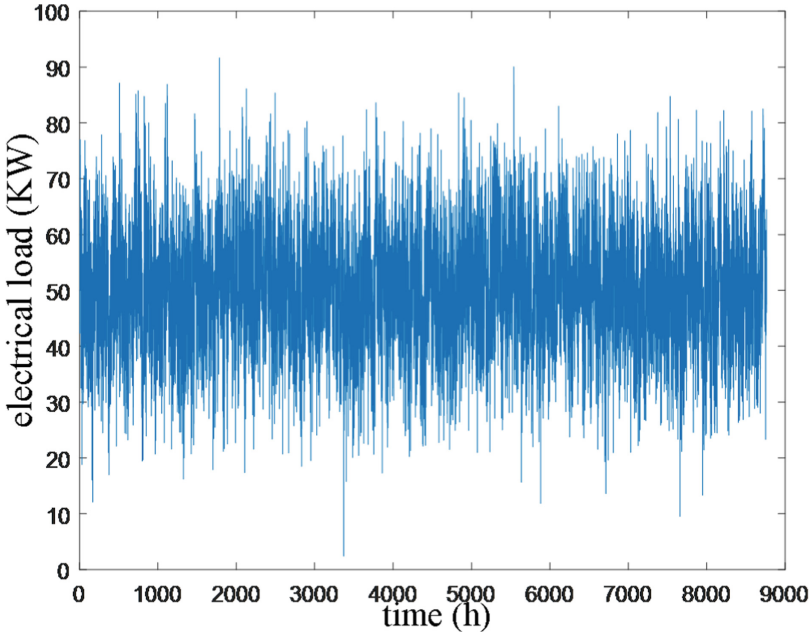

Fig. 7. Electric load data for the full year after discrete

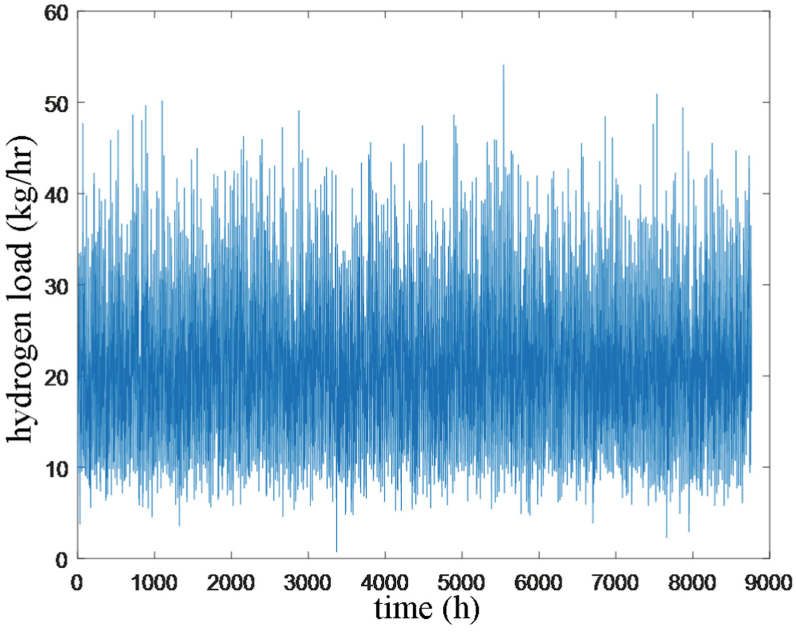

Fig. 8. Hydrogen load data for the full year after discrete

Table 4. Capacity configuration results of the microgrid system

Project	1	2	3	4
Wind turbine generator (table)	2	4	2	2
Solar PV cell (kW)	2000	–	2000	2500
Lithium-ion battery (block)	86	86	108	1000
Electric tank (kW)	2800	2700	3000	950
Hydrogen container (kg)	600	600	600	450
Changer (kw)	2682	2292	2786	692
Control strategy	LF	LF	CC	CC
Total net and present cost (one million yuan)	138.75	155.38	145.04	3908
Investment cost (one million yuan)	57.12	65.85	59.42	2565
Operation & maintenance cost (one million yuan)	52.87	61.43	54.58	743.3
Renewable energy utilization rate is (%)	100	100	100	100

From Table 4, it can be concluded that after the HOMER simulation software sets specific conditions and performs system simulation, the optimal combination scheme of microgrid system equipment is 2 wind turbines, 2000 kW solar photovoltaic battery, and 2000 kW lithium-ion battery capacity. 86 pieces, electrolyzer capacity 2800 kW, hydrogen storage tank capacity 600 kg converter 2682kW, system control operation strategy is load following control strategy. In this scenario, the total net cash cost of the microgrid system is 138.75 million yuan. In all simulation schemes, the utilization rate of renewable energy is 100% because they are based on wind energy and solar energy, which ensures the non-polluting of the microgrid system, which is in line with the "carbon peak and carbon neutrality" advocated by the current society. Dual carbon policy.

In the optimal system configuration scheme, the electric energy in the microgrid is mainly supplied by wind energy and solar energy jointly, but in other combination schemes, the electric energy is only supplied by wind energy or solar energy alone. A microgrid system where energy sources are mixed for power supply has more economic advantages than a single system. In the microgrid system, the distributed power generation units are all renewable resources. With the continuous development of distributed renewable power technology, the corresponding microgrid costs will continue to decline, so the integrated microgrid system technology has a very broad development. Prospect: From the results of the scheme in Table 4, the total net cash cost of the optimal scheme and the capacity configuration of the related equipment in the microgrid system can be obtained. The summary chart of the cash flow of the microgrid system according to different investment cost types of the optimal scheme is shown in Fig. 9. As shown in the figure, it can be concluded that in the initial investment cost, wind turbines account for the largest proportion of 38.28%, the investment cost of solar photovoltaic cell systems accounts for 14.85%, and the investment cost of electrolyzers accounts for 23.82%. The investment cost of the hydrogen storage tank accounted for 9.92%, the investment cost

of the converter accounted for 8.25%, and the investment cost of the lithium-ion battery energy storage system accounted for 4.88%. It is comprehensively explained that the wind turbine system occupies most of the investment cost in the microgrid system, so it is also the main power generation unit of the microgrid system.

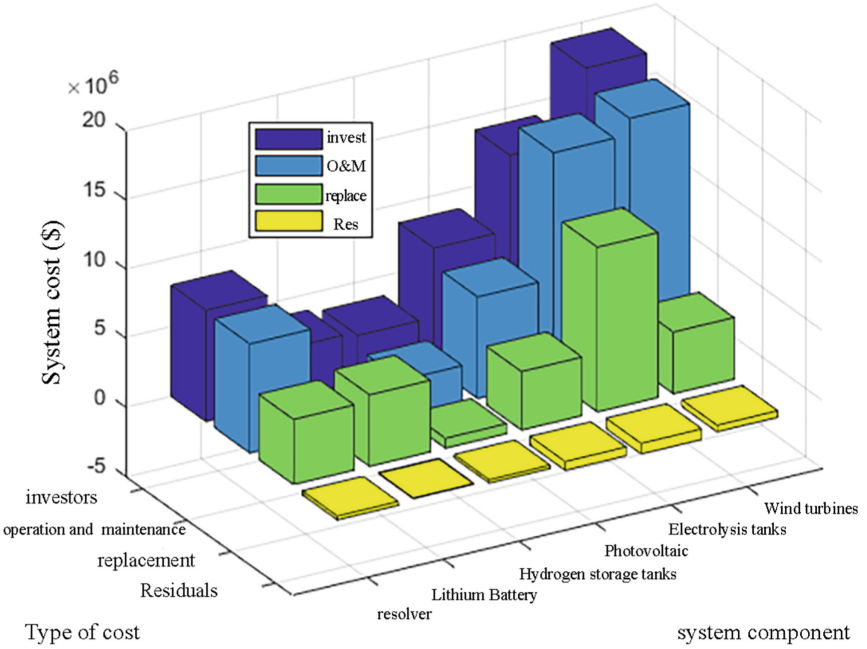

Fig. 9. Summary of system cash flow distinguished by cost type

From Fig. 9, it can be clearly seen that, except for the lithium-ion battery energy storage system, the initial investment cost of related equipment in the microgrid system is far greater than the maintenance and replacement costs of the equipment. The maintenance cost and replacement cost of the lithium-ion battery energy storage system are far greater than the initial investment cost, which is completely different from the total cost distribution of other related equipment. The initial investment cost, replacement cost and operation and maintenance cost of the lithium-ion battery energy storage system account for the proportion of its own total investment cost is 23.69%, 42.28% and 34.03% respectively. The replacement cost of the fan system and the solar photovoltaic cell system is far greater than the operation and maintenance cost of the equipment.

Figure 10 shows the cash summary of the microgrid system according to the operating years. It can be concluded that the initial investment in the microgrid system is 13.96 million yuan, the equipment replacement cost is 3.777 million yuan, the operation and maintenance cost is 139,700 yuan, and the system recovery cost is 173.5 10,000 yuan, Fig. 10 shows the cash flow of the hybrid microgrid system over its useful life.

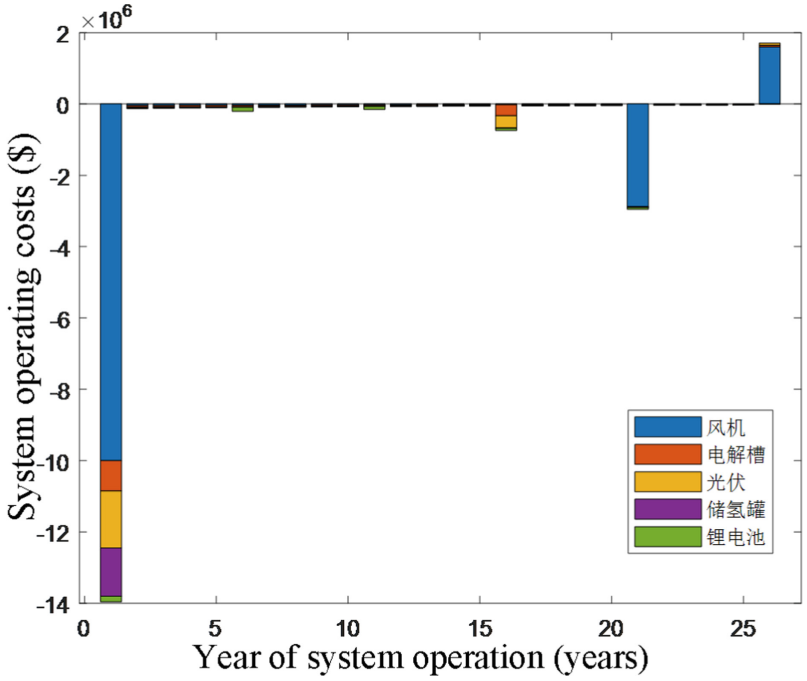

Fig. 10. Annual cash flow by component

4.4.2 Optimum Scheme Determination and Analysis

On the premise of the known wind energy, light energy resources and the specific cost of related equipment, the simulation software has made the best equipment configuration plan: 2 wind turbines, 2000 kW solar photovoltaic battery capacity, 86 lithium-ion battery capacity, Electrolyzer capacity 2800 kW, hydrogen storage tank capacity 600 kg and converter 2682 kW. In the optimal combined configuration system, the power generation amount and the power generation proportion of the relevant power generation units in the system operation for one year are shown in Table 5. From the data in the table, it can be concluded that the power generation proportion of the wind turbine system is 80.6%, and the solar photovoltaic power generation proportion is 80.6%. The power generation of the battery accounts for 19.4%, which is far less than the power generation of the wind turbine system. Therefore, the wind turbine plays the main role of power generation in the microgrid system.

The output of the power generation unit in each month of the year is shown in Fig. 11. From the figure, the output of the power generation unit in each month can be obtained. The output of the wind turbine system is much larger than that of the photovoltaic cell. However, the output of photovoltaic cells is greatly affected by the environment. From June to September, the power generation of photovoltaic cells accounts for a larger proportion than other times of the year. The power generation ratio of wind turbines is relatively small from June to September compared with other times. Therefore, the wind-solar complementary power generation method can make up for the volatility and

Table 5. Power generation and proportion of power generation units of the microgrid system

Equipment	Power generation (kWh/year)	Power generation ratio is (%)
Solar photovoltaic cell system	3690613	19.4
Wind turbine system	15382070	80.6
Aggregate	19072683	100

intermittent shortcomings of natural resources to a certain extent, and ensure sufficient power generation. Ensure the stable operation of the microgrid system. Figures 12 and 13 show the heat maps of wind turbines and solar photovoltaic cells in the microgrid system at different times of the year. From Fig. 12, it can be concluded that in spring and winter, the power generation output of wind turbines is relatively sufficient, which is more in line with the local wind energy situation of the research object. From Fig. 13, it can be concluded that the power generation of solar photovoltaic cells in a day varies greatly, generally concentrated between 11:00 and 14:00. In the horizontal time span, solar photovoltaic cells generate more electricity during summer than at other times.

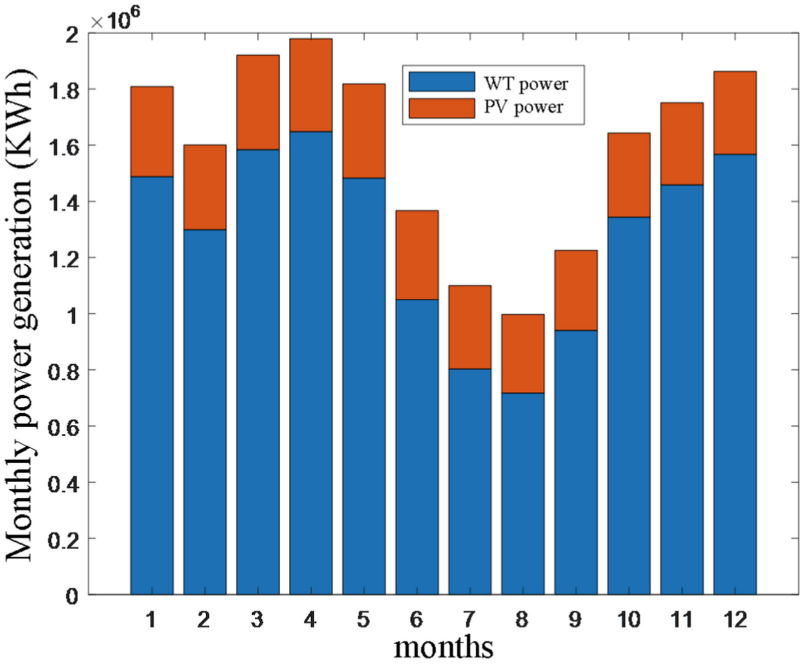

Fig. 11. Monthly power generation of the system components in the optimal configuration

When the simulation software is used to configure the capacity of the microgrid, the hydrogen storage level of the hydrogen storage tank and the SOC state change of the lithium-ion battery in the system for 8760 h in a year are obtained, which are shown in

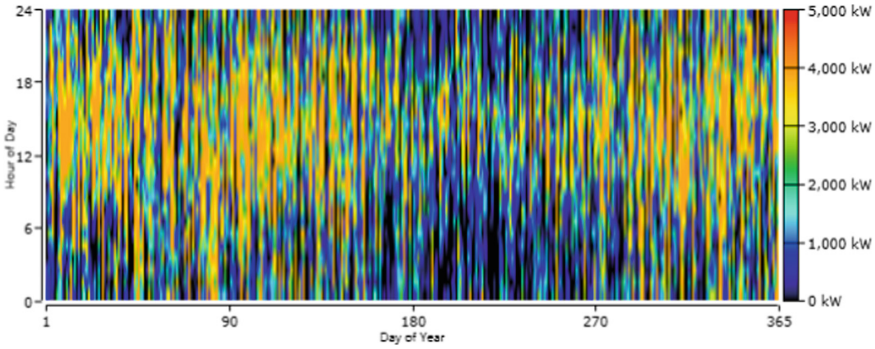

Fig. 12. Heat map of wind turbine

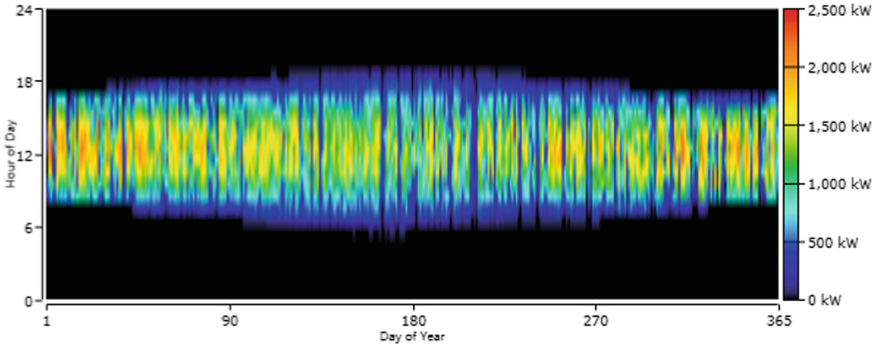

Fig. 13. Heat map of power generation of solar photovoltaic cells

Figs. 14 and 15, respectively. From the pictures, it can be seen that the hydrogen storage capacity of the hydrogen storage tank in summer and autumn is less than that in spring and winter, but the hydrogen storage capacity of the system can well meet the hydrogen demand of the hydrogen filling station, which proves that the relevant capacity selection of the system is correct. The overall level of the SOC state of lithium-ion batteries in summer and autumn is lower than that in spring and winter. Therefore, compared with the two seasons of summer and autumn, the power supply in spring and winter is more abundant, and the reliability of power supply of the system is more stable.

4.5 Hydrogen's Ability to Replace Gasoline and Reduce Carbon Emissions

From the hydrogen produced by the microgrid system, the amount of gasoline that can be replaced with hydrogen as a transport fuel can be calculated. From this, it is possible to calculate the amount of carbon dioxide and carbon monoxide emissions that can be reduced by using hydrogen as a fuel. The specific results are shown in the following table. According to the data in the table, the use of hydrogen as fuel can replace 495.21 tons of gasoline every year, which can lead to a reduction of 1138.98 tons and 3.80 tons of carbon dioxide and carbon monoxide emissions respectively. It can greatly reduce

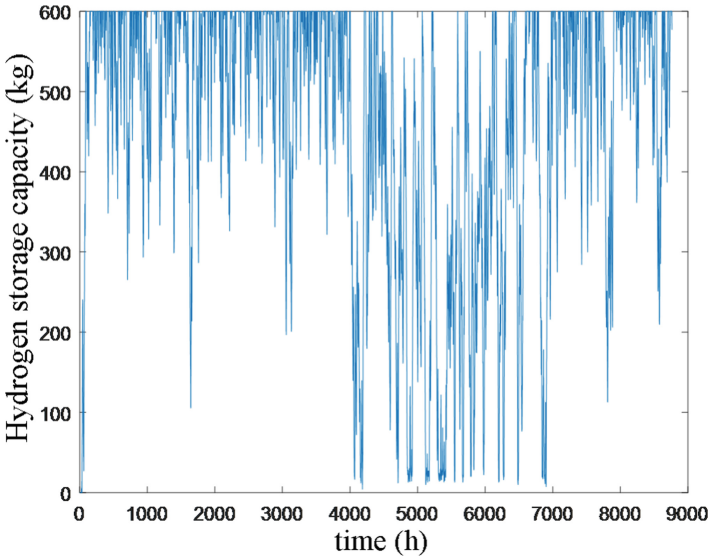

Fig. 14. Hydrogen storage capacity of hydrogen storage tank

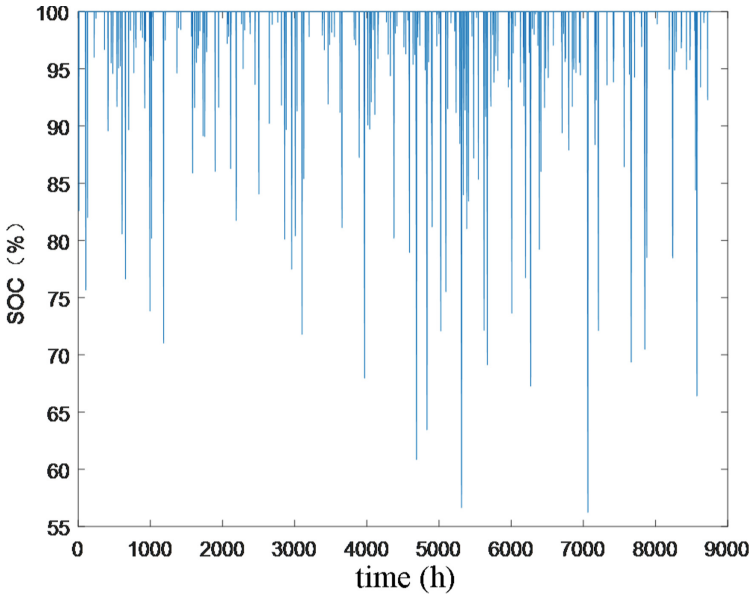

Fig. 15. Annual SOC change of lithium battery

carbon emissions, which is more in line with the “dual carbon” policy advocated by the government (Table 6).

Table 6. Annual gasoline replacement and carbon emission reduction

Hydrogen production (ton/year)年)	Gasoline replaced (ton/year)	CO_2 reduction (ton/year)	CO reduction (ton/year)
264.89	495.21	1138.98	3.80

5 Conclusion

In this study, the simulation results show that the optimized hybrid microgrid system consists of 2000 kW photovoltaic modules, 2 wind turbines, 86 batteries, 2682 kW inverter, 2800 kW electrolyzer and 600 kg hydrogen tank. The total net cash cost and renewable energy utilization rate of the optimized microgrid system are 138.75 million yuan and 100%, respectively. In this way, the supply of hydrogen bus fuel during the Winter Olympics is guaranteed, and it is also in line with the dual-carbon policy of "carbon peaking and carbon neutrality" advocated by the current society. At the same time, the annual hydrogen production of the micro-grid system can replace the use of 495.21 tons of gasoline, and it is expected to reduce carbon dioxide and carbon monoxide emissions by 1,138.98 tons and 3.80 tons, respectively.

References

1. Du, X.: Interpretation and thinking of my country's "Energy Production and Consumption Revolution Strategy (2016–2030)". China Econ. Trade Tribune (15), 44–45 (2017)
2. Qi, Y., Shang, X., Nie, J., Huo, X., Wu, B., Su, W.: Operation optimization of combined cooling, heating and power microgrid based on improved multi-objective gray wolf algorithm. Electr. Meas. Instrum. 1–10 (2022)
3. Peng, C., Xie, P., Zhan, J., Sun, H.: Robust economic scheduling of microgrids based on improved bacterial foraging algorithm. Power Grid Technol. **38**(09), 2392–2398 (2014)
4. Pan, W., Li, J., Fang, K.: An optimization method for independent microgrid capacity allocation considering subsidies. Power Grid Technol. **42**(07), 2206–2213 (2018)
5. Wang, C., Liu, Y., Li, X., et al.: Energy management system for stand-alone diesel-wind-biomass microgrid with energy storage system. Energy **97**, 90–104 (2016)
6. Fan, H., Yu, Y., Zhang, Y.: Multi-time-scale optimization of island microgrid. Modern Electron. Technol. **44**(07), 32–36 (2021)
7. Yu, D., Zhang, J., Wang, X., Gao, Y.: Capacity optimization of grid-connected wind-solar-storage hybrid power generation system. J. Electr. Power Syst. Autom. **31**(10), 59–65 (2019)
8. Shao, Z., Zhao, Q., Zhang, Y.: Optimization of independent microgrid source-load coordination configuration. Power Grid Technol. **45**(10), 3935–3946 (2021)
9. Zhang, Z., Fan, W., Liu, J., Zhou, T., Shi, J.: Capacity optimization of wind-solar-water-storage hybrid power generation system in remote mountainous areas. J. Power Sour. **16**(05), 138–146 (2018)
10. Tan, Y., Lv, Z., et al. Stand-alone micro-grid distributed generator optimization with different battery technologies. In *The 34th China Control Conference*
11. Hassan, Z., et al.: Optimal hybrid renewable energy design in autonomous system using modified electric system cascade analysis and Homer software. Energy Convers. Manag. **126**, 909–922 (2016)

12. Srinivas, Ch.L.S., Sreeraj, E.S.: A maximum power point tracking technique based on ripple correlation control for single phase photovoltaic system with fuzzy logic controller. Energy Procedia **90** (2016)
13. Suresh, V., Muralidhar, M., Kiranmayi, R.: Modelling and optimization of an off-grid hybrid renewable energy system for electrification in a rural areas. Energy Rep. **6** (2020)
14. Liu, X.: Analysis of main types and application technologies of wind turbines. Electr. Manuf. **45**(09), 18–20 (2009)
15. Cai, G., Xi, Y., Wang, Y., Yang, D., Chen, J.: Feature analysis and probability distribution optimal modeling of wind speed and wind power output in Heilongjiang region. J. Solar Energy **40**(11), 3250–3257 (2019)
16. Yu, J.: Optimal configuration and operation control of electricity-hydrogen multi-energy complementary microgrid. Southwest Jiaotong University (2019)
17. Dai, H.: Improving the photoelectric conversion efficiency of photovoltaic cells. China New Commun. **18**(11), 94–95 (2016)
18. Ju, S.: Research on the optimal design of multi-energy complementary community microgrid. Dalian University of Technology (2021)
19. Siyal, S.H., Mentis, D., Howells, M.: Economic analysis of standalone wind-powered hydrogen refueling stations for road transport at selected sites in Sweden. Int. J. Hydrogen Energy **40**, 9855e65 (2015)
20. Dincer, I., Acar, C.: Review and evaluation of hydrogen production methods for better sustainability. Int. J. Hydrogen Energy **40**(34), 11094e111 (2015)
21. Liu, B., Huang, X., Li, J.: Optimal configuration of island microgrid power supply considering time-shiftable loads. Chin. J. Electr. Eng. **34** No. 504(25), 4250–4258 (2014)
22. Engineering_toolbox: Fuels—higher and lower calorific values, p. 1e2 (2021). Accessed 16 Feb 2021
23. Ayodele, T.R., Ogunjuyigbe, A.S.O.: Increasing household solar energy penetration through load partitioning based on quality of life: the case study of Nigeria. Sustain. Cities Soc. **18**, 21e31 (2015)
24. Yan, G., Tan, X., Li, J., Wang, Z., Gao, Y.: Planning and geographical site selection of photovoltaic combined power generation system. Electr. Measur. Instrum. **52**(20), 15–19+26 (2015)
25. Dorrah, H.T., El-Rahman, N.M.A., Fahmy, F.H., El-Madany, H.T.: Optimization and feasibility analysis of satellite earth station power system using Homer. Telkomnika Telecommun. Comput. Electron. Control **10**(2) (2012)
26. Mekonnen, A.: Optimal configuration of photovoltaic/wind power grid-hybrid system based on Homer software. J. Energy Sci. **1**(8) (2019)

Multivariate Based Alkaline Electrolyzer Digital Twin Model Construction

Tao Liang[1], Zicong Liu[1(✉)], Hexu Sun[2], and Jianxin Tan[3]

[1] School of Artificial Intelligence, Hebei University of Technology, Tianjin 300130, China
2656107095@qq.com
[2] School of Electrical Engineering, Hebei University of Science and Technology, Shijiazhuang 050018, China
[3] Hebei Construction & Investment New Energy Group Co, Ltd., Shijiazhuang 050006, China

Abstract. Electrolytic water hydrogen production systems are highly coupled and operate under complex and dangerous conditions, making it difficult to carry out extreme experiments on physical objects. In this paper, the alkaline electrolyzer is studied and mathematical and three-dimensional models are developed for it. The System operation data shows that temperature, pressure and alkaline flow rate all have effects on the hydrogen concentration in oxygen and voltage. Among them, hydrogen concentration in oxygen is one of the important factors affecting the safety of the system, and changing both pressure and alkali flow rate respectively will cause significant changes in hydrogen concentration. Based on the system operation data, a multivariate nonlinear fitting of the empirical equation using Matlab was performed to establish the voltage model, Faraday efficiency model, hydrogen concentration in oxygen model and system pressure model of the alkaline electrolyzer. And the model simulation results were analyzed and verified theoretically, which were consistent with the actual engineering. The mathematical model of the alkaline electrolyzer is combined with the 3D model, and the digital twin model of the alkaline electrolyzer is controlled in real time by PLC. The mapping of the alkaline electrolyzer in the virtual space is realized, which provides an experimental platform for the subsequent study of wide power fluctuation.

Keywords: Alkaline electrolyzer · Digital twins · Mathematic model · Multivariate · Nonlinear

1 Introduction

As the "ultimate energy source for mankind", hydrogen energy has the advantages of high calorific value, recyclability, cleanliness and non-pollution, which have strengthened the position of hydrogen energy in the future energy system in various countries [1]. Globally, more and more cities are actively adopting hydrogen strategies, and the development and innovation of hydrogen production technology is in full swing [2, 3]. "Green hydrogen, which is produced by powering electrolytic cells with renewable energy sources such as wind and light, is favored by scholars worldwide because of its low cost and zero carbon emission [4, 5]. The alkaline solution with high capacity and low cost is widely used

H. Sun et al. (Eds.): WHTC 2023, SPPHY 393, pp. 269–280, 2024.
https://doi.org/10.1007/978-981-99-8631-6_27

to produce hydrogen by electrolysis [6], but due to the randomness and fluctuation of wind and light, the safety parameters of the system will exceed the critical value after acting directly on the alkaline electrolyzer, and the efficiency of hydrogen production will be greatly reduced by frequent starting and stopping, so the alkaline electrolyzer is not well adapted to the wide power fluctuation of renewable energy sources. In order to better study the control strategy to adapt to the wide power fluctuation, it is necessary to build a high-power alkaline electrolytic water hydrogen production digital twin system to realize the virtual mapping of the hydrogen production system in order to test the safe and stable operation conditions of the alkaline electrolyzer with wide power.

Alkaline electrolyzers with wide power fluctuations can reduce the efficiency of hydrogen production and increase the hydrogen content in oxygen of the system, thus increasing the danger of the system, and a lot of studies have been conducted at home and abroad to investigate the factors affecting the hydrogen concentration in oxygen. Zhang et al. [7] found that the system pressure can affect the hydrogen content in oxygen by experimenting with a 250 kW electrolyzer, and the electrolyzer can be operated stably at a wide power range of 30–100% by adjusting the system pressure, but they did not compare the effects of other process parameters. Ning et al. [8] conducted an experimental study on the electrolyzer with wide power from the perspective of safety and showed that proper adjustment of lye flow could stabilize the hydrogen content in oxygen within the safety range, but the system pressure was not considered. In order to study the control method of wide power, the establishment of mathematical model of the electrolyzer is particularly important. Fang et al. [9] proposed and simulated a control strategy for a modular switching electrolyzer based on the empirical equation given by Ulleberg [10], and the simulation results showed that this control strategy improved the hydrogen production rate. Ulleberg [10] established a thermal model and a mathematical model of the alkaline electrolyzer based on thermodynamics, heat transfer and electrochemical theory, and this model is applicable and has been widely used in the study of mathematical models of electrolytic cells. However, Ulleberg only considered the effect of temperature and ignored the effect of other factors on the electrolyzer. Mónica et al. [12] added the effect of system pressure to Ulleberg's model and developed a semi-empirical mathematical model for a 15KW electrolyzer, but this literature did not consider the alkaline flow rate, which was shown to have an effect on the hydrogen content in oxygen [8, 14]. Jiang et al. [11] developed a digital twin model of an alkaline electrolyzer based on experiments and principles with temperature as a variable, but did not visualize and control the model results in real time.

In this paper, the alkaline electrolyzer is studied and its mathematical model and three-dimensional model are established. The mathematical model includes voltage model, Faraday efficiency model, hydrogen concentration in oxygen model and system pressure model. The voltage model and the hydrogen concentration in oxygen model not only consider the pressure and temperature, but also take into account the alkali flow rate which has a great influence on both of them; the alkali flow rate is also used as one of the variables in the Faraday efficiency model, but the influence is very small. In this paper, a three-dimensional model of the hydrogen production system is also developed, since few studies have shown the mathematical model more visually and have controlled and tested it in a simple way. Therefore, a more accurate mathematical model of the alkaline

electrolyzer is developed, simulated and validated, and finally combined with the 3D model to form a digital twin model of the alkaline electrolyzer.

2 Alkaline Electrolyzer Digital Twin Model Framework

The digital twin model of the alkaline electrolyzer will be divided into a physical object layer, a data acquisition and control entity layer, an alkaline electrolyzer digital twin core entity layer, and an alkaline electrolyzer digital twin model application layer. The layers are interconnected with each other and progress towards the electrolyzer digital twin model layer by layer. The framework of the digital twin model of the alkaline electrolyzer is shown in Fig. 1.

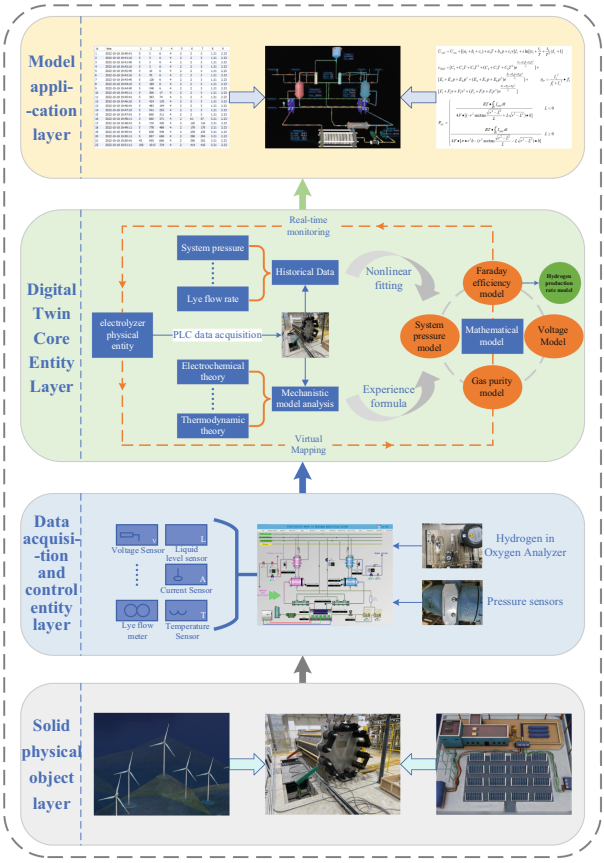

Fig. 1. Alkaline electrolyzer digital twin model framework

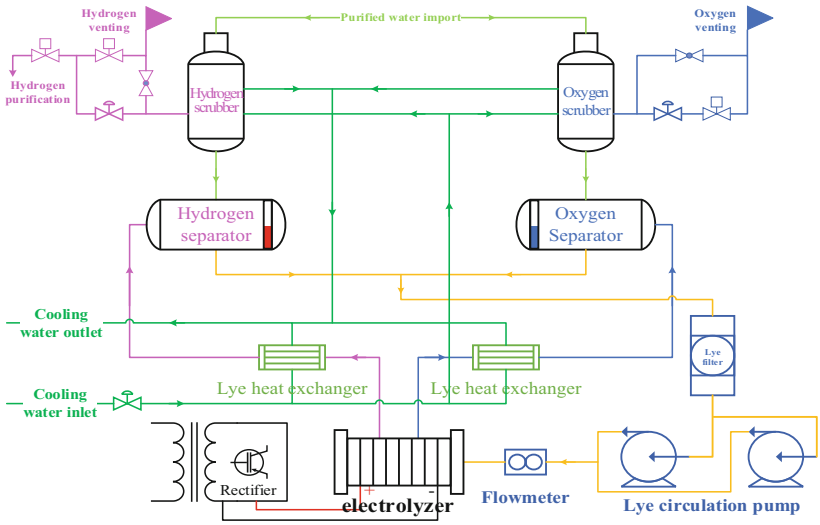

Fig. 2. Process flow chart of electrolytic water to hydrogen system

2.1 Alkaline Electrolyzer Digital Twin Model Hierarchy

The physical object layer is the physical object of the alkaline electrolytic cell. The hydrogen production system of electrolytic water studied in this paper mainly includes alkaline electrolytic cell, gas-liquid separation and post-processing system. The process diagram of the hydrogen production system of electrolytic water is shown in Fig. 2. The power supply supplies direct current to the electrolytic cell, and the gas produced by the alkaline electrolytic cell flows to the gas separator and scrubber through the alkaline liquid heat exchanger. The lye brought out by the gas is returned to the electrolytic cell through the lye filter under the action of the lye circulating pump. The data acquisition and control entity layer is the various sensors and control flow in the hydrogen production system of electrolytic water. This paper focuses on the core entity layer of digital twins. The established mathematical model is tested in the virtual simulation platform, and the model is controlled and verified by PLC. Finally, the running data are transmitted to the three-dimensional model in real time to realize the construction of the digital twin application layer of the hydrogen production system.

2.2 Mathematical Modeling Framework for Alkaline Electrolyzer

The mathematical modeling process of alkaline electrolyzer integrates the methods of mechanism modeling and data modeling, updates the empirical equation based on experimental data and theoretical analysis, and then uses the operational data of the hydrogen production system to fit the empirical equation nonlinearly, and finally establishes the mathematical model of alkaline electrolyzer.

The mechanism modeling is based on the operation mechanism of the alkaline electrolyzer, the derivation and demonstration of the equations using the knowledge in the

field of electrochemistry. The final mathematical model is suitable for the studied alkaline electrolyzer.

3 Alkaline Electrolyzer Digital Twin Model Construction

3.1 Alkaline Electrolyzer Mathematical Model Construction

Modeling of alkaline electrolyzer voltage characteristics

The most commonly used voltage model was proposed in 2003 by Ulleberg [10], who derived an empirical equation for the voltage model of alkaline electrolyzers based on thermodynamics and electrochemical properties of alkaline electrolyzers, as shown in Eq. (1):

$$U = U_{rev} + \frac{r_1 + r_2 T}{A} I + s \ln\left(\frac{t_1 + t_2/T + t_3/T^2}{A} I + 1\right) \tag{1}$$

where U_{rev} is the reversible voltage, T is the bath temperature, I is the given current, and A is the area of the electrode. s is a specific factor, related to the type and power of the electrolytic bath.

Ernesto Amores et al. [12] based on experiments with a 15KW alkaline electrolyzer, proposed that the voltage model should incorporate the effect of system pressure, but still does not consider the effect of lye flow rate on voltage. The magnitude of the flow rate directly affects the conductivity of the lye and thus the voltage of the alkaline electrolyzer. Therefore, the voltage model of the alkaline electrolyzer should include the effect of the lye flow rate, as in Eq. (2):

$$U_{cell} = U_{rev} + (a + b + c) I_s + s \ln[(t_1 + \frac{t_2}{T} + \frac{t_3}{T^2}) I_s + 1] \tag{2}$$

In Eq. (2):

$$a = a_1 + a_2 T \tag{3}$$

$$b = b_1 + b_2 p \tag{4}$$

$$c = c_1 + c_2 v \tag{5}$$

In Eq. (5), v is the alkaline flow rate, and including the alkaline flow rate as a variable in the model will make the voltage model of the alkaline electrolyzer more accurate.

$$U_{cell} = U_{rev} + [(a_1 + b_1 + c_1) + a_2 T + b_2 p + c_2 v] I_s + s \ln[(t_1 + \frac{t_2}{T} + \frac{t_3}{T^2}) I_s + 1] \tag{6}$$

Equation (6) is the voltage of each cell, and the total voltage of the alkaline electrolyzer is the number of cells multiplied by the cell voltage.

$$U_{elec} = n_{cell} \cdot U_{cell} \tag{7}$$

Modeling of Faraday efficiency characteristics of alkaline electrolyzer

In electrolytic water hydrogen production systems, the amount of hydrogen produced per unit time is closely related to the amount of electricity consumed by the alkaline electrolyzer per unit time, and the Faraday efficiency is defined as the ratio of the actual hydrogen produced by the system per unit time to the theoretical amount of hydrogen produced per unit time, which can be expressed by an empirical equation, derived by Ulleberg et al. [10]:

$$\eta_F = \frac{I_s^2}{f_1 + I_s^2} \cdot f_2 \tag{8}$$

To take the role of temperature and flow rate into account, Eq. (8) is modified by updating f_1, f_2 as a function of temperature and flow rate as variables:

$$f_1 = f_{11} + f_{t1}T + f_{v1}v \tag{9}$$

$$f_2 = f_{22} + f_{t2}T + f_{v2}v \tag{10}$$

Modeling of hydrogen concentration characteristics in oxygen in alkaline electrolyzer

In this paper, we address the modeling of hydrogen concentration in oxygen. According to the previous discussion, the hydrogen content in oxygen can be modeled theoretically based on temperature, pressure, and lye flow rate, etc. Hug et al. [13] in 1993 gave an empirical formula for calculating the hydrogen concentration in oxygen:

$$c_{HIO} = C_1 + C_2T + C_3T^2 + (C_4 + C_5T + C_6T^2)e^{\frac{C_7 + C_8T + C_9T^2}{I_s}} \tag{11}$$

Mónica et al. [12] adds the effect of system pressure, but still does not take into account the effect of alkali flow, this paper adds the effect of alkali flow on the basis of Eqs. (11), (12) makes the calculation of hydrogen concentration in oxygen more accurate.

$$\begin{aligned} c_{HIO} = {} & [C_1 + C_2T + C_3T^2 + (C_4 + C_5T + C_6T^2)e^{\frac{C_7 + C_8T + C_9T^2}{I_s}}] \\ & + [E_1 + E_2p + E_3p^2 + (E_4 + E_5p + E_6p^2)e^{\frac{E_7 + E_8p + E_9p^2}{I_s}}] \\ & + [F_1 + F_2v + F_3v^2 + (F_4 + F_5v + F_6v^2)e^{\frac{F_7 + F_8v + F_9v^2}{I_s}}] \end{aligned} \tag{12}$$

3.2 Alkaline Electrolyzer 3D Model Construction

In this paper, we firstly established a 3D model of the hydrogen production system by using Sketch Up, and then imported the established 3D model into the corresponding topology editor. Based on the established 3D model, this paper uses HT for Web to bring the 3D model closer to the physical entity, mainly by using WebGL and other technologies to visualize the flow of liquid in the system and the circulation pump operation and other physical movements, as shown in Fig. 3.

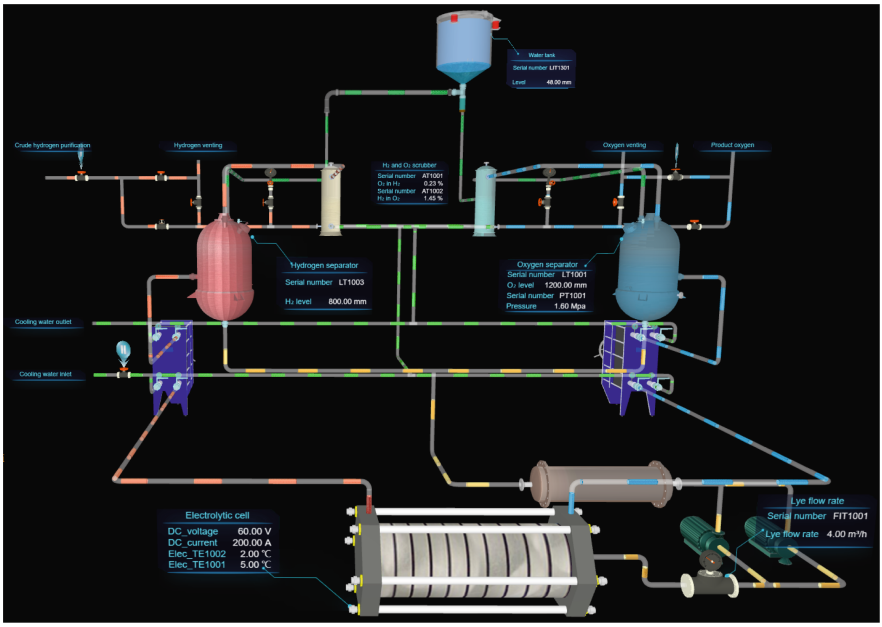

Fig. 3. HT for web-based digital twin model for hydrogen production system

4 Simulation Study of Digital Twin Model of Alkaline Electrolyzer

In this paper, the parameters of the constructed mathematical model of the alkaline electrolyzer were determined based on the single-day operating data of the 1MW alkaline electrolyzer in Chongli, Zhangjiakou, by using Matlab to perform multiple nonlinear regression on the model. The fitting results are also elaborated and analyzed. The parameters of the alkaline electrolyzer are shown in Table 1.

Table 1. Parameters of 1 MW alkaline electrolyzer.

Main features	Value	Unit
Capacity of hydrogen production	200	m^3/h
Maximum operating pressure	1.9	MPa
Rated voltage	600	V
Rated current	1650	A
Rated power	1	MW

4.1 Alkaline Electrolyzer Voltage Model Simulation Study

The simulation of the voltage model is carried out according to Eq. (6), and there are four parameters in the updated voltage model, so two of them are fixed separately,

and the surface plot of the voltage model is drawn with the other two parameters as variables. As shown in Fig. 4, this paper analyzes the factors affecting the alkaline electrolyzer voltage with (temperature-current density), (pressure-current density), and (lye flow-current density) as variables, respectively.

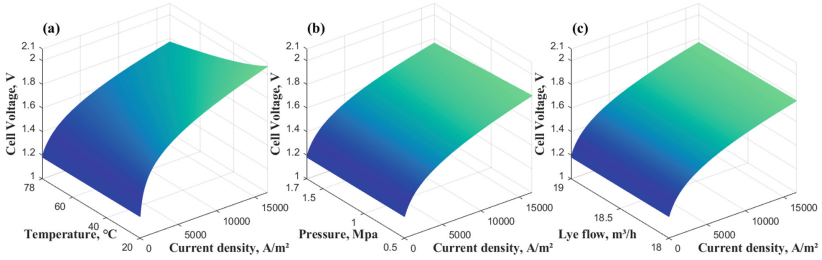

Fig. 4. Results of the voltage model by fixing different parameters: (a) (P = 1.5 MPa, v = 18.5 m^3/h); (b) (T = 78 °C, v = 18.5 m^3/h); (c) (P = 1.5 MPa, T = 78 °C)

Figure 5 shows more clearly the effect of temperature, pressure and flow on the cell voltage, from which it can be seen that temperature has the most dramatic effect on pressure, which is the reason why the literature [10] only uses temperature as the only variable in the cell voltage model. In Fig. 5(a, b, c) are taken for different temperature, pressure and flow rate to observe the variation of the cell voltage. Where Fig. 5(c) plots the cell voltage for different lye flow rates, it can be seen that there is a slight decrease in voltage as the lye flow rate increases. The increase in the lye flow rate leads to an increase in the amount of lye cooled per unit time, which leads to a decrease in the lye temperature. The voltage tends to increase as the temperature decreases, which is also shown in Fig. 4(a). On the other hand, the increase in the flow of lye will take away the air bubbles adhering to the electrode in time, which will lower the resistance and therefore the voltage of the cell. It can be seen that the latter cause has a greater effect on the voltage than the former one, because the change in resistance directly affects the voltage, and therefore it will present a slight decrease in voltage.

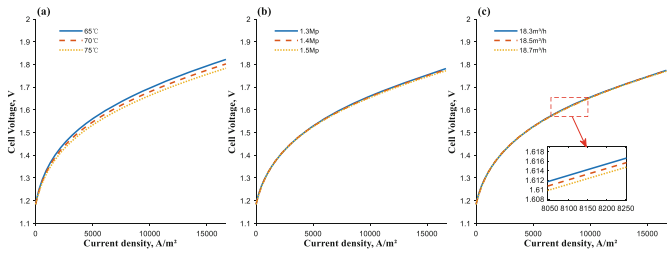

Fig. 5. Cell voltage at different parameter values: (a) temperature; (b) pressure; (c) lye flow

4.2 Simulation Study of Faraday Efficiency Model for Alkaline Electrolyzer

The simulation study of Faraday efficiency model was carried out according to Eqs. (8), (9) and (10), and the Faraday efficiency of alkaline electrolyzer was plotted with (temperature-current density) and (alkali flow-current density) as variables, respectively, as shown in Fig. 6.

In Fig. 7(a), since an increase in temperature leads to a faster movement of the anions and cations in the alkali solution, the resistance of the electrolyte decreases, which can lead to a small amount of current not being used to produce hydrogen and therefore leads to a decrease in Faraday efficiency. In Fig. 7(b), it can be seen that the effect of alkali flow rate on Faraday efficiency is not very large. It was stated earlier that an increase in the lye flow rate leads to a decrease in temperature, but it also leads directly to a decrease in resistance, a cause also explained in the voltage model, and these two causes have opposite effects on the Faraday efficiency of similar order of magnitude. Therefore, the effect of the lye flow rate on the Faraday efficiency is weak.

4.3 Model Simulation Study of Hydrogen Content in Oxygen

According to the mathematical model of hydrogen concentration in oxygen established in this paper, such as Eq. (12), the variation law of hydrogen concentration in oxygen is plotted with temperature, pressure, and lye flow as variables, as shown in Fig. 8(a), (b), and (c) in Fig. 9 respectively plot the curves of the hydrogen concentration in oxygen varying with the current density under different temperatures, pressures, and lye flow rates. In Fig. 9(a), the current is fixed, and as the temperature increases, the concentration of hydrogen in oxygen increases, and the increase in temperature causes the hydrogen dissolved in the alkali solution to escape and the thermal motion of the gas molecules to accelerate, thereby increasing the diffusion rate. An increase in pressure will lead to an increase in the solubility of the gas, but it will also increase the diffusion rate of gas molecules, as shown in Fig. 9(b). The final result is that the increase in pressure will increase the hydrogen content in oxygen. The lye circulates between the electrolytic cell and the separator under the action of the lye circulation pump. If the flow rate of the lye increases, the amount of lye returned to the hydrogen-oxygen separator per unit time will also increase. Moreover, the high permeability of hydrogen will cause a small amount of hydrogen to dissolve in the lye, which will lead to an increase in the concentration of hydrogen in oxygen, as shown in Fig. 9(c).

5 Conclusions

Based on the data and mechanism, this paper constructs a digital twin model of a 1MW alkaline electrolyzer, including a voltage model, a Faraday efficiency model, a hydrogen concentration model in oxygen, and a system pressure model. The construction of the model is based on data and mathematical formulas, and the simulation results are consistent with the theoretical analysis.

In this paper, we use digital twin technology to simulate the operating characteristics of the alkaline electrolyzer to ensure the safety of the real system operation. The operation

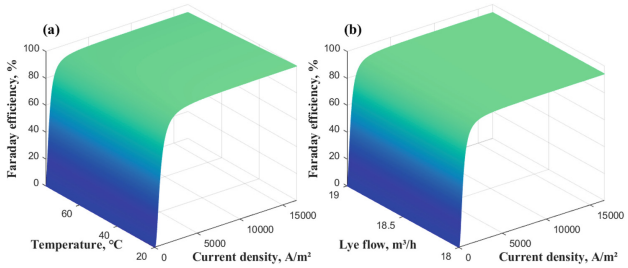

Fig. 6. Results of the Faraday efficiency model by fixing different parameters: (a) v = 18.5 m^3/h; (b) T = 78 °C

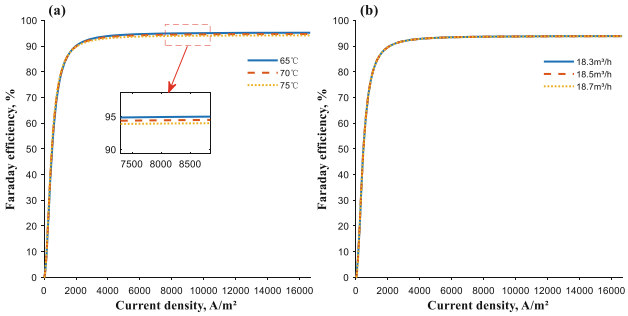

Fig. 7. Faraday efficiency at different parameter values: (a) temperature; (b) lye flow

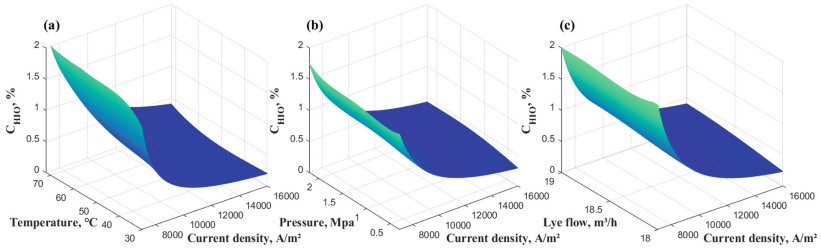

Fig. 8. Results of the hydrogen content in oxygen model by fixing different parameters: (a) (P = 1.5 MPa, v = 18.5 m^3/h); (b) (T = 78 °C, v = 18.5 m^3/h); (c) (P = 1.5 MPa, T = 78 °C)

characteristics of the hydrogen production system are complex, and the mathematical models of the valve separator and compressor have not been completed, and the digital twin model of the whole hydrogen production system is yet to be solved.

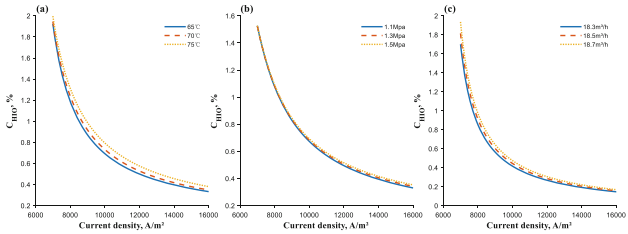

Fig. 9. Hydrogen content in oxygen at different parameter values: (a) temperature; (b) pressure; (c) lye flow

Acknowledgment. This research was supported by the Science and Technology Plan Project of Hebei Province of China (Grant No. 19210108D, 19214501D, 20314501D, F2021202022).

References

1. Cheng, W.J., Zhao, L., Xi, H., et al.: Research on hydrogen energy policy and water-electrolytic hydrogen under the 14th Five Year Plan. Therm. Power Gener. **51**(11), 181–188 (2022)
2. Peng, Y., Bai, X.M.: Cities leading hydrogen energy development: the pledges and strategies of 39 Chinese cities. NPJ Urban Sustain. **2**(1) (2022)
3. Acharya, A.: Scaling-up green hydrogen development with effective policy interventions. J. Sustain. Dev. **15**(5), 135 (2022)
4. Wang, P.C., Wan, L., Xu, Q., et al.: Hydrogen production based-on anion exchange membrane water electrolysis: a critical review and perspective. CIESC J. **72**(12), 6161–6175 (2021)
5. Zheng, Y., You, S., Bindner, H.W., Münster, M.: Optimal day-ahead dispatch of an alkaline electrolyser system concerning thermal–electric properties and state-transitional dynamics. Appl. Energy **307**, 118091 (2022)
6. Hong, Z., Wei, Z., Han, X.: Optimization scheduling control strategy of wind-hydrogen system considering hydrogen production efficiency. J. Energy Storage **47**(Mar) (2022)
7. Zhang, C., Wang, J.Y., Ren, Z.B., Yu, Z.Y., Wang, P.J.: Wind-powered 250 kW electrolyzer for dynamic hydrogen production: a pilot study. Int. J. Hydrogen Energy **46**(70), 34550–34564 (2021)
8. Ning, N.: Research on hydrogen generation system by water electrolysis under wide power fluctuation. Ship Sci. Technol. **39**(11), 133–136 (2017)
9. Fang, R.M., Liang, Y.: Control strategy of electrolyzer in a wind-hydrogen system considering the constraints of switching times. Int. J. Hydrogen Energy **44**(46), 25104–25111 (2019)
10. Øystein, U.: Modeling of advanced alkaline electrolyzers: a system simulation approach. Int. J. Hydrogen Energy **28**(1), 21–33 (2003)
11. Jiang, Y., Shen, X.J., Lü, H., Zhang, C.M.: Construction and simulation of operation digital twin model for alkaline water electrolyzer. Trans. China Electrotech. Soc. **37**(11), 2897–2908 (2022)
12. Mónica, S., Ernesto, A., Lourdes, R., Carmen, C.: Semi-empirical model and experimental validation for the performance evaluation of a 15 kW alkaline water electrolyzer. Int. J. Hydrogen Energy **43**(45), 20332–20345 (2018)

13. Hug, W., Bussmann, H., Brinner, A.: Intermittent operation and operation modeling of an alkaline electrolyzer. Int. J. Hydrogen Energy **18**(12) (1993)
14. Huang, D.G., Yin, Y.G., et al.: Effect of lye flow rate on water electrolyzer operation. Henan Chem. Ind. **33**(06), 26–28 (2016)

Construction and Simulation of Digital Twin Model and Electrolyzer Wide Power Adaptation Model for Alkaline Electrolytic Water Hydrogen Production

Zhe Zhang[1], Wenbo Yang[2], Liwei Wang[3(✉)], Tao Liang[2], and Zicong Liu[2]

[1] Science and Technology Innovation Research Academy (Hebei), CAICT Institute Co., Ltd., Baoding 071000, Hebei, China
[2] School of Artificial Intelligence, Hebei University of Technology, Tianjin 300130, China
[3] Guantao County Party Committee of Handan City, Hebei Province, Handan 057450, Hebei, China
100990449@qq.com

Abstract. Combining the framework of digital twin and the working mechanism of electrolytic water hydrogen production, a digital twin model of alkaline electrolytic water hydrogen production is constructed, and the influence of electrolyzer cell voltage by temperature and pressure is analyzed according to the mathematical model of electrolytic water hydrogen production. In order to improve the adaptability of the electrolyzer of the hydrogen production system to the power fluctuation of renewable energy input, a wide power adaptation model with multiple electrolyzers sharing one set of gas-liquid handling device is proposed. The case study shows that by reasonably selecting the electrolyzer model of the hydrogen production system, the use of the wide power adaptation model can effectively adapt to the fluctuation of wind power and improve the adaptation capability of the electrolyzer to wide power fluctuations.

Keywords: Electrolytic water to hydrogen · Digital twins · Electrolyzer · Wide power

1 Introduction

As a green energy source with high calorific value, diverse sources, clean and environmental protection, and high conversion efficiency, hydrogen energy has been recognized as a clean energy carrier with zero emission and zero pollution. Hydrogen energy, which is called the ultimate energy in the 21st century, has received attention and research from scholars all over the world, and more and more countries are putting the development of hydrogen energy in the forefront of energy development [1, 2].

Electrolytic water to hydrogen technology is widely used in the hydrogen production industry for its simple preparation process, clean product and high purity. To achieve large-scale hydrogen production from renewable energy sources, the input energy for

H. Sun et al. (Eds.): WHTC 2023, SPPHY 393, pp. 281–290, 2024.
https://doi.org/10.1007/978-981-99-8631-6_28

hydrogen production from electrolytic water is usually generated from renewable energy sources such as wind and light energy, whose input power is volatile and uncertain [3]. The electrolyzer is the core part of the electrolytic water hydrogen production process, and its performance has a great influence on the electrolytic hydrogen production system. Frequent fluctuations in the input power of the electrolyzer will cause the input current to fluctuate as well, resulting in frequent starts and stops of the electrolyzer, which will not only reduce the service life of the electrolyzer itself, but also lead to a decrease in its hydrogen production, and even affect the purity of the product and the concentration of hydrogen in oxygen, thus affecting the safety of the whole electrolytic water hydrogen production system [4]. Therefore, the mathematical model and simulation of hydrogen production from electrolytic water plays an important role in the safety of electrolytic water system. Ulleberg proposed an advanced mathematical model for alkaline electrolyzers based on basic thermodynamics, heat transfer theory and electrochemical relationships, which can be used to predict the voltage, hydrogen production, efficiency and operating temperature of electrolytic cells in electrolytic water systems [5]. Tijani et al. investigated the main parameters affecting the performance of the electrolyzer by means of basic thermodynamic and electrochemical reaction-related models [6]. Shen X. et al. developed a mathematical model of the equivalent impedance characteristics, electrothermal characteristics and power regulation characteristics of an alkaline electrolyzer [7]. Górecki et al. described the voltammetric characteristics of the electrolyzer and considered the effect of the concentration of potassium hydroxide solution on the hydrogen production, and verified the correctness of their model experimentally by varying the electrolyte concentration [8]. The electrolyzer model developed in the above literature provides a valuable reference for modeling and simulation of hydrogen production from alkaline electrolytic water, but does not take into account the effect of fluctuations in input power on the electrolyzer.

Since the operating condition of the electrolyzer is limited by the fluctuation of renewable energy input power, the lower power limit of the electrolyzer is generally set at 20–25% of the rated power to utilize as much renewable energy as possible. To improve the ability of electrolyzer to resist the fluctuation of renewable energy input power and to improve the hydrogen production rate of electrolytic water hydrogen production system, one can consider changing the electrode material of electrolyzer, increasing the surface area of electrode, optimizing the diaphragm material, using advanced electrolyte or adding new catalyst, etc. However, the research on the electrolyzer material is a long and complicated process, which cannot meet the demand of electrolyzer to adapt to wide power in the short term. Secondly, the feasibility of changing the structure of the electrolytic water hydrogen production system and optimizing the control strategy of the electrolytic system has been proved and more and more scholars have studied it. Fang R et al. proposed the combination of supercapacitor and modular control strategy to optimize the operation mode of the electrolyzer considering the effect of wind power fluctuation on the electrolyzer, thus extending the life of the electrolyzer and improving the hydrogen production [9]. Hong Z. et al. controlled the electrolyzer array by a segmented fuzzy control method as a way to improve the hydrogen yield of the electrolytic water hydrogen production system considering the efficiency of hydrogen production from wind power [10]. Shen et al. proposed a control strategy for the rotation

of alkaline electrolytic water hydrogen production electrolyzer arrays, which enables the electrolyzer arrays to operate or shut down in different operating states sequentially according to the rotation cycle, improving the safety of the electrolytic water hydrogen production system and extending the service life of the electrolyzer [11]. Liu et al. developed a wide power adaptation model for alkaline electrolyzers to improve the adaptability of electrolyzers to input power fluctuations and to improve the level of wind power consumption [12]. The above literature does not provide a clearer description of the power settings for the wide power model of the electrolyzer.

Based on the above research, this paper proposes a digital twin-based alkaline electrolytic water hydrogen production model and a multi-electrolyzer adaptive wide power model, which combines the working mechanism of alkaline electrolytic water hydrogen production and digital twin technology to construct a digital twin framework for alkaline electrolytic water hydrogen production. And it is verified by simulation that the wide power model proposed in the paper can improve the ability of the electrolyzer module to adapt to wind power fluctuations.

2 Alkaline Electrolytic Water Digital Twin Framework

Digital twin technology has attracted much attention in the fields of intelligent manufacturing and energy monitoring and analysis, and realizing information, digitalization and intelligence in the new energy field is a hot research topic in the energy field [13, 14]. Applying digital twin technology to the field of alkaline electrolytic water hydrogen production, which is a data visualization presentation of electrolytic water hydrogen production system, this paper gives the framework of renewable energy electrolytic water hydrogen production digital twin by combining the framework of digital twin and the working mechanism of electrolytic water hydrogen production.

As shown in Fig. 1, the renewable energy electrolytic water to hydrogen digital twin framework consists of four layers: the physical device layer, the data interaction layer, the model layer and the application layer. The physical equipment layer includes scenery power generation equipment, electrolytic water hydrogen production equipment and sensors, which realize data sensing through communication and IOT technologies. The data interaction layer consists of data transmission, data processing and data storage, which provides powerful data support for electrolytic water to hydrogen digital twin technology, involving transmission communication protocols and methods, processing of data and database storage and management, interconnecting the physical device layer, model layer and application layer. The model layer is divided into a mathematical model of electrolytic hydrogen production and a twin model. The mathematical model is a semi-empirical formula or equation fitted by data processing of historical data according to the working mechanism of electrolytic hydrogen production, and the twin model is a virtual three-dimensional model based on electrolytic hydrogen production equipment, which can simulate the process of electrolytic hydrogen production. The application layer includes production monitoring, report generation, intelligent warning and production forecasting, which presents the production status of electrolytic water hydrogen production in real time and is a visual representation of the digital twin of electrolytic water hydrogen production.

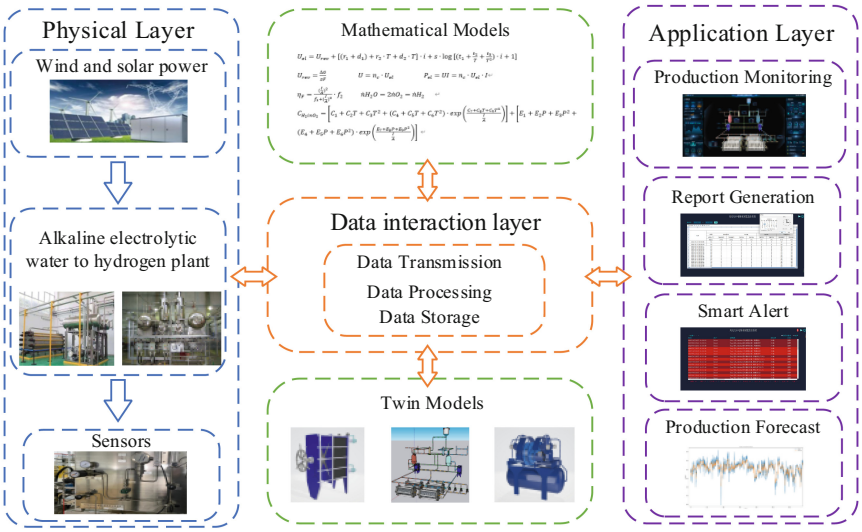

Fig. 1. Digital twin framework for hydrogen production from electrolytic water.

3 Model Construction

3.1 Mathematical Model of Alkaline Electrolyzer

The electrolyzer is the core component of the electrolytic water hydrogen production system. In the whole hydrogen production system, the electrolyzer is equivalent to a voltage sensitive non-linear DC load, so the I-U curve describing its voltage variation with current is one of the most important characteristics of the electrolyzer. To describe this characteristic of the electrolyzer, Ulleberg proposed a mathematical model of the electrolyzer voltage with respect to current and temperature to show the relationship between the electrolyzer voltage and its current and tank temperature. The electrical characteristics of the electrolyzer are also influenced by the pressure inside the electrolyzer, and the mathematical model proposed by Ulleberg was modified by Sánchez et al. to give the following Eq. (1) for its characteristics [15].

$$U_{el} = U_{rev} + \left[(r_1 + d_1) + r_2 \cdot T + d_2 \cdot P\right] \cdot \frac{I}{\mathrm{A}} + s \cdot \log\left[\left(t_1 + \frac{t_2}{T} + \frac{t_3}{T^2}\right) \cdot \frac{I}{\mathrm{A}} + 1\right] \tag{1}$$

where U_{el} represents the voltage of a single electrolyzer cell, U_{rev} is the reversible voltage of the electrolyzer, $r_1, r_2, d_1, d_2, s, t_1, t_2, t_3$ are its coefficients, I is the input current, and A is the electrolytic cell electrode surface area. When the electrolyzer is at a temperature of 25 °C and a pressure of 0.1 MPa, the reversible voltage can be found by the ratio of the Gibbs free energy ΔG to the product of the Faraday constant F and the number of electrons transferred z. The expression is shown in Eq. (2).

$$U_{rev} = \frac{\Delta \mathrm{G}}{\mathrm{zF}} \tag{2}$$

Considering that the reversible voltage (U_{rev}) has a tendency to decrease as the tank temperature increases, it can be derived from Eq. (3).

$$U_{rev} = -7.3 \times 10^{-4} \cdot T + 1.248 \tag{3}$$

3.2 Electrolytic Tank Wide Power Adaptation Model

Wind power is used directly as the input energy for alkaline electrolysis of water for hydrogen production, whose input power is stochastic and fluctuating. Frequent fluctuations of natural wind can lead to unstable operation of the cell, which not only directly affects the hydrogen production and purity, but also the safety of the hydrogen production system. Moreover, the technology of direct integration of large-scale wind power generation into electrolytic water for hydrogen production is gradually maturing, while large-scale hydrogen production equipment is gradually developing towards the many-to-one mode [16]. Thus, improving the wide power adaptability of electrolytic water hydrogen production systems is essential. In response to this problem, a "4-to-1" model of alkaline electrolytic hydrogen production is established based on four alkaline electrolytic cells sharing one gas-liquid unit in the hydrogen production system, shown in Fig. 2.

Power of the electrolyzer operation is limited by the purity of the product gas. To ensure the safety of the system, its minimum operating power is 20% of the rated power, and it cannot guarantee long-time operation. Meanwhile, the maximum operating power of the electrolytic cell can reach 110–130% of the rated power in a short period of time due to its overload characteristics. In this paper, we only study the case where the upper power limit of the electrolyzer is the rated power, and consider the operating power range of a single electrolyzer from 20 to 100% of the rated power, without considering its start-stop characteristics. As shown in Fig. 2, where 4 electrolytic cells of the same size share one set of gas-liquid unit, the power range that this electrolytic cell module can accommodate is extended from its full 20–100% of its capacity to 5–100%.

Based on the operation of the electrolyzer module and the renewable energy power, it is possible to express the relationship between the power required to operate the electrolyzer module and the power generated by renewable energy as well as the renewable energy power not absorbed by the electrolyzer module.

$$P_w = k \cdot P_E + P_{waste} \quad k = 0, 1, 2, 3, 4 \tag{4}$$

where P_w is the input power of renewable energy to the electrolyzer module, k indicates the number of electrolyzers operating at rated power, P_E is the rated power of a single electrolyzer, and P_{waste} is the power not absorbed by the electrolyzer module.

Electrolyzer operating power is limited by the purity of the product air, whose minimum operating power is 20% of the nominal power. The lower limit of operating power of the proposed electrolyzer module consisting of four electrolytic cells is 20% of the rated power of a single electrolyzer, which is 5% of the full power of the electrolyzer module. In case the full operating power of the electrolyzer module is $\sum P_E$, the lower limit of its operating power can be expressed as Eq. (5).

$$P_{min} = 5\% \sum P_E = 20\% P_E \tag{5}$$

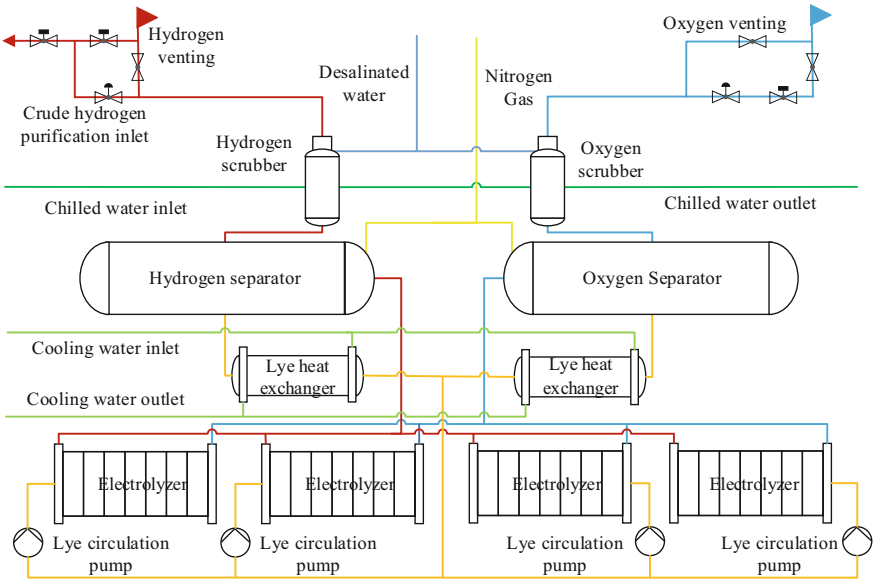

Fig. 2. Simple diagram of "4-to-1" hydrogen production plant in alkaline electrolyzer.

In Eq. (4), when all four cells in the electrolyzer module are operating at full power and the renewable energy power is greater than the power required by the electrolyzer module, the power is overloaded. The renewable energy power not absorbed by the electrolyzer at this point is Eq. (6).

$$P_{waste} = P_w - \sum P_E \tag{6}$$

While the power is not overloaded, according to the power dissipation of the electrolyzer module, it is classified into 3 operating conditions: low power, high power and full power. Expressing the number of electrolytic cells of the same size as i ($i = 1, 2, 3, 4$), the power operation condition of the cell module is Eq. (7).

$$\begin{cases} P_{el} = P_{wave} & i = 1 \\ P_{el} = k \cdot P_E + P_{wave} & i = 2, 3, 4, k = 1, 2, 3 \\ P_{el} = k \cdot P_E & i = 4, k = 4 \end{cases} \tag{7}$$

where P_{el} is the operating power of the electrolyzer module, k indicates the number of electrolyzers operating at rated power, and P_E is the rated power of one electrolyzer. P_{wave} is the fluctuating power at which an electrolyzer can operate and the fluctuating power is greater than the minimum operating power of the electrolyzer and less than the rated power of the electrolyzer, $P_{min} \leq P_{wave} \leq P_E$.

Equation (7) indicates that the electrolyzer module is in a low power operation state, when the input power of renewable energy to the electrolyzer module is less than the rated power of the electrolyzer, and only one electrolyzer module works in this state. If the fluctuating power is equal to the lower limit of the operating power of a

single electrolyzer, $P_{wave} = P_{min}$, which is 5% of the rated power, and 5% $\sum P_E$ is the minimum running power of the electrolyzer module. When the renewable energy power is less than the electrolyzer operating power, $P_w < P_{wave}$, P_w is the power not absorbed by the electrolyzer module, $P_{waste} = P_w$.

Equation (7) represents the electrolyzer module in high power operation, where the renewable energy input power to the electrolyzer module is less than the full power value of the electrolyzer module. The operating state of the electrolyzer module under high power includes two electrolyzers, three electrolyzers and four electrolyzers, and only one electrolyzer in each case is operating at less than its rated power, while the rest of the operating electrolyzers are operating at rated power. If the electrolyzer module has k cells at rated power and $(P_w - k \cdot P_E)$ is less than the minimum running power of cell, the power not absorbed by the cell module can be expressed as Eq. (8).

$$P_{waste} = P_w - k \cdot P_E \quad k = 1, 2, 3 \tag{8}$$

Equation (7) means that the electrolyzer module is in full power operation, at this time, all four electrolyzers are working at rated power, all renewable energy power is consumed by the electrolyzer module, and the operating power of the electrolyzer module reaches 100%.

4 Simulation and Analysis

To verify the adaptability of the above models, the electrical model and wide power adaptation model are experimented and analyzed based on the mathematical models developed in Sect. 3.

4.1 Electrical Model Analysis

The relationship between electrolyzer cell voltage (U_{el}) and current density is analyzed according to Eqs. (1–3), and Fig. 3(a) and (b) show the curves of electrolyzer cell voltage with current density under different temperatures and different pressures, respectively. The temperature is set to 45–75 °C and the pressure is fixed at 0.5 MPa, as shown in Fig. 3(a) the voltage of the cell increases with the increase of current density and decreases with the increase of temperature. The chemical reaction of electrolytic water is affected by temperature, and the redox reaction of electrolytic water is easier to achieve at high temperature, so the electrolytic voltage required is slightly lower than at low temperature. The pressure in Fig. 3(b) is set to 0.5–2.0 MPa and the temperature is fixed at 75 °C. The variation of the cell voltage with current density has the same trend as its variation under the influence of temperature, but the convergence of applying different pressures on the cell voltage almost does not affect the electrical performance of the cell voltage.

4.2 Alkaline Electrolytic Water to Hydrogen Wide Power Model Analysis

According to the wide power model of alkaline electrolytic water hydrogen production described in Eqs. (4–8) and the output power of a certain 1.6 MW wind turbine, two

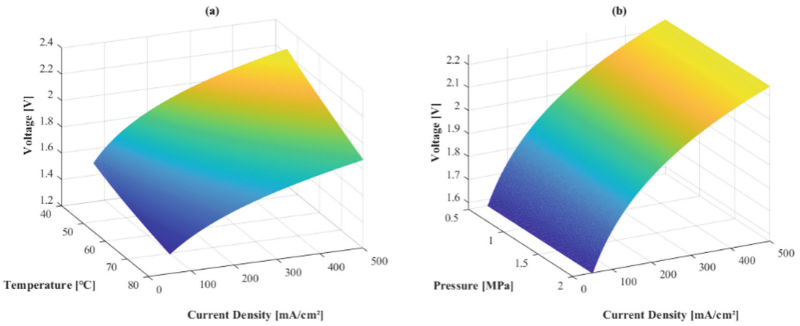

Fig. 3. Small chamber voltage variation curve with current density (a: pressure 0.5 MPa, b: temperature 75 °C).

different sets of electrolytic cells are selected for the hydrogen production system. The first group is one electrolyzer with a rated power of 1500 kW and the second group is an electrolyzer module with a total power of 1500 kW consisting of four electrolyzers with a rated power of 375 kW. The output power of a 1.6 MW wind turbine in a wind farm in Zhangbei area for a certain month is directly used as the input power of two sets of electrolyzer modules. The range of wind power that a single electrolyzer can withstand is 20–100% of its rated power, so the minimum operating power for a 1500 kW electrolyzer is 300 kW and for a 375 kW electrolyzer is 75 kW.

Figure 4 shows the power curves consumed by the two electrolyzer sets for operation. The power curves consumed by the two electrolyzer sets and the fan wind power curves basically overlap below 1500 kW, with a small deviation in the low power range. The reason for this is that the power consumption level of the electrolyzer depends on the output of wind power since the wind turbine power generation is directly supplied to the electrolyzer, so its power consumption curve goes in the same direction as the wind power basically. In the low power range, the power consumption curve of the electrolyzer set deviates from the wind power curve, and the wind power absorbed by the electrolyzer set for wide power hydrogen production is higher than the wind power absorbed by the electrolyzer set without wide power hydrogen production. Due to the limitation of the minimum operating power of the electrolytic cell, wind power below the minimum operating power of the electrolytic cell will not be absorbed by the cell. From the figure, the overlap between the power consumption curve and wind power curve of four 375 kW electrolyzer modules is higher than that between the power consumption curve and wind power curve of one 1500 kW electrolyzer, which also indicates that the level of wind power dissipation by the modules of the cells can be improved by using a wide power model.

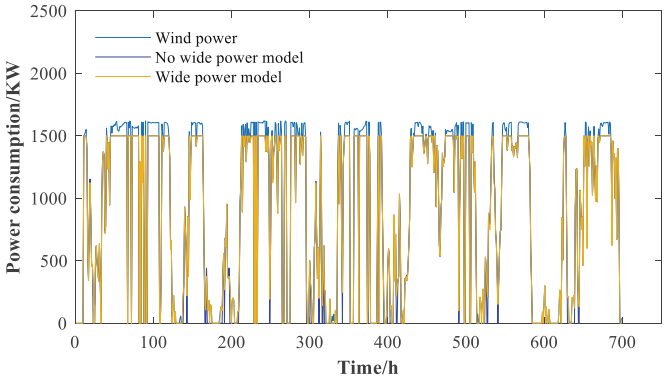

Fig. 4. Electrolyzer power dissipation curve.

5 Conclusion

This paper combines digital twin technology and the working mechanism of electrolytic water hydrogen production, constructs a digital twin framework for alkaline electrolytic water hydrogen production, and describes the technical method of digital twin of electrolytic water hydrogen production. A model of alkaline electrolytic water hydrogen production with multiple electrolyzers to adapt to wide power is established, and the analysis shows that the wide power adaptation of the multiple electrolyzer wide power model is better than that without the wide power model, and the power dissipation level is high. This paper has some reference value in the problems of digital twin application and wide power adaptation of electrolytic cells for hydrogen production from electrolytic water.

Acknowledgment. This research was supported by the Science and Technology Plan Project of Hebei Province of China (Grant No. 19210108D, 19214501D, 20314501D, F2021202022).

References

1. Cao, F., Chen, K., Guo, T., et al.: Research on technological path of hydrogen energy industry development. Distrib. Energy **5**(01), 1–8 (2020)
2. Shao, Z., Yi, B.: Developing trend and present status of hydrogen energy and fuel cell development **34**(04), 469–477 (2019)
3. Ge, L., Cui, Q., Li, M., et al.: Review on water electrolysis for hydrogen production powered by fluctuating wind power and PV. Integr. Smart Energy **44**(05), 1–14 (2022)
4. Ning, N.: Adaptation study of wide power fluctuation in water electrolysis hydrogen production unit. Ship Sci. Technol. **39**(11), 133–136 (2017)
5. Ulleberg, Y.: Modeling of advanced alkaline electrolyzers: a system simulation approach. Int. J. Hydrogen Energy **28**(1), 21–33 (2003)
6. Tijani, A., Yusup, N., Rahim, A.: Mathematical modelling and simulation analysis of advanced alkaline electrolyzer system for hydrogen production. Procedia Technol. **15**, 798–806 (2014)

7. Shen, X., Zhang, X., Lie, T., et al.: Mathematical modeling and simulation for external electrothermal characteristics of an alkaline water electrolyzer. Int. J. Energy Res. **42**(12), 3899–3914 (2018)
8. Górecki, K., Górecka, M., Górecki, P.: Modelling properties of an alkaline electrolyser. Energies **13** (2020)
9. Fang, R., Liang, Y.: Control strategy of electrolyzer in a wind-hydrogen system considering the constraints of switching times. Int. J. Hydrogen Energy **44**(46) (2019)
10. Hong, Z., Wei, Z., Han, X.: Optimization scheduling control strategy of wind-hydrogen system considering hydrogen production efficiency **47** (2021)
11. Shen, X., Nie, C., Lv, H.: Coordination control strategy of wind power-hydrogen alkaline electrolyzer bank considering electrothermal characteristics. Trans. China Electrotech. Soc. **36**(3), 463–472 (2021)
12. Liu, Y., Fan, Y., Hao, J., et al.: Capacity configuration and optimal scheduling of a wind-photovoltaic-hydrogen-thermal virtual power plant based on a wide range power adaptation strategy for an alkaline electrolyzer. Power Syst. Prot. Control **50**(10), 48–60 (2022)
13. Tang, W., Chen, X., Qian, T., et al.: Technologies and applications of digital twin for developing smart energy systems. Strateg. Study Chin. Acad. Eng. **22**(04), 74–85 (2020)
14. Shen, C., Jia, M., Chen, Y., et al.: Digital twin of the energy internet and its application. Global Energy Interconnection **3**(01), 1–13 (2020)
15. Sánchez, M., Amores, E., Rodríguez, L., et al.: Semi-empirical model and experimental validation for the performance evaluation of a 15 kW alkaline water electrolyzer. Int. J. Hydrogen Energy **43**(45), 20332–20345 (2018)
16. Yang, C., Ma, J., Li, G., et al.: Application and practice of many-to-one large-scale alkaline water electrolysis hydrogen production equipment. Solar Energy (05), 103–14 (2022)

Penetration Behavior Analysis of Resin During the Impregnation Progress of Expanded Graphite Plates

Runlin Fan, Junsheng Zheng(✉), and Zize Zhan

Tongji University, Shanghai 201804, China
jszheng@tongji.edu.cn

Abstract. Resin impregnation is an important process in the manufacture of composite graphite bipolar plates to reduce their porosity and improve their air tightness as well as flexural strength. In order to improve the filling efficiency of resin into expanded graphite plates and to investigate the factors influencing the resin penetration process, we compare the penetration rate and the upper limit of absorption of epoxy resin, acrylic resin and water in graphite plates. It was found that capillary force is part of the driving forces for resin penetration into the graphite plates, while the boundary layer is the main source of resistance. The higher viscosity of the resin not only leads to a lower resin flow rate, but also results in the formation of a thicker boundary layer, creating additional resistance. Further, the pores are not permeable by resin when the thickness of the boundary layer is greater than the pore size, which is an important reason why the expanded graphite plate is difficult to be filled by resin adequately.

Keywords: Impregnation progress · Flow behavior analysis · Boundary layer · Composite graphite plates

1 Introduction

With good corrosion resistance, low thickness and low fabrication cost, composite graphite bipolar plates (CGPs) have good potential for application in proton exchange membrane fuel cells. However, due to its poor electrical and mechanical properties and long production cycle, CGPs have not yet been wildly adopted.

Those CGPs prepared based on expanded graphite plates combined with impregnation progress tend to form a better conductive network between graphite particles, which in turn leads to higher electrical conductivity [1]. In addition, impregnation would reduce the porosity within the CGPs, which in turn improves the mechanical strength and air tightness of the CGPs [2]. However, the key for improving the air tightness and mechanical properties of CGPs through the impregnation process is that the graphite plates were filled by resin adequately. A number of methods have been developed to enhance the resin filling efficiency, mainly by reducing the viscosity of the impregnating solution [3]

H. Sun et al. (Eds.): WHTC 2023, SPPHY 393, pp. 291–296, 2024.
https://doi.org/10.1007/978-981-99-8631-6_29

and coupling the impregnation and molding process [4, 5]. However, the factors influencing the flow behavior of resin during impregnation and the resin filling efficiency have not been fully discussed yet.

In this study, graphite plates with different pore characteristics were prepared, and the penetration rate and upper limits of resin penetration into these graphite plates by various types of resins were measured. Based on Darcy's law and boundary layer theory, the influence of pore structure and resin viscosity on the resin penetration process was analyzed.

2 Experiment

The graphite plates were produced by molding the mixture of flake graphite (median particle size of 21.4 μm) and expanded graphite (300 times expansion) with a mass ratio of 4:1 and pure expanded graphite, respectively, and the molding pressure was 80 MPa. These graphite plates were named as flake graphite plate (FGP) and expand graphite plate (EGP). To investigate the effect of the viscosity of the resin on the impregnation process, epoxy resin solution and acrylic acid-based solution were prepared separately. Among them, the epoxy resin was 6002-bisphenol A type epoxy resin (purchased from Sinopharm), abbreviated as EP; with glycidyl methacrylate (purchased from Sinopharm) as diluent, abbreviated as GMA; while the acrylic resin used DB41812 type microporous filler (purchased from Huizhou Docbond New Material Co., Ltd.), abbreviated as AR.

The pores size within the graphite plates were tested using the mercury-pressure method according to Mauran [6]. The viscosity of the resin solution was tested using a rotational viscometer. The surface tension of the resin solution and its contact angle to the graphite plate were measured using a dynamic surface tensiometer (DCAT-25, DataPhysics Instruments GmbH). The resin penetration rate was recorded using the mechanism shown in Fig. 1(a), moving the liquid pool until the liquid surface was in horizontal contact with the lower surface of the graphite plate, and recording the mass growth rate of the graphite plate using a microgram balance. The size of graphite plates was 30 * 15 * 0.65 mm. The viscosity, contact angle and penetration rate of EP were tested at 20 °C and 120 °C, respectively. In addition, the penetration rate of deionized water at 20 °C and 75 °C was also recorded.

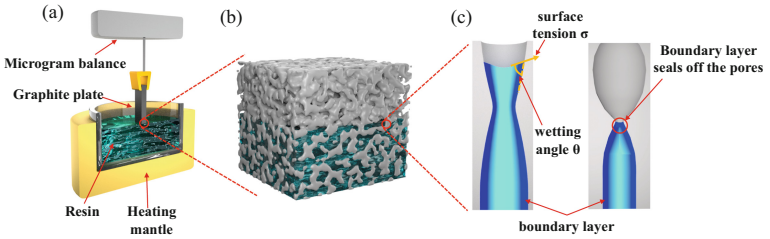

Fig. 1. Schematic diagram of resin penetration process into graphite plate: (a) resin penetration process testing mechanism; (b) resin penetration into the pores inside the graphite plate; (c) the effect of capillary force and boundary layer on the penetration process.

3 Result and Discussion

3.1 Pore Characteristics of Graphite Plates and Resin Penetration Behavior

The test results of the pore size distribution of FGP and EGP based on the mercury-pressure method were shown in Fig. 2. The pores within the graphite plates were mainly distributed between 27–700 μm and 5 nm–4.2 μm. EGP exhibited higher porosity and was mainly reflected in those pores with the size less than 1 μm.

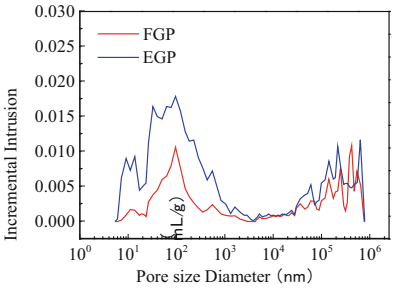

Fig. 2. The pore size distribution of FGP and EGP

The penetration rates of different liquids at different temperatures and their physical parameters were illustrated in Fig. 3, where the rapid rise in the initial stage was related to the surface tension of the resin liquid surface. As the temperature increases, the viscosity and surface tension of the EP decreased significantly, while its penetration rate and upper limit mass of saturation absorption were increased. When 15 wt% GMA was added as diluent, its viscosity decreased from 63.28 to 35.66 mPa s, however, the contact angle with graphite changed to 96.12°, while EP was unable to penetrate into the graphite plates. The viscosity of AR was 7.5 mPa s and exhibited better wettability to graphite, showing higher penetration rate and higher upper limit mass of saturation absorption, for FGP reaching saturation absorption of 30.74 mg at ~ 3600 s and EGP reaching 15.94 mg at ~ 4800 s. In addition, the penetration process of deionized water on graphite plates at 20 and 75 °C was recorded, as shown in Fig. 3(e)–(f). The viscosity of water was much lower than that of resin, while exhibited a higher penetration rate as well as an upper limit mass of saturation absorption. Comparing the penetration rates for different graphite plates, the penetration rates of almost all liquids were higher for FGP than for EGP, except for the penetration rates of water at 75 °C. A significant higher penetration rate and saturation absorption were obtained in EGP when deionized water was heated at 75 °C.

Combining the porosity characteristics of these graphite plates and the penetration behavior of different types of resins, it can be seen that the lower viscosity of the resin was not only beneficial to raise the penetration rate, but also to be more fully filled in the graphite plates. The pore structure of the graphite plate also has a direct impact on the penetration behavior, and EGP has more pore structures with a size less than 1 μm, which exhibited a lower penetration rate. Despite the higher porosity in EGP, it still

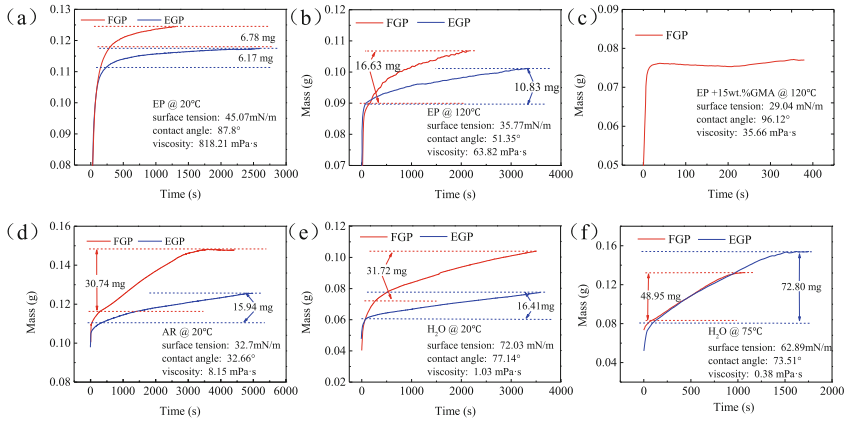

Fig. 3. Penetration rates of different types of liquids into the graphite plate at different temperatures: (a) EP @20 °C; (b) EP @120 °C; (c) EP + 15 wt% GMA @120 °C; (d) AR @20 °C; (e) H_2O @20 °C; (f) H_2O @75 °C

exhibited a lower upper limit of saturation absorption. In addition, when the viscosity of water decreased to 0.38 mPa s, it exhibited a rapid increase in both the penetration rate and the upper limit of saturation absorption.

3.2 Penetration Behavior Analysis

The penetration behavior of liquids in porous structures is usually described using Darcy's law, as shown in Eq. (1) [6]:

$$\overline{u} = -\frac{K}{\mu}\nabla p \tag{1}$$

where $\overline{u}$ represented the volume flow rate; K was the permeability coefficient related to the pore structure; μ was the liquid viscosity and p was the pressure driving the liquid flow. In the penetration process shown in Fig. 1(a), gravity was a resistance to flow and there was no other pressure gradient, so the effect of capillary forces (P_c) on the resin penetration behavior needs to be considered. In addition, the forces formed by the solid-liquid interaction, such as capillary forces, have also been confirmed to be an important component in driving/obstructing the penetration process, which also makes it exhibited nonlinear characteristics [7]. P_c was calculated by Eq. (2):

$$Pc = \frac{2\sigma \cdot \cos\theta}{r} \cdot \pi r^2 = 2\pi r \cdot \sigma \cdot \cos\theta \tag{2}$$

where σ was the surface tension of resin or water; θ was the contact angle and r was the radius of the pore. Based on Eq. (2), the capillary force for the penetration of EP into the pore with a pore size of 20 μm at 120 °C was 7 kPa, and the capillary force for the penetration of AR into this pore size at 20 °C was 8.5 kPa. The capillary forces for water at 20 °C and 75 °C were 5.0 kPa and 5.6 kPa, respectively. When the contact angle

was greater than 90°, the resin would not penetrate into the graphite plate effectively. This indicated that the capillary force was the main driving force. However, the higher capillary force of the resin exhibited a lower permeation rate and upper limit of saturation absorption, indicating that flow resistance has a more remarkable effect on the penetration process.

Boundary layer was a phenomenon that occurs at the solid-liquid interface, where the liquid flow velocity was significantly reduced due to intermolecular interaction forces. It has been confirmed that when the pore size reached the micron-meter level, the effect of the boundary layer on the resistance of liquid flow was not negligible, and the liquid flow in the pore was distinguished into a low flow rate region near the solid-liquid interface and a uniform flow rate region located in the middle region [8, 9], as illustrated in Fig. 1(c). And as the pore size decreased, the proportion of the boundary layer in the flow channel gradually increased, and the flow resistance would rise significantly [10]. It is worth noting that when the pore radius was equal to the thickness of the boundary layer, the liquid in the pore cannot flow through the pore under the influence of the boundary layer, and the pressure needs to be further increased to reduce the thickness of the boundary layer so that the liquid could flow through the pores [11, 12].

When we focused on the resin penetration process in graphite plate, the boundary layer gradually became thinner as the viscosity decreased, and the penetration rate increased significantly. At the same time smaller pores could be penetrated and the graphite plate showed a higher upper limit of absorption by the resin or water. In contrast, EGP possessed a more abundant microporous structure, the boundary layer forms a higher flow resistance, and more pores were not permeable, so it exhibited a lower permeation rate compared to FGP, and a lower saturation absorption. The impermeable pores at high viscosity changed to be permeated when the viscosity of water decreases to 0.38 mPa s, so it exhibited a significantly higher saturation absorption.

4 Conclusion

In this study, the penetration rates and upper limits of absorption of epoxy resins, acrylic resins and water into graphite plates with different pore structures were analyzed. The influence factors of penetration behavior were also analyzed in combination with capillary forces and boundary layers. The results showed that the penetration rate and the upper limit of absorption into the graphite plate increased significantly with the decrease of resin viscosity. As the EGP possessed more pores less than 1 μm, the flow resistance was significantly increased under the influence of the boundary layer and more pores were impermeable, thus exhibiting a lower penetration rate as well as an upper limit of absorption. Further, in order to achieve a more adequate impregnation of EGP by resin, the volume fraction of small pores should be reduced by adjusting the graphite particles, applying a lower viscosity resin as the infiltration agent as well as higher infiltration process pressure should also be concerned.

Acknowledgement. The authors would like to acknowledge the financial supports from the Key Technologies Research and Development Program (2020YFB1505904).

References

1. Du, C.: Preparation and properties of thin epoxy/compressed expanded graphite composite bipolar plates for proton exchange membrane fuel cells. J. Power Sour. **195**(16), 794–800 (2010)
2. Fan, R.: The conductive network optimization of composite graphite plates and its morphological analysis. Chem. Eng. J. **446**, 136652 (2022)
3. Lee, H.E.: Feasibility study on carbon-felt-reinforced thermoplastic composite materials for PEMFC bipolar plates. Compos. Struct. **180**, 378–385 (2017)
4. Du, C.: The preparation technique optimization of epoxy/compressed expanded graphite composite bipolar plates for proton exchange membrane fuel cells. J. Power Sour. **195**(16), 5312–5319 (2010)
5. Wang, X.: Collective enhancements on thermal-electrical and mechanical properties of graphite-based composite bipolar plates through the coupled manipulations of molding and impregnation pressures. Membranes (Basel) **12**, 222 (2022)
6. Mauran, S.: Application of the Carman-Kozeny correlation to a high-porosity and anisotropic consolidated medium: the compressed expanded natural graphite. Transp. Porous Med. **43**, 355–376 (2001)
7. Niessner, J.: Comparison of two-phase Darcy's law with a thermodynamically consistent approach. Transp. Porous Med. **88**, 133–148 (2011)
8. Pertsin, A.: Water−graphite interaction and behavior of water near the graphite surface. J. Phys. Chem. B **108**(4), 1357–1364 (2004)
9. Xiao, L.: Characteristics of boundary layer under microscale flow and regulation mechanism of nanomaterials on boundary layer. J. Mol. Liq. **368**, 120616 (2022)
10. Xu, S.: Influence of boundary-layer fluid on the seepage characteristic of low-permeability reservoir. J. Xian Shiyou Univ. **22**(2), 26–28 (2007)
11. Wang, X.: Experimental and theoretical investigation of nonlinear flow in low permeability reservoir. Procedia Environ. Sci. **11**, 1392–1399 (2011)
12. Song, F.: Nonlinear flow in low permeability reservoirs: modelling and experimental verification. Adv. Geo-Energy Res. **3**(1), 76–81 (2019)

Thermal Analysis and Optimization of Cold-Start Process of Alkaline Water Electrolysis System

Xintao Deng(✉), Fuyuan Yang, Yangyang Li, Jian Dang, and Minggao Ouyang

State Key Lab of Automotive Safety and Energy, Tsinghua University, Beijing 100084, People's Republic of China
dxt20@mails.tsinghua.edu.cn

Abstract. In this paper, a thermal model of commercial alkaline water electrolysis system is presented, including energy and mass balance model between system components and a two-stage graybox model of alkaline electrolyzer. The aim of this work is to study and improve the thermal behavior during cold-start process of electrolysis system. The model is used to simulate the cold-start process under various parametric settings such as electrolyte flow rate and electrolyte volume. Then, several optimization schemes are proposed and evaluated to be promising.

Keywords: Alkaline water electrolysis · Thermal analysis · Hydrogen production · System simulation

1 Introduction

The world is undergoing low-carbon energy transition. During the transition, hydrogen plays a fundamental role helping balance renewable electricity supply and demand, serving as long-term seasonal storage, raw material in industry and fuel in transportation [1, 2]. However, the commercial zero-carbon green hydrogen still faces uncertainties in production, transportation and storage technologies. With the characteristics of clean, efficient and capacity flexibility, water electrolysis stands out as one of the most promising and fast-growing technologies for renewable energy utilization. According to IRENA's forecast, in order to achieve the goal of limiting global warming within 1.5 °C by 2050, almost 5000 GW of hydrogen electrolyzer coupling with renewable energy will be needed by 2050, while the number was only 0.3 GW in 2021 [3].

When combined with renewable energy, the fluctuation and intermittent nature of input power needs to be paid extra attention. Solar energy fluctuates within days, while wind power is even more varying and intermittent. The efficient utilization of renewable energy puts forward requirements for the dynamic response capabilities of water electrolyzer [4]. Dynamic capabilities can be divided in two aspects. One is fast load regulation following the fluctuating power input. Literatures have shown that both alkaline and PEM electrolyzer have the ability to absorb fluctuating power as they can respond

H. Sun et al. (Eds.): WHTC 2023, SPPHY 393, pp. 297–311, 2024.
https://doi.org/10.1007/978-981-99-8631-6_30

fast enough to the load change [5–8]. Another is fast start-stop capability of the electrolysis system, which will be needed when considering off-grid scenarios and intermittent energy source such as solar and wind power. Slow start-up will lead to waste of renewable energy due to poor efficiency under low temperature. Currently, the cold-start of alkaline electrolysis system is especially retarded, mainly because of the low power density and large amount of liquid electrolyte stored in the systems [7]. According to previous studies, cold-start of alkaline electrolyzer generally requires more than one hour, sometimes with additional heating power, which further raises the energy consumption of hydrogen production [9, 10].

To seek for improvements, we need to firstly figure out the comes and goes of heat during alkaline electrolyzer operation. Previous studies have setup models to predict supplied power distribution and thermal characteristics of the system. Sakas et al. proposed a parameter adjustable dynamic mass and energy balance simulation model of an industrial alkaline water electrolysis system. The simulation results showed that 11.2% of supplied power was lost due to shunt current, 20.3% was lost due to overpotential [11]. Sánchez et al. developed a alkaline electrolysis plant model using Aspen Plus, finding that the system efficiency is 53.3% under 75 °C, 7bar, comparing with stack efficiency of 53% [12]. Diéguez et al. studied the thermal performance of a commercial alkaline water electrolysis system. He found that the power dissipated as heat can be reduced by 50–67% when supplied with higher quality DC current [13]. Jang et al. developed alkaline electrolysis system model to capture the temperature effect on the system performance. He pointed out that the system efficiency will increase from 75.86 to 77.01% under high electrolyte flow rate [14].

Aforementioned researchers have developed models to simulate thermal behavior of alkaline water electrolysis system. However, most of their concerns lied on the effect of temperature on electrochemical process instead of the dynamicity of system. To further understand and accelerate cold-start operation, more detailed and intrinsic thermal characteristics of electrolysis system remains to be investigated.

In this work, a steady state thermal model with modular components of an alkaline electrolysis system was developed and validated through dynamic testing data. Simulations have been carried out, and the cold-start processes under various parametric settings were evaluated. Finally, we investigated several schemes that can potentially bring the cold-start time down to 30 min.

2 Model Description

As our concentration was on the thermal behavior of the system, our model simplified the system to several components that primarily affect heat flow, including metal pipelines, gas-liquid separators, electrical heaters, and electrolysis stack. These components have either large surface area and thermal conductivity or exist as thermoelectric conversion devices. The following diagram shows the connections between major components (Fig. 1).

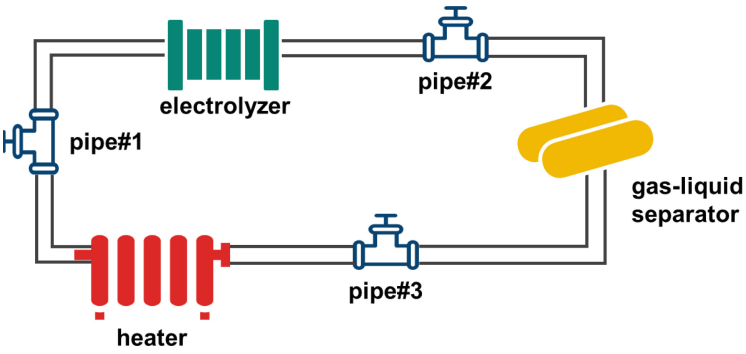

Fig. 1. Representative diagram of alkaline electrolysis system.

2.1 Thermal Model

Thermal liquid module of Matlab Simscape was used to setup our model. The thermal liquid module can couple the liquid mass flow with heat dissipation and absorption. We used controlled mass and heat flow source as the electrolyte flow rate and heating power input interface.

The heater used in the system consists of a cast aluminum external heater and a heat exchange pipe, as shown in Fig. 2 a), where all energy flow was indicated. The situation was basically the same in the electrolyzer, as shown in Fig. 2 b).

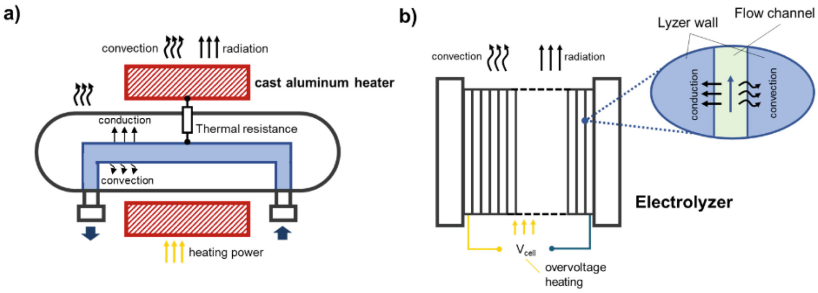

Fig. 2. Composition of heat flow in a) electrolyte heater; b) electrolyzer.

The heat transfer between flowing liquid and container wall can be wrote as in [15].

$$Q_H = Q_{conv} + Q_{cond} \tag{1}$$

where Q_{conv} is convective heat transfer, Q_{cond} is conductive heat transfer. With incompressible hypothesis we have:

$$Q_{conv} = \dot{m} c_p (T_{wall} - T_{fluid}) \left(1 - e^{-\frac{hA_{in}}{\dot{m}c_p}}\right) \tag{2}$$

$$Q_{cond} = \frac{k_{fluid} A_{in}}{D}(T_{wall} - T_{fluid}) \tag{3}$$

where $\dot{m}$ is mass flow rate of the fluid, c_p is specific heat, T_{wall} is container wall temperature and T_{fluid} is liquid temperature, A_{in} is container's inner surface area and A_{out} denotes the outer. h is heat transfer coefficient and depends on the Nusselt number $h = Nu\frac{k_{fluid}}{D}$, where k_{fluid} is thermal conductivity of the fluid and D is hydraulic diameter of the flow field.

The heat convection and radiation between components wall and environment were wrote as below.

$$Q_C = k_{conv,env} A_{out}(T_{wall} - T_{env}) \tag{4}$$

$$Q_R = k_{ra,env} A_{out}(T_{wall}^4 - T_{env}^4) \tag{5}$$

where $k_{conv,env}$ is convective heat transfer coefficient and $k_{ra,env}$ is radiation coefficient. A_{out} is container's outer surface area. T_{env} is environment temperature.

2.2 Electrochemical Model

The electrolyzer in the system will also be taken as a heat generative component, for its overpotential will convert into heat during hydrogen production. Part of the heat is absorbed by electrolyzer itself, another to the electrolyte and the rest is released into the environment through convection and radiation.

To simulate the thermal behavior of electrolyzer stack, we need to model its electrochemical characteristics. We developed a graybox two-stage model based on empirical equation and radial basis function fitting methods. The input of the model including current density, pressure, temperature and electrolyte flow rate, and it can predict polarization curve within a wide range of inputs, while only few experiment data and system knowledge were needed. The work flow of the model is shown in Fig. 3.

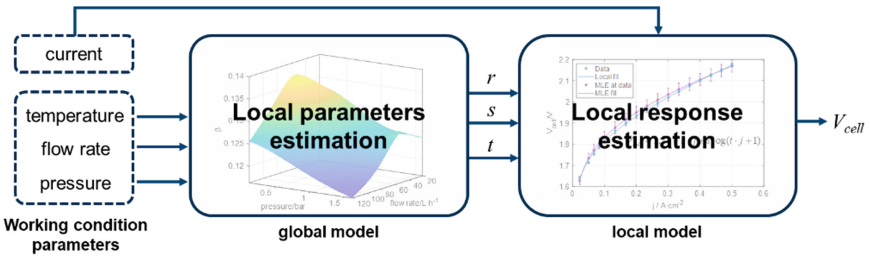

Fig. 3. Work flow of two-stage model.

The local model consists of an empirical equation. We adapted the three-parameter model following [16, 17].

$$V_{cell} = 1.23 + r \cdot j + s \log(t \cdot j + 1) \tag{6}$$

where r, s, t is the model parameter. r and t are related to temperature according to the author. According to previous works, we took all three parameters as the function of model variables [18–20].

We used sobol sequence [21] to generate experiment points across the parameter space. 22 experiment points were generated in current density range of 0.03–0.4 A/cm^2, temperature range of 40–80 °C, flow rate range of 20–120 L/h and gauge pressure range of 0–16 bar. The flow rate was restricted under high temperature to guarantee stable experimental condition, as well as avoiding gas purity problems [22] (Fig. 4).

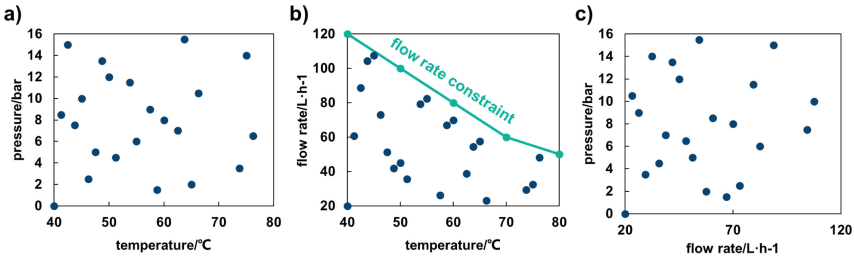

Fig. 4. Experiment design based on sobol sequence. Green line indicates flow rate constraint.

Radial basis function (RBF) was used to predict the model parameters across the working condition space. Then 7 sets of validation data were used for validation (Fig. 5).

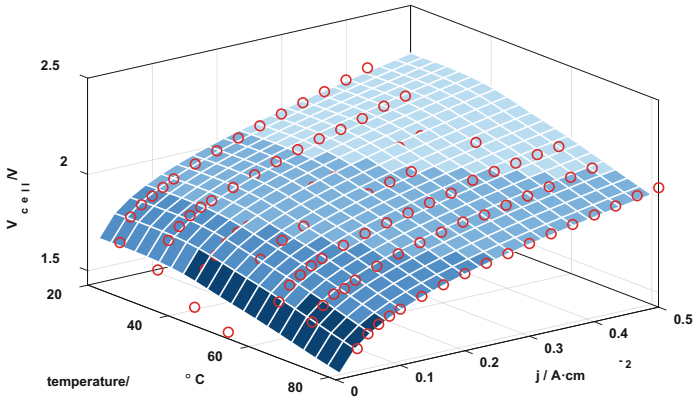

Fig. 5. Cell voltage prediction with respect to temperature. Red circles indicate validation data. The fitting RMSE is 0.026, normalized error sum of square was 16.2, log-likelihood function was 387.1. The RMSE of validation data prediction was 0.052.

The heat generated during electrochemical process was calculated from current, stack voltage and theoretical thermal neutral voltage. The thermal neutral voltage will

change with temperature. Following the equation proposed by [23], we have

$$\begin{cases} V_{tn} = V_{HHV} + \dfrac{3}{2nF}\dfrac{p_w}{p - p_w}Y \\ \ln p_w = 0.01621 - 0.1380m + 0.1933\sqrt{m} + 1.024\ln p_w^* \\ \ln p_w^* = 37.04 - \dfrac{6276}{T} - 3.416\ln T \\ Y = 42960 + 40.762T - 0.06682T^2 \end{cases} \tag{7}$$

The heating power of electrolyzer can be wrote as:

$$Q_{electrolyzer} = (V_{cell} - V_{tn})I_{cell} \tag{8}$$

Figure 6 shows the whole structure of our model.

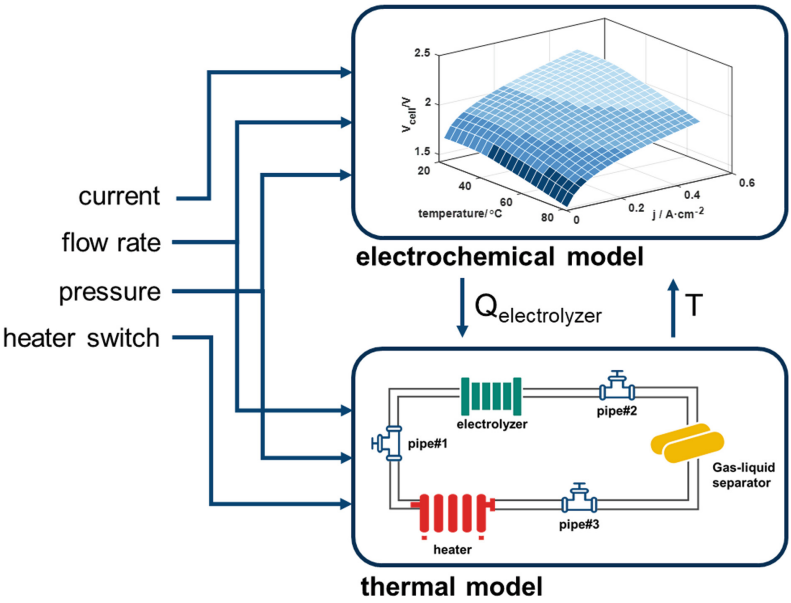

Fig. 6. Representative diagram of thermal model.

2.3 Model Validation

Actual system testing data was used to validate our thermal model. The tests were carried out on a commercial alkaline electrolysis system as shown in Fig. 7. The system has a 3.8 kW alkaline electrolyzer with an electrode area of 600 cm^2 and 8 single cells. Other system geometric parameters are listed in Table 1.

Three tests were carried out. In test I, only the heater was turned on; in test II, the heater and the electrolyzer were turned on and off simultaneously. During the test, the

Table 1. Component geometric parameters

Parameters	Value	Unit
Separator size	Φ200 × 1100	mm
Electrolyte pump flow rate range	0–150	L/h
Heat exchange pipe size	Φ108 × 820	mm
Electrolyzer size	Φ480 × 170	mm
Heater-electrolyzer pipe length	3000	mm
Electrolyzer-separator pipe length	1000	mm
Separator-heater pipe length	500	mm
Metal pipe size	1/2	in.

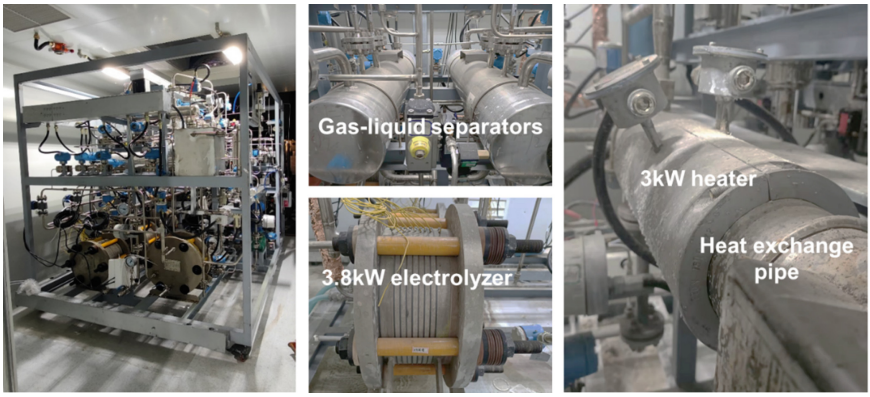

Fig. 7. Commercial alkaline electrolysis system

electrolyte pump power and system pressure remained unchanged. Data from test I and II were used to calibrate unknown system parameters. We focused on the heater outlet temperature and electrolyzer outlet temperature. Figure 8 shows the experiment data and calibrated simulation results. The parameters of calibrated model are listed in Table 2.

Another test III was an actual dynamic process, during which the heater, electrolyzer power and electrolyte flow rate varied with time. It was used to validate the simulation results. As can be seen in Fig. 10, the absolute error between predicted and experimental temperature was within 6 °C. The largest deviation was found to be in minutes after abrupt working condition change, particularly flow rate. This is mainly because the temperature was measured by platinum resistances in real system, which also have heat capacity but were neglected in simulations. The ignorance of temperature gradient inside the system component wall also accounts for simulation error (Fig. 9).

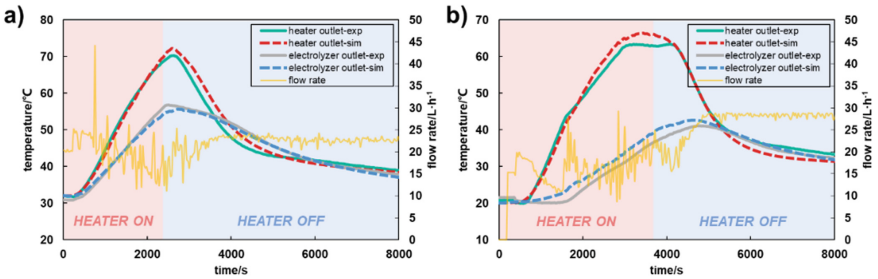

Fig. 8. Experiment and calibrated simulation result of a) test I; b) test II. Background color indicates the heater working state.

Table 2. Parameters used in model

Parameters	Value	Unit
Iron-air convective heat transfer coefficient	20	W/(m^2 K)
Heater-heat exchange pipe contact thermal resistance	0–150	L/h
Heater heat capacity	10	kJ/K
Heater-environment radiation coefficient	0.09	K/W
Heat exchange pipe heat capacity	8	kJ/K
Heat exchange pipe cross-sectional area	7854	mm^2
Heat exchange pipe hydraulic diameter	18	mm
Electrolyzer-environment radiation coefficient	8×10^{-8}	W/(m^2 K^4)
Electrolyzer heat capacity	88	kJ/K
Electrolyzer cross-sectional area	7040	mm^2
Electrolyzer hydraulic diameter	6	mm

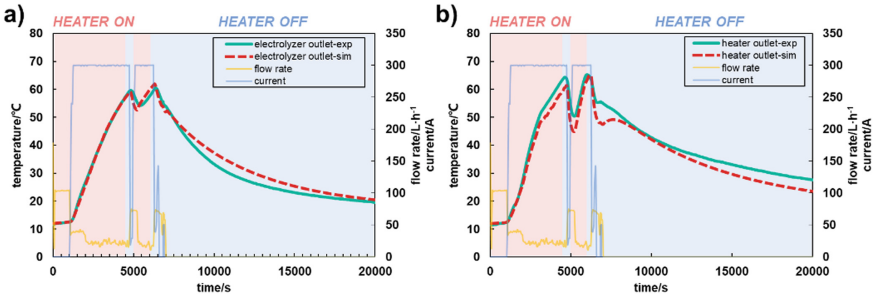

Fig. 9. Test III experiment and simulated result of a) electrolyzer outlet temperature; b) heater outlet temperature.

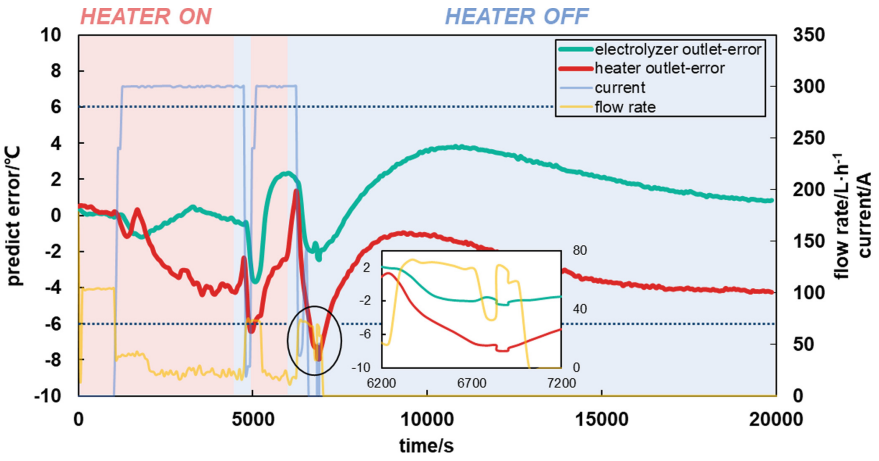

Fig. 10. Prediction error of test III. Subplot magnifies section with the greatest error.

3 Thermal Analysis

3.1 Cold-Start Process Analysis

Calibrated thermal model was used to derive the proportion of the heating power of each major component with a range of parameters of interest. We extracted the time spent before the electrolyzer outlet reaches 80 °C to assess cold-start speed. 80 °C was chosen because this is generally the acceptable operating temperature.

The effect of electrolyte flow rate and total liquid volume was evaluated as in Fig. 11. Lower flow rate is always better for cold-start because the slower electrolyte flows in electrolyzer channel, the more heat it receives from electrochemical overpotential. For the liquid volume, we represented it with the initial liquid volume in the separator. Under higher flow rate, larger liquid volume brought larger system heat capacity, so slower cold-start process. However, under low flow rate, less liquid made the cold-start faster. We investigated the temperature curve, finding that the electrolyzer inlet temperature with less liquid was higher, which made the heat transfer from electrolyte to electrolyzer more intense, along with more heat loss from electrolyzer surface to the environment. The inversion of liquid volume effect took place at flow rate of 2.5–2.75 m^3/h.

From the heat flow diagram in Fig. 11 b), we can learn that only 20.2% of total input electrical power was turned into heat, while the other part was consumed by electrochemical reaction. About a half of heating power was transferred to electrolyte, with 20.1% heat loss.

3.2 Optimization for Faster Cold-Start

In this section, we will evaluate several schemes to accelerate cold-start process. We set a cold-start time target of 30 min, which is comparable to commercial PEM system.

Constant current method

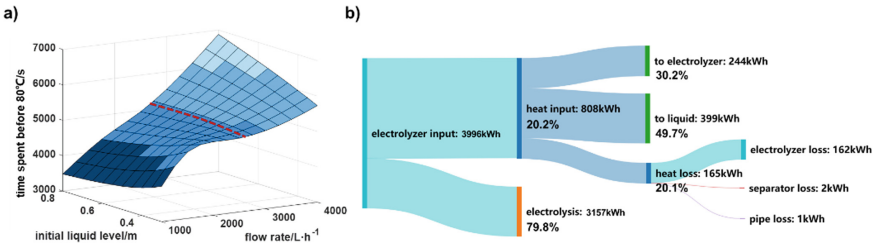

Fig. 11. a) Effect of flow rate and electrolyte volume on cold-start time; b) energy flow diagram of cold-start process.

The most intuitive method to accelerate cold-start is to apply larger current. We investigated several constant current densities from 2200 to 3500 A/m^2, and calculated the total energy consumption and its distribution ratio in different directions.

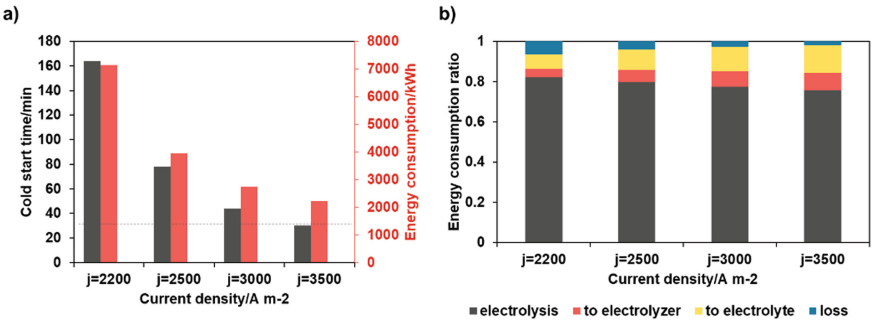

Fig. 12. a) Cold-start time and b) energy consumption ratio under different current densities.

It can be seen from Fig. 12 a) that the cold-start time was shorten to 30 min under 3500 A/cm^2. The energy consumption was reduced with the increasing current density, and the proportion of energy wasted on electrolysis as well as heat loss was also reduced. But the concern of constant current density method is that under low temperature, the electrode potential will be so high that it might cause irreversible damage to the catalyst.

Controlled voltage method

To eliminate the electrode degradation due to high potential, the controlled voltage method is proposed. The most common way is to gradually increase current density according to electrolysis voltage, called stepping current method. When the voltage control frequency is high enough, the stepping current becomes constant voltage method, which hold the electrolyzer voltage at constant level, as shown in Fig. 13 b). The cold-start time and energy consumption was shown in Fig. 13 a).

The cold-start time of stepping current method is shortened by 21.8% comparing to constant current, while it prevented the cell voltage from exceeding 2 V. The constant voltage of 2 V further shorten the cold-start time by 5.2%. If we wish to achieve

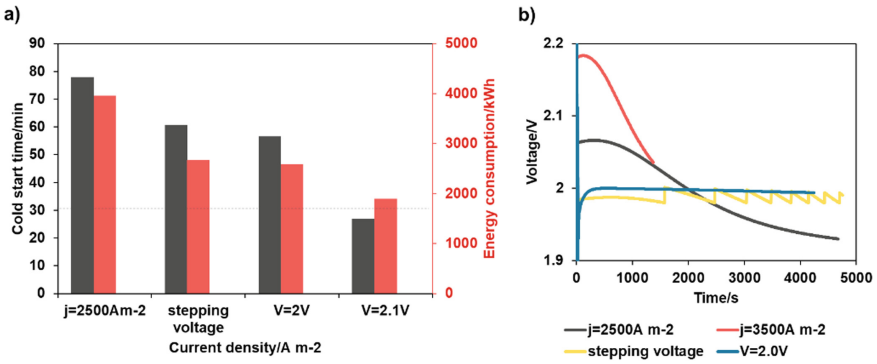

Fig. 13. a) Cold-start time and b) energy consumption ratio under different voltage control profile.

30 min cold-start, the constant voltage should be set to 2.1 V, and it saved 15.3% energy consumption comparing to constant current density of 3500 A/m^2.

Electrolyte heater

Installation of electrical heater seems to be a way to accelerate cold-start. We added a 300 kW heater before the inlet port of electrolyzer in the model. The results are shown in Fig. 14.

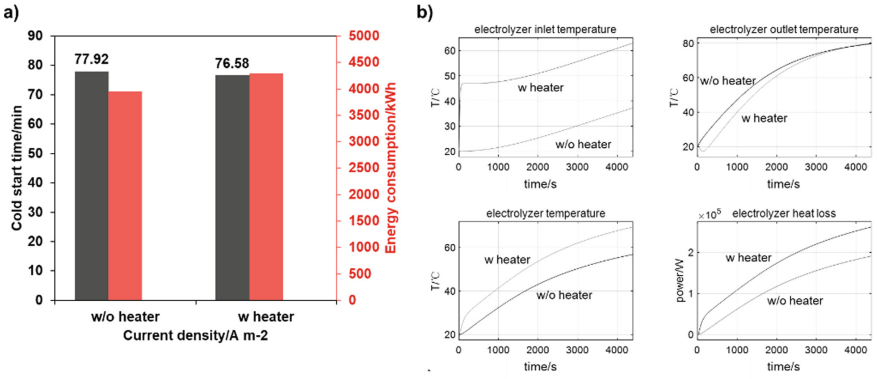

Fig. 14. a) Cold-start time with and without heater; b) system temperature curve during cold-start process.

The cold-start time with and without heater was close, but the case with heater consumed 8.6% more energy. We investigated the system temperature profiles as in Fig. 14 b), and found that the electrolyzer inlet temperature was much higher with the existence of heater. Hot electrolyte heated the electrolyzer so much, and finally reached a balance where the heat loss from electrolyzer surface offset the heater power. So, the heater method is not smart in commercial-scale system.

Dynamic resistance method

The largest portion of input energy waste is due to electrolysis reaction. If the reaction can be suppressed by increasing the internal resistance of electrolyzer, the utilization of input energy should be more efficient during heating process. We here proposed two ways of increasing internal ohmic resistance, one concerned with electron resistance and another ion resistance. The former method heats the electrolyzer bulk with the input power, and the latter transfers the power directly to electrolyte. The simulation results are shown in Fig. 15.

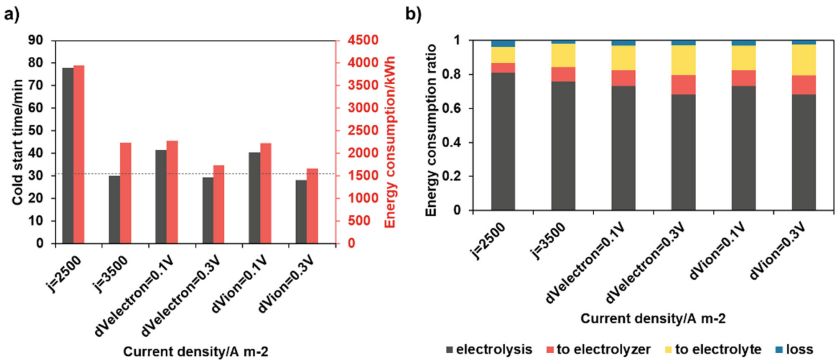

Fig. 15. a) Cold-start time and b) energy consumption ratio with and without dynamic resistance schemes.

The effect of increasing electron or ion resistance are similar. Increasing ohmic overpotential by 0.1 V reduced cold-start time by 46.2% and energy consumption by 42.0% comparing to constant current density of 3500 A/m^2. This improvement mainly attributed to the higher proportion of electrolyte-heating energy as in Fig. 15 b). To realize 30 min cold-start, the ohmic overpotential should be set to 0.3 V, and brought 24.0% energy saving comparing to 3500 A/m^2 constant current density.

The increased ohmic resistance should be eliminated at the end of cold-start. The way of achieving electron resistance adjustment may be through the dynamic control of compression force of electrolyzer with hydraulic compression system. As for the ion resistance, the application of stimuli-responsive smart gating membranes may be the solution, with which the ion resistance induced by porous membrane can be controlled [24].

4 Conclusion

In this paper, we studied the thermal behavior of alkaline water electrolysis system and the influence of flow rate and electrolyte volume on the cold-start process. Then we went through several methods that aims at accelerating cold-start. The conclusions drawn from the study are listed below.

1) During cold-start, only 20–30% of input power was used to generate heat (~10% to electrolyte), and 10–20% of heating power was lost.

2) Lowering the flow rate always gets faster cold-start, while the effect of electrolyte volume depends on the situation.
3) All accelerating schemes have their strength and weakness. We listed those methods that can potentially bring the cold-start time down to 30 min below (Table 3).

Table 3. Cold-start acceleration methods.

Strategy	Energy [kWh]	Strengths	Weakness
$j \geq 3500$ A m^2	2236	• Easy to implement;	• High risk of electrode irreversible degradation;
$V \geq 2.1$ V	1895	• Easy to implement;	• High electrode potential;
$\Delta V_{electron} \geq 0.3$ V	1737	• Low electrode potential; • Low energy consumption;	• Need of compression force control system;
$\Delta V_{ion} \geq 0.3$ V	1663	• No need of mechanical modification; • Lowest energy consumption;	• High electrode potential; • Need of advanced diaphragm;

References

1. Greene, D.L., Ogden, J.M., Lin, Z.: Challenges in the designing, planning and deployment of hydrogen refueling infrastructure for fuel cell electric vehicles. eTransportation **6** (2020). https://doi.org/10.1016/j.etran.2020.100086
2. Gao, W., Hu, Z., Huang, H., Xu, L., Fang, C., Li, J., et al.: All-condition economy evaluation method for fuel cell systems: system efficiency contour map. eTransportation **9** (2021). https://doi.org/10.1016/j.etran.2021.100127
3. I.R.E. Agency. World Energy Transitions Outlook: 1.5 °C Pathway. Journal (2021). https://www.irena.org/-/media/Files/IRENA/Agency/Publication/2021/Jun/IRENA_World_Energy_Transitions_Outlook_2021.pdf
4. Brauns, J., Turek, T.: Alkaline water electrolysis powered by renewable energy: a review. Processes **8** (2020). https://doi.org/10.3390/pr8020248
5. Carmo, M., Fritz, D.L., Mergel, J., Stolten, D.: A comprehensive review on PEM water electrolysis. Int. J. Hydrogen Energy **38**, 4901–4934 (2013). https://doi.org/10.1016/j.ijhydene.2013.01.151
6. Shen, X., Zhang, X., Li, G., Lie, T.T., Hong, L.: Experimental study on the external electrical thermal and dynamic power characteristics of alkaline water electrolyzer. Int. J. Energy Res. **42**, 3244–3257 (2018). https://doi.org/10.1002/er.4076
7. Tjarks, G., Mergel, J., Stolten, D.: Dynamic operation of electrolyzers—systems design and operating strategies. In: Hydrogen Science and Engineering: Materials, Processes, Systems and Technology, pp. 309–329 (2016)

8. Kiaee, M., Cruden, A., Infield, D., Chladek, P.: Utilisation of alkaline electrolysers to improve power system frequency stability with a high penetration of wind power. IET Renew. Power Gener. **8**, 529–536 (2014). https://doi.org/10.1049/iet-rpg.2012.0190
9. Buttler, A., Spliethoff, H.: Current status of water electrolysis for energy storage, grid balancing and sector coupling via power-to-gas and power-to-liquids: a review. Renew. Sustain. Energy Rev. **82**, 2440–2454 (2018). https://doi.org/10.1016/j.rser.2017.09.003
10. Varela, C., Mostafa, M., Zondervan, E.: Modeling alkaline water electrolysis for power-to-x applications: a scheduling approach. Int. J. Hydrogen Energy **46**, 9303–9313 (2021). https://doi.org/10.1016/j.ijhydene.2020.12.111
11. Sakas, G., Ibáñez-Rioja, A., Ruuskanen, V., Kosonen, A., Ahola, J., Bergmann, O.: Dynamic energy and mass balance model for an industrial alkaline water electrolyzer plant process. Int. J. Hydrogen Energy **47**, 4328–4345 (2022). https://doi.org/10.1016/j.ijhydene.2021.11.126
12. Sánchez, M., Amores, E., Abad, D., Rodríguez, L., Clemente-Jul, C.: Aspen Plus model of an alkaline electrolysis system for hydrogen production. Int. J. Hydrogen Energy **45**, 3916–3929 (2020). https://doi.org/10.1016/j.ijhydene.2019.12.027
13. Diéguez, P.M., Ursúa, A., Sanchis, P., Sopena, C., Guelbenzu, E., Gandía, L.M.: Thermal performance of a commercial alkaline water electrolyzer: experimental study and mathematical modeling. Int. J. Hydrogen Energy **33**, 7338–7354 (2008). https://doi.org/10.1016/j.ijhydene.2008.09.051
14. Jang, D., Choi, W., Cho, H.S., Cho, W.C., Kim, C.H., Kang, S.: Numerical modeling and analysis of the temperature effect on the performance of an alkaline water electrolysis system. J. Power Sour. **506** (2021). https://doi.org/10.1016/j.jpowsour.2021.230106
15. Çengel, Y.A.: Heat and Mass Transfer: A Practical Approach, 3rd edn. McGraw-Hill, Boston (2007)
16. Ulleberg, Ø., Mørner, S.O.: TRNSYS simulation models for solar-hydrogen systems. Solar Energy **59**, 271–279 (1997). https://doi.org/10.1016/S0038-092X(97)00015-7
17. Ulleberg, Ø.: Modeling of advanced alkaline electrolyzers: a system simulation approach. Int. J. Hydrogen Energy **28**, 21–33 (2003). https://doi.org/10.1016/S0360-3199(02)00033-2
18. Abdin, Z., Webb, C.J., Gray, E.M.: Modelling and simulation of an alkaline electrolyser cell. Energy **138**, 316–331 (2017). https://doi.org/10.1016/j.energy.2017.07.053
19. Zhang, D., Zeng, K.: Evaluating the behavior of electrolytic gas bubbles and their effect on the cell voltage in alkaline water electrolysis. Ind. Eng. Chem. Res. **51**, 13825–13832 (2012). https://doi.org/10.1021/ie301029e
20. Vogt, H.: The quantities affecting the bubble coverage of gas-evolving electrodes. Electrochim. Acta **235**, 495–499 (2017). https://doi.org/10.1016/j.electacta.2017.03.116
21. Mohd Azmin, F., Stobart, R.: Benefiting from sobol sequences experiment design type for model-based calibration. SAE Technical Papers, Apr 2015. https://doi.org/10.4271/2015-01-1640
22. Brauns, J., Turek, T.: Experimental evaluation of dynamic operating concepts for alkaline water electrolyzers powered by renewable energy. Electrochim. Acta **404** (2022). https://doi.org/10.1016/j.electacta.2021.139715
23. LeRoy, R.L., Bowen, C.T., LeRoy, R.L., Bowen, C.T., LeRoy, D.J.: The thermodynamics of aqueous water electrolysis. J. Electrochem. Soc. **127**, 1954–1962 (1980). https://doi.org/10.1149/1.2130044
24. Liu, Z., Wang, W., Xie, R., Ju, X.J., Chu, L.Y.: Stimuli-responsive smart gating membranes. Chem. Soc. Rev. **45**, 460–475 (2016). https://doi.org/10.1039/c5cs00692a

Effect of Flow Channel Blockage on the Scale-Up of Proton Exchange Membrane Fuel Cells

Bin Wang, Weitong Pan(✉), Longfei Tang, Guoyu Zhang, Yunfei Gao, Xueli Chen(✉), and Fuchen Wang

Institute of Clean Coal Technology, East China University of Science and Technology, 130 Meilong Road, Shanghai, China
{pwt,cxl}@ecust.edu.cn

Abstract. Optimizing flow field structure can effectively improve the performance of Proton Exchange Membrane Fuel Cell (PEMFC). Adding the block in the flow channel is one of the approaches. In this work, the enhanced transport characteristic of the block is re-examined, and its effect on the performance of the fuel cell scale-up is further revealed. The models of single-channel fuel cells with different lengths L and blockage ratio β are developed. Results show that the best cell performance exhibits when $\beta = 100\%$ due to the combined effect of the block and upstream zone. The convection appears below the block, and higher upstream pressure is induced, both of which increase the oxygen concentration at the catalyst layer. Besides, results indicate that the performance of the scaled-up fuel cell with blockage increases at a slower rate. Combined with the pump power, it is found that the addition of the block with $\beta = 100\%$ is indeed beneficial for the fuel cell scale-up. The findings of different blockage effects on different-sized cells provide guidelines for the flow field design.

Keywords: Proton exchange membrane fuel cell · Flow channel · Scale-up · Block · Net power

1 Introduction

Proton Exchange Membrane Fuel Cell (PEMFC) has a wide range of application prospects in stationary power plants, transportation, and other industries with the benefits of high power density and efficiency, no carbon emissions, moderate operating temperature, etc. [1, 2]. However, development bottlenecks exist in the commercialization of PEMFC, primarily in three technical indicators of performance, cost, and durability [3]. Optimizing flow field structure can effectively improve the performance of PEMFC.

The flow channel structure of Bipolar Plate (BP) has been extensively investigated throughout the years. The two most prevalent flow channel types could be classified as fine channel-type and pin-type [4]. In addition to the traditional parallel, serpentine, and interdigitated flow channel, the fine channel-type flow channel also comprises the flow channel with blocks (or baffles) and the bionic flow channel, etc. In the pin-type flow channel, a set of regularly spaced obstacles protrudes from the flow field plate. The

H. Sun et al. (Eds.): WHTC 2023, SPPHY 393, pp. 312–333, 2024.
https://doi.org/10.1007/978-981-99-8631-6_31

reactant gas flows in the flow channel formed by the set of obstacles, with the main flow characteristic being the bypass flow in the confined space rather than the inward flow in the fine channel. Benefits and drawbacks of the conventional flow channel are outlined in the literature [5–7]. The fine channel-type flow channel structure is the most frequently used in practice, notably the parallel flow channel, which is the most typical.

In the past decade, the modified version of parallel flow channels has been widely studied [8]. Adding blocks (or baffles) in the flow channel could effectively improve the transport of reactants to the porous electrode and thus improve the fuel cell performance. Li et al. [9] optimized the design of the flow channel with partially blocked blocks, and the results showed that when the number of blocks was 16, the net power density of the fuel cell reached the maximum. Ghanbarian et al. [10] considered the effect of various shapes of blocks (square, semicircular and trapezoidal) in the cathode flow channel on the performance of PEMFC. The staggered case outperformed the in-line case by 18% when Heidary et al. [11] compared the results of in-line and staggered configurations of blocks in the parallel flow channel. Chen et al. [12] investigated the impact of the backwind length of the baffle on the output power and the pressure loss.

Single channel is the most basic type of flow channel. Wu et al. [13] inserted different numbers of cuboid blocks laterally on the flow channel and found that the performance of the fuel cell was better under a reasonable pressure drop. Heidary et al. [14] numerically studied the effect of partially blocked and entirely blocked blocks on the performance of the fuel cell. Wang et al. [15] established a 3D multiphase fuel cell model with the Forchheimer inertial effect to simulate the baffle-induced convection more accurately. The results of Perng et al. [16] showed that the trapezoidal baffle with an angle of 60° and a height of 1.125 mm improved the net power the best among all designs of the trapezoidal baffle by about 90% compared to the conventional straight flow channel without baffles. Fan et al. [17] studied baffles of multi-plate structure and integrated structure using a 3D multiphase numerical model. Chen et al. [18] proposed a streamlined porous baffle-oriented flow channel to numerically investigate the performance of the fuel cell and water distribution in the straight flow channel. In contrast to the conventional straight flow channel, Guo et al. [19] demonstrated that both the single-block and the double-block flow channel could facilitate the removal of liquid water.

In conclusion, the placement of blocks in the flow channel could effectively enhance the transport of reactants from the flow channel to the gas diffusion layer, thus improving the performance of PEMFC. However, most of the studies focused on the enhanced transport characteristic in the block zone, while the effect of upstream pressure was not elucidated. In addition, the scale-up is a requirement for the commercialization of PEMFC. The study of the role of the block during the fuel cell scale-up is lacking.

Therefore, a systematic investigation is conducted for single-channel fuel cells with different lengths L and blockage β based on CFD software Fluent. The enhanced transport characteristic of the block is re-examined, and its effect on the performance of the fuel cell scale-up is further revealed.

2 Modeling and Simulation

2.1 Physic Model

A rectangular block is set inside the cathode flow channel (the width of the block is equal to the width of the flow channel), and the PEMFC model is established with different values of β (the height ratio of the block to the flow channel $\beta = \frac{h_{\text{block}}}{h}$, , i.e., the blockage ratio) and lengths L (25 mm, 50 mm, 100 mm, 150 mm, and 200 mm).

In Fig. 1, the computational domain and mesh of 25 mm PEMFC are displayed. Bipolar Plate (BP), Gas Diffusion Layer (GDL), Catalyst Layer (CL), and Proton Exchange Membrane (PEM) are all included in the computational domain. Hexahedron mesh is used in this model. The mesh for GDL, CL PEM is denser.

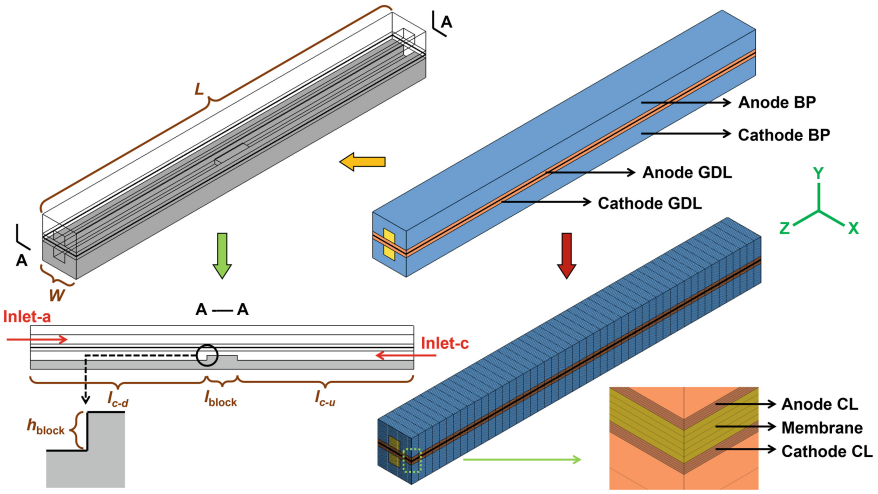

Fig. 1. Computational domain and mesh.

Geometric parameters of the PEMFC model are shown in Table 1. Operating parameters are adjusted according to the experiment of Wang et al. [20] in Sect. 2.6, and are shown in Table 2.

2.2 Numerical Model

Assumptions

For the convenience of computation, the following assumptions are made for the numerical model developed:

(1) The fuel cell operates under the steady-state condition.
(2) Raw material and product water are limited to the gas phase, and there is no phase transition during the operation.
(3) All gases are incompressible ideal gases and follow the ideal gas equation.

Table 1. Geometric parameters.

Geometric parameters	Physical quantities	Unit	Value
PEMFC length	L	mm	25/50/100/150/200
PEMFC width	W	mm	2.4
Flow channel length	l	mm	25/50/100/150/200
Flow channel width	w	mm	0.8
Flow channel height	h	mm	0.6
Rib width	s	mm	0.8
GDL thickness	δ_{GDL}	mm	0.2
CL thickness	δ_{CL}	mm	0.01
PEM thickness	δ_{PEM}	mm	0.03
BP thickness	δ_{BP}	mm	1.2
Block length	l_{block}	mm	2
Block width	w_{block}	mm	0.8
Block height	h_{block}	mm	0.3 ($\beta = 50\%$)/0.54 ($\beta = 90\%$)/0.6 ($\beta = 100\%$)
Length from block to cathode inlet	$l_{\mathrm{c\text{-}u}}$	mm	11.5/24/49/74/99
Length from block to cathode outlet	$l_{\mathrm{c\text{-}d}}$	mm	11.5/24/49/74/99

(4) The flow of fluid during the operation is laminar flow (Re $<$ 2000).
(5) The isotropic and uniform porous media structure in Membrane Electrode Assembly (MEA).

Governing Equations

Due to the constant flow and incompressibility assumptions, the mass conservation equation is

$$\nabla \cdot (\varepsilon \rho \vec{u}) = S_{\mathrm{m}} \tag{1}$$

where ε is the porosity of the porous media layer, $\varepsilon = 1$ in the flow channel; ρ is the density; $\vec{u}$ is the fluid velocity; S_{m} is the mass source term, which is solved separately according to different computational domains. $S_{\mathrm{m}} = 0$ for the flow channel and GDL; S_{m} for the anode and cathode CL is expressed by the following equation

$$\begin{aligned} S_{\mathrm{ma}} &= S_{\mathrm{H_2}} = -\frac{M_{\mathrm{H_2}}}{2F} i_{\mathrm{a}} \\ S_{\mathrm{mc}} &= S_{\mathrm{H_2O}} + S_{\mathrm{O_2}} = \frac{M_{\mathrm{H_2O}}}{2F} i_{\mathrm{c}} - \frac{M_{\mathrm{O_2}}}{4F} i_{\mathrm{c}}, \end{aligned} \tag{2}$$

Table 2. Operating parameters.

Operating parameters	Physic quantities	Unit	Value
Anode inlet temperature	t_a	K	353.15
Cathode inlet temperature	t_c	K	353.15
Operating temperature	t	K	353.15
Operating pressure	p	atm	1
Anode Inlet H_2/H_2O mass fraction	/	/	0.8/0.2
Cathode Inlet $O_2/H_2O/N_2$ mass fraction	/	/	0.2/0.1/0.7
GDL porosity	ε_{GDL}	/	0.5
GDL permeability	K_{GDL}	m^2	10^{-12}
CL porosity	ε_{CL}	/	0.5
CL permeability	K_{CL}	m^2	10^{-12}
Anode reference current density	${i_a}^{ref}$	A/m^2	7500
Cathode reference current density	${i_c}^{ref}$	A/m^2	20
Anode reference concentration	${c_a}^{ref}$	$kmol/m^3$	0.04
Cathode reference concentration	${c_c}^{ref}$	$kmol/m^3$	0.04
Anode concentration exponent	γ_a	/	0.5
Cathode concentration exponent	γ_c	/	1
Open-circuit voltage	V_{open}	V	1.0
Anode exchange coefficient	α_a	/	1
Cathode exchange coefficient	α_c	/	2

where M, F, and i are the molar mass, Faraday constant and the exchange current density, respectively. Subscripts a and c denote the anode and the cathode, respectively.

Momentum conservation equation is

$$\nabla \cdot (\varepsilon \rho \vec{u}\vec{u}) = -\varepsilon \nabla p + \nabla \cdot (\varepsilon \mu \nabla \vec{u}) + S_u \tag{3}$$

where p, μ, and S_u are the pressure, the viscosity, and the momentum source term, respectively. In the flow channel, $S_u = 0$; According to Darcy's law, in the porous media

$$S_u = -\frac{\mu}{\kappa}\varepsilon^2 \vec{u} \tag{4}$$

where κ is the permeability.

Energy conservation equation is

$$\nabla \cdot (\varepsilon \rho c_p \vec{u} T) = \nabla \cdot (k^{eff} \nabla T) + S_h \tag{5}$$

where T, c_p, and k^{eff} denote the temperature, the heat capacity at constant pressure, and the effective thermal conductivity, respectively. Due to the irreversible process during

the operation, not all chemical energy is utilized to provide the electrical work. The remaining energy conversion is incorporated into the source term S_h. S_h remains constant during the reaction process since there is no phase change. S_h is expressed by the following equation

$$S_h = h_{react} - i_{a,c}\eta_{a,c} + I^2 R_{ohm} \tag{6}$$

In this equation, the right three terms are the net enthalpy change of the reaction, the heat generated by the overpotential, and the ohmic heat generated by the conduction medium, respectively.

Species conservation equation is

$$\nabla \cdot (\varepsilon \vec{u} c_i) = \nabla \cdot \vec{J}_i + S_i \tag{7}$$

where c_i, $\vec{J}_i$, and S_i denote the species concentration, the vector of diffusion flux, and the species source term, respectively. The subscript i indicates species (at the anode indicates H_2 and H_2O, respectively and at the cathode indicates O_2, N_2, and H_2O, respectively). $\vec{J}_i$ Can be obtained from the Stefan-Maxwell equation [21]

$$\vec{J}_i = \sum_{j=1}^{N-1} D_{ij}^{eff} \nabla c_i \tag{8}$$

where D_{ij}^{eff} is the effective diffusion coefficient based on the binary species i-j, whose expression is [22]

$$D_{ij}^{eff} = \varepsilon^{1.5} D_{ij} \tag{9}$$

where the binary diffusion coefficient D_{ij} is expressed by[21]

$$D_{ij} = \frac{T^{1.75}\sqrt{\frac{1}{M_i} + \frac{1}{M_j}}}{p(\sqrt[3]{\sum v_i} + \sqrt[3]{\sum v_j})} \times 10^{-8} \tag{10}$$

where M is the molar mass and v_i is the diffusion volume of different gas species molecules.

The species source term S_i in Eq. (7) is 0 in the flow channel and GDL. In CL, the source terms for H_2, O_2, and H_2O are

$$S_{H_2} = -\frac{M_{H_2}}{2F} i_a,\ S_{O_2} = -\frac{M_{O_2}}{4F} i_c,\ S_{H_2O} = -\frac{M_{H_2O}}{2F} i_c \tag{11}$$

The core of electrochemical reaction model is the computation of electrochemical reaction rate, which is described using Butler-Volmer equation

$$i_a = \zeta_a i_{a,ref} \left(\frac{c_{H_2}}{c_{H_2,ref}}\right)^{0.5} \left(e^{\frac{\alpha_a F}{RT}\eta_a} - e^{-\frac{\alpha_c F}{RT}\eta_c}\right) \tag{12}$$

$$i_c = \zeta_c i_{c,ref} \left(\frac{c_{O_2}}{c_{O_2,ref}}\right) \left(-e^{\frac{\alpha_a F}{RT}\eta_a} + e^{-\frac{\alpha_c F}{RT}\eta_c}\right) \tag{13}$$

The above two equations consider the effects of the reactant concentration, temperature, and overpotential on the electrochemical reaction. Where η is the overpotential; ζ is the specific active surface area; i_{ref} is the reference exchange current density; c_{i}, $c_{\text{i,ref}}$ are the local molar concentration and the reference molar concentration of species i, respectively; α is the charge transfer coefficient.

The driving force of the electrochemical reaction is the difference between the potential of the solid phase and the potential of the membrane phase, both of which are called bipotential. On this basis, the corresponding two charge conservation equations are proposed for electron conduction in solid conducting materials (solid regions of Current Collector and porous layers) and proton transfer in the proton exchange membrane electrolyte in the form of

$$\nabla \cdot (\sigma_{\text{sol}} \nabla \phi_{\text{sol}}) + i_{\text{sol}} = 0 \tag{14}$$

$$\nabla \cdot (\sigma_{\text{pem}} \nabla \phi_{\text{pem}}) + i_{\text{pem}} = 0 \tag{15}$$

where Φ_{sol} and Φ_{pem} are the solid phase potential and the membrane phase potential, respectively; i_{sol} and i_{pem} are the electron current and the proton current source term, respectively, and $i_{\text{sol}} + i_{\text{pem}} = 0$; σ is the conductivity of the solid phase membrane phase. Current source terms are somewhat different at the anode and the cathode. At anode, $i_{\text{sol}} = -i_{\text{a}} < 0$ and $i_{\text{pem}} = i_{\text{c}} > 0$; at cathode, $i_{\text{sol}} = i_{\text{a}} > 0$ and $i_{\text{pem}} = -i_{\text{c}} < 0$.

The relationship between the overpotential of the anode and the cathode, bipotential, and electrode potential is

$$\eta_{\text{a}} = \phi_{\text{sol}} - \phi_{\text{pem}} \tag{16}$$

$$\eta_{\text{c}} = \phi_{\text{sol}} - \phi_{\text{pem}} - V_{\text{open}} \tag{17}$$

For the model of water transfer in PEM, the proton conductivity σ_{pem} in Eq. (15) can be expressed as

$$\sigma_{\text{pem}} = (0.514\lambda - 0.326) e^{1268\left(\frac{1}{303} - \frac{1}{T}\right)} \tag{18}$$

where λ is the number of water molecules per sulfonic acid group, and the relationship between it and the water saturation α is

$$\begin{aligned} &\lambda = 0.043 + 17.81\alpha - 39.85\alpha^2 + 36.0\alpha^3 (0 < \alpha \leq 1) \\ &\lambda = 14.0 + 1.4(\alpha - 1) (1 < \alpha \leq 3) \\ &\lambda = 16.8 \ (\alpha > 3) \end{aligned} \tag{19}$$

where the activity of water a is expressed by

$$a = \frac{p_{\text{wv}}}{p_{\text{sat}}} \tag{20}$$

where p_{wv} is the pressure of the water vapor; p_{sat} is the saturation vapor pressure.

The mode of water transfer in the membrane includes electromigration and differential concentration diffusion. The electromigration water flux is

$$N_{\mathrm{w}} = n_{\mathrm{d}} \frac{I}{F} \tag{21}$$

where $n_{\mathrm{d}} = \frac{2.5\lambda}{22}$,

n_{d} is the electromigration coefficient, i.e., the number of water molecules carried per transferred proton.

The differential diffusion water flux in PEM is

$$J_{\mathrm{w}}^{\mathrm{diff}} = -\frac{\rho_{\mathrm{m}}}{M_{\mathrm{m}}} M_{\mathrm{H_2O}} D_{\mathrm{l}} \nabla \lambda \tag{22}$$

where ρ_{m} and M_{m} are the density and the equivalent mass of the membrane, respectively. The diffusion coefficient of water in the membrane D_{l} is expressed by

$$D_{\mathrm{l}} = f(\lambda) e^{2416\left(\frac{1}{303} - \frac{1}{T}\right)} \tag{23}$$

where

$$\begin{aligned} f(\lambda) &= 10^{-10} (\lambda < 2) \\ f(\lambda) &= 10^{-10} [1 + 2(\lambda - 2)] (2 \leq \lambda \leq 3) \\ f(\lambda) &= 10^{-10} \times [3 - 1.67(\lambda - 3)] (3 < \lambda < 4.5) \\ f(\lambda) &= 1.25 \times 10^{-10} (\lambda > 4.5) \end{aligned} \tag{24}$$

2.3 Boundary Conditions

The inlet mass flow rate is set to 1.5×10^{-7} kg/s at the anode and 1.25×10^{-6} kg/s at the cathode for the 25 mm PEMFC, both of which increase proportionally with the length of the fuel cell.

The boundary conditions required for the computational domain are shown in Table 3. In addition, the no-slip boundary condition is set for all solid surfaces, and the isothermal condition is set for all walls.

2.4 Numerical Solution Method

The above control equations are solved using CFD software Fluent. In the numerical simulation, all differential equations are discretized by the finite volume method. The Semi-Implicit Method for Pressure Linked Equations (SIMPLE) algorithm for the pressure-velocity coupling is employed. Based on the constant pressure solution, the cathode voltage is set to a specific potential. The value starts at a voltage near the open-circuit voltage and gradually decreases, with each solution converging.

Table 3. Boundary conditions.

Zone	Boundary types	Boundary Conditions
Anode inlet	Mass flow inlet	[1.5 (25 mm)/3 (50 mm)/6 (100 mm)/9 (150 mm)/12 (200 mm)] $\times$ 10^{-7} kg/s
Cathode inlet	Mass flow inlet	[1.25 (25 mm)/2.5 (50 mm)/5 (100 mm)/7.5 (150 mm)/10 (200 mm)] $\times$ 10^{-6} kg/s
Anode outlet	Pressure outlet	$P_g = 0$ Pa
Cathode outlet	Pressure outlet	$P_g = 0$ Pa
Anode terminal	Wall	$\Phi_{sol} = 0$; $\partial\Phi_{pem}/\partial_y = 0$
Cathode terminal	Wall	$\Phi_{sol} = V_{cell}$; $\partial\Phi_{pem}/\partial_y = 0$
External boundary	Wall	$\partial\Phi_{pem}/\partial_x = 0$; $\partial\Phi_{pem}/\partial_z = 0$ $\partial\Phi_{sol}/\partial_x = 0$; $\partial\Phi_{sol}/\partial_z = 0$

2.5 Mesh Independence Test

To avoid the influence of mesh numbers on simulation results, the mesh independence test is required. The total mesh numbers are set to 98,400, 135,000, 390,000, and 765,000, respectively. Polarization curves are made for each setting of mesh numbers, as shown in Fig. 2. The current density at 0.3 V increases gradually as mesh numbers increase, with current density growth rates of 1.12%, 1.84%, and 0.50%, respectively. It can be seen that the growth rate of current density decreases when the mesh numbers increase from 390,000 to 765,000. The current densities are essentially comparable at these two settings of mesh numbers. Considering the computational resource comprehensively, a setting with mesh numbers of 390,000 is employed for the follow-up work.

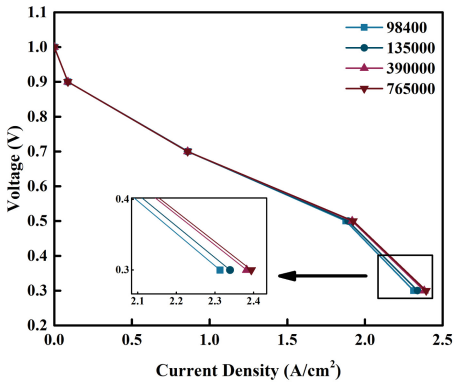

Fig. 2. Polarization curves at different settings of mesh numbers.

2.6 Model Validation

To validate the accuracy of the model, the polarization curve of the single-channel fuel cell obtained from the numerical simulation is compared with experimental values by varying corresponding simulation parameters according to the experimental conditions of Wang et al. [20]. The experiment of Wang et al. [20] was also used to validate the model in other simulation studies [23–25]. The comparison result is given in Fig. 3. It can be seen that numerical results are in good agreement with experimental data.

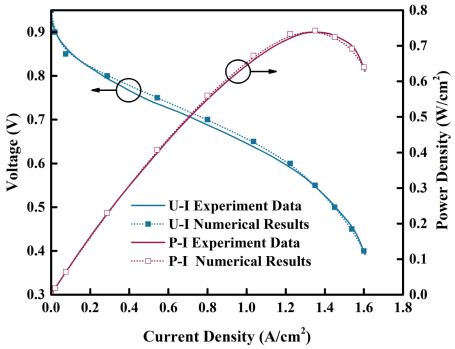

Fig. 3. Comparison of numerical results with experiment data from [20].

3 Results and Discussion

3.1 Effect of the Block on the Performance of PEMFC

Comparison of the Electrochemical Performance

A block is placed in the cathode flow channel for fuel cells with different lengths (25 mm, 50 mm, 100 mm, 150 mm, 200 mm). The distance from the block to the cathode inlet equals the distance from the block to the cathode outlet ($l_{\text{c-u}} = l_{\text{c-d}}$). Simulations are performed without the block ($\beta = 0\%$) and with $\beta = 50\%$, 90%, and 100%, respectively. Corresponding polarization curves are made (as shown in Fig. 4).

The polarization curves at $\beta = 50\%$ and $\beta = 0\%$ largely overlap, indicating that the block with $\beta = 50\%$ has almost no effect on the performance. The polarization curve shifts at $\beta = 90\%$, and the performance is improved. While at $\beta = 100\%$, the performance improvement is more obvious. Taking the 25 mm fuel cell as an example, the power density at 0.5 V operating voltage increases by 0.37% at $\beta = 50\%$, 1.30% at $\beta = 90\%$, and 13.26% at $\beta = 100\%$ compared to the case without the block.

Analysis for the Enhanced Transport Characteristic

Since the block with $\beta = 100\%$ has the best effect on the performance enhancement, the enhanced transport characteristic of this block setting is analyzed for the 25 mm fuel cell as an example. 0.5 V operating voltage is selected. The fuel cell is divided into three

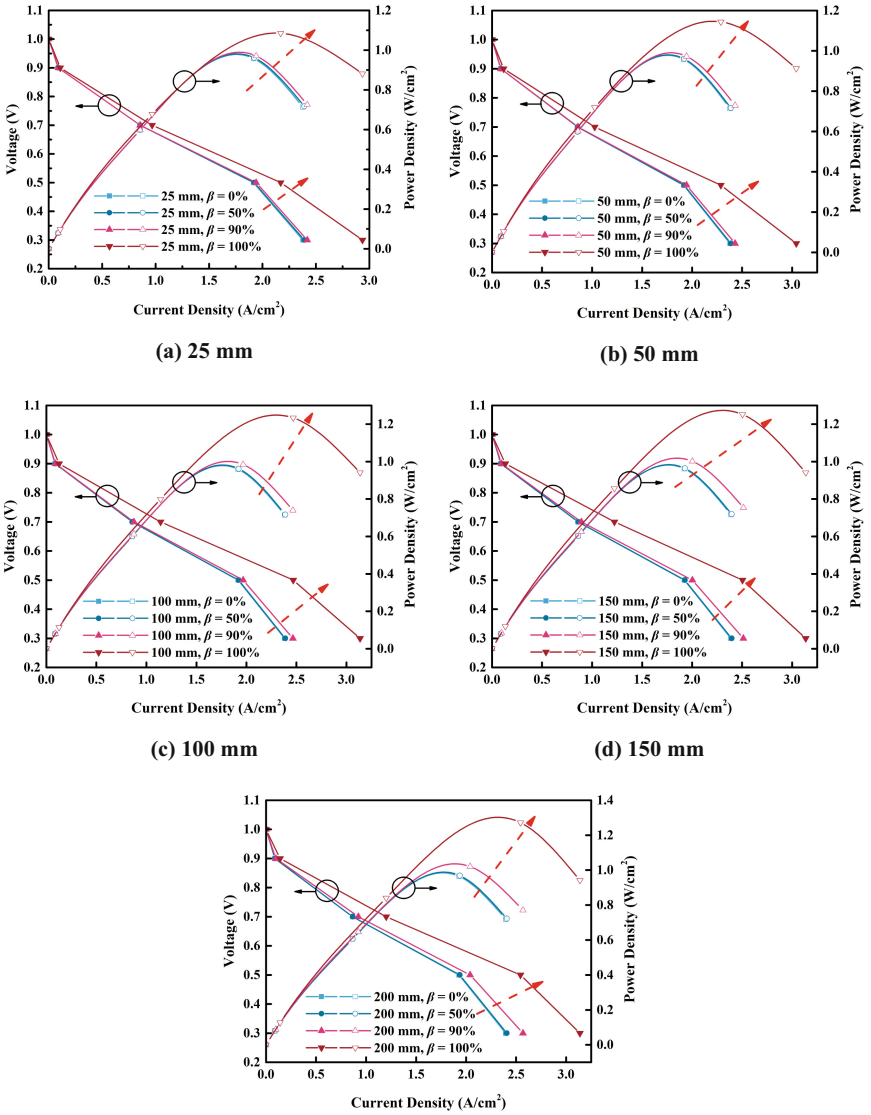

Fig. 4. Polarization curves of fuel cells with different lengths.

regions (as shown in Fig. 5): Upstream (0–9.5 mm), Block Zone (9.5–15.5 mm), and Downstream (15.5–25 mm). The division is based on the convection range (Section 0) of Block Zone.

The oxygen molar concentration distribution at the cathode GDL / CL interface (as shown in Fig. 6) shows that the oxygen concentration in the block zone and Upstream

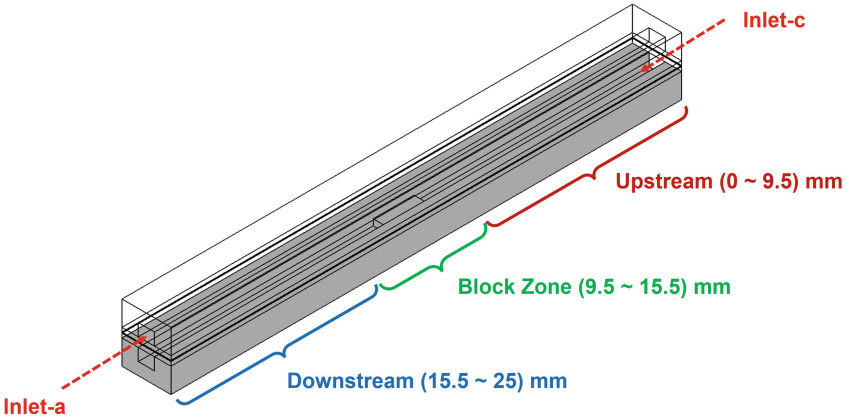

Fig. 5. Region division of the 25 mm fuel cell.

increases significantly after the addition of the block with $\beta = 100\%$, indicating that this block setting enhances the mass transfer of oxygen in the above two regions.

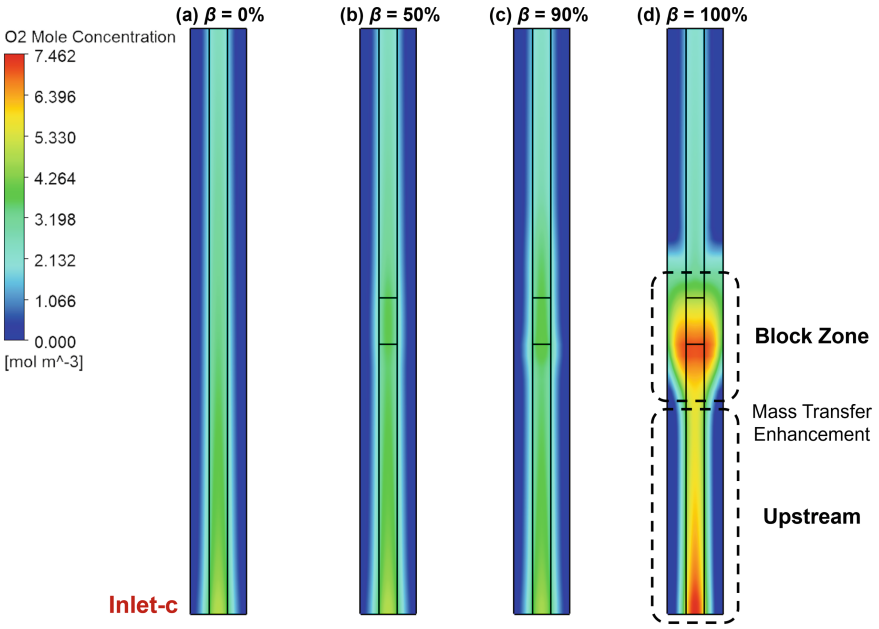

Fig. 6. Distribution of the oxygen molar concentration at the cathode GDL/CL interface.

Figure 7 shows the oxygen mass flow reduction rate in each region compared with the previous region (the previous region of the upstream flow channel is the flow channel inlet). After adding the block with $\beta = 100\%$, the oxygen mass flow reduction rate in the upstream flow channel and the block zone (from 15.35% to 18.97% and from 10.83%

to 15.21%, respectively) increases significantly, while in the downstream flow channel remains unchanged (from 17.99% to 17.29%). In general, the action range of the block is in the block zone and the Upstream. Next, the enhanced transport characteristics of the block with $\beta = 100\%$ in the block zone and Upstream will be analyzed in detail, respectively.

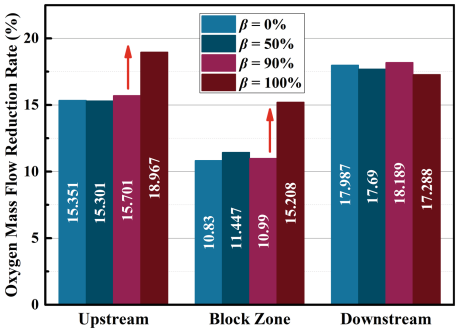

Fig. 7. Oxygen mass flow reduction rate in the flow channel of the 25 mm fuel cell.

Effect of the Block Zone

Figure 8 shows that the block with $\beta = 100\%$ completely blocks the flow channel, the reactant gas is forced to bypass the block and enter GDL. The mass transfer in the block zone is enhanced.

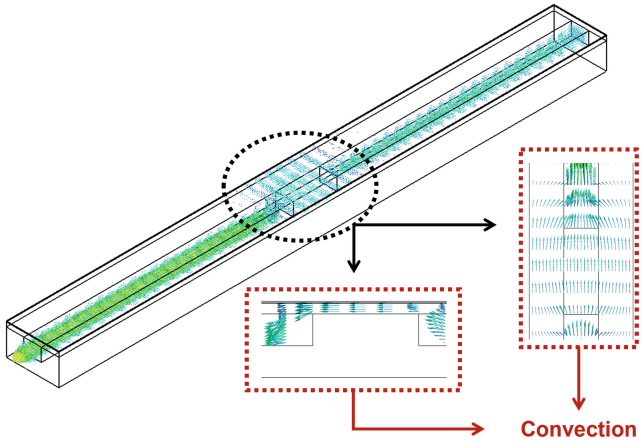

Fig. 8. Distribution of the velocity vector in the cathode flow channel, GDL, and CL.

Effect of the Upstream

Figure 9 presents the pressure in the cathode flow channel, GDL, and CL. The upstream pressure at $\beta = 90\%$ increases somewhat compared with that at $\beta = 0\%$ and 50%, but the increase is insignificant. While the block with $\beta = 100\%$ significantly increases the pressure in the upstream flow channel, GDL, and CL, and the maximum pressure in each region increases from 101,391.94 Pa, 101,374.27 Pa, and 101,373.38 Pa without the block to 187,249.47 Pa, 187,227.55 Pa, and 187,225.88 Pa, respectively. The pressure of each downstream component does not differ significantly at different β.

It is also observed that the upstream and downstream GDL and CL show pressure dip and surge regions in the local magnified view at $\beta = 100\%$, which is because this region is located at the junction of the upstream and downstream with the block zone and is affected by the convective effect of the block.

From the ideal gas equation, it is known that the increase of the pressure will drive the gas concentration to increase. As the increase of the upstream pressure, the oxygen concentration increases corresponding and thus improves the electrochemical performance.

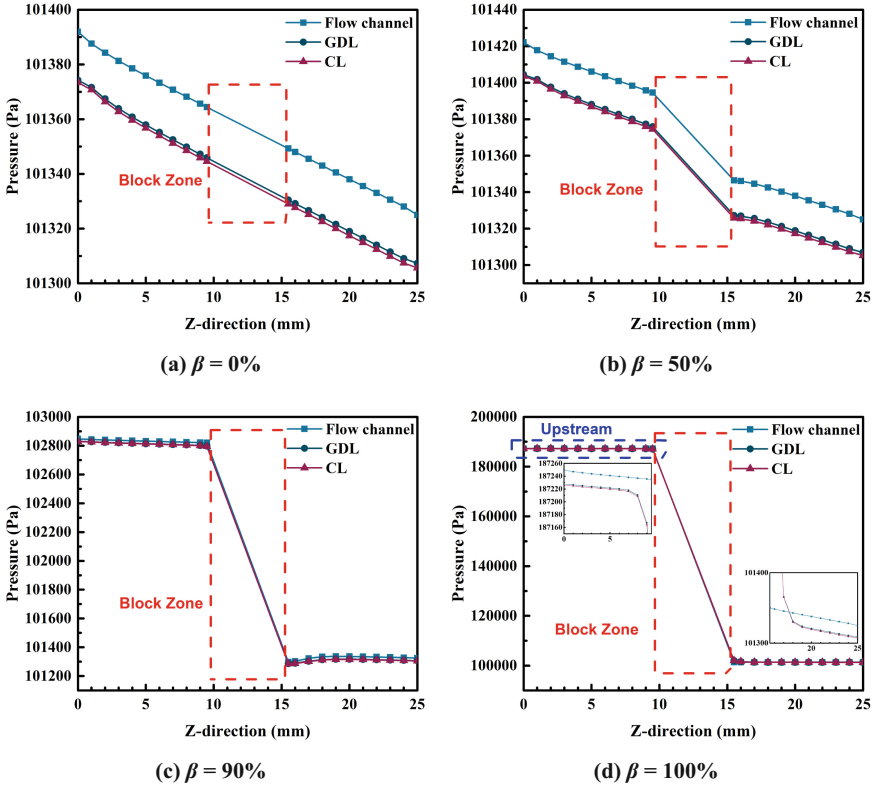

Fig. 9. Pressure in the cathode flow channel, GDL, and CL.

The enhanced transport characteristic of the Upstream on the performance of the fuel cell is further verified by the oxygen molar concentration in the cathode flow channel,

GDL, and CL (as shown in Fig. 10). At $\beta = 100\%$, the oxygen molar concentration in the upstream flow channel, GDL, and CL is significantly higher than that at the other three β. The maximum upstream concentration in the cathode flow channel, GDL, and CL increases from 5.81 mol·m^{-3}, 2.67 mol·m^{-3}, and 2.43 mol·m^{-3} without the block to 10.72 mol·m^{-3}, 4.33 mol·m^{-3}, and 3.82 mol·m^{-3}, respectively.

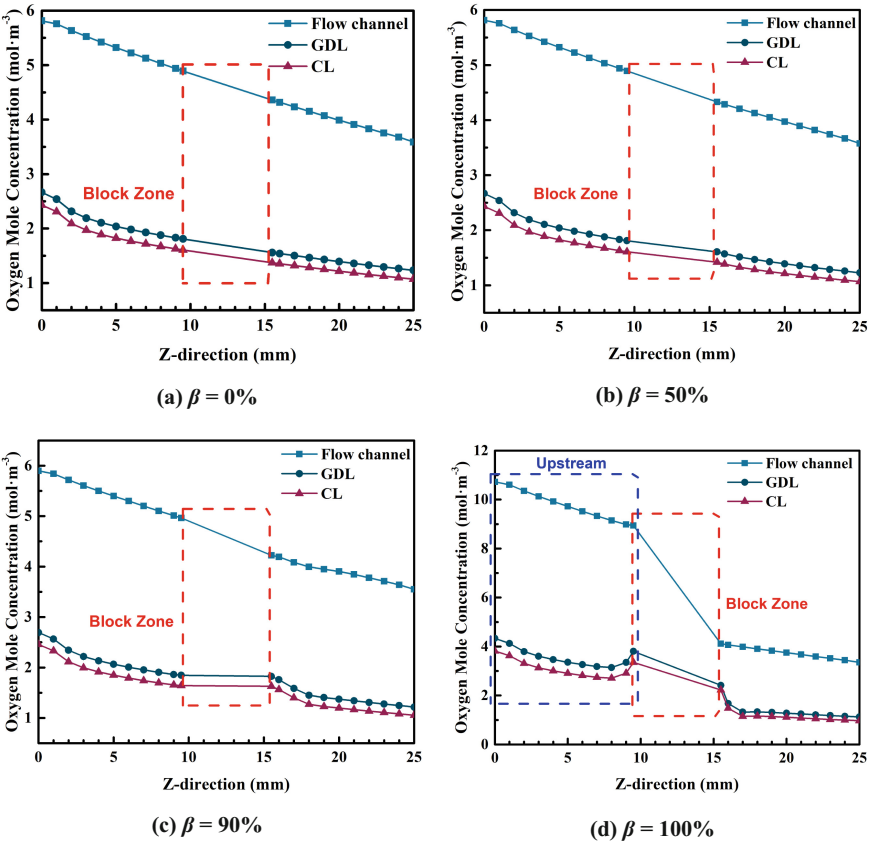

Fig. 10. Oxygen molar concentration in the cathode flow channel, GDL, and CL.

In summary, the enhanced transport characteristic of the block on the performance of the fuel cell is reflected in two aspects: on the one hand, the convection forms in the block zone, forcing more gas into GDL and thus into CL to participate in the reaction; on the other hand, higher upstream pressure is induced, the upstream oxygen concentration increases accordingly. Therefore, the electrochemical performance is improved.

It should be noted that since the scale-up is a requirement for the commercialization of PEMFC, the enhanced transport characteristic of the block on the single-channel PEMFC scale-up will be analyzed in Sect. 3.2.

3.2 Effect of the Block on the Performance of the Fuel Cell Scale-Up

Comparison of the Electrochemical Performance

Polarization curves of fuel cells with different lengths at different β are given in Fig. 11. At $\beta = 0\%$ and $\beta = 50\%$, the scale-up is almost unaffected. At $\beta = 90\%$, the block acts as a performance enhancement during the fuel cell scale-up. At $\beta = 100\%$, the block has a better effect during the fuel cell scale-up. At this blockage, the power density of the 200 mm fuel cell at 0.5 V operating voltage is improved by 3.08%, 11.19%, and 17.24% compared with that of the 100 mm, 50 mm, and 25 mm fuel cell, respectively.

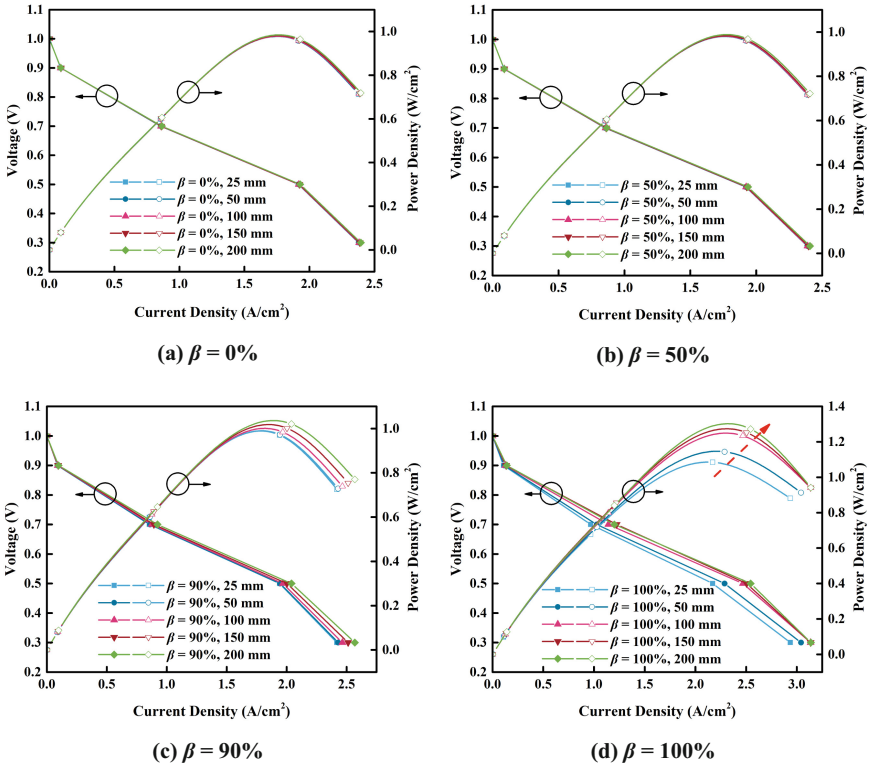

Fig. 11. Polarization curves of fuel cells with different lengths at different β.

Analysis for the Scale-Up

Since the block with $\beta = 100\%$ has the best effect on the improvement of the performance of the fuel cell during the scale-up, this block setting was selected for the subsequent analysis. The operating voltage is chosen to be 0.5 V. The upstream range of the 50 mm, 100 mm, 150 mm, and 200 mm fuel cell is set as (0–22) mm, (0–47) mm, (0–72) mm, and (0–97) mm, respectively; the block zone range is set as (22–28) mm, (47–53) mm, (72–78) mm, and (97–103) mm, respectively; the downstream range is set as (28–50) mm, (53–100) mm, (78–150) mm, and (103–200) mm, respectively.

The distribution of the oxygen molar concentration at the cathode GDL/CL interface with different lengths at $\beta = 0\%$ and $\beta = 100\%$ is shown in Figs. 12 and 13. The 50 mm, 100 mm, 150 mm, and 200 mm fuel cells are scaled by a factor of 0.5, 0.25, 0.167, and 0.125, respectively. It is observed that the distribution of the oxygen molar concentration at the GDL / CL interface is nearly same at $\beta = 0\%$, indicating that the performance during the fuel cell scale-up is unchanged.

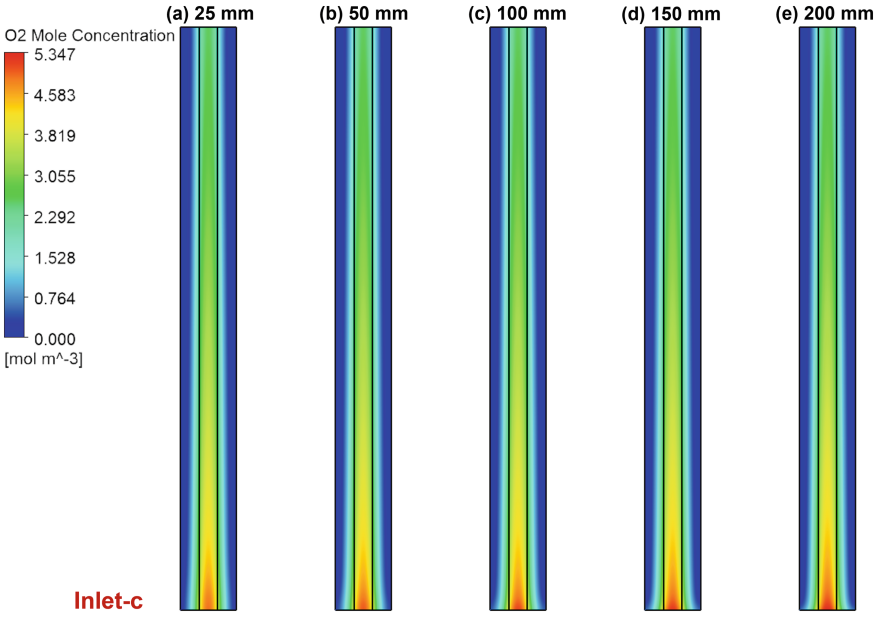

Fig. 12. Distribution of the oxygen molar concentration at the cathode GDL/CL interface with different lengths at $\beta = 0\%$.

At $\beta = 100\%$, it is observed that the oxygen molar concentration in the block zone and the Upstream gradually increases with length, indicating that the enhanced transport characteristic of the block during the fuel cell scale-up is also reflected in these two regions (the enhanced transport characteristic of the block has been explained in Sect. 3.1). The inlet mass flow rate increases during the scale-up according to the inlet boundary condition. The block obstructs the oxygen flow path in the flow channel, and it will further increase the upstream pressure and intensify the convective diffusion in the block zone as the flow rate increases.

It should be noted that the reinforcing effect of the block with $\beta = 100\%$ on the performance of the fuel cell gradually weakens (as shown in Fig. 14). The power density of fuel cells with different lengths is 1.085 W/cm^2, 1.144 W/cm^2, 1.234 W/cm^2, 1.252 W/cm^2, and 1.272 W/cm^2, respectively. The reason for this phenomenon is that the percentage of the block zone gradually decreases during the fuel cell scale-up (from 0.24 at 25 mm to 0.03 at 200 mm), decreasing the percentage of the convection range.

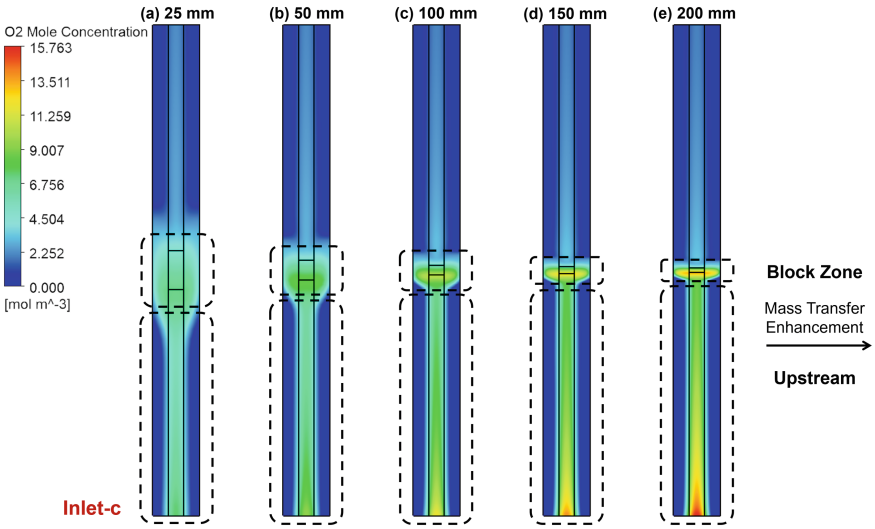

Fig. 13. Distribution of the oxygen molar concentration at the cathode GDL/CL interface with different lengths at $\beta = 100\%$.

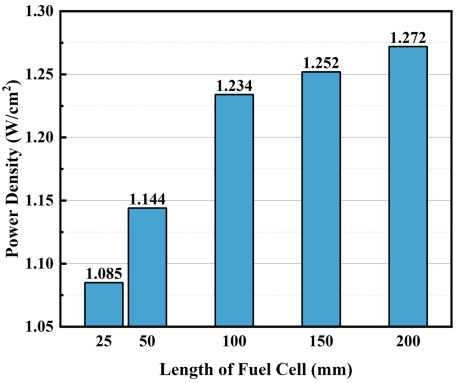

Fig. 14. Power density of fuel cells with different lengths at $\beta = 100\%$, $V_{\text{cell}} = 0.5$ V.

3.3 Net Power Density

The block with $\beta = 100\%$ will increase the upstream pressure and thus the pump power. It is necessary to calculate the net power density.

The net power density is calculated by the following equation [26]

$$P_{\text{net}} = P_{\text{cell}} - P_{\text{pump}} \tag{25}$$

$$P_{\text{pump}} = \frac{\xi\left(p_{\text{a,in}} \cdot v_{\text{a,in}} \cdot A_{\text{a,in}} + p_{\text{c,in}} \cdot v_{\text{c,in}} \cdot A_{\text{c,in}}\right)}{A_{\text{act}}} \tag{26}$$

where P_{net} represents the net power density of the fuel cell, W/m^2; P_{cell} represents the output power density of the fuel cell, W/m^2; P_{pump} represents the pump power density, W/m^2; ξ represents the conversion efficiency of the compressor (70% in this study); $p_{a,in}$ and $p_{c,in}$ represent the pressure of anode inlet and cathode inlet, Pa; $v_{a,in}$ and $v_{c,in}$ represent the velocity of anode inlet and cathode inlet, m/s; $A_{a,in}$ and $A_{c,in}$ represent the area of anode inlet and cathode inlet, m^2; A_{act} represents the activation area, m^2.

Table 4 shows the results of the net power calculation. For any given length of the fuel cell, the pump power increases accordingly as β increases. Regardless of the length, the block with $\beta = 100\%$ makes the net power maximum, indicating that such a setting is effective.

Table 4. Net power Density of fuel cells with different lengths.

β	25 mm		50 mm		100 mm	
	Pump power density (W/m^2)	Net power density (W/m^2)	Pump power density (W/m^2)	Net power density (W/m^2)	Pump power density (W/m^2)	Net power density (W/m^2)
0%	2.031	9577.969	8.088	9571.912	32.094	9557.906
50%	2.499	9612.501	9.238	9595.762	35.160	9579.840
90%	24.302	9680.698	67.354	9657.646	197.697	9642.303
100%	723.551	10126.449	921.999	10518.001	1100.815	11239.185

β	150 mm		200 mm	
	Pump power density (W/m^2)	Net power density (W/m^2)	Pump power density (W/m^2)	Net power density (W/m^2)
0%	71.108	9543.892	124.114	9520.886
50%	76.906	9563.094	133.625	9551.375
90%	363.420	9651.580	534.346	9670.654
100%	1202.655	11317.345	1281.097	11438.903

The trend of the net power density during the fuel cell scale-up is extracted in Fig. 15. At $\beta = 0\%$, the net power density gradually decreases during the scale-up. The net power densities of fuel cells with different lengths are 9577.969 W/m^2, 9571.912 W/m^2, 9557.906 W/m^2, 9543.892 W/m^2 and 9520.886 W/m^2, respectively. Conversely, at $\beta = 100\%$, the net power density gradually increases during the scale-up. The net power densities of fuel cells with different lengths are 10126.449 W/m^2, 10518.001 W/m^2, 11239.185 W/m^2, 11317.345 W/m^2, and 11438.903 W/m^2, respectively. Combined with the studies in Sects. 3.1 and 3.2, the addition of the block with $\beta = 100\%$ is indeed beneficial for the fuel cell scale-up.

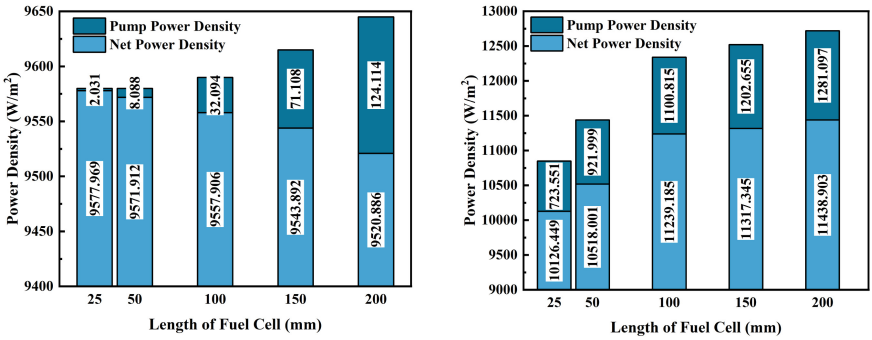

(a) $\beta = 0\%$ **(b) $\beta = 100\%$**

Fig. 15. Variation of the net power density during the scale-up.

4 Conclusion

The models of single-channel fuel cells with different lengths L and blockage ratio β are developed. The enhanced transport characteristic of the block is re-examined, and its effect on the performance of the fuel cell scale-up is further revealed. The way of effective utilization of the block is illustrated. The main conclusions are as follows:

(1) The most significant improvement in the performance of the fuel cell is achieved by the block with $\beta = 100\%$. The power density increased by 0.37% at $\beta = 50\%$, by 1.30% at $\beta = 90\%$, and by 13.26% at $\beta = 100\%$, respectively, compared with the case without the block for the 25 mm fuel cell. The enhanced transport characteristic of the block with $\beta = 100\%$ is reflected in two aspects: on the one hand, the convection forms in the block zone, forcing more reactant gas into GDL and enhancing the mass transfer; on the other hand, higher upstream pressure is induced, which in turn increases the upstream oxygen concentration at GDL/CL interface and improves the electrochemical performance.

(2) The block with $\beta = 100\%$ enhances the performance of the fuel cell during the scale-up. The power density of the 200 mm fuel cell at 0.5 V operating voltage increased by 3.08%, 11.19%, and 17.24% compared with that of the 100 mm, 50 mm, and 25 mm fuel cell, respectively. The increase of the mass flow rate during the fuel cell scale-up makes the upstream pressure increase and the convective diffusion in the block zone reinforced. It should be noted that the reinforcing effect of the block with $\beta = 100\%$ on the performance of the fuel cell gradually weakens. The reason for this phenomenon is that the percentage of the block zone gradually decreases during the fuel cell scale-up (from 0.24 at 25 mm to 0.03 at 200 mm), decreasing the percentage of the convection range.

(3) Considering the increase of the upstream pressure by adding the block with $\beta = 100\%$, the net power density calculation is performed. The net power density gradually decreases at $\beta = 0\%$, while the net power density gradually increases during the scale-up at $\beta = 100\%$. This indicates that the addition of the block with $\beta = 100\%$ is indeed beneficial for the fuel cell scale-up.

References

1. Alaswad, A., Dassisti, M., Prescott, T., Olabi, A.G.: Technologies and developments of third generation biofuel production. Renew. Sustain. Energy Rev. **51**, 1446–1460 (2015)
2. Alaswad, A., Baroutaji, A., Achour, H., Carton, J., Al Makky, A., Olabi, A.G.: Developments in fuel cell technologies in the transport sector. Int. J. Hydrogen Energy **41**(37), 16499–16508 (2016)
3. Shahgaldi, S., Hamelin, J.: The effect of low platinum loading on the efficiency of PEMFC's electrocatalysts supported on TiO_2–Nb, and SnO_2–Nb: an experimental comparison between active and stable conditions. Energy Convers. Manag. **103**, 681–690 (2015)
4. Pan, W., Wang, P., Chen, X., Wang, F., Dai, G.: Combined effects of flow channel configuration and operating conditions on PEM fuel cell performance. Energy Convers. Manag. **220**, 113046 (2020)
5. Li, X.G., Sabir, M.: Review of bipolar plates in PEM fuel cells: flow-field designs. Int. J. Hydrogen Energy **30**(4), 359–371 (2005)
6. Hamilton, P.J., Pollet, B.G.: Polymer electrolyte membrane fuel cell (PEMFC) flow field plate: design, materials and characterisation. Fuel Cells **10**(4), 489–509 (2010)
7. Liu, H.C., Yang, W.M., Tan, J., An, Y., Cheng, L.S.: Numerical analysis of parallel flow fields improved by micro-distributor in proton exchange membrane fuel cells. Energy Convers. Manag. **176**, 99–109 (2018)
8. Wang, Y., Sun, Z.Y., Yang, L.: Enhancement effects of the obstacle arrangement and gradient height distribution in serpentine flow-field on the performances of a PEMFC. Energy Convers. Manag. **252** (2022)
9. Li, W.Z., Yang, W.W., Wang, N., Jiao, Y.H., Yang, Y., Qu, Z.G.: Optimization of blocked channel design for a proton exchange membrane fuel cell by coupled genetic algorithm and three-dimensional CFD modeling. Int. J. Hydrogen Energy **45**(35), 17759–17770 (2020)
10. Ghanbarian, A., Kermani, M.J.: Enhancement of PEM fuel cell performance by flow channel indentation. Energy Convers. Manag. **110**, 356–366 (2016)
11. Heidary, H., Kermani, M.J., Advani, S.G., Prasad, A.K.: Experimental investigation of in-line and staggered blockages in parallel flowfield channels of PEM fuel cells. Int. J. Hydrogen Energy **41**(16), 6885–6893 (2016)
12. Chen, H., Guo, H., Ye, F., & Ma, C.F.: An experimental study of cell performance and pressure drop of proton exchange membrane fuel cells with baffled flow channels. J. Power Sources 472 (2020)
13. Wu, H.W., Ku, H.W.: The optimal parameters estimation for rectangular cylinders installed transversely in the flow channel of PEMFC from a three-dimensional PEMFC model and the Taguchi method. Appl. Energy **88**(12), 4879–4890 (2011)
14. Heidary, H., Kermani, M.J., Dabir, B.: Influences of bipolar plate channel blockages on PEM fuel cell performances. Energy Convers. Manag. **124**, 51–60 (2016)
15. Wang, X. F., Qin, Y. Z., Wu, S. Y., Xiang, S. G., Zhang, J. F., Yin, Y.: Numerical and experimental investigation of baffle plate arrangement on proton exchange membrane fuel cell performance. J. Power Sources **457** (2020)
16. Perng, S.W., Wu, H.W.: A three-dimensional numerical investigation of trapezoid baffles effect on non-isothermal reactant transport and cell net power in a PEMFC. Appl. Energy **143**, 81–95 (2015)
17. Fan, L., Niu, Z., Zhang, G., Jiao, K.: Optimization design of the cathode flow channel for proton exchange membrane fuel cells. Energy Convers. Manag. **171**, 1813–1821 (2018)
18. Chen, H., Guo, H., Ye, F., Ma, C.F.: A numerical study of orientated-type flow channels with porous-blocked baffles of proton exchange membrane fuel cells. Int. J. Hydrogen Energy **46**(57), 29443–29458 (2021)

19. Guo, Q.Y., Qin, Y.Z.: Numerical investigation of water droplet removal characteristics in novel block channels of PEMFC using dynamic wettability model. Int. J. Hydrogen Energy **46**(74), 36890–36902 (2021)
20. Wang, L., Husar, A., Zhou, T., Liu, H.: A parametric study of PEM fuel cell performances. Int. J. Hydrogen Energy **28**(11), 1263–1272 (2003)
21. Baricci, A., Mereu, R., Messaggi, M., Zago, M., Inzoli, F., Casalegno, A.: Application of computational fluid dynamics to the analysis of geometrical features in PEM fuel cells flow fields with the aid of impedance spectroscopy. Appl. Energy **205**, 670–682 (2017)
22. Berning, T., Djilali, N.: Three-dimensional computational analysis of transport phenomena in a PEM fuel cell—a parametric study. J. Power Sources **124**(2), 440–452 (2003)
23. Kuo, J.K., Yen, T.H., Chen, C.K.: Three-dimensional numerical analysis of PEM fuel cells with straight and wave-like gas flow fields channels. J. Power Sources **177**(1), 96–103 (2008)
24. Nguyen, P.T., Berning, T., Djilali, N.: Computational model of a PEM fuel cell with serpentine gas flow channels. J. Power Sources **130**(1), 149–157 (2004)
25. Hashemi, F., Rowshanzamir, S., Rezakazemi, M.: CFD simulation of PEM fuel cell performance: effect of straight and serpentine flow fields. Math. Comput. Model. **55**(3–4), 1540–1557 (2012)
26. Yong, Z., Shirong, H., Xiaohui, J., Yuntao, Y., Mu, X., Xi, Y.: Characteristics of proton exchange membrane fuel cell considering "dot matrix" gas distribution zones and waveform staggered flow field with cooling channels. Energy Convers. Manag. **267**, 115881 (2022)

Research on Space Regenerative Fuel Cell System and Comprehensive Energy Utilization Technology

Lei Feng(✉), Wen Chen, Jingrun Wang, Wen Xie, Qingxin Cui, Jingying Bai, and Cheng'an Wan

Beijing Spacecrafts, Beijing 100094, China
Lancefrye@163.com

Abstract. This paper introduces the application demands and research progress of fuel cells in the space field. Subsequently, an analysis of the comprehensive energy utilization modes of fuel cells from the aspects of water, gas, and heat is conducted. The fuel evaporated from the liquid hydrogen and liquid oxygen tanks of spacecraft can be used for fuel cell power generation, and the heat generated by fuel cells, together with the low-absorption and low-emissivity thermal control coatings, maintains the temperature of the spacecraft in the shadow area. The product water from fuel cells can be purified for reuse in thermal control, environmental control, and water electrolysis cells. The hydrogen and oxygen produced by electrolyzing water can be recycled for fuel cell power generation, and the oxygen can also be used for environmental control and life support, while the hydrogen can be used for methane production. To reduce system weight and achieve comprehensive utilization of energy and resources, integrated system design and research on regenerative fuel cell system principles are carried out. Finally, through the analysis of prototype performance parameters, the design scheme demonstrates the feasibility of energy and resource recycling.

Keywords: Fuel cell · Energy system · Comprehensive utilization · Integration · Aerospace

1 Introduction

With the advancement of manned space missions in China, there is a growing demand for energy systems with high output power and long working time to meet the operational requirements of spacecraft, especially in environments with extended periods of no sunlight, such as lunar nights. The integrated support system of spacecraft needs to have high specific energy and volumetric energy to reduce the spacecraft mass and increase payload capacity. Fuel cell technology has emerged as one of the key directions for the development of space power technology, both domestically and internationally [1–3]. Fuel cell power systems involve the conversion and utilization of multiple forms of energy, including water, gas, heat, and electricity. They can be used as independent power generation systems on spacecraft and can also integrate with spacecraft propulsion and thermal control systems to form a comprehensive energy system [4–6].

H. Sun et al. (Eds.): WHTC 2023, SPPHY 393, pp. 334–343, 2024.
https://doi.org/10.1007/978-981-99-8631-6_32

In this project, an analysis of energy transfer and resource sharing modes among subsystems, such as energy, propulsion, thermal control, and environmental control, is conducted from the perspectives of energy storage at the source end and energy consumption at the terminal end. Key technologies, including low-temperature propellant utilization, fuel cell power generation, product water purification, hydrogen and oxygen electrolysis regeneration, and heat recovery utilization, are studied through integrated analysis of energy utilization in subsystems such as power, propulsion, environmental control, and life support. A modular and replaceable prototype of a regenerative fuel cell integrated energy system is constructed, and ground demonstration and verification tests are conducted to provide technical reserves and design references for the future energy system of new manned spacecraft in China.

2 Energy Utilization Modes

The comprehensive utilization of energy encompasses the conversion of solar energy, chemical energy, electrical energy, and thermal energy, as well as the efficient utilization of hydrogen and oxygen, and the purification and utilization of product water. During the launch phase, the gaseous hydrogen and oxygen evaporated from the propulsion subsystem are supplied to the regenerative fuel cell system for power generation, which is used to supply the load while generating water for storage as a circulating substance in the regenerative fuel cell system [7].

During the lunar day period, solar energy is used as the primary energy source to power the bus load, and water is electrolyzed in the electrolysis cell, converting electrical energy into chemical energy for energy storage. This process enables the production of hydrogen and oxygen to meet the fuel cell power generation needs during the lunar night period. The excess hydrogen and oxygen can also be utilized to provide breathable oxygen for astronauts and hydrogen for reducing carbon dioxide in the environmental control and life support system. During the lunar shadow period without sunlight, the fuel cell system utilizes the stored hydrogen and oxygen for power generation, supplying power to the bus load as the main energy source, while generating water for storage after purification [8, 9]. The excess water can also be used as drinking water for the environmental control and life support system. The heat generated during the operation of the fuel cell can be used as a heat source for the thermal control subsystem during the lunar night period [10]. The comprehensive utilization of energy based on regenerative fuel cells is depicted in Fig. 1 [1].

3 Integrated Energy System Solution

The integrated system of combined heat, power, and environmental control is designed to integrate multiple subsystems including energy storage and generation, environmental control and life support, and thermal control. It consists of eight functional units, including power generation subsystem, gas supply and pressure regulation, gas regeneration, water purification, temperature and humidity control, ventilation and purification, environmental monitoring, and information processing and control. The system includes the following aspect (Fig. 2).

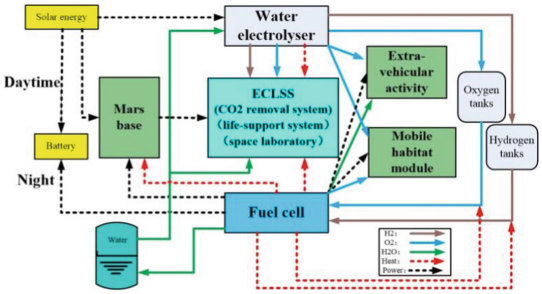

Fig. 1. Comprehensive energy utilization mode [1]

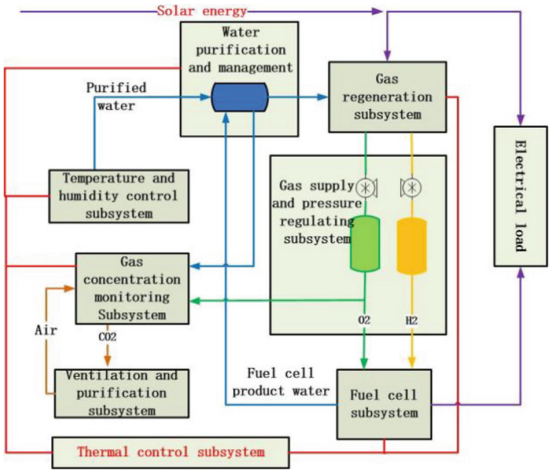

Fig. 2. Integrated energy system solution

3.1 Power Generation Function

The integrated energy system adopts a combined power generation method using fuel cells and lithium batteries. A 1000 W fuel cell is used as the main power source for external power supply, while lithium batteries serve as auxiliary power source for internal system power supply. When the system is started, the battery supplies power to the system components through a controller. Once the fuel cell stack reaches the operating state, it switches to supplying power to the controller and loads through voltage transformation/thermal backup, and enters the power generation state. When the battery is low on power, the fuel cell stack charges the battery through constant current and constant voltage DC-DC conversion.

3.2 Gas Supply and Pressure Regulation Function

Gas supply and pressure regulation mainly achieve gas supply for fuel cell power generation and environmental gas supply pressure regulation.

(1) The power generation process of the system requires providing hydrogen and oxygen gases with a stable pressure of about 100 ± 2 kPa for the internal reaction. The hydrogen and oxygen gases from the gas bottles are regulated by pressure reducing valves to stable pressure for fuel cell power generation.
(2) The integrated energy system provides oxygen for the sealed compartment through electrolysis of water. To meet the requirements of the living environment, the pressure inside the compartment is controlled at 94 kPa with an oxygen partial pressure of 20–24 kPa [11].

3.3 Gas Regeneration and Control

Gas regeneration and control mainly include pressure control and gas purification processes. During the electrolysis of water to produce hydrogen and oxygen gases, the pressure of the gases needs to be controlled to maintain a balanced pressure on both sides of the hydrogen and oxygen gases, which rises steadily and is input into the gas bottles. In addition, the hydrogen and oxygen gases produced by the electrolysis of water contain a large amount of water vapor and impurities. The membrane filter and dryer can recover water vapor from the gases, and palladium catalyst can remove impurities from the gases, achieving gas purification with hydrogen and oxygen purity of over 99.99%.

3.4 Water Regeneration and Purification

To improve water resource recovery efficiency, simplify management processes, and reduce system coupling to increase reliability, a unified water source, unified water quality, unified management, and unified distribution scheme are adopted for the system's water source. Water regeneration and purification mainly target the water from four processes, including product water from the power generation process, circulating water from the electrolysis process, condensate water from the temperature and humidity control process, and wastewater from daily use.

3.5 Temperature and Humidity Control Function

The temperature and humidity control function for the sealed compartment's atmosphere mainly includes temperature control, humidity control, condensate water collection, and cold source supply functions. According to the system's functional units, temperature and humidity are controlled through sensors and actuators, ensuring a comfortable living environment for the occupants. Condensate water, which is generated during the temperature and humidity control process, is collected and recycled for water regeneration and purification.

3.6 Ventilation and Purification Function

The ventilation and purification function is responsible for maintaining a clean and healthy air environment inside the sealed compartment. Air is circulated through filters to remove particulate matter and harmful gases. Carbon dioxide produced by human respiration is removed through a carbon dioxide removal system, and fresh oxygen

is supplied through the oxygen generation process. The ventilation and purification function ensures a continuous supply of fresh air and maintains a safe and healthy living environment.

3.7 Environmental Monitoring Function

The environmental monitoring function continuously monitors various parameters, such as temperature, humidity, air quality, and gas concentration, to ensure the system operates within the designated range. Data is collected and processed in real-time, providing feedback for system control and optimization. Any abnormal conditions are detected and addressed promptly to maintain the system's stability and reliability [12].

3.8 Information Processing and Control Function

The information processing and control function integrates all the subsystems and coordinates their operation. It includes data collection, processing, and control algorithms to ensure optimal performance of the integrated energy system. Real-time monitoring and control are performed to adjust system parameters and respond to changing conditions. The information processing and control function also includes human–machine interface (HMI) for operators to monitor system status and make manual adjustments when needed.

4 Regenerative Fuel Cell Energy System

In an integrated energy system, the regenerative fuel cell energy subsystem consists of the gas regeneration subsystem, gas supply and pressure regulation subsystem, and power generation subsystem. Currently, domestic regenerative hydrogen–oxygen fuel cell energy systems mainly face challenges such as insufficient specific energy, durability, and reliability that need further demonstration and verification. Based on the requirements of the application scenarios for the overall energy system and the preliminary analysis of the renewable energy system, the overall design adopts a split-type regenerative fuel cell system, where the electrolysis and power generation are carried out by separate fuel cell stacks, while the pipelines and controllers can be shared. The schematic diagram of the overall design principle is shown below. The regenerative fuel cell energy system mainly consists of five parts: the PEM water electrolysis subsystem, the hydrogen–oxygen fuel cell subsystem, the reactant storage subsystem, the environmental control subsystem, and the power regulation and control subsystem (Fig. 3).

4.1 Power Generation Function

The hydrogen–oxygen fuel cell subsystem directly converts the chemical energy of hydrogen and oxygen into electrical energy. To improve energy conversion efficiency, the generating power of fuel cell is 1000 W, and the generating efficiency is greater than 65%. The polarization curve of the fuel cell stack is shown in Fig. 4.

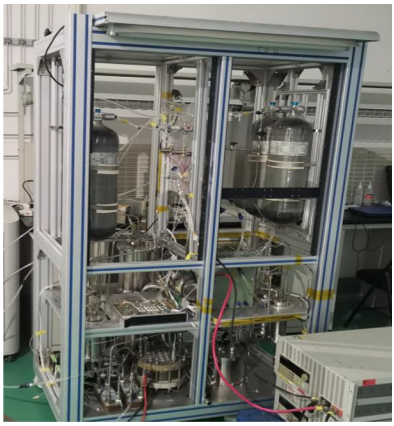

Fig. 3. Prototype of regenerative fuel cell principle

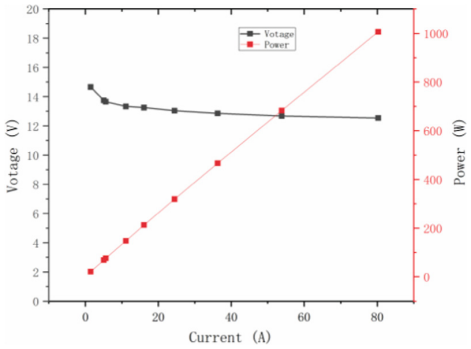

Fig. 4. Power generation performance of fuel cell

During the startup process of a hydrogen–oxygen fuel cell stack, liquid circulating water needs to be supplied. Therefore, the startup temperature of the stack needs to be above 0 °C. Additionally, the proton exchange membrane exhibits noticeable swelling phenomena at temperatures above 70 °C. To study the temperature sensitivity of a fuel cell stack within the temperature range of 10–65 °C, a preliminary design using MATLAB was conducted. Specific parameter conditions were set to evaluate the electrochemical performance of the stack at different temperatures. The obtained results were compared and analyzed against experimental measurements, the stack exhibits power generation capability within the temperature range of 10–65°C, with a difference of approximately 15% in power output and efficiency (Table 1).

The pressure of a single cell in the fuel cell stack is influenced by the partial pressures of hydrogen and oxygen gases. To analyze the electrochemical performance of the fuel cell stack under different gas pressures and evaluate its temperature sensitivity, simulations were conducted, and the results were compared with experimental measurements. According to the experimental results, the voltage of a single cell in the fuel cell stack is

Table 1. Comparison of electrochemical performance of a 1000W fuel cell stack with temperature variations

Temperature (°C)	Voltage (V) @ 200 mA/cm^2		Power (W) @ 80 A	
	Simulation values	Experimental measurements	Simulation values	Experimental measurements
10	0.709	/	907.52	/
20	0.731	0.743	935.68	951.04
30	0.753	0.765	963.84	979.20
40	0.776	0.774	993.28	990.72
50	0.798	0.791	1021.44	1012.48
60	0.820	0.810	1041.96	1036.80

observed to be 786 mV at a current density of 200 mA/cm^2 when the absolute pressure of hydrogen gas is 150 kPa. With an increase in the hydrogen gas absolute pressure to 250 kPa, the voltage of a single cell under the same current density reaches 815 mV. Therefore, within the range of 150–250 kPa, the fuel cell stack exhibits a difference of approximately 10% in terms of power generation efficiency and output (Table 2).

Table 2. Comparison of electrochemical performance of a 1000 W fuel cell stack with pressure variations

Pressure (kPa)	Voltage (V) @ 200 mA/cm^2		Power (W) @ 80 A	
	Simulation values	Experimental measurements	Simulation values	Experimental measurements
150	0.731	0.743	935.68	951.04
250	0.820	0.810	1041.96	1036.80

4.2 Efficient Utilization of Hydrogen and Oxygen

With a fuel cell power generation of 1000 W and an average single cell voltage of 0.8 V, the theoretical consumption of hydrogen and oxygen can be calculated using Faraday's law. Assuming intermittent exhaust, the collected exhaust gas can be used to calculate the utilization rate of hydrogen and oxygen. The calculation results are shown in Table 3.

4.3 Product Water Recovery

After adjusting the reaction gas pressure to the set value, the fuel cell stack is started and loaded to the rated power. After the fuel cell stack stabilizes, the working current of the stack and the number of single cells in the stack are recorded, as well as the weight

Table 3. Gas consumption volume and collection volume

	Hydrogen	Oxygen
Reaction time (h)	2	2
Theoretical consumption volume (L)	1046.4	523.2
Tail row collection volume (L)	1.2	2.4
Gas utilization rate (%)	99.87	99.47

of the recovered product water. By conducting a comparison between the theoretically calculated weight of water produced in a fuel cell and the actual weight of water collected, it is determined that the water recovery rate of the fuel cell is greater than 95% (Table 4).

Table 4. Quality of product water generation and collection

Time (min)	Water recovery weight (g)	Theoretical water production weight (g)	Product water recovery rate (%)
10	47.80	70.20	68.10
20	108.19	140.40	77.06
30	198.77	210.60	94.38
40	271.74	280.80	96.77
50	342.19	351.0	97.49
60	412.64	422.45	97.67

4.4 Hydrogen and Oxygen Production by Water Electrolysis

The water electrolysis subsystem re-electrolyzes water into hydrogen and oxygen using external electrical energy, and the gas production rate should meet the requirements of the fuel cell during eclipse periods. The electrolytic power of water cell is 1000 W, and the voltage efficiency is more than 90% (Fig. 5).

4.5 Hydrogen and Oxygen Purification

With a power of 1000 W for the water electrolysis cell, the gas produced at atmospheric pressure is purified through a purification device. The oxygen content in hydrogen gas and the hydrogen content in oxygen gas before and after purification are measured. The purification results are shown in Table 5.

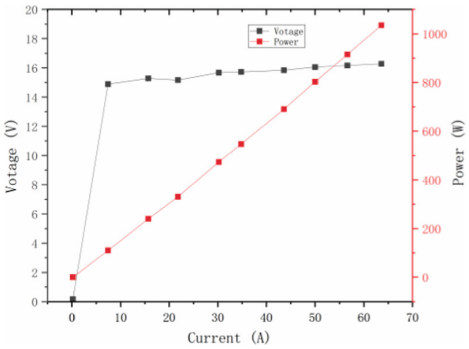

Fig. 5. Electrolytic performance of water electrolyzer

Table 5. Purity before and after gas purification

	Hydrogen (%)	Oxygen (%)
Before purification	99.95	98.05
After purification	99.99	99.99

5 Summary

Regenerative fuel cell systems offer high specific power and specific energy, making them well-suited for future manned space missions. These systems can achieve comprehensive material utilization through integration with propulsion, environmental control, and life support subsystems. Additionally, they can also integrate energy utilization with thermal control subsystems, resulting in an organic fusion of energy systems with other subsystems. By implementing multi-system integrated design, spacecraft launch weight can be reduced, and overall energy utilization efficiency can be improved throughout the spacecraft's lifecycle.

Regenerative fuel cell energy systems are a promising sustainable energy technology for future energy supply. However, they still face technical and engineering challenges in practical applications. To overcome these challenges, careful consideration should be given to system design, efficient power generation and hydrogen–oxygen utilization, advanced thermal control technology, reliable power regulation and control, durability, reliability, as well as regular maintenance and monitoring. By addressing these aspects, the performance and reliability of regenerative fuel cell energy systems can be enhanced, promoting their widespread adoption in various fields.

References

1. Feng, L., Shu, W.X., Xie, F., et al.: Study on renewable energy system based on mars resources. IOP Conf. Ser.: Earth Environ. Sci. **766**(1), 6 (2021)
2. Oh, T.H.: Effect of cathode conditions on performance of direct borohydride–hydrogen peroxide fuel cell system for space exploration. Renew. Energy **178** (2021)

3. Guo, H., Liu, X., Zhao, J.F., et al.: Experimental study of two-phase flow in a proton exchange membrane fuel cell in short-term microgravity condition. Appl. Energy **136**, 509–518 (2014)
4. Lai, J.S., Ellis, M.W.: Fuel cell power systems and applications. Proc. IEEE 1–25 (2017)
5. Montazerinejad, H., Eicker, U.: Recent development of heat and power generation using renewable fuels: a comprehensive review. Renew. Sustain. Energy Rev. **165** (2022)
6. Scott, J.H.: The development of fuel cell technology for electric power generation. Proc. IEEE **94**, 1815–1825 (2006)
7. Feng, L., Xie, W., Wen, C., et al.: Study on high-efficient utilization of heat energy of fuel cells in aerospace. Astronaut. Syst. Eng. Technol. 7(5) (2019)
8. Delgado-Bonal, A., Javier Martin-Torres, F., Vazquez-Martin, S., et al.: Solar and wind exergy potentials for Mars. Energy **102**, 550–558 (2016)
9. Zhang, Y.J., Mao, Z.Q., Xie, X.F., et al.: Research and application of regenerative fuel cells. Prog. Chem. **18**(5), 6 (2006)
10. Xie, W., Liu, J.F., Ma, Y.J.: Applicable to the space environment of PEMFC thermal management technology research. Dev. Innov. Mach. Electr. Prod. **30**(5), 3 (2017)
11. Jin, J., Hou, Y.Q.: The effect of oxygen supply mode on air pressure control of manned spacecraft. Spacecr. Environ. Eng. **32**(5), 469 (2015)
12. Guo, L.L.: In situ resource utilization technology for manned lunar and Mars exploration missions. China Space Navigation Press, China (2018)

Compatibilization of Carbon/Polymer Composites: Molecular Dynamics Simulation

Dongmei Yao[1], Cong Feng[2], Xiangmin Pan[3], Runlin Fan[1], Zize Zhan[1], Jing Chen[1], Junsheng Zheng[1(✉)], and Pingwen Ming[1]

[1] Clean Energy Automotive Engineering Center and School of Automotive Studies, Tongji University, 4800 Caoan Road, Shanghai 201804, China
jszheng@tongji.edu.cn

[2] College of Materials Science and Engineering, Tongji University, 4800 Caoan Road, Shanghai 201804, China

[3] Shanghai Motor Vehicle Inspection Certification and Technology Innovation Center, No. 68 Yutian South Road, Shanghai 201805, China

Abstract. The compatibilization of graphene/epoxy resin composites and carbon nanotube CNT/epoxy resin composite were studied based on the crystallized models with the molecular dynamics simulation in this paper. The effect of resin formula on compatibility parameter of carbon matrix was studied, and the combination of diglycidyl ether of bisphenol A (E51) resin with isophorone diamine (IPD) as the hardener achieved the best result. Further, the graphene/epoxy resin composite were constructed to investigate the effect of functional groups on components compatibility, conclude hydroxyl, carboxyl and amino. It was found that the functional groups had strong impact on compatibility parameter of graphene and CNT, whereas carboxylated graphene exhibits the best compatibility with the resin. This is due to the strong electronegativity of the carboxyl group, which induces a molecular interaction with the epoxy groups at the end of E51. The present study is expected to provide significant molecular insight into the relationship of compatibility between carbon matrix and epoxy resin for fuel cell composite bipolar plates.

Keywords: Compatibility · Composite bipolar plates · Molecular dynamics

1 Introduction

Carbon-based composite materials with resin are widely used in the preparation composite bipolar plates for fuel cell [1]. As expected, graphene is an ideal conductive filler and carbon nanotubes (CNTs) are also commonly added as additives to the preparation of composite plates to enhance the conductivity performance of the bipolar plates [2–4]. Epoxy resin (EP) is widely used in the production due to its excellent dynamic mechanics properties [5, 6]. Because EP undergoes a cross-linking reaction with the curing agent at high temperature to form a stable three-dimensional network structure [7, 8]. The commonly used resin types in the fuel cell field are diglycidyl ether of bisphenol A (E51) and 4,4′-diaminodiphenylmethane (AG80), and the commonly used curing agents are 4,4′-diaminodiphenyl Sulfone (DDS) and isophorone diamine (IPD) [8].

H. Sun et al. (Eds.): WHTC 2023, SPPHY 393, pp. 344–351, 2024.
https://doi.org/10.1007/978-981-99-8631-6_33

Many studies have shown that graphene-polymer interactions are major factor influencing the resulting properties of composites, which have been attempted to improve through the design of chemical structure of polymer as well as the tailor of graphene surface chemistry [9, 10]. Previous studies have shown that functional groups have a significant impact on the compatibility of carbon-based materials, such as hydroxyl, carboxyl, amino, methyl and epoxy with different grafting ratios were obtained [11]. From the view of thermodynamics, the compatibility of carbon matrix and polymer dominates filler dispersion and molded plate uniformity [12–14]. As a consequence, it is significant for us to study the compatibility of graphene and polymer [15]. The effect of functional groups on compatibility of graphene has not been reported in the literature science the quantification and accurate qualification of functional group is difficult through experimental methods because of heterogeneous structure of defective and functionalized graphene [16, 17]. With the development of computer technology, molecular simulation approaches based on classical physics or quantum physics theories have been widely used to study polymer composites [18]. Compared with traditional experiment methods with which the introduction of functional groups into graphene is difficult on account of the limitation of conditions, molecular dynamics (MD) simulation is a more effective method, especially for the quantification and qualification of functional groups [14]. Therefore, MD is potential to study the compatibility of defective and functionalized graphene especially for multicomponent solubility parameters [19, 20]. In this study, we firstly conducted a compatibility study on commonly used resins and curing agents to screen out the most suitable resin formula. Further, we elucidated the effect of defects and functional groups including hydroxyl (–OH), carboxyl (–COOH) and amino ($–NH_2$) on compatibility of graphene by MD simulation.

2 Methodology

2.1 Compatibility Parameters

For the MD simulations, a commercially available software Materials Studio (Accelrys, USA) with Dreiding forcefield was utilized, which expression is as follows [21]:

$$E = E_{val} + E_{nb} \tag{1}$$

$$E_{val} = E_B + E_A + E_T + E_I \tag{2}$$

$$E_{nb} = E_{vdw} + E_Q + E_{hb} \tag{3}$$

In the composite material system, E refers to the total energy, E_{val} refers to the interaction energy between the components and E_{nb} refers to the non-covalent interaction energy, respectively. The E_{val} is divided into several forms based on energy components, including bond stretch E_B, bond-angle bend E_A, dihedral angel torsion E_T and inversion terms E_I between covalent interactions. The E_{nb} includes van der Waals forces E_{vdw}, Coulomb interaction forces E_Q, and hydrogen bonding interactions E_{hb}.

In graphite blends, the better is the compatibility, the more uniform is the dispersion of one phase in another. The general expression for compatibility of mixing of a binary system is:

$$\frac{\Delta G}{RT} = \frac{\varnothing_b}{n_b}\ln\varnothing_b + \frac{\varnothing_s}{n_s}\ln\varnothing_s + x\varnothing_b\varnothing_s \tag{4}$$

$$x = \frac{E_{mix}}{k_B T} \tag{5}$$

where ΔG is the free energy of mixing (per mole), $\varnothing_i$ is the volume fraction of component i, n_i is the degree of polymerization of component i, χ is the interaction parameter, T is the absolute temperature, R is the gas constant, E_{mix} is the mix energy; that is the difference in free energy due to interaction between the mixed and pure state.

2.2 Model and Simulation Details

In the MD simulation process, the molecular models of carbon matrix and epoxy resin were constructed using the 3D atomistic document module in Materials Studio, and the models were geometrically optimized and energy minimized using the Forcite module. The optimized spatial structures of the monomers are shown in Fig. 1.

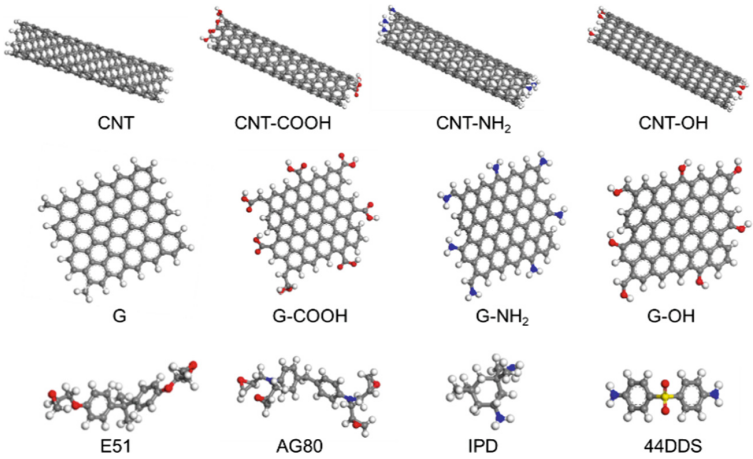

Fig. 1. The molecular structures of different CNTs, graphene, epoxy resin (E51, AG80) and curing agent (IPD, 44DDS) (grey: carbon atoms; white: hydrogen atoms; red: oxygen atoms; blue: nitrogen atoms; yellow: sulfur atoms).

3 Results and Discussion

3.1 3.1. Screening of Resin Type

Using carbon matrix as the base, epoxy resin and its curing agent as the screen in the Blend module, the interaction parameters χ, E_{mix}, and interaction energy distribution curves of each component obtained by simulating are shown in Figs. 2 and 3. E_{mix} and

χ values close to 0 indicate better compatibility of the composite system. From Fig. 2, it can be seen that the resin type has a greater impact on the mixing energy to temperature. The values of χ and E_{mix} for "E51 + IPD" are 183 and 109 kcal/mol, respectively, which are closer to 0 compared to other systems. Therefore, E51 and IPD are more easily blended with carbon matrix, which is consistent with the results for CNT.

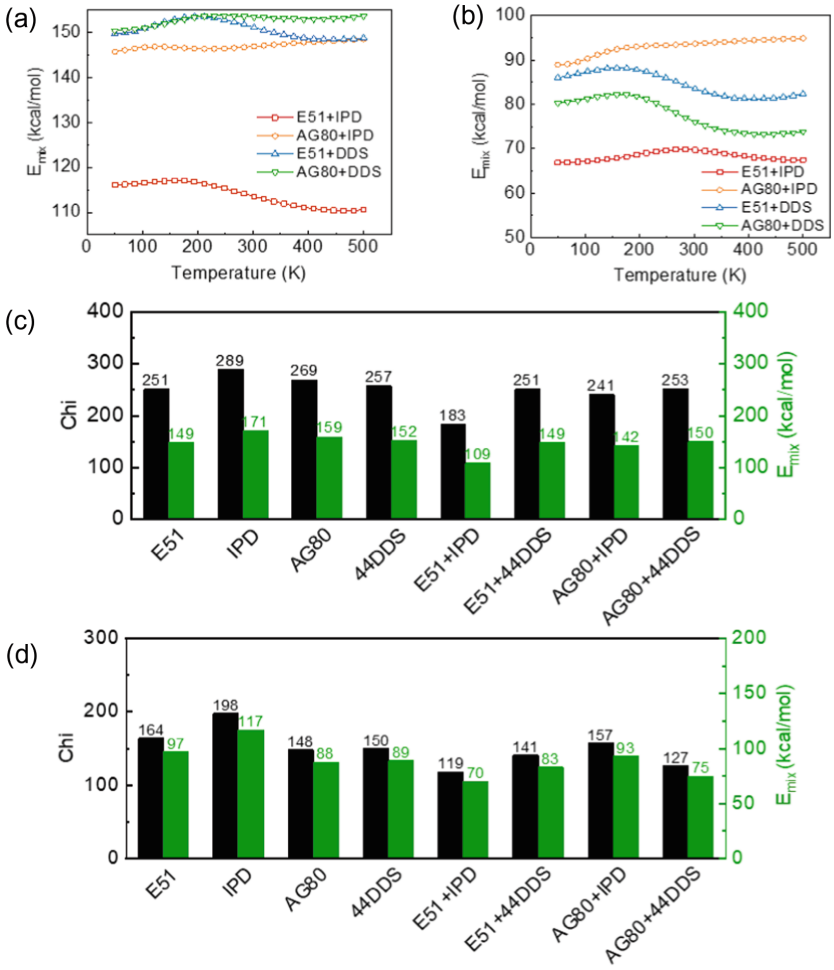

Fig. 2. The E_{mix} versus temperature (a). Phase diagram of two phases (b). Parameter Chi (χ) and E_{mix} of composite system at 273 K (c). Where graphite serves as the conductive substrate.

3.2 The Effect of Functional Groups

The compatibility between carbon-based matrix and resins with different functional groups was studied. As shown in Fig. 3(a), after the functional groups were modified,

the mixing energy with the resin was significantly reduced, among which the carboxyl modification resulted in a nearly 6 times decrease in mixing energy. This indicates that the introduction of functional groups can effectively increase the compatibility with the resin, and after the modification of functional groups, graphite is more easily mixed with the resin. However, for CNTs, a different effect was observed, where the introduction of functional groups resulted in a slight increase in mixing energy (Fig. 3b). To investigate this phenomenon, we studied the properties of different carbon materials themselves.

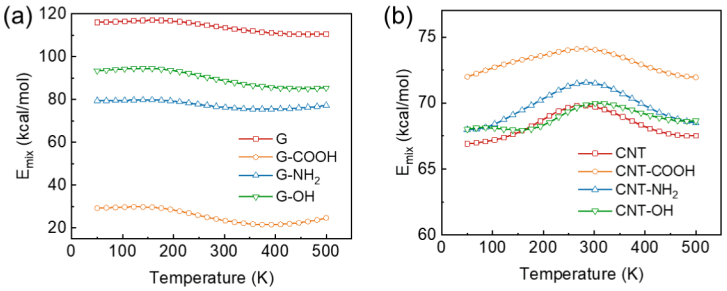

Fig. 3. The curve of mixing energy versus temperature for graphene (a) and CNT (b).

From Table 1, we can see that due to the strong electronegativity of the carboxyl functional group, the charge energy of carboxylated graphene is as high as 239.231 kcal/mol, much higher than other types of graphene, such as hydroxylated graphene with a charge energy of only 7.489 kcal/mol. This makes the total energy of carboxylated graphene, 183.579 kcal/mol, much lower than other types of graphene, and thus exhibits better compatibility with the resin. On the contrary, due to the unique cylindrical structure of CNTs, the introduction of functional groups increases the bond energy kcal/mol, and van der Waals energy of CNTs, while the change in charge energy is not significant. Therefore, the total energy of functionalized CNTs increases instead of decreasing, which weakens their compatibility with the resin, consistent with the above conclusion.

Table 1. Energy of the different carbon substrate models after reaching the equilibrium state

Type	E_{total} (kcal/mol)	$E_{valence}$ (kcal/mol)	E_b (kcal/mol)	$E_{non\text{-}bond}$ (kcal/mol)	E_v (kcal/mol)	E_e (kcal/mol)
G	282.4656	50.711	42.608	231.755	231.612	0.142
G-COOH	183.5787	136.313	49.087	47.266	286.497	− 239.231
G-NH_2	309.8638	78.786	45.672	231.078	249.021	− 17.943
G-OH	299.6241	68.047	43.803	231.577	239.066	− 7.489
CNT	2793.542	1939.526	167.528	854.016	863.14	− 9.124
CNT-COOH	2809.194	1976.005	173.917	833.189	879.284	− 46.095
CNT-NH_2	2829.036	1948.351	170.332	880.685	869.467	11.217
CNT-OH	2819.193	1944.715	169.031	874.478	864.915	9.562

4 Conclusion

Using MD simulation technology, it was confirmed that the compatibility of E51 as resin was combined with IPD as the curing agent in the carbon matrix were better than other resin. At the same time, as for the functionalization of carbon materials, introducing functional groups into graphene can significantly increase its compatibility with the resin, with carboxyl being the most effective due to its superior electronegativity, increasing compatibility by about 6 times. However, the effect of introducing functional groups on the compatibility of CNTs is minimal due to their unique cylindrical structure. The present study is expected to provide significant molecular insight into the relationship of compatibility between carbon matrix and epoxy resin for fuel cell composite bipolar plates.

Acknowledgment. This project is supported by the financial supports from the National Key R&D Program of China (2020YFB1505904).

References

1. Du, C., Ming, P., Hou, M., Fu, J., Fu, Y., et al.: J. Power. Sources. Power Sources **195**, 5312–5319 (2010)
2. F. Darıcık, A. Topcu, K. Aydın, S. Çelik, Int. J. Hydrogen Energy (2022)
3. Yao, K., Adams, D., Hao, A., Zheng, J.P., et al.: Energy Fuels **31**, 14320–14331 (2017)
4. Tan, Q.C., Shanks, R.A., Hui, D., Kong, I.: Compos. Part B Eng.. Part B: Eng. **90**, 315–325 (2016)
5. Lee, D., Lee, D.G.: J. Power. Sources. Power Sources **327**, 119–126 (2016)
6. Alo, O.A., Otunniyi, I.O., Pienaar, H.: Polym. Compos.. Compos. **41**, 3364–3375 (2020)
7. M. Laskoski, B. Dyatkin, N.C. Osti, J.K. Keum, E. Mamontov, et al., J. Polym. Sci. (2022)
8. Li, C., Strachan, A.: Polymer **51**, 6058–6070 (2010)
9. Cao, Y., Zhang, J., Feng, J., Wu, P.: ACS Nano **5**, 5920–5927 (2011)
10. Ren, S., Liu, X., Lin, P., Gao, Y., Erkens, S.J.M.: Design. Mater. Des.. Des. **223**, 111141 (2022)
11. Luo, Y., Wang, R., Wang, W., Zhang, L., Wu, S.: J. Phys. Chem. C. Phys. Chem. C **121**, 10163–10173 (2017)
12. Y. Qin, Y. Wang, J. Liu, F. Chen, A. Yao, et al., Macromol. Res. (2022)
13. Feng, Y., He, C., Wen, Y., Ye, Y., Zhou, X., et al.: Compos. Part A Appl. Sci. Manuf.. Part A: Appl. Sci. Manuf. **103**, 74–83 (2017)
14. Z. Wenqing, D. Xi, S. Gang, Y. Xiaoping, Carbon (2019)
15. Chartarrayawadee, W., Molloy, R., Ratchawet, A., Janmee, N., Butsamran, M., et al.: Polym. Compos.. Compos. **38**, 2272–2282 (2017)
16. Liu, Y.-T., Yang, J.-M., Xie, X.-M., Ye, X.-Y.: Mater. Chem. Phys.. Chem. Phys. **130**, 794–799 (2011)
17. Qiu, F., Hao, Y., Li, X., Wang, B., Wang, M.: Compos. Part B Eng.. Part B: Eng. **71**, 175–183 (2015)

18. A.P. William, S.R. Matthew, P. Sagar Umesh, M.O. Gregory, Compos. Part B: Eng. (2021)
19. Zhou, A., Tam, L.-H., Yu, Z., Lau, D.: Compos. Part B Eng.. Part B: Eng. **71**, 63–73 (2015)
20. J.E. Daniel, S. Filip, H. Andreas, et al., Chem. Eng. J. (2018)
21. Mayo, S.L., Olafson, B.D., Goddard, W.A.: J. Phys. Chem. **94**, 8897–8909 (1990)

Design of Charging Station System for Underwater High Energy Density Oxyhydrogen Fuel Cell

Zongju Cai(✉), Xiran Sun, Yuming Liu, and Chao Xu

Systems Engineering Research Institute CSSC, No. 1, Fengxian East Road, Haidian District, Beijing 100094, China
mmmb_000@163.com

Abstract. Based on the physical structure of the 20-foot container, this paper carries out the theoretical analysis of underwater charging station system about energy allocation of oxyhydrogen fuel cell and lithium batteries, and carries out the analysis of the equipment and components that have a great impact on the total weight of the charging station system, and summarizes the design principles to improve the energy density of the charging station system. The energy density of the underwater charging station is comprehensively improved in the aspects of technical design, material selection, structure and technology. The maximum structural configuration of hydrogen and oxygen gas storage vessel is carried out. The oxyhydrogen fuel cell and its auxiliary system realize the compact and lightweight design. The standard pressure chamber also achieves a lightweight design under the condition of 300m underwater pressure operation. The design and calculation results show that the charging station has high energy density, simple engineering implementation and can meet the requirements of underwater closed environment operation.

Keywords: Underwater power station · Oxyhydrogen fuel cell system · High energy density · Lightweight design

1 Introduction

For the long-term and small-volume requirements of power equipment, it is generally difficult to meet the system operation requirements by relying solely on high energy density batteries. In addition, considering that marine temperature is low, the discharge performance of the traditional battery is attenuated, and battery energy cannot meet the needs of more scenarios. The fuel cell is a representative energy with high energy density, which has the advantages of high energy conversion efficiency, low vibration noise, no exhaust emissions, and flexible module combination. The oxyhydrogen fuel cell is an energy conversion device that converts the chemical energy of hydrogen and oxygen into electrical energy through the electrode reaction, and its reaction process does not involve combustion, thus breaking the limit of power generation in a low temperature environment [1], which can be used for the development of underwater long range, large

H. Sun et al. (Eds.): WHTC 2023, SPPHY 393, pp. 352–363, 2024.
https://doi.org/10.1007/978-981-99-8631-6_34

navigation depth and high stealth closed cycle unmanned underwater charging station [2].

The power dynamic characteristics of oxyhydrogen fuel cells are soft, and the dynamic response speed is slow. The idea of adding lithium batteries to work with oxyhydrogen fuel cells is adopted, and the dynamic response of lithium batteries is fast to support the bidirectional charging and discharging characteristics. This paper designs an underwater high energy density fuel cell charging station system with hydrogen and oxygen as the main energy source, as shown in Fig. 1. The energy generated by oxyhydrogen fuel cells and lithium batteries are reasonably configured, which ensures the high energy density requirements of underwater power stations. The system is designed to withstand a standard pressure chamber with a water depth of 300 m. According to the function, three pressure chambers are arranged, including fuel cell cabin, battery electrical cabin and drainage cabin. In the fuel cell cabin, a set of hydrogen and oxygen fuel cell system with zero exhaust emission is realized to meet the operation requirements of closed cycle of underwater environmental charging power station system. In the battery electrical cabin, the power supply generated by the two kinds of energy is charged in parallel by the power electronic device.

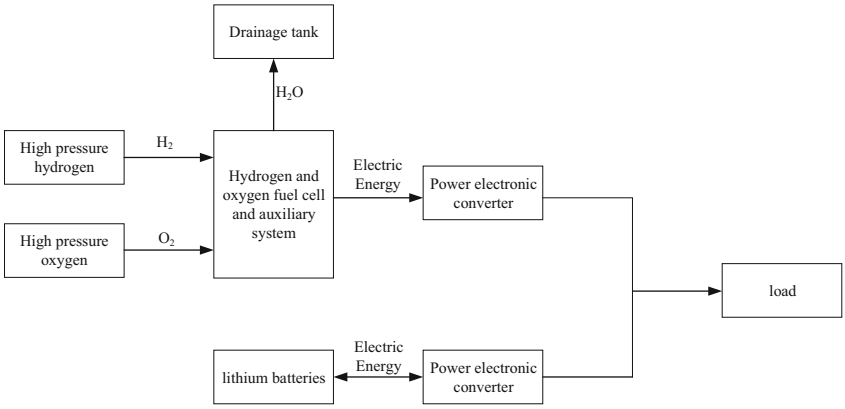

Fig. 1. Underwater high energy density fuel cell charging station system

2 Analysis of Factors Affecting Energy Density of Charging Station

2.1 Theoretical Analysis of Energy Allocation

Assume that a 20-foot 5.8 m * 2.3 m * 2.3 m container is used as the integration framework of the charging station. High pressure hydrogen storage and oxygen storage are selected as the energy storage methods for hydrogen and oxygen fuel. Assume the high pressure gas cylinder is 35 MPa/162 L gas cylinder with length of 1840mm and outer diameter of 410 mm. The lithium battery is a lithium iron phosphate battery pack with volume capacity of 270 Wh/L and energy density of 160 Wh/kg. In terms of energy space layout,

the lithium battery pack is arranged as a whole battery package, and the hydrogen and oxygen fuel is arranged in a modular way of "cylinder plus frame". The volume ratio of the hydrogen and oxygen fuel modules to the charging station is calculated, and the energy density of the charging station under different proportion conditions is analyzed.

Through the above calculation, the energy density of the whole charging station is obtained when the volume of oxyhydrogen fuel modules accounts for the proportion of the total volume of the whole charging station, and the change trend of the system energy density of oxyhydrogen fuel and lithium battery under different energy ratios is obtained, as shown in Fig. 2. It can be seen that the larger the volume of oxyhydrogen fuel modules, the higher the energy density of the whole charging station.

Therefore, in order to improve the energy density of the charging station, space of oxyhydrogen fuel modules should be increased as much as possible in combination with the characteristics of the platform structure. The energy transferred from oxyhydrogen fuel cells should also be the preferred energy source in the charging station system operation strategy.

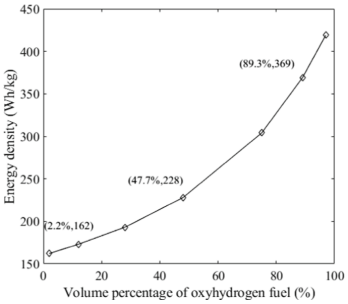

Fig. 2. Trend chart of oxyhydrogen fuel volume proportion and energy density of charging station

2.2 Theoretical Analysis of Weight Proportion

The charging station system mainly involves five parts: standard pressure chamber, oxyhydrogen fuel cell and its auxiliary system, oxyhydrogen fuel storage modules, lithium battery pack and power electronic converter. In order to deeply analyze the weight of each equipment, the weight specification parameters of each system and equipment were estimated during the design process, and the weight proportion of each system and equipment was calculated, forming the platform weight proportion analysis chart, as shown in Fig. 3.

According to the weight proportion analysis chart of each system and equipment, the proportion of hydrogen cylinders and valves, oxygen cylinders and valves, and standard pressure chamber occupies the top three, and the sum of the three accounts for more than 90% of the total weight, which is the key factor affecting the energy density of the entire system, Therefore, in the design and selection of hydrogen and oxygen storage modules and standard pressure chamber, the design principle of lightweight should be thoroughly implemented. Hydrogen and oxygen fuel cells, fuel cells auxiliary system,

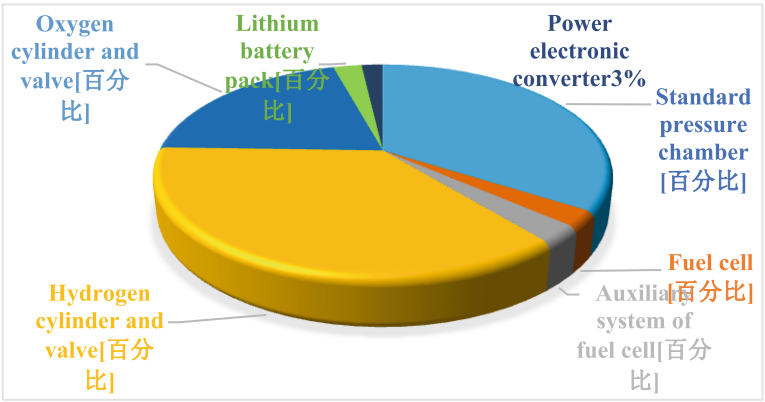

Fig. 3. Analysis of weight proportion of components and equipment

lithium batteries and power electronic converters each account for between 2% and 3% of the whole platform. The hydrogen and oxygen fuel cells and their auxiliary systems are in one pressure chamber, and the hydrogen and oxygen fuel cells account for about 50% of the weight of the fuel cell system, the lithium cells and power electronic converters are in another pressure chamber, and the lithium cells account for about 50% of the total weight of the equipment. As the core of the charging station, the lightweight design of oxyhydrogen fuel cell and lithium battery has a great impact on the weight reduction of the two core chambers.

2.3 Design Principles for Improving Energy Density

In order to improve the energy density of the charging station, the project takes into account the system design and equipment selection from several aspects such as the energy configuration of oxyhydrogen fuel modules and lithium battery, system function, material and component lightweight. It includes the following principles:

(1) Energy allocation: the capacity of lithium batteries should meet the basic requirements of the charging station control system for continuous power supply. In combination with the structural characteristics of the integration framework, hydrogen and oxygen fuel modules should be arranged as much as possible, in order to increase the proportion of hydrogen and oxygen fuel in the storage energy of the charging station, so as to improve the energy density of the system.
(2) System functions: adhere to the simplest way to achieve all the essential functions, reduce the number of components or parts, and thus reduce weight at the functional level. Deeply analyze and demonstrate the redundancy function, and minimize the redundancy design. On the basis of realizing the functions, the simplest structure is adopted to realize the lightweight of the overall structure of the charging station [3].
(3) Lightweight materials: on the premise of meeting the use requirements and reasonable redundancy, select the light material that meets the strength. The weight reduction of materials can be achieved by cutting the weight reduction hole in the plate, drilling the weight reduction hole in the square tube, and hollowing out the

plate to maximize the material performance. For parts such as pressure chambers that have a great impact on the weight of the system, the material shall be reasonably selected considering corrosion resistance, safety and lightweight.

(4) Lightweight components: for a large number of hydrogen and oxygen cylinders and valves, new lightweight materials such as carbon fiber should be actively explored. The lightweight design of hydrogen and oxygen fuel cells should be achieved by introducing new lightweight materials such as composite carbon fiber materials. Lightweight plastic products should be chosen as much as possible in the gas-liquid separator.

3 Design of Hydrogen and Oxygen Fuel Cell Charging Station System

3.1 Maximum Configuration Structure Design of Hydrogen and Oxygen Fuel

In the integrated frame of the 20-inch container, combined with the structural characteristics of the charging station, high-pressure hydrogen and oxygen storage containers are arranged below, using domestic 35 MPa carbon fiber III bottles, the inner layer is sealed with aluminum tank gas, the middle layer is carbon fiber reinforced resin to ensure the compressive strength, and the surface layer is glass fiber reinforced resin layer to protect the surface. Combined with the marine environment, carbon fiber high-pressure gas cylinders have excellent corrosion resistance characteristics, acid, alkali, salt and atmospheric corrosion resistance, and are safer to use [4].

At present, the general product is type III carbon fiber gas cylinder with a pressure resistance of 35 MPa. The conventional product is 162 L, with a valve length of 1830 mm and an outer diameter of 410 mm. This type of gas cylinder is selected as a high-pressure hydrogen and oxygen storage container. After three-dimensional modeling and calculation, a total of 18 hydrogen and oxygen gas storage containers with the specification of 35 MPa/162 L can be arranged, as shown in Fig. 4. Among them, 12 hydrogen gas storage containers are distributed on the left and upper sides of the pressure chambers, and 6 oxygen gas storage containers are distributed on the right side of the pressure chamber.

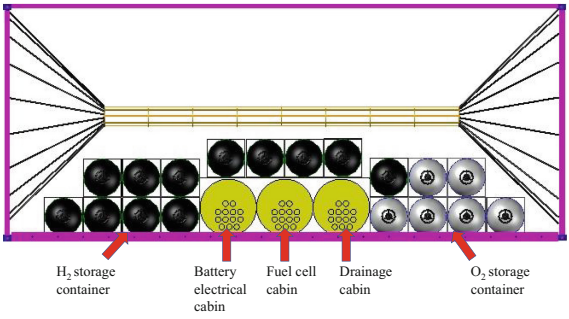

Fig. 4. The maximum configuration of hydrogen and oxygen gas storage vessels in the overall structure of the platform

3.2 Hydrogen and Oxygen Fuel Cell and Its Auxiliary System Design

Hydrogen and oxygen fuel cell and its auxiliary system mainly include hydrogen and oxygen fuel cell, hydrogen supply cycle system, oxygen supply cycle system, cooling cycle system, water collection system, hydrogen and oxygen tail gas absorption system and control system, as shown in Fig. 5 [5, 6]. The various components of system are arranged in the closed chamber with the specified space length $\leq$ 1500 mm and inner diameter $\leq$ 570 mm in the pressure chamber, to ensure the separation of gas, water and electricity, and to disperse the heat generated by the hydrogen and oxygen fuel cell in time, and to ensure that the liquid water generated can be discharged in time. The oxyhydrogen fuel cell and its auxiliary system have adopted compact design and lightweight design to comprehensively improve the energy density of the oxyhydrogen fuel cell and its auxiliary system.

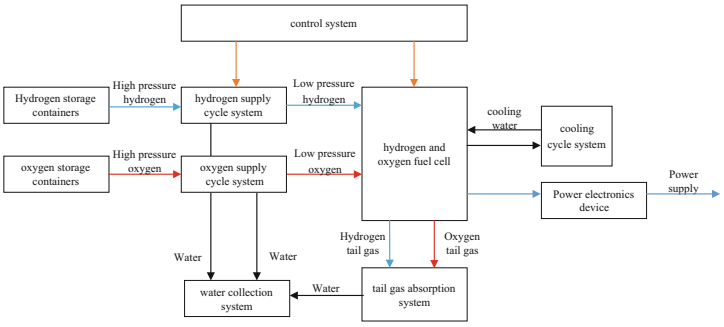

Fig. 5. Schematic diagram of oxyhydrogen fuel cell and its auxiliary system

(1) Compact design

In the fuel cell cabin, the size of the pressure chamber is taken as the size boundary of the layout, and the reasonable layout is divided into eight areas, as shown in Fig. 6, which ensures the separation of gas, water and electricity, and at the same time, the heat generated by the hydrogen and oxygen fuel cells can be dispersed in time.

The radiator (area1) is arranged on the right side of the system, and sticked to the surface of the pressure chamber, making full use of the low temperature sea out of pressure bulkhead for heat dissipation. Considering that the interfaces of the gas, electricity and the cooling of the oxyhydrogen fuel cell are all integrated on the left side, the oxyhydrogen fuel cell is set at the rightmost end of the frame (area 2). The cooling cycle system, including water pump, deionizer and thermostat, is arranged at the lower side of the oxyhydrogen fuel cell (area 3), which reduces the electrical risk caused by leakage and makes comprehensive use of the bottom space.

Gas-liquid separator and three-way pipeline are arranged in the middle of the cabin (area 4). The gas-liquid separator is arranged at the bottom of the system to facilitate the collection of water. The hydrogen and oxygen supply cycle systems, including supply pipeline, gas circulation pump and three-way pipeline, are arranged in the middle and

upper part of the pressure chamber (area 5). The hydrogen and oxygen fuel cell considers the convenience of water management, and the gas circuit adopts the cycle way of upper inlet and lower outlet. Water collection system is arranged in area 6, including water tank and drainage pump.

The control system is arranged on the left side of the pressure chamber (area 7) to integrate the system controller and power supply module. The left side is close to the pressure chamber flange, which is convenient for the external output and connection of the system cable. The hydrogen and oxygen tail gas absorption system is arranged at the left upper part of the pressure chamber (area 8), including the hydrogen and oxygen absorber, fan, hydrogen concentration sensor and pipeline. Considering the low hydrogen density, leakage is easy to gather on the top. When exhaust gas needs to be treated, the fan is used to circulate the mixed gas in the forced sealing chamber through the hydrogen and oxygen absorber and undergo catalytic combustion to consume hydrogen and oxygen in the chamber.

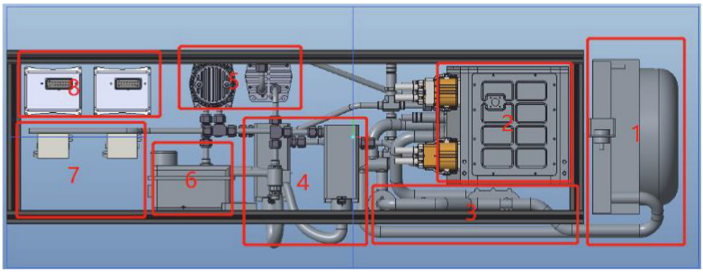

Fig. 6. Compact design of oxyhydrogen fuel cell and auxiliary system

(2) Lightweight design

The lightweight design of the fuel cell system has been realized by adopting six series aluminum alloy hollow frame structure, lightweight hydrogen and oxygen fuel cell, and new normal temperature hydrogen eliminator.

Since the oxyhydrogen fuel cell and auxiliary system are arranged inside the pressure chamber, all equipment and components are installed on the integrated frame, which adopts a hollow frame structure, reducing the weight of the entire frame. The frame is made of six-series aluminum alloy. Six-series aluminum alloy is the most widely used alloy with magnesium and silicon as the main added elements and Mg2Si as the main strengthening phase. 6061 and 6082 aluminum alloys in the six-series aluminum alloys are heat-treatable and can be strengthened. They have good formability, weldability, machinability, and medium strength. They can still maintain good operability after annealing. It is widely used in various industrial structural parts requiring certain strength and high corrosion resistance.

The stress distribution of the end face structure of the oxyhydrogen fuel cell is determined by simulation, and the reduction preparation method is adopted to reduce the end face materials as much as possible, and then the weight reduction goal is achieved

by introducing new lightweight materials such as composite carbon fiber materials; At the same time, it forms a unified design with the end face fluid distribution port, connector and sensor structure attached to the oxyhydrogen fuel cell to realize the function and structure modularization.

At present, the commonly used hydrogen removal methods include catalytic combustion, alloy hydrogen storage and auxiliary hydrogen and oxygen fuel cell absorption [7, 8]. For large-capacity power generation system, multiple hydrogen storage alloy devices will be equipped, greatly increasing the size and weight of the equipment. The auxiliary hydrogen and oxygen fuel cell absorption method needs to be equipped with auxiliary small fuel cells, which are connected in series with the fuel cell body used for power generation to consume the remaining anode gas and cathode gas in the reaction of the fuel cell body used for power generation. The auxiliary hydrogen and oxygen fuel cell needs to be equipped with gas supply system, cooling system, etc. to achieve a large number of components, the overall system is relatively complex, and the efficiency is low, which needs to occupy a large amount of volume space. The hydrogen removal method adopted in this system is to directly pass the hydrogen-containing mixture into the catalytic device at low temperature or normal temperature, without external heat source heating, and the heat generated by the catalytic process can accelerate the hydrogen removal reaction rate. The hydrogen removal device adopts compact and miniaturized design, with catalytic efficiency of more than 95% and weight of only 800 g. There is no need to replace or supplement hydrogen removal substances and desiccant, which eliminates replacement/supplement operation steps, prolongs the operation cycle of the system and reduces the maintenance cost.

3.3 Standard Pressure Chamber Design

Considering the working water depth of the charging station, the cylindrical structure is adopted in the structure shape, the end of one side is welded with a cover plate, and the end of the inlet and outlet cables is sealed and installed with a flange plate. The pressure chamber is designed as a cylinder, which is mainly based on the advantages of high radial pressure resistance, low axial underwater upstream resistance, and easy processing. The pressure chamber prototype is composed of a cylinder, two end covers and watertight connectors on the end cover. Each end cover and cylinder are connected uniformly on the circumference with screws, and the end face is sealed with O-ring. The pressure chamber of its underwater charging station is shown in Fig. 7.

The pressure chamber is made of 6061 aluminum alloy. As the pressure water depth is not less than 300 m, the working pressure p_w is 3MPa, that is, the design pressure of chamber $p_c = 1.1p_w = 3.3$ MPa. According to the national standard GB 150.1-150.4-2011 <Pressure Vessel>, the cylinder thickness is calculated according to the strength failure design:

$$\delta = \frac{p_c D_i}{2[\sigma]^t \emptyset - p_c} = 11\,\text{mm}$$

The specific meaning of parameters in the formula is as follows:
p_c-design pressure of chamber, 3.3 MPa,

D_i-inner diameter of pressure chamber, 570 mm,
$[\sigma]^t$-allowable stress of the material, take $[\sigma_d]$ and $[\sigma_b]$ minimum value, 96.7,
Ø-the welding coefficient, 100% NDT is required for single butt joint, 0.9.

Considering that the roundness of the cylinder can not be guaranteed by actual machining, and there are uneven factors such as material and load distribution, combined with machining allowance, corrosion allowance and screw connection, δ is taken 20 mm, then the outer diameter of pressure chamber cylinder is 610 mm.

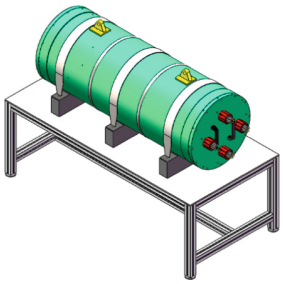

Fig. 7. 3D design drawing of pressure chamber of underwater charging station

4 Calculation of Energy Density of Charging Station System

The number of hydrogen moles is calculated by van der Waals gas equation. The hydrogen enthalpy value is used and the hydrogen fuel energy is calculated according to the efficiency obtained at the working point of the hydrogen and oxygen fuel cell. The project adopts a hydrogen cylinder with a volume of 162 L and a pressure of 35 MPa, which is substituted into the van der Waals gas equation:

$$\left(P + \frac{n^2 a}{V^2}\right)(V - nb) = nRT$$

The specific meaning of parameters in the formula is as follows:
P-Gas cylinder storage pressure, 35,000kPa,
V-Nominal volume of gas cylinder, 162 L,
a-parameter to measure intermolecular gravity, 24.32,
b-Sum of volumes of one mole of molecules, 0.027 L/mol,
n-molar weight, mol,
R-ideal gas constant, 8.314 J/(mol K),
T-temperature, 273.15 K.
Molar weight can be obtained by substituting the parameters.

$$n = 1876\,\text{mol}$$

According to the hydrogen low enthalpy value of 241 kJ/mol and the efficiency of hydrogen and oxygen fuel cell of 50%, the hydrogen fuel energy is calculated as follows:

$$Q_0 = \frac{\eta * n * q_{H2}}{3600} = 62.8\,\text{kWh}$$

It can be concluded that the complete consumption of hydrogen can provide 62.8 kWh of electric energy. The number of hydrogen cylinders is 12, and the calculation of all hydrogen fuel energy is

$$Q_1 = 12^*Q_0 = 753.5\,\text{kWh}$$

The lithium-ion battery pack with weight of 35 kg and storage capacity of 5 kWh is selected. Then the total energy reserve of the charging station is

$$Q = Q_1 + Q_2 = 758.5\,\text{kWh}$$

The system and equipment involved in the weight of the charging station, including the pressure chamber, the oxyhydrogen fuel cell and its auxiliary system, high pressure fuel cylinders under full load, the lithium battery pack and the power electronic converter, have been physically checked according to the weight of the prototype, and the results are shown in Table 1.

Table 1. Weight of five system and components

Code	Item	Number	Weight (kg)
M1	Pressure chamber	3	708
M2	Fuel cell and its auxiliary system	1	122
M3	High-pressure gas cylinders	12 + 6	1836
M4	Lithium battery pack	1	35
M5	Power electronic converter	3	46
M	Total		2747

The energy density of the underwater charging station is calculated as follows:

$$\rho = \frac{Q}{M} = 276\,\text{Wh/kg}$$

5 Conclusion

This paper designs an underwater high energy density fuel cell charging station system with hydrogen and oxygen as the main energy. By reasonably configuring hydrogen and oxygen fuel modules and the lithium batteries, the energy density of the underwater hydrogen and oxygen fuel cell charging station is 276 Wh/kg, and the main indicators of the system are shown in Table 2.

In the calculation process, although a large number of documents and materials have been consulted and the basic theories and related technologies of fuel cells and lithium batteries have been carefully studied, there are still some problems to be improved and further discussed, which can be summarized as follows:

Table 2. Main indicators of the system

Item	Number
Total weight	2747kg
Hydrogen energy	753.5 kWh
Lithium battery energy	5 kWh
System energy density	276 Wh/kg
Size of fuel cell chamber	Length 1500 mm, inner diameter 570 mm
Fuel cell output power	5 kW
Cylinder size	Length 1830 mm, outer diameter 410 mm

The calculation of hydrogen fuel energy is mainly based on the theoretical calculation of the van der Waals ideal gas formula, and the actual power generation of hydrogen fuel has not been tested and verified. The calculation results may differ from the actual operation data. In the next step, the hydrogen fuel energy will be further tested and verified in combination with the demonstration and verification system prototype.

This paper calculates the energy density of the system from the perspective of hydrogen storage and lithium battery storage, and assumes that all the energy is used for charging. It does not consider the specific charging and discharging operating conditions between the power generation end and the load end, nor does it consider the efficiency of electric energy in the transmission process. Therefore, it is necessary to further refine the power transmission efficiency according to the actual application.

These are the problems that need to be studied and solved in the future research. It is believed that with the development of hydrogen fuel and lithium battery energy storage technology and its application in underwater charging stations, the energy density of charging stations will make greater progress.

References

1. Shi, Y.-q., He, B., Cao, G.-j., et al.: A study on the energy management strategy for fuel cell electric vehicle based on instantaneous optimization. Autom. Eng. **30**(1), 30–35 (2008)
2. Gao, H.-z., Wang, Z.-j., Yin, S.-p., Lu, J., Wang, J.-g.: Energy management strategy simulation on underwater fuel cell power system. J. Unmanned Undersea Syst. **26**(3), 242–246 (2018)
3. Huang, Z., Wu, X., Lin, Z.: Review of hydrogen technology status and its development trend for fuel cell AIP system in submarine. J. Power Supply **41**(11), 1664–1666 (2017)
4. Bernd, K.: Lightweight Design: Calculation Foundation and Component Structure. Machinery Industry Press, Beijing (2010)
5. Wang, B.-j., Yuan, Y.: Hydrogen and oxygen fuel cell power system for underwater vehicles. Mar. Electr. Technol. **40**(1), 15–17 (2020)
6. Yuan, R.: Design of 10 kW Fuel Cell Powerplant for UUV. Harbin Engineering University
7. Li, J., Hu, Z., Fang, C., Xu, L., Ouyang, M.: Recycled fuel cell system. CN106058284 B (2019)
8. Wang, Z., Gao, Y., Wang, B., Wang, A., Li, H.: A hydrogen fuel cell hydrogen removal device and hydrogen removal method in closed environment. CN111799489 B (2021)

Study on Configuration and Control Strategy of Electrolyzers in Off-Grid Wind Hydrogen System

Tao Zhang[1], Lingjun Song[1(✉)], Fuyuan Yang[2], and Yangyang Li[2]

[1] School of Transportation Science and Engineering, Beihang University, Beijing 100191, China
songlingjun@buaa.edu.cn

[2] State Key Laboratory of Automotive Safety and Energy, Tsinghua University, Beijing 100084, China

Abstract. Multi-electrolyzers system is an effective method to address the problem that the lowest operating point of the alkaline water electrolyzer still is high when the water electrolysis system is coupled with renewable energy. This work proposed different configurations of nominal power and operating strategies of electrolyzers for an off-grid isolated stand-alone wind hydrogen system. The configurations contain different nominal power of electrolyzers rather than the same nominal power. An equal load strategy is proposed and simulated based on the operation characteristics of the alkaline electrolyzer. This strategy could reach the 99% of energy absorption rate.

Keywords: Alkaline electrolyzer · Off-grid wind hydrogen system · Capacity configuration · Control strategy

1 Introduction

The core problems of wind hydrogen are how to configure the nominal power and number of the electrolyzer and formulate operating strategies of multi-electrolyzers based on the operation law and characteristics of the alkaline electrolyzer. Varela et al. [1] solved a mixed-integer linear program to find the optimal number of electrolyzers and production schedules in a wind-hydrogen system. The results show that the optimal objective value and total energy absorption are obtained when 13 electrolyzers are configured in the system. Matute et al. [2] presented a multi-state model of electrolysis systems, optimal dispatch of hydrogen production plants is obtained, and the model was tested using real data from a wind farm, the results demonstrated that the model is a support tool to operate hydrogen production plants more profitably. The current studies mainly focus on the total capacity of the wind-hydrogen system [3, 4], few researchers make efforts to the comprehensive management between multiple electrolyzers, even if the multi-electrolyzers system has been considered, the nominal power of every electrolyzer is the same in most of the works [2–4].

H. Sun et al. (Eds.): WHTC 2023, SPPHY 393, pp. 364–369, 2024.
https://doi.org/10.1007/978-981-99-8631-6_35

2 Methodology

2.1 Multi-electrolyzers and Historical Data of Wind Turbine

The multi-electrolyzers have shared Bop (Bop, Balance of plant), and every electrolyzer has an independent power supply so that the state of the electrolyzer could be switched independently and flexibly. The control system will decide the operating state of electrolyzers depending on the Pout (Pout, output power of wind turbine), in this way water electrolysis system is operated safely and efficiently.

The distribution of Pout over time is shown in Fig. 1. The total capacity of electrolyzers in the system is subject to the historical and future Pout. Generally, the hydrogen production power of the electrolyzer shall be equal to the maximum Pout, while the maximum Pout is about 2.2475 MW, and the time that Pout exceeds 2 MW just is 442 h during 6000 h. Considering the balance between investment costs and energy absorption rate, the total capacity of electrolyzers is set to 2MW preliminary.

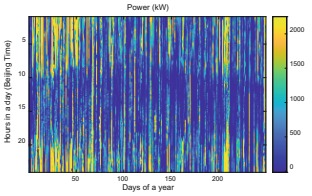

Fig. 1. Power distribution of wind turbine during 250 days.

2.2 Assumptions for the Alkaline Electrolyzer

In this work, the alkaline water electrolyzer is selected as hydrogen production equipment due to alkaline electrolyzer is currently the most mature and durable [5, 6].

There is an operating point with the lowest energy consumption (eop, operating point with the lowest energy consumption), which approximately is 60% of the nominal power of the electrolyzer [7]. When the Pin (Pin, input power of electrolyzer) increases from lop to eop, the energy consumption decreases gradually and once the Pin exceeds the eop, the energy consumption will continue to increase. When the Pin reaches the highest operating point, the electrolyzer has maximum energy consumption. Based on this fact, it's ruled that when the Pin is in the operating range of 20–60%, the energy consumption is 48 kWh/kgH_2, while the Pin is in the operating range of 60–100%, the energy consumption is 52 kWh/kgH_2 [8].

Generally, the lop of the electrolyzer is 20% of the nominal power, which is the reason why this work needs to be done. The lop could be reduced to 11% relying on some novel control methods [8, 9]. The following work will be based on that lop is 20% of the nominal power. Simultaneously, the impact of reducing lop to 11% of nominal power on the research results will also be explored.

2.3 Configurations and Control Strategy of the Electrolyzers

Considering the standardized manufacture of alkaline electrolyzers, it's assumed that the nominal power of the electrolyzers includes 0.5MW, 1MW, 1.5MW, and 2MW. And nA, nB, nC, and nD represent the number of electrolyzers with 0.5 MW, 1 MW, 1.5 MW, and 2 MW respectively. For hydrogen production system with a total capacity of 2MW:

$$0.5nA + nB + 1.5nC + 2nD = 2 \tag{1}$$

To solve Eq. (1), there are five configurations in this work. The configurations are listed in Table 1.

Table 1. Configurations of four electrolyzers.

Configuration	nA	nB	nC	nD	Total power (MW)
#1	0	2	0	0	2
#2	0	0	0	1	2
#3	1	0	1	0	2
#4	2	1	0	0	2
#5	4	0	0	0	2

2.4 Equal Load Strategy

In this work, an equal load strategy is proposed. For the sake of explanation, the electrolyzers are numbered EL1, EL2 until ELn according to the nominal power of electrolyzers from small to large, by the way, n represents the number of electrolyzers in the system. For this strategy, the controller needs to judge whether Pout exceeds lop of EL1, if the answer is yes, EL1 is started. Then the controller needs to calculate the result of Pout minus lop1 and if the calculation result exceeds lop2, EL2 will be started, and so on. The controller needs to repeat the calculation and judgment process after Pout changing. The core of strategy is to keep as more electrolyzers in operation as possible even if they can't be operated at nominal power. Figure 2 shows a schematic diagram of power distribution for three electrolytic cells as an example.

3 Results and Discussion

3.1 Comparison and Analysis of System Performance Under Different Configurations

Based on the characteristics of multi-electrolyzers systems, the theory of the Equivalent load lower limit (El) is proposed in this paper. EL can be represented by Eq. (2).

$$El = \frac{Pmin * 20\%}{Powertotal} \tag{2}$$

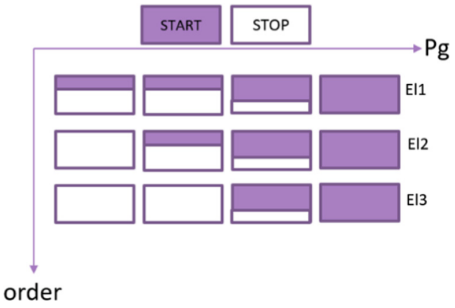

Fig. 2. Schematic diagram of equal load strategy.

The *Pmin* is nominal power of electrolyzer with lowest power, *Powertotal* is the total power of system.

The performance of hydrogen production systems can usually be measured by the following indicators: lower load limit (L); Hydrogen Production (P); Energy absorption rate (Ea); Average working hours per electrolyzer (Aw); Average times of starts and stops per electrolyzer (At). The operational indicators within 6000 h are listed in Table 2. This result shows that all indicators of the system with single electrolyzer are the worst. Multi-electrolyzer system has significant advantages in both hydrogen production and energy absorption rate. According to definition of Equivalent load lower limit, the energy absorption rate and minimum load of the system depend on the electrolytic cell with the lowest power.

When Pout (Output power of wind power) is the same, more electrolyzers could be started and the electrolyzers have the same operating point under this strategy, which results in electrolyzers being operated at a relatively low operating point with high efficiency. Though the #2, #3, #4 has same energy absorption, the hydrogen production show some differences. The hydrogen production is positively correlated with the number of electrolyzers with small nominal power under, the reason is that increasing the number of electrolyzers with small nominal power leads to the more chances for the electrolyzers to be operated at the operating point with high efficiency.

As for the average working hours per electrolyzer, the #4 has greater performance, which means that the electrolyzer will have a higher utilization rate using this configuration. In fact the difference of Aw of different configurations is small, the multi-electrolyzer system also couldn't solve the Relatively low utilization rate of electrolyzer in the scenario of wind power hydrogen production.

Frequent startup and shutdown of electrolyzer have a certain negative impact on the lifespan of the electrolyzer, so this indicator is also worth paying attention to. The #3 has minimal At, and the At will deteriorates as the number of 0.5 MW electrolyzer increases. However, Similar to Aw, the difference in At performance between different configurations is also relatively small.

The more electrolytic cells in the system, the higher the difficulty and cost of control, meanwhile, Bop also needs to be optimized accordingly. Thus # 3 maybe an ideal configuration based on a comprehensive comparison. Only two electrolyzers are configured in the system, and the overall performance is also very good.

Table 2. Hydrogen production in 6000 h and total costs of electrolyzers.

Configuration	N	EL (%)	HP (10^4 kg)	EA (%)	Aw (h)	At
#1	2	10	6.44	97.69	3035	454
#2	1	20	5.59	91.23	2676	457
#3	2	5	6.54	99.47	3229	437
#4	3	5	6.55	99.47	3284	442
#5	4	5	6.56	99.47	3218	444

4 Conclusion

This work proposed configurations and operating strategy of electrolyzers for an Off-grid isolated stand-alone wind hydrogen system. Based on the historical data of Pout, the total nominal power of the alkaline electrolyzer is determined to be 2 MW, and considering the electrolyzer will be manufactured standardized, five configurations of electrolyzers are obtained. According to the operation characteristics of alkaline electrolyzer, two operating strategies are proposed.

The single electrolyzer is a bad choice in the wind-hydrogen system due to its relatively high lop, but the multi-electrolyzers system performs well in the aspect of hydrogen production and energy absorptivity. Under equal load Strategy, the number of electrolyzers with small nominal power is positively correlated to hydrogen production.

By utilizing this configuration and control strategy, the system achieved an energy absorption rate of over 99% while working safely.

References

1. Varela, C., Mostafa, M., Zondervan, E.: Modeling alkaline water electrolysis for power-to-x applications: a scheduling approach. Int. J. Hydrogen Energy **46**(14), 9303–9313 (2021)
2. Matute, G., et al.: Multi-state techno-economic model for optimal dispatch of grid-connected hydrogen electrolysis systems operating under dynamic conditions. Int. J. Hydrogen Energy **46**(2), 1449–1460 (2021)
3. Fang, R., Liang, Y.: Control strategy of electrolyzer in a wind-hydrogen system considering the constraints of switching times. Int. J. Hydrogen Energy **44**(46), 25104–25111 (2019)
4. Shen, X., Nie, C., Lv, H.: Optimal control strategy of off-grid alkaline electrolyzer array for hydrogen production from wind power considering electrothermal characteristics. Trans. China Electrotech. Soc. **36**(3), 10 (2021)
5. Song, S., et al.: Production of hydrogen from offshore wind in China and cost-competitive supply to Japan. Nat. Commun. **12**(1), 1–8 (2021)
6. Buttler, A., Spliethoff, H.: Current status of water electrolysis for energy storage, grid balancing and sector coupling via power-to-gas and power-to-liquids: a review. Renew. Sustain. Energy Rev. **82**, 2440–2454 (2018)
7. Ursúa, A., et al.: Stand-alone operation of an alkaline water electrolyzer fed by wind and photovoltaic systems. Int. J. Hydrogen Energy **38**(35), 14952–14967 (2013)

8. Li, Y., et al.: Active pressure and flow rate control of alkaline water electrolyzer based on wind power prediction and 100% energy utilization in off-grid wind-hydrogen coupling system. Appl. Energy **328**, 120172 (2022)
9. Qi, R., et al.: Pressure control strategy to extend the loading range of an alkaline electrolysis system. Int. J. Hydrogen Energy **46**(73), 35997–36011 (2021)

Study on the High-Performance Catalyst for Sulfuric Acid Decomposition in the IS Cycle

Peng Zhang[1,2], Songzhe Chen[1], Laijun Wang[1], and Ping Zhang[1(✉)]

[1] Institute of Nuclear and New Energy Technology, Tsinghua University, Beijing 100084, China
zhangping77@tsinghua.edu.cn
[2] CHINERGY CO., LTD, Beijing 100193, China

Abstract. The iodine-sulfur cycle coupled with a high-temperature gas-cooled reactor is a clean and efficient hydrogen production technology. The sulfuric acid decomposition reaction is the highest temperature process in the iodine-sulfur cycle, which requires 850 °C high temperature and catalyst to carry out at a high conversion rate. This study prepared a series of loaded sulfuric acid decomposition catalysts using anatase TiO_2 and Ta_2O_5 as catalyst carriers and precious metal Pt as the active component. XRD, BET, and ICP-MS characterization of the catalysts demonstrated that the high calcination temperature could increase the crystallinity and content of the active components and decrease the specific surface area of the catalysts. The Pt/TiO_2-850 catalyst showed good performance under different feed concentrations, reaction temperatures, and particle sizes. In addition, the scale-up production does not affect the Pt/TiO_2-850 catalyst reaction performance. The Pt/TiO_2-850 catalyst was tested in a bayonet-tube SiC reactor with a 100-h high throughput lifetime, which proved that the Pt/TiO_2-850 catalyst has good stability.

Keywords: Iodine-sulfur cycle · Sulfuric acid decomposition · Catalyst · Stability

1 Introduction

Hydrogen is an important industrial raw material and an ideal energy carrier in the future, it is easy to store and transport as a secondary energy source and can be used directly as a fuel [1]. In addition to the traditional ammonia synthesis, methanol synthesis, and petroleum refining, hydrogen can be utilized on a large scale in hydrogen metallurgy, coal liquefaction, and fuel cell vehicles, providing the necessary technological support for these industries to reduce carbon emissions [2–4]. The utilization of nuclear energy for hydrogen production can achieve efficient, large-scale, and carbon-emission-free.

The hydrogen production technologies from nuclear energy using water as feedstock mainly include thermochemical cycles and high-temperature steam electrolysis. However, the iodine-sulfur (IS) cycle coupled with high-temperature gas-cooled reactors (HTGR) is considered the most suitable and promising hydrogen production technologies, which have been widely studied [5–8]. The IS cycle consists of three reactions, (1) the decomposition of H_2SO_4 into SO_2, O_2, and H_2O; (2) the decomposition of HI

H. Sun et al. (Eds.): WHTC 2023, SPPHY 393, pp. 370–382, 2024.
https://doi.org/10.1007/978-981-99-8631-6_36

into H_2 and I_2; and (3) the regeneration of HI and H_2SO_4 by the Bunsen reaction. The reaction of (1) recovered SO_2 and (2) recovered I_2 with H_2O to form HI and H_2SO_4 [9]. The IS cycle process showed in Fig. 1. The sulfuric acid (SA) decomposition reaction is a key process for coupling the IS cycle with a high-temperature heat source. The reaction needs to be carried out between 800 and 1000 °C. The SA decomposition process consists of a two-step reaction; first, SA decomposes to SO_3 and H_2O at about 400 °C; second, the SO_3 decomposes to SO_2 and O_2 above 800 °C. The first step reaction is fast and does not require a catalyst; the second step reaction is thermodynamically favorable, but the reaction rate is slow and requires a catalyst [10].

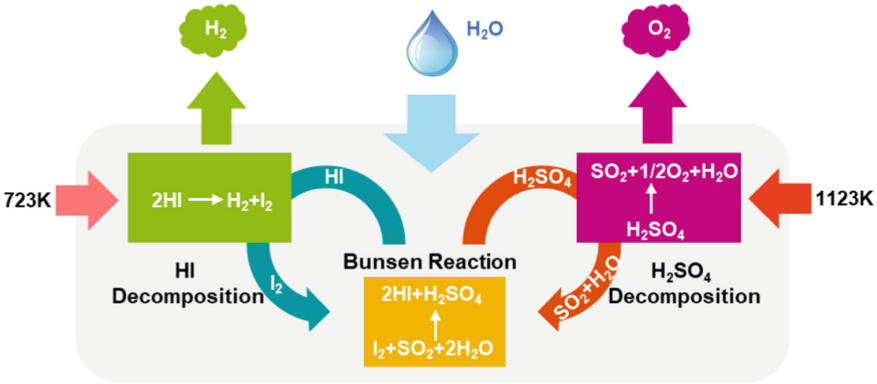

Fig. 1. The process of IS cycle

In addition to the IS cycle, other sulfur-containing cycles such as the mixed sulfur cycle and the bromine-sulfur cycle also contain SA decomposition reactions [11–13]. The SA decomposition process is a reaction that utilizes high-temperature heat in these cycles, and its energy consumption has a large impact on the overall process of hydrogen production efficiency. And the catalyst performance of the SO_3 decomposition process strongly affects the conversion rate and energy consumption. For this reason, a lot of research has been conducted on SO_3 decomposition catalysts, which are mainly divided into precious metal catalysts and oxide catalysts. Noble metals represented by Pt show excellent catalytic performance in SA decomposition reaction, and researchers have studied the SO_3 decomposition conversion rates of Pt, Pd, Rh, Ru, and Ir, and their activities are in the order of Pt > Pd > Rh > Ir > Ru [14]. Noble metal catalysts have good catalytic activity for SO_3 decomposition, but they are more expensive. For the consideration of economics and cost of hydrogen production under large-scale hydrogen production conditions, researchers have started to investigate non-precious metal catalysts. Non-precious metal catalysts mainly include oxides of Cr, Fe, Cu, Ce, V, Mn, Co, Zn, Al, etc., and studies have shown that the order of activity of various metal oxides is $Fe_2O_3 > V_2O_5 > CuO > MnO_2 > Cr_2O_3 > CeO_2 > CoO > ZnO > Al_2O_3$ [15]. These metal oxides are inexpensive but have an overall low catalytic activity. In order to further improve the conversion efficiency of oxide catalysts, researchers began to study composite metal oxides, and have explored the reaction activity of Fe/Al, Fe/Ti, Fe/Cu,

Fe/Cr, Cr/Cu, Cu/V, Ni/Fe, and other composite metal oxides [16–20]. The results show that these composite metal oxides can present high catalytic activity, some of them are even higher than the noble metal Pt, but their stability is generally poor. The reason is that during the long-time reaction process, the composite metal oxides decompose to generate monometallic oxides, and some even generate metal sulfates, which volatilize and agglomerate and thus lose catalytic activity. The catalysts for industrial applications need not only high catalytic activity but also good reaction stability to ensure the stable operation of industrial processes. All things considered, the development of catalysts for industrial applications ultimately requires the choice of noble metal catalysts. In order to reduce the price of noble metal catalysts and reduce the cost of hydrogen production, researchers loaded Pt on Al_2O_3, $BaSO_4$, SiC, and rutile phase TiO_2 carriers to study their reaction activity and stability, and the results showed that the carrier of Pt has an important influence on the activity and stability of the catalyst [21–25]. Because the catalysts are in a SA vapor environment, although Pt has good stability, the substrates are prone to sulfation and poisoning. Therefore, the carrier matrix loaded with Pt must be free from sulfation at high temperatures and have very good stability.

By testing different oxide carriers, researchers found that anatase TiO_2 and Ta_2O_5 have better stability at low temperatures (600 °C) but lower conversion efficiency [26, 27]. To effectively utilize the HTGR process heat for efficient hydrogen production, the SA decomposition process in the IS cycle needs to be carried out at about 850 °C, a temperature that ensures that the SA decomposition has a high decomposition efficiency and matches the exit temperature of the HTGR [28–30]. Second, the SA decomposition process is affected by various factors under the closed operation of the IS cycle, and the catalytic performance of the SA decomposition catalyst under different reaction conditions needs to be investigated. In addition, the long-term reaction stability of the catalyst is a prerequisite to ensure that the catalyst can be further applied, and the reaction lifetime of the catalyst needs to be tested. Based on this, a series of different SA decomposition catalysts were prepared with Pt-loaded anatase TiO_2 and Ta_2O_5, and their compositional analysis, structural characterization, and surface properties were investigated. The catalysts were tested for their SA decomposition performance at high temperatures, and suitable SA decomposition catalysts were selected. The selected catalysts were tested under different reaction conditions to comprehensively evaluate their reaction performance. Finally, the catalysts were scaled up for production and tested for long time stability life.

2 Materials and Methods

2.1 Preparation of Catalyst

The anatase TiO_2 (Ta_2O_5) was added to 1.0 wt% H_2PtCl_6 aqueous solution under stirring. After impregnation for 3 h, the suspension was dried by evaporation at 80 °C using a rotary evaporator. Then the dried samples were warmed up to 120 °C using an oven and kept for 4 h. The samples were then placed in a muffle furnace and calcined at 450 °C (650 °C, 850 °C) for 4 h. The obtained catalysts were named Pt/TiO_2-450, Pt/TiO_2-650, and Pt/TiO_2-850 (Pt/Ta_2O_5-450, Pt/Ta_2O_5-650, and Pt/Ta_2O_5-850).

2.2 Analytical Instruments

X-ray diffraction (XRD) was used for phase analysis of samples, the instrument model used was Rigaku D/MAX 2500H (Japan), and the scanning range was 10–90°. The specific surface area of the catalyst was analyzed by Quanta Autosorb-iQ (USA). The metallic platinum content of the catalysts was measured using an Agilent Technologies 8800 (USA). Scanning electron microscopy (SEM) was used to analyze the catalyst surface structure, and the instrument model used was Hitachi SU-8010 (Japan).

2.3 Catalytic Activity Test

The catalytic activity of the catalyst was evaluated in a fixed bed reactor. The catalyst was loaded in the middle of the quartz reaction tube and the tubular reactor was heated using an electric heater, the temperature of which was controlled by a thermocouple and a controller. The SA was pumped into the tubular reactor using a peristaltic pump, and the bottom part of the reactor was connected to a condenser and a tail gas absorption device. At the end of the reaction, the undecomposed SA solution at the bottom outlet of the condenser was collected and its concentration was measured, and then the SA decomposition conversion of the catalyst was calculated. The SA decomposition conversion is calculated by the following equation:

$$\eta = (1 - m_1 \times C_1 / m_0 \times C_0) \times 100\%$$

where m_1 and C_1 denote the mass and molar mass concentration of collected SA, and m_0 and C_0 denote the mass and molar mass concentration of concentrated SA entering the reactor.

3 Results and Discussion

3.1 Characterization of Catalysts

There is a relationship between the structure of the catalyst and the catalytic performance. In order to investigate the conformational relationship of Pt-loaded metal oxide catalysts, XRD analysis, specific surface area, and Pt content measurements were performed on the prepared catalysts to analyze their structures and compositions. Figure 2 shows the XRD spectra of the catalysts. The catalysts had distinctive diffraction peaks of anatase TiO_2 crystals and Ta_2O_5 crystals, and increasing the calcination temperature did not change the crystalline phase of the metal oxide carriers. The characteristic diffraction peaks of Pt crystals also appear in the catalysts. In the catalyst series of the same carrier, the increase of calcination temperature increases the intensity of the characteristic diffraction peaks of Pt crystals and promotes the crystallization of Pt nanoparticles. It is shown that the intensity of the characteristic diffraction peaks of Pt crystals on the catalysts with TiO_2 as the carrier is stronger than that of the catalysts with Ta_2O_5 as the carrier. It could be concluded from this that the high temperature is favorable for the crystallization of Pt nanoparticles, and the catalyst calcined at 850 °C has the best crystallinity of Pt nanoparticles. Compared with the carrier Ta_2O_5, the Pt nanoparticles loaded on TiO_2 have better crystallinity.

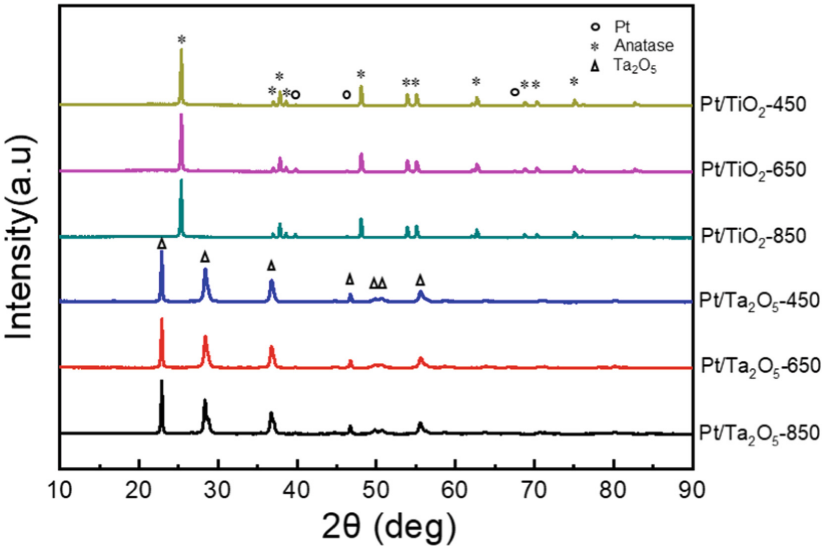

Fig. 2. XRD spectrum of the catalyst

Specific surface area and active component content are important properties of catalysts. Table 1 shows the specific surface area and Pt content of different catalysts. It could be seen that for the catalysts with the same carrier, the specific surface area of the catalysts gradually decreased and the Pt content gradually increased with the increase of calcination temperature. The reason could be that increasing the calcination temperature induces the Pt nanoparticles to migrate and fuse, and the small particles become large particles, thus decreasing the specific surface area of the catalyst [31]. In addition, high calcination temperature could make the impurities in the catalyst volatilize and increase the Pt content in the catalyst. The specific surface area and Pt content of Pt/TiO_2 series catalysts were higher than those of Pt/Ta_2O_5 series catalysts, which was possible because the specific surface area of Ta_2O_5 was smaller, which also resulted in less loading of Pt on Ta_2O_5 and the Pt content was lower. In general, the larger the specific surface area of the catalyst and the higher the content of active components, the higher its conversion efficiency [32]. Therefore, the reaction performance of Pt/TiO_2 series catalysts is better than that of Pt/Ta_2O_5 series catalysts. In order to verify the characterization results, the catalysts need to be tested for SA decomposition experiments to compare their catalytic performance.

3.2 Catalytic Activities of Catalysts

The catalysts have different conversion efficiency under different reaction conditions, therefore, the catalytic activity of the catalysts should be evaluated under various reaction conditions, including feed rate, feed concentration, reaction temperature, and catalyst particle size. Considering that the feed rate has a great influence on the catalytic performance of the catalysts, this study first carried out experiments at different weight hourly space velocities (WHSV) to screen out the catalysts with the best catalytic performance

Table 1. The specific surface area and Pt content of catalysts

Catalysts	BET surface area (m^2/g)	Pt content (μg/g)
Pt/TiO_2-450	13.144	6724
Pt/TiO_2-650	11.779	8013
Pt/TiO_2-850	11.227	9561
Pt/Ta_2O_5-450	6.295	4013
Pt/Ta_2O_5-650	6.339	7003
Pt/Ta_2O_5-850	4.503	7253

for SA decomposition and then tested the performance of the screened catalysts under the reaction conditions of feed concentration, reaction temperature, and particle diameter to comprehensively evaluate the catalytic activity.

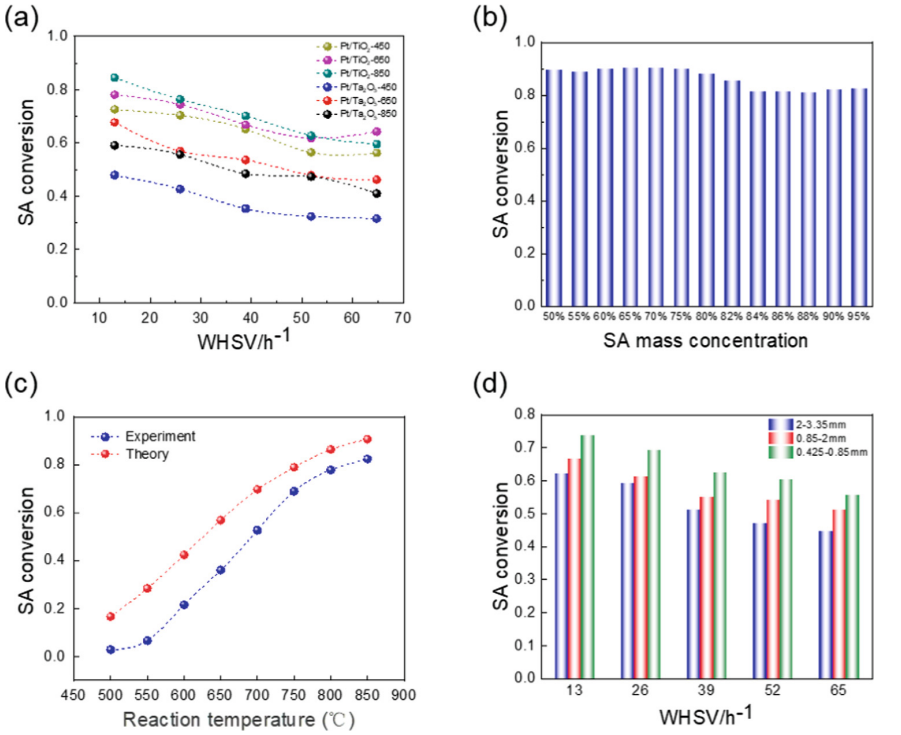

Fig. 3. (a) The conversion efficiency of catalysts at different WHSV. (b) The conversion efficiency of Pt/TiO_2-850 under different feed concentrations. (c) The conversion efficiency of Pt/TiO_2-850 at different temperatures. (d) The conversion efficiency of Pt/TiO_2-850 with different particle diameters.

The catalytic activity of catalysts at different weight hourly space velocities. In order to screen the best catalytic performance of the SA decomposition catalyst, the decomposition efficiency of the catalyst was tested at different WHSV at 850 °C. The results are shown in Fig. 3(a), where the decomposition efficiency of the catalyst gradually decreases as the SA feed rate increases. The faster the feed rate, the shorter the time for SO_3 to contact the catalyst, thus causing the decomposition efficiency of the catalyst to decrease. When the WHSV is 13 h^{-1}, the conversion efficiency of the catalyst is the highest. The conversion efficiency of the Pt/TiO_2 series catalyst was higher than that of the Pt/Ta_2O_5 series catalyst, which was consistent with the results of the specific surface area and Pt content analysis. The Pt/TiO_2-850 catalyst had the highest overall SA decomposition efficiency. The reason could be that the high calcination temperature induced the reduction of PtO_x in the catalyst to the active component Pt atoms, thus improving the catalytic performance of Pt/TiO_2. Although the specific surface area of the Pt/TiO_2-850 catalyst was the smallest, the crystallinity and content of Pt nanoparticles in the Pt/TiO_2-850 catalyst were the highest, indicating that the crystallinity and content of Pt nanoparticles had more influence on the catalytic performance than the specific surface area.

The catalytic activity of Pt/TiO_2-850 at different feed concentrations. The SA decomposition experiments at different WHSV determined that the Pt/TiO_2-850 catalyst has the highest conversion efficiency. During the experiment, 98%wt concentrated SA was used, and the feed concentration of the SA decomposition unit during the IS cycle was difficult to reach 98%wt. Even if the SA feed concentration could reach 98%wt, it would consume a lot of heat and increase the economic cost of the process. Therefore, it is necessary to explore the conversion efficiency of the catalyst under low concentration SA feed conditions. Based on this, different concentrations of SA were prepared in this study, and Pt/TiO_2-850 catalyst was selected as the object of study to test the effect of SA feed concentration on the catalytic performance of the catalyst under the reaction conditions at a temperature of 850 °C and a WHSV of 13 h^{-1}, and the results are shown in Fig. 3(b). When the SA feed concentration was between 50%wt and 75%wt, the conversion efficiency of Pt/TiO_2-850 was around 90%; when the SA feed concentration was higher than 75%wt, the conversion efficiency of Pt/TiO_2-850 started to decrease, and finally stabilized at around 80%. According to the experimental results, the SA decomposition using this catalyst during the IS cycle could concentrate the SA generated from the Bunsen reaction to 80% wt. This can ensure the catalyst has high conversion efficiency and reduce the heat of concentrated SA, thus reducing the heat consumption of the whole process.

The catalytic activity of Pt/TiO_2-850 at different temperatures. The IS cycle eventually needs to be coupled with a HTGR to heat the SA decomposition process using high-temperature helium. Compared with electric furnace heating, high-temperature helium heating would cause heating instability problems and does not ensure that the catalyst bed temperature is always maintained at 850 °C. Therefore, the effect of heating temperature on the catalytic performance of Pt/TiO_2-850 is required to be investigated. The temperature range of 500–850 °C was selected to test the SA decomposition conversion of Pt/TiO_2-850 catalyst, and the experimental results were compared with the

theoretical equilibrium conversion of the SA decomposition reaction, and the results are shown in Fig. 3(c) [33]. As the temperature increases, the conversion efficiency of the catalyst increases gradually, which is consistent with the fact that SA decomposition is a thermally absorbing reaction. In the temperature range of 750–850 °C, the difference between the conversion rate of the catalyst and the equilibrium conversion rate is around 10%; when the temperature is lower than 750 °C, the difference between the conversion rate of the catalyst and the equilibrium conversion rate is around 20%, and the high temperature is favorable to the Pt/TiO_2-850-catalyzed SA decomposition reaction. In order to ensure the SA decomposition with high conversion efficiency ($\geq$70%), it is necessary to ensure at least the SA decomposition catalyst bed temperature above 750 °C.

The catalytic activity of Pt/TiO_2-850 with different particle sizes. In addition to feeding concentration and temperature, catalyst particle size is also an important factor affecting conversion efficiency. In the previous experiments, the catalyst particle sizes of 0.25–0.425 mm (40–60 mesh) were used. In order to investigate the effect of particle size on the conversion efficiency, three different Pt/TiO_2-850 catalyst particles were prepared in the experiment, their particle sizes were respectively 0.425–0.85 mm (20–40 mesh), 0.85–2 mm (10–20 mesh) and 2–3.35 mm (6–10 mesh). The conversion efficiencies of the catalysts with different particle sizes at different WHSV were experimentally investigated, and the results are shown in Fig. 3(d). With the particle size increasing, the conversion efficiency of Pt/TiO_2-850 decreased gradually, and the conversion efficiency of 0.25–0.425 mm particles was the highest. The larger the catalyst particle size, the lower the stacking density of the catalyst bed. Part of the SO_3 gas passed through the catalyst bed without decomposition, resulting in lower decomposition efficiency. However, if the particle size of the catalyst is too small, the pressure drop of the catalyst bed would be too large, which would increase the operating cost of the equipment and be detrimental to the subsequent scale-up of the process. Therefore, 0.25–0.425 mm was finally chosen as the catalyst particle diameter used for the reaction.

3.3 Scale-Up Production and Stability Study of Pt/TiO_2-850

Previous studies have tested the SA decomposition efficiency of Pt/TiO_2-850 catalysts under different reaction conditions and confirmed that Pt/TiO_2-850 catalysts have excellent catalytic performance. However, in order to apply the catalyst to real industrial production, it is equally important that the catalysts can be produced in batch scale-up and have good stability in addition to having excellent catalytic performance. Based on this, in this study, Pt/TiO_2-850 catalysts were batch-scaled up to obtain catalysts in the order of kilograms. The scale-up produced catalysts were tested for SA decomposition experiments under different WHSV and temperature, and the results were compared with the catalysts prepared in the laboratory, and the comparison results are shown in Fig. 4(a) and (b). The scaled-up produced Pt/TiO_2-850 catalysts also have high conversion efficiency, and the scaled-up production process does not have a great impact on the reaction performance.

The above researches confirmed the good reaction performance of the scaled-up produced Pt/TiO_2-850 catalyst, and then the stability of Pt/TiO_2-850 catalyst was explored. The stability test was carried out on the IS-100 device previously built by the research

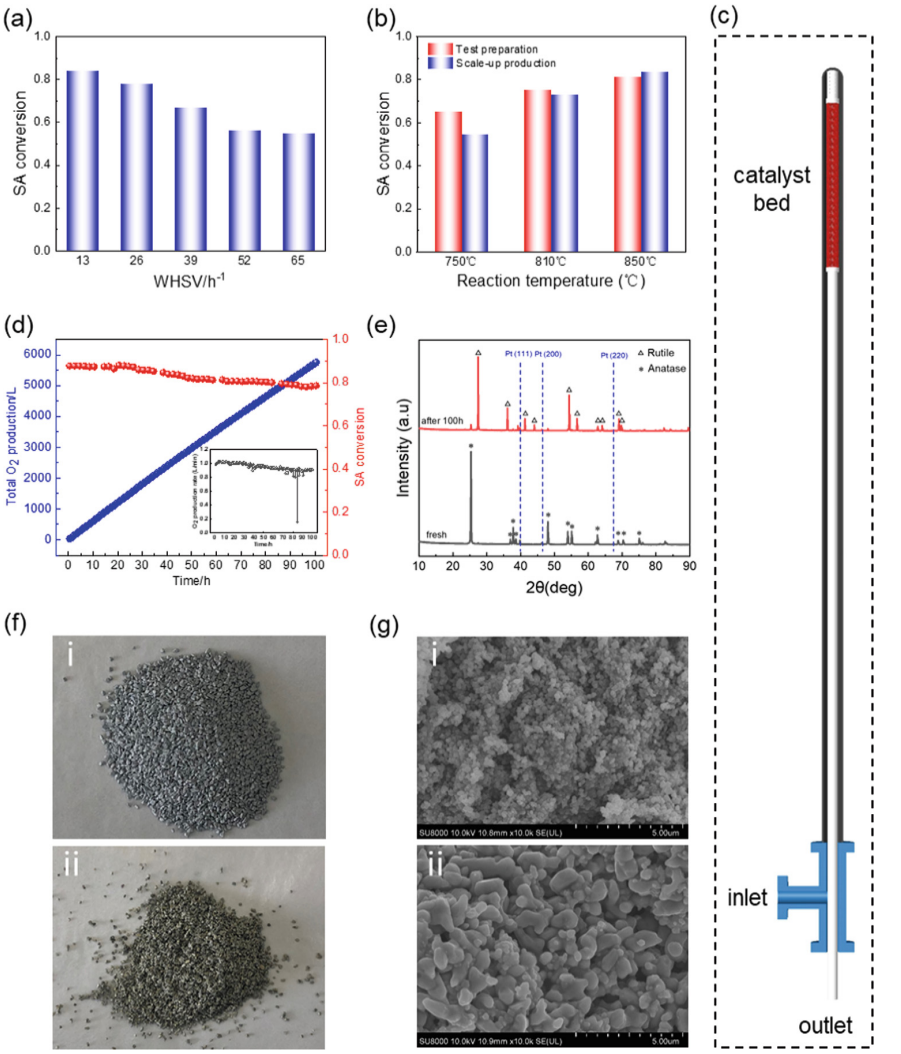

Fig. 4. (a) The conversion efficiency of scaled-up Pt/TiO_2-850 at different WHSV. (b) The conversion efficiency of scaled-up Pt/TiO_2-850 at different temperatures. (c) The schematic diagram of bayonet tube SA reactor. (d) SA decomposition conversion rate, instantaneous O_2 production flow and cumulative production in 100 h. (e) The XRD spectra of Pt/TiO_2-850 before and after 100 h reaction. (f) i The fresh Pt/TiO_2-850, ii The reacted Pt/TiO_2-850. (g) i The SEM image of fresh Pt/TiO_2-850, ii The SEM image of reacted Pt/TiO_2-850.

group. The SA decomposition reactor used a bayonet-tube reactor, and its structure is shown in Fig. 4(c). Compared with general fixed-bed reactors, the bayonet-tube reactor enables heat recovery of the reaction products and improve the process heat utilization efficiency. The material of the reactor is SiC, an industrial material with high hardness,

high heat transfer coefficient, and resistance to SA corrosion [34, 35]. Previous simulation studies have shown that bayonet-tube reactor can better utilize heat and improve the conversion efficiency of SA decomposition reactions [29]. A 100 h SA decomposition experiment was carried out in the bayonet tube SiC reactor to test the stability of the Pt/TiO_2-850 catalyst. The instantaneous and cumulative flow rates of O_2 were recorded by a mass flow meter during the reaction. The results are shown in Fig. 4(d). The reaction produced 5726 L O_2 for 100 h, which is higher than the initial target of 5000 L. The average conversion rate of the Pt/TiO_2-850 catalyst was 82.6%, and the O_2 instantaneous flow rate was maintained at about 0.95 L/min. The initial conversion efficiency of Pt/TiO_2-850 reached 87.7%, which was higher than that of the quartz fixed-bed reactor. Although the conversion efficiency of the catalyst decreased with increasing reaction time, the catalytic performance showed a stable trend in the later stage of the reaction, and the conversion efficiency of the catalyst remained stable at about 78.6% at the end of the reaction. Compared with the Pt/SiC, $CuCr_2O_4$, and $CuFe_2O_4$ SA decomposition catalysts previously studied in the laboratory, Pt/TiO_2-850 showed good stability. Combined with its excellent catalytic performance and easy scale-up production, Pt/TiO_2-850 can be used as a SA decomposition catalyst for the pilot scale-up of the IS cycle.

The SA decomposition reaction is in a high-temperature, strongly acidic environment, which is a great challenge to the stability of the catalyst. The Pt/TiO_2-850 catalyst still maintains high catalytic performance after 100 h of high-temperature SA decomposition reaction. Investigating the structural changes of Pt/TiO_2-850 catalysts before and after the reaction and understanding their conformational relationships are important guidelines for the design and development of high-performance and low-cost industrial catalysts for SA decomposition. Based on this, the specific surface area and metal Pt content of the SA decomposition catalysts were tested after 100 h of reaction in this study. After 100 h of reaction, the specific surface area of Pt/TiO_2-850 catalyst was 8.333 m^2/g, and the Pt content was 5650 $\mu g/g$. Compared with that before the reaction, the specific surface area and Pt content of the catalyst decreased. To further investigate the changes of Pt/TiO_2-850 catalyst before and after the reaction, XRD and SEM characterization were performed and the results were compared with the fresh catalysts as shown in Fig. 4(e)–(g). After a 100 h high-temperature SA decomposition reaction, the carrier of the catalyst changed from the anatase phase to the rutile phase. Macroscopically, the catalyst changed from gray particles to yellow-brown particles without any obvious change in particle size. Microscopically, the catalyst was agglomerated from uniform nanoparticle size to larger irregularly shaped particles, which indicated that the catalyst had appeared "sintering" phenomenon, and this result was consistent with the specific surface area. Although the "sintering" of the catalyst occurred after the reaction, the conversion efficiency of Pt/TiO_2-850 did not decrease significantly. The stability of Pt/TiO_2 is better than that of other Pt-loaded catalysts with carriers such as Al_2O_3, SiC, SiO_2, and $BaSO_4$. The reasons for this could be: (1) TiO_2 has good acid resistance and would not be dissolved by SA; (2) Pt and TiO_2 have strong metal-carrier interactions at high temperatures, and the carrier TiO_2 would encapsulate the Pt nanoparticles to prevent Pt loss and "sintering" [36]. These factors ensure the stability of Pt/TiO_2. In addition, the comparison of the catalysts before and after the reaction shows that the change in the crystalline structure of the carrier and the decrease in the specific surface area and

Pt content during the reaction do not cause the deactivation of the Pt/TiO_2-850 catalyst, which provides a direction for the subsequent Pt-loaded SA decomposition catalysts.

4 Conclusion

In this study, a series of SA decomposition catalysts were prepared using anatase TiO_2 and Ta_2O_5 as carriers and precious metal Pt as the active component. All catalysts exhibited SA decomposition catalytic performance at 850 °C. Among the many catalysts, Pt/TiO_2-850 catalyst had the highest reactivity and its conversion efficiency reached up to 84%. It was demonstrated that the Pt/TiO_2-850 catalysts had good catalytic activity under different reaction conditions. Furthermore, the scaled-up production of Pt/TiO_2-850 catalysts does not affect the catalytic performance. The Pt/TiO_2-850 catalyst was tested in a bayonet-tubular SiC reactor with a high throughput lifetime of 100 h. Its conversion efficiency still reached 78.6% at the end of the reaction, which proved that the Pt/TiO_2-850 catalyst has good stability. This work researched a SA decomposition catalyst with high reaction performance, easy to scale-up production, and good stability, which laid a solid foundation for the industrial application of SA decomposition catalyst.

References

1. Kovač, A., Paranos, M., Marciuš, D.: Hydrogen in energy transition: a review. Int. J. Hydrogen Energy **46**, 10016–10035 (2021)
2. Okolie, J.A., Patra, B.R., Mukherjee, A., Nanda, S., Dalai, A.K., Kozinski, J.A.: Futuristic applications of hydrogen in energy, biorefining, aerospace, pharmaceuticals and metallurgy. Int. J. Hydrogen Energy **46**, 8885–8905 (2021)
3. Hou, P., Zhou, Y., Guo, W., Ren, P., Guo, Q., Xiang, H., et al.: Rational design of hydrogen-donor solvents for direct coal liquefaction. Energy Fuels **32**, 4715–4723 (2018)
4. Fan, L., Tu, Z., Chan, S.H.: Recent development of hydrogen and fuel cell technologies: a review. Energy Rep. **7**, 8421–8446 (2021)
5. Ping, Z., Laijun, W., Songzhe, C., Jingming, X.: Progress of nuclear hydrogen production through the iodine–sulfur process in China. Renew. Sustain. Energy Rev. **81**, 1802–1812 (2018)
6. Zhang, P., Xu, J., Shi, L., Zhang, Z.: Nuclear hydrogen production based on high temperature gas cooled reactor in China. Strateg. Study Chinese Acad. Eng. **21**, 20–28 (2019)
7. Gabriel, K.S., El-Emam, R.S., Zamfirescu, C.: Technoeconomics of large-scale clean hydrogen production—a review. Int. J. Hydrogen Energy (2021)
8. Pinsky, R., Sabharwall, P., Hartvigsen, J., O'Brien, J.: Comparative review of hydrogen production technologies for nuclear hybrid energy systems. Prog. Nucl. EnergyNucl. Energy **123**, 103317 (2020)
9. Dehghani, S., Sayyaadi, H.: Energy and exergetic evaluations of Bunsen section of the sulfur–iodine thermochemical hydrogen production plant. Int. J. Hydrogen Energy **38**, 9074–9084 (2013)
10. Huang, C., Ali, T.: Analysis of sulfur–iodine thermochemical cycle for solar hydrogen production. Part I: decomposition of sulfuric acid. Sol. Energy **78**, 632–646 (2005)
11. Tebibel, H., Medjebour, R.: Comparative performance analysis of a grid connected PV system for hydrogen production using PEM water, methanol and hybrid sulfur electrolysis. Int. J. Hydrogen Energy **43**, 3482–3498 (2018)

12. Beghi, G.: A decade of research on thermochemical hydrogen at the Joint Research Centre-Ispra. Hydrogen Systems, pp. 153–171. Elsevier (1986)
13. Pen, M., Gomez, J., Fierro, J.L.G.: New catalytic routes for syngas and hydrogen production. Appl. Catal. A: Gen. **144**, 7–57 (1996)
14. Rashkeev, S.N., Ginosar, D.M., Petkovic, L.M., Farrell, H.H.: Catalytic activity of supported metal particles for sulfuric acid decomposition reaction. Catal. Today. Today **139**, 291–298 (2009)
15. Ishikawa, H., Ishii, E., Uehara, I., Nakane, M.: Catalyzed thermal decomposition of H_2SO_4 and production of HBr by the reaction of SO_2 with Br_2 and H_2O. Int. J. Hydrogen Energy **7**, 237–246 (1982)
16. Kim, T.H., Gong, G.T., Lee, B.G., Lee, K.Y., Jeon, H.Y., Shin, C.H., et al.: Catalytic decomposition of sulfur trioxide on the binary metal oxide catalysts of Fe/Al and Fe/Ti. Appl. Catal. ACatal. A **305**, 39–45 (2006)
17. Ping, Z., Bo, Y., Lei, Z.: Mechanism of oxygen releasing of copper ferrite in the formation of the corresponding oxygen-deficient compound. Sci. China Chem. **101** (2009)
18. Bo, Y.U., Zhang, P., Zhang, L., Chen, J., Xu, J.: Studies on the preparation of active oxygen-deficient copper ferrite and its application for hydrogen production through thermal chemical water splitting. 中国科学: 化学英文版 **9** (2008)
19. Banerjee, A.M., Pai, M.R., Bhattacharya, K., Tripathi, A.K., Kamble, V.S., Bharadwaj, S.R., et al.: Catalytic decomposition of sulfuric acid on mixed Cr/Fe oxide samples and its application in sulfur–iodine cycle for hydrogen production. Int. J. Hydrogen Energy **33**, 319–326 (2008)
20. Abimanyu, H., Jung, K.D., Jun, K.W., Kim, J., Yoo, K.S.: Preparation and characterization of Fe/Cu/Al_2O_3-composite granules for SO_3 decomposition to assist hydrogen production. Appl. Catal. ACatal. A **343**, 134–141 (2008)
21. Banerjee, A., Pai, M., Tewari, R., Raje, N., Tripathi, A., Bharadwaj, S., et al.: A comprehensive study on Pt/Al_2O_3 granular catalyst used for sulfuric acid decomposition step in sulfur–iodine thermochemical cycle: changes in catalyst structure, morphology and metal-support interaction. Appl. Catal. BCatal. B **162**, 327–337 (2015)
22. Nagaraja, B.M., Jung, K.D., Ahn, B.S., Abimanyu, H., Yoo, K.S.: Catalytic decomposition of SO_3 over Pt/$BaSO_4$ materials in sulfur−iodine cycle for hydrogen production. Ind. Eng. Chem. Res. **48**, 1451–1457 (2009)
23. Lee, S.Y., Jung, H., Kim, W.J., Shul, Y.G., Jung, K.-D.: Sulfuric acid decomposition on Pt/SiC-coated-alumina catalysts for SI cycle hydrogen production. Int. J. Hydrogen Energy **38**, 6205–6209 (2013)
24. Noh, S.-C., Lee, S.Y., Shul, Y.G., Jung, K.-D.: Sulfuric acid decomposition on the Pt/n-SiC catalyst for SI cycle to produce hydrogen. Int. J. Hydrogen Energy **39**, 4181–4188 (2014)
25. Petkovic, L., Ginosar, D., Rollins, H., Burch, K., Pinhero, P., Farrell, H.: Pt/TiO_2 (rutile) catalysts for sulfuric acid decomposition in sulfur-based thermochemical water-splitting cycles. Appl. Catal. ACatal. A **338**, 27–36 (2008)
26. Nur, A.S., Matsukawa, T., Hinokuma, S., Machida, M.: Catalytic SO_3 decomposition activity and stability of Pt supported on anatase TiO_2 for solar thermochemical water-splitting cycles. ACS Omega **2**, 7057–7065 (2017)
27. Nur, A.S., Matsukawa, T., Funada, E., Hinokuma, S., Machida, M.: Platinum supported on Ta_2O_5 as a stable SO_3 decomposition catalyst for solar thermochemical water splitting cycles. ACS Appl. Energy Mater. **1**, 744–750 (2018)
28. Gao, Q., Sun, Q., Zhang, P., Peng, W., Chen, S.: Sulfuric acid decomposition in the iodine–sulfur cycle using heat from a very high temperature gas-cooled reactor. Int. J. Hydrogen Energy **46**, 28969–28979 (2021)

29. Sun, Q., Gao, Q., Zhang, P., Peng, W., Chen, S.: Modeling sulfuric acid decomposition in a bayonet heat exchanger in the iodine-sulfur cycle for hydrogen production. Appl. Energy **277**, 115611 (2020)
30. Sun, Q., Gao, Q., Zhang, P., Peng, W., Chen, S., Zhao, G., et al.: Numerical study of heat transfer and sulfuric acid decomposition in the process of hydrogen production. Int. J. Energy Res. **43**, 5969–5982 (2019)
31. Kim, S.S., Hong, S.C.: Relationship between the surface characteristics of Pt catalyst and catalytic performance on the H2 SCR. J. Ind. Eng. Chem. **16**, 992–996 (2010)
32. Somorjai, G.A., Li, Y.: Introduction to Surface Chemistry and Catalysis. Wiley (2010)
33. Schwartz, D., Gadiou, R., Brilhac, J.-F., Prado, G., Martinez, G.: A kinetic study of the decomposition of spent sulfuric acids at high temperature. Ind. Eng. Chem. Res. **39**, 2183–2189 (2000)
34. Takeuchi, Y., Park, C., Noborio, K., Yamamoto, Y., Konishi, S.: Heat transfer in SiC compact heat exchanger. Fusion Eng. Des. **85**, 1266–1270 (2010)
35. Wang, Z., Liu, Y., Zhang, H., Jiang, J., Lin, T., Liu, X., et al.: Joining of SiC ceramics using the Ni-Mo filler alloy for heat exchanger applications. J. Eur. Ceram. Soc. **41**, 7533–7542 (2021)
36. Khan, H.A., Kim, S., Jung, K.-D.: Origin of high stability of Pt/anatase-TiO_2 catalyst in sulfuric acid decomposition for SI cycle to produce hydrogen. Catal. Today. Today **352**, 316–322 (2020)

Modeling and Simulation of PEMFC Supply System with Oxygen and Air Mixing

Guangyao Tong[1], Fengxiang Chen[1(✉)], Tao Li[2], Shuo Xu[2], Wei Shen[3], and Su Zhou[1]

[1] School of Automotive Studies, Tongji University, Shanghai, China
fxchen@tongji.edu.cn
[2] Spintrol Technology (Shenzhen) Co., Ltd., Shanghai, Guangdong, China
[3] Shanghai TXJS Engineering Technology Co., Ltd., Shanghai, China

Abstract. With the growing energy crisis and environmental problems in recent years, the green energy technology represented by fuel cell technology has been developing rapidly. Since air contains a large amount of nitrogen that does not participate in the reaction, the circulation of nitrogen in the cathode gas supply system will increase the power consumption of the air compressor, resulting in a lower net power output of the fuel cell system. In order to improve the output performance of the fuel cell system, a new fuel cell cathode gas supply system with oxygen and air mixing is proposed in this paper, and the research results show that this topology can effectively increase the output power of the stack and reduce the power consumption of the air compressor, which can eventually increase the net power of the system to more than 10%. This study provides an effective theoretical guide for the design of fuel cell system and the optimal matching of cathode gas supply system.

Keywords: PEMFC · Cathode gas supply system · Structural optimization

1 Introduction

In recent years, hydrogen energy with high energy density and no pollution has gradually become an object of interest for researchers in various countries due to the increasingly severe problems of global warming and oil scarcity. Proton exchange membrane fuel cell (PEMFC) is an ideal power source for electric vehicles and household distributed power generation devices because of its fast start-up at conventional temperature, high efficiency (40–60%) and ability to quickly adjust output power according to power demand [1, 2]. With the application of electrolytic water for hydrogen production, it also results in a large amount of oxygen not being fully utilised. If this oxygen could be utilised, it would effectively improve the efficiency of distributed power generation units.

Based on the above ideas, the topology of a new fuel cell cathode gas supply system with oxygen and air mixing is proposed in this paper, and a simulation platform is built to study it.

H. Sun et al. (Eds.): WHTC 2023, SPPHY 393, pp. 383–389, 2024.
https://doi.org/10.1007/978-981-99-8631-6_37

2 Structure and System Model Building

2.1 Introduction of Topology of Cathode Gas Supply System

The topology of the new fuel cell cathode gas supply system with oxygen and air mixing proposed in this paper are shown in Fig. 1. Compared with the conventional air supply systems, this topology mixes the oxygen supplied by the oxygen source with the gas in the mixing cavity to a preset oxygen concentration and feeds it to the stack via ejector. The gas in the mixing cavity is a mixture of saturated water vapor discharged from the stack and dry air fed by an air compressor. At the same time the humidity of the gas is controlled by the air compressor.

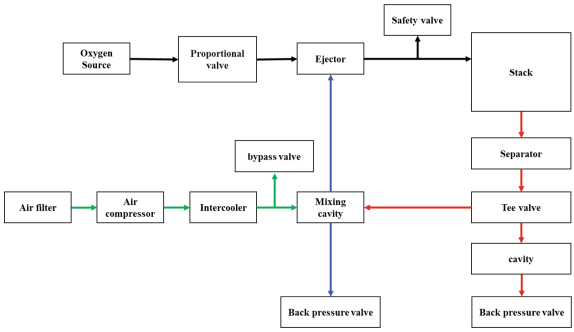

Fig. 1. The topology of the new fuel cell cathode gas supply system with oxygen and air mixing

2.2 Voltage Model of the PEMFC

The voltage model is based on the operating conditions of the stack and the cell voltage V_{cell} is calculated from the Nernst voltage E, activation loss η_{act}, ohmic loss η_{ohm} and concentration loss η_{conc} respectively, as shown in the following equations [3]:

$$V_{cell} = E - \eta_{act} - \eta_{ohm} - \eta_{conc} \tag{1}$$

The Nernst voltage can be expressed as follows [4]:

$$E = 1.229 - 2.302 \times 10^{-4}(T^{st} - 298.15) + 4.308 \times 10^{-5} T^{st} \ln\left(\left(p_{O_2}\right)^{\frac{1}{2}} p_{H_2}\right) \tag{2}$$

where T^{st} is the temperature of the stack, p_{O_2} is the partial pressure of oxygen at the cathode and p_{H_2} is the partial pressure of hydrogen at the anode.

The η_{act} is obtained by solving the following simplified Tafel equation:

$$\eta_{act} = \frac{RT^{st}}{2\alpha F} \ln\left(\frac{j}{j^0}\right) \tag{3}$$

where j is the current density and j^0 is the reference current density.

The η_{ohm} due to the resistance to proton transport within the proton exchange membrane can therefore be expressed as [5]:

$$\eta_{ohm} = j \times ASR \tag{4}$$

where ASR is the surface resistance, which depends mainly on the thickness of the film δ_{mem} and its conductivity σ_{mem}.

The η_{conc} caused by the consumption of reactants in the catalytic layer is expressed as follow [4]:

$$\eta_{conc} = \frac{RT^{st}}{2\alpha F} \ln\left(\frac{c^0_{O_2}}{c^{st\_cgdl}_{O_2}}\right) \tag{5}$$

where $c^0_{O_2}$ is the reference oxygen concentration within the catalytic layer.

2.3 Modeling the Gas Situation in the Stack

The molar flow rate of each component gas $\dot{n}_{x_2}$ ($x_2 = \{O_2, H_2, N_2\}$) in the stack can be obtained according to the mass conservation equation as follows:

$$\dot{n}^{ca/an}_{x_2} = \dot{n}^{ca/an\_i}_{x_2} - \dot{n}^{ca/an\_e}_{x_2} - \dot{n}^{ca/an\_react}_{x_2} \tag{6}$$

Part of the gas entering the stack is consumed by the electrochemical reaction and the flow rate can be expressed as:

$$\dot{n}^{react\_ca/an}_{x_2} = \begin{cases} \frac{n_{cell} I^{st}}{nF} & x_2 = \{H_2, O_2\} \\ 0 & x_2 = \{N_2\} \end{cases} \tag{7}$$

where n_{cell} is the number of cells, I^{st} is the output current, n is the number of participating electrons, and F is Faraday constant.

According to the mass conservation equation can be obtained separately from the cathode and anode within the molar flow of gaseous water:

$$\dot{n}^{ca}_{H_2O} = \dot{n}^{ca\_i}_{H_2O} - \dot{n}^{ca\_e}_{H_2O} + \dot{n}^{ca\_react}_{H_2O} - \dot{n}^{ca\_e}_{H_2O(l)} \tag{8}$$

$$\dot{n}^{an}_{H_2O} = \dot{n}^{an\_i}_{H_2O} - \dot{n}^{an\_e}_{H_2O} - \dot{n}^{an\_e}_{H_2O(l)} \tag{9}$$

The flow rate of liquid water at the cathode and anode is:

$$\dot{n}^{ca/an\_e}_{H_2O(l)} = \dot{n}^{ca/an\_e}_{H_2O} \times \frac{p^{ca/an}_{H_2O(l)}}{p^{ca/an}_{H_2O}} \tag{10}$$

where $p^{st\_ca}_{H_2O(l)}$ is the equivalent pressure under the same temperature conditions assuming that all liquid water in the cathode flow channel is converted to water vapor.

The channel pressure model uses a general gas cavity model with molar flow as input and pressure as output. The component pressures are calculated as shown below:

$$p_{x_2}^{ca/an} = \frac{\left(\int_0^t \dot{n}_{x_2}^{ca/an} d\tau\right) \times R \times T^{st}}{V^{st\_ca}} \tag{11}$$

Assuming that the water vapor in the channel reaches the saturation vapor pressure, the subsequent generation of water is all liquid water, water vapor partial pressure and the equivalent pressure of liquid water all converted to water vapor is shown below:

$$p_{\mathrm{H_2O}}^{ca/an} = \min\left(\frac{\left(\int_0^t \dot{n}_{\mathrm{H_2O}}^{ca/an} d\tau\right) \times R \times T^{st}}{V^{ca/an}}, p_{sat}\left(T^{st}\right)\right) \tag{12}$$

$$p_{\mathrm{H_2O}(l)}^{ca/an} = \frac{\left(\int_0^t \dot{n}_{\mathrm{H_2O}}^{ca/an} d\tau\right) \times R \times T^{st}}{V^{st\_ca/an}} - p_{\mathrm{H_2O}}^{ca/an} \tag{13}$$

The total pressure in the cathode and anode are shown below:

$$p_{total}^{ca} = p_{\mathrm{O_2}}^{ca} + p_{\mathrm{N_2}}^{ca} + p_{\mathrm{H_2O}}^{ca} \tag{14}$$

$$p_{total}^{an} = p_{\mathrm{H_2}}^{an} + p_{\mathrm{H_2O}}^{an} \tag{15}$$

3 Results and Discussion

In this work, a stack rated at 75 kW in the conventional topology was chosen as the object of simulation analysis, and its main parameters are shown specifically in Table 1. On the other hand, in the new topology, the oxygen concentration $\eta_{\mathrm{in}} = 40\%$, the lead ratio $\mu = 2.86$ and the opening of the electron tee $\theta = 0.2$.

3.1 Comparative Performance Analysis of New Topologies

Figure 2 shows that the new topology can effectively increase the output power of the stack because the increase in oxygen partial voltage effectively increases the Nernst voltage, reduces the activation loss and concentration loss, which ultimately increases the output power of the fuel cell. At the same time, as the current increases, the concentration loss is further reduced and the net power of the system is further increased. Overall, the increase is above 10% when the stack is at high current output. Figure 2(b) shows that the power consumption of the compressor in the new topology is reduced by nearly 50% compared to the conventional topology.

Table 1. Characteristic parameters of the stack

Parameters	Value
Quality of the stack	70 kg
Number of single cells	300
Rated current	412.5 A
Rated voltage	0.61 V
Rated power	75 kW
Oxygen excess ratio of the cathode at the rated point	1.8

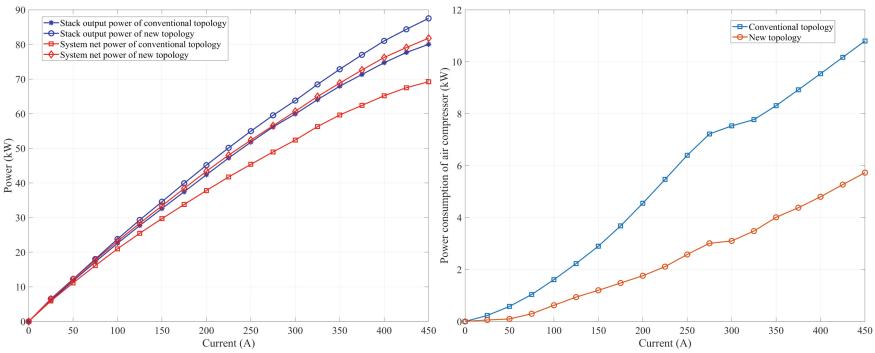

(a) Net power and Output power of stack (b) Power consumption of air compressor

Fig. 2. The characteristic curves of the two topologies

3.2 The Analysis of System Performance at Different Oxygen Excess Ratios

Figure 3 shows the variation of stack output power and system net power with Oxygen excess ratio λ, when $\eta_{\text{in}} = 40\%$, $I = 300\,A$, the output power of the stack increases as λ increases, but the growth rate gradually decreases. Meanwhile, the consumption of the air compressor increases with the increase of λ. This leads to the decrease of the net power of the system from $\lambda = 2.0$, and the molar fraction of oxygen η_{out} at cathode outlet is greater than 21%, the phenomenon of oxygen wastage occurs.

3.3 The Analysis of System Performance at Different Molar Fraction of Oxygen at the Cathode Inlet

Figure 4(a) shows the variation of stack output power and net power of system with different η_{in}, when $\lambda = 2.0$, $I = 300\,A$, as the η_{in} increases, the power consumption of the compressor decreases proportionally, and the net power growth rate of the system eventually decreases due to the decrease in the power growth rate of the stack output. Figure 4(b) shows that when the $\eta_{\text{in}} \geq 40\%$, the phenomenon of oxygen wastage occurs.

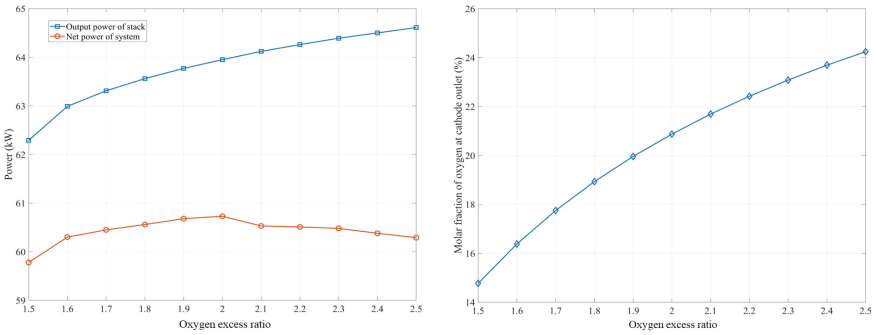

(a) Net power and Output power of stack (b) The molar fraction of O_2 at cathode outlet

Fig. 3. The characteristic curves at different oxygen excess ratio

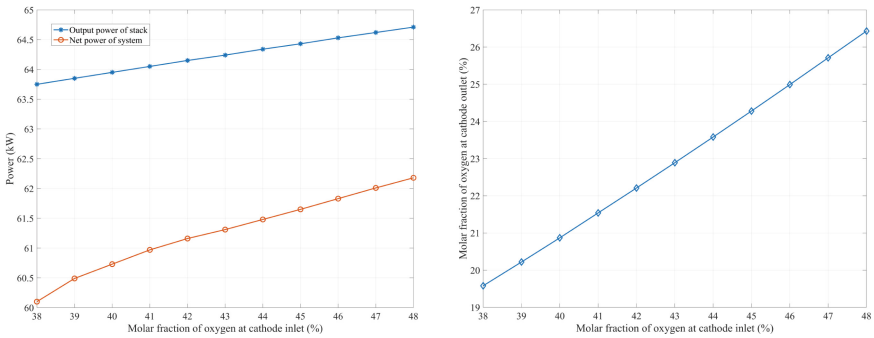

(a) Net power and Output power of stack (b) The molar fraction of O_2 at cathode outlet

Fig. 4. The characteristic curves at different oxygen concentration

4 Conclusion

In this work, a new fuel cell cathode gas supply system is proposed and mathematically modeled for study. Simulation and theoretical analysis show that this topology can effectively increase the output power of the stack and reduce the power consumption of the air compressor, which can eventually increase the net power of the system up to more than 10%. This provides a solid theoretical basis and guiding direction for fuel cell system performance optimization research and design development.

Acknowledgement. This study was supported by the National Natural Science Foundation of China under Grant U21A20166 and Science and Technology Planning Project of Ningbo under Grant 2022Z065.

References

1. Gong, D., Xu, S., Zhang, B.: Control strategies for prevention of PEMFC oxygen starvation: a review. SAE WCX Digital Summit (2021)
2. Barbir, F.: PEM Fuel Cells: Theory and Practice, 2nd ed., pp. 26–36. Elsevier, Amsterdam (2005)
3. Jiao, J., Chen, F., Yang, Y., et al.: Modeling and simulation of PEMFC stack dynamic performance. In: 2017 Chinese Automation Congress (CAC), pp. 2871–6. IEEE (2017)
4. O'Hayre, R., Cha, S.-W., Colella, W., Prinz, F.B.: Fuel Cell Fundamentals, pp. 116–127. Wiley, New Jersey (2016)
5. Springer, T.E., Zawodzinski, T.A., Gottesfeld, S.: Polymer electrolyte fuel cell model. J. Electrochem. Soc. **138**(8), 2334–2342 (1991)

Electrolysis Visualization and Performance Evaluation Platform for Commercial-Sized Alkaline Water Electrolyzer

Tao Wang(✉), Jinyi Wang, Pengjie Wang, Zhibo Ren, and Chao Peng

Huaneng Clean Energy Research Institute, CHNG Innovation Base, Changping District, Beijing 102209, China
t_wang@qny.chng.com.cn

Abstract. Alkaline water electrolysis (AWE) is promising for large-scale commercial production of green hydrogen, but large overpotential hinders their promotion. In order to reduce energy consumption, structure design of bipolar plate is crucial, which calls for a deep understanding of the flow behavior such as flow distribution and product bubble motion inside of the electrolyzers, thus requiring electrolysis visualization and evaluation. But due to challenge of structure design and proper sealing performance, related system/devices for commercial-sized electrolyzer are rare. In the present work, we construct an electrolytic visualization and performance testing system by using 3D computer aided design. Using precision CNC machining of transparent electrolyzer, the internal flow of different structures can be visualized, and the performance of the electrolyzer can be tested simultaneously. Based on the system, two common structured electrolyzer design are investigated, namely concave and convex bipolar plate (CCBP) and metal mesh support electrolyzer. The results indicate that a better flow uniformity is crucial for lower overpotential and the inferior performance of mesh structured electrolyzer at large current density results from bubble impediment in the mesh structure. The current platform can be applied as a general tool for convenient multi-phase investigation and performance evaluation of different structure design components during water electrolysis at a low cost.

Keywords: Green hydrogen · Water electrolysis · Electrolyzer · Flow visualization

1 Introduction

The production of green hydrogen is important for sustainable and eco-friendly energy. It has diverse applications in transportation, electricity generation, and industrial processes [1]. Green hydrogen is produced through water electrolysis using renewable energy sources, resulting in carbon-neutral fuel. Large-scale adoption of green hydrogen can significantly reduce carbon emissions, mitigate climate change, and enhance energy security by decreasing reliance on fossil fuels and increasing renewable energy use. In summary, green hydrogen production promotes a sustainable energy transition and resilient, eco-friendly energy system [2].

H. Sun et al. (Eds.): WHTC 2023, SPPHY 393, pp. 390–400, 2024.
https://doi.org/10.1007/978-981-99-8631-6_38

Alkaline water electrolysis is the most promising method for large-scale green hydrogen production, but faces challenges due to high costs [3–6]. The process requires substantial electricity, which can be prohibitively expensive if derived from non-renewable sources. Capital investment and equipment maintenance contribute to the high cost, making it less competitive than alternatives like steam methane reforming. Thus, reducing energy consumption is the main goal for developing alkaline water electrolyzers (AWEs).

To reduce energy consumption, the design of the electrolyzer's geometry structure is crucial. It determines electrolyte flow behavior and uniformity. Non-uniform flows can decrease reaction rates, cause uneven product distribution, and increase overpotential. The presence of product bubbles creates complex multiphase flow, influencing performance [7–9]. Therefore, optimizing the electrolyzer's geometry is essential to improve efficiency and reduce hydrogen production costs.

Optimizing the geometry structure requires understanding flow behavior, including uniformity and bubble motion. However, commercialized electrolyzers are assembled, making internal flow configurations invisible. Flow visualization setups are essential to investigate flow behavior and test structure designs. Yet, installing an accurate, reliable, and low-cost flow visualization system in large and complex commercial electrolyzers is challenging. Modifications to the electrolyzer design or additional components may be needed, which can be expensive and time-consuming. Flow visualization setups for water electrolysis are occasionally reported in small laboratory-scale electrolyzers [7, 10–12]. However, designing a visualization system for commercial-sized alkaline water electrolyzers is challenging due to difficulties in design, sealing, and high cost.

In the present study, a cost-effective, flexible, and convenient electrolysis visualization and testing system were established by using 3D computer-aided design and precise CNC machining. The flow behavior and performance of three structure designs of common alkaline water electrolyzers, namely, concave-convex bipolar plate (CCBP), metal mesh as well as blank electrolyzers were visualized and investigated based on the system. The current platform enables the study of flow behavior and the evaluation of the performance of the component, leading to more effective and sustainable electrolysis technologies. The proposed platform possesses the potential to serve as a comprehensive tool for investigating flow behavior and testing the performance of various components. Its application is anticipated to be of significant assistance in advancing the development of high-performance electrolyzers.

2 Electrolysis Visualization and Test Platform

The transparent electrolyzer module is the main component of the platform. Figure 1 shows the schematic diagram of the assembled transparent electrolysis cell, which provides an inexpensive and convenient experimental platform for studying flow behavior and optimizing novel electrolysis cell structures, including bipolar designs, mesh electrodes, and novel materials. The 3D structure of the transparent electrolysis cell was created using Solidworks software, allowing real-time modification and improvement of structural design parameters. The final design can be directly processed. The main components of the transparent electrolysis module are as follows:

1. Transparent PMMA plate: The default structure is a flat blank, but different electrode structures can be designed and tested. Electrode types can be 3D printed and tightly fitted inside the blank structure for comprehensive testing. The inner circle diameter of the transparent plate is 220 mm, which matches the electrode diameter. This size corresponds to commercial-sized alkaline water electrolyzers with a rated hydrogen production of 2 Nm^3/h.
2. Sealing rings: Made of transparent silicone or rubber, with a thickness of 0.6–1 mm, for efficient sealing between the PMMA plate and the Teflon sealing ring.
3. Teflon sealing ring: Made of PTFE material with grooves for placing the current collector ring and achieving effective sealing. The groove thickness is carefully determined for proper sealing.
4. Current collector ring: Connected to the power source to introduce current for hydrogen electrolysis. The outer dimensions must match the inner diameter of the collector ring sealing ring to ensure stable placement. The inside of the collector ring also has grooves for holding the electrode mesh, with a thickness matching that of the mesh.
5. Electrode mesh: Transmits current by contacting the collector ring and facilitates water electrolysis on the anode and cathode electrode meshes. Pure nickel mesh is used in this device.
6. Sealing ring: Made of silicone or rubber material, for efficient sealing between the electrode mesh and the diaphragm.
7. Diaphragm: Isolates hydrogen and oxygen produced during electrolysis to prevent the risk of explosion. PPS material is used as the diaphragm material in this device.

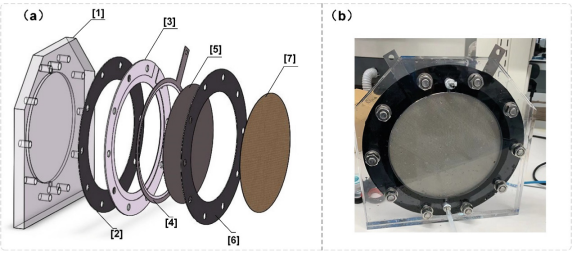

Fig. 1. Structure diagram of the main component of the electrolysis visualization test platform, the transparent PMMA electrolyzer:

The proposed transparent electrolyzer module can be used to test the performance of various components, including different geometry designs, electrode materials, and diagrams. In the following section, two common plate designs are investigated on the platform, namely concave-convex bipolar plate and metal 3D mesh, as shown in Fig. 2. And the results of the two are compared with one of the 'blank' electrolyzers with no geometry units. The geometry designs of CCBP and 3D metal mesh are intended to enhance the flow uniformity inside electrolyzers to improve electrolyzer efficiency. CCBP is a traditional geometry design in pressure filter electrolyzers with several concave and convex round units sculptured in the bipolar plates. This structure is simple and widely used in traditional commercial electrolyzers, but it is of high processing

cost. Recently, a novel structure design of a metal 3D mesh support body is developed for alkaline water electrolyzers, in which a 3D structured metal mesh is sandwiched between the flat bipolar plate and the electrodes. This design benefits the precision and speed of assembly. In the experimental section, the flow behavior and performance of the two designs would be investigated and compared.

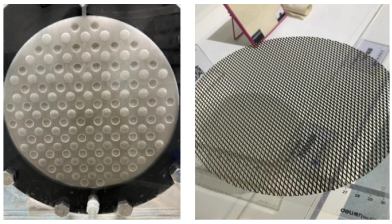

Fig. 2. Two common configurations of alkaline water electrolyzer: left, concave-convex bipolar plate (CCBP), right: metal 3D metal mesh.

3 Experiment

3.1 Experiment Setup

The assembled components of the electrolysis process visualization testing platform are secured with bolts to achieve efficient sealing. After passing the sealing test, experimental testing can be conducted. A schematic diagram of the electrolysis process visualization testing platform is shown in Fig. 3. The main equipment includes:

(1) Transparent electrolysis module for flow visualization;
(2) Peristaltic pump for circulating electrolytes;
(3) Constant temperature water bath for maintaining the constant temperature of the electrolysis process;
(4) Programmable DC power supply (ITECH, IT6724C, Auto range DC power supply) to generate constant current/voltage through the program to test the voltage of the electrolysis cell under different conditions;
(5) Computer for recording and processing experimental data.

3.2 Experiment Procedure

The experimental procedure is as follows: install and connect the equipment according to the schematic diagram, and use deionized water as the working fluid. Check the tightness of the entire system to ensure that there is no leakage. After confirming no leakage, replace the deionized water with 30% KOH as the electrolyte. Turn on the peristaltic pump to circulate the electrolyte inside the platform. The KOH electrolyte enters the transparent PMMA electrolyzer from the reagent bottle through the peristaltic pump, fills the cell, and flows out to the KOH reagent bottle to achieve the circulation of the alkaline

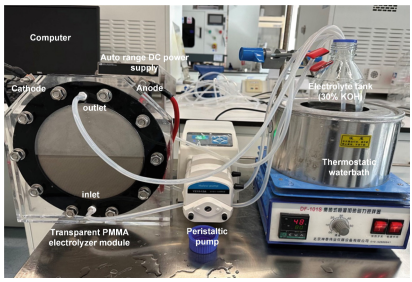

Fig. 3. Schematic diagram of experimental apparatus

solution. At the same time, turn on the water bath to ensure the temperature of the alkaline solution is constant. In this experiment, the temperature of the alkaline solution is set to a constant 80 °C. Before each group of experiments, set an appropriate flow rate for the alkaline solution and maintain it for more than 10 min to ensure the system reaches a steady state. Then, turn on the DC power supply, and use the programmed power supply strategy to experiment. Record the corresponding volt-ampere characteristic curve of the electrolyzer structure under different alkaline solution flow rates. Observe and record the gas-liquid flow state inside the transparent electrolyzer at the same time.

In this experiment, the output current of the DC power supply increases linearly, and the voltage of the electrolyzer is recorded every 15 s. Finally, the UI performance curve of the electrolyzer under the given conditions can be obtained. The experimental plan is attached in Table 1.

4 Result Discussion

4.1 Flow Behavior in the Blank Electrolyzer

Initially, we conducted flow visualization tests on a blank electrolyzer structure and observed the gas-liquid flow inside, as depicted in Fig. 4. At low current (1A), large gas bubbles formed within the electrolytic cell, adhering to the electrode plate walls. This is likely due to the limited upward movement of bubbles and the absence of strong circulation at low current density, resulting in mild gas motion. Consequently, bubbles stick to the electrode mesh and walls due to less drag force, as shown in the figure. As the current density increases, smaller bubbles are generated, exhibiting mist-like movements that are not directly visible to the naked eye. Simultaneously, internal gas bubbles display circulation within the electrolyzer, moving upward along the axial line of the cell. However, due to limited alkaline liquid discharge, a significant portion of bubbles cannot be expelled in time when reaching the outlet. As a result, they reverse direction along the electrolyzer's edge, creating an internal circulation driven by the density difference between gas and alkaline liquid, facilitated by lift force. This internal circulation disrupts the alkaline liquid flow, preventing bubble adhesion to the cell's walls and directing them towards the outlet alongside the alkaline liquid. Additionally, near the electrolyzer inlet, a circular region of lower gas-phase fraction (void zone) was observed. This occurs because the flow velocity is higher near the inlet, causing rapid upward movement of gas bubbles generated by the electrolyzer in that position (Fig. 4).

Table 1. Experimental plan in performance test

Group	Current (A)	Delay (s)
1	0.5	30
2	1	30
3	1.5	30
4	2	30
5	2.5	30
6	3	30
7	3.5	30
8	4	30
9	5	30
10	7	30
11	9	30
12	12	30
13	15	30
14	17	30
15	20	30

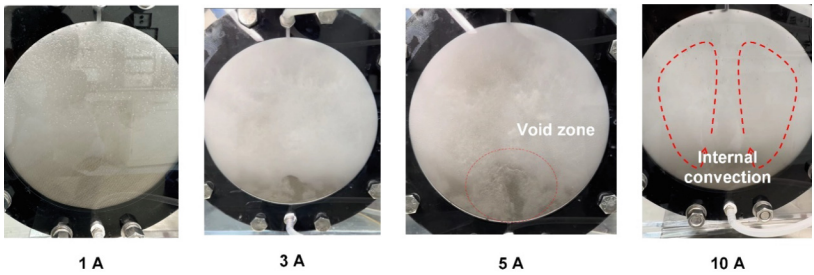

Fig. 4. Diagram of multi-phase flow behavior in the blank electrolyzer, showing a void zone near the entrance and internal convection of product gas bubbles at a higher current (I = 10A)

4.2 The Influence of Flow Rate for Blank Electrolyzer

We conducted voltammetric measurements on the blank electrolyzer at different flow rates, as depicted in Fig. 5. Increasing the flow rate of the alkaline solution leads to a decrease in cell voltage at the same current density, indicating enhanced electrolyzer performance. This is likely due to the improved removal of bubbles from the cell, reducing gas holdup and decreasing ohmic overpotential. However, our previous findings showed that increasing the flow rate reduces cell uniformity, which should increase the cell voltage and imply reduced performance. This paradox reflects the combined effects of various factors within the electrolyzer. As a highly nonlinear system, the electrolyzer's

performance is influenced by complex factors, resulting in different outcomes under different conditions. In our experiment with a small electrolyzer diameter, increasing the flow rate in the low range improves cell performance more significantly due to faster bubble removal, outweighing the performance reduction caused by decreased uniformity. Thus, an increase in the flow rate improves electrolyzer performance within this range. However, it is anticipated that continuing to increase the flow rate beyond a certain threshold will cause the performance improvement from bubble removal to be insufficient in compensating for the performance reduction due to decreased uniformity. At that point, electrolyzer uniformity becomes the controlling factor for performance. This conclusion requires further experimental verification.

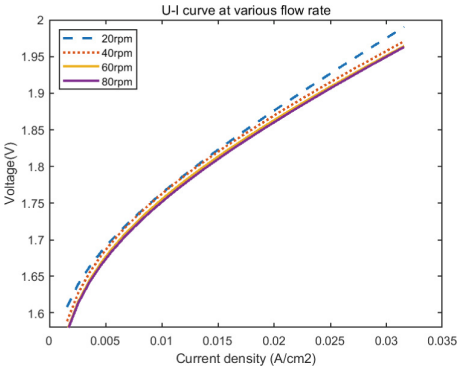

Fig. 5. Polarization curve measurement of blank electrolyzer at different inflow rates.

4.3 Influence of Different Geometries

Diagrams of multi-phase flow behavior in CCBP and mesh support electrolyzer are shown in Figs. 6 and 7, respectively. As shown in the figure, the void zone of the CCBP electrolyzer is much smaller than that of the blank electrolyzer, indicating an enhanced flow uniformity. From the observation, the flow uniformity in the mesh electrolyzer is the best of the three. The electrolyzer-scale internal convection of product bubbles is not obvious and is confined to the local area. Because of the geometries like CCBP and metal mesh, the internal convection inside of the electrolyzer is subdued, resulting in faster gas product ejectment. Thus, energy consumption is reduced. This is validated by polarization curve measurement, as is shown in Fig. 8. It can be observed that at the same current, the voltage of the blank structureelectrolyzer is significantly higher than that of the other structures, indicating higher resistance and poorer performance. Additionally, as the current gradually increases, the slope of the voltage increase for the blank structure electrolyzer is significantly larger than that of the other structures, indicating poorer performance. Combining the results of the visual experiments, the observed deficiencies in the performance of blank electrolyzer can be attributed to the absence of structural elements, leading to uneven lateral fluid distribution, circulating flow, and non-uniform distribution of fluid within the chamber, which results in the formation of dead zones.

The non-uniform flow distribution and resultant dead zones increases the residence time of the production bubbles, which causes considerable larger overpotential. Moreover, at lower currents, the 3D metal mesh structure electrolyzer has the lowest voltage, and as the current increases, the voltage of all the electrolyzer gradually increases. It was found that the voltage of the 3D metal mesh structureelectrolyzer gradually approaches that of the conventional CCBP, and when the current is 20 A, the voltage of the electrolyzer from high to low is blank structure, 3D metal mesh, and CCBP. Among them, the voltage of the 3D mesh structure electrolyzer is higher than that of the traditional CCBP structure, indicating its poorer performance. However, the fluid uniformity of the 3D metal mesh structure is superior to that of the CCBP structure, so why is its electrolysis performance worse than that of the CCBP structure? One possible reason is that through the visual experiment shown in Fig. 7, it was found that when the current density is high, due to the overly dense 3D mesh in the experiment, a large number of bubbles are generated and attached to the 3D metal mesh to form larger bubbles, as shown in Fig. 7, which increases the ohmic overpotential inside the electrolyzer, thereby reducing the performance of the electrolyzer. In summary, the above results confirm that improving the uniformity of fluid does indeed have a positive effect on the performance of the electrolyzer. However, at the same time, the uniformity of fluid flow is not the only factor affecting the performance of the electrolyzer. The structure inside the electrolyzer, such as the obstruction characteristics of product bubbles, also has an important impact on the performance of the electrolyzer. This also demonstrates the complexity of the electrolytic hydrogen production process (Fig. 8).

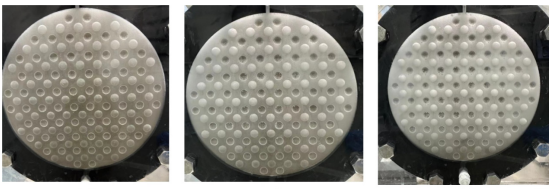

Fig. 6. Diagram of multi-phase flow behavior in CCBP electrolyzer, showing improved flow uniformity with reduced void zone area.

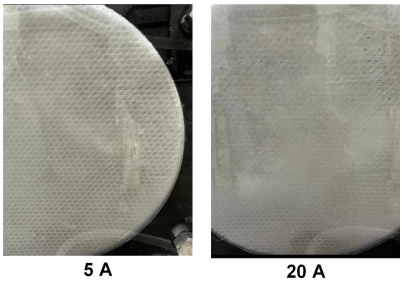

Fig. 7. Diagram of multi-phase flow behavior in mesh support electrolyzer, showing bubble impediment.

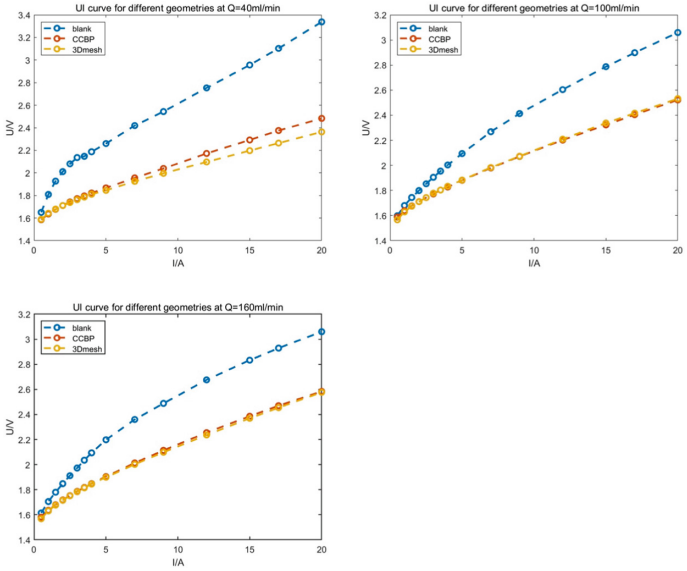

Fig. 8. Polarization curve measurement of CCBP, 3D metal mesh, and blank electrolyzers at different inflow rates.

5 Conclusion

To reduce the energy consumption of water electrolysis, it is important to design electrolyzers with improved flow uniformity, which requires a thorough understanding of flow behavior. Visualizing the flow behavior inside electrolyzers is crucial for this investigation. However, due to difficulties in sealing and fabrication as well as high cost, visualization systems for commercial-sized alkaline water electrolyzers are rare. In this study, an in-situ electrolysis visualization and performance evaluation platform were developed using 3D computer-aided design and precise CNC machining. The platform consists of a transparent bipolar plate and essential electrolyzer components, enabling in-situ observation of multiphase flow configurations during electrolysis and measurement of polarization curves. Two geometries, namely CCBP and 3D mesh electrolyzers,

were investigated and tested, and the results were compared with those obtained from a blank electrolyzer. In the blank electrolyzer, internal convection of product bubbles was observed, whereas the CCBP and 3D mesh geometries were effective in achieving improved flow uniformity. The polarization curve measurements indicated that the improved flow uniformity in CCBP and 3D mesh electrolyzers reduced the cell voltage. However, bubble impediment was observed in the 3D mesh electrolyzer, resulting in an inferior performance at higher current densities. The current platform enables the study of flow behavior and component performance, leading to more effective and sustainable electrolysis technologies, which can be applied as a general evaluation platform for the further development of high-performance electrolyzers, including structure design, electrode materials, and other components.

References

1. Zou, C., Li, J., Zhang, X., Jin, X., Xiong, B., Yu, H., et al.: Industrial status, technological progress, challenges, and prospects of hydrogen energy. Nat. Gas Ind. B **9**, 427–447 (2022)
2. Zhou, Y., Li, R., Lv, Z., Liu, J., Zhou, H., Xu, C.: Green hydrogen: a promising way to the carbon-free society. Chin. J. Chem. Eng. **43**, 2–13 (2022)
3. Lebrouhi, B.E., Djoupo, J.J., Lamrani, B., Benabdelaziz, K., Kousksou, T.: Global hydrogen development—a technological and geopolitical overview. Int. J. Hydrog. Energ. **47**, 7016–7048 (2022)
4. Rasul, M.G., Hazrat, M.A., Sattar, M.A., Jahirul, M.I., Shearer, M.J.: The future of hydrogen: challenges on production, storage and applications. Energ. Convers. Manage. **272**, 116326 (2022)
5. Shiva Kumar, S., Lim, H.: An overview of water electrolysis technologies for green hydrogen production. Energ. Rep. **8**, 13793–13813 (2022)
6. Ren, Z., Wang, J., Yu, Z., Zhang, C., Gao, S., Wang, P.: Experimental studies and modeling of a 250-kW alkaline water electrolyzer for hydrogen production. J. Power. Sour. **544**, 231886 (2022)
7. Wang, W., Yu, S., Li, K., Ding, L., Xie, Z., Li, Y., et al.: Insights into the rapid two-phase transport dynamics in different structured porous transport layers of water electrolyzers through high-speed visualization. J. Power. Sour. **516**, 230641 (2021)
8. Iwata, R., Zhang, L., Wilke, K.L., Gong, S., He, M., Gallant, B.M., et al.: Bubble growth and departure modes on wettable/non-wettable porous foams in alkaline water splitting. Joule **5**, 887–900 (2021)
9. Wang, T., Wang, J., Wang, P., Wang, F., Liu, L., Guo, H.: Non-uniform liquid flow distribution in an alkaline water electrolyzer with concave-convex bipolar plate (CCBP): a numerical study. Int. J. Hydrog. Energ. (2023)
10. Li, Y., Yang, G., Yu, S., Kang, Z., Talley, D.A., Zhang, F.-Y.: Direct thermal visualization of micro-scale hydrogen evolution reactions in proton exchange membrane electrolyzer cells. Energ. Convers. Manage. **199**, 111935 (2019)
11. Shigemasa, K., Atienza-Márquez, A., Inoue, K., Jang, S., Peña, F.I.R., Araki, T., et al.: Visualization of dragged water and generated hydrogen bubbles in a direct toluene electrohydrogenation electrolyzer. J. Power. Sour. **554**, 232304 (2023)
12. Ikeda, H., Misumi, R., Kojima, Y., Haleem, A.A., Kuroda, Y., Mitsushima, S.: Microscopic high-speed video observation of oxygen bubble generation behavior and effects of anode electrode shape on OER performance in alkaline water electrolysis. Int. J. Hydrog. Energ. **47**, 11116–11127 (2022)

Design of Membrane Electrode Assembly with Non-precious Metal Catalyst for Self-humidifying Proton Exchange Membrane Fuel Cell

Jing Liu and Tong Zhang(✉)

School of Automotive Studies, Tongji University, Shanghai 201804, China
tzhang@tongji.edu.cn

Abstract. High cost is one of the key factors restricting the industrialization and commercialization of proton exchange membrane fuel cells (PEMFCs). In this paper, a low-cost membrane electrode assembly (MEA) is prepared by using a self-made non-precious metal catalyst. Through the polarization curve test of fuel cell, the optimal loading of Fe-N-S-C catalyst and the optimal ratio with Nafion ionomer are studied. When the loading of Fe-N-S-C catalyst is 2.0 mg cm^{-2} and the ratio of Nafion ionomer to Fe-N-S-C catalyst is 3:7, the performance of the PEMFC is the best. The performance of MEA under different relative humidity (RH) and inlet pressure is also explored. The experimental results show that the MEA can still maintain good performance under the condition of 40% RH, which shows that this MEA has a certain self-humidifying ability. Because the non-precious metal catalyst layer is too thick, the performance of PEMFC can be improved by increasing the inlet pressure appropriately. The durability of MEA with non-precious metal catalyst is poor, and there is still a lot of work to be done to improve the stability and durability.

Keywords: Non-precious metal catalyst · MEA fabrication · Self-humidifying

1 Introduction

The proton exchange membrane fuel cell (PEMFC) is an energy conversion device that converts the chemical energy in hydrogen into electrical energy. It has the advantages of small size, light weight, fast start-up, high energy efficiency, and the generation of only water, making it an ideal power source for zero-emission vehicles (ZEV) [1]. However, high cost is the key factor to limit the industrialization and commercialization of PEMFCs, and society still prefers diesel locomotives to fuel cell vehicles before reducing the price of fuel cells. Current analysis of the cost structure of PEMFCs shows that in high-volume production, the proton exchange membrane (PEM) accounts for 11% of the stack cost and the platinum catalyst (Pt/C) accounts for 49% of the total cost [2]. In order to realize the commercialization of PEMFCs, it is necessary to reduce the material costs, including reducing the use of Pt catalysts, and seeking cheap catalysts, bipolar plates and proton exchange membranes. Therefore, the development of low platinum catalysts or non-noble metal catalysts has attracted increasing attention.

H. Sun et al. (Eds.): WHTC 2023, SPPHY 393, pp. 401–411, 2024.
https://doi.org/10.1007/978-981-99-8631-6_39

Pt/C is the catalyst commonly used in PEMFCs. This metal is selected because platinum is a relatively stable material, which can effectively accelerate the oxygen reduction reaction (ORR) at the cathode. Platinum is both expensive and scarce, with a price of $1500 per troy ounce [2]. More and more researches are devoted to reducing the content of platinum in fuel cell. One approach is to use platinum catalysts with different material carriers to enhance their performance, dispersibility and durability [3, 4]. These platinum carriers can be carbon particles, carbon nanotube particles, graphene and metal particles with a non-platinum metal core and a platinum shell structure. Another approach is to alloy platinum with cheaper metals such as palladium (Pd), ruthenium (Ru) and especially silver (Ag) [5, 6]. Recent studies even suggest that platinum may be completely replaced by non-platinum catalysts, which are low in cost, rich in raw materials, easy to synthesize and high in oxygen reduction performance [7, 8]. More and more scholars are studying and preparing high-performance non-noble metal catalysts. The common non-precious catalysts include non-precious metal sulfides, non-precious metal carbonitrides, non-precious metal oxides, non-precious metal nitride, non-precious metal nitrogen oxides, M-N/C catalysts, etc. Among them, M-N/C catalysts are the most likely non-precious metal catalysts to replace platinum catalysts [9].

The non-precious metal catalyst Fe-N-S-C can be used as an ORR catalyst for the preparation of the cathode catalyst layer (CL) of fuel cells. In this paper, the cathode CL is prepared by Fe-N-S-C catalyst, and the anode CL is prepared by low-load Pt/C catalyst. The prepared membrane electrode assembly (MEA) is assembled into fuel cells and its performance is tested. The effects of the Fe-N-S-catalyst loading and the ratio of Nafion ionomer to Fe-N-S-C catalyst on the performance of fuel cell are studied, and the effects of inlet pressure, operating temperature and inlet humidity on the performance of MEA of non-noble metal catalyst are investigated. The electrochemical impedance spectra (EIS) of the fuel cell at different humidity and different current loading are tested for reaction kinetics analysis. And the durability of the non-precious metal catalyst MEA is studied.

2 Experimental

2.1 Preparation of Fuel Cell

The preparation process of Fe-N-S-C catalyst has been described in detail in our previous work [9]. The non-noble metal catalyst Fe-N-S-C used to prepare the cathode CL of the fuel cell is prepared, and the anode CL is prepared using the low-load Pt/C (Pt 60 wt%, Johnson Matthey) catalyst. The Pt loading of the anode CL is 0.1 mg cm^{-2}, and the mass fraction of Nafion (5 wt%, Dupont) ionomer is 25 wt%. In order to investigate the optimal loading of Fe-N-S-C catalyst and the optimal ratio of Nafion ionomer to Fe-N-S-C catalyst, several MEAs are prepared for comparison. The non-precious metal catalyst MEAs used in this paper are all home-made in the laboratory. The two kinds of catalysts ink are sprayed on the Nafion 212 membrane, and then the catalyst coat membrane (CCM) and gas diffusion layer (GDL) are hot pressed at a constant temperature of 130 °C, a pressure of 500 psi and a hot-pressing time of 2 min. The reaction area of the fuel cell is 2 cm × 2 cm. The cells are assembled in order and the bolts are tightened in diagonal order with a torque wrench with a torque size of 5–7 N m.

2.2 Performance Evaluation and Electrochemical Measurements

The assembled fuel cell is connected to a fuel cell testing system, which includes a control system, gas supply system, a humidifying system and back pressure system. Firstly, before testing the polarization curve, the fuel cell is activated to improve the utilization ratio of the catalyst, and the membrane is humidified to establish the transmission channels of protons, electrons, reactants and products. The activation process of fuel cells generally adopts natural activation and forced activation, and the constant current forced activation is adopted in this experiment. When testing the polarization curves, the average value of each group of experiments is taken after three repetitions. EIS tests are carried out in the frequency range of 0.1 Hz–1 kHz with 5% loading current amplitude, and each EIS test is repeated three times.

3 Results and Discussion

3.1 Effect of Fe-N-S-C Loading on Cell Performance

The fuel cell performance is directly related to the cathode catalyst loading, and the effect of Fe-N-S-C catalyst loading on the fuel cell performance is explored here. The Pt loading of the anode CL is controlled to be 0.1 mg cm^{-2}, and the Fe-N-S-C catalyst loading of the cathode CL is 0.5 mg cm^{-2}, 1.0 mg cm^{-2}, 2.0 mg cm^{-2}, and 3.0 mg cm^{-2}, respectively. The fuel cell is operated at 70 °C, the relative humidity (RH) is 100%, and the hydrogen and oxygen flow rates were 100 and 200 mL min^{-1}, and the back pressure is 50 kPa. The current density-voltage curves and current density-power curves of the MEAs are shown in Fig. 1, and the maximum power density of each MEA is shown in Table 1.

It can be seen from the experimental results that when the loading of Fe-N-S-C catalyst is less than 2.0 mg cm^{-2}, the performance of the fuel cell will be improved with the increase of the loading, because more catalysts are involved in the ORR, which improves the electrochemical reaction rate, thus improving the energy density of the fuel cell. The cathode CL Fe-N-S-C with the loading of 2.0 mg cm^{-2} has obtained the fuel cell with the highest power density and the best performance. However, with the increasing load of non-precious metal catalyst, the performance of fuel cell does not increase, but decreases. Previous studies show that this Fe-N-S-C catalyst has a high specific surface area and a rich pore structure, and the thickness of the CL increases significantly with the increase of catalyst loading. When the catalyst loading exceeds 2.0 mg cm^{-2}, the thickness of the Fe-N-S-C CL exceeds 45 μm. Too thick CL will increase the internal resistance of the MEA, and hinder the transmission of reactants and products, leading to the decline of fuel cell performance. Therefore, the optimal loading capacity of Fe-N-S-C catalyst is 2.0 mg cm^{-2}, and this optimal loading capacity is selected for all the experiments.

3.2 Effect of Ionomer and Catalyst Ratios on Cell Performance

The influence of the ionomer loading on the fuel cell performance is very important. In this paper, the ratios of ionomer to Fe-N-S-C catalyst is 3:2, 3:3, 3:5 and 3:7, respectively.

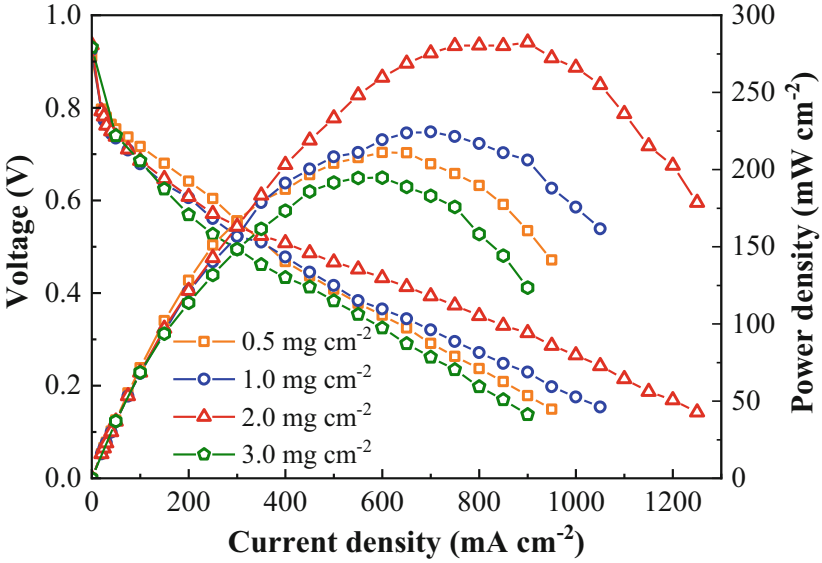

Fig. 1. Polarization curves of MEA with various Fe-N-S-C content at 70 °C and 100 mL min^{-1} of H_2 and 200 mL min^{-1} of O_2 flow rates under 100% RH, and gas pressure is 50 kPa.

Table 1. Maximum power density of MEA with different Fe-N-S-C catalyst loadings.

Anode (mg_{Pt} cm^{-2})	Cathode ($mg_{Fe\text{-}N\text{-}S\text{-}C}$ cm^{-2})	Maxmum power density (mW cm^{-2})
0.1	0.5	211.1
0.1	1.0	224.4
0.1	2.0	282.4
0.1	3.0	194.7

The performance of the prepared MEA is shown in Fig. 2, among which the ratio with the best cell performance is 3:7, and the power density of the fuel cell is 283 mW cm^{-2}, which is much higher than that of the MEA with other ratios, and the performance of several groups of MEA with higher ionomer loadings is poor.

On the one hand, the ionomer in the CL serves as an adhesive and provides a transport channel for hydrogen ions in the CL. The appropriate amount of ionomer in the CL is beneficial to form a good hydrogen ion transport channel, improve the utilization of the catalyst, and enhance the performance of the fuel cell. The proper ratio of ionomer to catalyst is beneficial to improve the performance of the membrane electrode. Excessive ionomer will severely block the pore structure of the catalyst surface, which will prevent the transfer of the reaction gas to the active site of the catalyst and reduce the rate of ORR, thus reducing the performance of the fuel cell. In addition, excess ionomer will retain the water generated from the cathode reaction in the CL, causing flooding, impeding the transport of the reaction gas and increasing the internal resistance of mass transfer.

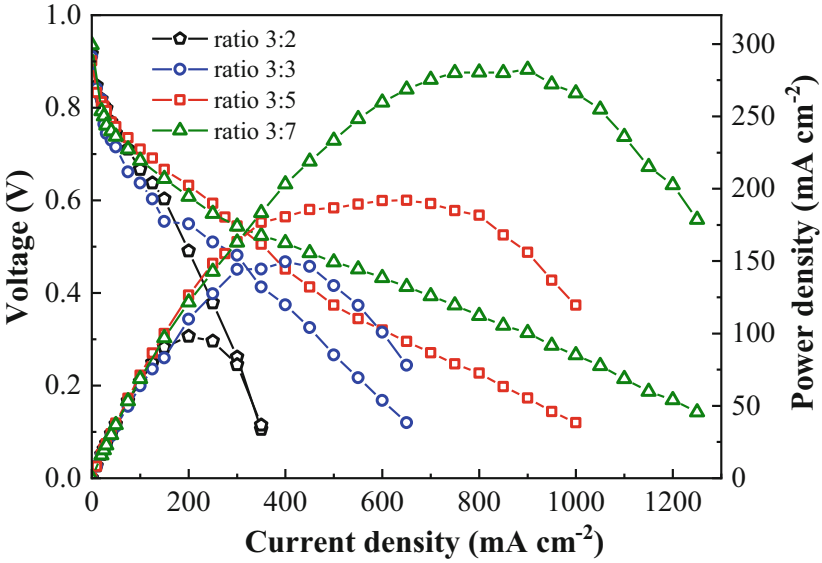

Fig. 2. Polarization curves of MEA with various mass ratio of Nafion and Fe-N-S-C catalysts at 70 °C and 100 mL min^{-1} of H_2 and 200 mL min^{-1} of O_2 flow rates under 100% RH, and gas pressure is 50 kPa.

3.3 Effect of Relative Humidity on Cell Performance

To investigate the cell performance of the non-precious metal catalyst at different RH, the polarization curves of the MEAs are tested at the inlet RH of 100, 80, 60, 40 and 20% for both cathode and anode, where the cathode Fe-N-S-C catalyst loading is 2.0 mg cm^{-2} and the anode Pt loading was 0.1 mg cm^{-2}, the operating temperature is 70 °C, the back pressure is 50 kPa, and the polarization curves of the non-precious metal film electrode at different RH are shown in Fig. 3.

From Fig. 3, it can be seen that the performance of the MEAs gradually improves as the RH of the inlet gas decreases. When the RH is 100%, the maximum power density of the membrane electrode is 217 mW cm^{-2}, when the RH drops to 40%, the maximum power density of the MEAs is 246 mW cm^{-2}, and when the RH of the inlet air continues to decrease, the power density drops slightly to 241 mW cm^{-2}. For the MEA which does not have self-humidification ability, it faces a sharp decrease or even loss of proton conduction ability under low humidity conditions. The experimental results show that the MEA with Fe-N-S-C catalyst as the cathode CL has a certain self-humidifying capability, which can ensure good performance under low humidity conditions. The self-humidifying performance of this MEA is related to the high specific surface area and abundant porosity of the Fe-N-S-C catalyst, and the specific reasons and self-humidifying performance have been explained in our previous work [10].

In order to further analyze and understand the electrochemical performance of the MEA at different RH, the EIS of the fuel cell is tested. The test results are shown in Figs. 4, and 5 shows the changes of activation loss, ohmic loss and concentration loss

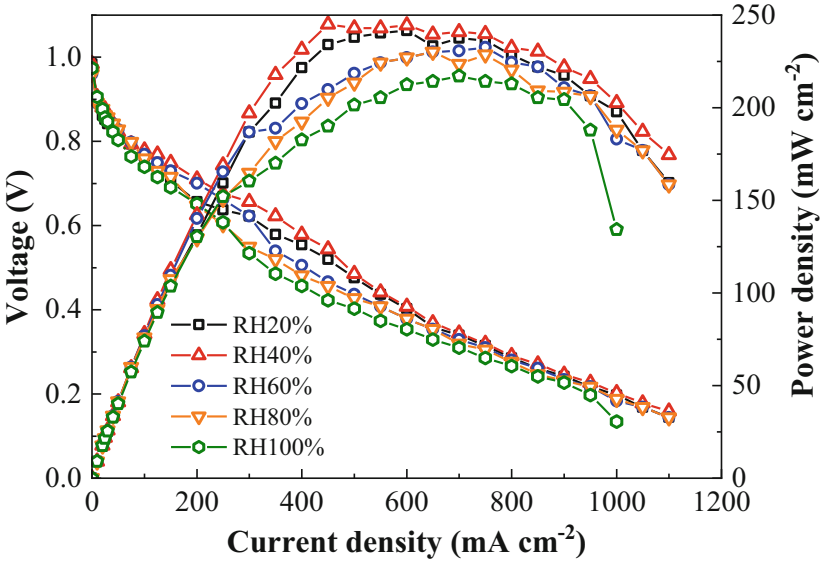

Fig. 3. Polarization curves of MEA under various RH (100, 80, 60, 40 and 20%) at 70 °C and 100 mL min^{-1} of H_2 and 200 mL min^{-1} of O_2 flow rates, and gas pressure is 50 kPa.

with time. The EIS is carried out when the current density of the fuel cell is 30 mA cm^{-2}, 300 mA $cm^{-2}$and 1000 mA cm^{-2}, respectively.

Comparing the EIS of the fuel cell at a current density of 30 mA cm^{-2}, it can be found that the ohmic resistance and charge transfer resistance of the fuel cell increase with the decrease of the RH of the fuel cell, because the cathode reaction rate is slow when the fuel cell is running at low current, and it can not generate enough water to wet the MEA. When the RH is 20%, the anode charge transfer resistance and cathode charge transfer resistance can be measured, indicating that the membrane electrode is extremely dehydrated and the proton conductivity is very low.

However, at a current density of 300 mA cm^{-2}, the resistance of each part of the MEA did not increase significantly, thanks to the self-humidifying ability of the Fe-N-S-C catalyst, which preserves the water from the gas supply and the water generated by the ORR, and when the membrane and the anode CL are water-starved, the water from the cathode is transferred to the anode through the diffusion effect generated by the water concentration gradient, thus ensuring the proton conduction ability of the membrane and ionomer.

When the cell is operated at high current density, the EIS can detect the mass transfer resistance of the MEA, and it can be seen from the figure that the ohmic resistance and charge transfer resistance of the fuel cell operating at 1000 mA cm^{-2} do not change significantly, but the mass transfer resistance of the MEA is the largest at a RH of 100%, which may be due to the water retention effect of the Fe-N-S-C CL that makes the MEA difficult to remove water in time under high humidity operating conditions, which causes flooding and hinders the reaction gas transfer of the fuel cell.

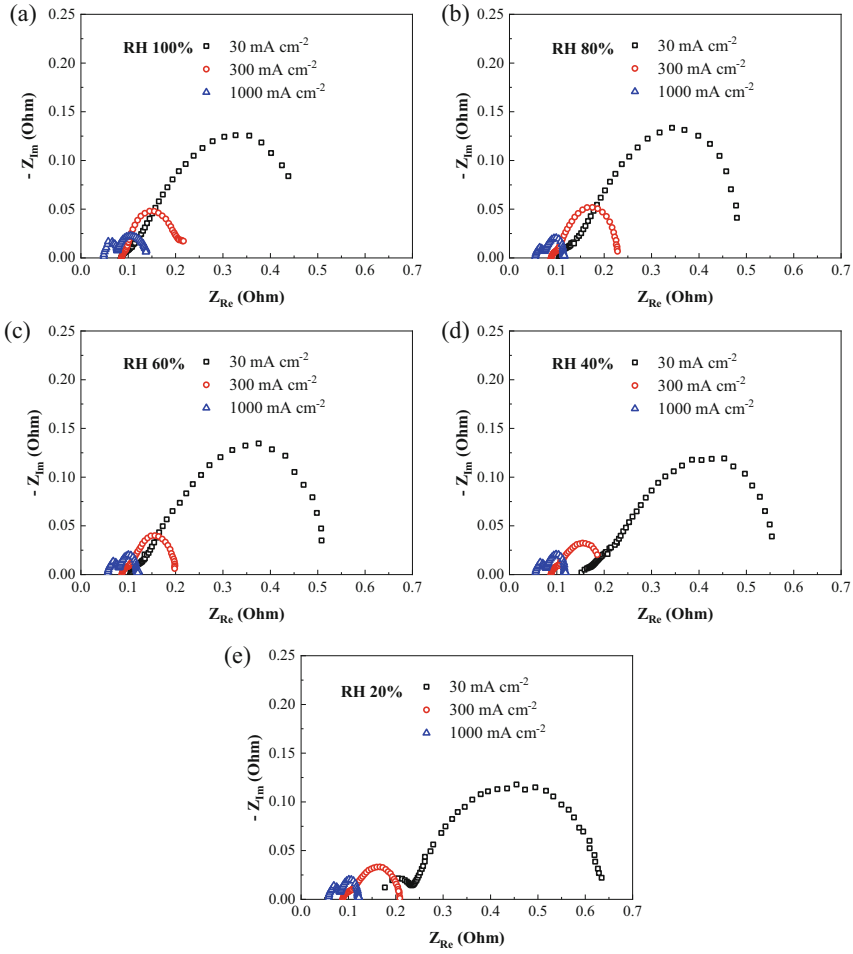

Fig. 4. Impedance spectra at 30, 300 and 1000 mA cm^{-2} of MEA at 70 °C and 100 mL min^{-1} of H_2 and 200 mL min^{-1} of O_2 flow rates under (a) 100%, (b) 80%, (c) 60%, (d) 40% and (e) 20% RH, and gas pressure is 50 kPa.

3.4 Effect of Inlet Pressure on Cell Performance

Generally, under the high current operating conditions, the voltage loss of the PEMFC is mainly caused by the transmission loss of reaction gas, and the performance of fuel cell can be improved by increasing the pressure of the reaction gas appropriately. The results of this study about the membrane electrode of non-precious metal catalyst are shown in Fig. 6.

The Fe-N-S-C loading of the membrane electrode is 2 mg cm^{-2} the Pt loading of the anode is 0.1 mg cm^{-2}. As can be seen from Fig. 6, the back pressure of the reaction gas has a very significant influence on the performance of the fuel cell. The maximum power density of the membrane electrode was 142 mW cm^{-2} when no back pressure

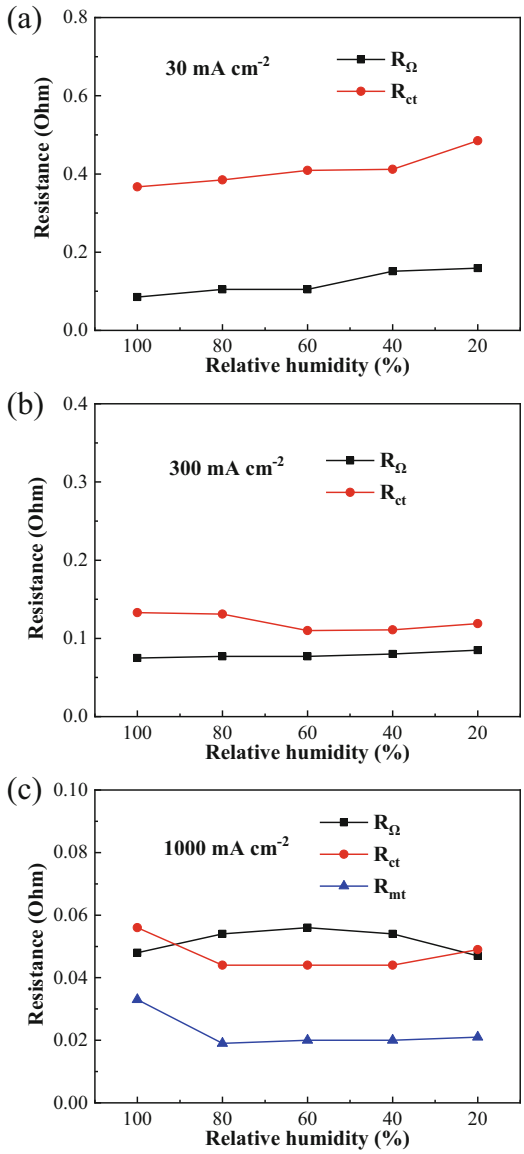

Fig. 5. Impedance spectra at (a) 30 mA cm^{-2}, (b) 300 mA cm^{-2} and (c) 1000 mA cm^{-2} of MEA.

was applied to the reaction gas, and as the back pressure of the reaction gas increased to 50 kPa, the maximum power density of the membrane electrode rose to 191 mW cm^{-2}, which was enhanced by 25%. When the back pressure of the reaction gas continued to increase to 100 kPa, the power density continued to rise by 17% to 223 mW cm^{-2} at 50 kPa. The experimental results showed that for this MEA with non-precious metal catalyst had a higher mass transfer resistance and exhibited poorer performance without

increasing the back pressure. This is because the Fe-N-S-C catalyst is porous and the CL is thicker, which hinders the transmission of the reaction gas to a certain extent.

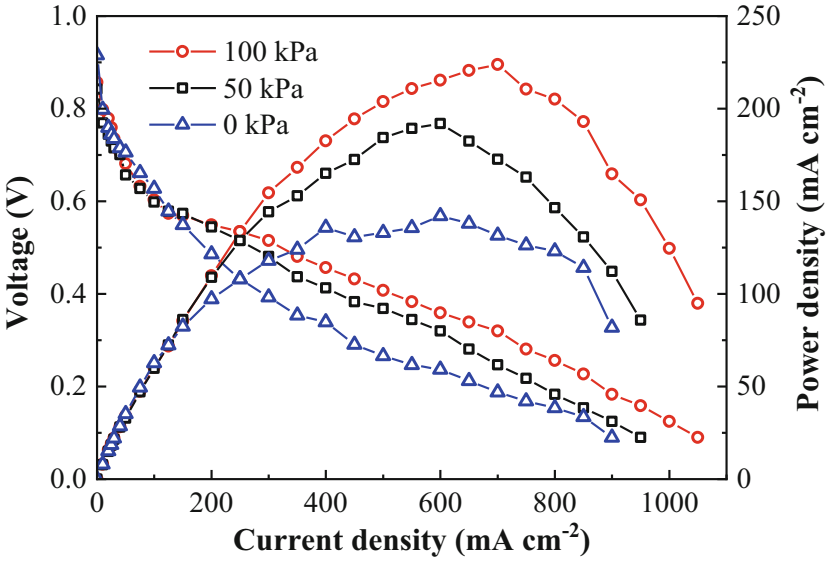

Fig. 6. Polarization curves of MEA under various gas pressure at 70 °C and 100 mL min^{-1} of H_2 and 200 mL min^{-1} of O_2 flow rates.

3.5 Durability of Fuel Cell with Non-precious Metal Catalyst

In the durability test of MEA with non-precious metal catalyst, its durability is not ideal, and voltage decays quickly in a short steady-state test. In this experiment, the voltage decay of MEA is studied over 50 h when operating at a current density of 200 mA cm^{-2}, and the experimental results are shown in Fig. 7. The voltage of the cell decayed by 40% in the first 30 h and remained basically stable in the next 20 h. The decay may be due to carbon corrosion, loss of catalytic active sites or oxidation of nitrogen atoms in the catalyst by hydrogen peroxide. Compared with the durability of MEA with noble metal catalysts, the durability of MEA with non-precious metal catalysts is much worse, and there is still much work to be done to improve the stability and corrosion resistance of the non-precious metal catalysts themselves.

4 Conclusions

In this paper, the MEA with Fe-N-S-C catalyst is successfully prepared. When the loading of Fe-N-S-C catalyst is 2.0 mg cm^{-2} and the ratio of Fe-N-S-C catalyst to Nafion ionomer is 7:3, the performance of MEA is the best. The performance of MEA under different RH conditions is tested, and it is found that it could still maintain good

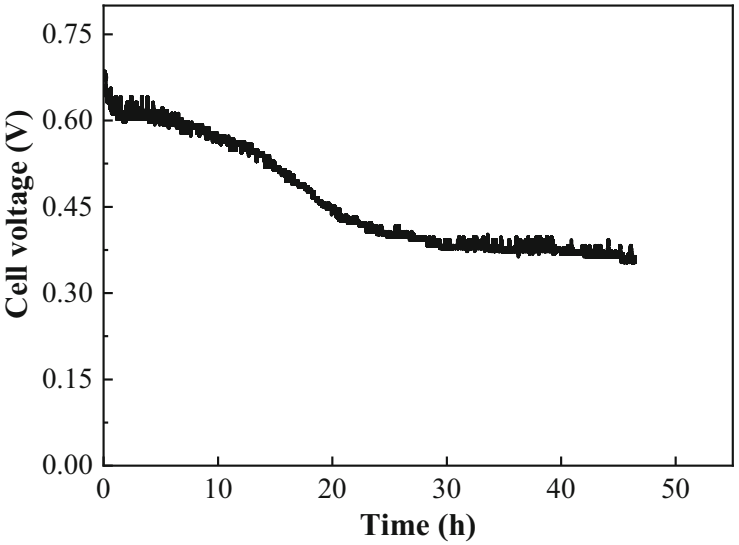

Fig. 7. Long-term discharge curves of MEA operated at 70 °C and 100% RH. The hydrogen and oxygen flow rates are 100 mL min^{-1} and 200 mL min^{-1}, respectively, and gas pressure is 50 kPa.

performance under low humidity conditions and has certain self-humidification ability. The influence of inlet pressure on the performance of MEA is studied. It is found that the performance of MEA is obviously improved with the increase of inlet pressure. The 50-h durability of fuel cell is tested at a current of 200 mA cm^{-2}. The voltage of the fuel cell decreased by 40% in the first 30 h and remained basically stable in the next 20 h. This shows that the durability of this Fe-N-S-C catalyst needs to be greatly improved.

References

1. Peighambardoust, S.J., Rowshanzamir, S., Amjadi, M.: Review of the proton exchange membranes for fuel cell applications. Int. J. Hydrogen Energ. **35**, 9349–9384 (2010)
2. Guerrero Moreno, N., Cisneros Molina, M., Gervasio, D., Pérez Robles, J.F.: Approaches to polymer electrolyte membrane fuel cells (PEMFCs) and their cost. Renew. Sustain. Energ. Rev. **52**, 897–906 (2015)
3. Antolini, E.: Graphene as a new carbon support for low-temperature fuel cell catalysts. Appl. Catal. B **123–124**, 52–68 (2012)
4. Liu, M., Zhang, R., Chen, W.: Graphene-supported nanoelectrocatalysts for fuel cells: synthesis, properties, and applications. Chem. Rev. **114**, 5117–5160 (2014)
5. Jiang, R., Moton, E., McClure, J.P., Bowers, Z.: A highly active and alcohol-tolerant cathode electrocatalyst containing Ag nanoparticles supported on graphene. Electrochim. Acta **127**, 146–152 (2014)
6. Godínez-García, A., Pérez-Robles, J.F., Martínez-Tejada, H.V., Solorza-Feria, O.: Characterization and electrocatalytic properties of sonochemical synthesized PdAg nanoparticles. Mater. Chem. Phys. **134**, 1013–1019 (2012)
7. Koh, J.-H., Abbaraju, R., Parthasarathy, P., Virkar, A.V.: Design and synthesis of degradation-resistant core–shell catalysts for proton exchange membrane fuel cells. J. Power Sour. **261**, 271–277 (2014)

8. Fofana, D., Natarajan, S.K., Hamelin, J., Benard, P.: Low platinum, high limiting current density of the PEMFC (proton exchange membrane fuel cell) based on multilayer cathode catalyst approach. Energy **64**, 398–403 (2014)
9. Zhu, Y., Chen, X., Liu, J., Zhang, J., Xu, D., Peng, W., et al.: Rational design of Fe/N/S-doped nanoporous carbon catalysts from covalent triazine frameworks for efficient oxygen reduction. Chemsuschem **11**(11), 2402–2409 (2018)
10. Yin, Y., Liu, J., Chang, Y., Zhu, Y., Xie, X., Qin, Y., et al.: Design of Pt-C/Fe-N-S-C cathode dual catalyst layers for proton exchange membrane fuel cells under low humidity. Electrochim. Acta **296**, 450–457 (2019)

Capacity Optimization of a Renewable Energy System Coupled with Large-Scale Hydrogen Production and Storage

Sheng Zhang[1(✉)], Xin Wang[2], Bo Li[1], Jianfeng Dai[1], and Jinyang Zheng[3]

[1] China Electric Power Planning and Engineering Institute, Beijing 100120, China
szhang@eppei.com
[2] Huadian Heavy Industries Co., LTD., Beijing 100071, China
[3] College of Energy Engineering, Zhejiang University, Hangzhou 310027, China

Abstract. Hybrid renewable energy and hydrogen energy systems have been proved to be a reliable and cost competitive option for power generation and hydrogen supply. However, the inappropriate capacity of hydrogen production and storage may result in out-of-balance of the power supply side and the hydrogen consumption side. In this paper, a simplified mathematical modeling of the hybrid energy system, including power generation, hydrogen production and storage has been presented to optimize the capacity of alkaline electrolyzer and hydrogen storage tank. Multi-objective functions are adopted in the capacity optimization model, including abandoned rate of renewable power, hydrogen supply fluctuation, and utilization efficiency of electrolyzer and hydrogen storage tank. A meta-heuristic algorithm (*i.e.*, improved multi-objective particle swarm optimization algorithm) is chosen to solve the model. A hybrid energy system with a distributed photovoltaic power station with the rated power of 7000 kW has been designed to satisfy the hydrogen demand of 720 kg/d of a chemical plant. The results reveal that the optimal capacity configuration of the hybrid energy system is 4971 kW for the alkaline electrolyzer and 937 Nm^3 for hydrogen storage tank during a period of 8760 h. Compared with the empirical model and single-objective optimization model, the proposed multi-objective optimization model is found helpful to optimize the capacity of hybrid energy system and gives better results regarding renewable energy utilization rate, equipment usage rate, and hydrogen supply stability.

Keywords: Capacity optimization · Renewable energy system · Hydrogen · Simulation model

1 Introduction

The rapid depletion of fossil fuel resources, the massive carbon emission and the environmental problems related with their burning have generated growing interest in renewable energy. However, an essential feature of most renewable energy is their intermittency, that decreases the reliability of electricity supply and hinders their large-scale applications.

H. Sun et al. (Eds.): WHTC 2023, SPPHY 393, pp. 412–421, 2024.
https://doi.org/10.1007/978-981-99-8631-6_40

One method of overcoming this disadvantage is to apply an energy storage system, such as pumped-storage power [1], electrochemical energy storage [2], and hydrogen energy [3]. Among these energy storage methods, hydrogen energy has several unique advantages including long term and large-scale energy storage, flexible hydrogen-electricity conversion, leading to increasing interest in hybrid renewable energy and hydrogen energy system [4, 5].

The focus on hybrid energy system is highlighted by many extensive studies, which cover economic analysis [6], system planning and design [7], and capacity optimization [8]. The capacity optimization of electrolyzer and hydrogen tank has a great effect on renewable energy utilization, hydrogen supply reliability, and net present cost. Much work so far has focused on capacity optimization of hybrid energy system using optimization algorithms and single-objective optimization. For example, flower pollination algorithm, particle swarm optimization (PSO) algorithm, and genetic algorithm are studied in previous studies, and show great results in capacity optimization [9]. However, single-objective optimization is difficult to take into account other requirements of hybrid energy system and to achieve simultaneous optimization [10], and the technical process concerning hydrogen is often oversimplified, which leads to distortion of optimization results for practical applications.

In this study, a distributed photovoltaic power station with rated power of 7000 kW and a chemical plant with hydrogen demand of 720 kg/d are chosen as the source side and hydrogen load side, respectively. Considering the energy utilization, hydrogen supply reliability, and the equipment usage rate, multi-objective optimization and PSO algorithm are used to optimize the capacity of electrolyzer and hydrogen tank. A comprehensive mathematical model of hybrid energy system is proposed to investigate the main parameters affecting the capacity optimization results during a period of 8760 h. The performance of proposed multi-objective optimization model is also compared with the empirical model and single-objective optimization model.

2 Mathematical Model of the Hybrid Energy System

The proposed hybrid energy system includes photovoltaic (PV) power, electrolyzer, hydrogen storage tank, compressor, power grid, and chemical plant, as shown in Fig. 1. The primary power source is PV power, and the power grid is the backup power source in case that the PV power is unable to fulfill the energy demand of the electrolyzer. Hydrogen produced by the electrolyzer is stored in the tank, and then compressed into high-pressure gas to meet the hydrogen demand of a chemical plant. The bi-converter acts as an inverter to convert AC power to DC to fulfill the DC load demand of electrolyzer. The detailed mathematical models of each part of the system are introduced as follows.

2.1 Solar Power System

The output power of PV panel (P_{sol}) depends on the solar radiation and atmospheric conditions, and it can be expressed as follows [11].

$$P_{pv}(t) = N_{pv} P_{rat} f_{loss} \frac{G_h(t)}{G_s} [1 + \alpha_P (T_c - T_s)] \tag{1}$$

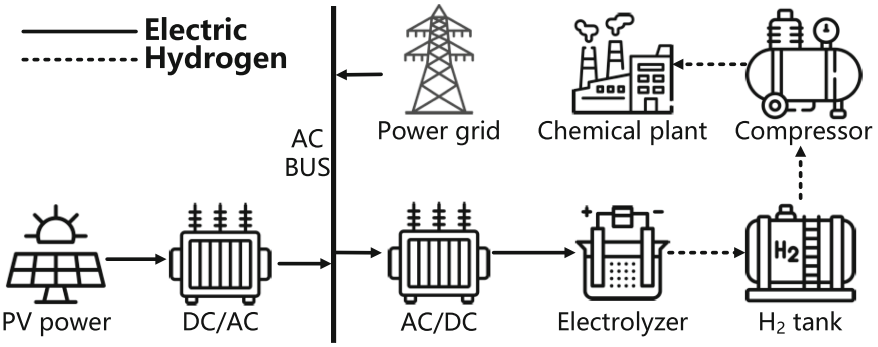

Fig. 1. Schematic diagram of the hybrid energy system.

where, N_{pv} is the number of PV panels, P_{rat} is the rated power of PV panel, f_{loss} is the loss factor of PV panel concerning shadow, dirt, and temperature, G_s is the standard incident radiation, $G_h(t)$ is the hourly solar radiation incident on the PV panel, α_P is the temperature coefficient of power, T_c is the PV cell real-time temperature, and T_s is the PV cell temperature under standard test conditions.

2.2 Electrolyzer

The electricity of solar system is used to produce hydrogen by electrolyzer. The power capacity of electrolyzer is considered as an optimization objective in this study.

The mass flow rate of produced hydrogen (ν_{e,H_2}) can be calculated as:

$$\nu_{e,H_2} = \frac{P_{pv}(t)\eta_{el} \times 3600}{HHV_{H_2}} \tag{2}$$

where, η_{el} is the efficiency of electrolyzer and HHV_{H_2} is the heating value of hydrogen.

2.3 Hydrogen Tank

Hydrogen generated by electrolyzer is stored in hydrogen tank, and hydrogen leakage during the storage is ignored. In terms of the capacity optimization, the storage capacity of hydrogen tank has been considered as an optimization objective.

2.4 Compressor

Power consumed by compressor (P_{comp}) is related with the inlet and output pressure of hydrogen, the flow rate of hydrogen, and the efficiency of compressor. It can be expressed as follow:

$$P_{comp} = C_{p,H_2} \frac{T_{comp}}{\eta_{comp}} \left[\left(\frac{P_{in}}{P_{out}} \right)^{\frac{k-1}{k}} - 1 \right] W_{comp} \tag{3}$$

where, $C_{p,\mathrm{H_2}}$ is the specific heat capacity of hydrogen, T_{comp} is the inlet ambient temperature, η_{comp} is the efficiency of compressor, P_{in} and P_{out} are the inlet and outlet pressure of hydrogen, k is the specific heat ratio of hydrogen at the standard condition, and W_{comp} is the gas flow rate.

3 Objective Functions, PSO Algorithm, and Constraints

3.1 Objective Functions

Considering the energy utilization rate of solar power, the hydrogen supply stability, and the equipment utilization rate of electrolyzer and tank, three objective functions (*i.e.*, abandonment rate of solar power, hydrogen supply shortage rate, and vacancy rate of equipment) are chosen and defined as:

$$\eta_{solar}^{AR} = \frac{1}{8760}\sum_{t=1}^{8760}\frac{P_{ex}(t)}{P_{pv}(t)} \tag{4}$$

$$\eta_{load}^{HSS} = \frac{1}{8760}\sum_{t=1}^{8760}\frac{M_{It,\mathrm{H_2}}(t)}{M_{load,\mathrm{H_2}}(t)} \tag{5}$$

$$\eta_{equ}^{vr} = 1 - \frac{1}{2\times 8760}\left(\sum_{t=1}^{8760}\frac{M_{tank}(t)}{M_{rated,tank}} + \sum_{t=1}^{8760}\frac{P_{el}(t)}{P_{rated,el}}\right) \tag{6}$$

where, η_{solar}^{AR} is the abandonment rate of solar power, P_{ex} is the excess solar power, η_{load}^{HSS} is the hydrogen supply shortage rate, $M_{It,\mathrm{H_2}}$ is the insufficient mass of hydrogen supply, $M_{load,\mathrm{H_2}}$ is the hydrogen demand, η_{equ}^{vr} is the vacancy rate of electrolyzer and tank, M_{tank} is the mass of stored hydrogen in the tank, $M_{rated,tank}$ is the rated hydrogen mass of the tank, P_{el} is the power of electrolyzer, $P_{rated,el}$ is the rated power of electrolyzer.

3.2 PSO Algorithm

PSO algorithm is based on the population of swarms in which each individual particle is a potential solution of the problem [12]. The best solution is found by the swarm of particles in a search space. The moving path of a particle in a D-dimensional space is adjusted according its own optimal value as well as the swarm's optimal value. The principle and steps of PSO algorithm have been thoroughly introduced in previous studies [12–14], and the control parameters in this study are presented in Table 1. PSO algorithm has been run for a maximum number of iterations of 200 for 1 h time interval during a whole year data set, *i.e.*, 8760 h.

It is worthwhile mentioning that a linear weighting method is adopted to convert the multi-objective problem (*i.e.*, three objectives in this study) into a single-objective one by using the following equation:

$$F_{mul} = w_1\eta_{solar}^{AR} + w_2\eta_{load}^{HSS} + w_3\eta_{load}^{HSS} \tag{7}$$

where, w_1, w_2, and w_3 are the weights of three objective functions, respectively, and the sum of three weights is equal to 1.

Table 1. Control parameters used in PSO algorithm

Parameters	Symbol	Value
Dimension of the problem	D	3
Population size	NS	200
Maximum iteration number	$IT_{\max}$	200
Weighting factors	c_1, c_2	1.5
Maximum inertia weight	$W_{\max}$	0.8
Minimum inertia weight	$W_{\min}$	0.4
Number of objective functions	OB	3

3.3 Constraints

Constraints including energy balance, hydrogen flow balance, input power and hydrogen storage capacity constraint should be carefully considered to ensure the accuracy of the model concerning practical applications.

Energy balance. It involves in solar power, auxiliary electricity from grid, and power consumed by electrolyzer and compressor at time t. It can be expressed as follow:

$$P_{pv}(t) + P_{ex}(t) = P_{el}(t) + P_{comp}(t) \tag{8}$$

where, P_{ex} is the auxiliary electricity from grid, P_{el} is the electrolyzer power.

Hydrogen flow balance. It is related to the supply, storage, and consumption of hydrogen, which can be further calculated as follow.

$$M_{e,\mathrm{H_2}}(t) = M_{tank}(t+1) - M_{tank}(t) + M_{load,\mathrm{H_2}}(t) - M_{ss,\mathrm{H_2}}(t) \tag{9}$$

where, $M_{\mathrm{e,H_2}}$ is the hydrogen generated by electrolyzer, M_{tank} is the stored hydrogen, $M_{\mathrm{load,H_2}}$ is the needed hydrogen of chemical plant, $M_{ss,\mathrm{H_2}}$ is the supply shortage of hydrogen.

Capacity constraints. The input power of electrolyzer cannot exceed the maximum power or be lower than the minimum starting power. The stored hydrogen in the tank cannot exceed its maximum capacity.

$$P_{el,\min} \le P_{el} \le P_{el,\max} \tag{10}$$

$$0 \le M_{\mathrm{tank}} \le M_{\mathrm{tank,max}} \tag{11}$$

where, $P_{el,\min}$ and $P_{el,\max}$ are the minimum and maximum power of electrolyzer, respectively, and $M_{\mathrm{tank,max}}$ is the maximum storage capacity of hydrogen tank.

4 Results and Discussions

The output power of PV system and hydrogen demand of the chemical plant in a typical week are shown in Fig. 2. The output power of PV system shows a strong volatility, which reaches the highest power at midday. The average hydrogen demand is about 30 kg/h, and the curve of hydrogen demand indicates the relatively small fluctuation. The resource data are further used in the capacity optimization.

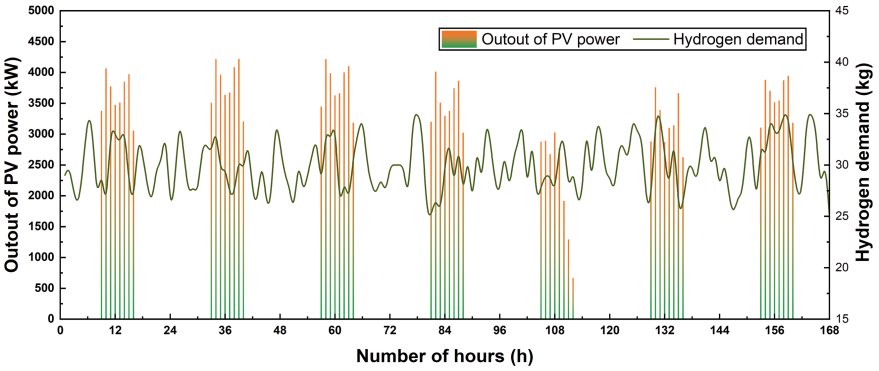

Fig. 2. Output power of PV system and hydrogen demand in a typical week.

Figure 3 reveals convergence characteristic of PSO algorithm with different objective functions. It is obvious that all the simulations converge in almost preliminary 30–100 iterations. Table 2 shows the capacity optimization results with different optimization methods, and the capacity configuration based on empiric value (*i.e.*, 80% of the rated PV power for electrolyzer power, and hydrogen yield in 12 h at the rated electrolysis power for the storage capacity of hydrogen tank) is also tested using the simulation model. The results show that the single-objective function is able to reach its corresponding optimal solution, but leads to the unbalance of other objective functions. For example, when selecting η_{equ}^{vr} as the objective function, the optimization results are 2942 kW for electrolyzer and 106 Nm^3 for hydrogen tank, and the η_{equ}^{vr} reaches the lowest. However, the storage capacity of hydrogen tank is too low to satisfy the electricity storage demand, resulting in a high abandonment rate of solar power. Compared with empiric value and single-objective function, multi-objective optimization shows a better performance, and the weighting factors of three objective functions (i.e., w_1, w_2, and w_3) are 0.3557, 0.3427, and 0.3016, respectively. Based on the simulation results of multi-objective optimization, the optimal capacity values are 4971 kW for electrolyzer and 937 Nm^3 for hydrogen tank. The η_{solar}^{AR}, η_{load}^{HSS}, and η_{equ}^{vr} for multi-objective optimization are 0.1737, 0.2484, and 0.7389, respectively, indicating the good performance of multi-objective optimization. It should be pointed out that even after the capacity optimization, the η_{equ}^{vr} is still too high because of the low annual utilization hours of solar power, and hybrid wind-photovoltaic complementary power generation is suggested to improve the usage rate of electrolyzer and hydrogen storage tank [15].

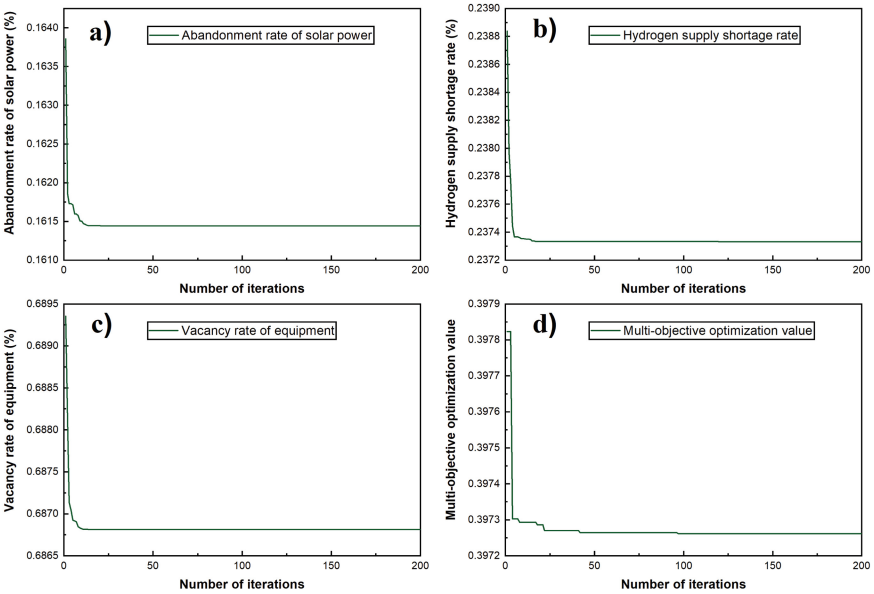

Fig. 3. Convergence characteristic of PSO algorithm with different objective functions. (a. abandonment rate of solar power, b. hydrogen supply shortage rate, c. vacancy rate of equipment, d. multi-objective function)

Table 2. Capacity optimization results with different optimization methods

Optimization method		Electrolyzer power (kW)	Capacity of tank (Nm^3)	η_{solar}^{AR}	η_{load}^{HSS}	η_{equ}^{vr}
Single-objective optimization	η_{solar}^{AR}	5078	2000	0.1617	0.2384	0.7833
	η_{load}^{HSS}	5313	2000	0.1622	0.2375	0.7845
	η_{equ}^{vr}	2942	106	0.3893	0.4566	0.6868
Multi-objective function		4971	937	0.1737	0.2484	0.7389
Empiric value		5600	823	0.1932	0.2640	0.7436

For further discussion, the capacity configuration obtained by multi-objective optimization has been chosen because of its better results. Figure 4 depicts the power input and output of the hybrid energy system in a typical week. It can be observed that the power of electrolyzer mainly depends on solar power generation, and when the PV power is insufficient or zero, auxiliary power from the grid is needed to supply power to the compressor. When the output power of PV is less than the minimum power of electrolyzer (*i.e.*, 40% of the rated power in this study), the electrolyzer is shut down, and the hydrogen supply mainly depends on the hydrogen stored in hydrogen tank.

In order to gain insight into the hydrogen management of the hybrid energy system, a complete data for a typical week concerning the hydrogen flow balance has been

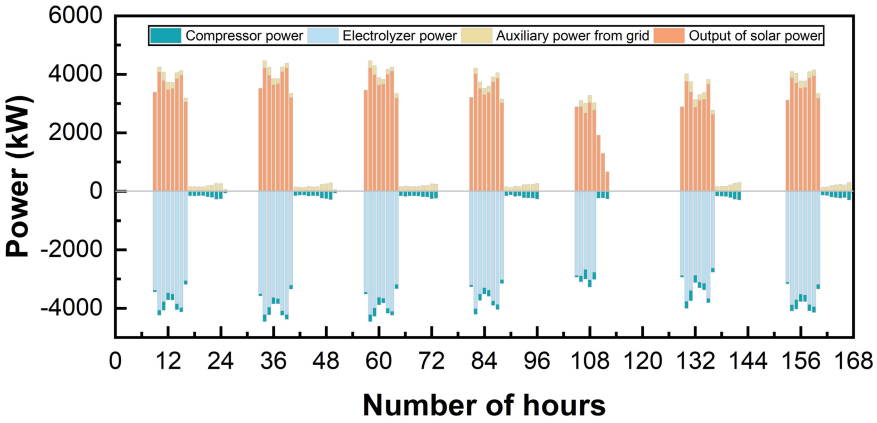

Fig. 4. Power input and output of hybrid energy system in a typical week.

selected. As shown in Fig. 5, the supply shortage of hydrogen usually occurs during the shortage of PV power generation or the startup stage of electrolyzer. Besides, the hydrogen produced by electrolyzer is significantly influenced by the remaining hydrogen stored in hydrogen tank, the hydrogen demand, and the output power of PV power system. As for 4971 kW electrolyzer, a maximum of 87.6 kg/h can be produced, and the highest hydrogen storage capacity of hydrogen tank is 1347 kg. Further, it can be concluded that with the increase of electrolyzer power and the storage capacity of hydrogen tank, the hydrogen supply shortage rate and the energy utilization rate of solar power increases, however, accompanied with the decrease of equipment utilization rate, *i.e.*, electrolyzer and hydrogen tank.

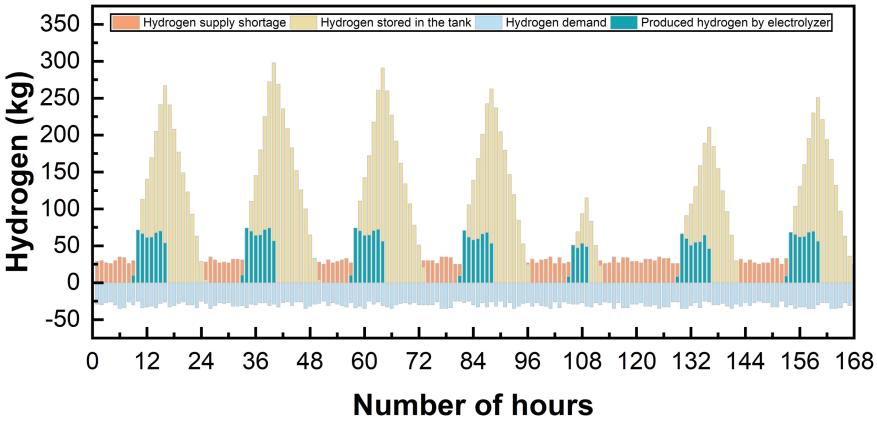

Fig. 5. Hydrogen balance of hybrid energy system in a typical week.

5 Conclusion

Based on PSO algorithm and multi-objective optimization, a hybrid energy system including solar energy and hydrogen energy is proposed. The optimization functions and the mathematical model are key issues in designing of high-efficiency and stable hybrid energy system. Compared with single-objective function optimization and empirical algorithm, multi-objective function optimization shows a better performance in terms of the balance of different optimization objectives. As to a 720 kg/d chemical plant with a distributed photovoltaic power station with rated power of 7000 kW, the optimal capacity configuration for the hybrid system is 4971 kW for electrolyzer and 937 Nm^3 for hydrogen tank according to the capacity optimization results. The proposed optimization model is promising in the capacity planning of hybrid energy system, which promotes large-scale applications of hydrogen energy in power industry.

References

1. Anagnostopoulos, J.S., Papantonis, D.E.: Simulation and size optimization of a pumped–storage power plant for the recovery of wind-farms rejected energy. Renew. Energ. **33**, 1685–1694 (2008)
2. Zhang, L., Hu, X., Wang, Z., Ruan, J., Ma, C., Song, Z., et al.: Hybrid electrochemical energy storage systems: an overview for smart grid and electrified vehicle applications. Renew. Sustain. Energ. Rev. **139**, 110581 (2021)
3. Kiryanova, N.G., Matrenin, P.V., Mitrofanov, S.V., Kokin, S.E., Safaraliev, M.K.: Hydrogen energy storage systems to improve wind power plant efficiency considering electricity tariff dynamics. Int. J. Hydrogen Energ. **47**, 10156–10165 (2022)
4. Eriksson, E.L.V., Gray, E.M.: Optimization and integration of hybrid renewable energy hydrogen fuel cell energy systems—a critical review. Appl. Energ. **202**, 348–364 (2017)
5. Singh, A., Baredar, P., Gupta, B.: Techno-economic feasibility analysis of hydrogen fuel cell and solar photovoltaic hybrid renewable energy system for academic research building. Energ. Convers. Manage. **145**, 398–414 (2017)
6. Kalinci, Y., Hepbasli, A., Dincer, I.: Techno-economic analysis of a stand-alone hybrid renewable energy system with hydrogen production and storage options. Int. J. Hydrogen Energ. **40**, 7652–7664 (2015)
7. HassanzadehFard, H., Tooryan, F., Collins, E.R., Jin, S., Ramezani, B.: Design and optimum energy management of a hybrid renewable energy system based on efficient various hydrogen production. Int. J. Hydrogen Energ. **45**, 30113–30128 (2020)
8. Zhang, W., Maleki, A., Rosen, M.A., Liu, J.: Optimization with a simulated annealing algorithm of a hybrid system for renewable energy including battery and hydrogen storage. Energy **163**, 191–207 (2018)
9. Moghaddam, M.J.H., Kalam, A., Nowdeh, S.A., Ahmadi, A., Babanezhad, M., Saha, S.: Optimal sizing and energy management of stand-alone hybrid photovoltaic/wind system based on hydrogen storage considering LOEE and LOLE reliability indices using flower pollination algorithm. Renew. Energ. **135**, 1412–1434 (2019)
10. Ruiming, F.: Multi-objective optimized operation of integrated energy system with hydrogen storage. Int. J. Hydrogen Energ. **44**, 29409–29417 (2019)
11. Das, U.K., Tey, K.S., Seyedmahmoudian, M., Mekhilef, S., Idris, M.Y.I., Van Deventer, W., et al.: Forecasting of photovoltaic power generation and model optimization: a review. Renew. Sustain. Energ. Rev. **81**, 912–928 (2018)

12. Wang, D., Tan, D., Liu, L.: Particle swarm optimization algorithm: an overview. Soft. Comput. **22**, 387–408 (2018)
13. Poli, R., Kennedy, J., Blackwell, T.: Particle swarm optimization: an overview. Swarm Intell. **1**, 33–57 (2007)
14. Du, K.-L., Swamy, M.N.S.: Particle swarm optimization. In: Search and Optimization by Metaheuristics: Techniques and Algorithms Inspired by Nature, pp. 153–73 (2016)
15. Shi, X., Qian, Y., Yang, S.: Fluctuation analysis of a complementary wind–solar energy system and integration for large scale hydrogen production. ACS Sustain. Chem. Eng. **8**, 7097–7110 (2020)

High Efficiency Fuel Cell Stack and Key Technologies of Power Module

Che-Jung Hsu[1](✉), Cheng-Huei Lin[1], Chih-Hung Lee[1], Li-Duan Tsai[2], and Chien-Ming Lai[2]

[1] CHUNG-HSIN Electric and Machinery mfg. corp. No.25, Wunde Rd., Gueishan Dist., Taoyuan City 333, Taiwan
TW013124@chem.com.tw

[2] Material and Chemical Research Laboratories, Industrial Technology Research Institute, Bldg.77, No.195, Sec.4, Chung Hsing Rd., Chutung, Hsinchu 310, Taiwan

Abstract. In this paper, the development of key technologies in fuel cell stacks and fuel cell power modules are reported, with emphasis on high-volume production (>10,000 units/year). Fuel cell stack design is focused on the development of high-efficiency membrane electrode assemblies ($\geqq$300 mA/cm^2 @0.8 V) suitable for continuous roll-to-roll manufacturing and high volumetric efficiency stacks (1.5 kW/L) with power rating of at least 10 kW. Power module design focuses on the union of liquid-cooled fuel cell stack, smart power conditioning technology, battery, hydrogen storage system and balance-of-plant into a fully-integrated, drop-in unit for MHE (Material Handling Equipment) systems. Technical verification was conducted by integrating the fuel cell power module into an automated guided vehicle as a turn-key replacement for the original power system. Power module performance was demonstrated with continuous current loading up to 240 A and peak current loading of 300 A. All core technologies of the fuel cell power module are deliverable as a free-standing total solution, expanding the potential applications beyond vehicle systems, and allowing rapid commercialization of related technologies.

Keywords: Fuel cell stack · Fuel cell power module · Material handling equipment · Turn-key replacement

1 Introduction

1.1 Technology Overview

This article reports on the technology of integrating fuel cells with secondary batteries and balance-of-plant components into a fuel cell power module for the material handling industry. The proton-exchange membrane fuel cell (PEMFC) is a well-researched and proven technology for a wide range of operating conditions. The BoP can be divided into three sub-systems: anode, cathode, and coolant. The anode sub-system includes hydrogen storage, re-circulation, and purging components. Hydrogen is compressed to 5000 PSI and is stored in an onboard tank. Re-circulation and purging are closely related,

H. Sun et al. (Eds.): WHTC 2023, SPPHY 393, pp. 422–428, 2024.
https://doi.org/10.1007/978-981-99-8631-6_41

where unconsumed hydrogen is recycled to the fuel cell stack inlet after excess water is separated and, along with other unwanted inert chemicals, is purged from the anode sub-system. The cathode sub-system includes air humidification and heat exchange components with the purpose of delivering humidified air to the fuel cell stack. The coolant sub-system is comprised of the thermal management components including coolant pump, fan, and radiator. Selection criteria for BoP components is intimately connected to fuel cell stack design and intended operating conditions, in addition to the cost and availability considerations discussed in the next sub-section.

2 Fuel Cell Stack and Power Module

This section introduces the key components of the fuel cell stack and the power module. Special emphasis is placed on the electro-chemical performance of the stack under different operating conditions. Since the power module consists of a fuel cell stack and a lithium-ion battery pack, the interaction between these two power sources during the operation of the propulsion system was also carefully examined.

2.1 Membrane-Electrode Assembly

The quality of the MEA design will affect the catalyst-use efficiency in the electrode, the flow rate requirements of fuel and air, the uniformity of current distribution, and the level of discharge efficiency.

The catalyst and the binder are uniformly coated by mixing and dispersing technology, and a highly dispersible catalyst slurry is prepared. Through the catalyst coating technology, the reaction triple phase boundary required for fuel cell reaction is constructed. The use of catalyst-coated membrane (CCM) continuous processing technology, such as Roll-to-Roll manufacturing in Fig. 1, greatly shortens the tedious batch processing time, improves the yield and increases the effective utilization of catalyst.

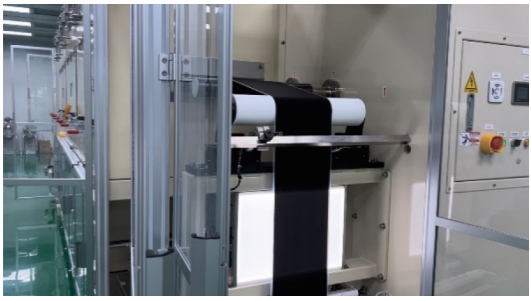

Fig. 1. CCM roll-to-roll manufacturing

This article exhibits a liquid-cooled fuel cell operating at 70 °C, referring to the DOE standard ($\geqq$300 mA/cm^2 @0.8 V) [1] for high-powered MEAs. The MEA was tested with reactant stoichiometry of 1.5X and 2.5X for hydrogen and oxygen, respectively.

A 5000-h constant current discharge mode life test has been completed. Under the discharge of 300 mA/cm^2, the ΔV/V performance of the MEA declined by 0.15%, and under the discharge of 360 mA/cm^2, the ΔV/V performance of the MEA declined by 2.55%, verifying the lifespan of the high-power MEA ≧5000 h, as shown in Fig. 2 performance-time graph.

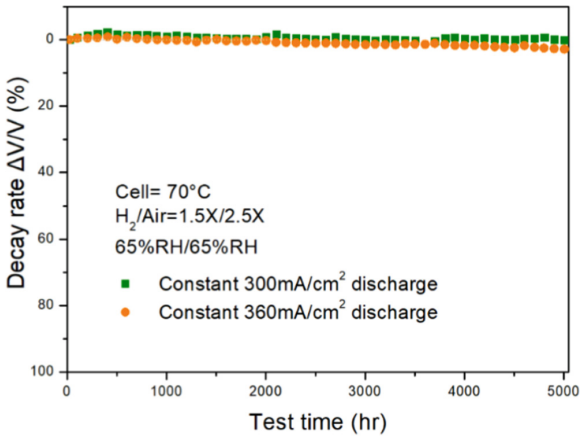

Fig. 2. Performance decay-time graph for MEA at 5000 h

2.2 Fuel Cell Stack

The design of a high-efficiency liquid-cooled fuel cell stack was based on the experience and assembly mechanism of existing traditional fuel cell stack designs. The requirements of the target industry include both the power requirements (≥10 kW) and the volume power density requirements of material handling vehicles and after testing three full-sized liquid-cooled fuel cell stacks were assembled for demonstration purposes (Fig. 3), to determine optimal stack operating conditions (Table 1), each fuel cell stack was activated through repeated current load cycling until maximum performance was achieved. The highest performance record measured by I-V curve is 12.5 kW (250 Amps @ 50 V) at the stoichiometric ratio of 1.2 and 2.0 for anode and cathode, respectively (Fig. 4). Using the measured stack volume (8.24 L) [2], the power volume density is 1.51 kW/L.

2.3 Fuel Cell Power Module

The fuel cell power module is mainly divided into five major items: liquid-cooled fuel cell stack, thermal management module, cathode air humidification module, hydrogen storage and delivery module, and energy storage module (Fig. 5).

Before assembling into a power module, each subsystem was assembled on a test bench for BoP component validation testing. The test bench is equipped with control boards, user interface, load banks and other testing equipment (錯誤! 找不到參照來

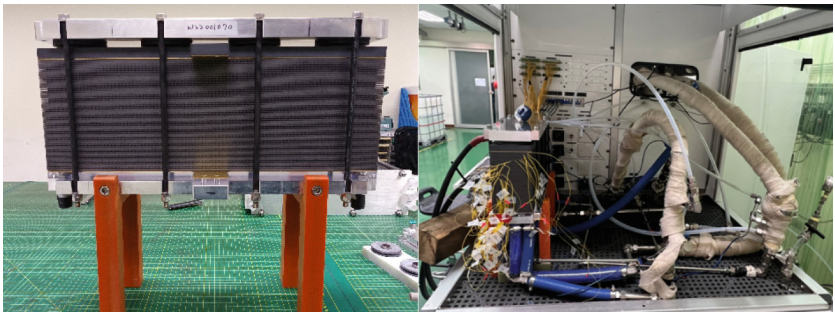

Fig. 3. Full-sized fuel cell stack and testing equipment

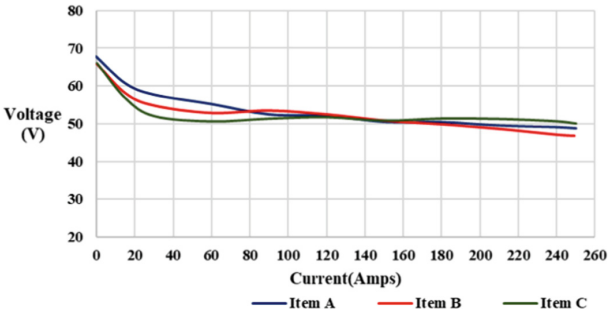

Fig. 4. Fuel cell stack performance curves

Table 1. Fuel cell stack operating parameters

	Item	Stoichoimetry	Temp./RH
Anode	A	1.5	65 °C/100RH%
	B	1.5	70 °C/50RH%
	C	1.2	70 °C/50RH%
Cathode	A	3	65 °C/100RH%
	B	3	70 °C/50RH%
	C	2	70 °C/50RH%
Coolant	A	–	65
	B	–	70
	C	–	70

源◦). The operating conditions of the power module system was simulated on the test bench through the user interface designed specifically for testing the system control. Various fuel cell stacks and BoP components were tested before deciding on the final BoP configuration. Once the whole system was tested and confirmed cooperating with

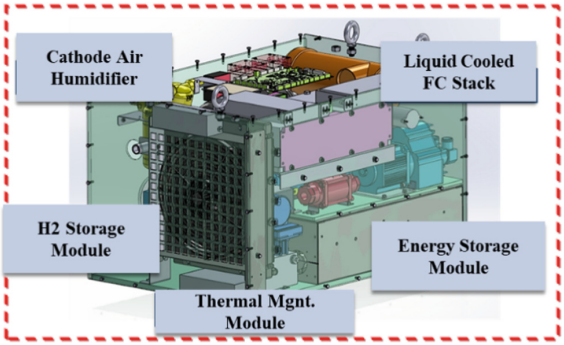

Fig. 5. Schematic diagram of the five major modules of a fuel cell power module

each other, functional stability tests, as shown in (Fig. 7), were conducted for tuning system-wide parameters. During the system testing, it was confirmed that the module can reach 10.6 kW net power, meeting the target design requirement for the material handling equipment AGV market needs (Fig. 6).

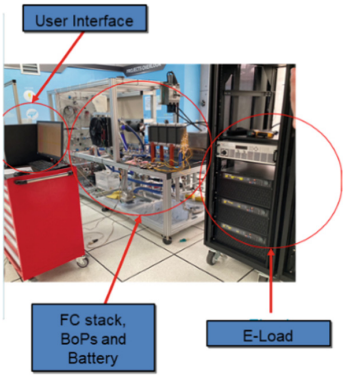

Fig. 6. Fuel cell stack with BoP components and battery on test bench

3 Power Module and AGV

The composition of the AGV system mainly includes two parts, namely the control system and the basic hardware. Furthermore, the control system can be mainly divided into the management and monitoring system, the vehicle controller and navigation system; the basic hardware mainly includes chassis, locomotion drivers, sensors, power units (secondary batteries or fuel cells), shelves, docks, network equipment and other parts. In order to complete the relevant technical verification, it is planned to integrate the power module into a commercial unmanned vehicle to replace the original secondary battery module. Integration includes not just the power module, but also a hybrid power control system, AGV system peripherals, and auxiliary components as shown in Fig. 8.

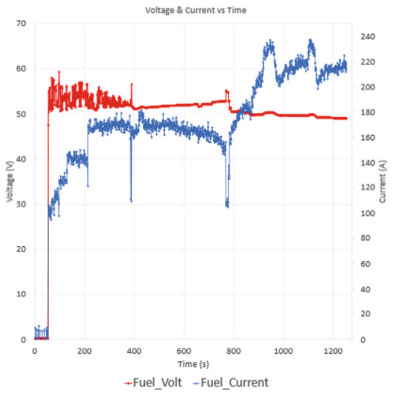

Fig. 7. System performance test output graph

During the integration and testing, empirical data will be collected, and a complete layout of the integration interface between the power module and the transport vehicle system will be developed. Once the integration interface is fully developed, the application of fuel cell power modules is planned to be extended to other products, and related technologies can be commercialized.

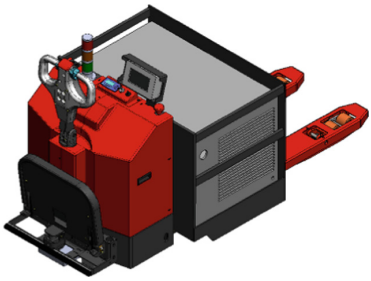

Fig. 8. AGV system with FC module

References

1. Hydrogen and Fuel Cell Technologies Office Multi-Year Research, Development, and Demonstration Plan of DOE, 3.4 Fuel Cells, 2016 (Updated May 2017)
2. Lan, H., Hao, D., Hao, W., He, Y.: Development and comparison of the test methods proposed in the Chinese test specifications for fuel cell electric vehicles. Energ. Rep. **8**, 565–579 (2022)

Effect of Fan Parameters on Forced-Convection Open-Cathode Proton Exchange Membrane Fuel Cells

Jiaxu Zhou, Zhifei Fang, and Huichao Deng(✉)

Beihang University, Beijing 100191, China
denghuichao@buaa.edu.cn

Abstract. Forced-convection open-cathode proton exchange membrane fuel cells have attracted much attention due to simple structure. The fan, as an important component of the stack, significantly influences the mass density and performance of the stack. Therefore, it is crucial to select the appropriate fan. In this study, the performance of stacks with different fans is compared and the optimal duty ratio and temperature of stacks under different load currents are determined. The experimental results show that excessive air volume reduces the performance of the stack, and the parasitic power should be taken into consideration. Additionally, the weight of the fan is is a significant factor that needs to be considered. Furthermore, the experimental results show that under the condition of sufficient air supply, the appropriate temperature rise is conducive to the improvement of stack performance. In order to reduce the weight of the stack, it is necessary to choose a reasonable fan.

Keywords: Forced-convection open-cathode proton exchange membrane fuel cell · Fan duty ratio · Net power density

1 Instruction

Proton exchange membrane fuel cell (PEMFC) has received a lot of attention in recent decades due to low temperature start-up, high efficiency and zero emissions [1]. PEMFC is a device that directly converts chemical energy to electric energy. Among several proton exchange membrane fuel cell types, forced-convection open-cathode PEMFC is more suitable for portable and unmanned aerial vehicles (UAV) energy because of removing the complex oxidant supply system [2]. The forced-convection PEMFC utilizes an axial fan as the air supply device. In addition to providing oxidant, the fan also serves to dissipate heat and remove water. Using only fans can make the stack more compact and reduce the mass of the stack and improve portability. However, because the cathode absorbs air directly from the atmosphere, the stack performance is sensitive to changes in cathode parameters, especially fans.

Water, thermal and gas management is critical for fuel cell. Fan air supply, heat dissipation and water remove coupling, water, thermal and gas management is more complex for forced-convection open-cathode PEMFC. Several studies have explored the

H. Sun et al. (Eds.): WHTC 2023, SPPHY 393, pp. 429–434, 2024.
https://doi.org/10.1007/978-981-99-8631-6_42

effect of air flow-rate selection [3–7]. These studies focused on performance performance and stack temperature variation. The research shown that the appropriate air flow rate can ensure the stack working at the optimum temperature without Membrane dehydration under adequate air supply. Other studies have explored the effects of parasitic power [8], fan placement parameters [9, 10].

In this work, we discussed the variation in the performance of three axial flow fans with different parameters installed on the same stack, and analyzed the possible causes of the variation in performance, and considered the weight of the fan as a factor in the selection of the fan. Finally, the relationship between fan duty ratio and fan temperature and performance is studied.

2 Experimental

2.1 Experimental Setup

For this work, we used a laboratory designed stack. The forced-convection OC-PEMFC consists of 15 cells. The 3 mm graphite was manufactured into bipolar plates using CNC (Computer Numerical Control) technology. The active area is 3.5 mm × 1.5 mm. Commercial MEA (Membrane Electrode Assembly) was used. Figure 1 shows the stack used in the experiment.

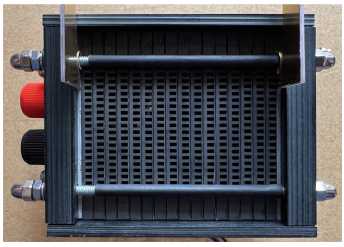

Fig. 1. Open-cathode stack

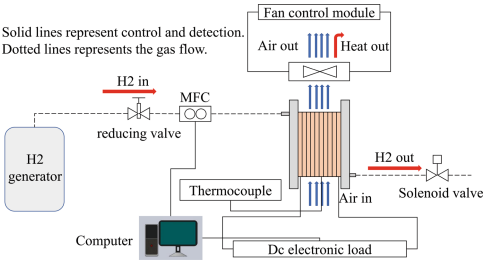

Fig. 2. Experimental schematic diagram

A hydrogen generator is used as the hydrogen source. The reducing valve is used to regulate the input pressure of the stack. An electronic load is used in order to obtain a polarization curve. A PWM controller is used to regulate air flow rate. Figure 2 shows the experimental schematic diagram.

2.2 Test Conditions

The forced-convection OC-PEMFC performance was tested with different axial flow fans. The fan parameters were shown in Table 1. Rated voltage of fan was 12 V. Temperature changes in the stack were measured using thermocouples inserted into the stack. The duty ratio varies from 100 to 30% to study the effect of the fan on the stack temperature and net power.

Table 1. Fan parameters

Fan model	Size (mm)	Actual power (W)	Air volume	Weight (g)
RB0412H12B-6	40*40*28	10.36656	50.4CFM	42
YS4015B12L	40*40*15	1.95408	14.83CFM	21
HD4010H12B	40*40*10	2.57712	13.95CFM	14

3 Results and Discussion

3.1 Effect of Different Fan on Stack Performance

In this work, we test the performance of the stack under different axial flow fans. The three axial fans have different parameters. Figure 3 shows the performance of stack. It is clearly observed that for the experimental stack, the performance of the stack does not change much under different fan conditions. From Table 1 we can see that the 4028 fan provides more air, but from Fig. 3 we can see that the excessive air flow slightly reduces the stack performance due to the excess water taken away.

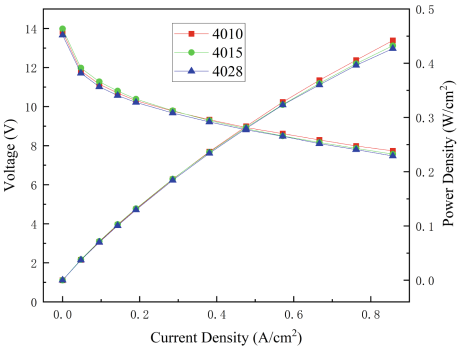

Fig. 3. Polarization curves

In open cathode stacks, the fan usually consumes the power generated by the stack. The net power density curve of the stack is shown in Fig. 4. After removing the parasitic

power of the fan, 4028 fan exhibited poor performance due to excessive parasitic power. It seems that the 4015 fan exhibits superior performance over the 4010 fan due to the smaller parasitic power. The performance gap between 4015 fan and 4010 fan decreases with the increase of load current. In addition, we can see from Table 1 that 4028 fan has the highest weight. This was followed by 4015 and 4010. The weight of the stack excluding the fan is 205 g. Comparatively speaking, 4015 and 4010 fans are better choices.

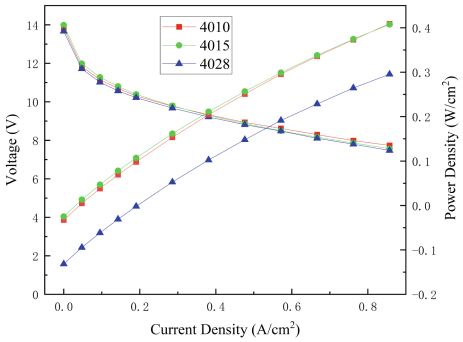

Fig. 4. Net power density curves

3.2 Effect of Fan Duty Ratio on Stack Temperature and Performance

Next, the influence of air flow rate variation on stack performance and temperature is analyzed. Adjust the air flow rate by adjusting the PWM duty ratio. The stack with 4015 fan was used for testing. Figure 5 shows the change of stack temperature with fan duty ratio at 2.5, 3 and 3.5 A. It can be seen from Fig. 3 that with the decrease of duty ratio, the temperature of the stack increases gradually, which can be attributed to the decrease of the heat dissipation capacity of the fan. Figure 6 shows the change curve of the net power density of the stack with the change of duty ratio under the load current conditions of 2, 2.5 and 3 A. It can be seen from Fig. 4 that with the reduction of duty ratio, the performance of the stack first improves and then begins to decline.

Combined with the temperature variation shown in Fig. 5, it can be considered that the performance variation is related to the temperature variation of the stack. Under sufficient oxidant conditions, with the increase of the stack temperature, the chemical reaction rate is accelerated, and the stack performance is improved. However, with the increase of the stack temperature, the high temperature will cause the membrane dehydration, the increase of ohmic resistance, and the stack performance is decreased. In addition, it can be seen that under the load current conditions of 2 A, 2.5 A and 3 A, the optimal operating temperature of the stack is about 44.3 °C, 49.8 °C and 49.5 °C, and the optimal duty ratio is about 30%, 40% and 50%, respectively.

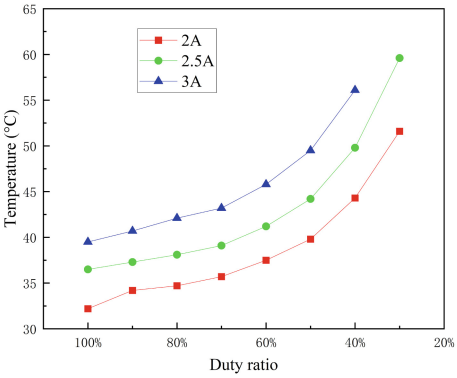

Fig. 5. The change of stack temperature with fan duty ratio

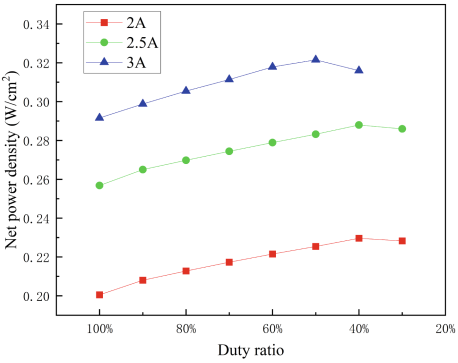

Fig. 6. The change of stack net power density with fan duty ratio

4 Conclusion

In this study, stacks with different fans were tested. The polarization curve and temperature of the stack were measured to investigate the effects of different fans and duty ratio. The experiment proves that the reasonable choice of fan is necessary. A suitable fan allows the stack to operate near the optimum operating point and effectively reduces the overall system weight.

References

1. Wang, Y., Ruiz Diaz, D.F., Chen, K.S., Wang, Z., Adroher, X.C.: Materials, technological status, and fundamentals of PEM fuel cells—a review. Mater. Today **32**, 178–203 (2020)
2. Kurnia, J.C., Chaedir, B.A., Sasmito, A.P., Shamim, T.: Progress on open cathode proton exchange membrane fuel cell: performance, designs, challenges and future directions. Appl. Energ. **283** (2021)
3. Wang, Z., Tongsh, C., Wang, B., Liu, Z., Du, Q., Jiao, K.: Operation characteristics of open-cathode proton exchange membrane fuel cell with different cathode flow fields. Sustain. Energ. Technol. Assess. **49** (2022)

4. Zeng, T., Zhang, C., Huang, Z., Li, M., Chan, S.H., Li, Q., et al.: Experimental investigation on the mechanism of variable fan speed control in Open cathode PEM fuel cell. Int. J. Hydrogen Energ. **44**, 24017–27 (2019). Author, F.: Contribution title. In: 9th International Proceedings on Proceedings, pp. 1–2. Publisher, Location (2010)
5. Song, Y., Zhang, C., Deshpande, A., Tan, K., Han, M.: Fixed air flow-rate selection by considering the self-regulating function of low power air-cooled PEMFC stack. Int. J. Heat Mass Transf. **158** (2020)
6. Huang, Z.-M., Su, A., Liu, Y.-C.: Development and testing of a hybrid system with a sub-kW open-cathode type PEM (proton exchange membrane) fuel cell stack. Energy **72**, 547–553 (2014)
7. Sasmito, A.P., Kurnia, J.C., Shamim, T., Mujumdar, A.S.: Optimization of an open-cathode polymer electrolyte fuel cells stack utilizing Taguchi method. Appl. Energ. **185**, 1225–1232 (2017)
8. Meyer, Q., Himeur, A., Ashton, S., Curnick, O., Clague, R., Reisch, T., et al.: System-level electro-thermal optimisation of air-cooled open-cathode polymer electrolyte fuel cells: air blower parasitic load and schemes for dynamic operation. Int. J. Hydrogen Energ. **40**, 16760–16766 (2015)
9. Ling, C.Y., Cao, H., Chen, Y., Han, M., Birgersson, E.: Compact open cathode feed system for PEMFCs. Appl. Energ. **164**, 670–675 (2016)
10. Zhao, C., Xing, S., Liu, W., Wang, H.: Air and H_2 feed systems optimization for open-cathode proton exchange membrane fuel cells. Int. J. Hydrogen Energ. **46**, 11940–11951 (2021)

Strategic Analysis of Hydrogen Energy Policies and Technology Layout in Major Countries

Xiao Han(✉), Hua-guang Yan, Jian-dong Kang, and Yang Li

China Electric Power Research Institute, Beijing 100192, China
hanxiao1118@126.com

Abstract. In the context of the global clean and low-carbon energy transition, hydrogen energy has become an important direction for energy technology innovation in the contemporary world. Many countries around the world have paid great attention to the development of hydrogen energy and leveraged it to the national strategies. This study firstly reviews the development of global hydrogen energy, focusing on the global hydrogen energy supply, hydrogen energy demand, the current situation and development trend of hydrogen energy. Secondly, based on data collected from government websites, key R&D institutions and well-known databases (e.g. CODIS database), a strategic analysis of hydrogen energy policies and technologies of main countries is conducted. In terms of policy, textual analysis is used to analyse the global hydrogen energy layout direction and the strategic positioning, strategic layout and strategic objectives of hydrogen energy in countries such as the United States, European Union, Japan and China. In terms of technology, the keyword search method is used to obtain data on scientific research projects in the field of hydrogen energy, and quantitative analysis is conducted to analyse the characteristics of the technical layout of global hydrogen energy research projects, and to analyse the funding of hydrogen energy projects and the focus of hydrogen energy technology research. Finally, suggestions for the future development of hydrogen energy are discussed.

Keywords: Hydrogen energy · Policy · Technology research and development · Strategy analysis

1 Introduction

With the acceleration of modern industrial processes and the increase in fossil fuel consumption leading to global warming, green and low-carbon development has become a global consensus [1]. In response to climate change, more than 130 countries and regions around the world have proposed carbon neutrality targets, and there is an unprecedented global determination and effort to accelerate the energy transition [2]. Compared with traditional fossil fuels, hydrogen energy is a new type of energy with the advantages of clean and zero carbon, long-term storage, flexibility and efficiency, multi-energy conversion and rich application scenarios [3]. Accelerating the development of hydrogen energy is an effective way to tackle the climate problem, reduce dependence on fossil

H. Sun et al. (Eds.): WHTC 2023, SPPHY 393, pp. 435–451, 2024.
https://doi.org/10.1007/978-981-99-8631-6_43

energy and help achieve deep decarbonization in areas that are difficult to reduce emissions, such as transport, industry and buildings [4]. In addition, with the development of renewable energy, hydrogen energy plays an increasingly important role in the new power system as a power medium and link [5].

Countries around the world attach great importance to the development of hydrogen energy. China, the United States, Europe, Japan and South Korea have elevated the development of hydrogen energy to a high level of national strategy and have continuously increased their support for hydrogen energy research and development and industrialization [6]. At the critical point of global carbon neutrality and economic downturn after the epidemic, hydrogen energy industry has become an important development area for many major countries/regions in the world to cope with global climate change and economic recovery after the epidemic [7, 8]. The literature [9–12] mainly analyzed the research in the field of hydrogen energy in the US, which is a global leader in the hydrogen fuel cell vehicle market and hydrogen refueling stations. The literature [13, 14] analyses Germany's national hydrogen energy strategy, which focuses on the transport, aviation, steel and chemical industries. The literature [15–17] analyses the development of hydrogen energy applications in Japan and South Korea. Due to the scarcity of resources and energy, both countries hope to develop a high level of hydrogen economy and move towards a hydrogen society. The literature [18, 19] analyses the advantages that Australia has in developing the hydrogen energy industry, and that new energy generation, hydrogen power generation and hydrogen export will be the main strategies for the development of hydrogen energy in Australia. China's hydrogen energy industry chain is currently focused on storage and transportation and hydrogen refueling, which drives the common development of upstream and downstream industries [20]. At present, the hydrogen energy industry chain with fuel cell as the main application has been initially commercialized globally, and it is expected that hydrogen energy will usher in an industrial explosion in the next 5 years [21].

The paper introduces the current situation and forecast of global hydrogen energy supply and demand, analyses the distribution and scale of hydrogen energy projects in operation, construction and planning worldwide, analyses the national hydrogen energy strategies of major countries in the world from the perspective of strategic positioning, strategic layout and strategic objectives, and analyses the progress and R&D direction of hydrogen energy technology in major countries around the world based on the funding of hydrogen technology projects and the focus of hydrogen technology research and development.

2 Overview of the Development of Hydrogen Energy Industry

2.1 Global Hydrogen Energy Supply

Global hydrogen production reaches 94 million tonnes in 2021, up 5% year-on-year, currently mainly from fossil energy sources. The International Energy Agency predicts that approximately 520 million tonnes of low-carbon hydrogen will be needed to achieve net zero global emissions by 2050. About 306 million tonnes of green hydrogen will come from renewable sources and 197.6 million tonnes of blue hydrogen from natural gas and coal combined with CCS technology; 16 million tonnes of low carbon electrolytic

hydrogen will be produced by electrolysis in nuclear and fossil fuel power plants with CCS. In comparison, 87 million tonnes of gray hydrogen is produced from natural gas and coal in 2020, mainly for the chemical and refining industries. The forecast for global hydrogen production in 2050 is shown (Fig. 1).

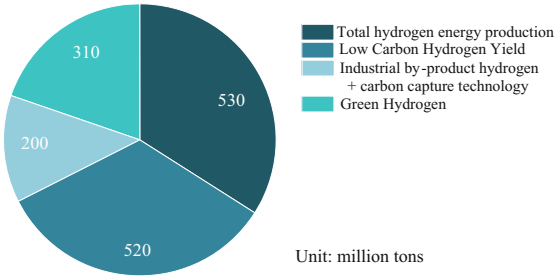

Fig. 1. Global hydrogen energy production forecast in 2050.

2.2 Global Hydrogen Energy Demand

In order to achieve net zero global emissions, the International Energy Agency predicts a total global demand for hydrogen energy of 528 million tonnes by 2050. The largest demand for hydrogen will come from transport, accounting for about 39% of the total, or 207 million tonnes, of which 91 million tonnes will be used for road transport, 90 million tonnes for shipping and 50 million tonnes of hydrogen for aviation. The industrial sector will use 187 million tonnes of hydrogen, about 35% of the total, of which 83 million tonnes will be used in the chemical industry, 54 million tonnes in the steel industry and 12 million tonnes in the cement industry. Power generation will account for approximately 19% of the total hydrogen demand, or 102 million tonnes per year. Hydrogen for construction and agriculture, 0.23 billion tonnes, is about 4% of the total. The forecast for global hydrogen demand in 2050 is shown (Fig. 2).

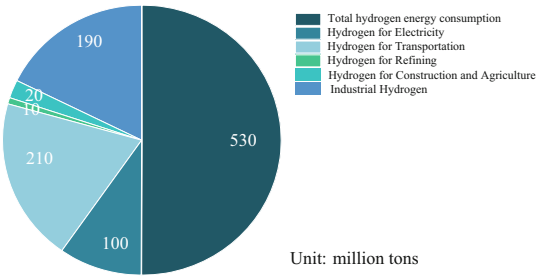

Fig. 2. Global hydrogen energy demand forecast in 2050.

2.3 Global Hydrogen Engineering

According to statistics, there are currently over 1400 hydrogen energy projects operating, constructed, and planned around the world. Among them, there are 227 hydrogen energy projects in operation, with a total hydrogen production scale of about 400 megawatts, mainly distributed in Europe, mainly producing hydrogen through electrolysis of water. The hydrogen produced is mainly used in transportation and industrial fields. The distribution of engineering areas for operation, construction, and planning are as shown in Fig. 3.

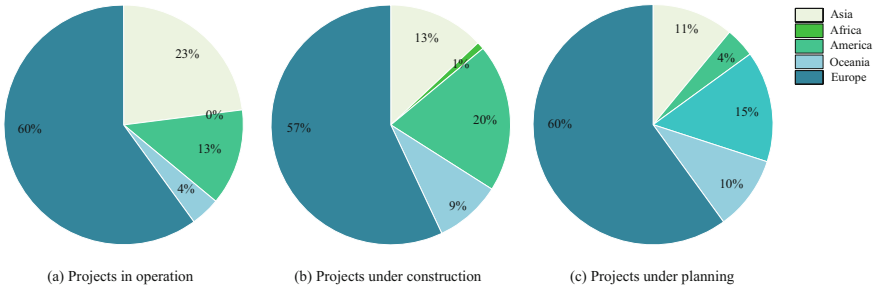

Fig. 3. Regional distribution of hydrogen energy engineering operations, construction, and planning around the world.

3 Strategic Analysis of Hydrogen Energy Policy

At present, the US, EU, Japan and other major economies in the world are actively laying out their hydrogen energy industries, and have released hydrogen energy development strategies and road maps, setting out a framework of action for hydrogen energy in terms of production, storage and transportation, application as well as technological innovation and investment.

3.1 Analysis of Global Hydrogen Energy Strategic Planning

As sustainable energy development and new energy technologies continue to advance, 35 countries and regions have issued strategies related to hydrogen energy by 2022.

In terms of the spatial layout of global hydrogen energy strategy reports, including 17 European countries, 6 Asian countries, 5 South American countries, 2 North American countries, 2 African countries and 2 Oceanian countries, it can be seen that the largest number of European countries have published hydrogen energy reports, accounting for about 50% of the world, becoming the global wind vane of hydrogen energy development. In terms of global hydrogen energy strategy report time promotion are as shown in Fig. 4, Japan took the lead in putting forward the Basic Hydrogen Energy Strategy in 2017, and in 2019, other countries put forward their national-level hydrogen energy

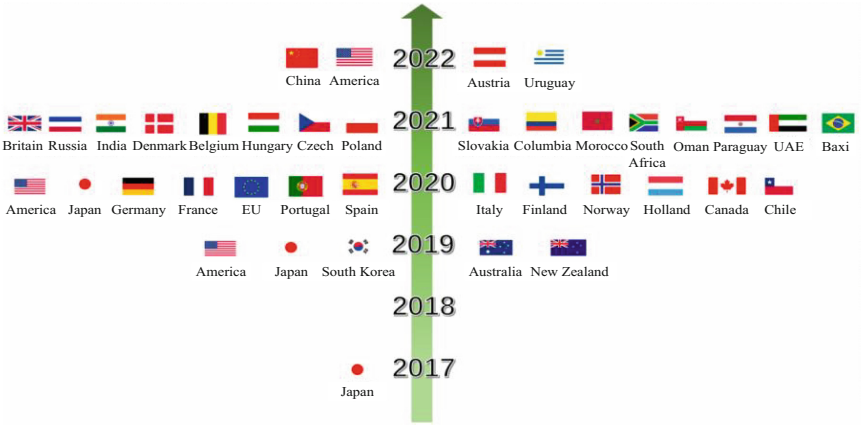

Fig. 4. Global hydrogen strategy release time.

strategic plans one after another, especially in 2020 and 2021 when the global hydrogen energy strategic plan release reaches its peak.

Through the analysis of the strategic planning reports on hydrogen energy in key countries and regions such as China, the US, Japan, Germany, France, the UK and the EU, it can be concluded that: countries generally formulate development strategies from the needs of decarbonization development, energy security, economic growth and the development of applied technologies, focusing on the directions of proton exchange membrane electrolytic hydrogen production, organic liquid hydrogen storage, low-temperature liquid hydrogen storage, hydrogen for power and scenic hydrogen production.

3.2 Analysis of Hydrogen Energy Policies in Major Countries

United States

In order to ensure leadership in emerging technologies, the US attaches great importance to the cultivation of technologies related to the upstream and downstream of the hydrogen energy industry chain, and policies continue to support research and development of hydrogen energy and fuel cell technologies. Table 1 shows the strategic policy and planning objectives for hydrogen energy in the US.

Through analysis, it can be concluded that the US hydrogen energy strategy is positioned as a reserve emerging technology. The US hydrogen energy is laid out in five main areas: transportation fuels, power generation and grid balancing, residential and commercial building fuel, industrial and long-distance transportation raw materials, and industrial fuel.

European Union

The development of hydrogen energy in the EU mainly relies on the large-scale development of renewable energy sources and perfect natural gas pipeline infrastructure to

Table 1. Hydrogen strategy policy of United States

Country	Strategic planning	Release time	Planning time	Development goals
United States	Road map to a US hydrogen economy	2019	2025	US $ 2 billion annual investment, 13 million tonnes of hydrogen demand, 150,000 FCEVs, 1000 hydrogen refueling stations
			2030	US $8 billion annual investment, 17 million tonnes of hydrogen demand, 1.2 million FCEVs, 4300 hydrogen refueling stations
			2050	68 million tonnes of hydrogen demand, representing 14% of US end-use energy demand and $750 billion in revenue
	Department of Energy Hydrogen Program Plan	2020	2030	The electrolyzer costs $300/kW and has a lifetime of 80,000 h, the PEMFC system costs $80/kW and has a lifetime of 25,000 h and the SOFC system costs $900/kW and has a lifetime of 40,000 h
	National clean hydrogen strategy and road map draft	2022	2030	10 million tonnes/year of clean hydrogen capacity at US$1/kg clean hydrogen cost
			2040	20 million tonnes/year of clean hydrogen capacity
			2050	50 million tonnes/year of clean hydrogen capacity

promote the construction of green hydrogen production and hydrogen energy storage and transportation systems, and to achieve the deep decarbonization of hydrogen energy in transport, industry and buildings to support the energy transition and the green and

low-carbon development of the European economy. Table 2 shows the strategic policies and planning objectives of the EU on hydrogen energy.

Through the analysis, it can be concluded that the EU's strategic positioning of hydrogen energy is to position hydrogen energy as an important guarantee to promote deep decarbonization and facilitate the energy transition. The EU hydrogen energy is laid out for decarbonization in industry, the application of hydrogen fuel cell vehicles such as heavy trucks and coaches, aviation and shipping transport, hydrogen power generation, and hydrogen for households and buildings.

Table 2. Hydrogen strategy policy of European Union

Country	Strategic planning	Release time	Planning time	Development goals
European Union	EU hydrogen strategy	2020	2024	At least 6 GW of renewable hydrogen energy electrolyzers with a renewable hydrogen production of 1 million tonnes
			2030	At least 40 GW of renewable hydrogen electrolyzers, 10 million tonnes of renewable hydrogen energy, EUR 24 billion–EUR 42 billion investment in electrolyzers, EUR 220 billion–EUR 340 billion scenery to provide electricity, EUR 65 billion hydrogen storage and transportation
			2050	About 1/4 of renewable energy generation will be used for renewable hydrogen production, €180 billion–€470 billion for hydrogen production and €850 million–€1 billion for hydrogen refueling stations

Japan

Japan is the first country in the world to have a national strategy for hydrogen energy development, with a clear policy orientation and progressive refinement of its content, due to the constraints of resource and energy scarcity, and a strong focus on the development of hydrogen energy-related technologies and the continued introduction of fiscal and tax incentives. Table 3 shows Japan's strategic policies and planning objectives regarding hydrogen energy.

Through the analysis, it can be concluded that: Japan's strategic positioning of hydrogen energy is to position hydrogen energy as an important way to guarantee energy security and consolidate industrial foundation. Japan's hydrogen energy is laid out in the fields of transportation (hydrogen fuel cell vehicles and hydrogen refueling stations), hydrogen energy power generation, and domestic fuel cell combined heat and power supply.

China

China has introduced a number of national-level planning policies to guide and encourage the development of the hydrogen energy industry and to accelerate the development of the whole industrial chain of hydrogen energy in "production, storage, transmission and transportation". Table 4 shows China's strategic policies and planning objectives for hydrogen energy.

Through the analysis, it can be concluded that the strategic positioning of hydrogen energy in China is to make hydrogen energy an important part of the future national energy system, an important carrier for the green and low-carbon transformation of energy-using terminals, a strategic emerging industry and a key development direction for future industries. China's hydrogen energy is laid out in the fields of transportation, energy storage, power generation and industry.

4 Strategic Analysis of Hydrogen Energy Technology

4.1 Analysis of Global Hydrogen Energy Technology Layout

The analysis of over 3000 hydrogen research projects from 2017 to 2022 is based on data collected from government websites, key R&D institutions and well-known databases (e.g. CODIS database) for major countries around the world.

The technological layout of global hydrogen research projects is characterized by the following: the range of hydrogen technologies for electricity involved in hydrogen energy projects in various countries is expanding; the investment in different technologies in hydrogen energy projects in various countries is gradually increasing; hydrogen energy projects in various countries are most deployed in the field of hydrogen for electricity, followed by electrolytic hydrogen production and hydrogen storage.

Table 3. Hydrogen strategy policy of Japan

Country	Strategic planning	Release time	Planning time	Development goals
Japan	Basic hydrogen strategy	2017	2025	320 hydrogen refueling stations, 200,000 fuel cell vehicles
			2030	30 yen/standard cube of hydrogen, 800,000 fuel cell vehicles, 1200 fuel cell buses, 10,000 fuel cell forklifts
			2050	Hydrogen Society
	Strategy for the development of hydrogen and fuel cell technologies	2019	2025	320 hydrogen refueling stations, 200,000 fuel cell vehicles
			2030	30 yen/scale-cube hydrogen supply cost, 900 hydrogen refueling stations, 800,000 fuel cell vehicles, 1200 fuel cell buses
			After 2030	20 yen/scale cube hydrogen power generation cost, 50,000 yen/kW electrolyzer
	Green growth strategy in conjunction with 2050 carbon neutrality	2020	2030	30 yen/scale-cube hydrogen energy cost, 3 million tonnes of hydrogen supply (including more than 420,000 tonnes of clean hydrogen)
			2050	20 yen/bbl (below) hydrogen, 20 million tonnes of hydrogen supply

4.2 Analysis of Hydrogen Energy Technology in Major Countries

United States

The emphasis on and support for hydrogen energy has increased each year from $13.06 million in 2018 to $7.1 billion in 2022 in the US. From 2018 to 2021, US hydrogen energy technology R&D funding focuses on advanced hydrogen production, storage and transportation, fuel cell technology, and hydrogen gas turbine research, and in

Table 4. Hydrogen strategy policy of China

Country	Strategic planning	Release time	Planning time	Development goals
China	Energy technology revolution innovation action plan	2016	2030	A service life of 10,000 h or more for PEMFC distributed generation systems and 40,000 h or more for SOFC distributed generation systems
			2050	Breakthroughs in hydrogen energy production with the widespread application of hydrogen energy and fuel cells
		2022	2025	Approximately 50,000 fuel cell vehicle holdings, 100,000–200,000 tonnes/year of renewable energy hydrogen production, and 1–2 million tonnes/year of CO_2 reduction
	Medium and long-term plan for the development of hydrogen energy industry		2030	A complete hydrogen energy industry technology innovation system, clean energy hydrogen production and supply system
			2035	To build an ecology of diverse hydrogen applications in transport, energy storage and industry and to increase the share of renewable energy in hydrogen production

2022 the US focuses on clean hydrogen production, hydrogen transportation and storage infrastructure, and end-use hydrogen including co-generation, and hydrogen power generation, as shown in Fig. 5 and expanding into emerging market applications for hydrogen energy, including medium and heavy duty trucks, data centers, ports, steel manufacturing, stationary power, and building heating.

In recent years, project development in the US has focused on electrolytic hydrogen production technology and hydrogen for electric power, with the number of projects in

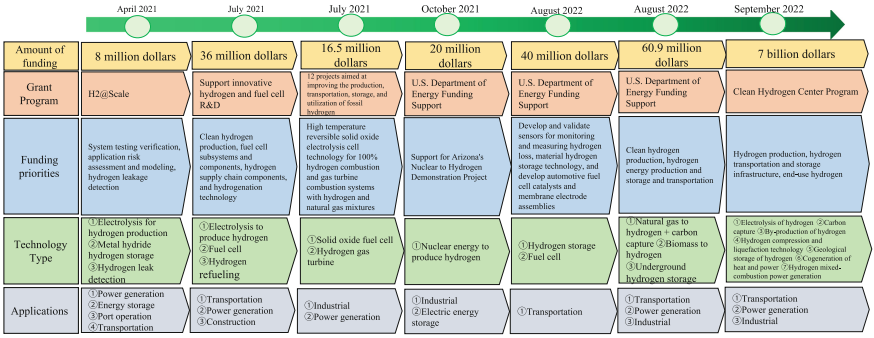

Fig. 5. Funding for hydrogen energy technology projects in the US.

these two categories accounting for over 70% of the total number of projects in the field of hydrogen for electric power. This is shown in Fig. 6.

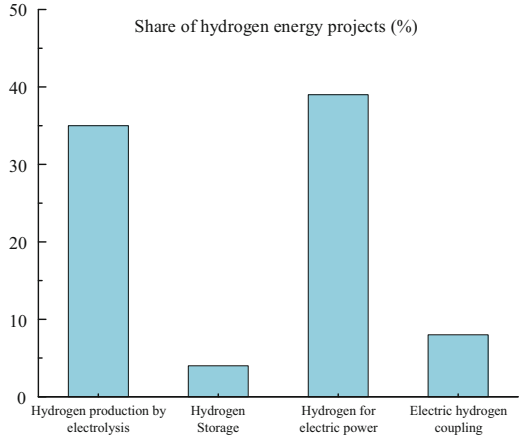

Fig. 6. Proportion of total projects in each sector of hydrogen energy in the US.

For hydrogen electrolysis technology, the US laid out both proton exchange membrane electrolysis hydrogen production technology from 2018 to 2020, and began to focus on solid oxide electrolysis hydrogen production technology from 2019. In 2019, the frontier laid out research on low-cost, durable electrode materials for alkaline anion exchange membrane electrolytic cell electrode material. In terms of hydrogen technology for electric power, the US laid out both proton exchange membrane fuel cell technology and solid oxide fuel cell technology from 2018 to 2022, and began to focus on hydrogen gas turbine and co-generation technology research and development in 2021 and 2022, respectively. In 2022, in addition to hydrogen production and use, the US focused on the layout of large-capacity, long-cycle hydrogen storage technology, with special attention to solid-state hydrogen storage and geological hydrogen storage Technologies.

Germany

The EU provides funding for hydrogen energy research and development in Germany through the EU research framework program “Horizon 2020” and “Horizon Europe”, with a focus on hydrogen production from renewable energy sources, high-capacity, long-cycle hydrogen storage and fuel cells for vehicles, as well as on the application of hydrogen energy in industry, transport and power generation, as shown in Fig. 7.

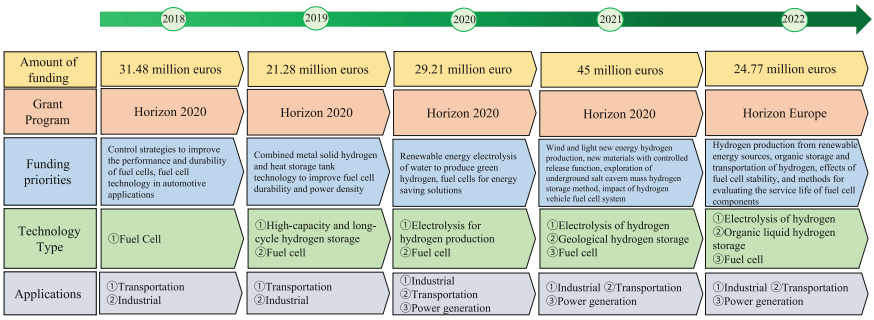

Fig. 7. Proportion of total projects in each sector of hydrogen energy in Germany.

In recent years, German projects in the field of hydrogen energy for electricity have focused on hydrogen technology for electricity, accounting for more than 50% of the total number of projects in the field of hydrogen energy for electricity, as shown in Fig. 8.

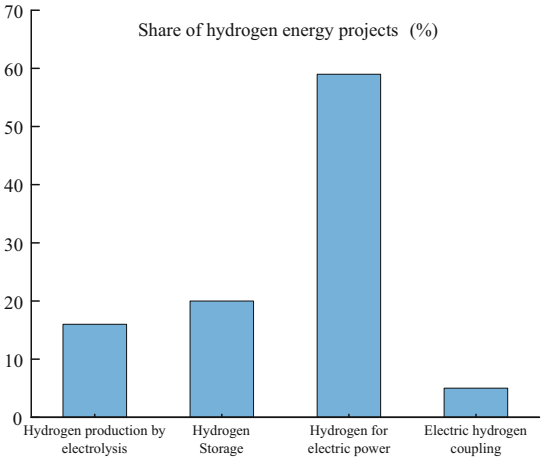

Fig. 8. Hydrogen energy in Germany by sector as a proportion of the total number of projects.

In terms of electrolytic hydrogen production technology, Germany has laid out solid oxide electrolytic hydrogen production technology for four consecutive years from 2019 to 2022, and in 2020, carried out R&D on low-cost and durable electrode materials for alkaline anion exchange membrane electrolyzers, but Germany has not laid out research on proton exchange membrane electrolytic hydrogen production technology.

In terms of hydrogen storage technology, Germany is focusing on low-temperature liquid hydrogen storage technology and metal solid hydrogen storage material R&D in 2018–2020, and on underground salt cavern hydrogen storage and organic liquid hydrogen storage technology in 2021 and 2022 respectively. In terms of hydrogen technology for electricity, Germany has laid out proton exchange membrane fuel cell technology and solid oxide fuel cell technology for four consecutive years from 2018 to 2021, carried out R&D on co-generation technology in 2021, and focused on hydrogen gas turbine technology from 2021 to 2022. In 2022, Germany mainly focuses on the layout of solid oxide electrolysis hydrogen production technology, proton exchange membrane fuel cell technology and hydrogen gas turbine technology.

Japan

Japan's New Energy Industry and Technology Development Organization (NEDO) has increased its funding for hydrogen energy year by year, from ¥15.1 billion in 2018 to ¥193.5 billion in 2022, with funding focused on hydrogen supply chains, fuel cells, hydrogen refueling stations, hydrogen gas turbines, etc. In 2022, it has funded research and development on the use of hydrogen in the steel-making process, focusing on the application of hydrogen energy in transport, industry, power generation and construction as shown in Fig. 9.

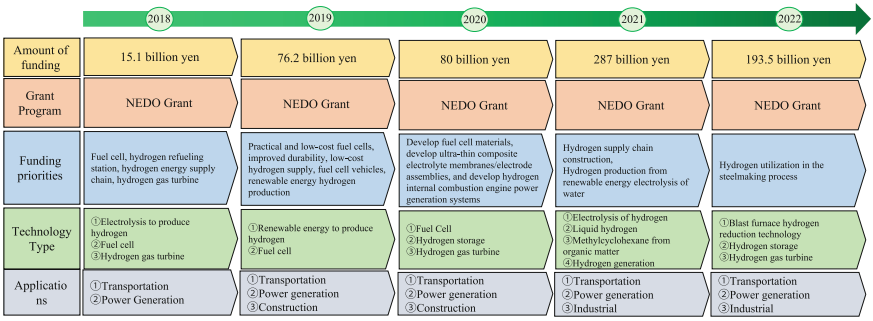

Fig. 9. Japanese hydrogen energy technology project funding.

In recent years, in the field of hydrogen for electricity, project development in Japan has also focused on hydrogen technology for electricity, accounting for more than 60% of the total number of projects in the field of hydrogen for electricity, as shown in Fig. 10.

For electrolytic hydrogen production technology, Japan conducted research and development on proton exchange membrane electrolytic hydrogen production technology and solid oxide electrolytic hydrogen production technology in 2018, and then focused mainly on research on proton exchange membrane electrolytic hydrogen production technology. For hydrogen for electricity, Japan has laid out proton exchange membrane fuel cell technology, solid oxide fuel cell technology and hydrogen gas turbine technology for five consecutive years from 2018 to 2022, with more than 70 projects deployed for proton exchange membrane fuel cell technology. In 2022, in addition to

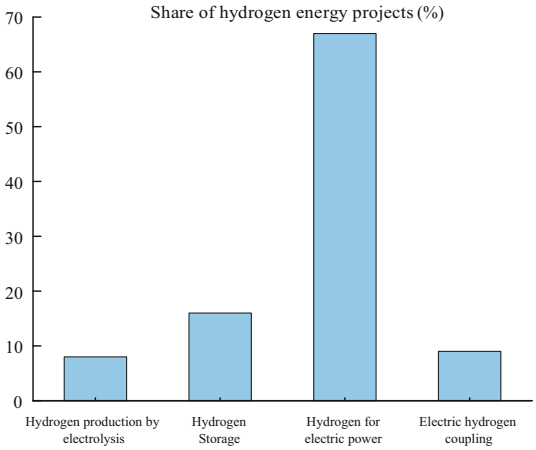

Fig. 10. Proportion of total projects in each sector of hydrogen energy in Japan.

hydrogen production and hydrogen use, Japan has also laid out organic liquid hydrogen storage and scenic hydrogen production technologies.

China

China's national key special project on hydrogen energy gradually increased R&D on hydrogen energy technologies from 2018, with research focus on proton exchange membrane electrolytic hydrogen production, low temperature liquid hydrogen storage, proton exchange membrane fuel cells, cogeneration and Power-to-X in the last five years, and hydrogen energy applications mainly focusing on power generation and transportation, with an all-round layout of R&D on power hydrogen production, storage, hydrogen use and electric-hydrogen coupling in 2021 and 2022 , as shown in Fig. 11.

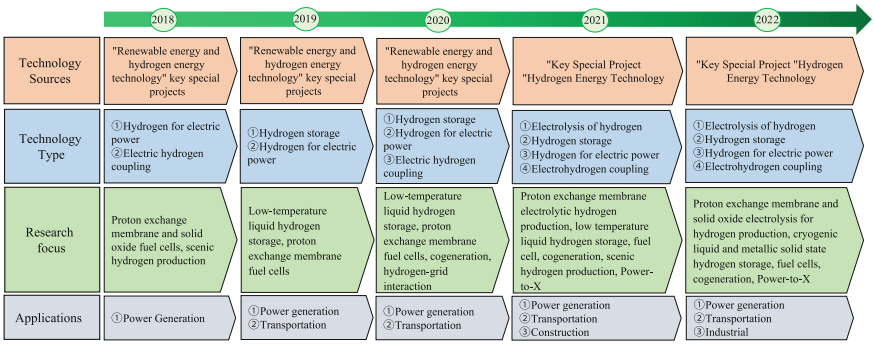

Fig. 11. Funding for China's hydrogen energy technology projects.

In recent years, in the field of hydrogen energy for electricity, project development in China has mainly focused on the field of hydrogen-using technology, with the number

of projects in this field accounting for 50% of the total number of projects in the field of hydrogen energy for electricity, as shown in Fig. 12.

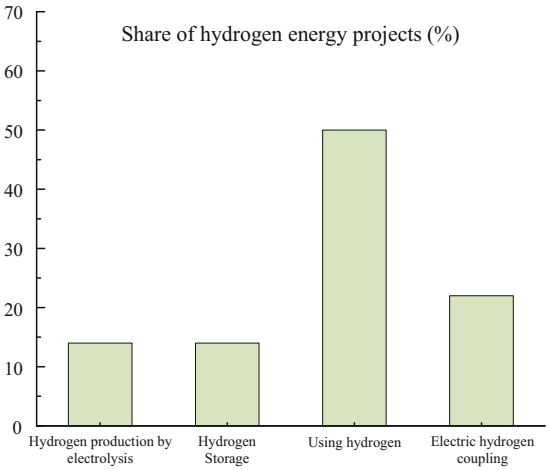

Fig. 12. Proportion of China's hydrogen energy projects in various fields to the total project.

For hydrogen production by electrolysis: China will start to lay out R&D on proton exchange membrane electrolysis technology from 2021 and increase R&D efforts in 2022; and lay out R&D on solid oxide electrolysis hydrogen production technology from 2022. For hydrogen storage: China will lay out the R&D of low-temperature liquid hydrogen storage technology every year from 2019, and focus on and lay out the R&D of metal solid hydrogen storage technology from 2022. For hydrogen use: China has been laying out R&D on proton exchange membrane and solid oxide fuel cell technologies since 2018, and on co-generation technologies every year since 2020. For electric-hydrogen coupling: China lays out R&D on hydrogen production technology for scenery in 2018 and 2021, focuses on and lays out R&D on Power-to-X technology from 2021, and lays out R&D on hydrogen-grid interaction technology in 2020 only. In 2022, China lays out R&D on electrolysis hydrogen production, hydrogen storage, hydrogen for power and electric-hydrogen coupling.

5 Summary and Outlook

In summary, in terms of global hydrogen energy strategic layout, countries that have issued hydrogen energy strategies have different development speeds and stages in this field, but the development trend is roughly the same, that is, promoting the improvement of hydrogen energy penetration in production and life, and ensuring the development of low-carbon, clean and sustainable energy. In terms of research and development of science and technology projects, different countries have different development priorities. Compared with other countries, China and Japan all focus on the field of hydrogen gas turbines. In addition, China has focused on co-generation.

With the accelerated development of renewable energy, hydrogen production from renewable energy will become an important direction of hydrogen energy development in the future, and will form different levels of coupling influence with the power grid. Establishing the coordination mechanism of electric-hydrogen coupling with clean electricity as the main source and hydrogen-based energy as the supplement, and building a new physical form of power system with "electricity as the main source and electric-hydrogen coupling", will promote the coupling application of hydrogen energy in the source, network, load and storage of the new power system, enhance the level of new energy consumption, realize the large capacity and long time storage of electric energy, and realize the interconnection and synergy optimization of various energy networks such as electricity, heating and fuel. It will realize the interconnection and optimization of various energy networks, such as electricity, heating and fuel, enhance the flexible regulation capability of the power grid, and ensure the safe and stable operation of the new power system.

Acknowledgment. This work is supported by a research and development project (Research on the Frontiers of Energy Power (Hydrogen Energy) Science and Technology and Development Trends JS83-22-002) of the China Electric Power Research Institute. The authors would like to thank the editors and reviewers for their constructive comments and suggestions to improve the quality of the paper.

References

1. Chien, F., Chau, K.Y., Ady, S.U., Zhang, Y., Tran, Q.H., Aldeehani, T.M.: Does the combining effects of energy and consideration of financial development lead to environmental burden: social perspective of energy finance. Environ. Sci. Pollut. Res. Int. **28**(30), 40957–40970 (2021)
2. Ceseña, E.A.M., Mancarella, P.: Energy systems Integration in smart districts: robust optimisation of multi-energy flows in integrated electricity, heat and gas networks. IEEE Trans. Smart Grid **10**(1), 1122–1131 (2019)
3. Yang, R., Zheng, X., Qin, M., et al.: A trifunctional Ni-P/Fe-P collaborated electrocatalyst enables self-powered energy systems. Adv. Sci. (Weinh) **9**(22), e2201594 (2022)
4. Huang, B., Xu, H., Jiang, N., et al.: Tensile-strained RuO_2 loaded on antimony-tin oxide by fast quenching for proton-exchange membrane water electrolyzer. Adv. Sci. (Weinh) **9**(23), e2201654 (2022)
5. Jia, Z., Qin, X., Chen, Y., et al.: Fully-exposed Pt–Fe cluster for efficient preferential oxidation of CO towards hydrogen purification. Nat. Commun. **13**(1), 6798 (2022)
6. Hydrogen Roadmap Europe. Hydrogen roadmap Europe: a sustainable pathway for the European energy transition. https://www.fch.europa.eu/sites/default/files/Hydrogen%20Roadmap%20Europe_Report.pdf. Accessed 10 Feb 2019
7. Lin, R., Hu, Q., Liu, Z., et al.: Integrated CuO/Pd nanospike hydrogen sensor on silicon substrate. Nanomaterials (Basel) **12**(9), 1533 (2022)
8. Wang, C., Sun, F.Q., Xu, Y., et al.: Analysis and enlightenment of hydrogen development strategy of world's major economies. World Sci-Tech. R&D **44**(5), 597–604 (2022)
9. Wang, Y., Gao, L., Liu, Y.: The inspiration of the national hydrogen energy roadmap of US. Fut. Dev. **39**(12), 22–29 (2015)

10. Liu, Y., Xu, F.: Fact sheet on hydrogen and the hydrogen economy. World Sci-Tech R & D **28**(1), 101–106 (2006)
11. Fu, G., Xiong, H.: The models of hydrogen energy development in Japan, Germany and the United States and enlightenments. Macroecon. Manage. **6**, 84–90 (2020)
12. Bao, J., Zhao, Z., Ma, Q.: Overview of the development trends of hydrogen energy technologies. Autom Digest **2**, 6–11 (2020)
13. Xia, F., Zhou, Y.: Current status and perspective of hydrogen energy and fuel cell technologies in Germany. Mar Electr Electron Eng **35**(2), 49–52 (2015)
14. Gronau, S., Hoelzen, J., Mueller, T., Hanke-Rauschenbach, R.: Hydrogen-powered aviation in Germany: a macroeconomic perspective and methodological approach of fuel supply chain integration into an economy-wide dataset. Intl. J. Hydrogen Energy **48**(14), 5347–5376 (2023)
15. Ding, M.: Characteristics, motivation, international coordination of Japan's hydrogen strategy. Contemp. Econ. Japan **4**, 28–41 (2021). (in Chinese)
16. Lei, C., Li, T.: Key technologies and development status of hydrogen energy utilization under the background of carbon neutrality. Power Gener. Technol. **42**(2), 207–217 (2021)
17. Wang, L., Cao, Y.: Utilization of hydrogen energy and its enlightenment to China's development. Shanghai Energy Conserv. **5**, 444–448 (2021)
18. Hartley, P.G., Au, V.: Towards a large-scale hydrogen industry for Australia. Engineering **6**(12), 1346–1348 (2020)
19. Xiong, H., Fu, G.: Four typical models of global hydrogen energy industries development and their references for China. Environ. Protect. **49**(1), 52–55 (2021)
20. Gao, X., An, R.: Research on the coordinated development capacity of China's hydrogen energy industry chain. J. Clean. Prod. **377**(134177), 0959–6526 (2022)
21. Fan, L., Tu, Z., Chan, S.H.: Recent development of hydrogen and fuel cell technologies: a review. Energy Rep. **7**, 421–8446 (2021)

Study on Optimization Operation of Micro-energy Network Considering Electro-ammonia Conversion

Shi Ruijing[1], Ren Peng[1(✉)], Fan Xiaochao[1], and Wang Jianglei[2]

[1] Xinjiang Institute of Engineering, Urumqi 830000, Xinjiang Uygur Autonomous Region, China
13199800705@163.com

[2] Xinjiang University, Urumqi 830000, Xinjiang Uygur Autonomous Region, China

Abstract. Micro energy networks are an important way to achieve the "carbon neutrality" goal. To further explore the potential of energy conversion in reducing carbon emissions, this article proposes an optimized operation model for micro energy networks with refined power-to-ammonia conversion. Based on the operation model considering carbon trading and comprehensive demand response, an optimization model for micro energy networks with refined power-to-ammonia conversion is established, with the objective of minimizing the system's operating cost and carbon emissions. Utilizing examples, various micro-source energy dispatch conditions are analyzed and the carbon emission costs, as well as the overall operating costs of the micro energy network, are calculated. The results show that compared with power-to-hydrogen conversion, using power-to-ammonia conversion in micro energy networks can effectively reduce system carbon emissions, with a decrease of 7.88% and a total operating cost reduction of 5.36%. This verifies the feasibility of the model and demonstrates that improving energy utilization can achieve the synergistic operation of the system's economy and low-carbon emissions.

Keywords: Micro energy grid · Electro-hydrogen conversion · Carbon emissions trading · Electro-ammonia conversion

1 Introduction

With the gradual maturity of hydrogen energy utilization technologies such as fuel cells, hydrogen energy, ammonia energy, heat energy and electric energy will realize flexible conversion and coupling development. Hydrogen energy and ammonia energy have clean and low-carbon properties and potential for cross-border applications. They can be widely used in transportation, industry and other fields. By widely promoting the application of hydrogen energy in energy terminals, greenhouse gas emissions will be effectively reduced. The concept of comprehensive demand response is evolved from the traditional demand response. It guides users to participate in the system regulation at a deeper level through the energy market price signal, calms the load fluctuation on the user

H. Sun et al. (Eds.): WHTC 2023, SPPHY 393, pp. 452–464, 2024.
https://doi.org/10.1007/978-981-99-8631-6_44

side, realizes resource coordination and optimization, and reduces costs and increases efficiency [1–4]. Document [5] has built a cost evaluation system of power balance with demand response, which provides a new way to solve the balance of power supply and demand. Literature [6] divides users participating in demand response into rigid load and price-sensitive load from load, indicating that demand response can effectively reduce the comprehensive cost of system operation. Literature [7] establishes an economic dispatch model considering thermal and electrical comfort and thermal power demand response, adjusts the thermal power load within the user's comfort range, eases energy consumption tension and reduces the system operation cost. Literature [8] uses the coupling and complementarity of multiple energy sources to change the user's energy use type but not the user's energy use plan, defines it as comprehensive demand response, and studies the direct transaction strategy between Micro Energy Grid (MEG) and suppliers, and verifies the advantages of integrated demand response (IDR). IDR can promote the cascade utilization of energy in the process of consumption and improve the efficiency of energy utilization [9]. According to the flexible and coupling characteristics of electricity, gas and heat loads, the document [10] establishes an optimal scheduling model considering the comprehensive demand response of electricity, gas and heat loads. Literature [11] optimizes the configuration of the energy storage system of the micro-energy network with coupled demand response of electricity, gas and heat, aiming at the minimum economic cost. The results show that the application of coupled demand response can improve the economy of the system.

In the above documents, while using the electricity-to-gas technology to promote the coupling between the power grid and the gas grid and the absorption of renewable energy such as wind and light, the pre-reaction of electricity-to-natural gas is not considered, and the benefits of electricity-to-hydrogen in the two-stage operation process are not considered. However, there are still some technical difficulties and safety problems in large-scale hydrogen storage and transportation, and ammonia has begun to receive attention. The molecular structure of ammonia is composed of one nitrogen atom and three hydrogen atoms, containing more hydrogen atoms. It is a natural hydrogen storage medium. Under normal pressure, it can be liquefied at −33 °C, which is convenient for safe transportation. To sum up, this paper comprehensively analyzes the process of converting electricity to hydrogen and hydrogen to natural gas, and uses fuel cells to produce heat and electricity to improve the energy utilization rate on the basis of considering the comprehensive demand response of the user side and the optimal operation strategy of the carbon trading mechanism; Because hydrogen energy is difficult to store and transport, it is proposed to introduce ammonia energy and replace the electric to gas equipment with electric to ammonia technology. Combined with an example, the two optimization operation strategies are verified and discussed in terms of minimum total operation cost and minimum carbon emissions.

1.1 MEG Structure

The MEG system established in this paper includes three types of energy: heat, electricity and gas. Its structure is shown in Fig. 1. The energy equipment in-cluded in the system mainly includes wind turbine (WT), photovoltaic (PV), gas turbine (GT) and gas boiler (GB); The energy storage system includes energy storage (ES), heat storage (HS) and gas

storage (GS); Energy conversion equipment includes waste heat boiler (WHB), electric boiler (EB), power to gas (P2G), etc.

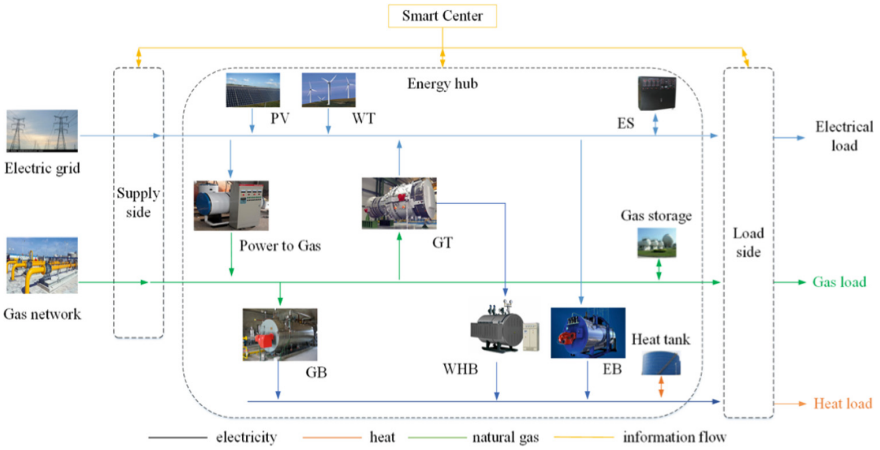

Fig. 1. Schematic diagram of micro-energy network structure.

Figure 1 shows that the micro energy grid integrates energy production, energy conversion, and energy consumption, and can operate independently or in parallel. Input electric energy and gas energy on the supply side to meet the load demands of electricity, gas, and heat on the load side.

The energy flow structure within the micro energy network is represented by a matrix:

$$\begin{bmatrix} P_{\text{load},t} \\ H_{\text{load},t} \\ G_{\text{load},t} \end{bmatrix} = \begin{bmatrix} 1 & 0 & \eta_{\text{GT}} \\ \eta_{\text{EB}} & 1 & \eta_{\text{GB}} \\ \eta_{\text{p2g}} & 0 & 1 \end{bmatrix} \begin{bmatrix} P_{\text{P},t} \\ P_{\text{H},t} \\ P_{\text{G},t} \end{bmatrix} + \begin{bmatrix} -P_{\text{chr},t} + P_{\text{dis},t} \\ -H_{\text{chr},t} + H_{\text{dis},t} \\ -G_{\text{chr},t} + G_{\text{dis},t} \end{bmatrix} \tag{1}$$

In the formula, $P_{\text{load},\,t}$, $H_{\text{load},\,t}$, $G_{\text{load},\,t}$ are the electricity, gas, and heat load requirements within the micro energy network at time t; $P_{\text{P},\,t}$, $P_{\text{H},\,t}$, $P_{\text{G},\,t}$ are the electric energy, thermal energy, and gas energy consumed by the micro energy network at time t; $P_{\text{chr},\,t}$, $P_{\text{dis},\,t}$, $H_{\text{chr},\,t}$, $H_{\text{dis},\,t}$, $G_{\text{chr},\,t}$, $G_{\text{dis},\,t}$ are the charging and discharging power of the electric storage equipment, heat storage equipment, and gas storage equipment in the micro energy network at time t.

2 Refined Models for Electrogas and Electroammonia Conversion

Most of the existing studies, when modeling electric to gas equipment, generally only consider the electric to methane process, without considering the electric hydrogen production process [12]. Hydrogen energy is a highly efficient energy source that does not generate carbon emissions. It has great application potential in the fields of chemical engineering, thermal power production, transportation, and other fields. The two-stage operation process of electricity to gas is shown in Fig. 2. Consider refining the MEG structure of the electro-gas con-version process as shown in Fig. 3, and the MEG structure of the electro-ammonia conversion process as shown in Fig. 4.

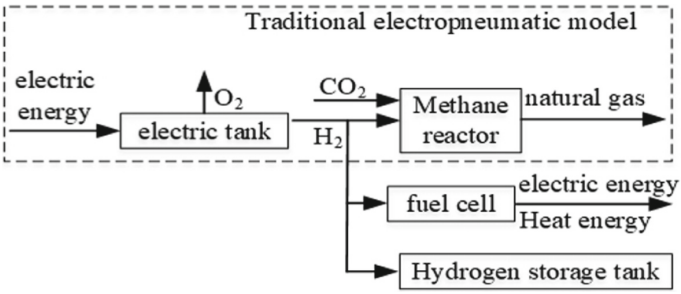

Fig. 2. Schematic diagram of micro-energy network structure.

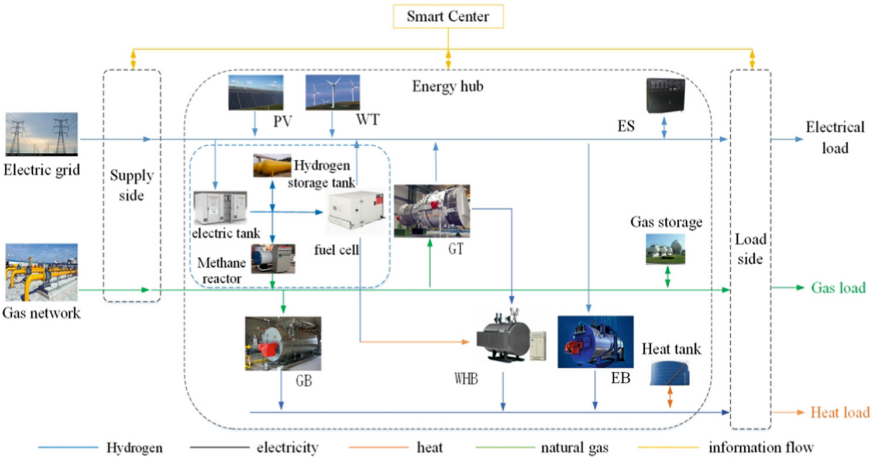

Fig. 3. MEG structure diagram considering electric to gas conversion.

2.1 MEG Structure

Methane Reactor (MR) uses hydrogen to reduce a certain amount of CO_2 to produce methane. The entire process is pollution-free and can consume a certain amount of CO_2. The flow chart is shown in Fig. 5. Methane can be supplied to system users and equipment.

This process is an exothermic process with low efficiency, and its model can be expressed as:

$$\begin{cases} MR_g(t) = \eta_{MR} P_{MR,H_2}(t) \\ P_{MR,H_2,min} \le P_{MR,H_2}(t) \le P_{MR,H_2,max} \\ \Delta P_{MR,H_2,min} \le P_{MR,H_2}(t+1) - P_{MR,H_2}(t) \le \Delta P_{MR,H_2,max} \end{cases} \tag{2}$$

In the formula, $P_{MR,\,H2}\ (t)$ is the hydrogen energy consumed by MR during the t period; $MR_g\ (t)$ is the natural gas power produced by MR during period t; η_{MR} is the conversion efficiency of MR; $P_{MR,\,H2,\,min}$ are the upper and lower limits of hydrogen

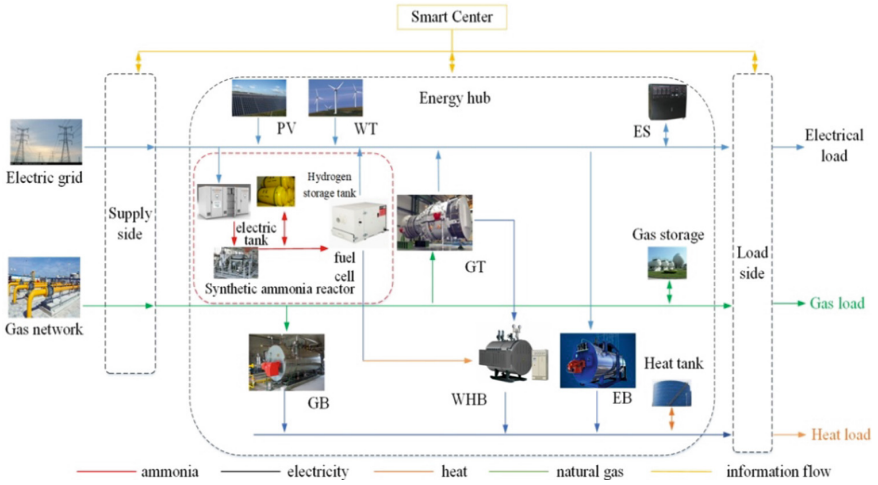

Fig. 4. MEG structure diagram considering electro-ammonia conversion.

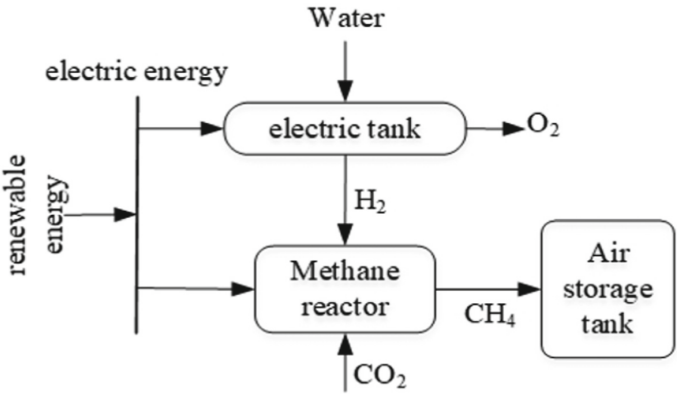

Fig. 5. Hydrogen to methane process.

energy consumption by MR; $\Delta P_{\mathrm{MR,H2,max}}$, $\Delta P_{\mathrm{MR,\,H2,\,min}}$ are the upper and lower limits of the MR output ramp.

2.2 Electroammonia Conversion Model

The process of producing ammonia from hydrogen is to synthesize nitrogen and hydrogen into ammonia through a Haber ammonia synthesis reactor. The flow chart is shown in Fig. 3. The process model can be expressed as:

$$E_{\mathrm{H_2}}(t+1) = E_{\mathrm{H_2}}(t) + \eta_{\mathrm{H_2,chr}} P_{\mathrm{H_2,chr}}(t+1) - \frac{P_{\mathrm{H_2,dis}}(t+1)}{\eta_{\mathrm{H_2,dis}}} \tag{3}$$

$$\begin{aligned} P_{\mathrm{H_2,chr,min}} &\le P_{\mathrm{H_2,chr}}(t) \le P_{\mathrm{H_2,chr,max}} \\ P_{\mathrm{H_2,dis,min}} &\le P_{\mathrm{H_2,dis}}(t) \le P_{\mathrm{H_2,dis\,max}} \end{aligned} \tag{4}$$

$$E_{\mathrm{H_2,min}} \le E_{\mathrm{H_2}}(t) \le E_{\mathrm{H_2,max}} \tag{5}$$

$$U_{\mathrm{H_2},dis}(t) + U_{\mathrm{H_2},chr}(t) \le 1 \tag{6}$$

In the formula, E_{H2} (t) is the capacity of the hydrogen storage tank at time t; $P_{\mathrm{H2,\ chr}}$ (t), $P_{\mathrm{H2,\ dis}}$ (t) are the input and output power of the hydrogen storage tank at time t, respectively; $\eta_{\mathrm{H2,chr}}$, $\eta_{\mathrm{H2,\ dis}}$: storage and discharge efficiency of hydrogen storage tanks; $\mathrm{E_{H2,\ max}}$, $\mathrm{E_{H2,\ min}}$ are the upper and lower limits of the hydrogen storage tank capacity; $U_{\mathrm{H2,\ chr}}$ (t), $U_{\mathrm{H2,\ dis}}$ (t) are respectively the charging and discharging states of the battery at time t, 0 represents the stop state, and 1 represents the operation state.

The ammonia storage tank model is similar to the hydrogen storage tank model and will not be described again.

3 Solution of Electric Heating Integrated Energy System

3.1 Objective Function

In order to analyze the economy and carbon emissions of the multi-energy coupled micro energy grid model established in this article, the objective function is to minimize the total operating cost of the system, including system energy purchase cost, equipment operation and maintenance cost, and carbon trading cost, while meeting the requirements for electricity, gas, and heat loads within the system and equipment constraints, namely:

$$F = \min(F_{\mathrm{grid}} + F_{\mathrm{gas}} + F_{\mathrm{op}} + F_{\mathrm{MEG}}) \tag{7}$$

In the formula, $\mathrm{F_{grid}}$—MEG power purchase cost; $\mathrm{F_{gas}}$—MEG gas purchase cost; $\mathrm{F_{op}}$—MEG operation and maintenance cost; $\mathrm{F_{MEG}}$—MEG carbon transaction cost.

(1) Grid interaction costs

$$F_{\mathrm{grid}} = \sum_{t=1}^{24} (v_{\mathrm{grid,b}}(t)P_{\mathrm{buy}}(t) + v_{\mathrm{grid,s}}(t)P_{\mathrm{sell}}(t)) \tag{8}$$

In the formula, $v_{\mathrm{grid,\ b}}$ (t)—the electricity purchase price at time t; $v_{\mathrm{grid,\ s}}$ (t)—the electricity selling price at the time of t; P_{buy} (t)—purchasing power at t time; P_{sell} (t)—Power sold at time t.

(2) Gas purchase cost

$$F_{\mathrm{gas}} = \sum_{t=1}^{24} v_{\mathrm{gas}}(t) \cdot G_{\mathrm{net}}(t)/LHV_{\mathrm{gas}} \tag{9}$$

In the formula, $v_{\mathrm{gas}}(t)$—the purchase price of gas at time t; $G_{\mathrm{net}}(t)$—gas purchasing power at time t; LHV_{gas}—Low calorific value of natural gas, taken as 9.78 kWh/m^3.

(3) Equipment operation and maintenance costs

$$F_{\mathrm{op}} = \sum_{n} K_n P_n(t) \tag{10}$$

In the formula, K_n refers to the unit operation and maintenance cost of equipment n (including gas turbine, battery, heat storage tank, gas storage tank, photovoltaic unit, wind turbine unit, gas boiler, waste heat boiler, methane reactor, fuel cell, hydrogen storage tank, ammonia storage tank, etc.); P_n (t)—The input power of the device n operating at time t.

3.2 Constraint Condition

On the basis of fully considering the operating characteristics of the respective subsystems of the electricity ammonia conversion model and the micro energy grid, the following constraints are selected:

(1) The electrical power balance constraint

$$\begin{aligned} &P_{\mathrm{WT}}(t) + P_{\mathrm{PV}}(t) + P_{\mathrm{GT}}(t) + P_{\mathrm{grid}}(t) - P_{\mathrm{bt,chr}}(t) + \\ &P_{\mathrm{bt,dis}}(t) - P_{\mathrm{eb}}(t) - P_{\mathrm{EL}}(t) + FC_{\mathrm{NH_3},e}(t) = Load_{\mathrm{ele}}(t) \end{aligned} \tag{11}$$

(2) Heat power balance constraints

$$\begin{aligned} &H_{\mathrm{GB}}(t) + H_{\mathrm{WHB}}(t) - H_{\mathrm{tst,chr}}(t) + H_{\mathrm{tst,dis}}(t) \\ &+H_{\mathrm{eb}}(t) + FC_{\mathrm{NH_3,h}}(t) = Load_{\mathrm{heat}}(t) \end{aligned} \tag{12}$$

(3) Ammonia power constraint

$$\mathrm{sum}(NR_{\mathrm{g}}) = \mathrm{sum}(P_{\mathrm{FC,NH_3}}) \tag{13}$$

In the formula, $P_{FC,\,NH3}$—ammonia energy input to the fuel cell. That is, the amount of electric ammonia conversion within an operating cycle is equal to the amount consumed by the fuel cell.

3.3 Solution Method

The research on optimal operation of micro energy networks includes two basic processes: modeling and solving. The methods for solving optimization problems include: (1) mathematical programming; (2) Heuristic optimization method.

The optimal operation of the micro energy network solved in this paper is a mixed integer linear programming problem, which constructs a comprehensive electric heating energy system model considering the carbon trading mechanism and user demand response; Fully consider the chemical characteristics between electric to gas and electric to ammonia conversion, establish a mathematical model, and incorporate it into the electrothermal comprehensive energy system model; Under the conditions of satisfying the output constraints of each module of the system and the energy balance of the power system, the Cplex solver is invoked on the Matlab platform using the Yalmip toolbox to solve the model.

4 Example Analysis

In order to verify the effectiveness of the model proposed in this article, the optimized operation model built in document [1] refined the electric to gas conversion process, adding fuel cells, hydrogen storage tanks, fuel cells, ammonia storage tanks, and other equipment. The parameters are shown in Table 1.

Table 1. Equipment parameters.

Micro power supply	Rated power/kW	Productiveness/%
Electric tank	800	0.85
Methane reactor	250	0.6
Electroammonia conversion	800	0.7
Fuel cell	600	0.65 (electricity)
		0.35 (heat)

To verify the effectiveness of the proposed model, this article intends to conduct a comparative analysis of the following two scenarios.

Scenario 1: Consider switching electricity to gas.
Scenario 2: Consider electricity ammonia conversion.

The actual carbon emissions and total cost under each working condition are shown in the Table 2. According to Table 2, compared to electric hydrogen conversion, using electric ammonia conversion in micro energy networks can effectively reduce system carbon emissions by 7.88% and total operating costs by 5.36%.

Table 2. Running cost.

Operating mode	Total cost/yuan	Power purchase cost/yuan	Gas purchase cost/yuan	Carbon emissions/kg
1	19,554	2161.97	14,919.22	11,482.06
2	18,014	1317.73	15,544.87	10,866.55

(1) The optimized scheduling results for electricity, gas, and heat in Scenario 1 are shown in Figs. 5, 6, and 7.

Figure 5 shows that during periods when users have less demand for electricity load (nighttime periods), due to the relatively rich output of wind power generation, electrolytic cell equipment converts it into hydrogen energy for storage, charging batteries, or heating through electric boilers; During peak hours of user electricity load, due to high electricity prices, the difference in electricity load demand is supplemented by fuel cells,

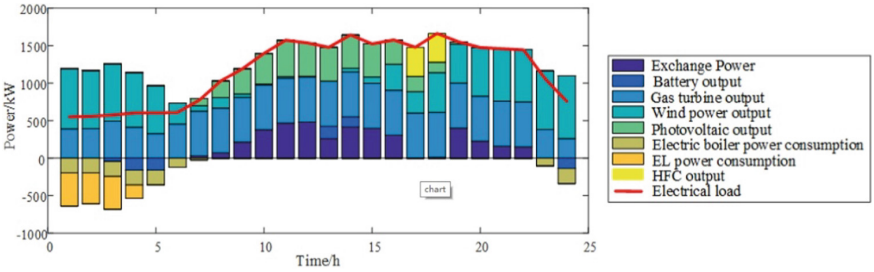

Fig. 6. Power dispatching results.

reducing the purchase of electricity from the large grid, and relying on the efficiency and cleanliness of hydrogen energy to reduce the carbon emissions of the system.

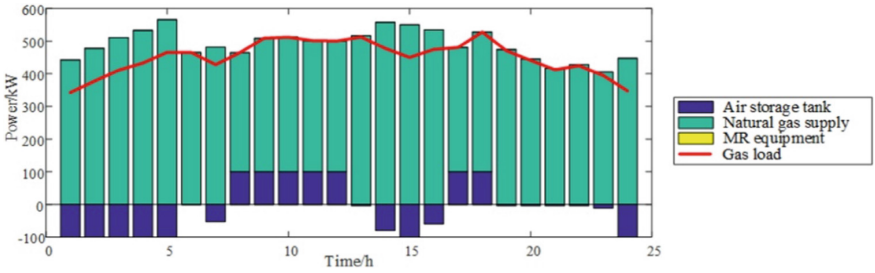

Fig. 7. Gas scheduling results.

Figure 6 shows that since hydrogen energy is produced from natural gas through a methane reactor and then heated and powered by GB and GT, there is a significant capacity loss during the energy conversion process, while fuel cells have a high efficiency in cogeneration, so fuel cells are preferred for producing electricity and heat.

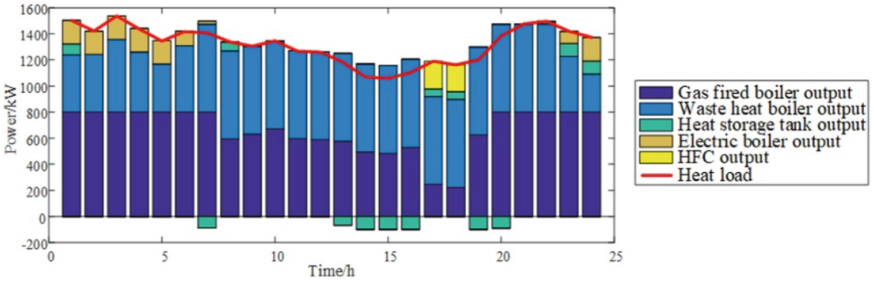

Fig. 8. Heat scheduling results.

Figure 7 shows that during the peak period of electrical load, due to the combined heat and power generation effect of fuel cells, while meeting the electrical load, a large

amount of heat energy is also produced, reducing the output of gas fired boilers at this time and reducing the consumption of natural gas.

(2) The optimized scheduling results for electricity, gas, and heat in Scenario 2 are shown in Figs. 8, 9, and 10.

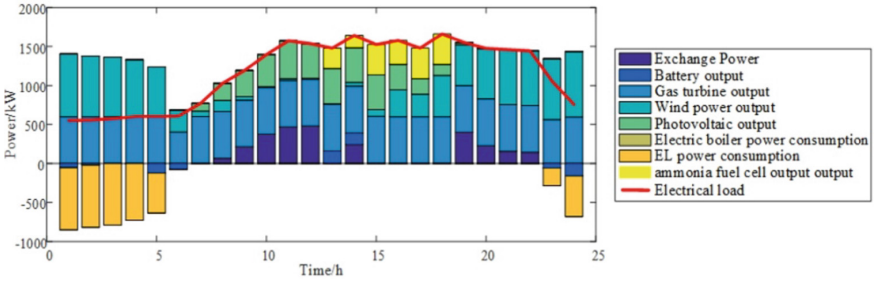

Fig. 9. Power dispatching results.

Figure 8 shows that during the low demand period for electricity load of users, due to the high output of wind power generation, electric ammonia production equipment is used to convert it into ammonia energy for storage or to charge the battery; The difference between the user's electricity load and the electricity load during peak electricity prices is supplemented by fuel cells to reduce the purchase of electricity from the large power grid. As ammonia is a carbon free fuel and is converted from clean energy, it can reduce the system's operating costs and reduce the system's carbon emissions.

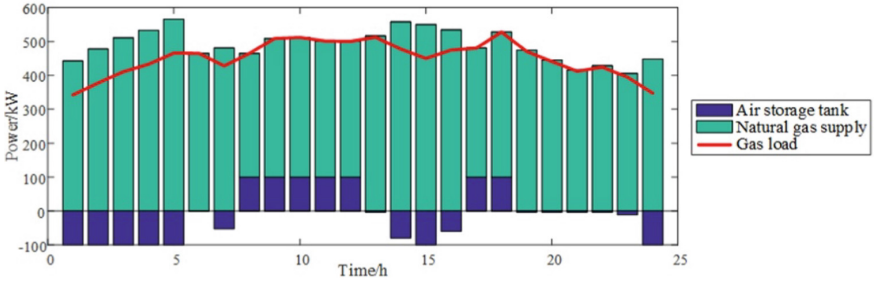

Fig. 10. Gas scheduling results.

Figure 9 shows that in this section, electric ammonia production equipment is used instead of traditional electric gas conversion equipment, and the conversion efficiency is high. Therefore, there is no conversion of electric energy to natural gas, but natural gas is relatively clean, so natural gas is still the main source of energy in the micro energy grid. Based on time-sharing gas prices, achieve low storage and high production.

Figure 10 shows that during the peak period of electrical load, due to the combined heat and power generation effect of fuel cells, while meeting the electrical load, a large

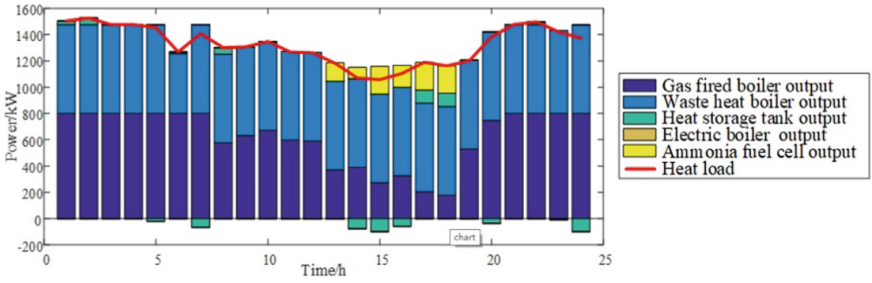

Fig. 11. Heat scheduling results.

amount of heat energy is also produced, reducing the output of gas fired boilers at this time, reducing the consumption of natural gas, thereby reducing the system operating costs and carbon emissions (Fig. 11).

5 Conclusion

This article first introduces the advantages of hydrogen and ammonia energy sources, expounds the production processes of electric conversion of methane and ammonia, and then selects equipment based on the types and characteristics of electrolytic cells, fuel cells, and hydrogen/ammonia storage tanks in combination with MEG requirements, and establishes corresponding mathematical models. Consider the impact of refining the electric to gas process and replacing traditional electric to gas equipment with electric to ammonia on the operation of the micro energy grid.

(1) Based on the optimization model of demand response, further consider refining the electro-gas conversion process, consider the advantages of high hydrogen energy density and high conversion efficiency, and reduce energy waste in the hydrogen to methane process. With the minimum operating cost and carbon emissions as the objective functions, establish a MEG optimization operation model, and use a Cplex solver to solve. Simulation results show that the optimized operation model can improve the utilization efficiency of renewable energy, reduce the use of fossil energy, and further reduce the carbon emissions of the system.

(2) The advantages of ammonia energy in the energy field are explained. Due to its carbon free, easy to obtain, easy to store and transport, and the bulk energy density of liquid ammonia far exceeds that of liquid hydrogen and hydrogen, it is proposed to use electric ammonia conversion equipment to replace traditional electric gas conversion equipment. On the premise of meeting the user's load requirements, with the minimum operating cost and carbon emissions as the objective function, a MEG optimization operation model is established and solved using a Cplex solver. The results of an example show that the optimization model can improve energy utilization efficiency, reduce system carbon emissions, and provide a new idea for the consumption of renewable energy in remote and transportation inconvenient areas on the basis of minimum operating costs.

Acknowledgement. This study is supported by the National Natural Science Foundation of China, with project number 52266018. This study is funded by the Xinjiang Autonomous Region with project number 2022B01019-1. This study is funded by the Science and Technology Department of Xinjiang Autonomous Region, with project number 2022A01001-2.

References

1. Yuan, W., Chen, L., Wang, C., et al.: Double-layer optimal scheduling of electric to ammonia coupled wind light fire integrated energy system based on ammonia energy storage technology. Chin. J. Electr. Eng. **2023**, 1–11 (2023)
2. Bloess, A.: Modeling of combined heat and power generation in the context of increasing renewable energy penetration. Appl. Energy **267**, 114727 (2020)
3. Yan, N., Ma, G., Li, X., et al.: Low-carbon economic dispatch method for integrated energy system considering seasonal carbon flow dynamic balance. IEEE Trans. Sustain. Energy **14**(1), 576–586 (2023)
4. Zhou, Y., Yu, H., Li, Z., et al.: Robust optimization of a distribution network location-routing problem under carbon trading policies. IEEE Access **8**, 46288–46306 (2020)
5. Dai, X., Han, X., Jin, X.: Cost benefit evaluation method for demand response participation in power balance. China Electric Power **55**(10), 170–177 (2022)
6. Huang, W., Liu, D., Li, S., et al.: Double level optimization of integrated energy systems with P2G and demand response under dual carbon targets. Electr. Measurem. Instrument. **59**(11), 8–17 (2023)
7. Wang, S., Liu, T., He, C., et al.: Comprehensive energy economic scheduling for parks based on comfort demand response and carbon trading. Electr. Measurem. Instrument. **59**(11), 1–7 (2022)
8. Liu, J., Liu, X., Gao, X., et al.: Multi-energy micro-energy network optimal collaborative scheduling considering comprehensive demand response. Power Energy Prog. **7**(6), 106–117 (2019)
9. Zhang, T., Guo, Y., Li, Y., et al.: Optimal dispatching of regional integrated energy systems considering electrical and thermal comprehensive demand response. Power Syst. Protect. Control **49**(01), 52–61 (2021)
10. Zeng, M., Wu, G., Li, R., Wang, H., et al.: Key issues and prospects for integrated demand side response in the energy internet. Power Grid Technol. **40**(11), 3391–3398 (2016)
11. Wu, Y., Lv, L., Xu, L., et al.: Comprehensive and optimized configuration of multiple energy storage capacities in a multi-energy microgrid considering electrical/thermal/pneumatic coupling demand response. Power Syst. Protect. Control **48**(16), 1–10 (2020)
12. Chen, J., Hu, Z., Chen, Y., et al.: Thermoelectric optimization of integrated energy systems considering a stepped carbon trading mechanism and electric hydrogen production. Electric Power Autom. Equip. **41**(09), 48–55 (2021)

Enhancement of Acidic HER by Fe Doped CoP with Bimetallic Synergy

Yuanfeng Gao, Hong Lv(✉), Yongwen Sun, Han Yao, Ding Hu, and Cunman Zhang

Clean Energy Automotive Engineering Center, School of Automotive Studies, Tongji University, Shanghai, China
lvhong@tongji.edu.cn

Abstract. Compared to single metal site catalysis, the bimetallic synergistic strategy can exploit the complementary ability of different active sites for active species uptake and desorption to develop excellent catalysts. Pure phase metal phosphides are a disadvantage as a promising electrocatalyst for platinum-free hydrogen precipitation with either too strong or too weak adsorption of hydrogen. Here, synthetic Fe-doped CoP particles anchored with MWCNTs, which exhibited excellent catalytic performance for HER, required an overpotential of 123 mV to reach 10 mA cm^{-2}, with a Tafel slope of 58.8 mV dec^{-1}. It was found experimentally that Fe doping improved the conductivity of the catalyst regulated the electronic structure of CoP, and optimized the overall hydrogen adsorption energy of the catalyst. The difference in hydrogen adsorption strength of Fe, Co is used to break the symmetry constraint of single active center and improve the intrinsic activity of the catalyst, a strategy that can be used to guide the preparation of inexpensive and high performance catalysts.

Keywords: Fe-doped CoP · HER · Synergistic strategy

1 Introduction

Traditional fossil fuel resources are dwindling, and their combustion produces large amounts of pollutants and greenhouse gases, which have a serious impact on the environment. Therefore, developing clean energy is a major challenge facing the world today. Hydrogen (H_2), with a calorific value of ≈282 kJ mol^{-1}, is a clean and sustainable energy source and an ideal substitute for fossil fuels [1–3]. The combustion of hydrogen does not produce greenhouse gases such as carbon dioxide, which can effectively reduce air pollution and greenhouse gas emissions [4]. Electrocatalytic hydrogen evolution can produce clean hydrogen through the reaction of splitting water into hydrogen and oxygen, which can be used as a clean energy medium [5].

The hydrogen evolution reaction (HER) to produce hydrogen gas from cheap electrons generated by renewable energy is a central issue in the manufacture of zero-carbon and carbon-neutral energy carriers [6]. Currently hindering the development of HER is the lack of catalysts with high performance and excellent stability. The current study

H. Sun et al. (Eds.): WHTC 2023, SPPHY 393, pp. 465–474, 2024.
https://doi.org/10.1007/978-981-99-8631-6_45

shows that noble metal-based catalysts (Pt, Ru, Ir, etc.) exhibit the best catalytic performance in electrochemical water splitting [7–10]. However, the scarcity of global reserves and high price of precious metals limit their wide application.

Attempts have been made to replace noble metal-based electrocatalysts with transition metals. Non-noble metal alloys, transition metal sulphides [11–15], phosphides [16–22], carbides [1, 23], and nitrides [24–28] have demonstrated their potential as efficient and durable HER catalysts. Among them, CoP is the most promising substitute due to its high catalytic activity and durability [29–31]. Although the morphology of phosphide has been tuned to obtain a large number of active sites, unfortunately, its performance and durability are still not ideal compared with the noble metal Pt.

In order to improve the intrinsic activity of metal phosphide HER, doping with metallic elements becomes a promising approach Charge transfer between external atoms and the host occurs, and the electronic structure is adjusted to enhance the kinetic process of HER. Most of the current studies focus on the doping of noble metal atoms to improve HER performance, and there is a lack of research on transition metal element doping. In addition, the limited enhancement of HER performance of transition metal-doped phosphides has hindered the research of cheap and durable CoP catalysts.

Fe^{3+} is more acidic among transition metals and can serve as lewis acid sites. Specifically, Fe^{3+} with higher acidity than Co^{2+} can pull electrons from the neighboring Co-P bond, reducing the electronic energy associated with Co^{2+} oxidation and causing a positive change in the corresponding Co redox [6]. Therefore, we hypothesize that the enhanced HER activity can be attributed to the introduction of more acidic substituents into more electron-rich Fe centers through inductive effects. The electron-rich Fe provides electrons to protons, which are easily trapped and form H_{ad} active material. After giving a certain voltage, enough Had is accumulated and then transferred to the electron-deficient Co sites, where Co is beneficial for proton desorption. Both of them have different tasks and synergistically improve the performance of HER. This bimetallic synergistic effect is helpful to guide us to discover more potential catalysts.

2 Experiment Section

2.1 Chemicals

Iron chloride hexahydrate ($FeCl_3 \cdot 6H_2O$), cobalt chloride hexahydrate ($CoCl_2 \cdot 6H_2O$), Sodium hypophosphite ($NaH_2PO_2 \cdot H_2O$), methanol (CH_3OH) and hexamethylenetetramine (HMT) were purchased from Sigma-Aldrich and directly used without further purification. Ultrapure deionized water (DI, 18.4 $M\Omega\ cm^{-1}$) was used in all experiments. MWCNTs were purchased from Tanfeng Tech. Inc (China). Cabon paper HCP020P were purchased from Shanghai Hesen Electric Co., Ltd (China).

2.2 Preparation of $Co_{1-x}Fe_xLDH$/MWCNTs

In a typical synthesis process of $Co_{0.75}Fe_{0.25}LDH$/MWCNTs, the total moles of Co and Fe are 2. The MWCNTs (100 mg) was dispersed into the water of 70 mL to form a dispersion solution under continuous ultrasonication. Subsequently, 0.5 mmol iron chloride

hexahydrate ($FeCl_3 \cdot 6H_2O$), 1.5 mmol cobalt chloride hexahydrate ($CoCl_2 \cdot 6H_2O$), and 0.875 mmol hexamethylenetetramine (HMT) were added into the above solution under vigorous stirring. The solution was refluxed at 100 °C for 5 h in an oil bath, and then the precipitates were collected by centrifugation for several times with water and alcohol. The samples were dried at 60 °C overnight to obtain $Co_{0.75}Fe_{0.25}$LDH/MWCNTs. For comparison, the bulky $Co_{0.75}Fe_{0.25}$LDH samples without MWCNTs were also obtained under the same conditions. Other CoFeLDH/MWCNTs, prepared by adjusting the proportion of Fe.

2.3 Preparation of $Co_{1-x}Fe_xP$/MWCNTs

To prepare the $Co_{0.75}Fe_{0.25}$P/MWCNTs, a low temperature phosphidation method was employed here. In details, 300 mg of $NaH_2PO_2 \cdot H_2O$ and as-synthesized $Co_{0.75}Fe_{0.25}$P/MWCNTs were placed in the quartz boats individually, and then placed in two separate positions within the tube furnace. The furnace was heated up to 300 °C with a temperature ramping rate of 5 °C/min and kept at 300 °C for two hour under an N_2 flow of 100 sccm.

2.4 Electrochemical Measurements

The catalyst ink was prepared by dispersing 4 mg of various catalysts into 1 mL of the mixed solvent containing water, ethanol and 5% Nafion with a volumetric ratio of 768:200:32. For the preparation of the catalytic electrodes, 10 μL of the catalyst ink was loaded onto a carbon paper (CP) electrode. A CHI760E electrochemical workstation was used to conduct all the electrochemical tests, with an CP as the working electrode, a graphite rod as the counter electrode, a Hg/Hg_2SO_4 electrode as the reference electrode, and 0.5 M H_2SO_4 as the electrolyte. The CV result is shown in Fig. S1. Before the electrochemical test, $E(RHE) = E(Hg/Hg_2SO_4) + 0.71$ V for 0.5 M H_2SO_4 electrolyte.

3 Results and Discussion

The morphology of the catalysts was characterized by SEM and TEM. The SEM images (Fig. 1a) showed that the nanoparticles were grown on the surface of the MWCNTs and the surface-grown catalysts encapsulated the MWCNTs to form a core-shell structure. This structure may provide more active sites for the HER reaction and is thought to improve the catalytic performance. As shown in Fig. 1b, the lattice spacings of $Co_{0.75}Fe_{0.25}$P/MWCNTs of 0.243, 0.238 and 0.283 nm correspond to [111], [201] and [002] crystal planes, respectively, which are very close to the lattice spacings of the corresponding crystal planes of $(CoFe)P_2$. The high-angle annular dark field image (HAADF) map shows that the nanoparticles are uniformly dispersed on the surface of MWCNTs (Fig. 1c), which also indicates that electrons can interact with the catalyst nanoparticles rapidly through the MWCNTs channels. The STEM-EDX map shows the same distribution area of Fe, Co and P elements, which proves that the products are uniformly distributed on the surface of MWCNTs, indicating that Fe doped CoP was successfully synthesized (Fig. 1d).

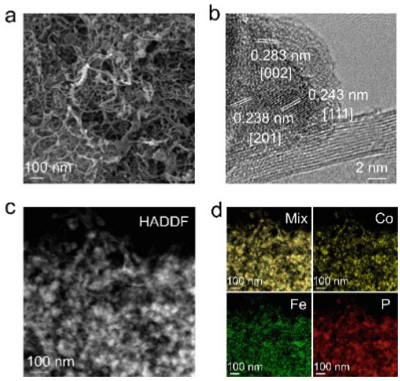

Fig. 1. (**a**) SEM and (**b**) HR-TEM image of $Co_{0.75}Fe_{0.25}P$/MWCNTs. (**c**) HAADF-STEM images and the corresponding. (**d**) STEM-EDX of $Co_{0.75}Fe_{0.25}P$/MWCNTs.

The surface composition and chemical properties of $Co_{0.75}Fe_{0.25}P$/MWCNTs were investigated by x-ray photoelectron spectroscopy (XPS). As shown in Fig. 2a, the Co 2p XPS spectra of $Co_{0.75}Fe_{0.25}P$/MWCNTs had characteristic peaks at 781.8 and 797.9 eV, which were assigned to Co^{3+} [32]. The Co 2p XPS spectra had characteristic peaks at 783.7 and 799.2 eV, which were assigned to Co^{2+}, and the other peak positions were assigned to satellite peaks. The characteristic peaks of Fe 2p XPS spectra (Fig. 2b) in $Co_{0.75}Fe_{0.25}P$/MWCNTs at 712.4 and 726.3 eV, which are attributed to Fe^{3+}. The characteristic peaks of Fe 2p XPS spectra at 710.2 and 724.5 eV, which are assigned to Fe^{2+}, and other peak positions are attributed to satellite peaks [33]. The Co 2p and Fe 2p XPS spectra of $Co_{0.75}Fe_{0.25}P$/MWCNTs indicate that the acidic Fe^{3+} pulls electrons out of the Co site, leading to a change in the electronic structure of the catalyst. The characteristic peaks of the O 2p XPS spectra (Fig. 2c) in $Co_{0.75}Fe_{0.25}P$/MWCNTs at 531.8 and 533.3 eV, respectively attributed to surface oxygen and exogenous oxygen. The lattice oxygen is not found in the O 2p XPS spectra, which indicates that no metal phosphate is formed [34]. P 2p XPS spectra at 130.1 and 131.2 eV for the low valence P [35] and higher binding energy at 134.3 eV are attributed to PO_4^{3-} or P_2O_5, which is attributed to the oxidation of the surface P element [36].

The HER activity of $Co_{0.75}Fe_{0.25}P$/MWCNTs in 0.5 M H_2SO_4 was determined by linear scanning voltammetry (LSV). For comparison, CoP/MWCNTs, FeP/MWCNTs and 20% Pt/C loaded on carbon paper (CP) substrates were prepared. The LSV (Fig. 3a) showed that $Co_{0.75}Fe_{0.25}P$/MWCNTs had a higher activity towards HER with an overpotential of only 126 mV at 10 mA cm^{-2}, which was significantly smaller than that on CoP/MWCNTs (233 mV) and FeP/MWCNTs (160 mV).

As shown in Fig. 3b, $Co_{0.75}Fe_{0.25}P$/MWCNTs delivered a small Tafel slope of 89.8 mV dec^{-1}, close to that for the commercially available Pt/C catalyst (48.9 mV dec^{-1}), which was lower than CoP/MWCNTs (102 mV dec^{-1}) and FeP/MWCNTs (100 mV dec^{-1}), indicating favorable HER activity. To predict the intrinsic catalytic reaction kinetics of the sample, the Tafel slope was derived from the corresponding polarization curve using the Tafel formula ($\eta = \mathbf{a} + \mathbf{b} \log \boldsymbol{j}$, where $\boldsymbol{b}$ is the Tafel slope, and $\boldsymbol{j}$ is the current density). A lower Tafel slope indicates more efficient hydrogen

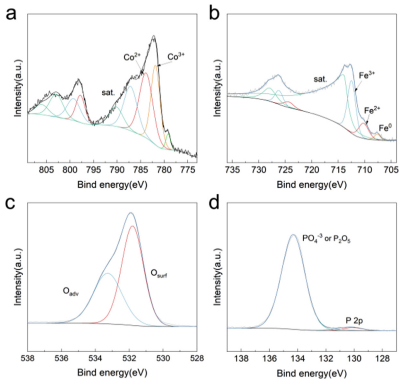

Fig. 2. (**a**) High-resolution XPS spectra of Co 2p, (**b**) Fe 2p, (**c**) O 2p and (**d**) P 2p for $Co_{0.75}Fe_{0.25}P$/MWCNTs.

reaction evolution dynamics, meaning that increasing the same current density requires smaller overpotentials.

It is well known that under a specific set of conditions, the HER mechanism is divided into two steps in acidic solution, which are electrochemical adsorption process (Volmer) and desorption process (Heyrovsky or Tafel). Generally, a Tafel slope of 120 mV dec^{-1} indicates that the Volmer step is the rate-determining step:

$$H^- + e^- + * \rightarrow *H_{ads}$$

This step is followed by either an electrochemical desorption step (Heyrovsky reaction, Tafel slope is 40 mV dec^{-1}) [37],

$$H^- + e^- + * + *H_{ads} \rightarrow H_2 + 2*$$

or a recombination step (Tafel reaction, Tafel slope is 30 mV dec^{-1}) [38, 39],

$$*H_{ads} + *H_{ads} \rightarrow H_2 + 2*$$

The rate-determining step of Pt/C follows the Volmer-Heyrovsky mechanism in 0.5 M H_2SO_4 solution according to the literature. The Tafel slope of CoP/MWCNTs and FeP/MWCNTs increased to 102 and 100 mV dec^{-1}, all of them indicated a tendency to limit the absorption of H^+ on active sites (Volmer Step). The slope of $Co_{0.75}Fe_{0.25}P$/MWCNTs (89.8 mV dec^{-1}) implies that the reaction mechanism is the Volmer-Heyrovsky mechanism in the HER, in which the rate-determining step is the desorption process and the reaction kinetics is optimized. Analysis of the overpotential and Tafel shows that Fe has a large effect on HER performance. In Fig. 3c, the practical H_2 yield is basically agreement with the theoretical value, giving a faradaic efficiency of nearly 99% for HER in 0.5 M H_2SO_4. The electrochemical impedance spectrum shows a charge transfer resistance of 7.1 Ω for $Co_{0.75}Fe_{0.25}P$/MWCNTs, which is close to Pt/C (7 Ω) and less than CoP/MWCNTs (10.2 Ω) and FeP/MWCNTs (8.9 Ω). This also indicates that Fe doping modulates the electronic structure of the catalysts, making the charge transport more efficient.

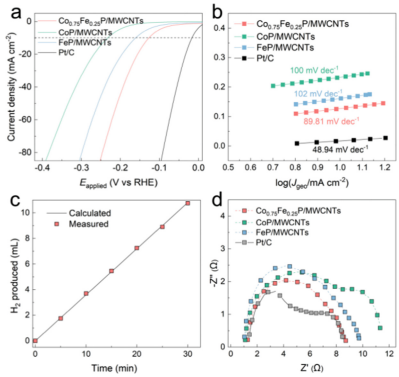

Fig. 3. (**a**) SEM and (**b**) HR-TEM image of $Co_{0.75}Fe_{0.25}P$/MWCNTs. (**c**) HAADF-STEM images and the corresponding (**d**) STEM-EDX of $Co_{0.75}Fe_{0.25}P$/MWCNTs. (**a**) HER-LSV curves of $Co_{0.75}Fe_{0.25}P$/MWCNTs, CoP/MWCNTs, FeP/MWCNTs and Pt/C. (**b**) Tafel plots of different samples. (**c**) Faraday efficiency of HER for $Co_{0.75}Fe_{0.25}P$/MWCNTs with constant current density of 100 mA cm^{-2}. (**d**) Nyquist plots for $Co_{0.75}Fe_{0.25}P$/MWCNTs, CoP/MWCNTs, FeP/MWCNTs and Pt/C.

The electrochemical double layer capacitance (C_{dl}) was determined by cyclic voltammetry (CV). As shown in Fig. 4a, b and c, $Co_{0.75}Fe_{0.25}P$/MWCNTs exhibited a larger C_{dl} of 3.2 mF cm^{-2} in contrast to CoP/MWCNTs (2.2 mF cm^{-2}) and FeP/MWCNTs (2.1 mF cm^{-2}). The larger electrochemically active surface area of $Co_{0.75}Fe_{0.25}P$/MWCNTs indicates that the Fe doped CoP is a dual active site.

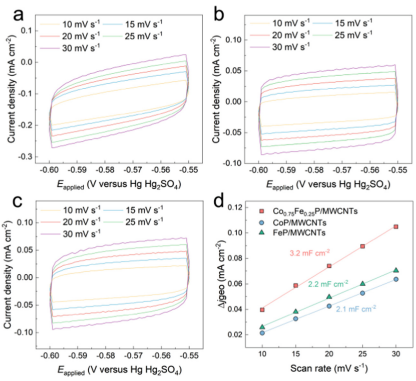

Fig. 4. CV curves at the non-Faradic region of (**a**) $Co_{0.75}Fe_{0.25}P$/MWCNTs, (**b**) CoP/MWCNTs and (**c**) FeP/MWCNTs. (**d**) Double-layer capacitance (Cdl) of $Co_{0.75}Fe_{0.25}P$/MWCNTs, CoP/MWCNTs and FeP/MWCNTs.

When evaluating HER electrocatalysts, the TOF value at the overpotential of −0.2 V versus RHE reveal the intrinsic activity of the catalyst. According to the estimated number of active sites, the TOF value (Fig. 5a) of each active site of $Co_{0.75}Fe_{0.25}P$/MWCNTs, CoP/MWCNTs and FeP/MWCNTs in 0.5 M H_2SO_4 was calculated. As shown in

Fig. 5a, the TOF value of $Co_{0.75}Fe_{0.25}P$/MWCNTs (0.18 s^{-1}) was higher than that of CoP/MWCNTs and FeP/MWCNTs, which further indicates the synergistic effect of the bimetallic sites. The ECSA-normalized specific activity (SA) at $\eta = -200$ mV is shown in Fig. 5b. $Co_{0.75}Fe_{0.25}P$/MWCNTs (SA = 556 μA cm^{-2}) offers higher specific activity than the bare CoP/MWCNTs (SA = 386 μA cm^{-2}) and FeP/MWCNTs (SA = 86 μA cm^{-2}), demonstrating the effectiveness of the bimetallic synergy strategy. Furthermore, the mass activity (MA) is calculated at the overpotential (η) of −200 mV (Fig. 5c), and $Co_{0.75}Fe_{0.25}P$/MWCNTs shows higher MA (107 A g^{-1}) than CoP/MWCNTs (MA = 52 A g^{-1}), and FeP/MWCNTs (MA = 11 A g^{-1}). The corresponding specific activity and mass activity of HER at the overpotential of −200 mV were showed in Fig. 5d, which demonstrating the bimetallic synergistic strategy is potentially applicable to the exploration of superior catalysts.

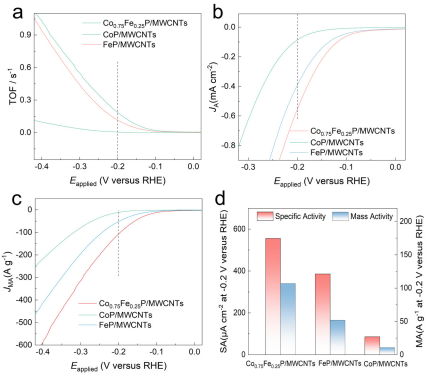

Fig. 5. **a** Turnover Frequency (TOF) plots of $Co_{0.75}Fe_{0.25}P$/MWCNTs, CoP/MWCNTs and FeP/MWCNTs. **b** OER-LSV curves for specific activity, and **c** mass activity of different catalysts. **d** The corresponding specific activity and mass activity of OER at the overpotential of −0.2 V versus RHE.

4 Conclusion

In summary, the $Co_{0.75}Fe_{0.25}P$/MWCNTs catalyst with heterogeneous structure and strong metal carrier interaction was synthesized by hydrothermal method. A series of physical characterization and chemical experiments showed that the unique bimetallic synergy of the $Co_{0.75}Fe_{0.25}P$/MWCNTs composite and the SMSI between the nano-nanoparticles and the MWCNTs substrate give the material superior electronic conductivity, abundant active sites and stable structure, which are the fundamental reasons for its high electrocatalytic HER activity and stability. The $Co_{0.75}Fe_{0.25}P$/MWCNTs catalysts have an overpotential of only 126 mV at a current density of 10 mA cm^{-2} in 0.5 M H_2SO_4 solution and TOF values as high as 0.18 s^{-1} at an overpotential of −200 mV. The bimetallic synergy can provide a promising strategy for the design of superior HER catalysts. Provides a promising strategy for the design of superior HER catalysts.

References

1. Li, J., et al.: Mechanistic insights on ternary $Ni_{2-x}Co_xP$ for hydrogen evolution and their hybrids with graphene as highly efficient and robust catalysts for overall water splitting. Adv. Func. Mater. **26**, 6785–6796 (2016). https://doi.org/10.1002/adfm.201601420
2. Dresselhaus, M.S., Thomas, I.L.: Alternative energy technologies. Nature **414**, 332–337 (2001). https://doi.org/10.1038/35104599
3. Holladay, J.D., Hu, J., King, D.L., Wang, Y.: An overview of hydrogen production technologies. Catal. Today **139**, 244–260 (2009). https://doi.org/10.1016/j.cattod.2008.08.039
4. Seh, Z.W., Kibsgaard, J., Dickens, C.F., Chorkendorff, I., Nørskov, J.K., Jaramillo, T.F.: Combining theory and experiment in electrocatalysis: Insights into materials design. Science **355**, eaad4998 (2017). https://doi.org/10.1126/science.aad4998
5. Turner, J.A.: Sustainable hydrogen production. Science **305**, 972–974 (2004). https://doi.org/10.1126/science.1103197
6. Yuan, S., et al.: Tunable metal hydroxide–organic frameworks for catalysing oxygen evolution. Nat. Mater. **21**, 673–680 (2022). https://doi.org/10.1038/s41563-022-01199-0
7. Liu, D., et al.: Atomically dispersed platinum supported on curved carbon supports for efficient electrocatalytic hydrogen evolution. Nat. Energy **4**, 512–518 (2019). https://doi.org/10.1038/s41560-019-0402-6
8. Alinezhad, A., et al.: Direct growth of highly strained Pt islands on branched ni nanoparticles for improved hydrogen evolution reaction activity. J. Am. Chem. Soc. **141**, 16202–16207 (2019). https://doi.org/10.1021/jacs.9b07659
9. Tiwari, J.N., et al.: Multicomponent electrocatalyst with ultralow Pt loading and high hydrogen evolution activity. Nat. Energy **3**, 773–782 (2018). https://doi.org/10.1038/s41560-018-0209-x
10. Liang, C., et al.: Exceptional performance of hierarchical ni–fe oxyhydroxide@NiFe alloy nanowire array electrocatalysts for large current density water splitting. Energy Environ. Sci. **13**, 86–95 (2020). https://doi.org/10.1039/C9EE02388G
11. Bonde, J., Moses, P.G., Jaramillo, T.F., Nørskov, J.K., Chorkendorff, I.: Hydrogen evolution on nano-particulate transition metal sulfides. Faraday Discuss. **140**, 219–231 (2009). https://doi.org/10.1039/B803857K
12. Sun, Y., Huang, C., Shen, J., Zhong, Y., Ning, J., Hu, Y.: One-step construction of a transition-metal surface decorated with metal sulfide nanoparticles: a high-efficiency electrocatalyst for hydrogen generation. J. Colloid Interface Sci. **558**, 1–8 (2020). https://doi.org/10.1016/j.jcis.2019.09.090
13. Guo, Y., et al.: Nanoarchitectonics for transition-metal-sulfide-based electrocatalysts for water splitting. Adv. Mater. **31**, 1807134 (2019). https://doi.org/10.1002/adma.201807134
14. Li, H., et al.: Systematic design of superaerophobic nanotube-array electrode comprised of transition-metal sulfides for overall water splitting. Nat. Commun. **9**, 2452 (2018). https://doi.org/10.1038/s41467-018-04888-0
15. Huang, C., et al.: Electrolyzer with hierarchical transition metal sulfide and phosphide towards overall water splitting. Mater. Today Phys. **11**, 100162 (2019). https://doi.org/10.1016/j.mtphys.2019.100162
16. Are metal chalcogenides: Nitrides, and phosphides oxygen evolution catalysts or bifunctional catalysts? ACS Energy Lett. **2**, 1937–1938 (2017). https://doi.org/10.1021/acsenergylett.7b00679
17. Tan, Y., et al.: Versatile nanoporous bimetallic phosphides towards electrochemical water splitting. Energy Environ. Sci. **9**, 2257–2261 (2016). https://doi.org/10.1039/C6EE01109H
18. Yan, L., et al.: Metal-organic frameworks derived nanotube of nickel–cobalt bimetal phosphides as highly efficient electrocatalysts for overall water splitting. Adv. Funct. Mater. **27**, 1703455 (2017). https://doi.org/10.1002/adfm.201703455

19. Feng, Y., Yu, X.-Y., Paik, U.: Nickel cobalt phosphides quasi-hollow nanocubes as an efficient electrocatalyst for hydrogen evolution in alkaline solution. Chem. Commun. **52**, 1633–1636 (2016). https://doi.org/10.1039/C5CC08991C
20. Ha, D.-H., et al.: Activity and stability of cobalt phosphides for hydrogen evolution upon water splitting. Nano Energy **29**, 37–45 (2016). https://doi.org/10.1016/j.nanoen.2016.04.034
21. Du, H., Kong, R.-M., Guo, X., Qu, F., Li, J.: Recent progress in transition metal phosphides with enhanced electrocatalysis for hydrogen evolution. Nanoscale **10**, 21617–21624 (2018). https://doi.org/10.1039/C8NR07891B
22. Lu, S.-S., et al.: Tungsten-doped ni–co phosphides with multiple catalytic sites as efficient electrocatalysts for overall water splitting. J. Mater. Chem. A **7**, 16859–16866 (2019). https://doi.org/10.1039/C9TA03944A
23. McKone, J.R., Sadtler, B.F., Werlang, C.A., Lewis, N.S., Gray, H.B.: Ni–mo nanopowders for efficient electrochemical hydrogen evolution. ACS Catal. **3**, 166–169 (2013). https://doi.org/10.1021/cs300691m
24. Xie, J., Xie, Y.: Transition metal nitrides for electrocatalytic energy conversion: opportunities and challenges. Chemistry **22**, 3588–3598 (2016). https://doi.org/10.1002/chem.201501120
25. Abghoui, Y., Skúlason, E.: Hydrogen evolution reaction catalyzed by transition-metal nitrides. J. Phys. Chem. C **121**, 24036–24045 (2017). https://doi.org/10.1021/acs.jpcc.7b06811
26. Yu, L., et al.: A universal synthesis strategy to make metal nitride electrocatalysts for hydrogen evolution reaction. J. Mater. Chem. A **7**, 19728–19732 (2019). https://doi.org/10.1039/C9TA05455C
27. Balogun, M.-S., Huang, Y., Qiu, W., Yang, H., Ji, H., Tong, Y.: Updates on the development of nanostructured transition metal nitrides for electrochemical energy storage and water splitting. Mater. Today **20**, 425–451 (2017). https://doi.org/10.1016/j.mattod.2017.03.019
28. Jin, H., et al.: Molten salt-directed catalytic synthesis of 2d layered transition-metal nitrides for efficient hydrogen evolution. Chem **6**, 2382–2394 (2020). https://doi.org/10.1016/j.chempr.2020.06.037
29. Zhang, H., Maijenburg, A.W., Li, X., Schweizer, S.L., Wehrspohn, R.B.: Bifunctional heterostructured transition metal phosphides for efficient electrochemical water splitting. Adv. Func. Mater. **30**, 2003261 (2020). https://doi.org/10.1002/adfm.202003261
30. Chu, S., et al.: Holey Ni-Cu phosphide nanosheets as a highly efficient and stable electrocatalyst for hydrogen evolution. Appl. Catal. B **243**, 537–545 (2019). https://doi.org/10.1016/j.apcatb.2018.10.063
31. Zhu, J., Hu, L., Zhao, P., Lee, L.Y.S., Wong, K.-Y.: Recent advances in electrocatalytic hydrogen evolution using nanoparticles. Chem. Rev. **120**, 851–918 (2020). https://doi.org/10.1021/acs.chemrev.9b00248
32. Xiao, Z., et al.: Operando identification of the dynamic behavior of oxygen vacancy-rich Co_3O_4 for oxygen evolution reaction. J. Am. Chem. Soc. **142**, 12087–12095 (2020). https://doi.org/10.1021/jacs.0c00257
33. Huang, G., Zhao, L., Yuan, S., Li, N., Jing, S.: Iron doped mesoporous cobalt phosphide with optimized electronic structure for enhanced hydrogen evolution. Int. J. Hydrogen Energy **47**, 14767–14776 (2022). https://doi.org/10.1016/j.ijhydene.2022.02.223
34. Zhai, Y., Ren, X., Sun, Y., Li, D., Wang, B., Liu, S.: Synergistic effect of multiple vacancies to induce lattice oxygen redox in NiFe-layered double hydroxide oer catalysts. Appl. Catal. B **323**, 122091 (2023). https://doi.org/10.1016/j.apcatb.2022.122091
35. Tang, C., et al.: Fe-doped cop nanoarray: A monolithic multifunctional catalyst for highly efficient hydrogen generation. Adv. Mater. **29**, 1602441 (2017). https://doi.org/10.1002/adma.201602441
36. Guan, C., et al.: Hollow Mo-doped CoP nanoarrays for efficient overall water splitting. Nano Energy **48**, 73–80 (2018). https://doi.org/10.1016/j.nanoen.2018.03.034

37. Dinh, C.-T., et al.: Multi-site electrocatalysts for hydrogen evolution in neutral media by destabilization of water molecules. Nat. Energy **4**, 107–114 (2019). https://doi.org/10.1038/s41560-018-0296-8
38. Men, Y., Li, P., Zhou, J., Cheng, G., Chen, S., Luo, W.: Tailoring the electronic structure of Co_2P by N doping for boosting hydrogen evolution reaction at all pH values. ACS Catal. **9**, 3744–3752 (2019). https://doi.org/10.1021/acscatal.9b00407
39. Men, Y., Li, P., Yang, F., Cheng, G., Chen, S., Luo, W.: Nitrogen-doped CoP as robust electrocatalyst for high-efficiency pH-universal hydrogen evolution reaction. Appl. Catal. B **253**, 21–27 (2019). https://doi.org/10.1016/j.apcatb.2019.04.038

An Optimal Energy Management Strategy for a Hybrid Train

Rui Chang[1], Yang Liu[2(✉)], Yufeng Cao[2], and Jianqiang Liu[1]

[1] Institute of Power Electronics and Electric Traction, Beijing Jiaotong University, Beijing 100044, China
21121411@bjtu.edu.cn, 11590069@ceic.com
[2] China Energy Railway Equipment Co., Ltd., Beijing 100091, China
liujq@bjtu.edu.cn

Abstract. The hybrid trains use hydrogen fuel cells and lithium-iron phosphate batteries as energy sources. The powertrain has the advantage of zero emissions and high energy efficiency due to optimizing the power distribution strategy and the recovery of braking energy. This paper proposes an energy management strategy based on the Dynamic Programming Algorithm (DPA) to optimize the power allocation of both power sources to guarantee the power performance of the train and achieve optimal operation at the cost. The method is based on a dynamic programming algorithm to determine the optimum output power of a hydrogen-fuelled engine. Based on the operating characteristics of the train and the characteristics of the respective power sources, the objective function and constraints are established, and the principles for selecting the parameters of the optimization algorithm are presented. Finally, as a driving condition, the train is operated on a specific line in a minimum time operation. The vehicle model and control strategy designed in Matlab/Simulink environment is jointly simulated and verified. Simulation results show that the proposed optimization strategy results in significant savings in hydrogen consumption for the hybrid train compared to the SOC equalization strategy and better meets the train power performance requirements.

Keywords: Hybrid trains · Hydrogen fuel cells · Lithium iron phosphate batteries · Energy management · Dynamic programming

1 Introduction

The transportation industry is actively developing hydrogen-fuelled hybrid trains to reduce pollution emission levels due to the green and efficient nature of new energy sources and the shift in energy layout. When used as a power source in vehicles, fuel cells have soft output characteristics and poor dynamic performance, so they are slow to transmit power and need to be used in conjunction with auxiliary energy sources such as batteries [1]. Hybrid systems offer high energy and power densities and better vehicle dynamics, but they also require energy management systems to distribute energy between multiple sources for optimum efficiency and performance [2]. Current hybrid energy management strategies have evolved into two main categories, namely rule-based control and optimization-based control.

H. Sun et al. (Eds.): WHTC 2023, SPPHY 393, pp. 475–484, 2024.
https://doi.org/10.1007/978-981-99-8631-6_46

The rule-based algorithm relies on knowledge of the operating characteristics of the hybrid system components as well as relevant engineering experiences, such as State Machine Control (SMC) and the Wavelet-fuzzy Logic Control (WFLC) type of strategy. Zhang et al. [3] proposed a power allocation algorithm based on wavelet decomposition for energy management. Caux et al. [4] tested an online fuzzy logic algorithm, and Erdinc et al. [5] built upon this research by integrating the algorithms of wavelet decomposition and fuzzy logic.

Optimization-based algorithms include Dynamic Programming (DP), Equivalent Consumption Minimization Strategy (ECMS), and Pontryagin's Minimum Principle (PMP), in which ECMS and PMP are instantaneous optimization algorithms and DP is a global optimization algorithm. Motapon et al. [6] discuss a comparative analysis between different optimal power allocation methods. A popular selection technique for optimal power allocation in hybrid vehicles is dynamic programming (DP). This method is widely used to control the degree of mixing between sources of vehicles, whether they are internal combustion engine (ICE) based or purely electric [7]. This algorithm is used to solve recursive problems, guarantees optimality within a certain tolerance range, and is easy to implement [8]. The main problem with DP is the dimensional catastrophe, where the number of states grows exponentially with time [9]. In [10], DP was used to test the impact of battery weight and storage capacity on the cost of operation.

2 Efficient Energy Management Strategies Based on Dynamic Programming Algorithms

2.1 General Formulas for Dynamic Programming

This paper investigates the problem of distributing the power of the fuel cell and the battery so that the cost function is minimized subject to constraints. The entire run time is discretized into T phases by step Δt, which are equally spaced along the length of the driving cycle.

The power of the fuel cell or the power of the battery can be considered as the control vector. By fixing one, the other can be derived from the power balance equation, so this power fixing method helps to solve the problem more easily and is easy to program. In this case, the fuel cell power is chosen as the control vector, and the control vector x consists of a range from the lower fuel cell power limit P_{fcL} to the upper fuel cell power limit P_{fcH} discretized in equal steps. The cell then satisfies the residual capacity requirement within the SOC constraint.

The total number of nodes is S × T, which depends on the number of selected states and time samples. Each of these nodes can be indexed according to its current stage position and corresponding state. For example, node Niuj corresponds to the node at step N and state uj. Equation (1) shows that the total Fiuj cost associated with each node at a certain time step is the sum of its node cost and the minimum value of all transition costs at the node from the previous time step.

$$F_{\mathrm{iuj}} = C_{\mathrm{iu_j}} + \min_{k}\left[R_{\mathrm{u}_k,\mathrm{iu}}\right] \quad i = 1:T; j,k = 1:\mathrm{S} \tag{1}$$

2.2 Equation Establishment and Constraint Implementation Method

To simplify the problem, the power required for the vehicle driveline, $P_{req} = P_{ele} + P_{aux}$, is first calculated and used as input to the optimization problem. P_{dc} is the control variable and SOC is the state variable.

Nodal costs and transition costs are defined. The nodal cost shown in (2) calculates the cost of the energy from the fuel cell and the battery. It also treats the braking energy as equivalent to the fuel cell energy. This is because the dissipated energy initially comes from the fuel cell. The cost of the fuel cell considers primarily the cost of hydrogen consumption. This cost also takes into account the cost of electricity in the charging and discharging phases of the battery.

$$J = \min \sum_{k=0}^{N-1} C_{\mathrm{fc,k}} + C_{\mathrm{bat,k}} \tag{2}$$

where Cfc and Cbat are the fuel cell and battery pack costs respectively. These two cost variables can be expressed as in Eq. (3).

$$\begin{cases} C_{\mathrm{fc}} = M_{\mathrm{h2}} b_{\mathrm{e}} P_{\mathrm{fc}} \Delta t \\ C_{\mathrm{bat}} = M_{\mathrm{ele}} P_{\mathrm{bat}} \left(\eta_{\mathrm{disavg}} \eta_{\mathrm{chgavg}}\right)^{-\mathrm{sgn}(P_{\mathrm{bat}})} \Delta t \end{cases} \tag{3}$$

M_{h2} and Mele are the prices of hydrogen and electricity in \$/g and \$/kWh.

Transition costs are associated with the feasibility of moving from one node to another. When a hop from node to node is infeasible, a very large cost is added to the switching cost. Conversely, if the link is feasible from node to node, the transition costs are low. For the hydrogen fuel cell hybrid system, the power of the fuel cell must be between its lower power limit $P_{fc,min}$ and upper power limit $P_{fc,max}$, and the rate of change of its power ΔP_{fc} must not be greater than the allowed range of the battery system. The battery also has a lower power limit $P_{bat,min}$ and upper power limit $P_{bat,max}$, and the power allocated to the battery must be within this range. The battery also has a limit on SOC, which should be between its permissible lower boundary SOC_L and upper boundary SOC_H. The introduction of the SOC end value constraint, which allows the battery SOC to be the same at the start and end moments to avoid additional charging processes, is important for the control of the power cell SOC during the operating cycle. Equation (4) lists all constraints.

The implementation of the constraint on the final SOC relies on imposing a large transition cost on the paths that deviate from the set value at the final moment T, and this transition cost increases with the degree of deviation, and is expressed as (5).

$$s.t. \begin{cases} SOC_0 = SOC_E = SOC_N \\ SOC_L < SOC < SOC_H \\ P_{fc,\min} < P_{fc} < P_{fc,\max} \\ P_{bat,\min} < P_{bat} < P_{bat,\max} \\ \left|\Delta P_{fc}\right| < \Delta P_{dc,lmt} \end{cases} \tag{4}$$

$$C_{\mathrm{SOC\_N,k}} = 10^{\gamma} \left|SOC - SOC_{\mathrm{N,k}}\right| \tag{5}$$

The implementation of the constraint on the battery SOC boundary and the constraint on the fuel cell power rate of change relies on imposing a large transition cost at each moment on all nodes that are outside the boundary, forcing the algorithm to find alternative paths, with the expressions as (6–8).

$$C_{\mathrm{SOC\_H,k}} = \alpha(SOC - SOC_{\mathrm{H}}), \quad SOC > SOC_{\mathrm{H}} \tag{6}$$

$$C_{\mathrm{SOC\_L,k}} = \beta(SOC_{\mathrm{L}} - SOC), \quad SOC < SOC_{\mathrm{L}} \tag{7}$$

$$C_{\mathrm{fc,\ var\ ,k}} = \theta\left(\left|\frac{P_{\mathrm{dc,k+1}} - P_{\mathrm{dc,k}}}{\Delta t}\right| - \Delta P_{\mathrm{dc,lmt}}\right)^2 \ \frac{P_{\mathrm{dc,k+1}} - P_{\mathrm{dc,k}}}{\Delta t} > \Delta P_{\mathrm{dc,lmt}} \tag{8}$$

The constraint on fuel cell power and the battery is achieved by relying on limiting the decision space to the power of the fuel cell only, which can be achieved indirectly through the power balance relationship on the busbar in Eq. (9).

$$\begin{aligned} x_{LB} &= \max(P_{fc\_\min}, P_{load} - P_{bat,\max}) \\ x_{UB} &= \min(P_{fc\_\max}, P_{load} + P_{bat,\min}) \end{aligned} \tag{9}$$

3 Simulation Validation and Comparative Analysis

3.1 Simulation Model Construction

In order to obtain valid simulation results, the electrical and mechanical parts of the power system of the new-energy hybrid trolley train need to be modeled, consisting of at least five different subsystems as shown in Table 1.

Table 1. Power system subsystems and their description

Subsystems	Description
Fuel cells	3*81 kW PEMC
Power batteries	460 Ah $LiFePO_4$ battery
DC/DC	Unidirectional boost DCDC converters
Motors	2*215 kW AC motor
Energy management systems	Implementation of energy management control algorithms

3.1.1 Fuel Cell System Modeling

The fuel cell model is calculated as follows: the system input variable is the fuel cell power and the output variables are the fuel cell voltage and the instantaneous hydrogen consumption. The fuel cell voltage can be obtained from the polarization curve and the efficiency corresponding to the current power can also be obtained (Fig. 1).

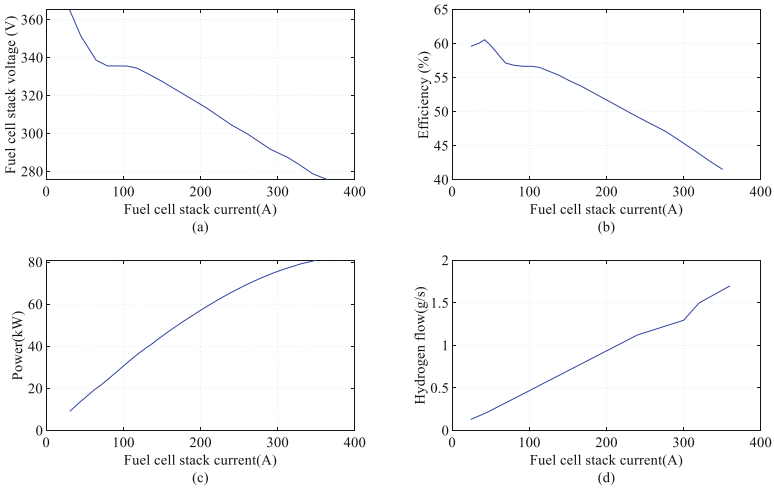

Fig. 1. Fuel cell characteristic curves. (**a**) FC voltage-current curve. (**b**) FC efficiency-current curve. (**c**) FC power-current curve. (**d**) FC hydrogen flow-current curve.

According to the power efficiency curve and (12), the instantaneous hydrogen flow rate can be found, and the instantaneous hydrogen consumption m_{H2}, LHV is the low heat value of hydrogen, which is taken as 120 kJ/g.

$$\Delta m_{\mathrm{H}_2} = \frac{P_{\mathrm{fc}}}{LHV\,\eta_{\mathrm{fc}}}, m_{\mathrm{H}_2} = \int \Delta m_{\mathrm{H}_2} dt \tag{10}$$

3.1.2 DC/DC Model

The DC/DC contains non-linear components. When studying the dynamic characteristics near the steady-state operating point, the system can be seen as approximately linear by means of small signal analysis methods. In this paper, the internal dynamics of the DC/DC are not studied and the joint model is solved by treating the DC/DC as a fixed efficiency.

3.1.3 Battery System

The battery is modeled using the Rint model, where the open circuit voltage, internal resistance, and battery power are functions of the SOC.

The current parameters of the equivalent circuit are calculated from the quadratic equation relating the open circuit voltage, the internal resistance, and the actual power, see (13).

$$I_{BT} = \frac{V_{oc} - \left(\sqrt{V_{oc}^2 - 4R_{BT}P_{BT}}\right)}{2R_{BT}} \tag{11}$$

The SOC is updated according to the current value entered into the block as shown in (14).

$$\mathrm{SOC}(t_k) = \mathrm{SOC}(0) - \frac{1}{C_{BT}} \int_{t_0}^{t_k} I_{BT}\, dt \tag{12}$$

Calculating the open-circuit voltage and internal resistance of the battery from the current SOC value and the temperature value by looking at the table. The battery parameters are shown in Fig. 2.

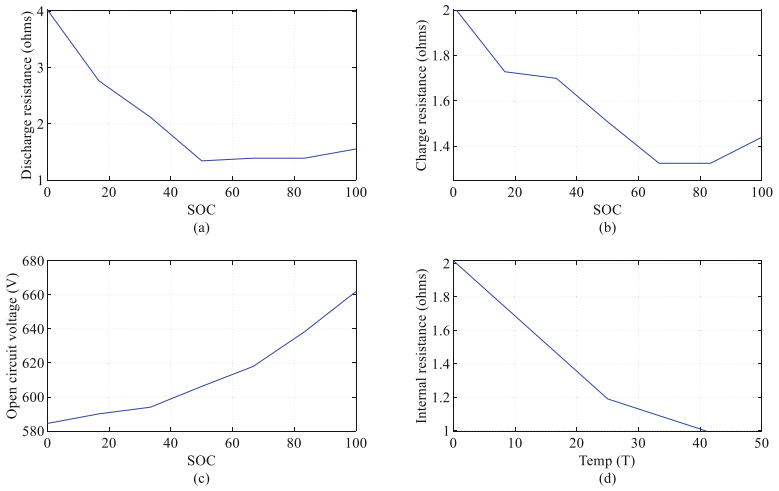

Fig. 2. Battery characteristics curve. (**a**) Discharge resistance curve. (**b**) Charge resistance curve. (**c**) Open circuit voltage curve. (**d**) Internal resistance–temperature curve.

3.2 Simulation Results and Comparison

In this paper, the power-time curve of a specific 20 km experimental line, derived using the minimum time operation approach discussed earlier, is used as the optimization object. The optimal strategy aims to minimize the hydrogen consumption cost of the line, and the effectiveness and applicability of the method are demonstrated by a large number of simulations and comparative experiments. The proposed method is compared with the SOC balancing strategy, which was proposed and tested by Zhang et al. [11].

3.2.1 The Impacts on Hydrogen Consumption Costs and Power Performance

The power distribution derived from the optimization algorithm and the SOC algorithm is shown in Fig. 3.

Using the hydrogen consumption cost and the system power index as the evaluation criteria, the cost of hydrogen consumption for the optimization algorithm for the whole working condition is about $34.13, while the cost of the SOC equalization algorithm is

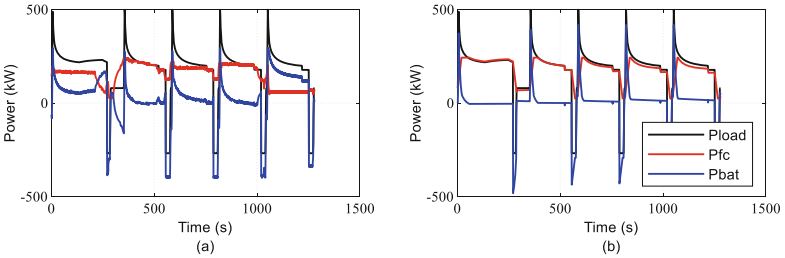

Fig. 3. Algorithm power allocation comparison chart. (**a**) Power distribution under the DP algorithm. (**b**) Power distribution under SOC balancing algorithm.

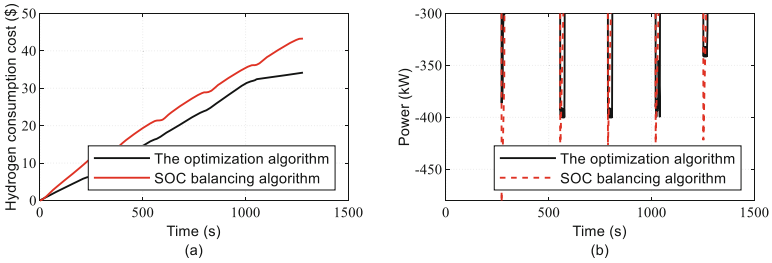

Fig. 4. Comparison of hydrogen consumption costs and battery power. (**a**) Comparison of hydrogen consumption costs. (**b**) Battery power distribution details.

about $43.26. The optimization algorithm saving of about 21%, as shown in Fig. 4(a). For the power distribution case, the SOC balancing algorithm has more aggressive requirements for the upper limit of power battery charging power, which can only be solved by limiting the power performance of the train or by means of braking resistors when the upper limit of power battery charging power cannot be met, whereas the optimization algorithm can achieve the characteristics of each system component through algorithmic constraints, as shown in Fig. 4(b). Therefore, the optimization algorithm has advantages over the SOC balancing algorithm, both in terms of cost savings and power performance.

3.2.2 Study of the Strength of the Terminal Value Constraint

Many scholars have proposed to make the initial SOC and the end-state SOC equal, but for a hydrogen-fuelled train, the cost of hydrogen is much higher than that of the battery, and an appropriate relaxation of the end-state SOC constraint can reduce the cost.

Where γ is the weighting factor presenting the degree of strain. A smaller weighting factor γ indicates a weaker degree of constraint. The SOC end-state value deviates downward from the preset value and the hydrogen cost decreases as shown in Fig. 5. At different levels of constraint, the optimization algorithm finds the path that minimizes the total cost. Rely on adjusting γ to find a balance between the game objectives of hydrogen cost and SOC end-state value.

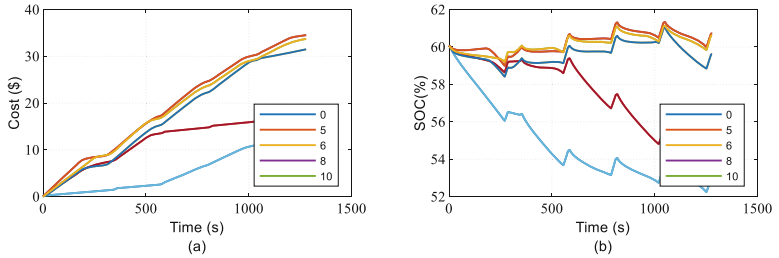

Fig. 5. Final value constraint effects. (**a**) Effect on cost. (**b**) Effect on SOC.

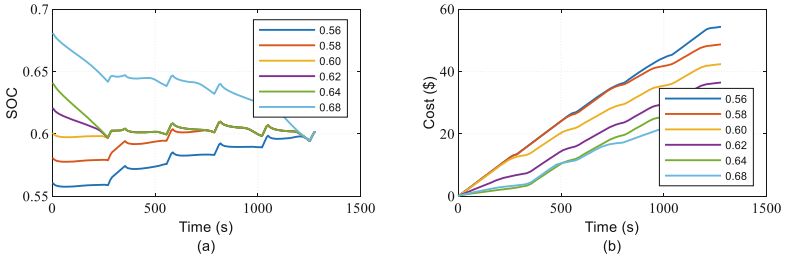

Fig. 6. Effect of different initial SOC. (**a**) Effect on SOC. (**b**) Effect on cost.

3.2.3 Effect of Different Initial SOC

The effect of different initial SOC on the hydrogen cost is also more significant, as can be seen from Fig. 6(a), where the algorithm can make the final SOC all converge to the same point for different initial SOC. As the SOC of the initial state increases, the hydrogen consumption cost will then decrease. The reason for this is that when returning to the same final SOC, the battery in the group with a higher initial SOC will discharge more, resulting in the need for the fuel cell to deliver less energy, so its overall cost shows a decreasing trend.

3.2.4 Comparison of Different Average Demand Powers

For the 20 km power-time line data, the mean power is 95.75 kW, beyond which the train has an auxiliary power portion that can be considered a constant power rating, which varies greatly in magnitude depending on the season and electrical equipment on board, and whose trend is analyzed by applying an offset of x kW to the 20 km time-power data. The curves for SOC under both algorithms shift from high to low as the average power increases, but the optimization algorithm's final state SOC is more biased toward being less than 60, whereas the SOC balancing algorithm is more biased toward being greater than 60, and it is clear that the curve of the optimization algorithm favors the choice of control sequence with lower costs of hydrogen consumption. Figure 7(c) shows that the optimization algorithm always has a lower hydrogen consumption than the SOC balancing algorithm at any mean power offset. The specific degree of improvement in hydrogen consumption cost of the optimization algorithm relative to the SOC balancing

algorithm is presented in Fig. 7, which ranges from 9% to 21%, demonstrating the significant effect of the optimization.

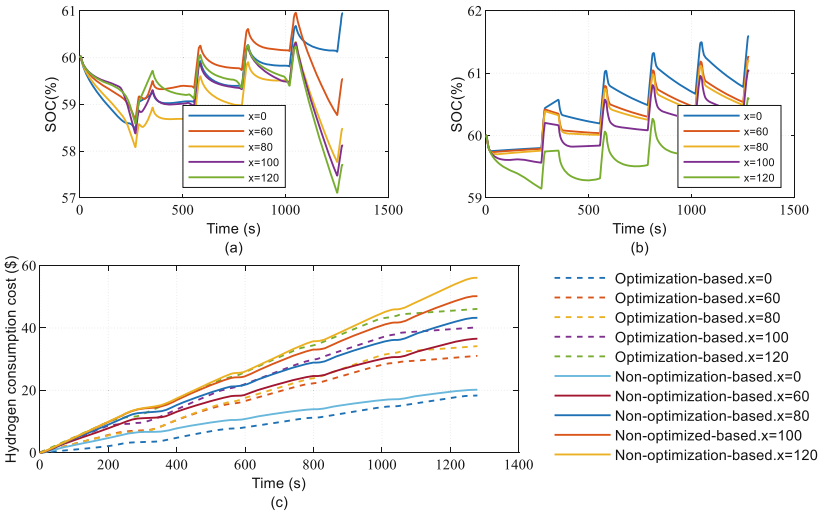

Fig. 7. Effect of different average demand powers. (**a**) Optimization algorithm. (**b**) SOC balancing algorithm. (**c**) Comparison of hydrogen consumption costs.

4 Conclusion

a. The optimization strategy can be used to derive the optimal solution of the cost function that satisfies the power constraints of each power source when the target power demand is known. The optimization strategy proposed is significantly more cost-effective than the SOC balancing strategy and can better meet the power performance requirements of the vehicle.
b. The effects of different end-value constraints of the optimization algorithm on the cost of hydrogen consumption and the final value of SOC are analyzed, and the results show that the optimization algorithm always obtains the control sequence that makes the cost-optimal for different weighting factors of the end-value constraints and the hydrogen consumption cost decreases with the weakening of the SOC end value constraint.
c. The characteristics of the optimization strategy for different initial SOC and different average demand power are investigated, and the effectiveness and superiority of the optimization algorithm are demonstrated by comparing it with the SOC equalization algorithm under different average demand power.

Acknowledgment. Supported by research fund for the scheme research program of advanced rail transit comprehensive test and research base of China Energy Railway Equipment Co., Ltd. (TZKY-21-16).

References

1. Li, B.: Research on energy management strategy of fuel cell vehicle based on driving condition prediction. Jilin University, Changchun (2021) (in Chinese)
2. Jiang, D.D.: Energy management of hybrid electric vehicles based on model predictive control. Zhejiang University, Hangzhou (2020) (in Chinese)
3. Zhang, X., Mi, C.C., Masrur, A., et al.: Wavelet-transform-based power management of hybrid vehicles with multiple on-board energy sources including fuel cell, battery and ultracapacitor. J. Power Sources **185**(2), 1533–1543 (2008)
4. Caux, S., Hankache, W., Fadel, M., et al.: On-line fuzzy energy management for hybrid fuel cell systems. Int. J. Hydrogen Energy **35**(5), 2134–2143 (2010)
5. Erdinc, O., Vural, B., Uzunoglu, M.: A wavelet-fuzzy logic based energy management strategy for a fuel cell/battery/ultra-capacitor hybrid vehicular power system. J. Power Sources **194**(1), 369–380 (2009)
6. Motapon, S., Dessaint, L.A., Al-Haddad, K.: A comparative study of energy management schemes for a fuel-cell hybrid emergency power system of more-electric aircraft. IEEE Trans Indust Electron **61**, 1320–1334 (2014)
7. Brahma, A., Guezennec, Y., Rizzoni, G.: Optimal energy management in series hybrid electric vehicles. In: Proceedings of the 2000 American Control Conference, vol. 1, p. 60–4 (2000)
8. Wood, A.J., Wollenberg, B.F.: Power generation operation and control, 2nd edn. Wiley, New York (1996)
9. Bellman, R.: Dynamic programming, 1st edn. Princeton University, Princeton (1957)
10. Rurgladdapan, J., Uthaichana, K., Kaewkham-ai, B.: Li-ion battery sizing and dynamic programming for optimal power-split control in a hybrid electric vehicle. In: 9th International Conference on electrical engineering/electronics, computer, telecommunications and information technology, p. 1–5 (2012)
11. Zhang, W.: Research on key technologies of fuel cell tram power system. Tsinghua University, Tsinghua (2017) (in Chinese)

H-Mg Bond Weakening Mechanism of Graphene-Based Single-Atom Catalysts on MgH_2(110) Surface

Shuai Dong[1,2], Hao Liu[1,2], Xinyuan Liu[1,2], Chaoqun Li[1,2], Zhengyang Gao[1,2], and Weijie Yang[1,2,2(✉)]

[1] School of Energy and Power Engineering, North China Electric Power University, Baoding 071003, Hebei, China
yangwj@ncepu.edu.cn

[2] Hebei Key Laboratory of Low Carbon and High Efficiency Power Generation Technology, North China Electric Power University, Baoding 071003, Hebei, China

Abstract. Solid-state hydrogen storage is gradually becoming an effective way for the large-scale storage and transportation of hydrogen energy. Magnesium hydride (MgH_2) has become a promising candidate among solid-state hydrogen storage materials due to its high hydrogen storage density, low cost and good safety. However, ambiguous H-Mg bond weakening mechanism of various catalysts on MgH_2 hinders the development of novel catalysts for MgH_2 dehydrogenation. To overcome this problem, we applied the model catalyst, single-atom catalyst with accurately characterizable coordination structure, to understand the interaction between catalyst and MgH_2 surface through spin-polarized density-functional theory calculation. We constructed heterogeneous interface structures between single-atom catalysts and MgH_2 surface including nine kinds of transition metal atoms. The interaction between single-atom catalysts and MgH_2 surface has been well explored through bond length, electron localization function, charge density difference and crystal orbital Hamiltonian population, providing the intrinsic information of H-Mg bond weakening mechanism over single-atom catalysts. This work can establish the foundational guide for the design of novel dehydrogenation catalysts.

Keywords: Single-atom catalysts · H-Mg bond · Weakening mechanism · Density-functional theory

1 Introduction

The burning of fossil energy is inevitably accompanied by the production of large amounts of carbon dioxide, which is the main culprit of the greenhouse effect. To achieve carbon neutrality and carbon peaking, it is necessary to get rid of the dependence on fossil energy. As an emerging clean energy source, hydrogen energy is considered the most promising alternative energy source due to its many advantages [1]. In the hydrogen energy cycle, hydrogen is used as a carrier and contains three main components:

H. Sun et al. (Eds.): WHTC 2023, SPPHY 393, pp. 485–496, 2024.
https://doi.org/10.1007/978-981-99-8631-6_47

preparation, storage and transportation, and application [2]. In contrast to hydrogen application and preparation technologies, hydrogen storage and transportation technologies are relatively underdeveloped. Among the hydrogen storage methods, solid-state hydrogen storage is a hot research topic in this field. And Magnesium hydride (MgH_2), as a popular research object among solid-state hydrogen storage materials, possesses high gravimetric hydrogen density (about 7.6 wt%) and volumetric hydrogen density (about 110 g/L), good reversibility and low cost characteristics [3–5].

However, poor dehydrogenation kinetics and thermodynamic properties have hindered its commercial application. In practical applications, its operating temperature is 450–550 °C [6]. To enhance the dehydrogenation performance of MgH_2, researchers have taken a series of measures, including alloying [7–10], nanostructuring [11], catalyzing [12–15], and construction of composite systems [16–18]. Among them, catalyst doping is considered as a promising improvement strategy. Catalysts can enhance the hydrogen release thermodynamic properties of MgH_2 by reducing the activation energy required for the chemical reaction. Common catalysts such as transition metals, metal oxides and carbon nanomaterials can be used to enhance the dehydrogenation performance of MgH_2. However, with the addition of catalysts also makes the gravimetric hydrogen storage density of the system significantly lower. The emergence of metal–carbon composites has emerged as one of the most promising solutions. Carbon-based single-atom catalysts offer the maximum atom utilization while allowing further enhancement of the gravimetric hydrogen storage density.

Single atom catalysts show excellent catalytic activity in many fields, and also have exceptional performance in promoting metal hydride dehydrogenation. Both experiments and theoretical calculations have found that single atom catalysts can enhance the dehydrogenation performance of MgH_2. However, the catalytic mechanism of single atom catalysts for the MgH_2 system is still unknown. In the experiment, Huang et al. successfully prepared highly dispersed metal catalysts synthesized on nitrogen doped carbon (M–N–C) [23]. It was found that the addition of the nickel based catalysts in MgH_2 reduced the activation energy to 87.2 ± 5.4 kJ mol^{-1}. Previous work found the "burst effect" of layer-by-layer dehydrogenation on the surface of $MgH_2(110)$ by DFT calculations, where the surface dehydrogenation energy barrier is maximum and then decreases layer by layer [19]. Then we constructed heterojunctions of nine single-atom catalysts with $MgH_2(110)$ and found that the surface dehydrogenation energy barrier of MgH_2 decreased a lot in the presence of catalysts [20]. In addition, Sun et al. [21] found that graphene doped with N, P, and S was also able to reduce the surface dehydrogenation energy barrier of MgH_2. Deng et al. [22]constructed a MgH_2/graphene heterojunction and introduced precious metals (Pd and Pt) to further improve dehydrogenation performance. Obviously, we can find that single atom catalysts have an ideal effect in improving the dehydrogenation performance of MgH_2. At the same time, it can also ensure the gravimetric hydrogen storage density of solid hydrogen storage materials.

Motivated by the above work, in this work, we constructed nine heterojunction structures. These heterojunction structures are composed of a single atom catalyst with graphene doped with three nitrogen atoms loaded with transition metal atoms as the substrate and a $MgH_2(110)$ surface. Firstly, we found the optimal interlayer distance for different heterojunctions, and then conducted structural optimization calculations for

all heterojunctions. After calculation, it was found that the catalyst-loaded metal atoms moved further toward the MgH_2 surface. At the same time, the H-Mg bond length on the MgH_2 surface slightly increased. Moreover, the degree of increase in H-Mg bonds varies slightly among different species. To further explore the intrinsic reasons for this phenomenon, electron localization function, charge density difference and crystal orbital Hamiltonian population analyses were performed on these heterojunction systems. These analyses were used to further improve the knowledge of the mechanism of catalyst-promoted dehydrogenation of MgH_2.

2 Computational Methods

In this work, the Projector Augmented Wave (PAW) technique and the Vienna Ab initio Simulation Package (VASP5.4.4) were used to calculate density functional theory (DFT). The Perdew–Burke–Ernzerhof (PBE) function is used to characterize the exchange–correlation energy in the generalized gradient approximation (GGA) [23–25]. The modeling of hydrogen adsorption and desorption by PBE is reasonably accurate and in good agreement with the experimental results from ultrahigh vacuum, according to prior benchmark studies and discussions [26, 27]. We also consider spin polarization and van der Waals corrections using the DFT-D3 method [28, 29]. The dipole moment is modified along the z-direction in each calculation. A $(4 \times 4 \times 1)$ Γ-centered k-point grid was used to achieve structural relaxation, and a plane wave basis set with a 500 eV energy cutoff was used to represent valence electrons. Geometries were considered relaxed whenever the sum of all atom forces fell below 0.02 eV $Å^{-1}$. To calculate the effect of spin polarization on the system, we set ISPIN = 2. Since there were dipole moments in the slabe model, which can have a certain impact on the results. Therefore, to make the results more accurate, we set LDIPOL = TRUE and IDIPOL = 3.

To investigate the charge change brought on by the addition of SACs ($\Delta\rho$), we calculated the charge density difference. Charge density difference, one of the most important techniques for studying electronic structures, was calculated using the formula:

$$\Delta\rho = \rho_{AB} - \rho_A - \rho_B \tag{1}$$

where $\Delta\rho$ represents the change value in charge density, ρ_{AB} represents the charge density when two fragments of A and B are together, and ρ_A and ρ_B respectively represent the charge densities when A and B are individually present at the same position. The Local Orbital Basis Suite towards Electronic-Structure Reconstruction (LOBSTER) software is used to calculate the Crystal Orbital Hamilton Population (COHP) approach, which is used to investigate the bonding mechanism of chemical bonds in the system [30–33].

In this work, we chose the most stable 110 surface of MgH_2 to study the dehydrogenation phenomenon [34]. The catalysts were loaded with transition metal atoms using three N_3-doped graphene 2*d* materials as substrates. To successfully establish a heterojunction structure between the catalyst and MgH_2, we constructed a 4×2 MgH_2 supercell (Fig. 1a). The size of the catalyst was also adjusted to 12.33×12.83 Å to reduce the lattice mismatch (Fig. 1b). A 15 Å vacuum layer was set up in the z-direction to separate the images. The heterojunction structure was optimized by setting different layer spacings, and it was found that the heterojunction layer spacing was about 2.75 Å

and the energy was about −834.06 eV after optimization (Fig. 2b). The final structure of this work is shown in Fig. 1c.

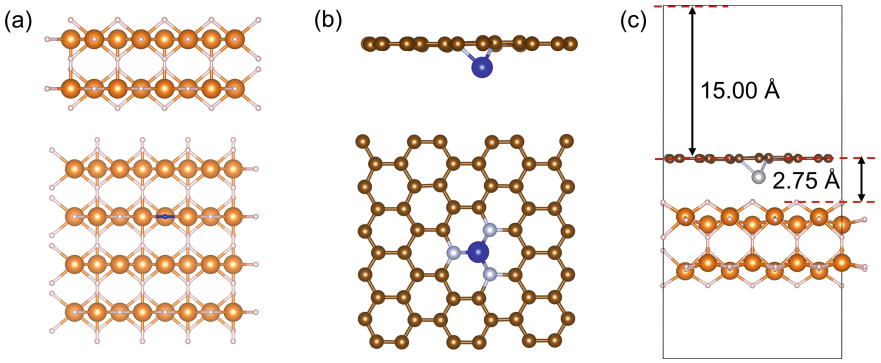

Fig. 1 **(a)** Side and top views of $MgH_2(110)$ surface. **(b)** Side and top views of a graphene-doped nitrogen substrate loaded with transition metal atoms. SACs-TM (TM = Ti, V, Cr, Mn, Fe, Co, Ni, Cu, and Zn). **(c)** Side view of an MgH_2/SACs-TM heterojunction. White and orange spheres represent H and Mg, respectively. Brown and blue spheres represent C and Ni (using Ni as an example), respectively

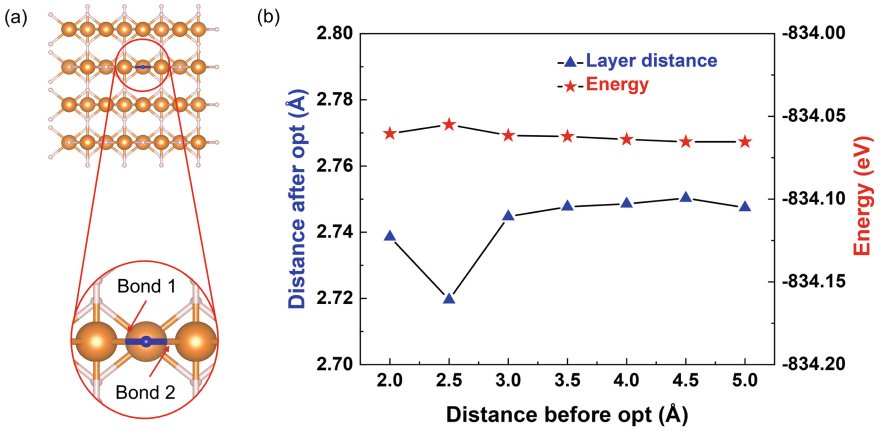

Fig. 2 **(a)** Illustrations of the Bond 1 and Bond 2 in MgH_2. White and orange spheres represent H and Mg, respectively. **(b)** Distance-energy relationship between MgH_2 and SACs-Ni

3 Results and Discussion

3.1 Performance of H-Mg Bond Length of Pure MgH_2 and MgH_2/SACs-TM

To understand what happens after the addition of SACs-TM, we performed structural optimization calculations for all heterojunction models. After convergence of the structural optimization, we found that the bond length of H-Mg in pure MgH_2 is 1.85 Å

(including Bond 1 and Bond 2). However, a significant increase in the bond length of H-Mg bond in MgH_2 occurs regardless of which single atom catalyst is added to MgH_2. The largest increase in the bond length of the H-Mg bond was observed for the addition of SACs-Ni, with the bond length reaching about 2.03 Å (Bond 2). In addition, the SACs-Co, V and Cu also increase the bond length of the H-Mg bond to about 2.01 Å (the maximum of Bond 1 and Bond 2), which is slightly less effective than Ni. SACs-Fe had a similar effect on Bond 1 and Bond 2. However, the other SACs-TM have slightly different effects on Bond 1 and Bond 2. Among them, SACs-TM (TM = Ti, V, Cr, Zn) has a stronger effect on Bond 1 and a slightly less effect on Bond 2. On the contrary, SACs-TM (TM = Mn, Co, Ni, Cu) have a stronger effect on Bond 2. We attribute the different effects of different single-atom catalysts on Bond 1 and Bond 2 to the fact that the structure of the heterojunction system will be somewhat different after optimization. It is easily found that in the presence of single-atom catalysts, the bond energy decreases as the bond length of H-Mg becomes longer, thus reducing the energy required to break the H-Mg bond. The addition of these single-atom catalysts weakens the H-Mg interactions and thus facilitates the dehydrogenation process (Fig. 3).

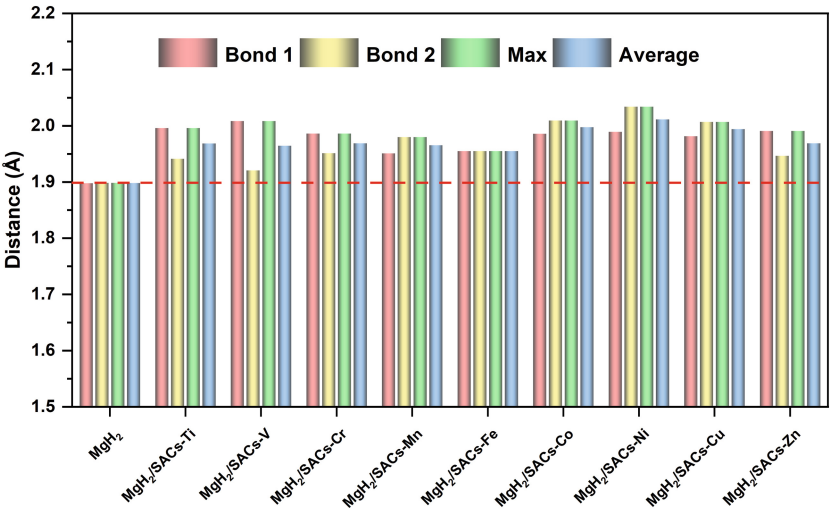

Fig. 3 Bond 1 and Bond 2 (H-Mg) bond length changes before and after the addition of SACs-TM (TM = Ti, V, Cr, Mn, Fe, Co, Ni, Cu, Zn)

3.2 Electron Localization Function of Pure MgH_2 and MgH_2/SACs-TM

To understand the mechanism of H-Mg bond weakening, we analyzed the catalytic mechanism of single-atom catalysts on the MgH_2 surface from another perspective. ELF is one of the means to study the electronic structure, where the strength of the H-Mg bond can be analyzed [35]. First, we performed electron localization function (ELF) analysis on pure MgH_2 to understand the charge distribution of H atoms on the 110 surface. Then,

we further performed ELF analysis on the heterojunction system with the addition of different single-atom catalysts to study the change of H atom charge distribution after the addition of SACs. The red region is used to indicate the higher electron density, while the blue region indicates the lower electron density. We can clearly see that there is a very full red region around the H-Mg bond on the MgH_2 surface without the addition of a single-atom catalyst. This indicates that there are more electrons distributed in this part, indicating that the H-Mg bond (bond 1 and bond 2 are very stable). In addition, the red region around the H-Mg bond in the second layer is slightly reduced, but the H-Mg bond here is still more stable. However, the red region around the H-Mg bond on the MgH_2 surface is greatly reduced after the addition of the monatomic catalyst. In particular, the red area around Bond 1 and Bond 2 shrinks to a greater extent, because this area is most affected by the catalyst. On the contrary, the red area around the H-Mg bond in the second layer has only a small change. Therefore, we believe that the single-atom catalyst mainly has a greater effect on the charge distribution on the MgH_2 surface. By the electron cloud distribution analysis, we can confirm that the H-Mg bonds (Bond 1 and Bond 2) on the surface of MgH_2(110) are weakened by the action of the monatomic catalyst. Among all the catalysts, the H-Mg bonds in the presence of SACs-Mn, Co, Cu and Ni are weakened more than the other transition metal atoms and there is almost no electron distribution above the bonds. This is consistent with the previous results on the bond length variation. Some studies [36] have pointed out that the interaction between the unsaturated d-layer electrons of metals and the valence electron of H will weaken the H-Mg bond, thus promoting the dehydrogenation process of MgH_2, which is consistent with the research results in this paper (Fig. 4).

3.3 Charge Density Difference of MgH_2/SACs-TM

To understand the mechanism of H-Mg bond weakening, we analyze the heterojunction system from the electronic structure level. Analysis of charge transfer is an essential method to determine whether the bond strength becomes weaker or not. Therefore, we performed charge density difference calculations for all heterojunction systems with doped catalysts. From the calculation results, it can be seen that charge transfer occurs in all the heterojunction systems after the addition of catalysts. The amount of charge transfer is more compared to the previous MgH_2/SACs system in the N_4 system [20]. Therefore, it is reasonable to believe that the dehydrogenation energy barrier is lower in this system. In detail, different charge transfers occur in different heterojunctions. Among them, both the catalyst and MgH_2 in the MgH_2/SACs-Ti system lose their charges, and the charges accumulate at the space layer between the heterojunction heterojunctions. However, most of the catalyst in the other heterojunction systems flows to MgH_2, while a small amount of charge accumulates at the space layer between the heterojunctions. This charge transfer may be one of the important reasons for the weakening of the H-Mg bond (Fig. 5).

3.4 Crystal Orbital Hamilton Population of Pure MgH_2 and MgH_2/SACs-TM

To further reveal the mechanism of H-Mg bond weakening, this work calculates the integral crystal orbital Hamiltonian population (ICOHP) integral values of H-Mg bonds

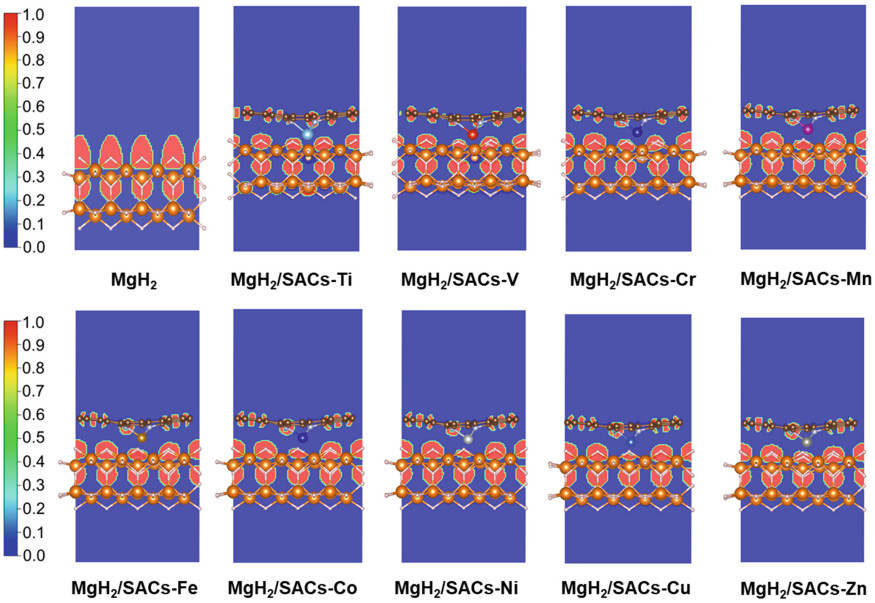

Fig. 4 ELFs of pure MgH_2 and MgH_2/SACs-TM (TM = Ti, V, Cr, Mn, Fe, Co, Ni, Cu, Zn). The section is the 010 plane of the H atom nearest to the metal atom. In the color bars, 1 represents a fully localized state, 0.5 represents a uniform electronic gas state, and 0 represents a fully non-localized state

in different systems by means of the COHP method. To facilitate the comparison, the ICOHP values of the H-Mg bonds (Bond 1 and Bond 2) in different systems were statistically analyzed. From the ICOHP values, the sizes of Bond 1 and Bond 2 of pure MgH_2 are almost identical at −0.49. Also, we found that the COHP analysis is almost identical and neither of them occupies the antibond orbital. Therefore, we can assume that the H-Mg bonds (Bond 1 and Bond 2) on the surface of pure MgH_2 (110) are very stable. However, all ICOHP values changed after the addition of single-atom catalysts. Also, the addition of monatomic catalysts leads to the appearance of antibonding orbitals as can be seen in the COHP analysis. Therefore, we can assume that the catalyst causes a decrease in the stability of the H-Mg bonds (Bond 1 and Bond 2). Compared to the results of previous studies, the value of ICOHP in this work is more variable and the weakening of the H-Mg bonds is more pronounced. We speculate that this phenomenon occurs because the single-atom catalysts in the present work carry metal atoms closer to the H atoms. This again confirms that SACs can promote MgH_2 dehydrogenation by weakening the H-Mg bond (Figs. 6, 7).

After the above analysis, it has been confirmed that the single atom catalyst doped with N_3 has a better weakening effect on the H-Mg bond. And further understanding of the weakening mechanism of H-Mg bonds. Next, study the effects of different coordination environments on catalysts to find a descriptor. Finally, we hope to design catalysts using the descriptor to provide theoretical guidance for the commercial application of Mg based solid hydrogen storage materials.

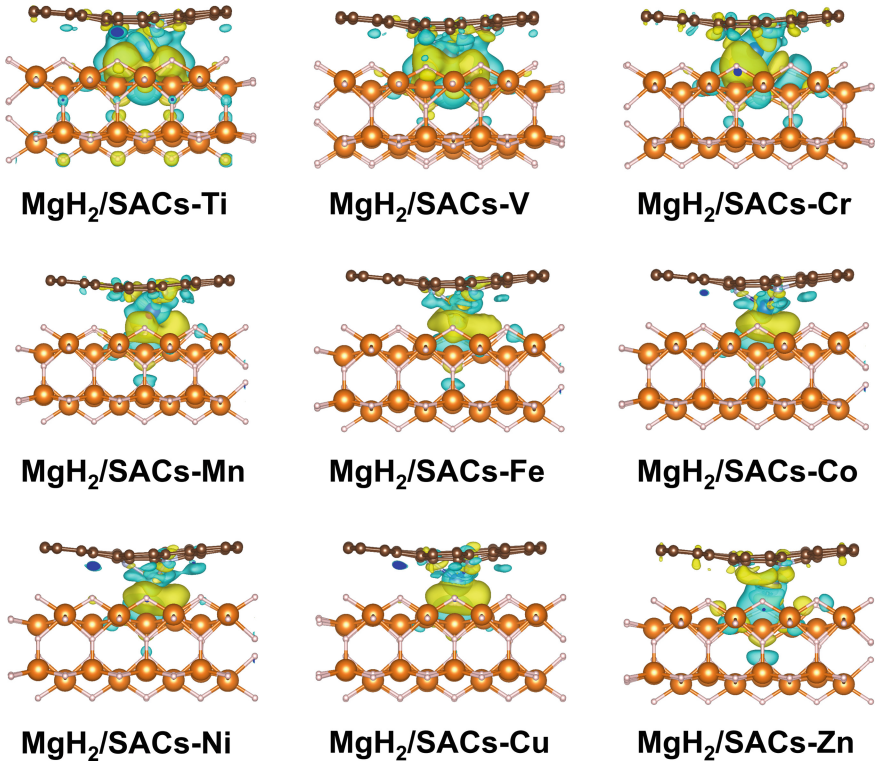

Fig. 5 Calculated charge density differences of MgH_2/SACs-TM (TM = Ti, V, Cr, Zn, Cu, Mn, Co, Fe, and Ni) induced by the addition of SACs. The yellow and blue isosurfaces indicate electron accumulation and loss, respectively. All the results are plotted with an isovalue of 0.01 e·Å^{-3}. White, orange, and brown spheres represent H, Mg, and C, respectively

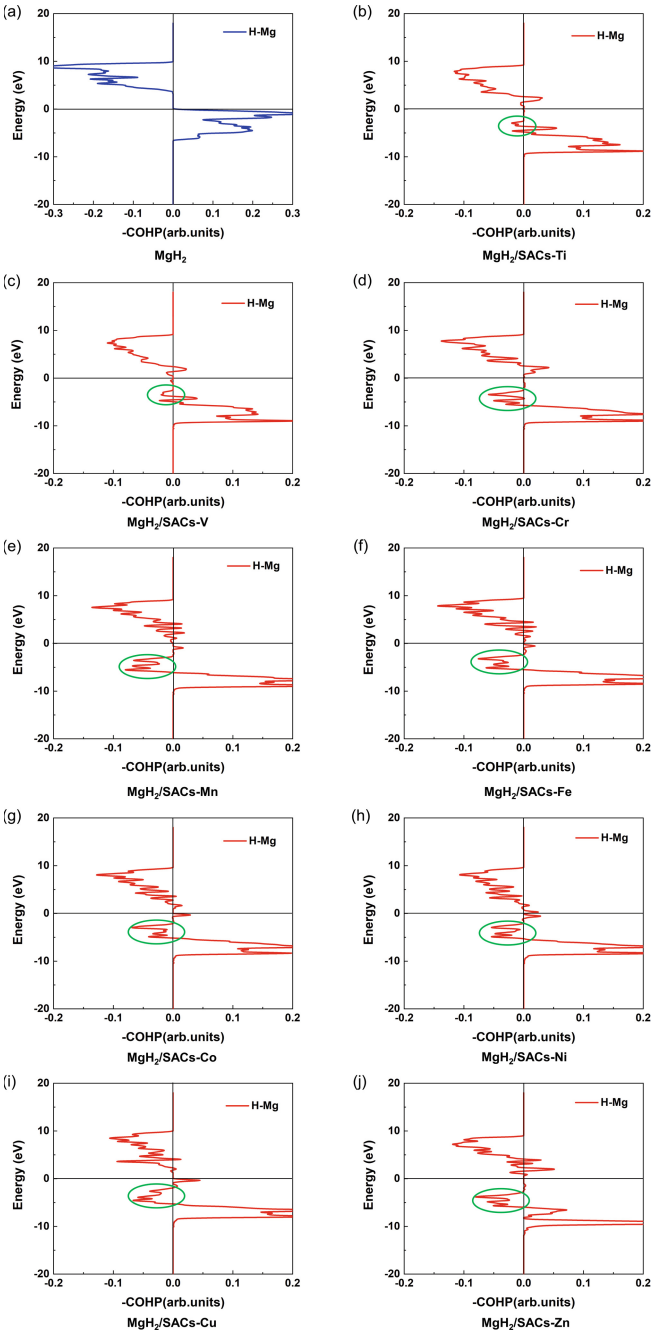

Fig. 6 (a–j) COHP analysis of the H-Mg Bond 1 and Bond 2 in MgH_2 and MgH_2/SACs-TM

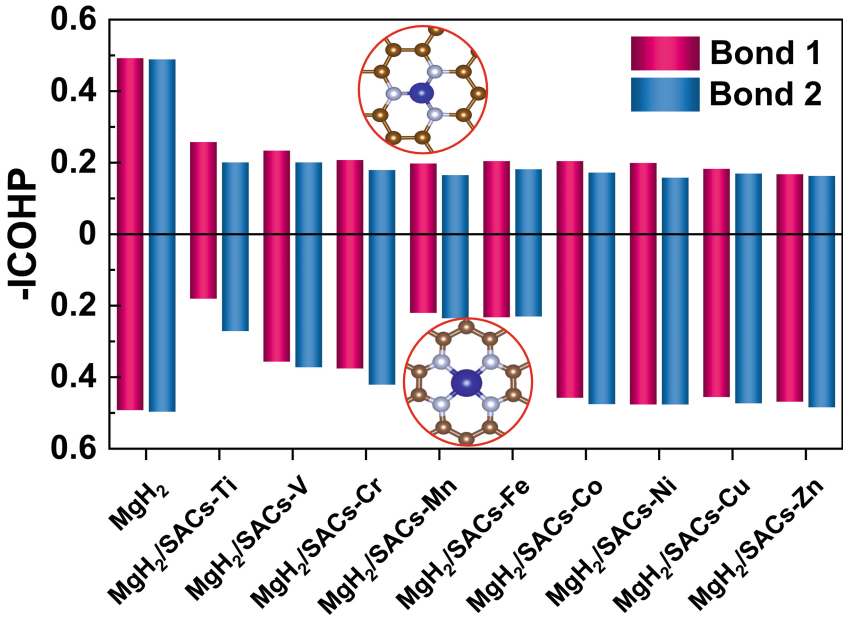

Fig. 7 Comparison of the integral values of H-Mg Bond 1 and Bond 2 between MgH_2 and MgH_2/SACs-TM in the system. The top half is from this work, using a N_3-doped catalyst, and the bottom half is from the previous work, using a N_4-doped catalyst

4 Conclusion

In summary, we optimized pure MgH_2 and nine MgH_2/SACs-TM heterojunction systems using DFT-D3 calculations of spin polarization, respectively. We found that the MgH_2 dehydrogenation performance of all heterojunction systems was improved by the addition of SACs. This was mainly manifested by a significant increase in the outermost H-Mg bond length of MgH_2(110) after the addition of the catalyst. However, the addition of different SACs-TM can have different effects on Bond 1 and Bond 2. We speculate that this is attributed to some differences in the conformation of different heterojunction systems after optimization. To in-depth analyze the binding properties of SACs and MgH_2 and the weakening mechanism of the H-Mg bond, electron localization function, charge density difference and crystal orbital Hamiltonian population analyses were performed on the heterojunction. Furthermore, this work provides important guidance for the design of novel MgH_2/SACs heterojunction materials and offers a solution for the slow kinetics of MgH_2 dehydrogenation in hydrogen storage.

References

1. Schlapbach, L., Züttel, A.: Hydrogen-storage materials for mobile applications. Nature **414**(6861), 353–358 (2001)
2. Lai, Q., Sun, Y., Wang, T.: How to design hydrogen storage materials? Fundamentals, synthesis, and storage tanks. Adv. Sustain **3**(9), 1900043 (2019)

3. Liang, G., Huot, J., Boily, S.: Catalytic effect of transition metals on hydrogen sorption in nanocrystalline ball milled MgH_2-TM (TM = Ti, V, Mn, Fe and Ni) systems. J. Alloys Compd. **292**(1–2), 247–252 (1999)
4. Zhang, J., He, L., Yao, Y.: Catalytic effect and mechanism of NiCu solid solutions on hydrogen storage properties of MgH_2. Renew. Energ. **154**, 1229–1239 (2020)
5. Galey, B., Auroux, A., Sabo-Etienne, S.: Enhancing hydrogen storage properties of the Mg/MgH_2 system by the addition of bis (tricyclohexylphosphine) nickel (II) dichloride. Int. J. Hydrog. Energy **44**(23), 11939–11952 (2019)
6. Zhang, J., Huang, Y.N., Mao, C.: Synergistic effect of Ti and F co-doping on dehydrogenation properties of MgH_2 from first-principles calculations. J. Alloys Compd. **538**, 205–211 (2012)
7. Li, S., Zhu, Y., Liu, Y.: Nano-inducement of Ni for low-temperature dominant dehydrogenation of Mg–Al alloy prepared by HCS+ MM. J. Alloys Compd. **819**, 153020 (2020)
8. Lin, H.J., Lu, Y.S., Zhang, L.T.: Recent advances in metastable alloys for hydrogen storage: a review. Rare Metals **41**(6), 1797–1817 (2022)
9. Mao, J., Huang, T., Panda, S.: Direct observations of diffusion controlled microstructure transition in Mg-In/Mg-Ag ultrafine particles with enhanced hydrogen storage and hydrolysis properties. Chem. Eng. J. **418**, 129301 (2021)
10. Osorio-García, M., Suárez-Alcántara, K., Todaka, Y.: Low-temperature hydrogenation of Mg–Ni–Nb_2O_5 alloy processed by high-pressure torsion. J. Alloys Compd. **878**, 160309 (2021)
11. Zhang, J., Zhu, Y., Lin, H.: Metal hydride nanoparticles with ultrahigh structural stability and hydrogen storage activity derived from microencapsulated nanoconfinement. Adv. Mater. **29**(24), 1700760 (2017)
12. Gao, H., Shi, R., Liu, Y.: Facet-dependent catalytic activity of two-dimensional $Ti_3C_2T_x$ MXene on hydrogen storage performance of MgH_2. J. Magnes. Alloy **11**(10), 3724–3735 (2022)
13. Zhao, Y., Liu, Z., Liu, J.: Improvement effect of reversible solid solutions $Mg_2Ni(Cu)/Mg_2Ni(Cu)H_4$ on hydrogen storage performance of MgH_2. J. Magnes. Alloy (2022). https://doi.org/10.1016/j.jma.2022.04.006
14. Ren, Z.H., Zhang, X., Gao, M.X.: Research progress in Ti-based catalysts-modified $NaAlH_4$ hydrogen storage materials. Chin. J. Rare Met. **45**(5), 569–582 (2021)
15. Yuan, J., Huang, H., Jiang, Z.: Ni-doped carbon nanotube-$Mg(BH_4)_2$ composites for hydrogen storage. ACS Appl. Nano Mater. **4**(2), 1604–1612 (2021)
16. Wang, Y., Chen, X., Zhang, H.: Heterostructures built in metal hydrides for advanced hydrogen storage reversibility. Adv. Mater. **32**(31), 2002647 (2020)
17. Kesarwani, R., Shukla, V., Hudson, M.S.L.: Improved hydrogen storage characteristics of magnesium hydride using dual auto catalysts (MgF_2+ CsH). Int. J. Hydrog. Energy **47**(63), 27049–27058 (2022)
18. Chen, W., Sun, Y., Xu, T.: Reversible hydrogen storage performance of $2LiBH_4$–MgH_2 enabled by dual metal borides. ACS Appl. Energy Mater. **5**(9), 10501–10508 (2022)
19. Dong, S., Li, C., Wang, J.: The, "burst effect" of hydrogen desorption in MgH2 dehydrogenation. J. Mater. Chem. A **10**(42), 22363–22372 (2022)
20. Dong, S., Li, C., Lv, E.: MgH_2/single-atom heterojunctions: effective hydrogen storage materials with facile dehydrogenation. J. Mater. Chem. A **10**(37), 19839–19851 (2022)
21. Li, Q., Qiu, S., Wu, C.: Computational investigation of MgH_2/graphene heterojunctions for hydrogen storage. J. Phys. Chem. C **125**(4), 2357–2363 (2021)
22. Deng, Y., Yang, M., Zaiser, M.: Enhancing dehydrogenation performance of MgH_2/graphene heterojunctions via noble metal intercalation. Int. J. Hydrogen Energy **48**(44), 16733–16744 (2023)

23. Kresse, G., Joubert, D.: From ultrasoft pseudopotentials to the projector augmented-wave method. Phys. Rev. B **59**(3), 1758 (1999)
24. Perdew, J.P., Burke, K., Ernzerhof, M.: Generalized gradient approximation made simple. Phys. Rev. Lett. **77**(18), 3865 (1996)
25. Kresse, G., Furthmüller, J.: Efficient iterative schemes for ab initio total-energy calculations using a plane-wave basis set. Phys. Rev. B **54**(16), 11169 (1996)
26. Wellendorff, J., Silbaugh, T.L., Garcia-Pintos, D.: A benchmark database for adsorption bond energies to transition metal surfaces and comparison to selected DFT functionals. Surf. Sci. **640**, 36–44 (2015)
27. Zheng, H., Li, H., Song, W.: Calculations of hydrogen associative desorption on mono-and bimetallic catalysts. J. Phys. Chem. C **125**(22), 12028–12037 (2021)
28. Becke, A.D., Johnson, E.R.: Exchange-hole dipole moment and the dispersion interaction. J. Chem. Phys. **122**(15), 154104 (2005)
29. Grimme, S., Antony, J., Ehrlich, S.: A consistent and accurate ab initio parametrization of density functional dispersion correction (DFT-D) for the 94 elements H-Pu. J. Chem. Phys. **132**(15), 154104 (2010)
30. Deringer, V.L., Tchougréeff, A.L., Dronskowski, R.: Crystal orbital Hamilton population (COHP) analysis as projected from plane-wave basis sets. J. Phys. Chem. A **115**(21), 5461–5466 (2011)
31. Dronskowski, R., Blöchl, P.E.: Crystal orbital Hamilton populations (COHP): energy-resolved visualization of chemical bonding in solids based on density-functional calculations. J. Phys. Chem. **97**(33), 8617–8624 (1993)
32. Maintz, S., Deringer, V.L., Tchougréeff, A.L.: LOBSTER: a tool to extract chemical bonding from plane-wave based DFT. J. Comput. Chem. **37**(11), 1030–1035 (2016)
33. Maintz, S., Deringer, V.L., Tchougréeff, A.L.: Analytic projection from plane-wave and PAW wavefunctions and application to chemical-bonding analysis in solids. J. Comput. Chem. **34**(29), 2557–2567 (2013)
34. Du, A.J., Smith, S.C., Yao, X.D.: Ab initio studies of hydrogen desorption from low index magnesium hydride surface. Surf. Sci. **600**(9), 1854–1859 (2006)
35. Gibbs, G.V., Cox, D.F., Ross, N.L.: Comparison of the electron localization function and deformation electron density maps for selected earth materials. J. Phys. Chem. A **109**(44), 10022–10027 (2005)
36. Liu, T., Zhang, T., Zhang, X.: Synthesis and hydrogen storage properties of ultrafine Mg–Zn particles. Int. J. Hydrogen Energy **36**(5), 3515–3520 (2011)

Correction to: The Preparation of Iridium-Based Catalyst with Different Melting Point-Metal Nitrate and Its OER Performance in Acid Media

Jiayao Deng[1,2], Xiao Hu[1,2], Guizhi Xu[1,2], Zhanfeng Deng[1], Lan Yang[1], Ding Chen[3], Ming Zhou[3], and Boyuan Tian[1(✉)]

[1] Beijing Institute of Smart Energy, Changping, Beijing 102209, China
tianboyuan@bise.hrl.an.cn
[2] State Key Laboratory of Advanced Transmission Technology, State Grid Smart Grid Research Institute Co.,Ltd., Changping, Beijing 102209, China
[3] State Grid Jiaxing Power Supply Company, Jiaxing, Zhejiang, China

Correction to:
Chapter 6 in: H. Sun et al. (Eds.): WHTC 2023, SPPHY 393, pp. 61–68, 2024.
https://doi.org/10.1007/978-981-99-8631-6_6

The original version of this chapter was published with an incorrect author name Gnauizhi Xu, which has now been corrected to Guizhi Xu. The chapter has been updated with the change.

The updated version of this chapter can be found at
https://doi.org/10.1007/978-981-99-8631-6_6

H. Sun et al. (Eds.): WHTC 2023, SPPHY 393, p. C1, 2024.
https://doi.org/10.1007/978-981-99-8631-6_48

Author Index

H. Sun et al. (Eds.): WHTC 2023, SPPHY 393, pp. 497–499, 2024.
https://doi.org/10.1007/978-981-99-8631-6